Series in BioEngineering

Ganesh Naik *Editor*

Biomedical Signal Processing

Advances in Theory, Algorithms and Applications

Springer

Series in BioEngineering

The Series in Bioengineering serves as an information source for a professional audience in science and technology as well as for advanced students. It covers all applications of the physical sciences and technology to medicine and the life sciences. Its scope ranges from bioengineering, biomedical and clinical engineering to biophysics, biomechanics, biomaterials, and bioinformatics.

More information about this series at http://www.springer.com/series/10358

Ganesh Naik
Editor

Biomedical Signal Processing

Advances in Theory, Algorithms and Applications

Springer

Editor
Ganesh Naik
MARCS Institute
Western Sydney University
Penrith, NSW, Australia

ISSN 2196-8861 ISSN 2196-887X (electronic)
Series in BioEngineering
ISBN 978-981-13-9096-8 ISBN 978-981-13-9097-5 (eBook)
https://doi.org/10.1007/978-981-13-9097-5

This Springer imprint is published by the registered company Springer Nature Singapore Pte Ltd.
The registered company address is: 152 Beach Road, #21-01/04 Gateway East, Singapore 189721, Singapore

Foreword

At the heart of biomedical analysis and engineering solutions, there is superb signal processing. Computational, mathematical, and engineering fields such as data analytics, machine learning, and AI, and biomedical engineering are developing rapidly. A comprehensive, accessible, and research-informed book on recent advances in biomedical signal processing is overdue. *Biomedical Signal Processing* edited by Dr. Ganesh Naik meets this need by reporting the latest advances in signal processing conveyed through examples of leading-edge research. Recent developments captured in the collection span new theoretical frameworks and algorithmic breakthroughs presented through specific applications.

Biomedical engineer Dr. Ganesh Naik is a vital researcher in the Biomedical and Human Technologies program in the research institute that I direct, the MARCS Institute for Brain, Behaviour and Development at Western Sydney University. MARCS Institute's programs of basic science and translational research are designed to advance knowledge and find sustainable solutions to the problems that matter most concerning humans and their interaction with other humans and technology. Unashamedly interdisciplinary, engineers, cognitive scientists, developmental psychologists, linguists, neuroscientists, and speech and music scientists come together to solve the problems that matter most through the themes: sensing and perceiving, interacting with each other, and technologies for humans (https://www.westernsydney.edu.au/marcs).

Dr. Naik joined the MARCS Institute at Western Sydney University in 2017 bringing his biomedical signal processing prowess to an industry-led project developing a noninvasive wearable for sleep apnea research. Ganesh joined the MARCS Institute for Brain, Behaviour, and Development as a skilled and talented engineer with expertise gained in labs in Sydney and Melbourne in Australia as well as Vellore Institute of Technology and Mysore University, India. External recognition of the rigor and quality of Ganesh's work includes fellowships from the University of Technology Sydney, Skills Victoria, IEEE Victoria, and an adjunct professor appointment at Vellore Institute of Technology. My background is cognitive science, and I have a particular interest in the human-machine nexus. In fact, Dr. Naik and I first met through an interdisciplinary research network funded

by the Australian Research Council on Human Communication Science. Funded for 5 years from 2004 to 2009, HCSnet was convened by Denis Burnham and me at Western Sydney University together with Robert Dale at Macquarie University.

The edited collection *Biomedical Signal Processing* is organized into four parts. Part I is devoted to recent developments in theories, algorithms, and extensions of EMG signal analysis. The part begins with a description of the state-of-the-art EMG signal processing and classification. Subsequent chapters discuss the application of EMG signal processing to robots for assistive rehabilitation, then force myography applied to human locomotion, and the final chapter in Part I reports a case study of maximum voluntary contraction (MVC) and triceps brachii and biceps brachii.

The second part focuses on brain-computer interface (BCI) and EEG signal processing. Applications include a BCI for classifying signals associated with motor imagery; artificial neural networks applied to EEG to detect effects of binaural stimuli; automated detection using wavelet filter banks of seizure versus nonseizure EEG; and automated identification of seizures using Fourier-Bessel series expansion-based empirical wavelet transform (FBSE-EWT).

In the third part, new ECG and cardiac applications are reported. These include a review of unipolar cardiac leads; classifying arrhythmia using long-duration ECG signal fragments analysis; data analytics applied to ECG; benefits of tensor-based methods in cardiac contexts; and ECG signal processing for remote monitoring of cardiovascular disease (CVD).

In the fourth part, biomedical signal processing is extended to proteomic applications.

Biomedical Signal Processing offers academic researchers and practitioners a comprehensive and contemporary account of developments in this fast-moving field. With authors from Australia, Brazil, Canada, China, India, North Africa, Poland, and the USA, the book reflects an international update on biomedical signal processing methods and applications. With the health and medical challenges faced by the world's growing and aging population, we need biomedical signal processing more than ever! This edited volume is a timely and excellent resource for undergraduate and graduate students as well as researchers working with a range of physiological, multidimensional, time-varying data, and signal processing techniques. I commend the edition to all who are interested in biomedical signal processing.

April 2019

Professor Catherine J. (Kate) Stevens, Ph.D.
Director, MARCS Institute for Brain, Behaviour,
and Development
Western Sydney University
Bankstown, NSW, Australia

Preface

The recent advances in modern signal processing techniques in medicine have improved the accuracy and reliability of medical diagnoses. Today, biomedical signal analysis is becoming one of the most important visualizations and interpretation methods in biology and medicine.

The goal of the present book is to present a complete range of proven and new methods that play a leading role in the improvement of biomedical signal analysis and interpretation. The book provides a forum for researchers to exchange their ideas and to foster a better understanding of the state of the art of the subject. This book is intended for biomedical, computer science, and electronics engineers (researchers and graduate students) who wish to get novel research ideas and some training in novel biomedical research areas, especially on ECG, EEG, and EMG signal applications. Additionally, the research results previously scattered in many scientific articles worldwide are collected methodically and presented in the book in a unified form.

The book is organized into four parts. The first part is devoted to recent developments in theories, algorithms, and extensions of EMG signal processing and human locomotion applications. In this part, we have collected four chapters with several novel contributions. The set of chapters include an insight on EMG signal processing, classification, and practical considerations the by *Angkoon, Evan* and *Eric*; estimation of ankle joint torque and angle based on EMG for assistive rehabilitation robots by *Palayil Baby et al.*; force myography and its application to human locomotion by *Anoop et al.*; and an application of EMG for stroke rehabilitation applications by *Naik et al*. The second part focuses on the various applications of EEG and its links to other relevant areas, such as BCI and epileptic seizure identification system. We have gathered five chapters in this part, and they are, respectively, EEG-based BCI to classify motor imagery signals by *Andrade et al.*, artificial neural networks on multi-channel EEG data to detect the effect of binaural stimuli in resting state by *Júnior et al.*, automated detection of seizure and nonseizure EEG using two band biorthogonal wavelet filter banks by *Bhati et al.*, automated identification of epileptic seizures from EEG using FBSE-EWT method by *Gupta et al.*, and DWT-based epilepsy seizures by *Sharmila* and *Geethanjali*.

The third part covers various cardiac and ECG signal processing applications, namely, unipolar cardiac leads ECG analysis by *Hussein et al.*, cardiac arrhythmias classification based on long-duration ECG signal fragments analysis by *Plawiak* and *Abdar*, artificial intelligence-enabled ECG big data mining for pervasive heart health monitoring by *Zhang*, tensor-based approaches in cardiac applications by *Padhy et al.*, syntactic methods for ECG diagnosis and QRS complexes recognition by *Hamdi et al.*, and extraction of ECG significant features for remote CVD monitoring by *Naresh* and *Acharyya*. The final part covers a chapter on accelerated computational approach in proteomics by *Bhardwaj, Gudur*, and *Acharyya*.

I want to thank the authors for their excellent submissions (chapters) to this book and their significant contributions to the review process, which have helped to ensure the high quality of this publication. Without their contributions, it would not have been possible for the book to come successfully into existence.

Penrith, NSW, Australia Ganesh Naik
April 2019

Contents

Myoelectric Signal Processing and Human Locomotion

Surface Electromyography (EMG) Signal Processing, Classification, and Practical Considerations

Angkoon Phinyomark, Evan Campbell and Erik Scheme

1 Introduction

Electromyography (EMG) is the process of measuring the electrical activity produced by muscles throughout the body using electrodes on the surface of the skin or inserted in the muscle. Motor intent deciphered from surface EMG signals has been employed as an intuitive control strategy for dexterous multi-functional prostheses [102] and gesture recognition interfaces [99]. Myoelectric prostheses relate residual limb muscle activity to the movement of a terminal device, sometimes, by employing pattern recognition approaches to identify repeatable and distinct EMG signatures for each motion class. State-of-the-art EMG pattern recognition systems for multi-function prostheses typically contain data pre-processing, data segmentation, feature extraction, dimensionality reduction, classification, and control blocks [62]. Conceptually, this architecture can facilitate intuitive control that mimics natural neural pathways. For decades, despite substantial research and development efforts in the literature, the only real commercial application of EMG signals has been prosthetics. Recently, with the release of wearable EMG gesture control and motion control devices, such as the Myo armband in 2013 (http://www.myo.com), new markets have been opened. Advancements in wearable technologies have increased the potential for myoelectric devices to permeate into everyday life; however, these emerging gesture recognition interfaces suffer from similar sensitivities to many real-world factors that have been identified in the field of prosthetics [75, 93].

Indeed, the real challenge for prostheses and gesture recognition interfaces are the dynamic factors that invoke changes in EMG signal characteristics. As a consequence of these factors, model inaccuracies are produced between the training

A. Phinyomark (✉) · E. Campbell · E. Scheme
Institute of Biomedical Engineering, University of New Brunswick, 25 Dineen Drive, Fredericton, NB, Canada
e-mail: aphinyom@unb.ca

E. Campbell
e-mail: evan.campbell1@unb.ca

E. Scheme
e-mail: escheme@unb.ca

G. Naik (ed.), *Biomedical Signal Processing*, Series in BioEngineering,
https://doi.org/10.1007/978-981-13-9097-5_1

phase and practical use. The common avoidance of these dynamic factors in laboratory settings creates a discrepancy between the performance of these devices in constrained settings and their reliability in regular daily use. Under ideal conditions, such as in a controlled virtual environment, the usability of multi-function prostheses has been reported to suffer when classification accuracy drops below 90% [31, 48]. While classification accuracy provides a benchmark in the laboratory, daily use invariably introduces dynamic variables not present in these conditions, leading to decreased accuracy and, ultimately, reliability of the device [29, 102]. From day to day, the reliability of previously trained models varies greatly depending on multiple factors including intra-subject repeatability, signal noise, different muscle contraction intensities and duration, limb position and forearm orientation, electrode shift, and muscle fatigue. Hands-busy conditions present additional challenges for gesture recognition tasks by introducing increased signal complexity. Furthermore, while the prostheses field has focused largely on within-user models, the widespread scaling of commercial devices for human-computer interaction would benefit from the development of multi-user classification models to eliminate the need for custom training and lengthy calibration protocols. In this chapter, state-of-the-art EMG signal processing and classification techniques that address these dynamic factors and practical considerations are presented, and directions for future research are outlined and discussed.

2 EMG Pattern Recognition

Pattern recognition systems, which generally consist of data pre-processing, data segmentation, feature extraction, dimensionality reduction, and classification stages (Fig. 1), have found widespread success across many fields of biomedical engineering, including myoelectric control [102].

Data pre-processing involves the strategic removal of confounding information or sources of data corruption. In EMG applications, after the raw EMG signals are prepared (Fig. 2), a number of data pre-processing steps are applied to reduce the influence of noise, which could compromise their interpretation. Sources of noise common to EMG applications include, but are not limited to, motion artefacts, power-line interference, and electronics noise inherent in the equipment. Pre-processing steps are used to reduce the impact of these sources of corruption and prepare the input data for further analysis [15, 96].

Data segmentation involves various techniques to further prepare the pre-processed EMG signals before applying classification techniques. This step is necessary due to the fact that the stochastic EMG signals, obtained as a time series in the time-amplitude domain, are non-stationary or exhibit "non-stationarity." Many feature extraction methods assume that the data are stationary, and so the longer EMG time series is partitioned into shorter EMG segments to estimate the properties of the signal. For real-time myoelectric control systems, however, the length of these segments plus any computation must be less than 300 ms to avoid noticeable delays

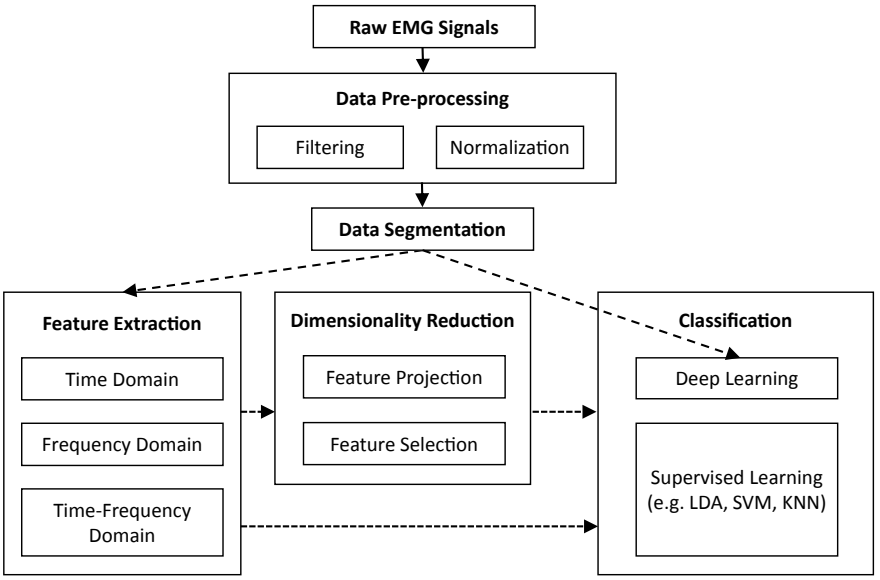

Fig. 1 A structure of EMG pattern recognition systems

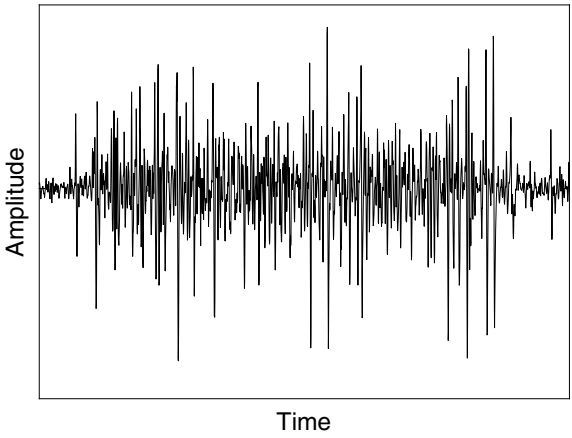

Fig. 2 An example of surface EMG signal recorded from extensor carpi radialis longus muscle when a subject performed hand open for two seconds

[17]. The two main techniques for data segmentation include adjacent windowing and overlapping windowing. In adjacent windowing, contiguous and disjoint segments of a predefined length are used. More commonly, overlapping windows with window increments less than the segment length, are used to improve the density of the resulting decision stream.

Feature extraction is the process of improving the information density of the processed signals, often transforming the signals from a higher dimensional input space into a lower dimensional feature space. The selection of appropriate features has a

tremendous impact on the performance of any pattern recognition system and the ideal feature set is heavily dependent on the classification task. Within the myoelectric control literature, EMG features have been commonly divided into three categories: time domain, frequency (spectral) domain, and time-scale (time-frequency) domain [74, 76, 81, 87]. The availability of high quality features that possess good class separability, minimal complexity, and are robust to dynamic factors is the most influential aspect of myoelectric control system performance [9, 117].

Dimensionality reduction is the process of either searching the computed feature space and selecting an optimal subset of high performing features (feature selection) or combining all initial features and projecting them based on some linear or non-linear mapping (feature projection) in order to maximize classification performance. Some commonly used dimensionality reduction techniques include sequential forward selection (SFS), genetic algorithms (GA), principal component analysis (PCA), and independent component analysis (ICA) [62, 64, 79].

Finally, classification involves the use of a boundary detector, or discriminant function learned through past events to estimate the class of a current event given the features presented. Substantial exploration and development of classification algorithms have been performed in myoelectric control, validating the viability of algorithms such as linear discriminant analysis (LDA), support vector machines (SVM), hidden Markov models (HMM), and artificial neural networks (ANN) [62, 79, 102].

3 Dynamic Factors in Hands-Free Control

Although classification rates of above 90% have been demonstrated in many studies, several problems must still be solved before practical and robust implementations of commercial myoelectric control systems can be realized. Consequently, four of the main challenges to deployable myoelectric control are discussed in detail in this chapter: (1) within-day and between-day variation, (2) noise, (3) variation in force, and (4) variation in limb position and forearm orientation.

3.1 Within-Day and Between-Day Variation

The re-usability and sustainability of myoelectric control systems pose a major concern for real-world applications as devices designed for long-term use often require frequent retraining. Indeed, the requirement to retrain these devices regularly has been seen as a hindrance to the commercialization and adoption of consumer-grade myoelectric control systems. Regardless of the model performance upon creation, the non-stationarity of EMG signals (i.e., their characteristics change throughout the day, and between days) gradually degrades its performance over time (up to 20–30% [60, 63]). The source of these natural variations over time has been attributed to many factors including spatial orientation (electrode shift), electro-physiological

Table 1 List of selected studies investigating the effect of time on myoelectric control systems

References	Number of days	Subjects	Number of movements	Number of electrodes
[100]	2	8N	6	6
[83]	4	20N	8 + rest	4
[120]	5	5N	6	4
[3]	5	5N	7 + rest	8
[63]	5	10N	7	14
[112, 113]	7	10N + 6A	6 + rest	5–6
[60]	8	7N	5 + rest	4
[54]	10	5N + 3A	12 + rest	4–6
[33]	11	8N + 2A	12 + rest	4–6
[97]	15	7N	6 + rest	8
[10, 38, 39, 87]	21	1N	11	4

Note N, able-bodied (non-amputee) subject; A, amputee subject

factors (muscle fatigue, sweating, skin impedance), user intent (muscle contraction effort), and many other potential factors. Most studies make the false assumption that EMG signals are a stationary process and thus have neglected to model any temporal variations in the signal over time. A common characteristic of these studies is their short collection period (i.e., a single or few sessions in one day) within constrained laboratory settings, thus largely avoiding these signal changes.

Over the last decade, approximately 30 experiments have been compiled that investigate the effect of time on myoelectric control systems (Table 1). Nevertheless, these studies can be categorized into three main research categories. The first category is the exploration of the nature of changes of time in pursuit of answers to (a) when changes occur, (b) the impact of these changes on classifier performance when not trained recurrently, and (c) the quantity and stratification of training data necessary to achieve stable parameter estimation that is representative of the true sampling distribution and reaches asymptotic accuracy. The second category is the identification of stable classification, feature extraction, and dimensionality reduction algorithms that are invariant to changes that occur over time. The third category is the development of adaptive algorithms that are able to actively retrain and/or relabel the classification model.

EMG classification performance for able-bodied and amputee populations continuously degrades as the period between training and testing increases [3, 10, 33, 83, 113]. However, there is no consensus on the amount of training data sufficient for a fixed classification model to reach an asymptote in accuracy. While Waris et al. [113] found a continuous decrease in performance over 7 days, a number of other studies have found that there may be periods when the classification performance is rather stable or even improves. Some have found that classification accuracy initially decreases exponentially, but then plateaus after 3 days [83], 4 days [3, 33], and 6 days [10] for able-bodied individuals, and 6–9 days for amputees [33]. A possible expla-

nation is the subject learning effect, wherein subjects begin to elicit more repeatable gestures after becoming familiarized with the process. Because this subject learning mainly occurs during the first several days [106], training data collected after this period could reduce the need for classification algorithms to compensate for user adaptation. For example, Milosevic et al. [60] found that training a classifier with data after 4 and 5 days of use provided better results for later days (testing on the 6th) than training with data from the 1st and the 2nd days of use (and testing on the 3rd day). Of note, learning persisted in most studies irrespective of whether external feedback was provided during the performed gesture or not [33]. The plateauing of classification performance occurred at different times across studies, potentially due to differences in subject learning abilities, coaching, or feedback, which may vary with the sample population, experimenter, and experiment (i.e., the higher the learning ability of a subject, the faster he or she may reach a stable accuracy).

Boschmann et al. [10] also remarked that classification accuracy begins to drop again once the period between training and testing reaches more than 10 days. Such studies on the long-term effects of classification performance have ranged from two to twenty-one days (Table 1); however, they are few and remain relatively short when compared to real prolonged usage in daily life. Consequently, longer experiments may yield more consistent results across subjects and studies regarding whether or not the performance curve would plateau. Evaluation of such longer-term EMG effects over months and years is warranted as using more available data to train classifiers could lead to more accurate and stable parameter estimation that more closely represents the true sample distribution [92]. For an extended coverage of methods used to identify the probability density functions and the stationarity of EMG signals, the reader is encouraged to consult [109] and [89], respectively.

Numerous studies on time-invariant classification, feature extraction, and dimensionality reduction algorithms have culminated in an understanding of techniques effective for dealing with changes in signal properties. Kaufmann et al. [38] and Waris et al. [112] investigated the behaviour of five state-of-the-art classifiers: LDA, SVM, ANN, *k*-nearest neighbour (*k*NN), and decision tree (DT) when applied to EMG signals recorded over 21 and 7 consecutive days, respectively. Kaufmann et al. [38] found that classification accuracies dropped to less than 80% when trained exclusively with data collected on the first day and validated against subsequent days' data. The performance degraded with an increasing period between training and testing data and dropped gradually (more than 10%) if not being retrained. This was relatively consistent for all classifiers examined, with the exception of LDA which dropped by only 3.6%. Within an alternative analysis, Kaufmann et al. [38] found distinguishable performance differences between fixed and retrained classification models after three days; retrained classifiers used either the most recently collected data or all preceding data for training. In contrast, Waris et al. [112] found that an ANN yielded the highest classification accuracies in the context of between-day fluctuations, followed by LDA. In addition to the five aforementioned classifiers, Kaufmann et al. [39] demonstrated that an evolvable hardware (EHW) classifier was able to compete with the state-of-the-art classifiers in terms of classification performance over time. Zia ur Rehman et al. [97] showed that a convolutional neural net-

work (CNN) with raw bipolar EMG samples as the inputs outperformed both LDA and stacked sparse autoencoders (SSAE) for classification of EMG signals from six hand gestures over two sessions per day for 15 consecutive days. Similarly, Zhai et al. [118] showed that CNN with spectrograms as the inputs outperformed SVM for the classification of EMG signals from the NinaPro database [6]. For an extended coverage of deep learning methods and considerations, the reader is encouraged to consult [92].

During an investigation of 10 hand gestures over the span of 21 days, Phinyomark et al. [87] found that sample entropy (SampEn) outperformed a set of fifty other EMG features extracted from the time domain and frequency domain when using an LDA classifier. The average classification accuracy across the duration was 93.4% when using a static model obtained during initial training. This fixed model suffered only a 2.4% performance decrease when compared to periodic retraining schemes. Inclusion of three additional features in the feature vector: root mean square (RMS), waveform length (WL), and the fourth order cepstrum coefficient (CC), further increased the classification accuracy to 98.9%; the four feature fixed model achieved the same accuracies as the retrained models without requiring the collection of new training data each day. Moreover, this study confirmed that the LDA classifier yielded better performance than other state-of-the-art classifiers including SVM, ANN, KNN, DT, quadratic discriminant analysis (QDA), and random forests (RFS) in the classification of time-varying signal properties.

Dimensionality reduction techniques have also been explored in the context of their robust to non-stationary effects. In their work, Zhang et al. [120] evaluated an adaptive feature extraction method based on wavelet packet transforms (WPT), local discriminant basis (LDB) algorithms, and PCA. Phinyomark et al. [83] compared seven state-of-the-art feature sets in both the time domain and time-scale domain. Time domain feature sets achieved above 80% accuracy in the presence of non-stationary effects when uncorrelated linear discriminant analysis (ULDA) was used for dimensionality reduction prior to LDA classification, whereas time-scale domain features achieved less than 70% accuracy. In addition to PCA and ULDA, Liu et al. [54] proposed another dimensionality reduction method called kernel Fisher discriminant analysis (KDA), a kernelized version of LDA, to extract time invariant characteristics from EMG features.

Adaptive algorithms, able to retrain and/or relabel the classification model, have been proposed to enhance the longevity of myoelectric control systems. LDA has been most heavily explored in this area, such as when Jain et al. [36] proposed an adaptive LDA classifier that updated the training data during the detection of slow concept drift and performed label correction during detection of fast changes in the signal. Chen et al. and He et al. [13, 35] also proposed adaptive/self-enhancing LDA and QDA classifiers that continuously updated their model parameters, such as the class mean vectors, the class covariances, and the pooled covariance. Gu et al. [27] proposed a new adaptation mechanism called representative sample based LDA by using a new sample set instead of the whole training (an incremental learning-based LDA). Zhang et al. [119] proposed an unsupervised LDA adaptation strategy based on probability weighting and cycle substitution. Liu et al. [51] applied a domain

adaptation (DA) framework, which reused the models trained in previous days as input (nine days in this study) for a new LDA classifier trained on the 10th day of the experiment. Although the results from all of these studies have shown that adaptive LDA classifiers significantly outperform their static counterparts, most [13, 27, 35, 36, 119] evaluated their performance on data recorded over only 4–11 h from a single day. Moreover, in practice, the user will have at least visual feedback and will likely experience self-adaptation in the form of reflexive error correction and longer-term learning. This suggests a system where both the user and algorithms are adapting, which may create unstable conditions. Future investigations should, therefore, explore appropriate adaptation schemes that can coexist with user adaptation in the presence of visual feedback and with the dynamics factors introduced during actual use [111].

3.2 Noise

The majority of EMG signal processing and pattern recognition algorithms assume that the EMG data are of high quality, which can lead to invalid results or interpretations if this assumption is incorrect. It is widely acknowledged that noise contamination of EMG signals is an unavoidable problem involved in the recording data. In other words, raw EMG signals typically contain not only useful information but also some irrelevant or confounding information that adds ambiguity. The raw signal cannot, therefore be used directly, and data pre-processing is necessary to reduce the effect of noise and to improve the spectral resolution of the EMG signal. Common noise contaminants in the EMG signal can be categorized into many forms [15, 23, 59, 109], for example; (a) motion artefacts, (b) electrocardiogram (ECG) interference, (c) power line interference, (d) quantization noise, (e) analog-to-digital converter clipping, (f) amplifier saturation, (g) spurious background spikes, and (h) additive white Gaussian noise (AWGN).

Research works related to these noise contaminants in myoelectric control systems have roughly focused on three main research topics. The first topic is the investigation of the quality of the EMG signal by (a) determining whether the noise is present in the signal, (b) identifying the noise type, and (c) providing an estimate of the severity of noise. The second topic is the development of algorithms that either reduce the noise within the recorded signal or focus on the useful parts of the signal for classification purposes. The third topic is the identification of robust feature extraction and classification methods that are tolerant of noise.

Verification of the EMG signal quality is often performed by human operators using visual inspection during or after the acquisition in combination with some quantitative measures such as signal-to-noise ratio (SNR). Fraser et al. [23], however, developed an approach to automatically differentiate clean from contaminated EMG signals. The proposed method used a one-class SVM and a feature vector of WL, mean absolute value (MAV), two of 10-bin histogram (HIST), and two of 10-bin averaged power spectral density (PSD). This contaminant detection method was

shown to be successful in identifying whether a noise is present in the signal; EMG signals were classified as noise-free when the SNR was above 10 dB, and as contaminated when the SNR was found to be below 10 dB. The same research group [22, 59] expanded on these previous methods by also identifying noise type. The output of seven quantitative measures: SNR, signal-to-motion artefact ratio (SMR), maximum drop in power density (DPR), power spectrum deformation (OHM), signal-to-power line ratio (SPR), signal-to-ECG ratio (SER), and Pearson correlation coefficient test for normality (CCN), were used as features for the SVM classifier that identified the noise type. Specifically, SMR, SNR, OHM, and SER were able to detect motion artefacts, but suffered some confusion with ECG interference. Power line interference is best identified by SPR, while CCN can be used to detect amplifier saturation. AWGN is detected by DPR, but DPR is sensitive to changes in all of the contaminants. This extended contaminant detection method, however, identified noise types at only very low SNRs (below 0 dB), with the performance beginning to drop at 0 dB and approaching random chance at higher SNRs. Moreover, both methods can be used to identify the presence of only a single noise type. In real-world situations, it is likely that multiple types of noise are present simultaneously in the signal, and additional work on noise detection methods for myoelectric control systems is necessary.

If the signal quality is found to be inadequate, appropriate pre-processing approaches are necessary. Fortunately, several types of noise manifest outside of the useful energy band of the EMG signal or only in a narrow specific frequency band of the signal. For instance, power line interference is clustered around 50 Hz or 60 Hz (depending on geographic location), while motion artefacts tend to be bandlimited in the frequency range of 0–20 Hz [96]. Use of conventional filters such as finite-impulse response (FIR) and infinite-impulse response (IIR) filters can therefore reduce these types of noise with minimal impact on the usable EMG signal [30, 55]. For example, De Luca et al. [55] recommended using a Butterworth filter with a corner frequency of 20 Hz and a slope of 12 dB/oct to filter movement artefact and baseline noise contamination. Powar et al. [94] used an FIR filter with coefficients that lead to the extraction of high kurtosis EMG, and that increased the classification performance by 20.5%. Adaptive digital filters, such as least mean square (LMS) and recursive least square (RLS) algorithms, have also been proposed to remove these kinds of noise [21, 61, 121].

Other sources of noise whose frequency components are random in nature range in the usable energy band of EMG frequencies from 0 to several thousand Hz (depending on measurement method). This kind of noise cannot efficiently and effectively be eliminated using conventional filters. In this case, the random noise can be reduced using high-quality electronic components, intelligent circuit design, and careful manufacturing techniques, but not entirely eliminated. Hence, it may cause problems when extracting robust features, making it difficult to yield high classification performance for myoelectric control systems. Wavelet transforms, and adaptive filters have been commonly used as powerful tools in the removal of random noise in non-stationary signals. Adaptive filters suffer from the complexity of devising automated procedures as their performance depends on a reference input signal, which is

difficult to apply in real-world applications. In contrast, the wavelet transform does not require any reference signals, and so pre-processing based on wavelet denoising of EMG has been proposed for pattern recognition with good success (e.g. [40, 57, 80]). Combining both Wavelet transforms, and adaptive filters could also improve the classification performance [28].

To yield the best performance with wavelet-based denoising algorithms, five parameters must be optimized: (1) the wavelet basis function, (2) the decomposition level, (3) a threshold selection rule (4) a threshold rescaling method, and (5) a thresholding function. All of these parameters have been examined comprehensively [84] highlighting a compromise between two points of view, denoising and classification, as follows: (1) the wavelet basis functions: Daubechies 2, 7, Symlets 2, 5, Coiflet 4, BiorSplines 5.5 and ReverseBior 2.2 [67, 71, 73]; (2) the decomposition level: 4 [67, 71, 73]; (3) the threshold selection rules: the weighted universal method with $w = 0.55$ [80] and the global scale modified universal method [68]; (4) the threshold rescaling methods: the level dependent for wavelet coefficient length and the first level or the level dependent for standard deviation of noise [67]; (5) the thresholding functions: the adaptive shrinkage method [72] and the firm shrinkage method [78]. These wavelet denoising approaches not only reduced the effect of noise in EMG pattern recognition but also significantly increased the classification performance by 2–50% depending on the SNR level. For extended coverage of wavelet denoising methods and review of wavelet denoising in EMG signal processing and classification, the reader is encouraged to consult [84].

Another kind of noise that occurs when using multi-channel EMG systems is cross-talk. Blind source separation methods, such as PCA and ICA, can be used to reduce this so-called noise [18, 19], however, it should be noted that muscle cross-talk could also add discriminatory spatial information that may improve classification performance [29].

Due to the limited number of noise removal options in the pre-processing stages of EMG pattern recognition, employing robust feature extraction and classification methods that are tolerant of noise may be required to improve the robustness of myoelectric control systems. Based on comprehensive investigations of state-of-the-art EMG features, the Willison amplitude (WAMP) [66, 69] and modified mean and median frequency (MMNF and MMDF) [70] EMG features have been recommended as being most tolerant of power line interference and additive white Gaussian noise. Geng et al. [25] also showed that a sparse representation-based classification algorithm outperformed a number of state-of-the-art classifiers such as LDA, KNN, RF, and SVM when the signals were contaminated by white Gaussian noise.

3.3 Variation in Force

Conventional myoelectric control schemes use an EMG amplitude estimator (such as MAV and RMS [91]) to map the intensity of the contraction of the underlying muscles to the velocity or position of a cursor or device [105]. Pattern recognition

Table 2 List of selected studies investigating the effect of force on myoelectric control systems

References	Force levels (%MVC)	Subjects	Number of movements	Number of electrodes
[56]	2: 10, 50	8N	5	4
[110]	2: 25, 65	8N	4	Two 4-by-3 grids
[50]	3: 20, 50, 80	3N	4 + rest	4
[49]	3: 20, 50, 80	3N	5	32
[5]	3: 20, 50, 80	5N	6 + rest	6
[34]	3: 20, 50, 80	9N	8 + rest	8
[3]	3: 30, 60, 90	5N	7 + rest	8
[1]	3: low, medium, high	2A	4 + rest	12
[2]	3: low, medium, high	9A	6	8
[42]	3: low, medium, high	10N + 1A	6	6
[43]	3: low, medium, high	12N + 1A	6	6
[102]	7: 20, 30, 40, 50, 60, 70, 80	11N	9 + rest	8

Note that MVC, maximum voluntary contraction; N, able-bodied (non-amputee) subject; A, amputee subject

based myoelectric control, however, relies on clustering repeatable patterns of EMG activity into recognizable classes. Contractions performed at different force levels may result in drastically different features, resulting in a considerable impact on the performance of a classifier.

Some researchers have made efforts towards solving this problem during the past decade (Table 2), which can again be categorized into three main research categories. The first category is the investigation of the effect of changing force levels on the performance of pattern recognition based myoelectric control. The second category is the design of training strategies to mitigate the effect of force changes. The third category is the development of feature extraction methods that are invariant to these different force levels.

In a study by Scheme et al. [102], the ability of pattern recognition based myoelectric control to recognize human gestures in the presence of deviations in contraction intensity deviation was explored. EMG from 10 gestures was recorded at intensities ranging from 20 to 80% of maximum voluntary contraction (MVC) from 11 able-bodied subjects using an 8-channel wearable EMG armband. To test the ability of EMG pattern recognition to handle unseen force levels, the classifier was trained with each force level and then tested with each and all force levels. As expected, classification accuracy was maximized when the classifier was trained and tested with similar force levels, while the presence of contractions from unseen force levels increased the error considerably (between 32 and 44%). These results were later reit-

erated when Al-Timemy et al. [1] investigated the effect of force variation with two transradial amputees. Similarly, their results showed that classification performance is degraded by up to 60% when the force level is varied. Importantly, the classification accuracies were found to be lower for high force levels as the amputees struggled when generating this high, and unsustainable levels [1].

To counteract this severe degradation in performance, an obvious strategy is to train the classifier using all force levels [1, 3, 102] or to train parallel classifiers using different force levels and then categorize the input EMG signals into a target classifier for recognition [50]. Although incorporating multiple levels in the training protocol improves the classification accuracy, the increased training time and burden may limit the clinical viability of this approach. Scheme et al. [102, 103] therefore recommended the use of dynamically varying 'ramp' contractions which captured features across the full range of force levels during training. Using these ramp contractions have been found to be a highly successful and simple training strategy to reduce the effect of force variation and to introduce added natural variability during training.

Extracting features that are invariant to force levels is an alternative solution to maintaining classification performance without incorporating extra training samples. Tkach et al. [110] studied the stability of twelve commonly used time-domain features with an LDA classifier during low and high levels of force and suggested a set of four features consisting of WL, log detection (LD), slope sign change (SSC), and AR features. The 76% accuracy obtained in the classification of four gestures, however, suggests the need for alternative feature extraction methods. Li et al. [49] proposed the use of common spatial patterns (CSP) method and showed better robustness against force variation with an improvement of 5.3% in classification accuracy. In addition to time domain features, Lv et al. [56] showed that frequency domain (improved discrete Fourier transform) features were better than commonly used time domain features for wrist EMG classification. He et al. [34] proposed two novel feature extraction methods, based on the property of muscle coordination in the frequency domain, to extract angular rather than amplitude information. These features were found to increase accuracy by approximately 11% (from 80 to 91%) when classifying nine gestures with three different force levels (20, 50, and 80% MVC). These features were motivated by the observation that the frequency response of muscle activation patterns is invariant over a range of force levels. Al-Timemy et al. [2] proposed another set of features based on the orientation between a set of spectral moment descriptors extracted from the original EMG signal and an additional non-linearly mapped version of these moments (TD-PSD features). Based on Parseval's theorem, the power spectral density was computed directly in the time domain to reduce computational cost. This feature set achieved significant improvements of around 6–8% in classification accuracy as compared to other commonly used features. These features have since been shown to extract information that is unique from other amplitude based features [65]. Asogbon et al. [5] also proposed a different set of features based on Parseval's theorem and showed an increase in classification accuracies as compared to commonly used time-domain feature sets (6.7–13.5%). Similarly, features based on chaos theory and fractal analysis could be

used to increase the robustness of pattern recognition to contraction level as these methods measure the self-similarity and complexity of the signal [4, 77, 85, 86]. For example, Phinyomark et al. [82] found that detrended fluctuation analysis (DFA) can yield a better classification performance when the amplitude level of the EMG signal is low. More details about functional groups of EMG features can be found in [65].

3.4 Variations in Limb Position and Forearm Orientation

The same hand and wrist gestures can also generate substantially different signal patterns when performed in different limb positions and forearm orientations, increasing classification error, and reducing robustness in real-life use [12, 20, 43, 52, 104]. It has been noted, however, that the impact of changes in limb position is less pronounced in amputees than with able-bodied subjects [26, 37]. Nevertheless, several studies have proposed three main methods to address this problem (Table 3): (1) training the classifier using EMG signals recorded from different pre-defined static positions or during dynamic motion between pre-defined positions; (2) using accelerometers to measure arm positions and orientations; and (3) developing robust feature extraction, dimensionality reduction, and classification algorithms that can suppress the impact of position and orientation variations.

As with force level, a similarly successful strategy has been to inform classifier boundaries of the effect of limb positions and forearm orientations by including exemplars from each position and orientation during training [12, 20, 43, 104]. For instance, Scheme et al. [104] trained an LDA classifier using EMG recorded in 8 different limb positions to discriminate eight different gestures. Within-position accuracy was found to be best with the arm hanging straight down while the position that provided the worst accuracy was when the elbow was bent at 90°. Khushaba et al. [43] trained an SVM classifier using EMG recorded from 3 different forearm orientations (i.e., wrist fully supinated, at rest, and fully pronated) to discriminate

Table 3 List of selected studies investigating the effect of limb position and forearm orientation on myoelectric control systems

References	Number of positions	Subjects	Number of movements	Number of electrodes
[52]	2	4N	4 + rest	4
[43]	3	12N + 1A	6	6–8
[115]	5	8N	8 + rest	8
[20]	5	17N	7 + rest	8
[12, 26]	5	5A	6 + rest	8
[104]	8	8N	7 + rest	8
[7]	9	3N	4 + rest	8

Note that N, able-bodied (non-amputee) subject; A, amputee subject

six different gestures. Recently, Yang et al. [115] investigated the effect of both limb positions and forearm orientations, and found that the classification performance of hand and fingers gestures are more highly impacted by forearm orientation than limb position. This result is intuitive given the proximity of extrinsic hand muscles, widely used as primary EMG sites, to the pronator and supinator muscles. Although incorporating different positions in training protocols has been shown to improve the classification accuracy, the training time and burden again limit the clinical viability of such systems [7]. Using either a dynamic motion between predefined positions or free movement of the arm in the 3-dimensional (3D) space while eliciting training gestures is therefore seen as a preferred training strategy [24, 95, 101].

Scheme et al. [104] also proposed the use of accelerometers to measure the positions of the arm. Fougner et al. [20] extended this work by proposing two approaches integrate accelerometer information: (1) two-stage position-aware classification, wherein limb position is first detected using the accelerometer information, followed by position-specific gesture classification using EMG, and (2) single-stage position-aware classification wherein a classifier is trained using a combination of features from accelerometers and EMG signals. The first approach creates multiple position-specific classifiers, requiring the selection and collection of discrete positions, whereas the second increases the dimensionality of the feature space to accomodate the position effect. In a similar approach, Geng et al. [26] used mechanomyography signals to first determine the arm position, finding that both the 1- and 2-stage approaches outperform EMG information alone. Although adding extra information from accelerometers may improve the classification accuracy, their integration with EMG information must be carefully considered. Due to the increased dimensionality of the problem, their inclusion can result in a worse performance than EMG alone if too few training data and positions are included [95].

As with other perturbations, researchers have also attempted to identify and develop feature extraction, dimensionality reduction, and classification algorithms that are robust to the impact of arm position [7, 14, 43, 45, 46, 52, 53]. Liu et al. [52] investigated the robustness of six state-of-the-art time-domain feature sets and found that position had a significant impact on the performance of the classifier for all the feature sets. The TD-PSD features that have been shown to be invariant to force levels [2] have also performed well in the presence of limb position and forearm orientation variations as compared to commonly used feature sets [43, 45, 46]. Canonical correlation analysis (CCA) methods have also been successfully shown to reduce the number of positions required when training a new user [14]. Further, a number of novel classifiers: mixed-LDA [116], conditional Gaussian mixture models (CGMM) [53], sparse representation classification (SRC) [7], and extreme learning machine (ELM) with adaptive sparse representation classification (EASRC) [8] have been shown to significantly outperform traditional EMG classifiers (such as LDA) in limb positions not explicitly seen during training.

4 Hands-Busy Conditions

Given a historical focus on prosthetic applications, myoelectric control has been predominantly explored in hands-free conditions. As new applications emerge, however, the need for EMG recognition during simultaneous interactions with other objects is beginning to arise. Traditional human-computer interfaces, like keyboards, mice, and joysticks, rely on the physical and dedicated interaction of the hands and fingers, precluding the simultaneous control of alternate inputs. It is possible that this limitation may be overcome through the use of EMG pattern recognition, thus facilitating multitasking. In other words, even when a user's hands are busy with other objects, EMG-based human-computer interfaces may be able to classify a set of unique gestures or contractions. Given the nascence of this emerging field of application, few studies have been conducted with the aim of developing gesture recognition interfaces capable of performing under these 'hands-busy' conditions.

Hands-busy conditions were explored by Saponas et al. [99] when twelve participants performed pinch gestures in combination with a travel mug and a weighted bag to emulate object interactions with a small tool-sized object and a large heavier object. Their experiment comprised 25 trials of finger gestures for each object, where each trial contained a sample of the index, middle, ring, and pinky finger pinch gestures in random order. Using an SVM classifier, four finger (index, middle, ring, pinky) and three finger (excluding pinky) pinch grips were recognized 65 and 77% while interacting with the travel mug. Classification accuracies during the weighted bag interaction were 86 and 91% for four and three finger gesture experiments, respectively. These experiments indicated that loading of the hand by object weight does not negatively impact gesture recognition performance. In fact, classification accuracies were higher under larger loads, alluding to more separable classes. Another study conducted by Khushaba et al. [44] developed an EMG control scheme to alleviate driver distraction by replacing button controls with decoded muscle activity. Eight-channel EMG was collected from 8 subjects to decode 14 gestures during hands-busy conditions in a simulated driving environment. Fuzzy neighborhood discriminant analysis (FNDA), orthogonal FNDA, LDA, locality sensitive discriminant analysis (LSDA), PCA, and neighborhood preserving embedding (NPE) was utilized for the projection of 136 EMG features to 13 features. FNDA and orthogonal FNDA were found to significantly outperform other feature projection techniques ($p < 0.05$) and achieved less than 7% classification error during an online experiment.

Given the potential broad applications in human-computer and human-machine interaction, further hands-busy condition studies are required to fully identify object characteristics that impact gesture recognition; however, these hands-busy conditions may benefit from techniques explored in previous force level, limb position, and forearm orientation studies. While object properties like stiffness may have minor affects on EMG signal characteristics, the primary confounding factors are likely the multiple positions and forces adopted to facilitate comfortable interaction with objects.

5 Cross-User Classification Models

Inherent differences in physiology and behaviour, among other factors, affect the elicitation of muscle potentials and result in substantial differences in EMG patterns between individuals, even for the same gestures. This has necessitated the adoption of user-specific data collection and training phases within myoelectric control protocols. In prosthetics, physiological changes due to amputation or differences due to congenital absence contribute to additional variations in muscle geometry, the composition of subcutaneous fats, muscle, and skin, tendon attachment points, and innervation zones. As such, in clinical practice, numerous appointments donning, articulating, and doffing prostheses in the presence of expert guidance are expected to establish a confident classification model for each user. The growth of other EMG applications, in particular, commercial gesture recognition interfaces, would be greatly hindered if the same expertise, resources, and maintenance were required. Indeed, the adoption of EMG-based devices would be greatly facilitated by the forgoing of lengthy or custom training protocols. In pursuit of a solution, the development of cross-user classification models has been a keen area of research within the past decade.

The proof-of-concept of cross-user classification models was performed by Saponas et al. [98], where a forearm electrode cuff was used to capture hand and finger gestures from 12 subjects. A 12-fold, leave-one-subject-out, cross-validation provided the framework for the assessment of model robustness and signal variance between subjects. Recognition of six finger lift gestures from previously unseen subjects achieved average classification rates of 57%. Despite the relatively poor performance of the system (relative to common within-subject results), the model performed considerably better than chance (1 in 6, or 17%), suggesting the potential for developing cross-user classification models for myoelectric control systems. Kim et al. [47] later corroborated that the standard classification models, without implementing additional methods to extract the user-independent EMG patterns, can yield classification rates above chance (41% for a four-class classification problem) and that the further development of novel algorithms for cross-user classification models are necessary.

Xiang et al. [114] identified a set of gestures that were more user-independent that could be coupled with cross-user classification models. In an offline experiment, data from 4 subjects collected over 5 days were used to train a classifier to recognize gestures from 6 unseen subjects. Eleven different user-independent gesture sets containing five, six, or eight gestures were evaluated. The range of gesture set classification accuracies achieved, 76–90%, indicated the user-independence of these gesture sets approaching a usable standard for commercial applications. Upon further inspection, gesture class separability was non-uniform across subjects; three test subjects achieved good class separability, whereas others suffered from poor performance. In an online experiment, data from 10 subjects collected over 4 days were used to recognize two sets of 6 and 8 user-independent gestures from 50 unseen subjects using a set of time-domain features (MAV and the fourth-order AR model coeffi-

cients) and a linear Bayes classifier. Facilitated by the user-independent gestures and increased numbers of training subjects, cross-user classification rates achieved 90.7% and 81.3%, respectively. Hand gestures found to provide strong user-independence include flexion and extension of the wrist, hyper-extension of palm, and hand grasp.

An alternative solution was proposed by Matsubara and Morimoto [58] through the segmentation of motion-dependent and user-dependent information using a bilinear model. This procedure involved adapting a parameter matrix that segmented motion-dependent and user-dependent information for each gesture. Afterward, this matrix was used to effectively remove user-dependent information from unseen subjects; thus removing the necessity for user-specific data collection and classifier training. Using the user-independent features extracted from the bilinear EMG model with an SVM classifier, the proposed method increased performance from 54 to 73% while decreasing the learning time from 830 to 6 s as compared with the standard classification model.

A subsequent study employed CCA driven by a similar motivation [41]. CCA devises a pair of linear transformations that maximize the correlation of similar-class feature matrices between subjects in the transformed space. Following the same cross-validation method as Saponas et al. [98], CCA was validated using 10 able-bodied subjects as the expert users to recognize 12 finger gestures from 6 transradial amputees (with varying levels of amputation). The proposed CCA framework produced comparable or better results for the amputee test subjects in the absence of subject-specific training data (average classification accuracies greater than 82% across all subjects). Another CCA-based study examined the combination of user- and position-independence [14]. The position-independent CCA algorithm was assessed using 10 new subjects and achieved an LDA classification accuracy improvement of 44.2% over the same algorithm in the absence of CCA.

Deep learning architectures have begun to be tailored for EMG in an attempt to develop cross-user classification models [92]. Traditionally, deep learning was not used on EMG signals due to the lengthy training procedures required to amass the necessary amount of samples; however, transfer learning serves as a solution to aggregate a sufficiently large dataset by learning general features from multiple subjects [16]. Cross-user transfer learning achieved 98.3% classification accuracy for 7 hand and wrist gestures collected from 17 subjects. Additionally, using the Ninapro database, this deep-learning architecture achieved 65.6% classification accuracy for 18 hand and wrist gestures collected from 10 participants using the Myo armband device.

In addition to these efforts to identify user-independent EMG patterns, individual differences in EMG signals due to human factors, including gender, age, and anthropometric variables, have also been reported. For gender and age differences in muscle activation via EMG signals, for example, Harwood et al. [32] and Theou et al. [107] found that older adults exhibit greater EMG burst activity, with higher mean amplitudes, as compared to younger adults. These age-related changes are also emphasized in women. For anthropometric variables, Thongpanja et al. [108] found that the linear relationship between the force of contraction and the MNF and MDF features varied from person to person. These results could be due to human physical

variations (i.e., different anatomical and physiological properties of the muscles) as a number of anthropometric variables can be used to identify subgroups of subjects based on these relationships. Phinyomark et al. [88] found that it is feasible to use anthropometric variables as an input to calibrate or adapt EMG pattern recognition systems. Significant and strong correlations between several commonly used EMG features and anthropometric variables were found including the circumference of the forearm and biceps. These variables could benefit the design of cross-user classification models that include this added context. Such a system could leverage additional sensors in an EMG armband that also measure the circumference of the band itself [11]. For other anthropometric variables that cannot be measured directly using a wearable device, it could be possible to estimate anthropometric data for individual subjects using published anthropometric tables [90].

6 Concluding Remarks and Future Directions

In this chapter, we have reviewed and discussed several signal processing and classification techniques for myoelectric control systems. In particular, the practical considerations of how to handle the dynamic factors prevalent in real-world scenarios were emphasized. In particular, within-day and between-day variations, signal noise, variations in force, and variations in limb position and forearm orientation were highlighted. Additional emerging conditions, such as the implications of hands-busy usage scenarios and the construction of cross-user classification models were also explored.

Despite the exciting work in many of these areas, remaining research is needed to extend the robustness and applications of myoelectric devices. Further exploration of the effects of *within-day and between-day variations* is necessary for the development of long-term commercial use devices. In particular, the controversy among researchers regarding the performance profile exhibited using a fixed classification model should be analyzed for longer periods between training and testing. Moreover, subject-learning, induced through longer collection and training procedures, could provide insight into possible frameworks for adaptive systems that are robust to non-stationary EMG signals.

Limitations with current signal processing techniques for the detection and removal of *noise* remain the scenarios in which one-class classifiers can distinguish types of noise. In the case where noise is large (low SNR) and visual inspection can effectively be used to assess signal contaminants, the classifier is unnecessary; however, when the signal quality is high (high SNR), and contaminants are unable to be distinguished through visual inspection, the one-class classifier fails. Adaptations to this novel technique will facilitate targeting signal contaminants and empowering accompanying pattern recognition systems for applications like gesture recognition. The tradeoffs between these noise levels, their recognition, and their impact on performance should also be further explored.

The state-of-the-art techniques for minimizing the effect of *contraction intensity* are facilitated by either strategic data collection along with quantized or dynamic force levels or the extraction of features that are invariant to contraction intensity level, both of which have drawbacks. The sampling of additional force levels involves an additional parameter to be varied throughout data collection, increasing the length of the training procedure. Contraction intensity invariant features implemented under practical conditions may be sensitive to other dynamic factors or lack valuable amplitude information, thus decreasing their usability. Future possible directions for contraction intensity invariant classification models follow the trends of other dynamic factors in the implementation of adaptive systems. In particular, as in the development of cross-user models, CCA or similar approaches may facilitate intensity invariance with little or no added training burden.

Advancements in *limb position* methods have allowed for gesture classification in numerous positions. Techniques identified as position invariant avoid additional data collection under a range of positions, thus shortening the training protocol. Adaptive techniques, like CCA and CGMM, also provide improved accuracy under the effects of various limb positions while minimizing the training protocol. While these techniques provide higher classification accuracy as compared to their absence, advancements are necessary to guarantee usability (accuracy >90%) under all limb positions and forearm orientations.

It is important to note that most current EMG feature sets provide sufficient class separability to tolerate these added sources of variability, suggesting that proper population of feature space during training remains one of the predominant challenges for myoelectric control.

Previous works exploring the classification of EMG during *hands-busy conditions* have improved classification models for the intent of facilitating multitasking; however, many of the practical robustness issues outline herein have yet to be examined in this context. Further studies are required to identify whether object interactions that accompany gestures invoke characteristic behaviours or whether those two are non-stationary.

Cross-user classification models remain a lofty and worthy goal for pattern-recognition based myoelectric control. CCA has demonstrated exciting potential as a possible framework for preceding user-specific training by learning a set of transformations that maximize the correlation between subjects. There remains the necessity for user-specific training data to be collected to initialize the set of transformations for a new user. This requirement could be rectified through an adaptive system capable of providing estimation for the set of transformations based on anthropomorphic variables. In conjunction with an online self-enhancing parameter estimation technique that customize the statistical parameters to the user in real-time, a myoelectric control system could be employed in the absence of any initial training procedure.

As previous research has typically studied the effects of these dynamic factors in isolation, the investigation of the combined effect of various confounding factors (including intra and inter-subject repeatability, noise, variation in force, variation in limb position and orientation, and electrode shift) remains needed [27, 43].

References

1. Al-Timemy, A.H., Bugmann, G., Escudero, J., Outram, N.: A preliminary investigation of the effect of force variation for myoelectric control of hand prosthesis. In: Proceedings of 2013 35th Annual International Conference of the IEEE Engineering in Medicine and Biology Society (EMBC), pp. 5758–5761 (2013). https://doi.org/10.1109/EMBC.2013.6610859
2. Al-Timemy, A.H., Khushaba, R.N., Bugmann, G., Escudero, J.: Improving the performance against force variation of emg controlled multifunctional upper-limb prostheses for transradial amputees. IEEE Trans. Neural Syst. Rehabil. Eng. **24**(6), 650–661 (2016). https://doi.org/10.1109/TNSRE.2015.2445634
3. Amsüss, S., Paredes, L.P., Rudigkeit, N., Graimann, B., Herrmann, M.J., Farina, D.: Long term stability of surface EMG pattern classification for prosthetic control. In: Proceedings of 2013 35th Annual International Conference of the IEEE Engineering in Medicine and Biology Society (EMBC), pp. 3622–3625 (2013). https://doi.org/10.1109/EMBC.2013.6610327
4. Arjunan, S.P., Kumar, D.K.: Decoding subtle forearm flexions using fractal features of surface electromyogram from single and multiple sensors. J. NeuroEng. Rehabil. **7**(1), 53 (2010). https://doi.org/10.1186/1743-0003-7-53
5. Asogbon, M.G., Samuel, O.W., Geng, Y., Idowu, P.O., Chen, S., R, N.G., Feng, P., Li, G.: Enhancing the robustness of EMG-PR based system against the combined influence of force variation and subject mobility. In: Proceedings 2018 3rd Asia-Pacific Conference on Intelligent Robot Systems (ACIRS), pp. 12–17 (2018). https://doi.org/10.1109/ACIRS.2018.8467236
6. Atzori, M., Gijsberts, A., Castellini, C., Caputo, B., Hager, A.G.M., Elsig, S., Giatsidis, G., Bassetto, F., Mller, H.: Electromyography data for non-invasive naturally-controlled robotic hand prostheses. Sci. Data **1**, 140,053 (2014). https://doi.org/10.1038/sdata.2014.53
7. Betthauser, J.L., Hunt, C.L., Osborn, L.E., Kaliki, R.R., Thakor, N.V.: Limb-position robust classification of myoelectric signals for prosthesis control using sparse representations. In: Proceedings of 2016 38th Annual International Conference of the IEEE Engineering in Medicine and Biology Society (EMBC), pp. 6373–6376 (2016). https://doi.org/10.1109/EMBC.2016.7592186
8. Betthauser, J.L., Hunt, C.L., Osborn, L.E., Masters, M.R., Lvay, G., Kaliki, R.R., Thakor, N.V.: Limb position tolerant pattern recognition for myoelectric prosthesis control with adaptive sparse representations from extreme learning. IEEE Trans. Biomed. Eng. **65**(4), 770–778 (2018). https://doi.org/10.1109/TBME.2017.2719400
9. Boostani, R., Moradi, M.H.: Evaluation of the forearm EMG signal features for the control of a prosthetic hand. Physiol. Meas. **24**(2), 309 (2003)
10. Boschmann, A., Kaufmann, P., Platzner, M., Winkler, M.: Towards multi-movement hand prostheses: combining adaptive classification with high precision sockets. In: Proceedings of Technically Assisted Rehabilitation (TAR) (2009)
11. Cannan, J., Hu, H.: Using forearm circumference for automatic threshold calibration for simple EMG control. In: Proceedings of 2013 IEEE/ASME International Conference on Advanced Intelligent Mechatronics, pp. 1476–1481 (2013). https://doi.org/10.1109/AIM.2013.6584303
12. Chen, L., Geng, Y., Li, G.: Effect of upper-limb positions on motion pattern recognition using electromyography. In: Proceedings of 2011 4th International Congress on Image and Signal Processing, vol. 1, pp. 139–142 (2011). https://doi.org/10.1109/CISP.2011.6100025
13. Chen, X., Zhang, D., Zhu, X.: Application of a self-enhancing classification method to electromyography pattern recognition for multifunctional prosthesis control. J. NeuroEng. Rehabil. **10**(1), 44 (2013). https://doi.org/10.1186/1743-0003-10-44
14. Cheng, J., Wei, F., Li, C., Liu, Y., Liu, A., Chen, X.: Position-independent gesture recognition using sEMG signals via canonical correlation analysis. Comput. Biol. Med. (2018). https://doi.org/10.1016/j.compbiomed.2018.08.020

15. Chowdhury, R.H., Reaz, M.B.I., Ali, M.A.B.M., Bakar, A.A.A., Chellappan, K., Chang, T.G.: Surface electromyography signal processing and classification techniques. Sensors **13**(9), 12431–12466 (2013). https://doi.org/10.3390/s130912431
16. Côté-Allard, U., Fall, C.L., Drouin, A., Campeau-Lecours, A., Gosselin, C., Glette, K., Laviolette, F., Gosselin, B.: Deep learning for electromyographic hand gesture signal classification by leveraging transfer learning (2018). arXiv:1801.07756
17. Englehart, K., Hudgins, B.: A robust, real-time control scheme for multifunction myoelectric control. IEEE Trans. Biomed. Eng. **50**(7), 848–854 (2003). https://doi.org/10.1109/TBME.2003.813539
18. Farina, D., Fevotte, C., Doncarli, C., Merletti, R.: Blind separation of linear instantaneous mixtures of nonstationary surface myoelectric signals. IEEE Trans. Biomed. Eng. **51**(9), 1555–1567 (2004). https://doi.org/10.1109/TBME.2004.828048
19. Farina, D., Lucas, M., Doncarli, C.: Optimized wavelets for blind separation of nonstationary surface myoelectric signals. IEEE Trans. Biomed. Eng. **55**(1), 78–86 (2008). https://doi.org/10.1109/TBME.2007.897844
20. Fougner, A., Scheme, E., Chan, A.D.C., Englehart, K.: Stavdahl, Ø: Resolving the limb position effect in myoelectric pattern recognition. IEEE Trans. Neural Syst. Rehabil. Eng. **19**(6), 644–651 (2011). https://doi.org/10.1109/TNSRE.2011.2163529
21. Fraser, G.D., Chan, A.D.C., Green, J.R., Abser, N., MacIsaac, D.: CleanEMG power line interference estimation in sEMG using an adaptive least squares algorithm. In: Proceedings of 2011 Annual International Conference of the IEEE Engineering in Medicine and Biology Society, pp. 7941–7944 (2011). https://doi.org/10.1109/IEMBS.2011.6091958
22. Fraser, G.D., Chan, A.D.C., Green, J.R., MacIsaac, D.T.: Biosignal quality analysis of surface EMG using a correlation coefficient test for normality. In: Proceedings of 2013 IEEE International Symposium on Medical Measurements and Applications (MeMeA), pp. 196–200 (2013). https://doi.org/10.1109/MeMeA.2013.6549735
23. Fraser, G.D., Chan, A.D.C., Green, J.R., MacIsaac, D.T.: Automated biosignal quality analysis for electromyography using a one-class support vector machine. IEEE Trans. Instrum. Meas. **63**(12), 2919–2930 (2014). https://doi.org/10.1109/TIM.2014.2317296
24. Gazzoni, M., Celadon, N., Mastrapasqua, D., Paleari, M., Margaria, V., Ariano, P.: Quantifying forearm muscle activity during wrist and finger movements by means of multichannel electromyography. PLoS ONE **9**(10), 1–11 (2014). https://doi.org/10.1371/journal.pone.0109943
25. Geng, Y., Ouyang, Y., Samuel, O.W., Chen, S., Lu, X., Lin, C., Li, G.: A robust sparse representation based pattern recognition approach for myoelectric control. IEEE Access **6**, 38326–38335 (2018). https://doi.org/10.1109/ACCESS.2018.2851282
26. Geng, Y., Zhou, P., Li, G.: Toward attenuating the impact of arm positions on electromyography pattern-recognition based motion classification in transradial amputees. J. NeuroEng. Rehabil. **9**(1), 74 (2012). https://doi.org/10.1186/1743-0003-9-74
27. Gu, Y., Yang, D., Huang, Q., Yang, W., Liu, H.: Robust EMG pattern recognition in the presence of confounding factors: features, classifiers and adaptive learning. Expert Syst. Appl. **96**, 208–217 (2018). https://doi.org/10.1016/j.eswa.2017.11.049
28. Hamedi, M., Salleh, S., Ting, C., Astaraki, M., Noor, A.M.: Robust facial expression recognition for MuCI: a comprehensive neuromuscular signal analysis. IEEE Trans. Affect. Comput. **9**(1), 102–115 (2018). https://doi.org/10.1109/TAFFC.2016.2569098
29. Hargrove, L., Scheme, E., Englehart, K.: Myoelectric Prostheses and Targeted Reinnervation, chap. 15, pp. 291–310. Wiley-Blackwell (2013). https://doi.org/10.1002/9781118628522.ch15
30. Hargrove, L., Scheme, E., Englehart, K., Hudgins, B.: Filtering strategies for robust myoelectric pattern classification. In: CMBES Proceedings, vol. 31 (2008)
31. Hargrove, L.J., Scheme, E.J., Englehart, K.B., Hudgins, B.S.: Multiple binary classifications via linear discriminant analysis for improved controllability of a powered prosthesis. IEEE Trans. Neural Syst. Rehabil. Eng. **18**(1), 49–57 (2010). https://doi.org/10.1109/TNSRE.2009.2039590

32. Harwood, B., Edwards, D.L., Jakobi, J.M.: Age- and sex-related differences in muscle activation for a discrete functional task. Eur. J. Appl. Physiol. **103**(6), 677–686 (2008). https://doi.org/10.1007/s00421-008-0765-z
33. He, J., Zhang, D., Jiang, N., Sheng, X., Farina, D., Zhu, X.: User adaptation in long-term, open-loop myoelectric training: implications for EMG pattern recognition in prosthesis control. J. Neural Eng. **12**(4), 046,005 (2015)
34. He, J., Zhang, D., Sheng, X., Li, S., Zhu, X.: Invariant surface EMG feature against varying contraction level for myoelectric control based on muscle coordination. IEEE J. Biomed. Health Inform. **19**(3), 874–882 (2015)
35. He, J., Zhang, D., Zhu, X.: Adaptive pattern recognition of myoelectric signal towards practical multifunctional prosthesis control. In: Su, C.Y., Rakheja, S., Liu, H. (eds.) Intelligent Robotics and Applications, pp. 518–525. Springer, Berlin, Heidelberg (2012)
36. Jain, S., Singhal, G., Smith, R.J., Kaliki, R., Thakor, N.: Improving long term myoelectric decoding, using an adaptive classifier with label correction. In: Proceedings of 2012 4th IEEE RAS EMBS International Conference on Biomedical Robotics and Biomechatronics (BioRob), pp. 532–537 (2012). https://doi.org/10.1109/BioRob.2012.6290901
37. Jiang, N., Muceli, S., Graimann, B., Farina, D.: Effect of arm position on the prediction of kinematics from EMG in amputees. Med. Biol. Eng. Comput. **51**(1), 143–151 (2013). https://doi.org/10.1007/s11517-012-0979-4
38. Kaufmann, P., Englehart, K., Platzner, M.: Fluctuating EMG signals: investigating long-term effects of pattern matching algorithms. In: Proceedings of 2010 Annual International Conference of the IEEE Engineering in Medicine and Biology, pp. 6357–6360 (2010). https://doi.org/10.1109/IEMBS.2010.5627288
39. Kaufmann, P., Glette, K., Gruber, T., Platzner, M., Torresen, J., Sick, B.: Classification of electromyographic signals: comparing evolvable hardware to conventional classifiers. IEEE Trans. Evol. Comput. **17**(1), 46–63 (2013). https://doi.org/10.1109/TEVC.2012.2185845
40. Khezri, M., Jahed, M.: Surface electromyogram signal estimation based on wavelet thresholding technique. In: Proceedings of 2008 30th Annual International Conference of the IEEE Engineering in Medicine and Biology Society, pp. 4752–4755 (2008). https://doi.org/10.1109/IEMBS.2008.4650275
41. Khushaba, R.N.: Correlation analysis of electromyogram signals for multiuser myoelectric interfaces. IEEE Trans. Neural Syst. Rehabil. Eng. **22**(4), 745–755 (2014). https://doi.org/10.1109/TNSRE.2014.2304470
42. Khushaba, R.N., Al-Timemy, A., Kodagoda, S.: Influence of multiple dynamic factors on the performance of myoelectric pattern recognition. In: Proceedings of 2015 37th Annual International Conference of the IEEE Engineering in Medicine and Biology Society (EMBC), pp. 1679–1682 (2015). https://doi.org/10.1109/EMBC.2015.7318699
43. Khushaba, R.N., Al-Timemy, A., Kodagoda, S., Nazarpour, K.: Combined influence of forearm orientation and muscular contraction on EMG pattern recognition. Expert Syst. Appl. **61**, 154–161 (2016). https://doi.org/10.1016/j.eswa.2016.05.031
44. Khushaba, R.N., Kodagoda, S., Liu, D., Dissanayake, G.: Muscle computer interfaces for driver distraction reduction. Comput. Methods Programs Biomed. **110**(2), 137–149 (2013). https://doi.org/10.1016/j.cmpb.2012.11.002
45. Khushaba, R.N., Shi, L., Kodagoda, S.: Time-dependent spectral features for limb position invariant myoelectric pattern recognition. In: Proceedings of 2012 International Symposium on Communications and Information Technologies (ISCIT), pp. 1015–1020 (2012). https://doi.org/10.1109/ISCIT.2012.6380840
46. Khushaba, R.N., Takruri, M., Miro, J.V., Kodagoda, S.: Towards limb position invariant myoelectric pattern recognition using time-dependent spectral features. Neural Netw. **55**, 42–58 (2014). https://doi.org/10.1016/j.neunet.2014.03.010
47. Kim, J., Cho, D., Lee, K.J., Lee, B.: A real-time pinch-to-zoom motion detection by means of a surface EMG-based human-computer interface. Sensors **15**(1), 394–407 (2015). https://doi.org/10.3390/s150100394

48. Kuiken, T.A., Miller, L.A., Lipschutz, R.D., Lock, B.A., Stubblefield, K., Marasco, P.D., Zhou, P., Dumanian, G.A.: Targeted reinnervation for enhanced prosthetic arm function in a woman with a proximal amputation: a case study. The Lancet **369**(9559), 371–380 (2007). https://doi.org/10.1016/S0140-6736(07)60193-7
49. Li, X., Fang, P., Tian, L., Li, G.: Increasing the robustness against force variation in EMG motion classification by common spatial patterns. In: Proceedings of 2017 39th Annual International Conference of the IEEE Engineering in Medicine and Biology Society (EMBC), pp. 406–409 (2017). https://doi.org/10.1109/EMBC.2017.8036848
50. Li, X., Xu, R., Samuel, O.W., Tian, L., Zou, H., Zhang, X., Chen, S., Fang, P., Li, G.: A new approach to mitigate the effect of force variation on pattern recognition for myoelectric control. In: Proceedings of 2016 38th Annual International Conference of the IEEE Engineering in Medicine and Biology Society (EMBC), pp. 1684–1687 (2016). https://doi.org/10.1109/EMBC.2016.7591039
51. Liu, J., Sheng, X., Zhang, D., He, J., Zhu, X.: Reduced daily recalibration of myoelectric prosthesis classifiers based on domain adaptation. IEEE J. Biomed. Health Inform. **20**(1), 166–176 (2016). https://doi.org/10.1109/JBHI.2014.2380454
52. Liu, J., Zhang, D., He, J., Zhu, X.: Effect of dynamic change of arm position on myoelectric pattern recognition. In: Proceedings of 2012 IEEE International Conference on Robotics and Biomimetics (ROBIO), pp. 1470–1475 (2012). https://doi.org/10.1109/ROBIO.2012.6491176
53. Liu, J., Zhang, D., Sheng, X., Zhu, X.: Quantification and solutions of arm movements effect on sEMG pattern recognition. Biomed. Signal Process. Control **13**, 189–197 (2014). https://doi.org/10.1016/j.bspc.2014.05.001
54. Liu, J., Zhang, D., Sheng, X., Zhu, X.: Enhanced robustness of myoelectric pattern recognition to across-day variation through invariant feature extraction. In: Proceedings of 2015 37th Annual International Conference of the IEEE Engineering in Medicine and Biology Society (EMBC), pp. 7262–7265 (2015). https://doi.org/10.1109/EMBC.2015.7320068
55. Luca, C.J.D., Gilmore, L.D., Kuznetsov, M., Roy, S.H.: Filtering the surface emg signal: movement artifact and baseline noise contamination. J. Biomech. **43**(8), 1573–1579 (2010). https://doi.org/10.1016/j.jbiomech.2010.01.027
56. Lv, B., Sheng, X., Guo, W., Zhu, X., Ding, H.: Towards finger gestures and force recognition based on wrist electromyography and accelerometers. In: Huang, Y., Wu, H., Liu, H., Yin, Z. (eds.) Intelligent Robotics and Applications, pp. 373–380. Springer International Publishing, Cham (2017)
57. Maier, J., Naber, A., Ortiz-Catalan, M.: Improved prosthetic control based on myoelectric pattern recognition via wavelet-based de-noising. IEEE Trans. Neural Syst. Rehabil. Eng. **26**(2), 506–514 (2018). https://doi.org/10.1109/TNSRE.2017.2771273
58. Matsubara, T., Morimoto, J.: Bilinear modeling of EMG signals to extract user-independent features for multiuser myoelectric interface. IEEE Trans. Biomed. Eng. **60**(8), 2205–2213 (2013). https://doi.org/10.1109/TBME.2013.2250502
59. McCool, P., Fraser, G.D., Chan, A.D.C., Petropoulakis, L., Soraghan, J.J.: Identification of contaminant type in surface electromyography (EMG) signals. IEEE Trans. Neural Syst. Rehabil. Eng. **22**(4), 774–783 (2014). https://doi.org/10.1109/TNSRE.2014.2299573
60. Milosevic, B., Farella, E., Benatti, S.: Exploring arm posture and temporal variability in myoelectric hand gesture recognition. In: Proceedings of 2018 7th IEEE International Conference on Biomedical Robotics and Biomechatronics (Biorob), pp. 1032–1037 (2018). https://doi.org/10.1109/BIOROB.2018.8487838
61. Ortolan, R.L., Mori, R.N., Pereira, R.R., Cabral, C.M.N., Pereira, J.C., Cliquet, A.: Evaluation of adaptive/nonadaptive filtering and wavelet transform techniques for noise reduction in EMG mobile acquisition equipment. IEEE Trans. Neural Syst. Rehabil. Eng. **11**(1), 60–69 (2003). https://doi.org/10.1109/TNSRE.2003.810432
62. Oskoei, M.A., Hu, H.: Myoelectric control systems—a survey. Biomed. Signal Process. Control **2**(4), 275–294 (2007). https://doi.org/10.1016/j.bspc.2007.07.009

63. Palermo, F., Cognolato, M., Gijsberts, A., Mller, H., Caputo, B., Atzori, M.: Repeatability of grasp recognition for robotic hand prosthesis control based on sEMG data. In: Proceedings of 2017 International Conference on Rehabilitation Robotics (ICORR), pp. 1154–1159 (2017). https://doi.org/10.1109/ICORR.2017.8009405
64. Phinyomark, A., Hu, H., Phukpattaranont, P., Limsakul, C.: Application of linear discriminant analysis in dimensionality reduction for hand motion classification. Meas. Sci. Rev. **12**(3), 82–89 (2012). https://doi.org/10.2478/v10048-012-0015-8
65. Phinyomark, A., Khushaba, R.N., Ibáñez-Marcelo, E., Patania, A., Scheme, E., Petri, G.: Navigating features: a topologically informed chart of electromyographic features space. J. R. Soc. Interface **14**(137) (2017). https://doi.org/10.1098/rsif.2017.0734
66. Phinyomark, A., Limsakul, C., Phukpattaranont, P.: EMG feature extraction for tolerance of white Gaussian noise. In: Proceedings of International Workshop and Symposium Science Technology, pp. 178–183 (2008)
67. Phinyomark, A., Limsakul, C., Phukpattaranont, P.: A comparative study of wavelet denoising for multifunction myoelectric control. In: Proceedings of 2009 International Conference on Computer and Automation Engineering, pp. 21–25 (2009). https://doi.org/10.1109/ICCAE.2009.57
68. Phinyomark, A., Limsakul, C., Phukpattaranont, P.: EMG denoising estimation based on adaptive wavelet thresholding for multifunction myoelectric control. In: Proceedings of 2009 Innovative Technologies in Intelligent Systems and Industrial Applications, pp. 171–176 (2009). https://doi.org/10.1109/CITISIA.2009.5224220
69. Phinyomark, A., Limsakul, C., Phukpattaranont, P.: EMG feature extraction for tolerance of 50 Hz interference. In: Proceedings of PSU-UNS International Conference on Engineering Technologies, pp. 289–293 (2009)
70. Phinyomark, A., Limsakul, C., Phukpattaranont, P.: A novel feature extraction for robust EMG pattern recognition. J. Comput. **1**(1), 71–80 (2009)
71. Phinyomark, A., Limsakul, C., Phukpattaranont, P.: An optimal wavelet function based on wavelet denoising for multifunction myoelectric control. In: Proceedings of 2009 6th International Conference on Electrical Engineering/Electronics, Computer, Telecommunications and Information Technology, vol. 02, pp. 1098–1101 (2009). https://doi.org/10.1109/ECTICON.2009.5137236
72. Phinyomark, A., Limsakul, C., Phukpattaranont, P.: EMG signal estimation based on adaptive wavelet shrinkage for multifunction myoelectric control. In: Proceedings of 2010 7th International Conference on Electrical Engineering/Electronics, Computer, Telecommunications and Information Technology, pp. 322–326 (2010)
73. Phinyomark, A., Limsakul, C., Phukpattaranont, P.: Optimal wavelet functions in wavelet denoising for multifunction myoelectric control. ECTI Trans. Electr. Eng. Electron. Commun. **8**(1), 43–52 (2010)
74. Phinyomark, A., Limsakul, C., Phukpattaranont, P.: Application of wavelet analysis in EMG feature extraction for pattern classification. Meas. Sci. Rev. **11**(2), 45–52 (2011). https://doi.org/10.2478/v10048-011-0009-y
75. Phinyomark, A., Khushaba, R.N., Scheme, E.: Feature extraction and selection for myoelectric control based on wearable EMG sensors. Sensors **18**(5), 1615 (2018). https://doi.org/10.3390/s18051615
76. Phinyomark, A., Nuidod, A., Phukpattaranont, P., Limsakul, C.: Feature extraction and reduction of wavelet transform coefficients for EMG pattern classification. Elektron. Elektrotech. **122**(6) (2012). https://doi.org/10.5755/j01.eee.122.6.1816
77. Phinyomark, A., Phothisonothai, M., Phukpattaranont, P., Limsakul, C.: Critical exponent analysis applied to surface EMG signals for gesture recognition. Metrol. Meas. Syst. **18**(4), 645–658 (2011)
78. Phinyomark, A., Phukpattaranont, P., Limsakul, C.: EMG signal denoising via adaptive wavelet shrinkage for multifunction upper-limb prosthesis. In: Proceedings of 3rd Biomedical Engineering International Conference, pp. 35–41 (2010)

79. Phinyomark, A., Phukpattaranont, P., Limsakul, C.: A review of control methods for electric power wheelchairs based on electromyography signals with special emphasis on pattern recognition. IETE Techn. Rev. **28**(4), 316–326 (2011). https://doi.org/10.4103/0256-4602.83552
80. Phinyomark, A., Phukpattaranont, P., Limsakul, C.: Wavelet-based denoising algorithm for robust EMG pattern recognition. Fluct. Noise Lett. **10**(2), 157–167 (2011). https://doi.org/10.1142/S0219477511000466
81. Phinyomark, A., Phukpattaranont, P., Limsakul, C.: Feature reduction and selection for EMG signal classification. Expert Syst. Appl. **39**(8), 7420–7431 (2012). https://doi.org/10.1016/j.eswa.2012.01.102
82. Phinyomark, A., Phukpattaranont, P., Limsakul, C.: Fractal analysis features for weak and single-channel upper-limb EMG signal. Expert Syst. Appl. **39**(12), 11156–11163 (2012). https://doi.org/10.1016/j.eswa.2012.03.039
83. Phinyomark, A., Phukpattaranont, P., Limsakul, C.: Investigating long-term effects of feature extraction methods for continuous EMG pattern classification. Fluct. Noise Lett. **11**(4), 1250,028 (2012). https://doi.org/10.1142/S0219477512500289
84. Phinyomark, A., Phukpattaranont, P., Limsakul, C.: The usefulness of wavelet transform to reduce noise in the SEMG signal. In: Schwartz, M. (ed.) EMG Methods for Evaluating Muscle and Nerve Function, chap. 7. IntechOpen, Rijeka (2012). https://doi.org/10.5772/25757
85. Phinyomark, A., Phukpattaranont, P., Limsakul, C.: Applications of variance fractal dimension: a survey. Fractals **22**(01n02), 1450,003 (2014). https://doi.org/10.1142/S0218348X14500030
86. Phinyomark, A., Phukpattaranont, P., Limsakul, C., Phothisonothai, M.: Electromyography (EMG) signal classification based on detrended fluctuation analysis. Fluct. Noise Lett. **10**(3), 281–301 (2011). https://doi.org/10.1142/S0219477511000570
87. Phinyomark, A., Quaine, F., Charbonnier, S., Serviere, C., Tarpin-Bernard, F., Laurillau, Y.: EMG feature evaluation for improving myoelectric pattern recognition robustness. Expert Syst. Appl. **40**(12), 4832–4840 (2013). https://doi.org/10.1016/j.eswa.2013.02.023
88. Phinyomark, A., Quaine, F., Charbonnier, S., Serviere, C., Tarpin-Bernard, F., Laurillau, Y.: A feasibility study on the use of anthropometric variables to make musclecomputer interface more practical. Eng. Appl. Artif. Intell. **26**(7), 1681–1688 (2013). https://doi.org/10.1016/j.engappai.2013.01.004
89. Phinyomark, A., Quaine, F., Charbonnier, S., Serviere, C., Tarpin-Bernard, F., Laurillau, Y.: Feature extraction of the first difference of EMG time series for EMG pattern recognition. Comput. Methods Programs Biomed. **117**(2), 247–256 (2014). https://doi.org/10.1016/j.cmpb.2014.06.013
90. Phinyomark, A., Quaine, F., Laurillau, Y.: The relationship between anthropometric variables and features of electromyography signal for humancomputer interface. In: Naik, G. (ed.) Applications, Challenges, and Advancements in Electromyography Signal Processing, chap. 15. IGI Global, Hershey, PA (2014). https://doi.org/10.4018/978-1-4666-6090-8.ch015
91. Phinyomark, A., Quaine, F., Laurillau, Y., Thongpanja, S., Limsakul, C., Phukpattaranont, P.: EMG amplitude estimators based on probability distribution for muscle-computer interface. Fluct. Noise Lett. **12**(3), 1350,016 (2013). https://doi.org/10.1142/S0219477513500168
92. Phinyomark, A., Scheme, E.: EMG pattern recognition in the era of big data and deep learning. Big Data Cogn. Comput. **2**(3), 21 (2018). https://doi.org/10.3390/bdcc2030021
93. Phinyomark, A., Scheme, E.: A feature extraction issue for myoelectric control based on wearable EMG sensors. In: Proceedings of 2018 IEEE Sensors Applications Symposium (SAS), pp. 1–6 (2018). https://doi.org/10.1109/SAS.2018.8336753
94. Powar, O.S., Chemmangat, K., Figarado, S.: A novel pre-processing procedure for enhanced feature extraction and characterization of electromyogram signals. Biomed. Signal Process. Control **42**, 277–286 (2018). https://doi.org/10.1016/j.bspc.2018.02.006
95. Radmand, A., Scheme, E., Englehart, K.: On the suitability of integrating accelerometry data with electromyography signals for resolving the effect of changes in limb position during dynamic limb movement. J. Prosthet. Orthot. **26**(4), 185–193 (2014). https://doi.org/10.1097/JPO.0000000000000041

96. Reaz, M.B.I., Hussain, M.S., Mohd-Yasin, F.: Techniques of EMG signal analysis: detection, processing, classification and applications. Biol. Proced. Online **8**(1), 11–35 (2006). https://doi.org/10.1251/bpo115
97. Zia ur Rehman, M., Waris, A., Gilani, S.O., Jochumsen, M., Niazi, I.K., Jamil, M., Farina, D., Kamavuako, E.N.: Multiday EMG-based classification of hand motions with deep learning techniques. Sensors **18**(8), 2497 (2018). https://doi.org/10.3390/s18082497
98. Saponas, T.S., Tan, D.S., Morris, D., Balakrishnan, R.: Demonstrating the feasibility of using forearm electromyography for muscle-computer interfaces. In: Proceedings of the SIGCHI Conference on Human Factors in Computing Systems, CHI '08, pp. 515–524. ACM, New York, NY, USA (2008). https://doi.org/10.1145/1357054.1357138
99. Saponas, T.S., Tan, D.S., Morris, D., Balakrishnan, R., Turner, J., Landay, J.A.: Enabling always-available input with muscle-computer interfaces. In: Proceedings of 22nd Annual ACM Symposium on User Interface Software and Technology, UIST '09, pp. 167–176. ACM, New York, NY, USA (2009). https://doi.org/10.1145/1622176.1622208
100. Saponas, T.S., Tan, D.S., Morris, D., Turner, J., Landay, J.A.: Making muscle-computer interfaces more practical. In: Proceedings of the SIGCHI Conference on Human Factors in Computing Systems, CHI '10, pp. 851–854. ACM, New York, NY, USA (2010). https://doi.org/10.1145/1753326.1753451
101. Scheme, E., Biron, K., Englehart, K.: Improving myoelectric pattern recognition positional robustness using advanced training protocols. In: Proceedings of 2011 Annual International Conference of the IEEE Engineering in Medicine and Biology Society, pp. 4828–4831 (2011)
102. Scheme, E., Englehart, K.: Electromyogram pattern recognition for control of powered upper-limb prostheses: state of the art and challenges for clinical use. J. Rehabil. Res. Dev. **48**(6), 643–660 (2011). https://doi.org/10.1682/JRRD.2010.09.0177
103. Scheme, E., Englehart, K.: Training strategies for mitigating the effect of proportional control on classification in pattern recognition based myoelectric control. J. Prosthet. Orthot. **25**(2), 76–83 (2013). https://doi.org/10.1097/JPO.0b013e318289950b
104. Scheme, E., Fougner, A., Stavdahl, Ø., Chan, A.D.C., Englehart, K.: Examining the adverse effects of limb position on pattern recognition based myoelectric control. In: Proceedings of 2010 Annual International Conference of the IEEE Engineering in Medicine and Biology, pp. 6337–6340 (2010). https://doi.org/10.1109/IEMBS.2010.5627638
105. Scheme, E., Lock, B., Hargrove, L., Hill, W., Kuruganti, U., Englehart, K.: Motion normalized proportional control for improved pattern recognition-based myoelectric control. IEEE Trans. Neural Syst. Rehabil. Eng. **22**(1), 149–157 (2014). https://doi.org/10.1109/TNSRE.2013.2247421
106. Tabor, A., Bateman, S., Scheme, E.: Evaluation of myoelectric control learning using multi-session game-based training. IEEE Trans. Neural Syst. Rehabil. Eng. **26**(9), 1680–1689 (2018). https://doi.org/10.1109/TNSRE.2018.2855561
107. Theou, O., Edwards, D., Jones, G.R., Jakobi, J.M.: Age-related increase in electromyography burst activity in males and females. J. Aging Res. **2013**, 720,246 (2013). https://doi.org/10.1155/2013/720246
108. Thongpanja, S., Phinyomark, A., Hu, H., Limsakul, C., Phukpattaranont, P.: The effects of the force of contraction and elbow joint angle on mean and median frequency analysis for muscle fatigue evaluation. ScienceAsia **41**(4), 263–272 (2015). https://doi.org/10.2306/scienceasia1513-1874.2015.41.263
109. Thongpanja, S., Phinyomark, A., Quaine, F., Laurillau, Y., Limsakul, C., Phukpattaranont, P.: Probability density functions of stationary surface EMG signals in noisy environments. IEEE Trans. Instrum. Meas. **65**(7), 1547–1557 (2016). https://doi.org/10.1109/TIM.2016.2534378
110. Tkach, D., Huang, H., Kuiken, T.A.: Study of stability of time-domain features for electromyographic pattern recognition. J. Neuroeng. Rehabil. **7**(1), 21 (2010). https://doi.org/10.1186/1743-0003-7-21
111. Vidovic, M.M., Hwang, H., Amsss, S., Hahne, J.M., Farina, D., Mller, K.: Improving the robustness of myoelectric pattern recognition for upper limb prostheses by covariate shift adaptation. IEEE Trans. Neural Syst. Rehabil. Eng. **24**(9), 961–970 (2016). https://doi.org/10.1109/TNSRE.2015.2492619

112. Waris, A., Niazi, I.K., Jamil, M., Englehart, K., Jensen, W., Kamavuako, E.N.: Multiday evaluation of techniques for EMG based classification of hand motions. IEEE J. Biomed. Health Inform. 1–1 (2018). https://doi.org/10.1109/JBHI.2018.2864335
113. Waris, A., Niazi, I.K., Jamil, M., Gilani, O., Englehart, K., Jensen, W., Shafique, M., Kamavuako, E.N.: The effect of time on EMG classification of hand motions in able-bodied and transradial amputees. J. Electromyogr. Kinesiol. **40**, 72–80 (2018). https://doi.org/10.1016/j.jelekin.2018.04.004
114. Xiang, C., Lantz, V., Kong-Qiao, W., Zhang-Yan, Z., Xu, Z., Ji-Hai, Y.: Feasibility of building robust surface electromyography-based hand gesture interfaces. In: Proceedings of 2009 Annual International Conference of the IEEE Engineering in Medicine and Biology Society, pp. 2983–2986 (2009). https://doi.org/10.1109/IEMBS.2009.5332524
115. Yang, D., Yang, W., Huang, Q., Liu, H.: Classification of multiple finger motions during dynamic upper limb movements. IEEE J. Biomed. Health Inform. **21**(1), 134–141 (2017). https://doi.org/10.1109/JBHI.2015.2490718
116. Yu, Y., Sheng, X., Guo, W., Zhu, X.: Attenuating the impact of limb position on surface EMG pattern recognition using a mixed-LDA classifier. In: Proceedings of 2017 IEEE International Conference on Robotics and Biomimetics (ROBIO), pp. 1497–1502 (2017). https://doi.org/10.1109/ROBIO.2017.8324629
117. Zardoshti-Kermani, M., Wheeler, B.C., Badie, K., Hashemi, R.M.: EMG feature evaluation for movement control of upper extremity prostheses. IEEE Trans. Rehabil. Eng. **3**(4), 324–333 (1995). https://doi.org/10.1109/86.481972
118. Zhai, X., Jelfs, B., Chan, R.H.M., Tin, C.: Self-recalibrating surface EMG pattern recognition for neuroprosthesis control based on convolutional neural network. Front. Neurosci. **11**, 379 (2017). https://doi.org/10.3389/fnins.2017.00379
119. Zhang, H., Zhao, Y., Yao, F., Xu, L., Shang, P., Li, G.: An adaptation strategy of using LDA classifier for EMG pattern recognition. In: Proceedings of 2013 35th Annual International Conference of the IEEE Engineering in Medicine and Biology Society (EMBC), pp. 4267–4270 (2013). https://doi.org/10.1109/EMBC.2013.6610488
120. Zhang, X., Chen, X., Zhao, Z., Li, Q., Yang, J., Lantz, V., Wang, K.: An adaptive feature extractor for gesture SEMG recognition. In: Zhang, D. (ed.) Medical Biometrics, pp. 83–90. Springer, Berlin, Heidelberg (2007)
121. Zhou, P., Lock, B., Kuiken, T.A.: Real time ECG artifact removal for myoelectric prosthesis control. Physiol. Meas. **28**(4), 397 (2007)

Estimation of Ankle Joint Torque and Angle Based on S-EMG Signal for Assistive Rehabilitation Robots

Palayil Baby Jephil, Paras Acharaya, Lian Xu, Kairui Guo, Hairong Yu, Mark Watsford, Song Rong and Steven Su

Abstract Surface Electromyography (S-EMG) has shown the advantages of robotic rehabilitation. Robotic rehabilitation can be significantly improved if the intended body movement of the patients can be well identified. In this chapter, we first use the SVM classifier to identify the intended motion patterns, which are plantarflexion and dorsiflexion, by using three wireless EMG sensors placed at the tibialis anterior, gastrocnemius lateralis and gastrocnemius medialis muscles. To estimate the ankle joint torque as well as the joint angle for both plantarflexion and dorsiflexion, this chapter also develops nonlinear mathematical models for joint torque estimation and utilises Swarm Techniques to identify model parameters for each movement pattern of the ankle. During rehabilitation, once the intended motion is recognised, the activation functions extracted from an individual associated EMG channel can be

P. Baby Jephil · P. Acharaya · L. Xu · K. Guo · H. Yu · S. Su (✉)
School of Biomedical Engineering, Faculty of Engineering and IT, University of Technology Sydney, Ultimo, Australia
e-mail: Steven.Su@uts.edu.au

P. Baby Jephil
e-mail: Jephil.B.palayil@student.uts.edu.au

P. Acharaya
e-mail: Paras.Acharya@student.uts.edu.au

L. Xu
e-mail: Xu.Lian@uts.edu.au

K. Guo
e-mail: Kairui.Guo@student.uts.edu.au

H. Yu
e-mail: Hairong.Yu@student.uts.edu.au

M. Watsford
Department of Sports and Exercise Science, Faculty of Health, University of Technology Sydney, Ultimo, Australia
e-mail: Mark.Watsford@uts.edu.au

S. Rong
School of Biomedical Engineering, Sun Yat-sen University, Guangzhou 510006, China
e-mail: songrong@mail.sysu.edu.cn

G. Naik (ed.), *Biomedical Signal Processing*, Series in BioEngineering,
https://doi.org/10.1007/978-981-13-9097-5_2

used to estimate both the torque and angle by using the established nonlinear models. Experimental results demonstrated the effectiveness of the proposed approach.

Keywords Ankle rehabilitation · Particle swarm optimization · Machine learning

1 Introduction

The human ankle joint is a complex structure, an articulation formed between the talus and the tibia [43], which provides dynamic linkage allowing interaction of the lower limb with the ground. Despite the constant high compressive and shear forces experienced during the gait cycle, the ankle joint is considered to be less susceptible to the degenerative process compared to the hip or knee joint [6]. A systematic review by Fong et al. also shows that the ankle is the most common site of injuries in 24 of 70 sports studied [12]. Additionally, apart from common sprain and fractures, diseases and conditions like osteoarthritis, peripheral nervous compression, peripheral nerve trauma, peripheral neuropathy, cerebrovascular accident, and spinal cord injuries can also result in ankle dysfunction or disability [2].

The conventional ankle rehabilitation methods are hands-on physiotherapy techniques-joint mobilisation, joint manipulation, muscle stretching, neurodynamic, massages, and soft tissue techniques and physiotherapy instrument mobilisation [22]. These hands-on techniques have exposed several disadvantages and limitations, as the integration of external factors (patient position, table height and so on) and internal factors (generated motion and force of practitioner arms and forearms and so on) may be significantly different than for those of similar or higher stature than their patients. The ability to generate adequately controlled force, acceleration and displacement from the practitioner's upper extremities, particularly the hands, to facilitate therapeutic benefit in the patient may require proportionally more exertion and effort and may exceed, in some cases, the practitioner's capacity when the patient's size presents a physical challenge. To overcome these problems, researchers are trying to optimise rehabilitation procedures by using automated robots. Many mechanical devices incorporated with sensors and actuators are increasing surfacing to help physiotherapists and other medical professionals with the rehabilitation process [40]. Also, studies have demonstrated some level of success in various robotic control strategies such as impedance control [47], adaptive control [3], and challenge-based haptic simulation [4]. However, the responses for each control method differ with different impairments. The most effective control strategy for specific ankle disability has not been explicitly addressed.

Furthermore, studies [10, 33, 34] have revealed that rehabilitation robots operating on multiple bio signal sources have a high potential in improving diagnostics and physiotherapy outcome. Using physiological signals offers the advantage over

traditional physiotherapy, which increases the preciseness of the support, as well as minimises the changes between movement repetitions. It also provides quantitative measures of the patient's recovery state after an injury [47].

Estimating how the forces are dissipated to the articulating surfaces is the first step of understanding the joint mechanics, their functions, and related injuries and diseases. Several dynamic models have been developed to estimate the forces (internal and external) applied to a joint. However, it is far more difficult to determine given the uncertain nature of the joint [20, 25]. Muscle forces cannot be determined based on objective function alone, as it cannot account for individual muscle activation patterns. For the past several years, biomechanical models such as the Hill-based muscle model were developed to represent a mathematical model of muscle mechanics [11, 35], and its use is still ongoing and very relevant in the present context as well [36]. However, electromyography (EMG), in conjunction with an appropriate anatomical model, is considered to be the most prominent solution [7, 15, 20]. McGill et al. 1995 and Lyod and Buchanan 1996 were the early applicants of EMG signal in conjunction with an appropriate anatomical model to estimate forces produced in each muscle [8, 21]. In recent years, several biomechanical models, such as Hill-based muscle model was developed to represent a mathematical model of muscle mechanics [5, 42], which dramatically increases the estimation error as the EMG signal varies from one individual to another.

Since developing robotic assistive devices requires a multidisciplinary approach, techniques from various backgrounds such as software engineering, control engineering and mechanical engineering have been applied to improve the design. In recent years, machine learning algorithms are implemented to provide a better strategy for patients during and after the treatment [1]. As Table 1 shows, for the last decade, researchers have investigated different optimisation techniques like Genetic Algorithm, Simulated Annealing, Levenberg Marquardt and Particle Swarm Optimization. These methods are used to establish the non-linear mathematical models and create the relationship between ankle torque/force and s-EMG [27, 28, 39].

This chapter presents a design of an assistive ankle rehabilitation robot based on the EMG signal that predicts the joint forces (torque and angle) based on the EMG signal using a minimum number of constraints using SVM classification combined with particle swarm optimisation for intention detection and prediction of required angle and torque.

2 Methodology

2.1 Overview

The model designed investigates two motions, namely, ankle plantarflexion and ankle dorsiflexion. S-EMG signal was acquired from three muscles specifically- tibialis anterior, lateral, and medial gastrocnemius are used as the input of the system.

Table 2.1 Studies related to rehabilitation using EMG signals and machine learning

Authors	Application	Algorithm	Results
Liu and Young [17, 18]	Modelling: EMG-movements	The adaptive neuro-fuzzy inference system	The accuracy of 97, 99, 87.9 and 81.8% for four subjects for upper arm EMG signal and corresponding movement
Rahatabad et al. [26]	Modelling: EMG-force	Genetic Algorithm + Fuzzy Logic	Reduced root mean square error to 12.4% of Hill-based muscle model
Allard et al. [9]	Robotic arm guidance	Convolution Neural Network	97.9% accuracy with 18 subjects performing 7 gestures
Zhai et al. [46]	Neuroprosthesis control	Convolution Neural Network	10.8 and 2.99% increase in classification accuracy in intact (50 movement type) and amputee (10 movement type) with consistent higher absolute performance
Xia et al. [44]	Limb movement estimation	Convolution Neural Network + Recurrent Neural Network	The 3D trajectory estimation was best using Recurrent Neural Network for all eight healthy subjects used compared to support vector regression and Convolution Neural Network alone

The model is designed in such a way that it can be easily tailored for any joint and any individual with given appropriate anatomical and physiological data overcoming the discomforts experienced with the current techniques such as calibration process and the complexity of sensor placement which is achieved by machine learning, optimisation techniques, and decreased sensor numbers. The first stage of the system is the intent classification that provides empirical data for the selection of the appropriate model, decreasing the execution and processing time, thereby making the system more robust and adaptive. Classification of the patient's intent is done by implementing a machine learning algorithm, Support Vector Machine (SVM). The acquired s-EMG following the classification is converted to muscle activation which is then fed into different non-linear mathematical models whose outputs are

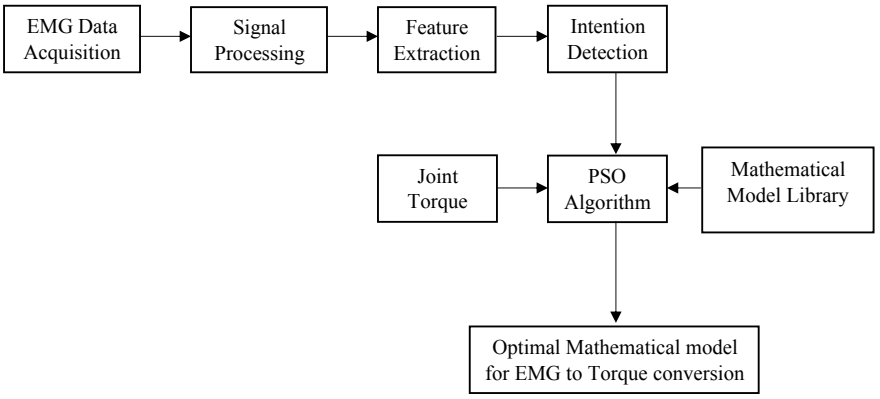

Fig. 1 System overview

respective torque value at that instance of time. The system chooses from two different sets of mathematical models depending on the intent of the user. Particle swarm optimisation is used, to optimise the mathematical models by iteratively improving the solutions within the confined boundary of the search space.

The overall idea and the overview is shown in Fig. 1.

2.2 Intention Detection

Before estimating the joint torque and angle, it is necessary to understand the intended direction in which the patient wants to move the ankle. To detect the intended direction, EMG data is acquired on three muscles location selected which are tibialis anterior, lateral, and medial gastrocnemius. Based on the literature [29, 31, 37] four features are selected to train the data. All the features are extracted using an overlapping hamming window. The four features are mean absolute value (MAV), waveform length (WL), root mean square (RMS) and Integrated EMG (IEMG)

- Mean absolute value (MAV) is taken for the amplitude of the EMG signal. It is used as an onset to detect muscle activity and is defined as:

$$MAV = \frac{1}{N}\sum_{n=1}^{N} x_n$$

where,

N is the total sample size and
x_n is the acquired EMG signal.

- Waveform length (WL) is the length of the waveform over a specified period. The equation of (WL) is defined as:

$$WL = \sum_{n=1}^{N-1} |x_{n+1} - x_n|$$

where,

N is the total sample size,
x_{n+1} is the following EMG signal and
x_n is the acquired EMG signal.

- Root Mean Square (RMS) is similar to standard deviation and is expressed as:

$$\text{RMS} = \sqrt{\frac{1}{N} \sum_{n=1}^{N} x_n^2}$$

where,

N is the total sample size
x_n is the acquired EMG signal.

Integrated EMG (IEMG) is the summation of the absolute value of the amplitude of the EMG signal, and it is defined as:

$$IMEG = \sum_{n=1}^{N} |x_n|$$

where,

N is the total sample size and
x_n is the acquired EMG signal.

Once the features are extracted from all the channels, these features are combined to form a vector Z = [MAV, WL, RMS, IEMG]. The data was collected from four healthy males between the age group 20–25 during dorsiflexion, plantarflexion, and at rest using DELSYS wireless system placed at tibialis anterior, lateral and medial gastrocnemius. The extracted features were trained and classified using multiclass SVM. SVM seeks to find the optimal separating hyperplane between classes by following the maximised margin criterion [38]. One-Versus-One Approach was used in this project to classify the data using a radial basis function using MATLAB toolbox. After the intention of the patient is detected, the next stage is to determine the torque and angle of the ankle for the intended movement.

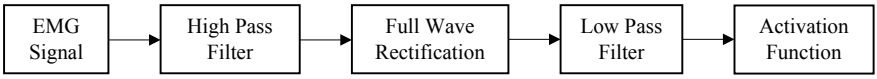

Fig. 2 s-EMG signal processing

2.3 Estimation of Joint Ankle Torque

To estimate ankle joint torque, the EMG signal is firstly pre-processed using a high-pass filter to remove motion artefacts and rectified so that the envelope of the EMG signal can be considered to be a net neural drive to the muscle. It is then filtered using a low pass filter to smoothen the envelope, which gives the corresponding activation dynamics. Next, the pre-processed EMG signal is converted to an activation function which is explained in the next session of the paper. Figure 2 shows the process of extracting the activation function.

2.3.1 EMG to Activation Function

The activation function represents the elemental muscle activation dynamics. Activation dynamics correspond to the transformation of neural excitation to the activation of the contractile apparatus, which is a specialised structure for contraction consisting of the sarcomere [45]. The activation function is used to describe the linear or non-linear relationship between EMG and force and the activation equation in this paper is proposed by [20, 21]:

$$a_j(t) = \frac{e^{Au_j(t)} - 1}{e^A - 1}$$

where,

$a_j(t)$ is the activation of muscle j
$u_j(t)$ is the post-processed EMG of muscle j at time t
A is the non-linear shape factor constraint to $-3 < \mathrm{A}_j < 0$.

Additionally, Ruijven and Weijus 1990, Guimaraes et al. 1995 and Herzog et al. 1998 showed a poor prediction alone from the rectified EMG signal and had a shorter duration than the resulting force. However, their study has suggested the addition of muscle twitch to the activation function can give a better prediction of the muscle forces [13, 14, 41]. Miler brown et al. 1973 and Rabiner and Gold 1975 have suggested that a critically damped linear second-order discrete linear model can be used to represent muscle twitches and which can be expressed in the discrete form by using backward difference [24, 30]. D. G. Lloyd and T. F. Beiser 2003 have used a second order discrete linear model to model muscle excitation from the activation function in the form of a recursive filter given by [20]:

$$u_j(t) = \alpha e_j(t-d) - \beta_1 u_j(t-1) - \beta_2 u_j(t-2)$$

where,

$e_j(t)$ is the pre-processed EMG of muscle j at time t
$u_j(t)$ is the post-processed EMG of muscle j at time t
α is the gain coefficient for muscle j
β is the recursive coefficients for the muscle j
d is the electromechanical delay

where,

$\beta 1 = C1 + C2$,
$\beta 2 = C1 \cdot C2$.

Such that |C1| < 1 and |C2| < 1
And,
$\alpha - \beta_1 - \beta_2 = 1$; maintains a unit gain of the recursive filter.

Once the activation function of the EMG has been obtained, we input this signal to 3 sets of mathematical models for each movement. The best mathematical model that predicts the estimated torque would be selected using an algorithm called partial swarm optimisation (PSO).

2.3.2 Mathematical Model of EMG to Torque Conversion

The mathematical is based on the assumption that the relationship between the s-EMG signal and the joint torque is nonlinear [23]. Based on this assumption, three nonlinear equations for estimating the joint torque from the EMG signal are included. The nonlinear equations are based on previous similar studies [19, 39].

$$MM_1 = x_1 + x_2 \cdot \sqrt{u_i}$$

$$MM_2 = x_1 + x_2 \cdot sine(u_i)$$

$$MM_3 = x_1 \cdot u_i^{x_2} + x_3 \cdot u_i^{x_4}$$

where,

u_i Processed EMG data.
x_i as a random value parameter associated with the selected mathematical model.

2.3.3 Fitness Function

An objective function shown below is set as a fitness function-Sum of Squared Error (SSE). The function defined below is used to summarise how close the mathematical

model is for predicting the EMG signal. It also guides our algorithm towards an optimal solution.

$$SSE = \sum_{k=0}^{n} (Actual\ Torque - Predicted\ Torque)^2$$

where,

i	data samples.
Predicted torque	torque value estimated from a mathematical model.

An isokinetic dynamometer (Biodex System 4 New York, USA) was used to measure continuous ankle torque. The ankle joint is manually forced in the upward direction to record the highest torque value generated after the maximum position of the ankle joint during dorsiflexion was achieved. This was done to determine whether our mathematical model could achieve the maximum torque value with the recorded s-EMG signal.

2.3.4 Partial Swarm Optimization

Partial Swarm Optimization (PSO) is a metaheuristic computational method that iteratively improves the candidate solutions known and particles by continually moving them around in a defined search space based on mathematical equation defining the position of the candidate solution (particle) and its velocity at a certain point of time in that space. The advantage of using PSO over other optimisation technique is that it requires primitive mathematical operators making it computationally expensive regarding computational memory and storage [16], which makes it is convenient for real-time implementation. Additionally, PSO does not use the gradient of the problem is optimised, and it makes few or no assumptions about the problem being optimised [32]. With their exploration and exploitation algorithm, the particle of the swarm fly through the defined hyperspace and have two essential reasoning capabilities: their memory of their own best position—local best (lb) and knowledge of the global or their neighbourhood's best—global best (gb). The position of the particle is influenced by velocity. The position of the particle "i" in the search space at the time step; is denoted by $x_i(t)$ where denotes the discrete the time steps. The position of the particle is changed by adding a velocity, i.e., $v_i(t)$, to the current position;

$$x_i(t+1) = x_i(t) + v_i(t+1)$$

where,

$$v_i(t) = v_i(t-1) + c_1 r_1(lb(t) - x_i(t-1)) + c_2 r_2(gb(t) - x_i(t-1))$$

c_1 and c_2 acceleration coefficient.

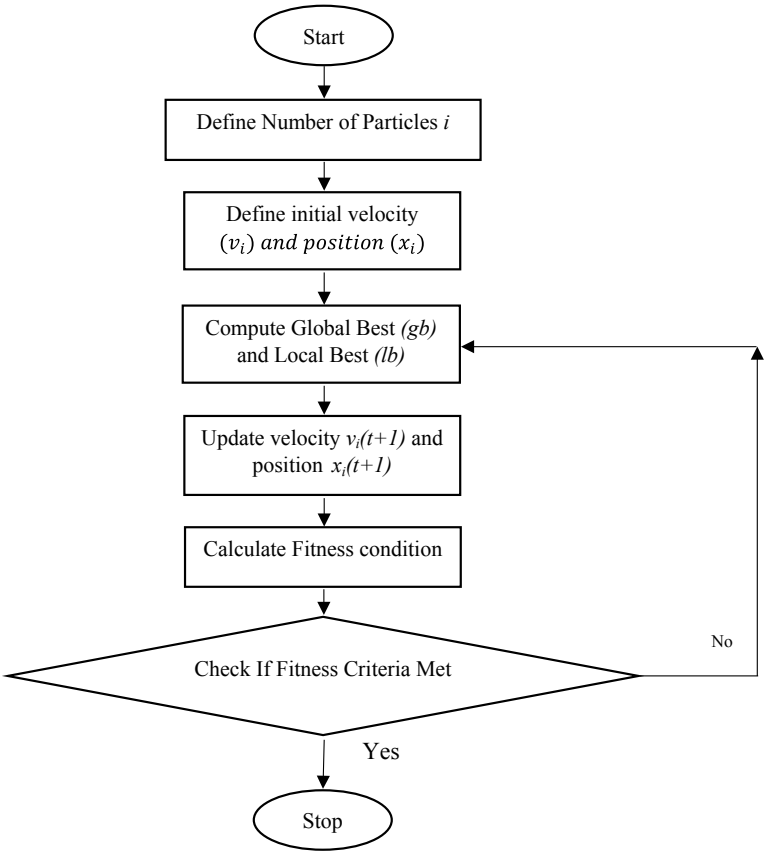

Fig. 3 PSO flowchart

r_1 and r_2 random vectors.

The flowchart of partial swarm optimisation is illustrated in Fig. 3.

Since two motions of the ankle joint: dorsiflexion and plantarflexion are considered, the mathematical models described above are divided into two categories one each for a particular motion. Each mathematical model is activated, depending on the output from the SVM. Consequently, if the intended movement is dorsiflexion first set of the determined mathematical model will be used whereas, if the intention is plantarflexion the second set of the determined mathematical model will be selected. Contrarily, if the patient is relaxed, the output torque will be zero (Fig. 4).

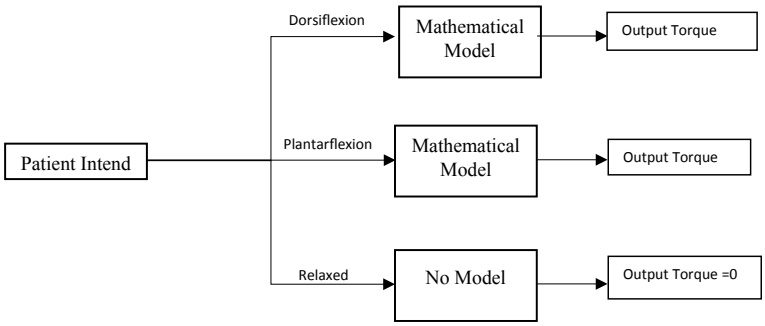

Fig. 4 System overview

2.4 Estimation of Ankle Joint Angle

For a continuous movement of the ankle joint, it is necessary to estimate the joint ankle. During dorsiflexion, the muscle activity is higher, and the corresponding joint torque and joint ankle are increased simultaneously. The same can be seen for plantar flexion as well as the joint torque, and the joint ankle is changed with the joint torque, and the joint can be assumed to be closely proportional to each other [48], and it is expressed as,

$$\theta_j = k\tau_i$$

where,

θ_j Estimated Joint Ankle Angle
τ_i Estimated Torque of Ankle Joint
k adjustable constant.

3 Results

Figure 5 shows the conversion of the s-EMG signal to the Activation function. As mentioned earlier, activation function helps in better prediction of forces due to the delay as s-EMG has a shorter duration than the resulting force.

The figures below show the estimated joint torque from the three mathematical models. The illustrated Fig. 6 depicts that the torque value predicted using the mathematical model almost accurately supersede the data collected via dynamometer during both planter and dorsiflexion. Additionally, the minor shifts in the graph are due to inconsistent sampling configuration of the EMG signal collected and dynamometer. In the future, we are planning to use the DELSYS system at lower sampling configuration to reduce the data points thereby increasing the processing

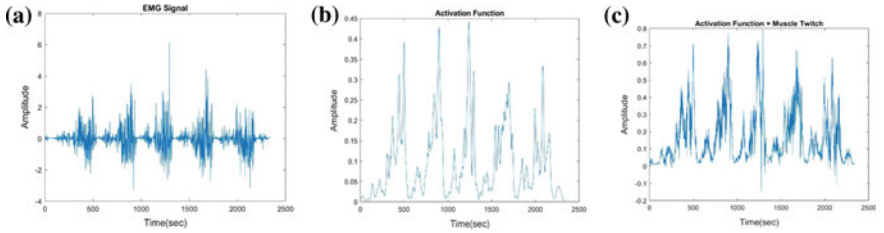

Fig. 5 EMG signal associated with dorsiflexion

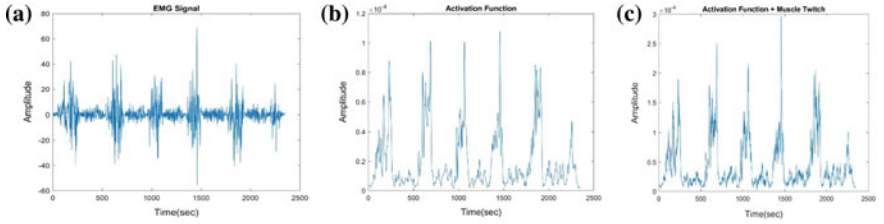

Fig. 6 EMG signal associated with plantarflexion

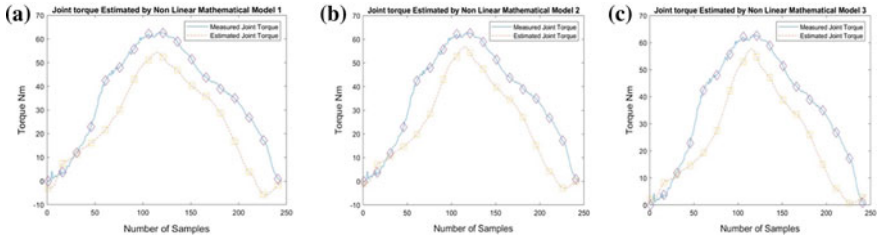

Fig. 7 Estimated and actual joint torque for dorsiflexion using the mathematical models

time and conversely, decreasing the number of iterations making the response time of the overall system accuracy. The error difference between the predicted and the measured torque was an average of 18% for dorsiflexion and an average of 27% for plantarflexion.

The second set of figures, i.e. Figs. 7 and 8 show the relationship between the predicted angle obtained using $\theta_j = k\tau_i$. The results show that the predicted angle follows the measured angle more explicitly compared to the predicted torque. An average error percentage of only *8%* was observed between the predicted angle and measured angle during dorsiflexion. However, *a 14%* average error was calculated for dorsiflexion (Figs. 9 and 10).

The table below shows the stat for each mathematical model. The execution time for both dorsiflexion and plantarflexion is increased with XN, where N = 1, 2, 3 and 4 are the variables linked with each mathematical model. Mathematical model 2 with X1 = −1.59E+1 and X2 = 3.52E+3 for dorsiflexion and X1 = −1.23E+1

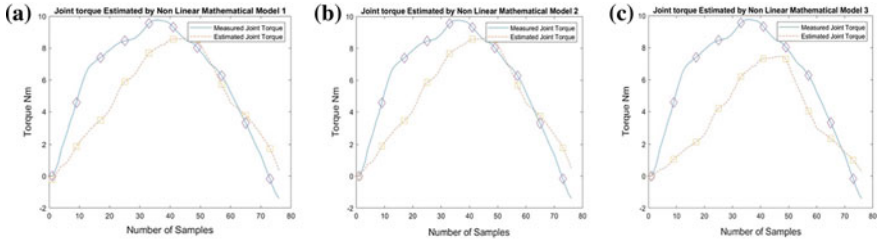

Fig. 8 Estimated and actual joint torque for plantarflexion using the mathematical models

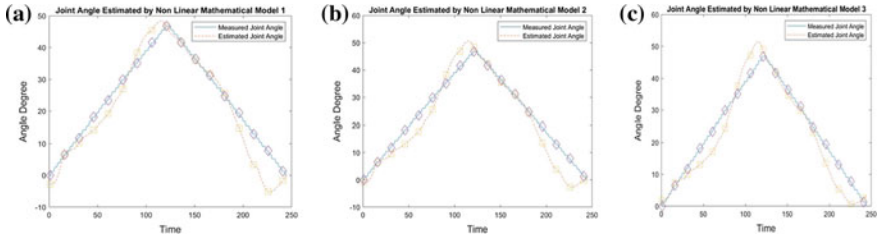

Fig. 9 Estimated and actual ankle torque for plantarflexion using the mathematical models

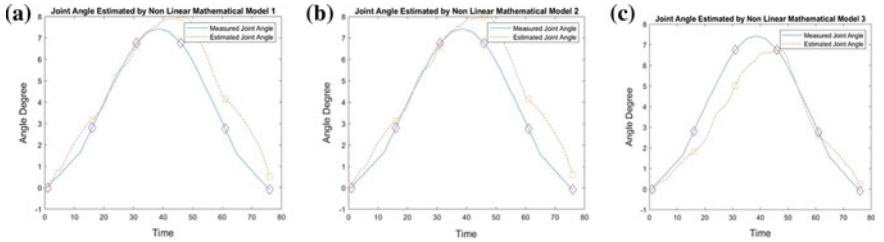

Fig. 10 Estimated and actual ankle torque for plantarflexion using the mathematical models

and X2 = 3.64E+1 for plantarflexion has the least execution time of 0.4741 ms and 0.2798 ms for dorsiflexion and plantarflexion, respectively. However, the variable size and number of iterations seem independent of each other as mathematical model 1 for dorsiflexion has the maximum number of iterations:205 with only two variables compared to mathematical model 4 whose number of iterations is only 190 with four variables. The same can be seen for plantarflexion as mathematical model 1 has the maximum number of iterations with two variables, i.e., 387 and mathematical model 3 with four variables has the least number of iterations of 158.

The results indicate that by integrating PSO and SVM classification, both joint ankle torque and angle can be accurately predicted. The proposed approach can significantly reduce the number of different types of sensors, which has great potential to provide a more straightforward and efficient rehabilitation solution. Table 2 also presents that the selected mathematical models for dorsiflexion may require some

Table 2 Results of Mathematical models used

Dorsiflexion			Plantarflexion		
Mathematical model 1 $MM_1 = X_1 + X_2 \cdot \sqrt{U_i}$	X1	−6.47E+01	Mathematical model 1	X1	−2.69E+01
	X2	8.43E+02		X2	4.54E+01
	Number of iteration	205		Number of iteration	387
	Execution time (s)	0.5437		Execution time (s)	0.3868
Mathematical model 2 $MM_2 = X_1 + X_2 \cdot sine(U_i)$	X1	−1.59E+01	Mathematical model 2	X1	−1.23E+01
	X2	3.52E+03		X2	3.64E+01
	Number of iteration	158		Number of iteration	273
	Execution time (s)	0.4741		Execution time (s)	0.2798
Mathematical model 3 $MM_3 = X_1 \cdot U_i^{X_2} + X_3 \cdot U_i^{X_4}$	X1	9.94E+08	Mathematical model 3	X1	−2.23E+11
	X2	1.02E+09		X2	5.14E+11
	X3	1.32E+04		X3	2.98E+01
	X4	1.41E+00		X4	2.57E+00
	Number of iteration	190		Number of iteration	158
	Execution time (s)	1.9821		Execution time (s)	0.4741

adjustments for higher accuracy. Since the model is well established that the relationship between joint torque and S-EMG signal is non-linear [23], to include more non-linear equations using fewer variables shall be considered for future improvement.

4 Conclusion

The paper presents an EMG-based real-time estimation of ankle joint torque during plantarflexion and dorsiflexion. The real-time classification of the intention of the user using multi-class SVM added an extra layer of certainty is minimising the failure rate for the selection of a mathematical model, thereby reducing the processing and execution time. The selected mathematical model is based on the nonlinear relationship between s-EMG and joint torque. PSO based on common fitness function accurately solves the nonlinear equation.

For future works, the immediate step would be to convert the estimated joint torque into a joint angle. Many papers have suggested that the ankle joint and the

ankle torque has a linear equation. Furthermore, the main focus will be to implement the model real-time and to develop an algorithm that selects the best mathematical model based on the signal strength of the user in real-time with very few delays.

Since s-EMG signals are full of noise, we think that there should be a mechanism that stabilises the motor once the predetermined angle is reached. We are planning to use an in-house designed accelerometer with a Kalman filter that removes the jerky motion that was experienced when testing out the results with our EC motor.

Acknowledgements This work was supported by the Australia–China Joint Institute for Health Technology and Innovation established by the University of Technology Sydney (UTS) and Sun Yat-sen University (SYSU).

References

1. Argha, A., Savkin, A., Liaw, S.T., Celler, B.G.: Effect of seasonal variation on clinical outcome in patients with chronic conditions: analysis of the Commonwealth Scientific and Industrial Research Organization (CSIRO) National Telehealth Trial. JMIR Med. Inform. **6**(1), e16 (2018). https://doi.org/10.2196/medinform.9680
2. Baumhauer, J.F., Alosa, D.M., Renstrom, A.F., Trevino, S., Beynnon, B.: A prospective study of ankle injury risk factors. Am. J. Sports Med. **23**(5), 564–570 (1995). https://doi.org/10.1177/036354659502300508
3. Blaya, J.A., Herr, H.: Adaptive control of a variable-impedance ankle-foot orthosis to assist drop-foot gait. IEEE Trans. Neural Syst. Rehabil. Eng. **12**(1), 24–31 (2004). https://doi.org/10.1109/TNSRE.2003.823266
4. Boian, R.F., Deutsch, J.E., Chan Su, L., Burdea, G.C., Lewis, J.: Haptic effects for virtual reality-based post-stroke rehabilitation. In: Proceedings of 11th Symposium on Haptic Interfaces for Virtual Environment and Teleoperator Systems. HAPTICS 2003, 22–23 Mar 2003, pp. 247–253 (2003). https://doi.org/10.1109/haptic.2003.1191289
5. Borst, J., Forbes, P.A., Happee, R., Veeger, D.H.: Muscle parameters for musculoskeletal modelling of the human neck. Clin. Biomech. (Bristol, Avon) **26**(4), 343–351 (2011). https://doi.org/10.1016/j.clinbiomech.2010.11.019
6. Brockett, C.L., Chapman, G.J.: Biomechanics of the ankle. Orthop. Trauma **30**(3), 232–238 (2016). https://doi.org/10.1016/j.mporth.2016.04.015
7. Buchanan, T.S., Lloyd, D.G., Manal, K., Besier, T.F.: Neuromusculoskeletal modeling: estimation of muscle forces and joint moments and movements from measurements of neural command. J. Appl. Biomech. **20**(4), 367–395 (2004)
8. Cholewicki, J., McGill, S.M., Norman, R.W.: Comparison of muscle forces and joint load from an optimization and EMG assisted lumbar spine model: towards development of a hybrid approach. J. Biomech. **28**(3), 321–331 (1995). https://doi.org/10.1016/0021-9290(94)00065-c
9. Côté Allard, U., Nougarou, F., Fall, C.L., Giguere, P., Gosselin, C., Laviolette, F., Gosselin, B.: A convolutional neural network for robotic arm guidance using sEMG based frequency-features (2016). https://doi.org/10.1109/iros.2016.7759384
10. Coyle, D.: Neural network based auto association and time-series prediction for biosignal processing in brain-computer interfaces. IEEE Comput. Intell. Mag. **4**(4), 47–59 (2009). https://doi.org/10.1109/MCI.2009.934560
11. Fleischer, C., Wege, A., Kondak, K., Hommel, G.: Application of EMG signals for controlling exoskeleton robots. Biomed. Tech. (Berl) **51**(5–6), 314–319 (2006). https://doi.org/10.1515/BMT.2006.063

12. Fong, D.T., Hong, Y., Chan, L.K., Yung, P.S., Chan, K.M.: A systematic review on ankle injury and ankle sprain in sports. Sports Med. **37**(1), 73–94 (2007). https://doi.org/10.2165/00007256-200737010-00006
13. Guimaraes, A.C., Herzog, W., Allinger, T.L., Zhang, Y.T.: The EMG-force relationship of the cat soleus muscle and its association with contractile conditions during locomotion. J. Exp. Biol. **198**(4), 975 (1995)
14. Herzog, W.: History dependence of force production in skeletal muscle: a proposal for mechanisms. J. Electromyogr. Kinesiol. **8**(2), 111–117 (1998). https://doi.org/10.1016/s1050-6411(97)00027-8
15. Hof, A.L., Van den Berg, J.: EMG to force processing I: an electrical analogue of the hill muscle model. J. Biomech. **14**(11), 747–758 (1981). https://doi.org/10.1016/0021-9290(81)90031-2
16. Kennedy, J., Eberhart, R.: Particle swarm Optimization, vol. 4 (1995). https://doi.org/10.1109/icnn.1995.488968
17. Liu, H-J., Young, K.: An Adaptive Upper-Arm EMG-Based Robot Control System, vol. 12 (2010)
18. Liu, H.-J., Young, K.-Y.: Upper-limb EMG-based robot motion governing using empirical mode decomposition and adaptive neural fuzzy inference system. J. Intell. Robot. Syst. **68**(3–4), 275–291 (2012). https://doi.org/10.1007/s10846-012-9677-6
19. Liu, L., Liu, P., Moyer, D.V., Clancy, E.A.: System identification of non-linear, dynamic EMG-torque relationship about the elbow. In: 2011 IEEE 37th Annual Northeast Bioengineering Conference (NEBEC), 1–3 Apr 2011, pp. 1–2 (2011). https://doi.org/10.1109/nebc.2011.5778638
20. Lloyd, D.G., Besier, T.F.: An EMG-driven musculoskeletal model to estimate muscle forces and knee joint moments in vivo. J. Biomech. **36**(6), 765–776 (2003). https://doi.org/10.1016/s0021-9290(03)00010-1
21. Lloyd, D.G., Buchanan, T.S.: A model of load sharing between muscles and soft tissues at the human knee during static tasks. J. Biomech. Eng. **118**(3) (1996). https://doi.org/10.1115/1.2796019
22. Mattacola, C.G., Dwyer, M.K.: Rehabilitation of the ankle after acute sprain or chronic instability. J. Athl. Train. **37**(4), 413–429 (2002)
23. Metral, S., Cassar, G.: Relationship between force and integrated EMG activity during voluntary isometric anisotonic contraction. Eur. J. Appl. Physiol. **46**(2), 185–198 (1981). https://doi.org/10.1007/bf00428870
24. Milner-Brown, H.S., Stein, R.B., Yemm, R.: Changes in firing rate of human motor units during linearly changing voluntary contractions. J. Physiol. **230**(2), 371–390 (1973)
25. Nam Jo, Y., Jeong Kang, M., Hee Yoo, H.: Estimation of muscle and joint forces in the human lower extremity during rising motion from a seated position. J. Mech. Sci. Technol. **28**(2), 467–472 (2014). https://doi.org/10.1007/s12206-013-1111-x
26. Nowshiravan Rahatabad, F., Jafari, A.H., Fallah, A., Razjouyan, J.: A fuzzy-genetic model for estimating forces from electromyographical activity of antagonistic muscles due to planar lower arm movements: the effect of nonlinear muscle properties. Biosystems **107**(1), 56–63 (2012). https://doi.org/10.1016/j.biosystems.2011.09.004
27. Nurhanim, K., Elamvazuthi, I., Vasant, P., Ganesan, T., Parasuraman, S., Khan, M.K.A.A.: Joint torque estimation model of Surface Electromyography (sEMG) based on swarm intelligence algorithm for robotic assistive device. Procedia Comput. Sci. **42**, 175–182 (2014). https://doi.org/10.1016/j.procs.2014.11.049
28. Oyong, A.W., Parasuraman, S., Jauw, V.L.: Robot assisted stroke rehabilitation: estimation of muscle force/joint torque from EMG using GA. In: 2010 IEEE EMBS Conference on Biomedical Engineering and Sciences (IECBES), 30 Nov–2 Dec 2010, pp. 341–347 (2010). https://doi.org/10.1109/iecbes.2010.5742257
29. Phinyomark, A., Phukpattaranont, P., Limsakul, C.: Feature reduction and selection for EMG signal classification. Expert Syst. Appl. **39**, 7420–7431 (2012). https://doi.org/10.1016/j.eswa.2012.01.102
30. Rabiner, L.R., Gold, B.: Theory and Application of Digital Signal Processing. Prentice-Hall (1975)

31. Reaz, M.B.I., Hussain, M.S., Mohd-Yasin, F.: Techniques of EMG signal analysis: detection, processing, classification and applications. Biol. Proced. Online **8**(1), 11–35 (2006). https://doi.org/10.1251/bpo115
32. Rini, D.P., Shamsuddin, S.M., Yuhaniz, S.: Particle swarm optimization: technique, system and challenges. Int. J. Comput. Appl. **14**(1) (2011). https://doi.org/10.5120/ijais-3651
33. Sárkány, N., Tihanyi, A., Szolgay, P.: The design of a mobile multi-channel bio-signal measuring system for rehabilitation purposes. In: 2014 14th International Workshop on Cellular Nanoscale Networks and their Applications (CNNA), 29–31 July 2014, pp. 1–2 (2014). https://doi.org/10.1109/cnna.2014.6888644
34. Shabani, A., Mahjoob, M.J.: Bio-signal interface for knee rehabilitation robot utilizing EMG signals of thigh muscles. In: 2016 4th International Conference on Robotics and Mechatronics (ICROM), 26–28 Oct 2016, pp. 228–233 (2016). https://doi.org/10.1109/icrom.2016.7886851
35. Shin, D., Kim, J., Koike, Y.: A myokinetic arm model for estimating joint torque and stiffness from EMG signals during maintained posture. J. Neurophysiol. **101**(1), 387–401 (2009). https://doi.org/10.1152/jn.00584.2007
36. Siebert, T., Stutzig, N., Rode, C.: A hill-type muscle model expansion accounting for effects of varying transverse muscle load. J. Biomech. **66**, 57–62 (2018). https://doi.org/10.1016/j.jbiomech.2017.10.043
37. Subasi, A.: Classification of EMG signals using combined features and soft computing techniques. Appl. Soft Comput. **12**(8), 2188–2198 (2012). https://doi.org/10.1016/j.asoc.2012.03.035
38. Suykens, J.A.K., Vandewalle, J.: Least squares support vector machine classifiers. Neural Process. Lett. **9**(3), 293–300 (1999). https://doi.org/10.1023/A:1018628609742
39. Ullah, K., Jung-Hoon, K.: A mathematical model for mapping EMG signal to joint torque for the human elbow joint using nonlinear regression. In: 2009 4th International Conference on Autonomous Robots and Agents, 10–12 Feb 2009, pp. 103–108 (2000). https://doi.org/10.1109/icara.2000.4803995
40. Valadao, C.T., Loterio, F., Cardoso, V., Bastos, T., Frizera-Neto, A., Carelli, R.: Robotics as a tool for physiotherapy and rehabilitation sessions**Authors acknowledge the financial support from FAPES, CAPES and CNPq. IFAC-PapersOnLine **48**(19), 148–153 (2015). https://doi.org/10.1016/j.ifacol.2015.12.025
41. van Ruijven, L.J., Weijs, W.A.: A new model for calculating muscle forces from electromyograms. Eur. J. Appl. Physiol. **61**(5–6), 479–485 (1990)
42. Veeger, D., Yu, B., An, K.N, Rozendal, H.R.: Parameters for modeling the upper extremity. J. Biomech. **30**, 647–652 (1997). https://doi.org/10.1016/s0021-9290(97)00011-0
43. Wu, G., Siegler, S., Allard, P., Kirtley, C., Leardini, A., Rosenbaum, D., Whittle, M., D'Lima, D.D., Cristofolini, L., Witte, H., Schmid, O., Stokes, I.: ISB recommendation on definitions of joint coordinate system of various joints for the reporting of human joint motion—Part I: ankle, hip, and spine. International Society of Biomechanics. J. Biomech. **35**(4), 543–548 (2002)
44. Xia, P., Hu, J., Peng, Y.: EMG-based estimation of limb movement using deep learning with recurrent convolutional neural networks. Artif. Organs **42**(5), E67–E77 (2018). https://doi.org/10.1111/aor.13004
45. Zajac, F.E.: Muscle and tendon: properties, models, scaling, and application to biomechanics and motor control. Crit. Rev. Biomed. Eng. **17**(4), 359–411 (1989)
46. Zhai, X., Jelfs, B., Chan, R.H.M., Tin, C.: Self-recalibrating surface EMG pattern recognition for neuroprosthesis control based on convolutional neural network. Front. Neurosci. **11**, 379 (2017). https://doi.org/10.3389/fnins.2017.00379
47. Zhang, M., Davies, T.C., Xie, S.: Effectiveness of robot-assisted therapy on ankle rehabilitation—a systematic review. J. Neuroeng. Rehabil. **10**, 30 (2013). https://doi.org/10.1186/1743-0003-10-30
48. Zhao, X., Sun, H., Ye, D.: Ankle rehabilitation robot control based on biological signals. In: 2017 29th Chinese Control and Decision Conference (CCDC), 28–30 May 2017, pp. 6090–6095 (2017). https://doi.org/10.1109/ccdc.2017.7978264

Force Myography and Its Application to Human Locomotion

Anoop Kant Godiyal, Vinay Verma, Nitin Khanna and Deepak Joshi

1 Introduction

Locomotion is a highly skillful task that we humans perform using our two limbs to commute from one place to another. Millions of years ago, our ancestors used to live in trees and used all four limbs to walk. Over the years, we have learned to walk on two limbs and evolved gradually. In the modern day, with immense technical advancement, our lives became easier, resulting in an unhealthier lifestyle that leads to serious diseases. Diabetes is one such disease, which is one of the major causes of amputation [47]. The second most important cause of amputation is traumatic injuries [70]. With the loss of limb, an amputee faces serious challenges in his day-to-day life; thus a declined quality of life. The situation worsens when the amputation is particularly of the lower limb as it affects their locomotion capabilities. Locomotion is an important factor for an individual's independence. To enhance the quality of amputee's life, it is important to design a robust but simple and affordable prosthesis that can provide a wide range of acceptability and better human-machine interface.

In the United States alone, there were 1.4 million lower limb amputees in the year 2012, which is estimated to double in the next 35 years. The lower limb disability is prominent amongst the amputation related disabled population worldwide. To aid their hampered lives owing to disability, a variety of prostheses are commercially available. These are categorized into two types- passive and active prosthesis. Passive

A. K. Godiyal · D. Joshi (✉)
Centre for Biomedical Engineering, Indian Institute of Technology, Delhi, India
e-mail: joshid@iitd.ac.in

V. Verma · N. Khanna
Electrical Engineering, Indian Institute of Technology Gandhinagar, Ahmedabad, Gujarat, India

D. Joshi
Department of Biomedical Engineering, All India Institute of Medical Sciences, New Delhi, India

G. Naik (ed.), *Biomedical Signal Processing*, Series in BioEngineering,
https://doi.org/10.1007/978-981-13-9097-5_3

prosthesis cosmetically mimics the actual leg but lacks in capability as it requires extra effort for driving and maintaining the balance. This results in unnatural gait patterns and higher metabolic energy. These limitations of a passive prostheses can be resolved to a great extent, using an active prosthesis, resulting in an active area of research. The most important part of any active prosthesis is to recognize the modes and gait events during locomotion, for seamlessly controlling the prosthesis and timely adjusting the mode [3, 44, 59, 60].

Interestingly, the sensing technology is an integral and the most important part of the active prosthesis. Over the years, many sensing technologies like electromyography (EMG) [1, 22], inertial sensors [24, 33], capacitance sensors [9, 68] etc. have been used to acquire the signal from the individual's body and identify the different locomotion modes along with the gait events during locomotion. To ensure the safe walking, the locomotion modes and the gait events should be recognized as accurately as possible, which mainly depends on the sensing technology used. Surprisingly, there is one of the other limitations of each sensing technology. Therefore, the quest to an alternate cost-effective sensing technology with minimal limitations is the utmost need and thus, remains a highly demanding area of research. This chapter gives insight into the identification of locomotion modes and the gait events during the locomotion using an emerging sensing technique called the force myography (FMG). In FMG, the change in the gross volume of the limb is captured via a strap tied to it. This change in volume is due to the contraction and relaxation of the skeletal muscles while performing the activities of daily living (ADL).

2 Background

To identify the human locomotion and detect gait events during the locomotion, various signals are acquired from the subject's body. After detecting the gait events and locomotion modes, the signals are then used to drive the prosthesis for safe and efficient locomotion. This human locomotion and gait event determination is also helpful to assess movement disorders such as Parkinson's disease, cerebellar ataxia, multiple sclerosis, and other gait related disorders. Electromyography (EMG) is considered the gold standard system to assess limb activity because it is well established and widely known. EMG is a technique to measure the electrical activity that occurs in the skeletal muscles during the contraction and relaxation motion. EMG has been widely used in prosthetics, rehabilitation, driving exoskeleton, and many human-machine interfaces [20, 21, 29, 39, 57]. Especially in the control of prosthetics, EMG is used to capture the muscle movements as it appears before any other motion occurs. Though being popular, it suffers from some major limitations such as sensitivity to anatomical locations, movement artifacts, cross-talk between muscles, degradation due to external noise, and electromagnetic noise [12, 58]. It is also dependent on environmental conditions such as humidity and dust, which restrict it's global acceptability. To obtain quality EMG signal, the signal to noise ratio should be high, which requires well-designed hardware resulting in an exponential increase

in the cost of the system. Though cheaper surface electromyography (sEMG) systems are available, these systems provide poor quality signals and hence, resulting in poor accuracy in the identification of locomotion modes and gait events.

Recently mechanical sensors like inertial sensors [18, 43, 45], capacitance sensors [9, 68], and force myography [11, 16, 17, 26] are used as they provide an upper hand in overcoming the limitations of the EMG system. The inertial measurement unit is a combination of accelerometer and gyroscope that are fused into a single chip to provide a better understanding of the real-world problems with their use. With the advancement in technology, these sensors have become compact, lightweight and affordable because of which researchers can acquire the data autonomously and continuously even outside the laboratory environment. The limitation associated with the inertial sensors is the noise component that is due to the external factors and shifting of the sensors. To attain higher accuracy, the complementary information is fed to the system, i.e., extra sensors are added with an independent source of the noise. As the inertial sensor responds to the motion of the human body part, so the intent to move cannot be collected using the inertial measurement unit (IMU), thus, it lags behind the EMG. In addition, the inertial sensors do not acquire any of the body parameters, and hence they cannot determine fatigue.

Due to these limitations, the researchers are endeavoring to the better sensing technology that has benefits of EMG being intuitive and compact, lightweight and affordable with good accuracy as IMU. The researchers have come up with two solutions—capacitive sensing and FMG. Currently, the capacitance sensing is in the primitive stage for the identification of human locomotion. Very few studies have been done to identify the human locomotion, gait events, and the forearm motions using the capacitive sensing [66–68]. FMG has been extensively explored for the upper limb applications [14, 26, 27, 62, 63]. When compared to other available technologies, FMG has a greater potential for being applied in prosthesis development, rehabilitation, and various human-machine interfaces. The FMG technology is advantageous over EMG as—there is no requirement of skin preparation for putting the FMG strap, no effect of humidity, sweating, and dust on the sensors due to their lamination and contact separation as they are not put directly on the skin [5, 55]. Additionally, there is no issue of cross-talk because the FMG is acquired through the strap that is tied on the periphery of the limb, thus is homogeneous [5]. Moreover, the literature reveals that FMG is not only capable but superior in determining the fatigue in the muscles when compared with the EMG and is not affected by the socket shift [56]. Above all, FMG is cost-effective, simple to design, easy to use, lightweight, and stable over time. Keeping these factors in mind, the hardware required to design the FMG system is simple and less complicated. To date, FMG systems are not commercially available, a prototype for collecting FMG signal costs less than US $50 [6]. With these immense advantages, FMG puts its strong candidacy for rehabilitation and movement monitoring, especially for persons with disabilities.

3 Design and Development

3.1 FMG Instrumentation

FMG uses force sensitive resistors (FSRs) to measure the gross volume change in the limb during a particular motion. FSRs are the combination of electrodes, spacer and a conductive-resistive polymer. The resistance of FSR will decrease with the increase in force applied to it. When the force is applied on the top/bottom of the FSR, it compresses, and the conductive-resistive polymer is exposed to the electrodes leading to a decrease in resistance from infinity. On the application of larger force, the conductive-resistive polymer comes more in contact with the electrodes resulting in a further decrease in the resistance. The advantage of using FSR lies in its flexible nature and low cost. In the development of the FMG system, we have used a flexible and stretchable strap with 8 FSRs (FSR 400, sensitivity 0.2–20N, Interlink Electronics Inc., Camarillo United States) placed at equidistance to each other on the inner periphery of the strap. Each FSR was supported by a thin layer of leather ($20 \times 20 \times 1.5$ mm) to provide rigid support. Here in this experiment, the strap was tied on the thigh of the healthy and the amputee subjects, keeping in mind that we have designed a strap of length 40 cm, which can be stretched to a length of 55 cm. Therefore, a single FMG strap can accommodate a large population for the collection of the data.

To convert the stretchable strap to a non-stretchable strap, an additional strap was tied on to the top of the strap for the healthy individuals using the Velcro. This scheme was automatically provided with the socket for the amputee population as shown in Fig. 1. During any movement, the change in force results in a change in the resistance, which is captured through a voltage divider circuit and converted to the voltage variation. A base resistance (10 KΩ in our case) was chosen to vary the sensitivity of the system. An operational amplifier was used to amplify the acquired signal and then send it to the analog pin of the Arduino Nano microcontroller. The data acquired was then wirelessly transmitted to the base system via a Bluetooth module (Bluefruit EZ-Link) at a sampling frequency of 100 Hz. To detect the transmission loss, the data was coupled with the reference signal and then validated at the receiver station. If any abnormality with the reference signal was found then that trial was considered to be a false trial. For example, in some of the trials, we found sudden peaks from base value or non-uniformity in the reference signal, which may be due to wireless data transmission, these trails were discarded during our data collection.

3.2 Footswitches Insoles

In the study related to gait analysis, the foot switches play a critical role, as they become the markers to identify the gait events. So, to this end, we had designed a customized foot insole that is having three tactile switches. The placement of the switches was in such a way that they can efficiently segment the swing and the stance

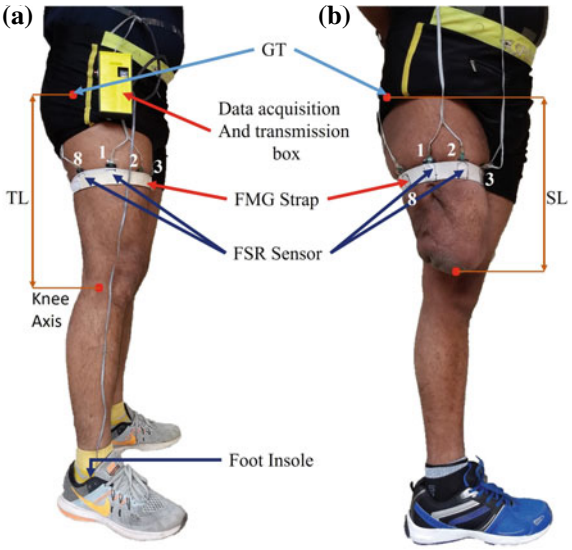

Fig. 1 Sensor placement. **a** Placement of FMG strap on the thigh of the able-bodied individual. **b** Placement of FMG strap on the residual stump of the amputee. GT—Greater Trochanter. TL—Thigh Length. SL—Stump Length

phase. The first switch was placed at the heel, which serves as the basis to identify the heel strike. The second and third switches were placed at the 1st metatarsal and big toe respectively, as shown in Fig. 2. These two markers served as the reference point for the toe-off marker. The 1st metatarsal marker was added to avoid any missing of big toe switch during the walking. The customized insole serves dual purpose i.e. could be used for the segmenting the gait cycles or could also be used as the ground truth for estimation of gait events (heel strike, HS, and toe off, TO). The insole was drawn on the coral draw and printed using the silk screen printing. To detect the

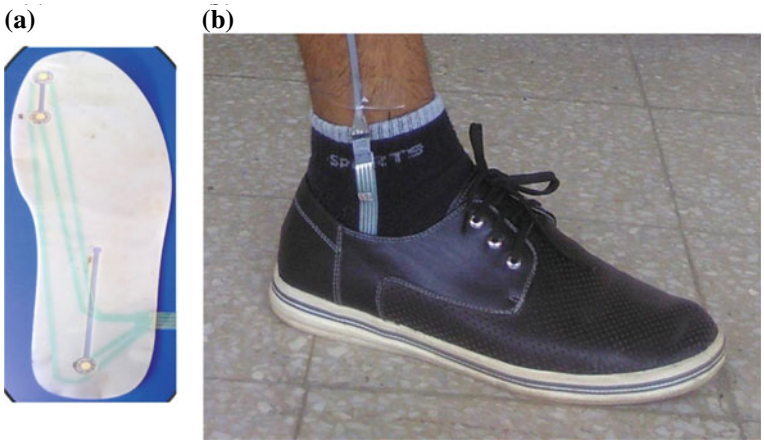

Fig. 2 **a** Footswitch insole. **b** Configuration during the experiment

status of a tactile switch the debouncing circuit is used and then the signal was sent to the digital pin of the same Arduino Nano microcontroller from where the data was sent wirelessly.

4 Applications

4.1 Application of FMG in Locomotion Classification

Recently there is a great advancement in lower limb prosthesis design. Although modern-day prosthesis provides improved stability, still the commercially available low-cost prosthesis is passive in nature. One of the major limitations associated with passive prosthesis is that it consumes relatively higher metabolic energy and offers an asymmetrical gait, which results in several spine related problems [3]. Though modern day active prosthesis had solved some of the inherent problems that were associated with the passive prosthesis [37]. For active prosthesis to perform safe and efficient locomotion, locomotion classification becomes an inherent part of the prosthesis [65]. Various sophisticated algorithms are adopted to identify locomotion modes using different sensors. When it comes to selecting a signal that can be utilized for locomotion classification, the first choice becomes the EMG signal due to its inherent origin before the actual motion, thus being intuitive. However, the EMG signal suffers from some of the major limitations that were discussed in Sect. 2, which restricts its wide acceptability [1, 22]. Mechanical sensors have also been explored in the literature for the locomotion classification [9, 50]. However, the limitation with this type of sensors is that they provide the information when the action/motion has occurred and thus lead to lagging in the EMG signal.

We have reported the in-house developed force myography system to classify various locomotion modes like level walking (LW), ramp ascent (RA), ramp descent (RD), stair ascent (SA), and stair descent (SD) [34]. All the locomotion modes were performed by eight healthy individuals (age 25 $\pm$ 3 years, height 170 $\pm$ 11.5 cm, weight 66.9 $\pm$ 11.43 kg) and two unilateral transfemoral amputees (25.5 $\pm$ 0.5 years). In the process of locomotion classification, we have used FMG strap, which was donned on the dominant limb at 50% of thigh length (TL) from the greater trochanter (GT) of the able-bodied subject as shown in Fig. 1a. All able-bodied subjects involved in the study were found to be the right limb dominant. For the amputee, the strap was first tied on the residual stump at 50% of the stump length (SL) from the GT, and then the socket was donned on by the amputee, as shown in Fig. 1b. The mentioned five different locomotion modes, i.e., LW, RA, RD, SA, and SD, were performed by each of the participants. Five trials of each locomotion mode were conducted for each participant, and after each trial, the subject was given a rest for a minimum of 2 min. Each trial started with a standing period of 10 s followed by a walk corresponding to the particular locomotion mode (LW/RA/RD/SA/SD) and standing period of 10 s at the end. Later, 10 s of standing periods at the beginning and end of each trial were

removed before any further analysis. The instructions for initiating and stopping the locomotion were verbally provided by the experimenter. All the data were collected at user's self-selected speed. The subject walked for 100 ft on a level platform. The ramp had an inclination of 5° and a length of 60 ft. The total length of the stair was 12 ft with a step width of 12 inches and a step height of 6 inches. A pictorial description of each locomotion mode with the corresponding measurements is shown in Fig. 3.

The gait cycle was segmented by the foot switch signals for each trial. As the subject walks at a self-selected speed, each segmented gait cycle length varies. Therefore, to make it similar, we interpolated the gait cycle data using the spline interpolation. The time axis was also normalized to the duration of the gait cycle and expressed in percentage. Additionally, we have assessed the repeatability of FMG by calculating variance ratio (VR) within a locomotion mode. This ratio is measured from intra-subject variability, reflecting the repeatability of gait waveforms over a number of gait cycles. It has been widely used for gait analysis applications [15, 23]. The mathematical expression was explained in our earlier manuscript [16]. The value of VR varies from zero to one, where zero signifies the highly matched and repeatable waveforms, while one suggests the highly unmatched or random waveforms of gait cycles.

The locomotion classification modes include—gait segmentation using footswitch signals, feature extraction, and testing of a trained classifier (Fig. 4). In this study, only stance phase data has been used for classifying the locomotion modes to compensate for the delay in the control of prosthesis [41] in real-time scenario. Now, after segmenting the gait cycle by footswitch signal, we have extracted eight time-domain features: minimum (min), maximum (max), mean, standard deviation (std), root mean square (RMS), waveform length (WL), number of slope sign changes (SSC), and mean absolute deviation (MAD) [61] from each gait cycle, resulting a total of 64 features (8 features $\times$ 8 sensors $=$ 64 features). Finally, linear discriminant analysis (LDA) has been used as a classifier to classify the locomotion modes. For the validation, leave one out cross validation (LOOCV) method was adopted. The LDA classifier is computationally efficient, has good performance, and can be easily implemented in real-time [10, 22]. Then for the leave one out cross validation, we have selected four trials among the five trials of each of the five locomotion modes (LW, RA, RD, SA, and SD) for training the classifier. Thus, the remaining trial is used as a testing dataset for evaluating classification accuracy. The classifi-

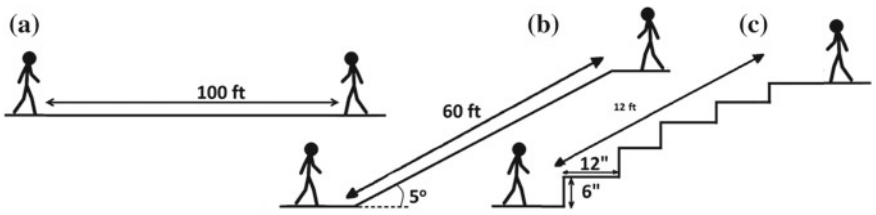

Fig. 3 Experimental protocol. **a** LW. **b** Ramp walk (ascent/descent). **c** Stair walk (ascent/descent)

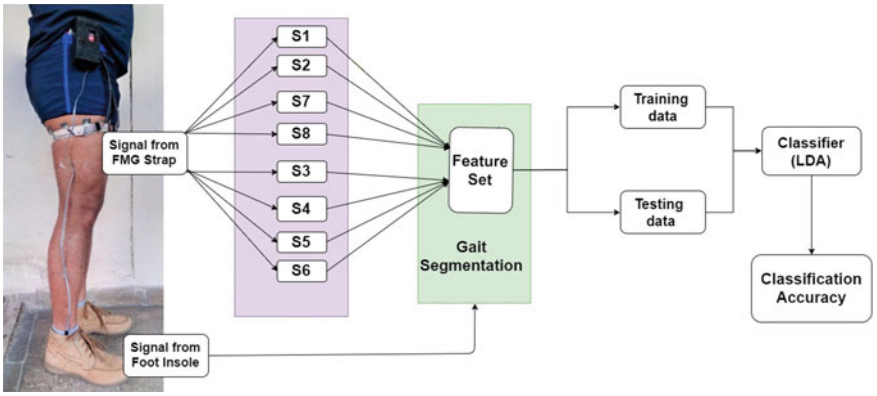

Fig. 4 Block diagram of locomotion mode classification

cation accuracy was then averaged across all trials to calculate the subject-specific classification accuracy and overall classification accuracy has been finally assessed from averaging all subject-specific accuracies. We computed the confusion matrix for the actual and estimated class to quantify error distribution where a high value of diagonal element indicates higher accuracy to estimate that locomotion mode.

The FMG signal for a typical able-bodied and a unilateral transfemoral amputee for each locomotion mode and sensor is shown in Fig. 5. Each sensor (S1–S8) response is obtained by averaging the gait cycle across the five trials. For visualization purpose, each sensor was normalized to its maximum value. The FMG sensors detect the volumetric changes of thigh muscles. Therefore, the sensors placed on the thigh have various loading responses of muscles during heel strike, mid stance, terminal stance, pre-swing, and swing segments of a gait cycle. Thus, forming different FMG patterns at different sensor locations for different locomotions. Noticeably, the loading pattern of each signal was more distinct in stance phase than the swing phase as most of the body weight exerts in the stance phase only. It has also been observed that the variation in FMG pattern was more in able-bodied subjects when compared to amputee depicting a "flatter trajectory" (Fig. 5). This variation may be due to the absence of relevant muscles in amputee that utilizes more power through remaining muscles.

The FMG patterns are usually consistent; however, the difference in walking patterns results in variations across the subjects. Table 1 represents the variance ratio (VR) of all sensors for all locomotion modes in able-bodied and amputee subjects. Observations show that the FMG signal of LW, RA, and RD comprise a low VR (close to zero) with minimal std, exhibit consistency leading to the high repeatability in most of the locomotion modes except S4 sensor. The variability of the S4 sensor may be due to its anatomical placement on the abductor muscle which has a role to adduct and rotate the thigh [38], hence influence the walk. The range of VR up to 0.3 is considerably good, as reported in EMG based gait studies [23]. As we know, for staircase walking the pattern of a gait cycle depends on the contact area of the

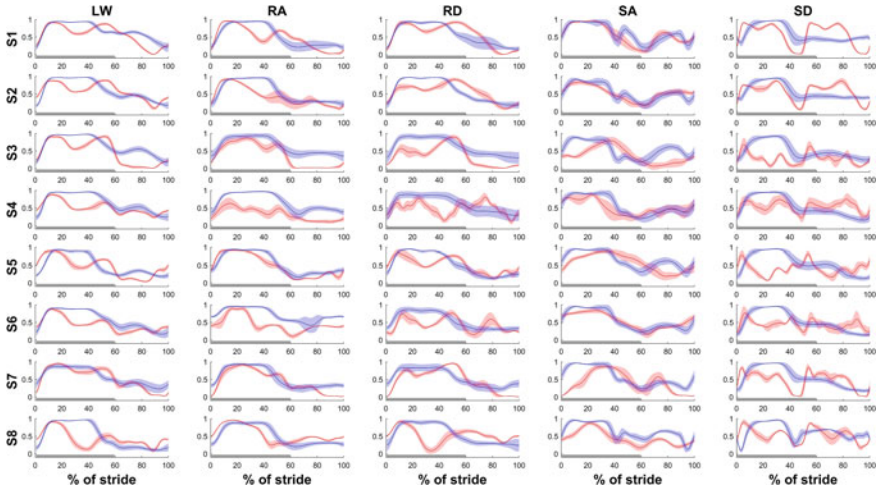

Fig. 5 Normalized FMG signals from FMG strap, S1–S8 denotes the sensors within the strap. The horizontal axis represents the gait cycle in percentage. The Red line shows the mean across the gait cycle while the shaded region (red) represents the standard deviation of the signal for the able-bodied subject. The blue line shows the mean across the gait cycle while the shaded region (blue) represents the standard deviation of the signal for the amputee subject. The gray-shaded region on the x-axis denotes the stance phase of the gait cycle

foot to the stair which may vary in every step resulting in higher VR in stair walking [52, 53].

Remarkably, we have achieved classification accuracies of 99.5 and 96.1% for able-bodied and amputees respectively, using simplified and low computational features of FMG technique. This system has a high potential for sensing various terrain as the classification accuracy for stairs was 99.2% (average of SA and SD in Fig. 6a) in case of able-bodied and 97.9% (average of SA and SD in Fig. 6b) in case of amputees. It was noted that being a physiological signal, EMG produces a classification accuracy of 85–90% for classifying locomotion modes whereas the mechanical sensors can give classification accuracy of more than 90% for able-bodied and amputee subjects [1, 9, 10, 22, 29]. The high sensitivity to anatomical placement, more susceptible to motion artifacts, and disturbance by sweating may be the cause of lesser classification accuracy of EMG. In contrast, FMG signals are produced due to the volumetric changes of muscle with slow variation and hence, represented by simple time-domain features.

To conclude, the reasons which make FMG a better alternative sensing technique lies under three predominant criteria:

(i) Improved accuracy than the standard EMG and other mechanical sensors;
(ii) No issue of humidity as well as sweating as FMG strap is laminated with a thin non-compressible layer over the FSR sensors, overcoming the main limitation of EMG sensing technique; and

Table 1 Variance ratio (mean ± std) for all sensors during different locomotion modes

	LW	RA	RD	SA	SD
(a) Able-bodied					
S1	0.02 ± 0.01	0.03 ± 0.02	0.03 ± 0.01	0.10 ± 0.09	0.03 ± 0.01
S2	0.04 ± 0.01	0.13 ± 0.10	0.08 ± 0.04	0.13 ± 0.08	0.08 ± 0.02
S3	0.02 ± 0.01	0.05 ± 0.05	0.07 ± 0.04	0.17 ± 0.10	0.30 ± 0.10
S4	0.08 ± 0.02	0.27 ± 0.12	0.35 ± 0.23	0.33 ± 0.18	0.53 ± 0.23
S5	0.04 ± 0.02	0.03 ± 0.01	0.13 ± 0.06	0.15 ± 0.09	0.24 ± 0.09
S6	0.06 ± 0.03	0.10 ± 0.08	0.26 ± 0.10	0.10 ± 0.06	0.58 ± 0.10
S7	0.04 ± 0.03	0.04 ± 0.02	0.04 ± 0.03	0.15 ± 0.10	0.13 ± 0.07
S8	0.08 ± 0.04	0.04 ± 0.01	0.13 ± 0.09	0.13 ± 0.07	0.20 ± 0.09
(b) Amputee					
S1	0.05 ± 0.02	0.09 ± 0.06	0.1 ± 0.08	0.21 ± 0.10	0.15 ± 0.08
S2	0.04 ± 0.02	0.05 ± 0.03	0.03 ± 0.02	0.19 ± 0.09	0.14 ± 0.09
S3	0.06 ± 0.02	0.16 ± 0.09	0.17 ± 0.09	0.20 ± 0.11	0.17 ± 0.09
S4	0.08 ± 0.05	0.10 ± 0.08	0.29 ± 0.19	0.50 ± 0.14	0.11 ± 0.11
S5	0.04 ± 0.03	0.05 ± 0.03	0.04 ± 0.03	0.17 ± 0.10	0.12 ± 0.10
S6	0.07 ± 0.05	0.19 ± 0.09	0.15 ± 0.10	0.11 ± 0.09	0.08 ± 0.06
S7	0.13 ± 0.09	0.09 ± 0.08	0.15 ± 0.12	0.11 ± 0.11	0.08 ± 0.07
S8	0.03 ± 0.03	0.07 ± 0.05	0.09 ± 0.07	0.14 ± 0.10	0.14 ± 0.08

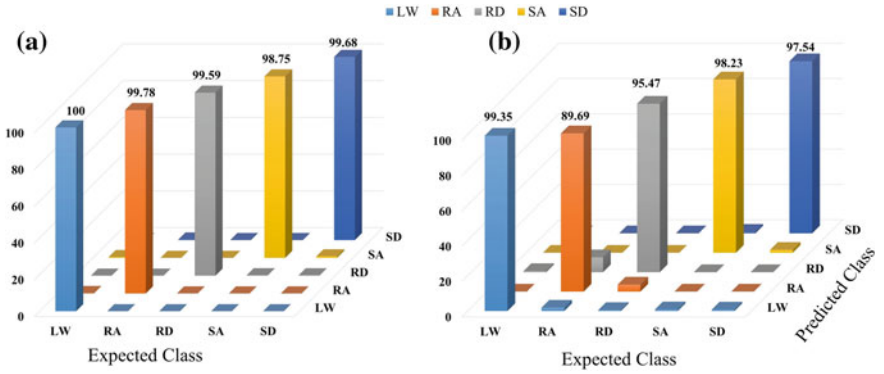

Fig. 6 Confusion matrix for locomotion modes classification using the LDA classifier for; **a** able-bodied, and **b** amputee

(iii) Acquisition of simple time domain features resulting in minimal signal processing, which leads to an efficient sensing system for low power applications.

Therefore, FMG would be a promising sensing technique having low cost and high accuracy with a wide range of biomechanical applicability. Although the hardware design is under a primitive stage, it is difficult to mount on the thigh of the transfemoral amputee. Therefore, customized FMG strap is indeed a necessary futuristic step for this highly valuable sensing technique.

4.2 Application of FMG in Gait Event Detection

The utility of the FMG signal has noticeably important directions in terms of gait event detection. Gait event detection forms a crucial basis for applications like prosthesis and orthosis [18, 28], rehabilitation [35], activity monitoring [7, 48], and exoskeleton [32]. In a single gait cycle, two gait events occur i.e. heel strike (HS) and toe-off (TO). These are the markers that define the stance and swing phase during the gait cycle. To define the spatiotemporal parameter of the gait cycle, these events need to be identified accurately. The conventional ways to measure the HS and TO such as ground reaction force (GRF) [8] and motion capture systems, are highly accurate but come with certain major limitations:

(1) The subject has to be restricted in a laboratory setting environment. Therefore, they cannot perform the activity of daily living in restricted conditions.
(2) While performing the experiment, the subject becomes conscious, so the experimenter does not accurately acquire the real gait characteristics.
(3) It requires a skilled person to operate the system, and
(4) The cost of the system is very high.

Identification of the gait events in any condition outside/inside is essential for gait analysis. In the past, the insoles have been used to identify the gait events outside the laboratory and got the same place as that of the camera-based system. However, the major limitations associated with this type of system are—firstly, their size dependency which requires a proper alignment for accurate identification of gait events. Secondly, the insole is subjected to wear and tear as they are worn inside the shoe, so it tends to get damaged over a period of time. Therefore, the quest for another technique to resolve limitations related to the insole, a motion capture system, and GRF is still a matter of exploration. Although the researchers have used EMG for the identification of gait events, it comes with the inherent limitations which restrict its applicability. Recently, mechanical sensors are gaining importance due to miniaturization, no effect of sweating, and ability to wear. The IMU, which is a combination of accelerometer and gyroscope, has been used to identify the gait events in the various applications [2, 4, 32, 36, 43, 45]. Recently, to a little extent, capacitance sensing has been explored for the gait event detection by putting it on the thigh and shank [67].

Therefore, an alternate sensing method needs to be explored which could be cost-effective, independent of the laboratory settings and foot size, wearable, easy to implement, and convenient to operate by a non-professional person. For the same in this work, we have used force myography to identify the gait event during the level walk, ramp walking, and also the transition between them. In addition, we have further explored whether a single FSR sensor in the FMG strap has the potential to identify the gait events. A recent study also showed the ability to force myography to detect gait events during the slow speed of walking in a healthy population [25].

The study of gait event detection has recruited five able-bodied male adults (mean $\pm$ std, age: 25 $\pm$ 3 years, height: 170 $\pm$ 11.5 cm, and weight: 66.9 $\pm$ 11.43 kg) with no movement related disorders. The FMG strap was wrapped on the thigh of the dominant limb at mid of the thigh length, where thigh length is measured from the greater trochanter and ends at the knee axis. All the sensors within the sensor strap were mapped to the corresponding thigh muscles as—R1-Vastus Lateralis, R2-Iliotibial tract, R3-Biceps femoris, R4-Semitendinosus, R5-Adductor Magnus, R6-midway of Gracilis and adductor Longus, R7-Vastus Medialis, and R8-Rectus Femoris. The subject walked on three different terrains, i.e., Level walk (LW), ramp ascent (RA), and ramp descent (RD), and four trials of each activity were taken. The length of the LW, RA, and RD was 50 feet, 80 feet, and 80 feet long, respectively. In the RA and RD walk, the 10 feet walk at the starting, and the end was of LW, and the rest 60 feet was the ramp. The ramp had an inclination of 5 degrees. The LW at the starting and end of the ramp walk is added to detect the four transitions in between them namely LW-to-RA, RA-to-LW, LW-to-RD, and RD-to-LW, as shown in Fig. 7. In each trial, the subject stood for 10 s at the initial position, then he walked at self-selected speed in the respective terrain, and again after reaching the final position the rest of 10 s was provided. During the experiment, the instruction to initiate and stop the trial was verbally provided by the experimenter. After each trial, minimum 2 min rest was provided for each participant.

The block diagram for the entire event detection framework is shown in Fig. 8. A system with low computational complexity was developed to assist the real-time development and deployment of the system in the prosthesis. The complete FMG data of walking is divided into the training and testing database. For each of the training and testing trials, the data has to be first pre-processed with a fourth-order low pass Butterworth filter with a cut off of 20 Hz, and then a seven-point moving average filter is applied. The two-stage filtering is applied to remove the high-frequency noise from the FMG signal. After the pre-processing of the FMG signal, a signature vector is estimated, and then each of the signatures is normalized to zero mean and unit variance. Normalization is done to avoid any possibility of signal variation as the walking pattern may vary from trial to trial and also due to the difference in the placement of FMG sensors. The training of the gait event detection for locomotion is dependent on the actual gait events that were taken from the reference system (foot insole system) from the 1st trial of that locomotion mode (LW, RA, and RD). The collection of these reference signatures is named as a signature database. The reference signature has two sub-database (1) HS database and (2) TO database.

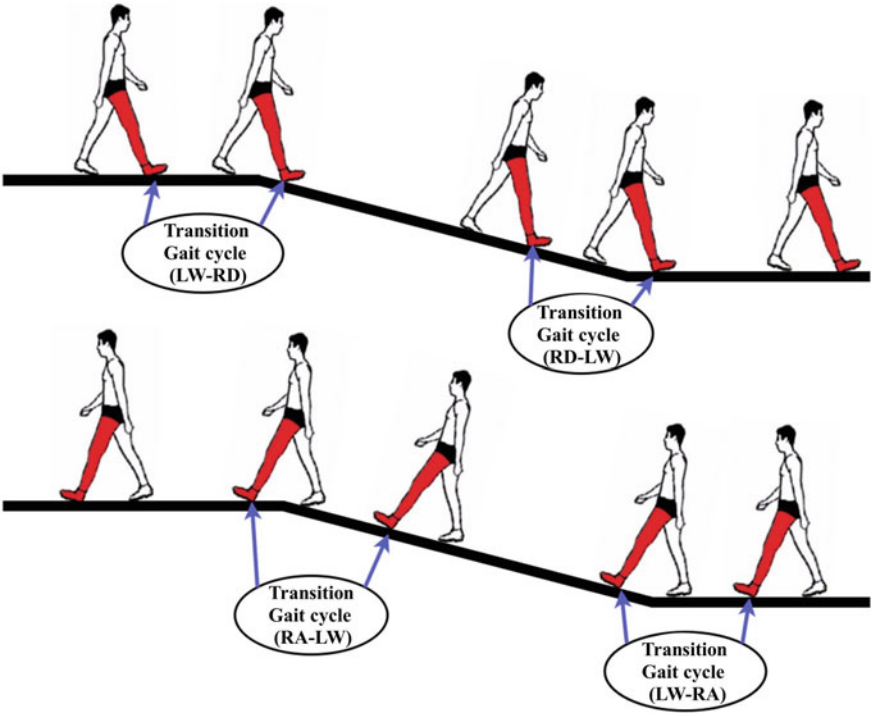

Fig. 7 Experimental protocol; locomotion platform with transitions (total four transitions LW–RA, RA–LW, LW–RD, and RD–LW)

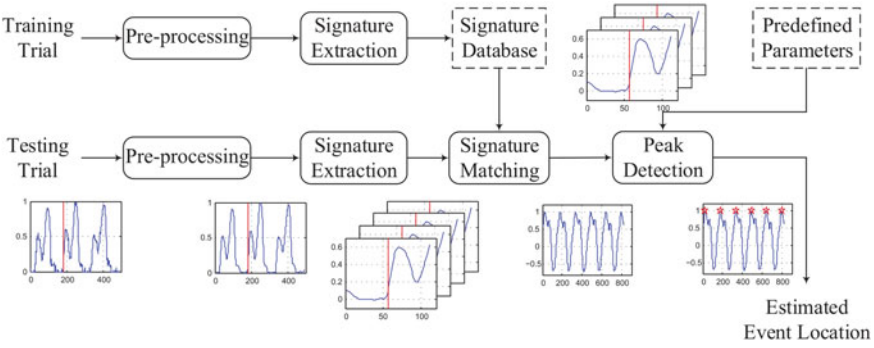

Fig. 8 Block diagram of the event detection framework

During the testing of the trial of any locomotion mode, the signal is passed through the pre-processing and signature extraction of each sample, the signature of the testing sample is then compared with the signature database which determines whether the signature resembles the HS, TO or none. This comparison or signature matching is performed using a detector based on the normalized correlation. If a particular time instance corresponds to any of the events (HS or TO), then the signature corresponding to that time instance will have a high correlation value; otherwise, it will have a low correlation value. These correlation values were then stored, and a peak detection algorithm is applied to the stored correlation values. The peak detection algorithm determines the highest correlated values and finally gives the location of the occurrence of the gait events during that locomotion mode. To validate the accuracy of the algorithm, the time difference between the actual gait events and the estimated gait events is calculated. To remove the biasing, the error is computed in the form of mean absolute error (MAE) for a subject and then averaged across the total number of subjects in order to report the overall error. The transition MAE reported for a subject is the overall average MAE obtained by averaging the error corresponding to each of the four transition phases for that individual. More details about each step can be found in our earlier research work [17].

For different locomotion modes, the MAE for estimating TO and HS is shown in Fig. 9a, b. The figure depicts that using sensor R8 leads to minimal error among all the other sensors R1–R7. The superiority of R8 among the other sensors might be due to the rectus femoris muscle, as the rectus femoris muscle is majorly responsible for the walking in the sagittal plane, which is aligned to the R8 sensor. In addition, it can be noted that the placement of sensors is affecting the performance of the system. As R8 being the most efficient and R2, R6, and R7 being the least efficient in estimating the gait events. Given the fact that we have used eight sensors in the FMG strap, the shifting on the strap will not have any effect on the overall performance. As the strap is homogeneous, any shifting can result in the other sensor replacing the R8 sensor in the FMG strap and hence not affecting the system performance.

The variation of MAE for different locomotion modes along with the transition for heel strike and toe-off using the R8 sensor is shown in Fig. 9c, d. The overall MAE for estimating TO in LW, RA, RD, and Transition is 16.99 ± 18.12, 15.65 ± 18.05, 11.41 ± 11.76, and 17.29 ± 21.92 ms respectively and is shown in Fig. 9c. Similarly, the overall MAE for estimating the HS for LW, RA, RD, and Transition is 9.66 ± 8.29, 9.03 ± 8.09, 9.66 ± 10.30 and 13.94 ± 18.95 ms respectively and is shown in Fig. 9d. Table 2 shows the detailed variation of MAE for HS and TO within/across the subjects for different locomotion modes and the transitions. Note that in the estimation of the mean for overall MAE, we need to take weighted mean because the number of TO (or HS) events is not exactly the same for each of the participants. This difference in the number of events across the participants is as expected because participants walk at their self-selected speeds. Since the algorithm is terrain independent and the variability in the stride time is large for a particular locomotion mode, the MAE has a relatively higher standard deviation. Although, the terrain dependent algorithm might be used to reduce the standard deviation but

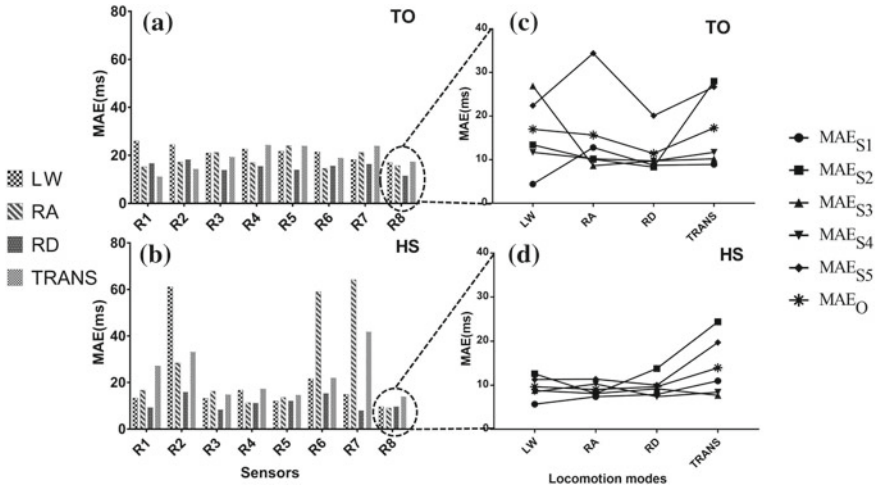

Fig. 9 MAE in estimation of heel strike and toe-off for different locomotion modes and transitions with FMG sensors (R1–R8) at corresponding locations around the thigh; **a** Toe-off; **b** Heel strike; MAE for all locomotion modes and transitions, using sensor R8 only, for five subjects; the solid lines show the mean absolute error for MAE_{S1}-Subject1, MAE_{S2}-Subject2, MAE_{S3}-Subject3, MAE_{S4}-Subject4, MAE_{S5}-Subject5 and MAE_O-average across all five subjects; **c** Toe-off; **d** Heel strike; LW—Level walk, RA—Ramp Ascent, RD—Ramp Descent, TRANS-transitions i.e. transition from LW–RA, RA–LW, LW–RD and RD–LW)

Table 2 Variation of MAE within the subjects for different locomotion modes and transitions

	MAE_{S1}	MAE_{S2}	MAE_{S3}	MAE_{S4}	MAE_{S5}	MAE_O
(a) Toe-off						
LW	4.4 ± 5.1	13.4 ± 12.7	26.9 ± 22.3	11.7 ± 9.5	22.4 ± 21.3	16.99 ± 18.12
RA	12.8 ± 11.6	10.1 ± 14.5	8.6 ± 14.6	10.2 ± 7.1	34.4 ± 22.1	15.65 ± 18.05
RD	8.7 ± 7.0	8.3 ± 9.9	9.7 ± 10.8	9.7 ± 8.7	20.1 ± 15.9	11.41 ± 11.76
TRANS	8.9 ± 12.6	28 ± 36.8	10.2 ± 14.6	11.7 ± 13.5	26.7 ± 15.4	17.29 ± 21.92
(b) Heel strike						
LW	5.7 ± 5.7	12.6 ± 7.6	8.8 ± 9.0	8.5 ± 6.4	11.3 ± 9.6	9.66 ± 8.29
RA	7.4 ± 7.3	8.1 ± 6.5	8.1 ± 7.2	10.3 ± 8.5	11.4 ± 10.2	9.03 ± 8.09
RD	7.9 ± 7.0	13.8 ± 15.7	9.2 ± 7.3	7.4 ± 8.4	10.0 ± 10.1	9.66 ± 10.3
TRANS	11.0 ± 8.1	24.4 ± 34.2	7.7 ± 7.3	8.4 ± 5.7	19.7 ± 17.3	13.94 ± 18.95

terrain independent algorithm is rather suitable for real-time applications. This is in concordance with the previous literature [4, 24, 30, 42, 46, 54].

Also, it is clearly seen from Fig. 9c, d that, compared to LW, RA, and RD, the MAE_O (i.e. mean absolute error of all 5 subjects) for transition (TRANS) is the largest in both the cases, toe-off, and heel strike. One of the factors leading to relatively larger MAE for transition (TRANS) is a lesser number of gait cycles containing transition, as in a single trial, only two transition gait cycles occur. The transition gait event

analysis is important because this is the event when the person is transitioning from one locomotion mode to another. It is one of the most common situations leading to the falling of the amputees and the elderly persons [19, 49]. Till now, this [35] is the only study that reports the estimation of HS error while performing the transition and shows an improvement in the TO estimation as compared to our previous work [30].

When comparing the FMG based system to the other available gait event detection systems FMG system offers the lowest error among all. However, the error obtained using the accelerometer is comparable to the FMG system, but the accelerometer suffers from the inherent problem of drifting, so another sensor is added to compensate for the drift, which leads to a limitation of the study and FMG gaining its importance. Since the current approach is completely based on the heuristic approach when compared with other methods, so the FMG puts its strong candidacy for real-time implementation.

The advantages associated with the present FMG system are that there is no issue of sweating and humidity as the FMG strap need not be placed directly on the skin, there is no issue related to drift and alignment as compared to inertial sensors. The most important feature of the FMG system is that it uses minimal signal processing to estimate the gait events while performing the locomotion mode; hence it puts less burden on the processing unit and leads to longer battery lives. The results are promising; however, the current FMG system needs design modification for the use of the amputee population. The present study focused on healthy individuals, which can be further enhanced and verified for the larger dataset and amputee population. Also, gait events in more complex gait patterns must be analyzed.

4.3 Other Applications of FMG

The FMG is very advantageous in terms of its multidirectional applicability. Some of the other current and prospective applications of FMG include gesture recognition, rehabilitation, and prosthesis control. This chapter focused on FMG application in the lower limb as a primary example; however, it has used in the upper limb extensively, as discussed below.

Currently, the majority of the available systems that are focusing on gesture control are using the camera (simple/infrared) for acquiring the data. For recognizing finger gestures [34] and hand gesture [69], these systems record a huge volume of data and also suffer from occlusion and increased complexity, thus making it difficult for the real-time applications involving classification of gestures. The other sensing modality that has been widely used for monitoring the hand and wrist gestures since the past decade is electromyography [31]. The limitations that were associated with the EMG have already been discussed earlier (Sect. 2). Recently the FMG has been used extensively for gesture recognition. The primary gestures that are the hot topics for the researchers are hand gestures, finger gestures, and wrist gestures [11, 14, 26, 40, 51, 63]. For most of the applications, the FMG system is worn on the forearm

section as it provides a large area for the radial displacement for the data collection. FMG has also been used to identify the grasp and non-grasp [55] and estimation of elbow, forearm, and wrist positions [64]. Researches have also compared FMG with the existing commercially available sEMG systems for distinguishing 48 hand motions of both the hands along with the wrist. The results state that the FMG system is at par with the sEMG system, and they have also noted that the classification accuracy is similar for both the forearm and the wrist [13].

Motivated from the previous results of the FMG, Cho et al. [11] conducted a study where they used the FMG signals to classify the grip patterns of the transradial amputees and achieved an accuracy of 70% in classifying the various grip patterns using the residual muscles only. These results make the candidacy of the FMG suitable for prosthesis control.

The FMG can also be used in the field of exoskeleton and rehabilitation. As we have already seen that the FMG is capable of determining various gestures involved in upper limb activities and lower limb applications, it can identify the gait events and locomotion classification [16, 17]. These features of grasping, pinching, walking and other activities of daily living could be used by the rehabilitation experts. These movements are used in rehabilitation to strengthen the body muscles, especially in the case of neuromuscular disorders like stroke, spinal cord injury, multiple sclerosis, Parkinson's disease. Therefore, FMG can also be used as the standard for quantification of the degree of improvement and feedback during the rehabilitation therapies.

5 Conclusion

In this chapter, we have shown the use of the FMG for two of the lower limb applications, i.e., locomotion classification and gait event detection. To achieve this, we have developed an in-house FMG strap to acquire the FMG data. For the classification of locomotion, this system offers good accuracy despite simple design. It is clearly established from the experiments conducted during this study that the information of muscle activities of a residual limb can be used as a method of locomotion-mode classification or intent recognition during ambulation. Thus, it may prove to be a viable and inexpensive alternative to EMG and mechanical-sensor-based systems. Remarkably, a novel FMG based gait event detection system has also been proposed in this chapter. Experiments conducted on healthy subjects validated the effectiveness of the proposed system over the existing works. To the best of our knowledge, the error levels attained by the proposed system were comparable to the lowest error achieved so far in the literature. Although tested on healthy subjects, it offers enough substance to be employed with exoskeletons, orthoses, and prostheses. The simple design of FMG strap and its placement around thigh makes it suitable for mounting it even inside the socket of the above knee (AK) and below knee (BK) amputees. It can be concluded that the proposed FMG based system is a promising method for gait event detection in a real-world scenario.

Acknowledgements Deepak Joshi would like to thank the Department of Science and Technology, Government of India for funding the present work through Early Career Research Award (ECR/2016/001282), and would also like to thank Indian Council of Medical Research (ICMR) for supporting the work via grant number 5/20/13/Bio/2011-NCD-1.

Nitin Khanna would like to thank the Indian Institute of Technology Gandhinagar as this material is based upon work partially supported by internal research grant IP/IITGN/EE/NK/201516-06.

Any opinions, findings, and conclusions or recommendations expressed in this material are those of the author(s) and do not necessarily reflect the views of the funding agencies. Address all correspondence to Deepak Joshi at joshid@iitd.ac.in.

References

1. Afzal, T., Iqbal, K., White, G., Wright, A.B.: A method for locomotion mode identification using muscle synergies. IEEE Trans. Neural Syst. Rehabil. Eng. **25**(6), 608–617 (2017). https://doi.org/10.1109/TNSRE.2016.2585962
2. Asbeck, A.T., Schmidt, K., Galiana, I., Wagner, D., Walsh, C.J.: Multi-joint soft exosuit for gait assistance. In: IEEE International Conference pn Robotics and Automation, pp. 6197–6204
3. Au, S.K., Weber, J., Herr, H.: Powered ankle-foot prosthesis improves walking metabolic economy. IEEE Trans. Rob. **25**(1), 51–66 (2009). https://doi.org/10.1109/TRO.2008.2008747
4. Aung, M.S.H., Thies, S.B., Kenney, L.P.J., Howard, D., Selles, R., Findlow, A.H., Goulermas, J.Y.: Automated detection of instantaneous gait events using time frequency analysis and manifold embedding. IEEE Trans. Neural Syst. Rehabil. Eng. **21**(6), 908–916 (2013)
5. Castellini, C., Artemiadis, P., Wininger, M., Ajoudani, A., Alimusaj, M., Bicchi, A., Caputo, B., et al.: Proceedings of the first workshop on peripheral machine interfaces: going beyond traditional surface electromyography. Front. Neurorobot. **8**(AUG), 1–17 (2014). https://doi.org/10.3389/fnbot.2014.00022
6. Castellini, C., Ravindra, V.: A wearable low-cost device based upon force-sensing resistors to detect single-finger forces. In: 5th IEEE RAS/EMBS International Conference on Biomedical Robotics and Biomechatronics, pp. 199–203 (2014). https://doi.org/10.1109/BIOROB.2014.6913776
7. Chan, C.W., Rudins, A.: Foot biomechanics during walking and running. Mayo Clin. Proc. **69**(5), 448–461 (1994). https://doi.org/10.1016/S0025-6196(12)61642-5
8. Chang, Y.H., Huang, H.W., Hamerski, C.M., Kram, R., McN, A.R., Jayes, A.S., Biewener, A.A., et al.: The independent effects of gravity and inertia on running mechanics. J. Exp. Biol. **203**(Pt 2), 229–238 (2000). https://doi.org/10.1016/0021-9290(80)90019-6
9. Chen, B., Zheng, E., Fan, X., Liang, T., Wang, Q., Wei, K., Wang, L.: Locomotion mode classification using a wearable capacitive sensing system. IEEE Trans. Neural Syst. Rehabil. Eng. **21**(5), 744–755 (2013). https://doi.org/10.1109/TNSRE.2013.2262952
10. Chen, B., Zheng, E., Wang, Q.: A locomotion intent prediction system based on multi-sensor fusion. Sensors (Switzerland) **14**(7), 12349–12369 (2014). https://doi.org/10.3390/s140712349
11. Cho, E., Chen, R., Merhi, L.-K., Xiao, Z., Pousett, B., Menon, C.: Force myography to control robotic upper extremity prostheses: a feasibility study. Front. Bioeng. Biotechnol. **4**(March), 1–12 (2016). https://doi.org/10.3389/fbioe.2016.00018
12. Chowdhury, R., Reaz, M., Ali, M., Bakar, A., Chellappan, K., Chang, T.: Surface electromyography signal processing and classification techniques. *Sensors* **13**(9), 12431–12466 (2013). https://doi.org/10.3390/s130912431
13. Connan, M., Ruiz Ramírez, E., Vodermayer, B., Castellini, C.: Assessment of a wearable force and electromyography device and comparison of the related signals for myocontrol. Front. Neurorob. **10**(NOV), 1–13 (2016). https://doi.org/10.3389/fnbot.2016.00017
14. Englehart, K., Scheme, E.: A proportional control scheme for high density force myography. J. Neural Eng. **15**(4) (2018). https://doi.org/10.1088/1741-2552/aac89b

15. Erni, T., Colombo, G.: Locomotor training in paraplegic patients: a new approach to assess changes in leg muscle EMG patterns. Electroencephalogr. Clin. Neurophysiol. Electromyogr. Motor Control **109**(2), 135–39 (1998). https://doi.org/10.1016/S0924-980X(98)00005-8
16. Godiyal, A.K., Mondal, M., Joshi, S.D., Joshi, D.: Force myography based novel strategy for locomotion classification. IEEE Trans. Hum. Mach. Syst. **48**(6), 648–657 (2018). https://doi.org/10.1109/THMS.2018.2860598
17. Godiyal, A.K., Verma, H.K., Khanna, N., Joshi, D.: A force myography-based system for gait event detection in overground and ramp walking. IEEE Trans. Instrum. Meas. **67**(10), 2314–2323 (2018). https://doi.org/10.1109/TIM.2018.2816799
18. Goršič, M., Kamnik, R., Ambrožič, L., Vitiello, N., Lefeber, D., Pasquini, G., Munih, M.: Online phase detection using wearable sensors for walking with a robotic prosthesis. Sensors (Switzerland) **14**(2), 2776–2794 (2014). https://doi.org/10.3390/s140202776
19. Gottschall, J.S., Nichols, T.R.: Neuromuscular strategies for the transitions between level and hill surfaces during walking. Philos. Trans. R. Soc. Lond. Ser. B Biol. Sci. **366**(1570), 1565–1579 (2011). https://doi.org/10.1098/rstb.2010.0355
20. Gupta, R., Agarwal, R.: Electromyographic signal-driven continuous locomotion mode identification module design for lower limb prosthesis control. Arab. J. Sci. Eng. **43**(12), 7817–7835 (2018). https://doi.org/10.1007/s13369-018-3193-3
21. Ha, K.H., Varol, H.A., Goldfarb, M.: Volitional control of a prosthetic knee using surface electromyography. IEEE Trans. Bio-Med. Eng. **58**(1), 144–151 (2011). https://doi.org/10.1109/TBME.2010.2070840
22. Huang, H., Kuiken, T.A., Lipschutz, R.D.: A strategy for identifying locomotion modes using surface electromyography. IEEE Trans. Bio-Med. Eng. **56**(1), 65–73 (2009). https://doi.org/10.1109/TBME.2008.2003293
23. Hwang, S., Lee, H.M., Cherng, R.J., Chen, J.J.J.: Electromyographic analysis of locomotion for healthy and hemiparetic subjects—study of performance variability and rail effect on treadmill. Gait Posture **18**(1), 1–12 (2003). https://doi.org/10.1016/S0966-6362(02)00071-1
24. Jasiewicz, J.M., Allum, J.H.J., Middleton, J.W., Barriskill, A., Condie, P., Purcell, B., Li, R.C.T.: Gait event detection using linear accelerometers or angular velocity transducers in able-bodied and spinal-cord injured individuals. Gait Posture **24**(4), 502–509 (2006). https://doi.org/10.1016/j.gaitpost.2005.12.017
25. Jiang, X., Chu, Kelvin H.T., Khoshnam, M., Menon, C.: A wearable gait phase detection system based on force myography techniques. Sensors (Switzerland) **18**(4), 1279 (2018). https://doi.org/10.3390/s18041279
26. Jiang, X., Merhi, L.K., Menon, C.: Force exertion affects grasp classification using force myography. IEEE Trans. Hum. Mach. Syst. **48**(2), 219–226 (2018). https://doi.org/10.1109/THMS.2017.2693245
27. Jiang, X., Merhi, L.K., Xiao, Z.G., Menon, C.: Exploration of force myography and surface electromyography in hand gesture classification. Med. Eng. Phys. **41**, 63–73 (2017). https://doi.org/10.1016/j.medengphy.2017.01.015
28. Joshi, D., Mishra, A., Anand, S.: ANFIS based knee angle prediction: an approach to design speed adaptive contra lateral controlled AK prosthesis. Appl. Soft Comput. **11**(8), 4757–4765 (2011). https://doi.org/10.1016/j.asoc.2011.07.007
29. Joshi, D., Nakamura, B.H., Hahn, M.E.: High energy spectrogram with integrated prior knowledge for EMG-based locomotion classification. Med. Eng. Phys. **37**(5), 518–524 (2015). https://doi.org/10.1016/j.medengphy.2015.03.001
30. Joshi, D., Nakamura, B.H., Hahn, M.E.: A novel approach for toe off estimation during locomotion and transitions on ramps and level ground. IEEE J. Biomed. Health Inform. **20**(1), 153–157 (2016). https://doi.org/10.1109/JBHI.2014.2377749
31. Ju, Z., Liu, H.: Human hand motion analysis with multisensory information. IEEE/ASME Trans. Mechatron. **19**(2), 456–466 (2014). https://doi.org/10.1109/TMECH.2013.2240312
32. Jung, J.Y., Heo, W., Yang, H., Park, H.: A neural network-based gait phase classification method using sensors equipped on lower limb exoskeleton robots. Sensors (Switzerland) **15**(11), 27738–27759 (2015). https://doi.org/10.3390/s151127738

33. Khandelwal, S., Wickstrom, N.: Gait event detection in real-world environment for long-term applications: incorporating domain knowledge into time-frequency analysis. IEEE Trans. Neural Syst. Rehabil. Eng. **24**(12), 1363–1372 (2016). https://doi.org/10.1109/TNSRE.2016.2536278
34. Kim, D., Hilliges, O., Izadi, S., Butler, A.D., Chen, J., Oikonomidis, I., Olivier, P.: Digits: freehand 3D interactions anywhere using a wrist-worn gloveless sensor. In: Proceedings of the 25th Annual ACM Symposium on User Interface Software and Technology—UIST'12, p. 167 (2012). https://doi.org/10.1145/2380116.2380139
35. Kimmeskamp, S., Hennig, E.M.: Heel to toe motion characteristics in parkinson patients during free walking. Clin. Biomech. **16**(9), 806–812 (2001). https://doi.org/10.1016/S0268-0033(01)00069-9
36. Kotiadis, D., Hermens, H.J., Veltink, P.H.: Inertial gait phase detection for control of a drop foot stimulator inertial sensing for gait phase detection. Med. Eng. Phys. **32**(4), 287–297 (2010). https://doi.org/10.1016/j.medengphy.2009.10.014
37. Lawson, B.E., Mitchell, J., Truex, D., Shultz, A., Ledoux, E., Goldfarb, M.: A robotic leg prosthesis: design, control, and implementation. IEEE Robot. Autom. Mag. **21**(4), 70–81 (2014). https://doi.org/10.1109/MRA.2014.2360303
38. Leighton, R.D.: A functional model to describe the action of the adductor muscles at the hip in the transverse plane. Physiother. Theory Pract. **22**(5), 251–262 (2006). https://doi.org/10.1080/09593980600927385
39. Leonardis, D., Barsotti, M., Loconsole, C., Solazzi, M., Troncossi, M., Mazzotti, C., Castelli, V.P., et al.: An EMG-controlled robotic hand exoskeleton for bilateral rehabilitation. IEEE Trans. Haptics **8**(2), 140–151 (2015). https://doi.org/10.1109/TOH.2015.2417570
40. Li, N., Yang, D., Jiang, L., Liu, H., Cai, H.: Combined use of FSR sensor array and SVM classifier for finger motion recognition based on pressure distribution map. J. Bionic Eng. **9**(1), 39–47 (2012). https://doi.org/10.1016/S1672-6529(11)60095-4
41. Liu, Z., Lin, W., Geng, Y., Yang, P.: Intent pattern recognition of lower-limb motion based on mechanical sensors. IEEE/CAA J. Autom. Sinica **4**(4), 651–660 (2017). https://doi.org/10.1109/JAS.2017.7510619
42. Mannini, A., Genovese, V., Sabatini, A.M., Member, S.: Online decoding of hidden markov models for gait event detection using foot-mounted gyroscopes. IEEE J. Biomed. Health Inform. **18**(4), 1122–1130 (2014)
43. Maqbool, H.F., Husman, M.A.B., Awad, M.I., Abouhossein, A., Iqbal, N.: A real-time gait event detection for lower limb prosthesis control and evaluation. IEEE Trans. Neural Syst. Rehabil. Eng. **25**(9), 1500–1509 (2017)
44. Martinez-villalpando, E.C., Herr, H.: Agonist-antagonist active knee prosthesis: a preliminary study in level-ground walking **46**(3), 361–373 (2009). https://doi.org/10.1682/JRRD.2008.09.0131
45. Mo, S., Chow, D.H.K.: Accuracy of three methods in gait event detection during overground running. Gait Posture **59** (October 2017), 93–98 (2018). https://doi.org/10.1016/j.gaitpost.2017.10.009
46. Novak, D., Reberšek, P., Rossi, S.M.M.D., Donati, M., Podobnik, J., Beravs, T., Lenzi, T., Vitiello, N., Carrozza, M.C., Munih, M.: Automated detection of gait initiation and termination using wearable sensors. Med. Eng. Phys. **35**(12), 1713–1720 (2013). https://doi.org/10.1016/j.medengphy.2013.07.003
47. Paisey, R.B., Abbott, A., Levenson, R., Harrington, A., Browne, D., Moore, J., Bamford, M., Roe, M.: Diabetes-related major lower limb amputation incidence is strongly related to diabetic foot service provision and improves with enhancement of services: peer review of the south-west of england. Diabet. Med. **35**(1), 53–62 (2018). https://doi.org/10.1111/dme.13512
48. Panahandeh, G., Mohammadiha, N., Leijon, A., Handel, P.: Continuous hidden markov model for pedestrian activity classification and gait analysis. IEEE Trans. Instrum. Meas. **62**(5), 1073–1083 (2013). https://doi.org/10.1109/TIM.2012.2236792
49. Peng, J., Fey, N.P., Kuiken, T.A., Hargrove, L.J.: Anticipatory kinematics and muscle activity preceding transitions from level-ground walking to stair ascent and descent. J. Biomech. **49**(4), 528–536 (2016). https://doi.org/10.1016/j.jbiomech.2015.12.041

50. Preece, S.J., Goulermas, J.Y., Kenney, L.P., Howard, D.: A comparison of feature extraction methods for the classification of dynamic activities from accelerometer data. IEEE Trans. Biomed. Eng. **56**(3), 871–879 (2009). https://doi.org/10.1109/TBME.2008.2006190
51. Radmand, A., Scheme, E., Englehart, K.: High-density force myography: a possible alternative for upper-limb prosthetic control. J. Rehabil. Res. Dev. **53**(4), 443–456 (2016). https://doi.org/10.1682/JRRD.2015.03.0041
52. Ramstrand, N., Nilsson, K.A.: A comparison of foot placement strategies of transtibial amputees and able-bodied subjects during stair ambulation. Prosthet. Orthot. Int. **33**(4), 348–355 (2009). https://doi.org/10.3109/03093640903074891
53. Riener, R., Rabuffetti, M., Frigo, C.: Stair ascent and descent at different inclinations. Gait Posture **15**(1), 32–44 (2002). https://doi.org/10.1016/S0966-6362(01)00162-X
54. Sabatini, A.M., Martelloni, C., Scapellato, S., Cavallo, F.: Assessment of walking features from foot inertial sensing. IEEE Trans. Biomed. Eng. **52**(3), 486–494 (2005)
55. Sadarangani, G.P., Menon, C.: A preliminary investigation on the utility of temporal features of force myography in the two-class problem of grasp versus no-grasp in the presence of upper-extremity movements. BioMed. Eng. Online **16**(1), 1–19 (2017). https://doi.org/10.1186/s12938-017-0349-4
56. Sanford, J., Patterson, R., Popa, D.O.: Concurrent surface electromyography and force myography classification during times of prosthetic socket shift and user fatigue. J. Rehabil. Assist. Technol. Eng. **4** (2017). https://doi.org/10.1177/2055668317708731
57. Sarasola-Sanz, A., Irastorza-Landa, N., Lopez-Larraz, E., Bibian, C., Helmhold, F., Broetz, D., Birbaumer, N., Ramos-Murguialday, A.: A hybrid brain-machine interface based on EEG and EMG activity for the motor rehabilitation of stroke patients. Int. Conf. Rehabil. Rob. (ICORR) **2017**, 895–900 (2017). https://doi.org/10.1109/ICORR.2017.8009362
58. Sensinger, J.W., Lock, B.A., Kuiken, T.A.: Adaptive pattern recognition of myoelectric signals: exploration of conceptual framework and practical algorithms 12. IEEE Trans. Neural Syst. Rehabil. Eng. **17**(3), 270–278 (2009)
59. Varol, H.A., Sup, F., Goldfarb, M.: Multiclass real-time intent recognition of a powered lower limb prosthesis. IEEE Trans. Biomed. Eng. **57**(3), 542–551 (2010). https://doi.org/10.1109/TBME.2009.2034734
60. Varol, H.A., Sup, F., Goldfarb, M.: Powered sit-to-stand and assistive stand-to-sit framework for a powered transfemoral prosthesis. In: 2009 IEEE International Conference on Rehabilitation Robotics, ICORR 2009, pp. 645–651 (2009). https://doi.org/10.1109/ICORR.2009.5209582
61. Veer, K., Sharma, T.: A novel feature extraction for robust EMG pattern recognition. J. Med. Eng. Technol. **40**(4), 149–154 (2016). https://doi.org/10.3109/03091902.2016.1153739
62. Wininger, M.: Pressure signature of forearm as predictor of grip force. J. Rehabil. Res. Dev. **45**(6), 883–892 (2008). https://doi.org/10.1682/JRRD.2007.11.0187
63. Xiao, Z.G., Menon, C.: Towards the development of a wearable feedback system for monitoring the activities of the upper-extremities. J. NeuroEng. Rehabil. **11**(1), 1–13 (2014). https://doi.org/10.1186/1743-0003-11-2
64. Xiao, Z.G., Menon, C.: Performance of forearm FMG and SEMG for estimating elbow, forearm and wrist positions. J. Bionic Eng. **14**(2), 284–295 (2017). https://doi.org/10.1016/S1672-6529(16)60398-0
65. Young, A.J., Simon, A.M., Hargrove, L.J.: A training method for locomotion mode prediction using powered lower limb prostheses. IEEE Trans. Neural Syst. Rehabil. Eng. **22**(3), 671–677 (2014). https://doi.org/10.1109/TNSRE.2013.2285101
66. Zheng, E., Mai, J., Liu, Y., Wang, Q.: Forearm motion recognition with noncontact capacitive sensing. Front. Neurorob. **12**(July), 1–13 (2018). https://doi.org/10.3389/fnbot.2018.00047
67. Zheng, E., Manca, S., Yan, T., Parri, A., Vitiello, N., Wang, Q.: Gait phase estimation based on noncontact capacitive sensing and adaptive oscillators. IEEE Trans. Biomed. Eng. **99**, 1–12 (2017). https://doi.org/10.1109/TBME.2017.2672720
68. Zheng, E., Wang, Q.: Noncontact capacitive sensing-based locomotion transition recognition for amputees with robotic transtibial prostheses. IEEE Trans. Neural Syst. Rehabil. Eng. **25**(2), 161–170 (2017). https://doi.org/10.1109/TNSRE.2016.2529581

69. Zhou, R., Junsong, Y., Jingjing, M., Zhengyou, Z.: Robust part-based hand gesture recognition using kinect sensor. IEEE Trans. Multimed. **15**(5), 1110–1120 (2013). https://doi.org/10.1109/TMM.2013.2246148
70. Ziegler-Graham, K., MacKenzie, E.J., Ephraim, P.L., Travison, T.G., Brookmeyer, R.: Estimating the prevalence of limb loss in the United States: 2005–2050. Arch. Phys. Med. Rehabil. **89**(3), 422–429 (2008)

Comparison of Independence of Triceps Brachii and Biceps Brachii Between Paretic and Non-paretic Side During Different MVCs—A Case Study

Ganesh Naik, Rifai Chai, Steven Su, Song Rong and Hung T. Nguyen

Abstract Stroke is one of the major causes of permanent disability in adults. Physical training and rehabilitation help stroke survivors to carry out their day-to-day tasks. Surface electromyography (sEMG) has been widely used for stroke rehabilitation and assessment of muscle activities for different force levels. In this regard, it is very important to know the function and differences between various muscles involved in the stroke rehabilitation process. Hence, this study investigated the independence between biceps and triceps brachii for paretic and non-paretic sides during different muscle voluntary contractions (MVCs). Source separation technique using independent component analysis (ICA) and time domain features such as root mean square (RMS), mean absolute value (MAV), and integrated absolute value (IAV) were used to measure the muscle activities. The results show that biceps brachii muscles are more independent than triceps brachii muscles for different MVCs. The findings of this study could be used for measuring independence between muscles, which would help to identify and treat the specific muscle during stroke rehabilitation procedures.

Keywords Stroke rehabilitation · Electromyography · Independent component analysis · RMS · Triceps brachii · Biceps brachii

G. Naik (✉)
MARCS Institute for Brain, Behaviour and Development Institute, Western Sydney University, Penrith, NSW, Australia
e-mail: ganesh.naik@westernsydney.edu.au

R. Chai · H. T. Nguyen
Faculty of Engineering and IT, Swinburne University of Technology, Melbourne, VIC, Australia

S. Su
Faculty of Engineering and IT, University of Technology Sydney, Sydney, NSW, Australia

S. Rong
School of Biomedical Engineering, Sun Yat-Sen University, Guangzhou, China

G. Naik (ed.), *Biomedical Signal Processing*, Series in BioEngineering,
https://doi.org/10.1007/978-981-13-9097-5_4

1 Introduction

Stroke is one of the main causes of a cerebrovascular problem and is one of the major reasons for permanent disability in adults. The stroke affects the quality of life and stroke survivors have to deal with several issues related to muscles and body, which include spasticity, weakness, loss of dexterity, and pain at the paretic (stroke affected) side. Research shows that nearly 70–80% of people who sustain a stroke suffer from limb impairment undergo continuous rehabilitation and medical care to lessen their physical impairment [2, 16].

Post-stroke rehabilitation is a tedious process. Due to functional limitations, stroke survivors usually have a low quality of life as compared to healthy people [11]. Hence, post-stroke rehabilitation helps stroke survivors to recover their upper limb motor functions and get back to near normal day to day life [12]. Kinematic analysis is one of the widely used tools for stroke rehabilitation. Also, there exist several methods to rehabilitate stroke survivors, which include: target point reaching tasks, robot-based therapy, and trajectory tracking, etc. [1, 15].

Although kinematic analysis helps in understanding the external performance of neuromuscular functions, it is also essential to understand the effect of stroke-induced sensory-motor functions or muscle activities. Surface electromyography (sEMG) is an electrical signal captured from the surface of the skin during muscle activation [3]. Surface EMG provides a clear understanding of physiological processes neuromuscular functions of stroke-affected muscles and helps in the stroke rehabilitation process. Surface EMG has been used for several applications which include, muscle fatigue detection, amputee gesture recognition, device control, neuro-muscular disease classification, etc. [5]. Surface EMG features have also been used for stroke rehabilitation, such as identification of muscle activation level, muscle contractions, muscle coherence, and neuromuscular disorder identification after stroke [4, 17].

An agonist to antagonist muscle activation helps in understanding the coordination of muscle activities [14]. However, crosstalk associated with these muscles, especially in the stroke-affected side (paretic), makes it difficult. A multivariate technique such as independent component analysis (ICA) has been used for crosstalk reduction and source separation of EMG signals. ICA is one of the blind source separation (BSS) techniques and helps in separating the sources without the knowledge of how they are mixed. This characteristic of ICA is very useful in EMG signal analysis where mixed sources can be separated into individual sources, and during that process crosstalk between muscles is minimized [13].

In this research, we investigated the independence of biceps and triceps brachii between paretic and non-paretic side during different maximal voluntary contractions (MVCs). This knowledge helps to understand the coordination between biceps and triceps brachii muscles and might help in rehabilitating the patients who suffered from a stroke and neuromuscular disorders.

2 Theory

ICA is one of the BSS techniques which aim to express the mixed (observed) data in terms of a linear combination of mutually independent latent variables, also known as independent components (ICs). In the simplest form of this problem, suppose we have n observations (mixtures or recordings) containing different instantaneous linear mixtures of n original sources and assuming that the original sources are independent of each other. In this case, we can use ICA to tackle this problem. Mathematically, we express this as $x = As$, where x and s are n-dimensional real vectors, and A is a non-singular mixing matrix [8]. ICA determines unmixing matrix W to estimate the unknown sources u (up to permutation and scaling): $u = Wx$. There exist various ICA algorithms in literature such as FastICA [8], Infomax [9], Jade [18], etc. This research uses the FastICA algorithm [8] due to its quick computational time as compared to other ICA algorithms.

3 Methods

3.1 Subjects

University Human Research Ethics Committee approved the experimental protocol for this study. Four patients affected with stroke participated in this study. An information sheet was given, and all the participants signed a consent form prior to the experiment.

3.2 Data Acquisition

Subjects seated in the chair with the hand gripping a dynamometer (refer to Fig. 1) and performed MVCs. Subjects generated and maintained the grip force at 25, 50 and 75% of maximal grip force (MGF) according to the feedback of the ratio to MVCs. The sEMG signals were recorded from both paretic (stroke-affected) and non-paretic hands. The eight muscles that involve in the flexion and extension of the hand, they are triceps brachii, biceps brachii, anterior deltoid, posterior deltoid, flexor carpi radialis, extensor carpi radialis, flexor digitorum superficialis, and extensor digitorum communis. The placement of electrodes was configured according to SENIAM guideline [6]. The trials each lasting for 5 s were repeated 3 times at each level. EMG signals were recorded from 8 muscles on upper extremities, which were sampled at 1000 Hz.

Fig. 1 Electrodes connection during the sEMG experiment

4 Data Processing and Feature Extraction

For this research, we investigated triceps brachii and biceps brachii muscles. EMG data were processed using Matlab R2015a software. A 4th order Butterworth band-pass filter with a frequency range of 20–450 Hz was applied to reject any frequency outside this range. FastICA algorithm was applied to extract ICs from two-channel (triceps brachii and biceps brachii) sEMG data for each MVCs. Time domain features of moving the window of 500 ms duration are extracted to evaluate the independence of paretic and non-paretic muscle activities for each MVCs, which include: (i) Root mean square (RMS), (ii) Mean absolute value (MAV) and (iii) Integrated absolute value (IAV). The feature details are summarized in Table 1. The RMS, MAV, and IAV were averaged over the 3 trials for each subject.

Table 1 Time domain features used for sEMG analysis

Features	Equations
RMS	$\sqrt{\frac{1}{N}\sum_{n=1}^{N} x(n)^2}$
MAV	$\frac{1}{N}\sum_{n=1}^{N} \lvert x(n)\rvert$
IAV	$\sum_{n=1}^{N-1} \lvert x(n)\rvert$

$x(n)$ = recorded/segmented sEMG signal at time n
n = time index of recorded sEMG signal
N = Total number of samples to be analyzed

5 Results and Discussion

The mean and standard deviation (SD) results for RMS, MAV, and IAV for both non-paretic and paretic sides are provided in Table 2 and Table 3 respectively. The same is plotted in Figs. 2, Fig. 3 and Fig. 4, respectively.

Figure 2 and Table 2 display the average ICA separated RMS of triceps brachii and biceps brachii muscles. From the results, it can be seen that biceps brachii values are independent and remain almost the same for both paretic and non-paretic sides for different MVCs. On the other hand, there is a decline in triceps brachii values for higher MVCs which indicate dependency for higher forces (MVCs). For full MVCs (100%) paretic side shows lower triceps brachii values as compared to the non-paretic side. It is understood that the reduction in sEMG activation level for triceps brachii during higher MVCs was mostly due to the increased muscle force, which attributed to the decrease in excessive muscle activations [7].

Figure 3 and Table 2 show the average MAV features of triceps brachii and biceps brachii muscles for ICA separated data. From the results, it can be seen that biceps brachii s exhibit almost the same muscle activities for both paretic and non-paretic sides for different MVCs. Conversely, similar to RMS features, there is a decline in triceps brachii values for higher MVCs. The decline in MAV is probably due to the stiffness of triceps brachii muscle and reduced co-contractions for higher forces [7, 10].

Table 2 Average time domain feature values for non-paretic side during different MVCs

Features	25% MVCs		50% MVCs		75% MVCs		100% MVCs	
	Triceps brachii	Biceps brachii	Triceps brachii	Biceps brachii	Triceps brachii	Biceps brachii	Triceps brachii	Biceps brachii
RMS (mv)	0.98 ± 0.12	1.00 ± 0.09	0.88 ± 0.19	0.97 ± 0.15	0.75 ± 0.17	0.97 ± 0.15	0.71 ± 0.13	0.93 ± 0.15
MAV (mv)	0.75 ± 0.16	0.87 ± 0.09	0.73 ± 0.14	0.79 ± 0.12	0.55 ± 0.15	0.82 ± 0.13	0.53 ± 0.11	0.78 ± 0.13
IAV (μv)	376.89 ± 78.99	437.33 ± 46.90	363.94 ± 79.82	395.67 ± 83.47	316.54 ± 63.26	408.07 ± 75.16	288.41 ± 61.70	391.88 ± 64.25

Table 3 Average time domain feature values for paretic side during different MVCs

Features	25% MVCs		50% MVCs		75% MVCs		100% MVCs	
	Triceps brachii	Biceps brachii	Triceps brachii	Biceps brachii	Triceps brachii	Biceps brachii	Triceps brachii	Biceps brachii
RMS (mv)	0.94 ± 0.13	0.96 ± 0.13	0.91 ± 0.09	0.93 ± 0.19	0.75 ± 0.15	0.98 ± 0.11	0.65 ± 0.16	0.99 ± 0.12
MAV (mv)	0.80 ± 0.13	0.82 ± 0.12	0.76 ± 0.12	0.79 ± 0.09	0.59 ± 0.1	0.86 ± 0.11	0.55 ± 0.12	0.87 ± 0.08
IAV (μv)	399.56 ± 87.38	412.33 ± 88.11	382.44 ± 85.09	395.35 ± 82.03	275.31 ± 83.16	427.66 ± 96.93	243.22 ± 80.64	434.81 ± 56.80

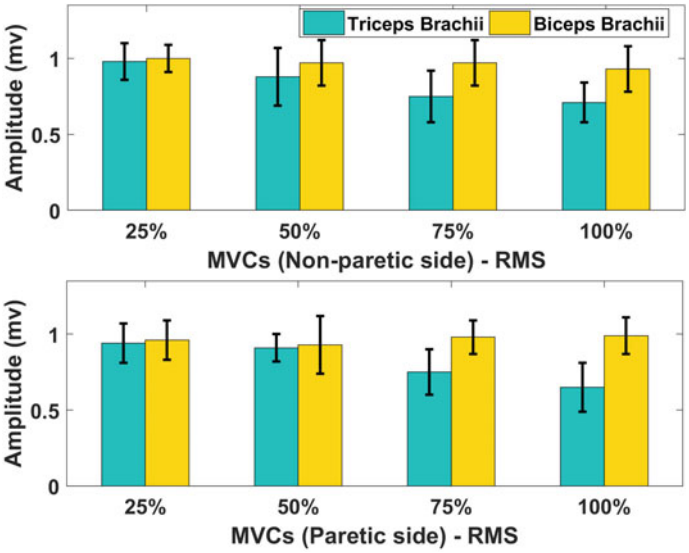

Fig. 2 Average RMS values for paretic and non-paretic sides during different MVCs

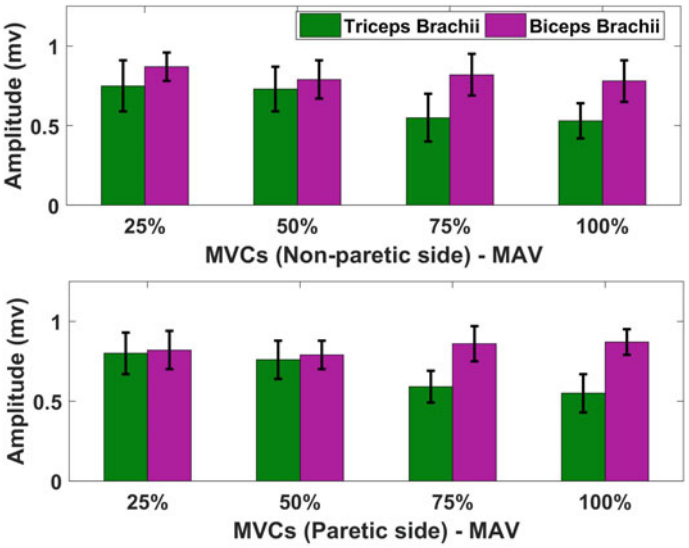

Fig. 3 Average MAV values for paretic and non-paretic sides during different MVCs

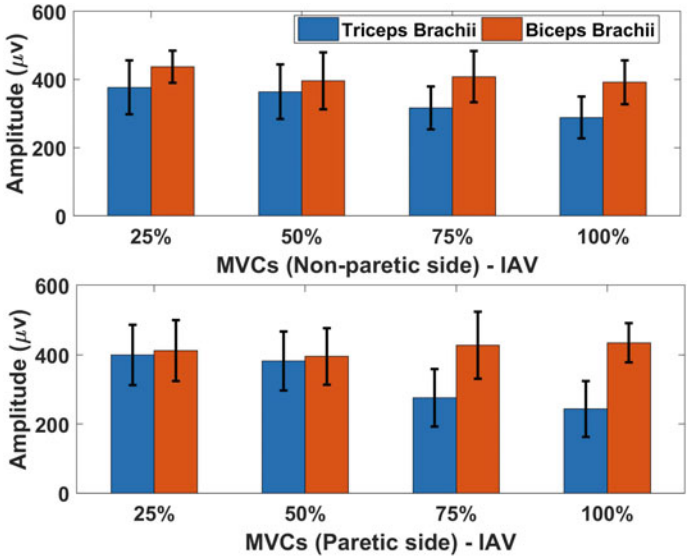

Fig. 4 Average IAV values for paretic and non-paretic sides during different MVCs

Figure 4 and Table 2 show the average IAV features of triceps brachii and biceps brachii muscles for ICA separated data. From the results, it can be observed that biceps brachii values remain identical for all MVCs for both paretic and non-paretic sides. On the contrary, there is a sharp decline in triceps brachii values for 75 and 100% MVCs of the paretic side. Paretic triceps brachii muscle exhibits dependency as compared to non-paretic side. For stroke-affected patients decline in triceps brachii muscle indicates a decrease in motor performance and this may have a significant effect on their upper extremity performances [10].

6 Results and Discussion

This study has produced clinically useful information on the effects of triceps brachii and biceps brachii muscles for a stroke affected patients. Both triceps brachii and biceps brachii muscles play a significant role in the stroke rehabilitation process. Information on their independence, co-contraction, and correlated motor performance are vital for after stroke rehabilitation process. The findings of this indicate that biceps brachii muscles exhibit more independence as compared to triceps brachii muscles in stroke patients. Additionally, the findings suggest that co-contraction of biceps brachii and triceps brachii muscles might be strongly correlated; this is in agreement with previous studies by [18]. However, further research using more sub-

jects and investigation on more muscles are needed to identify independent muscles, which would help in finding suitable muscles for the stroke rehabilitation process.

References

1. Aprile, I., Rabuffetti, M., Padua, L., Di Sipio, E., Simbolotti, C., Ferrarin, M.: Kinematic analysis of the upper limb motor strategies in stroke patients as a tool towards advanced neurorehabilitation strategies: a preliminary study. BioMed. Res. Int. **2014** (2014)
2. Cesqui, B., Tropea, P., Micera, S., Krebs, H.I.: EMG-based pattern recognition approach in post stroke robot-aided rehabilitation: a feasibility study. J. Neuroeng. Rehabil. **10**, 1 (2013)
3. Criswell, E.: Cram's Introduction to Surface Electromyography. Jones & Bartlett Publishers (2010)
4. Dipietro, L., Ferraro, M., Palazzolo, J.J., Krebs, H.I., Volpe, B.T., Hogan, N.: Customized interactive robotic treatment for stroke: EMG-triggered therapy. IEEE Trans. Neural Syst. Rehabil. Eng. **13**, 325–334 (2005)
5. Farina, D., Jiang, N., Rehbaum, H., Holobar, A., Graimann, B., Dietl, H., Aszmann, O.C.: The extraction of neural information from the surface EMG for the control of upper-limb prostheses: emerging avenues and challenges. IEEE Trans. Neural Syst. Rehabil. Eng. **22**, 797–809 (2014)
6. Hermens, H.J., et al.: European recommendations for surface electromyography. Roessingh Res. Dev. **8**, 13–54 (1999)
7. Hu, X., Tong, K.Y., Song, R., Tsang, V.S., Leung, P.O., Li, L.: Variation of muscle coactivation patterns in chronic stroke during robot-assisted elbow training. Arch. Phys. Med. Rehabil. **88**, 1022–1029 (2007)
8. Hyvärinen, A., Oja, E.: A fast fixed-point algorithm for independent component analysis. Neural Comput. **9**, 1483–1492 (1997)
9. Lee, T.-W., Girolami, M., Sejnowski, T.J.: Independent component analysis using an extended infomax algorithm for mixed subgaussian and supergaussian sources. Neural Comput. **11**, 417–441 (1999)
10. Leonard, C., Gardipee, K.A., Koontz, J.R., Anderson, J.-H., Wilkins, S.A.: Correlation between impairment and motor performance during reaching tasks in subjects with spastic hemiparesis. J. Rehabil. Med. **38**, 243 (2006)
11. Li, X., Liu, J., Li, S., Wang, Y.C., Zhou, P.: Examination of hand muscle activation and motor unit indices derived from surface EMG in chronic stroke. IEEE Trans. Biomed. Eng. **61**, 2891–2898 (2014)
12. Miller, L.C., Dewald, J.P.: Involuntary paretic wrist/finger flexion forces and EMG increase with shoulder abduction load in individuals with chronic stroke. Clin. Neurophysiol. **123**, 1216–1225 (2012)
13. Naik, G.R., Kumar, D.K., Palaniswami, M.: Signal processing evaluation of myoelectric sensor placement in low-level gestures: sensitivity analysis using independent component analysis. Expert Syst. **31**, 91–99 (2014)
14. Simoneau, E.M., Longo, S., Seynnes, O.R., Narici, M.V.: Human muscle fascicle behavior in agonist and antagonist isometric contractions. Muscle Nerve **45**, 92–99 (2012)
15. Song, R., Tong, K.Y.: EMG and kinematic analysis of sensorimotor control for patients after stroke using cyclic voluntary movement with visual feedback. J. Neuroeng. Rehabil. **10**, 1 (2013)
16. Sun, R., Song, R., Tong, K.: Complexity analysis of EMG signals for patients after stroke during robot-aided rehabilitation training using fuzzy approximate entropy. IEEE Trans. Neural Syst. Rehabil. Eng. **22**, 1013–1019 (2014)

17. Woodford, H., Price, C.: EMG biofeedback for the recovery of motor function after stroke. Cochrane Database Syst. Rev. **2** (2007)
18. Ziehe, A., Laskov, P., Nolte, G., Müller, K.R.: A fast algorithm for joint diagonalization with non-orthogonal transformations and its application to blind source separation. J. Mach. Learn. Res. **5**, 777–800 (2004)

BCI and EEG Signal Processing Applications

An EEG Brain-Computer Interface to Classify Motor Imagery Signals

Maria Karoline Andrade, Maíra Araújo de Santana, Giselle Moreno, Igor Oliveira, Jhonnatan Santos, Marcelo Cairrão Araújo Rodrigues and Wellington Pinheiro dos Santos

Abstract Considering the increase in life expectancy, people started to invest in technologies capable of improving the quality of life. One of these technologies is the Brain-Machine Interface. Combined with EEG signals, this technique may allow individuals with some motor disabilities to perform activities of daily living. Motor Imagery came up as an important tool to support this population. So they may send commands to external devices by using their brain voluntary activity. In this chapter, the performance of an Imagery EEG-based BCI engine was accessed by applying Wavelet transform to the signals and extracting metrics used to describe digital signals. We used signals from the motor imagery of the right hand, left hand and foot movements. Different intelligent classifiers were tested. We achieved results greater than 99% of accuracy and Kappa above 0.99. The method is promising and can be used for future evaluations with several individuals to verify reproducibility.

1 Introduction and Motivation

According to the World Health Organization (WHO), more than 2 billion people will need at least one assistive device until 2030. This estimation duplicates for the elderly [9, 12, 24, 47, 54, 68, 69]. WHO also points out that nowadays, only one in every 10 poor people may have access to this kind of technology. That is due to the high costs associated with this technology and the lack of awareness about the use of the devices [9, 12, 24, 47, 54, 68, 69]. Despite these numbers, the development of new technologies is increasing year by year. These innovations aim to improve the quality of life of people with all kinds of disabilities.

M. K. Andrade · M. A. de Santana · G. Moreno · I. Oliveira · J. Santos · M. C. A. Rodrigues
W. P. dos Santos (✉)
Universidade Federal de Pernambuco, Recife, Brazil
e-mail: wellington.santos@ufpe.br

M. K. Andrade
e-mail: karoline.andrade@ufpe.br

G. Naik (ed.), *Biomedical Signal Processing*, Series in BioEngineering,
https://doi.org/10.1007/978-981-13-9097-5_5

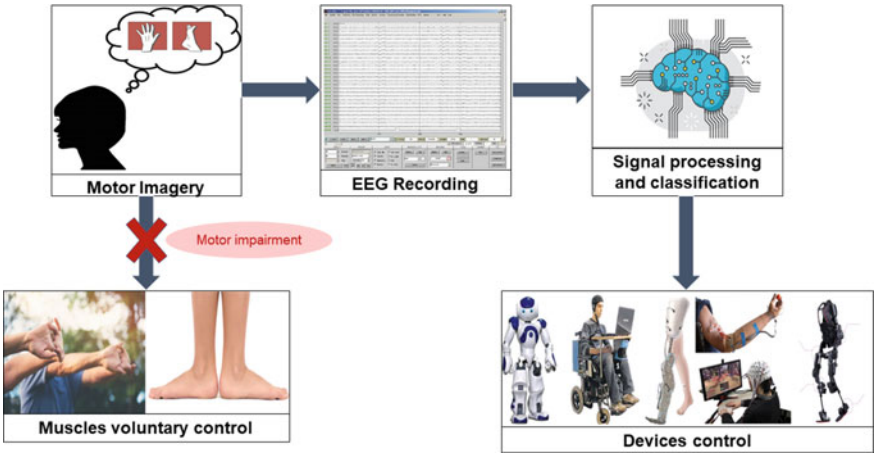

Fig. 1 Motor imagery combined to artificial intelligence techniques to control interfaces. *Source* Authors

Nowadays, many commercialized prostheses use myoelectric signals to control the movements. This kind of device requires remaining musculature, which turns it unfeasible for people with total limb loss. One possible solution to this limitation is prosthesis that uses Brain-Computer Interface (BCI) combined with Electroencephalogram (EEG) signals. This approach may allow these people to control interfaces (hardwares or softwares) using their brain activity, such as shown in Fig. 1. Several groups worldwide have been working on this kind of technology. There is still a lot to be done since it needs to provide the largest mobility combined to a real-time response [4, 5, 10, 17, 22, 29, 37, 41, 42, 45, 67].

The brain-machine interface has proved to be a promising tool. According to Brain/Neural Computer Interaction (BNCI), it may have applications in the following areas: neural rehabilitation, brain-to-brain interface, robotics, and assistive technologies, space applications, clinical applications and miscellaneous. For assistive technologies, we can mention the following applications: BCI-controlled robot, BCI-controlled prosthetic, Controlling humanoid robots, driving wheelchairs [8, 11, 21, 43, 46, 51–53, 59, 66, 74, 75, 77].

Electrocorticography (ECoG), functional near-infrared spectroscopy (fNIRS), and other kinds of signals may be used to control BCI, however, EEG is still one of the most used. EEG acquisition process is non invasive, has a low cost, and has a good temporal resolution. Even though it is a good technique, there are several challenges in using EEG-based BCI. Two of the main ones are the non real-time response and the brain unstable dynamics [43, 70]. The way to overcome these problems is to optimize artificial intelligence techniques to achieve the best possible performance.

2 Materials and Methods

This study was divided into four (4) main steps. The first one consists of the signal recording using EEG. The second phase was the signal segmentation, in which we prepared the signal to the following steps. Each segment of the signal was subject to several procedures, to acquire some quantitative information from it. These information (features) were then used as entries for the classification step. During the classification, the features are used to describe each signal. The classifier's challenge is to learn some patterns to differentiate the instances of each group. Their main goal is to correctly group the signals. In this case, satisfactory classification rates mean that the intelligent system is capable of identifying imagined movements using only brain activity. The method is briefly described in Fig. 2.

2.1 Signals Acquisition Protocol

EEG was recorded using a g.tec g.Hiamp amplifier at a sampling rate of 256 Hz. A notch filter at 60 Hz and a bandpass filter between 0.5 and 60 Hz were applied during recording. Twenty-seven electrodes plus reference (placed on right ear) were used. The electrodes were placed over the sensorimotor area of the subject, according to Fig. 3. We observe the sensorimotor area since it is activated by the imagination of movements [56].

The dataset has information from five (5) sections of EEG recordings. We performed all sections with the same subject. In each section, the subject was placed in front of a computer screen. Randomly spaced commands were given to the subject by indicative arrows to the right, left, or upwards (see Fig. 4). The arrows appeared on the screen.

We associated the different arrows directions to imagined movements of his right hand, his left hand, or his foot, respectively. These movements were chosen since the brain area responsible for them are well separated, as may be seen in Fig. 5.

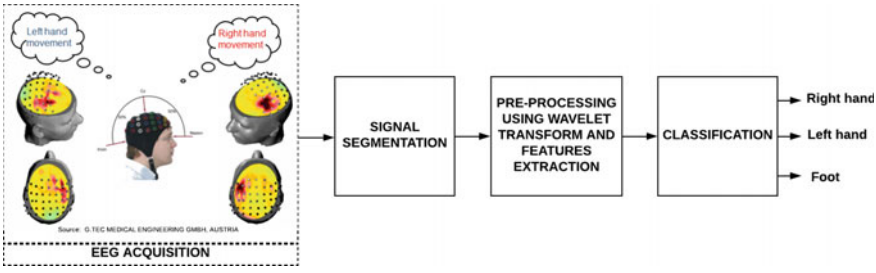

Fig. 2 Methods brief description. *Source* Authors

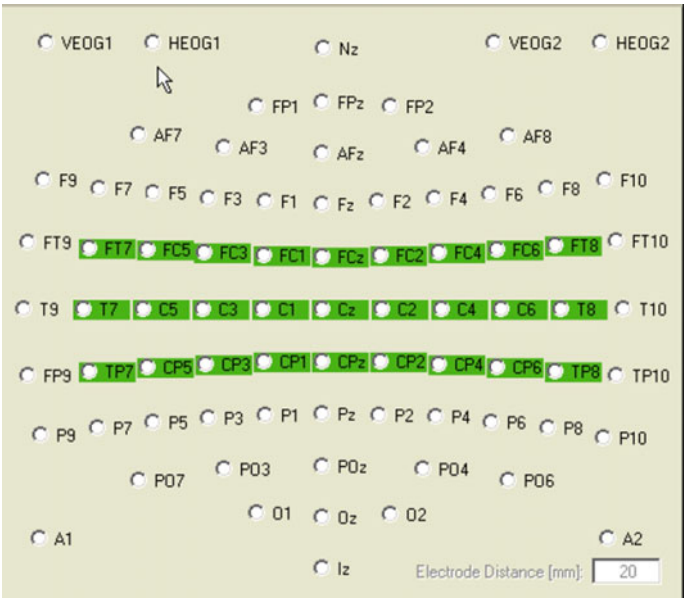

Fig. 3 Electrodes positioning. *Source* [30] (under permission)

The subject was asked to imagine the movement after seeing its respective arrow. We provide subject all this explanation before performing the experiment.

Each command lasts eight (8) seconds (Fig. 6). This time is enough to give the subject time to imagine the movement and record his brain activity. The subject was exposed to 60 commands in each section.

2.2 Signal Segmentation

In this step, we split each trial from EEG recordings. We used an 8 s window to catch the whole trial. It was done in order to separate the signals into the three classes, according to the respective imagined movement. We acquired a total of 100 recordings for the right hand, 98 of the left hand and 100 instances for foot imagined movement.

2.3 Pre-processing and Features Extraction

Considering that the Wavelet transform has a good resolution in the domains of frequency and temporal space [3, 16, 20, 49], after splitting the signal, we applied

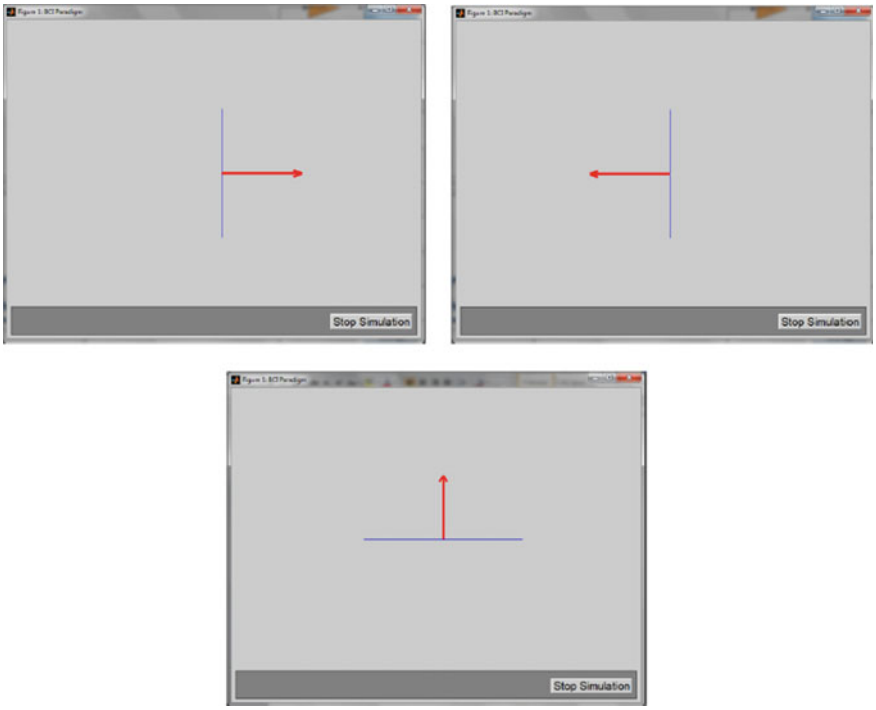

Fig. 4 Indicative arrows used to indicate which movement the subject should imagine. The upper left image shows the right arrow. The left arrow is shown in upper right image. The bottom image presents arrow upwards. *Source* [30] (under permission)

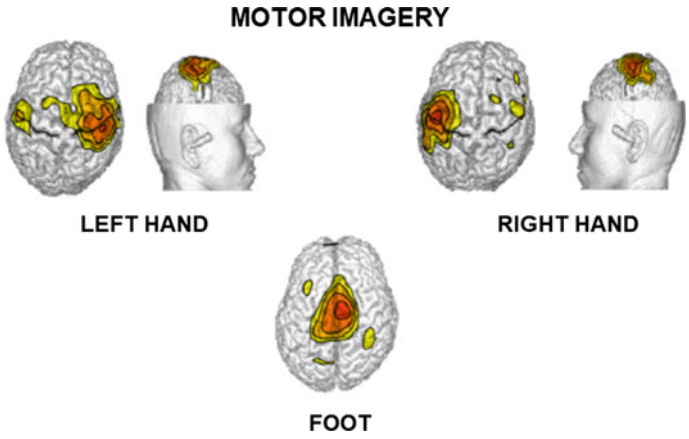

Fig. 5 Brain areas activated by the imagination of right hand, right arm and foot movements. *Source* Based on [58]

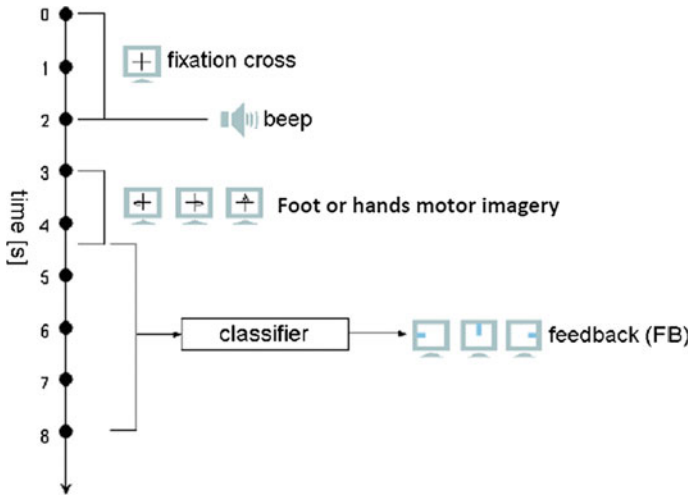

Fig. 6 Scheme of trial used to record brain activity during movement imagination using EEG. *Source* [30] (under permission)

the Wavelet transform with seven (7) levels. Then, we calculated the following attributes: Fourier Fast Transform coefficient, Standard Deviation, Energy, Entropy, Mean, Range, and Skewness. They were chosen since they are widely used in digital signal processing approaches [1, 44, 72, 76].

2.4 Classification

For the classification phase we performed experiments using nine (9) different algorithms and varying some of their parameters (see Table 1 for further information): Bayes Net, Naive Bayes, Multilayer Perceptron (MLP), Support Vector Machine (SVM), J48, Random Forest, Random Tree, Extreme Learning Machine (ELM) and Morphological Extreme Learning Machine (mELM).

Naive Bayes and Bayes Net are classifiers based on Bayes theory. They use conditional probability to create a data model. In a Bayes Net algorithm, we access the probability of a class node by checking the values given by other nodes (features). It assumes dependencies among the attributes. Its main parameter is the type of search that will be performed. Naive Bayes, on the other side, assumes that all attributes are independent of each other and are only connected to the class. It is considered 'naive' since it does not allow dependencies among the features [15].

The Support Vector Machine (SVM) performs a nonlinear mapping of the dataset into a higher dimension space. Then, it creates a hyperplane to separate the distinct classes. It is common to change the function that will build this boundary to see which one fits better to the dataset [14, 32].

Table 1 Classifiers configuration

Classifier	Parameters
BayesNet	–
NaiveBayes	–
MLP	Hidden layers: none, 1 and 2
	Learning rate: 0.3
	Momentum: 0.2
	Iterations: 500
SVM	Polynomial kernel: exponent (E) = 1–5
	RBF kernel
J48	–
RandomForest	Trees: 10, 50 and 100
RandomTree	–
ELM	Sigmoid kernel
mELM	Neurons in the hidden layer: 100
	Kernel: dilatation and erosion

Multi-Layer Perceptrons (MLPs) consist of complex artificial neural networks with multiple layers of neurons. An MLP has a set of sensory units that makes up the input layer, an intermediate layer (hidden layer), and the output layer. This neural network usually learns information through a backpropagation algorithm [32]. The state-of-the-art demonstrates that diverse architectures of multi-layer perceptrons trained with several algorithms are able to aid to distinguish different classes of data, with especially high accuracy in biomedical applications [7, 18–20, 61–65, 73].

J48 is a classifier that aims to build a decision tree from a database. It does that to get knowledge and thereby to shape decision-making. In this approach, the most significant attribute is called the root of the tree [55]. Random Forest also uses decision trees to perform classification. This classifier consists of a combination of trees, which hierarchically split the data. Considering an input vector and after generating a certain number of trees, each one cast a vote for a class of the problem. Then, the most voted class will be chosen in the classifier's prediction. In this classifier, the user may change the number of trees that will vote during classification [13]. A Random Tree is a decision tree that considers only some features for each node of the tree. These attributes are randomly selected [28].

The Extreme Learning Machine (ELM) is a training approach for single-layer neural networks. This classifier randomly generates input weights. Therefore, it is usually associated with fast learning phases. This characteristic may be relevant in applications that require several trainings iterations [25, 27, 34–36, 39, 48, 50, 78].

Proposed by Azevedo et al. [7], the mELM consists of applying non-linear kernels based on mathematical morphological operators. These operators perform procedures of dilatation and erosion on the dataset [7].

We tested ELM and mELM algorithms through GNU Octave, version 4.0.3. This software is an open-source environment for scientific computing developed by Eaton [23].

For the other algorithms, we performed tests using the Waikato Environment for Knowledge Analysis (WEKA), version 3.8.1. This software was released by the University of Waikato (New Zealand) and is licensed by the General Public License [26, 31, 33].

In order to access an appropriate statistical analysis, we run each configuration 30 times. To check classifiers' performance, we compared accuracy, Kappa statistic and confusion matrix. The accuracy consists of the percentage of correctly classified instances. Kappa statistic stands for the agreement coefficient. It measures the correlation between the expected results and the achieved ones. The confusion matrix, in turn, provides information regarding the rates of false positive, false negative, true positive, and true negative.

All tests were performed using K-fold cross-validation as a test method. In this approach, the algorithm splits the dataset into K subgroups. Then, it takes one by one to train the classifier and builds the testing set using the remaining subgroups. The final performance consists of the mean from the K tests [38].

3 Related Works

As mentioned before, non-invasive EEG signals are the most used in BCI. Most EEG electrodes require the use of a gel solution to balance impedance between skin and electrode. This gel may cause discomfort, and its application takes some time. Based on this, Spüler [71] performed an experiment using dry electrodes. He combined BCI based on Visual Evoked Potentials (VEPs), one-class Support Vector Machine (OCSVM), and euclidean distance. The tests performed achieved results up to 76% of mean accuracy and the mean communication speed of 46 bit/min. Expressive results, even though less satisfying than the ones obtained using gel-based electrodes.

There are several EEG-based BCI techniques, one of which is the Motor Imagery EEG-based BCI. In their study, Khalaf et al. [40] combined this technique with functional transcranial ultrasound Doppler (fTCD) to differentiate the imagined movements of the right and left arms. They wanted to access the system's ability to differentiate the imaged movement from a baseline and each other. The obtained results were up to 89.48%, using SVM. This result corresponds to the differentiation of left-arm imagined movement in relation to a baseline. Their results were similar to previous literature for EEG-fNIRS hybrid BCIs, but they achieved a better response time.

Qureshi et al. [57] used independent component analysis (ICA) to classify EEG signals of motor imagery of four movements: left hand, right hand, both feet, and tongue. Eight (8) subjects participated in the tests. They obtained a mean accuracy of 94.29% and individual accuracy of up to 97.80%. These results were accessed using ELM as a classifier. Roman-Gonzalez [58], in turn, achieved accuracy up to

96.77%. He used LDA and autoregressive parameters to classify movements from the right hand, left hand, and foot.

One challenge of using the EEG-based BCI is the distinction between more refined movements, such as finger movements of one hand. Alazrai et al. [6] used the Choi-William distribution (CWD) and the quadratic time-frequency distribution (QTFD). They analyzed EEG signals from eight (8) subjects who performed 20 finger movements with the right hand. Using a two-layer classification framework (2LCF), they obtained a mean accuracy of 87.2%. The less satisfying result was 79% for ring finger movements. Samuel et al. [60] extracted attributes of time and frequency domains from EEG signals of motor imagery. In this study, they obtained results of up to 99% accuracy to identify five hand movements.

One of the practical applications for EEG-based BCI is the control of robots. Ai et al. [2] combined common spatial pattern (CSP), local characteristic-scale decomposition (LCD) and functional brain networks. The attributes extracted had information from the frequency and spatial domains of the signal. Robot movements were related to the following tasks of the motor imagery: Feet movement (forward), right-hand movement (right), left-hand movement (left), tongue movement (backward). The best result was an accuracy of 89.7% and Kappa of 0.86.

4 Results and Discussion

Table 2 shows the classifiers' performance for all tested configurations. The best and worse configuration are highlighted in green and red, respectively.

After analysing all the results we selected the best configuration for each classifier. To do so, we compared accuracy, kappa, the standard deviation associated with them. Parameters complexity was also checked, in a way that we prioritized less computational costing configurations. Finally, we plot these configurations in order to graphically visualize data and access some statistical information. Figure 7 shows the results for accuracy while Kappa results are presented in Fig. 8.

As may be seen from the results, most classifiers configuration had an outstanding performance for both accuracy and Kappa statistic. Many classifiers achieve results really close to the maximum (100% for accuracy and 1.0 for Kappa). Both Bayesian classifiers had less satisfying performance, while SVM, ELM, and mELM performed better. The main difference between each configuration lies in the data dispersion. Again, SVM, ELM, and mELM (kernel dilatation) were more consistent, presenting very low dispersion. The tree-based classifiers and Bayesian networks showed more data dispersion than the others.

Table 3 presents the confusion matrix for the best (SVM—poly kernel E = 3) and worse (Naive Bayes) results in the classification phase. From the matrices we can observe almost none confusion for the best result, agreeing with the previous presented results. For the worse result, we may note that there is almost none confusion between right and left hands imagined movement. This result matches our expectations since it is assumed that the brain activation area associated with these

Table 2 Mean and Standard Deviation (SD) of accuracy and Kappa statistic for all tested configurations

CLASSIFIER	Configuration	ACCURACY		KAPPA STATISTIC	
		Mean	SD	Mean	SD
Bayes Net	-	90.75%	5.10	0.86	0.08
Naive Bayes	-	74.62%	5.65	0.62	0.08
MLP	Hidden layers: none	98.79%	2.12	0.98	0.03
	Hidden layers: 1	92.24%	6.57	0.88	0.10
	Hidden layers: 2	87.39%	9.54	0.81	0.14
	Hidden layers: 'a' *	99.28%	1.70	0.99	0.02
SVM	Polynomial kernel (E=1)	96.90%	3.16	0.95	0.05
	Polynomial kernel (E=2)	99.17%	1.57	0.99	0.02
	Polynomial kernel (E=3)	99.38%	1.42	0.99	0.02
	Polynomial kernel (E=4)	99.27%	1.61	0.99	0.02
	Polynomial kernel (E=5)	98.97%	1.99	0.98	0.03
	RBF kernel	75.67%	5.81	0.63	0.09
J48	-	94.53%	4.39	0.92	0.06
Random Forest	Trees: 10	98.08%	2.76	0.97	0.04
	Trees: 50	98.77%	2.17	0.98	0.03
	Trees: 100	98.83%	2.03	0.98	0.03
Random Tree	-	94.94%	4.55	0.92	0.07
ELM	Sigmoid kernel	99.31%	1.50	0.99	0.02
mELM	Dilatation kernel	99.17%	1.53	0.99	0.02
	Erosion kernel	98.77%	2.14	0.98	0.02

*'a' = (attribs + classes) / 2 = 29

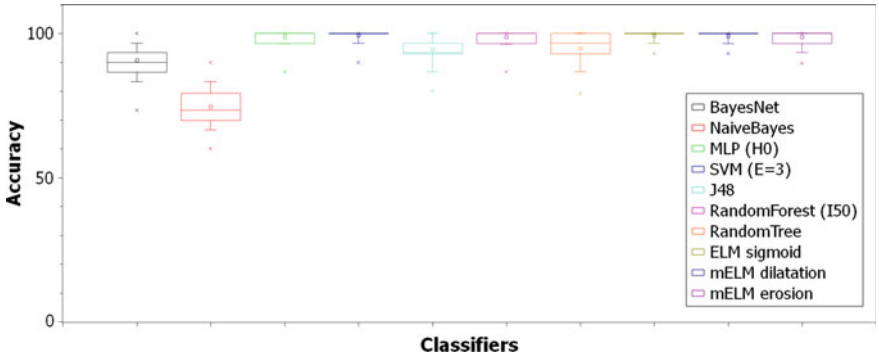

Fig. 7 Accuracy for classifiers best configuration. *Source* Authors

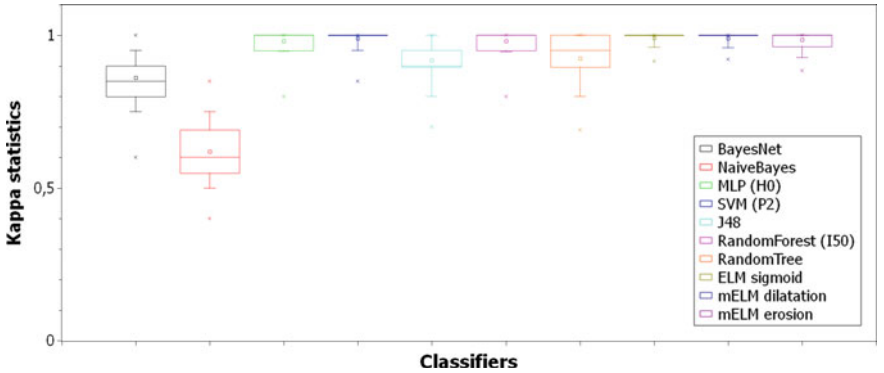

Fig. 8 Kappa statistic for classifiers' best configurations. *Source* Authors

Table 3 Confusion matrices for the best and worse results obtained during classification

		Right hand	Left hand	Foot
BEST RESULT	**Right hand**	99	0	1
	Left hand	1	97	0
	Foot	1	0	99
WORST RESULT	**Right hand**	90	10	0
	Left hand	3	93	2
	Foot	56	5	39

movements are quite far from each other, becoming easily differentiated. Imagined foot movement, however, was dramatically confused with right-hand imagery in this trial.

5 Conclusions

The approach used here showed that the chosen attributes combined with the Wavelet transform provide satisfying results in the differentiation of hand and foot movements. The promising results indicate that the method may be feasible for an application in assistive technology. On the other hand, from an application perspective, there are crucial points that still need to be analyzed. The first one is the low possibility of generalization, due to the particularities of each human brain. This aspect is well explored in Spüler [71], cited above, where different individuals had individual accuracy values from 2.3 to 82.8%.

For more complex applications, with more refined movements, there is still a lot to be improved. Alazrai et al. [6] approach confirm this need, even obtaining a good accuracy, with average results per finger being up to 87.2%, they have not reached

an ideal result yet. This is due to the fact that the execution of finger movements requires simultaneity. In the case of motor imagery, the response waves are slow, thus becoming another challenge to a rapid processing and immediate response.

It is worth mentioning that the EEG signal used here has a good temporal resolution, but it has limitations on spatial resolution. We observed that this characteristic did not limit the results since we achieve an accuracy of up to 99%. This was similar to the results obtained by Samuel et al. [60]. We consider that this spatial limitation deserves to be better evaluated since it may disrupt the achievement of desirable characteristics for BCI.

Acknowledgments We are grateful to the Brazilian research-funding agencies CAPES, CNPq and Facepe, for the partial support for this research.

References

1. Acharya, U.R., Oh, S.L., Hagiwara, Y., Tan, J.H., Adeli, H.: Deep convolutional neural network for the automated detection and diagnosis of seizure using EEG signals. Comput. Biol. Med. **100**(1), 270–278 (2018)
2. Ai, Q., Chen, A., Chen, K., Liu, Q., Zhou, T., Xin, S., Ji, Z.: Feature extraction of four-class motor imagery EEG signals based on functional brain network. J. Neural Eng. (2019). https://doi.org/10.1088/1741-2552/ab0328
3. Akay, M.: Wavelet applications in medicine. IEEE Spectr. (1997)
4. Al-Timemy, A.H., Bugmann, G., Escudero, J., Outram, N.: A preliminary investigation of the effect of force variation for myoelectric control of hand prosthesis. In: 2013 35th Annual International Conference of the IEEE Engineering in Medicine and Biology Society (EMBC), pp. 5758–5761. IEEE (2013)
5. Al-Timemy, A.H., Khushaba, R.N., Bugmann, G., Escudero, J.: Improving the performance against force variation of EMG controlled multifunctional upper-limb prostheses for transradial amputees. IEEE Trans. Neural Syst. Rehabil. Eng. **24**(6), 650–661 (2016)
6. Alazrai, R., Alwanni, H., Daoud, M.I.: EEG-based BCI system for decoding finger movements within the same hand. Neurosci. Lett. **698**, 113–120 (2019)
7. Azevedo, W.W., Lima, S.M., Fernandes, I.M., Rocha, A.D., Cordeiro, F.R., da Silva-Filho, A.G., dos Santos, W.P.: Fuzzy morphological extreme learning machines to detect and classify masses in mammograms. In: 2015 IEEE International Conference on Fuzzy Systems (FUZZ-IEEE), pp. 1–8. IEEE (2015)
8. Bashashati, A., Fatourechi, M., Ward, R.K., Birch, G.E.: A survey of signal processing algorithms in brain-computer interfaces based on electrical brain signals. J. Neural Eng. **4**(2), R32 (2007)
9. Bauer, S.M., Elsaesser, L.J., Arthanat, S.: Assistive technology device classification based upon the World Health Organization's, International Classification of Functioning, Disability and Health (ICF). Disabil. Rehabil. Assist. Technol. **6**(3), 243–259 (2011)
10. Bergmeister, K.D., Hader, M., Lewis, S., Russold, M.F., Schiestl, M., Manzano-Szalai, K., Roche, A.D., Salminger, S., Dietl, H., Aszmann, O.C.: Prosthesis control with an implantable multichannel wireless electromyography system for high-level amputees: a large-animal study. Plast. Reconstr. Surg. **137**(1), 153–162 (2016)
11. Birbaumer, N., Cohen, L.G.: Brain-computer interfaces: communication and restoration of movement in paralysis. J. Physiol. **579**(3), 621–636 (2007)
12. Borg, J., Larsson, S., Östergren, P.O.: The right to assistive technology: for whom, for what, and by whom? Disabil. Soc. **26**(2), 151–167 (2011)

13. Breiman, L.: Random forests. Mach. Learn. **45**(1), 5–32 (2001)
14. Cauwenberghs, G., Poggio, T.: Incremental and decremental support vector machine learning. In: Advances in Neural Information Processing Systems, pp. 409–415 (2001)
15. Cheng, J., Greiner, R.: Learning Bayesian belief network classifiers: algorithms and system. In: Stroulia, E., Matwin, S. (eds.) Advances in Artificial Intelligence, pp. 141–151. Springer, Berlin, Heidelberg (2001)
16. Chui, C.K.: An Introduction to Wavelets, 1st edn. Academic Press, New York (1992)
17. Controzzi, M., Clemente, F., Barone, D., Ghionzoli, A., Cipriani, C.: The SSSA-MyHand: a dexterous lightweight myoelectric hand prosthesis. IEEE Trans. Neural Syst. Rehabil. Eng. **25**(5), 459–468 (2017)
18. Cordeiro, F.R., dos Santos, W.P., da Silva-Filho, A.G.: Segmentation of mammography by applying GrowCut for mass detection. Stud. Health Technol. Inform. **192**, 87–91 (2013)
19. Cordeiro, F.R., Santos, W.P., Silva-Filho, A.G.: A semi-supervised fuzzy GrowCut algorithm to segment and classify regions of interest of mammographic images. Expert Syst. Appl. **65**, 116–126 (2016)
20. Cruz, T., Cruz, T., Santos, W.: Detection and classification of lesions in mammographies using neural networks and morphological wavelets. IEEE Lat. Am. Trans. **16**(3), 926–932 (2018)
21. Daly, J.J., Wolpaw, J.R.: Brain-computer interfaces in neurological rehabilitation. Lancet Neurol. **7**(11), 1032–1043 (2008)
22. Dyson, M., Barnes, J., Nazarpour, K.: Myoelectric control with abstract decoders. J. Neural Eng. (2018)
23. Eaton, J.W., Bateman, D., Hauberg, S.: GNU Octave manual version 3: a high-level interactive language for numerical computations. Netw. Theory (2008)
24. Eide, A.H., Øderud, T.: Assistive technology in low-income countries. In: Disability & International Development, pp. 149–160. Springer (2009)
25. Feng, G., Huang, G.B., Lin, Q., Gay, R.K.L., et al.: Error minimized extreme learning machine with growth of hidden nodes and incremental learning. IEEE Trans. Neural Netw. **20**(8), 1352–1357 (2009)
26. Fong, S., Biuk-Aghai, R.P., Millham, R.C.: Swarm search methods in Weka for data mining. In: Proceedings of the 2018 10th International Conference on Machine Learning and Computing, ICMLC 2018, pp. 122–127. ACM, New York, NY, USA (2018). https://doi.org/10.1145/3195106.3195167
27. de Freitas, R.C., Alves, R., da Silva-Filho, A.G., de Souza, R.E., Bezerra, B.L.D., dos Santos, W.P.: Electromyography-controlled car: a proof of concept based on surface electromyography, extreme learning machines and low-cost open hardware. Comput. Electr. Eng. **73**, 167–179 (2019)
28. Geurts, P., Ernst, D., Wehenkel, L.: Extremely randomized trees. Mach. Learn. **63**(1), 3–42 (2006)
29. Ghazaei, G., Alameer, A., Degenaar, P., Morgan, G., Nazarpour, K.: Deep learning-based artificial vision for grasp classification in myoelectric hands. J. Neural Eng. **14**(3), 036,025 (2017)
30. (g.tec), G.T.: Common Spatial Patterns 3-class BCI, vol. v2.16.00. Guger Technologies, Schiedlberg, Austria (2016)
31. Hall, M., Frank, E., Holmes, G., Pfahringer, B., Reutemann, P., Witten, I.H.: The WEKA data mining software: an update. ACM SIGKDD Explor. Newsl. **11**(1), 10–18 (2009)
32. Haykin, S.: Neural Networks: A Comprehensive Foundation. Prentice Hall, New York (1999)
33. Holmes, G., Donkin, A., Witten, I.H.: Weka: a machine learning workbench. In: Proceedings of the 1994 Second Australian and New Zealand Conference on Intelligent Information Systems, 1994, pp. 357–361. IEEE (1994)
34. Huang, G.B., Zhou, H., Ding, X., Zhang, R.: Extreme learning machine for regression and multiclass classification. IEEE Trans. Syst. Man Cybern. Part B (Cybernetics) **42**(2), 513–529 (2012)
35. Huang, G.B., Zhu, Q.Y., Siew, C.K.: Extreme learning machine: a new learning scheme of feedforward neural networks. In: Proceedings of 2004 IEEE International Joint Conference on Neural Networks, 2004, vol. 2, pp. 985–990. IEEE (2004)

36. Huang, G.B., Zhu, Q.Y., Siew, C.K.: Extreme learning machine: theory and applications. Neurocomputing **70**(1–3), 489–501 (2006)
37. Ison, M., Artemiadis, P.: The role of muscle synergies in myoelectric control: trends and challenges for simultaneous multifunction control. J. Neural Eng. **11**(5), 051,001 (2014)
38. Jung, Y., Hu, J.: A K-fold averaging cross-validation procedure. J. Nonparametric Stat. **27**, 167–179 (2015)
39. Kasun, L.L.C., Zhou, H., Huang, G.B., Vong, C.M.: Representational learning with extreme learning machine for big data. IEEE Intell. Syst. **28**(6), 31–34 (2013)
40. Khalaf, A., Sejdic, E., Akcakaya, M.: A novel motor imagery hybrid brain computer interface using EEG and functional transcranial Doppler ultrasound. J. Neurosci. Methods **313**(1), 44–53 (2019)
41. Khushaba, R.N., Al-Timemy, A., Kodagoda, S., Nazarpour, K.: Combined influence of forearm orientation and muscular contraction on EMG pattern recognition. Expert Syst. Appl. **61**, 154–161 (2016)
42. Khushaba, R.N., Krasoulis, A., Al-Jumaily, A., Nazarpour, K.: Spatio-temporal inertial measurements feature extraction improves hand movement pattern recognition without electromyography. In: 2018 40th Annual International Conference of the IEEE Engineering in Medicine and Biology Society (EMBC), pp. 2108–2111. IEEE (2018)
43. Lécuyer, A., Lotte, F., Reilly, R.B., Leeb, R., Hirose, M., Slater, M.: Brain-computer interfaces, virtual reality, and videogames. Computer **41**(10), (2008)
44. Li, J., Sun, S.: Energy feature extraction of EEG signals and a case study. In: 2008 IEEE International Joint Conference on Neural Networks (IEEE World Congress on Computational Intelligence), pp. 2366–2370 (2008)
45. Liu, J.: Feature dimensionality reduction for myoelectric pattern recognition: a comparison study of feature selection and feature projection methods. Med. Eng. Phys. **36**(12), 1716–1720 (2014)
46. Lotte, F., Congedo, M., Lécuyer, A., Lamarche, F., Arnaldi, B.: A review of classification algorithms for EEG-based brain-computer interfaces. J. Neural Eng. **4**(2), R1 (2007)
47. Martin, S., Kelly, G., Kernohan, W.G., McCreight, B., Nugent, C.: Smart home technologies for health and social care support. Cochrane Database Syst. Rev. **4**(2) (2008)
48. Martínez-Martínez, J.M., Escandell-Montero, P., Soria-Olivas, E., MartíN-Guerrero, J.D., Magdalena-Benedito, R., GóMez-Sanchis, J.: Regularized extreme learning machine for regression problems. Neurocomputing **74**(17), 3716–3721 (2011)
49. Massopust, P.R.: Fractal Functions, Fractal Surfaces and Wavelets, 1st edn. Academic Press, New York (1994)
50. Miche, Y., Sorjamaa, A., Bas, P., Simula, O., Jutten, C., Lendasse, A.: OP-ELM: optimally pruned extreme learning machine. IEEE Trans. Neural Netw. **21**(1), 158–162 (2010)
51. Middendorf, M., McMillan, G., Calhoun, G., Jones, K.S.: Brain-computer interfaces based on the steady-state visual-evoked response. IEEE Trans. Rehabil. Eng. **8**(2), 211–214 (2000)
52. Millán, J.d.R., Rupp, R., Müller-Putz, G., Murray-Smith, R., Giugliemma, C., Tangermann, M., Vidaurre, C., Cincotti, F., Kubler, A., Leeb, R., et al.: Combining brain-computer interfaces and assistive technologies: state-of-the-art and challenges. Front. Neurosci. **4**, 161 (2010)
53. Nicolas-Alonso, L.F., Gomez-Gil, J.: Brain computer interfaces: a review. Sensors **12**(2), 1211–1279 (2012)
54. Organization, W.H.: International classification of functioning, disability, and health: children & youth version: ICF-CY. World Health Organization (2007)
55. Pahwa, P., Papreja, M., Miglani, R.: Performance analysis of classification algorithms. Int. J. Comput. Sci. Mobile Comput. **3**(4), 50–58 (2014)
56. Pfurtscheller, G., Neuper, C.: Motor imagery activates primary sensorimotor area in humans. Neurosci. Lett. **239**, 65–68 (1997)
57. Qureshi, M.N.I., Cho, D., Lee, B.: EEG classification for motor imagery BCI using phase-only features extracted by independent component analysis. In: 2017 39th Annual International Conference of the IEEE Engineering in Medicine and Biology Society (EMBC), pp. 2097–2100 (2017). https://doi.org/10.1109/EMBC.2017.8037267

58. Roman-Gonzalez, A.: EEG signal processing for BCI l. In: Hippe, Z.S., Kulikowski, J.L., Mroczek, T. (eds.) Human-Computer Systems Interaction: Backgrounds and Applications 2: Part 1, pp. 571–591. Springer, Berlin, Heidelberg (2012)
59. Saha, S., Mamun, K.A., Ahmed, K., Mostafa, R., Naik, G.R., Khandoker, A., Darvishi, S., Baumert, M.: Progress in brain computer interfaces: challenges and trends (2019). arXiv:1901.03442
60. Samuel, O.W., Geng, Y., Li, X., Li, G.: Towards efficient decoding of multiple classes of motor imagery limb movements based on eeg spectral and time domain descriptors. J. Med. Syst. **41**(12), 194 (2017)
61. dos Santos, M.M., da Silva Filho, A.G., dos Santos, W.P.: Deep convolutional extreme learning machines: filters combination and error model validation. Neurocomputing **329**, 359–369 (2019)
62. dos Santos, W.P., de Assis, F.M., de Souza, R.E., Mendes, P.B., de Souza Monteiro, H.S., Alves, H.D.: A dialectical method to classify Alzheimer's magnetic resonance images. In: Evolutionary Computation. InTech (2009)
63. dos Santos, W.P., de Assis, F.M., de Souza, R.E., dos Santos Filho, P.B.: Evaluation of Alzheimer's disease by analysis of MR images using Objective Dialectical Classifiers as an alternative to ADC maps. In: 30th Annual International Conference of the IEEE Engineering in Medicine and Biology Society, 2008, EMBS 2008, pp. 5506–5509. IEEE (2008)
64. dos Santos, W.P., de Assis, F.M., de Souza, R.E., Santos-Filho, P.B., de Lima Neto, F.B.: Dialectical multispectral classification of diffusion-weighted magnetic resonance images as an alternative to apparent diffusion coefficients maps to perform anatomical analysis. Comput. Med. Imaging Graph. **33**(6), 442–460 (2009)
65. dos Santos, W.P., de Souza, R.E., dos Santos Filho, P.B.: Evaluation of Alzheimer's disease by analysis of MR images using multilayer perceptrons and Kohonen SOM classifiers as an alternative to the ADC maps. In: 29th Annual International Conference of the IEEE Engineering in Medicine and Biology Society, 2007, EMBS 2007, pp. 2118–2121. IEEE (2007)
66. Schalk, G., McFarland, D.J., Hinterberger, T., Birbaumer, N., Wolpaw, J.R.: BCI2000: a general-purpose brain-computer interface (BCI) system. IEEE Trans. Biomed. Eng. **51**(6), 1034–1043 (2004)
67. Scheme, E., Englehart, K.: Electromyogram pattern recognition for control of powered upper-limb prostheses: state of the art and challenges for clinical use. J. Rehabil. Res. Dev. **48**(6) (2011)
68. Scherer, M.J.: Assessing the benefits of using assistive technologies and other supports for thinking, remembering and learning. Disabil. Rehabil. **27**(13), 731–739 (2005)
69. Scherer, M.J., Glueckauf, R.: Assessing the benefits of assistive technologies for activities and participation. Rehabil. Psychol. **50**(2), 132 (2005)
70. Schwartz, A.B., Cui, X.T., Weber, D.J., Moran, D.W.: Brain-controlled interfaces: movement restoration with neural prosthetics. Neuron **52**, 205–220 (2006)
71. Spüler, M.: A high-speed brain-computer interface (BCI) using dry EEG electrodes. Plos One **12**(2), 1–12 (2017)
72. Trakoolwilaiwan, T., Behboodi, B., Lee, J., Kim, K., Choi, J.W.: Convolutional neural network for high-accuracy functional near-infrared spectroscopy in a brain-computer interface: three-class classification of rest, right-, and left-hand motor execution. Neurophotonics **5**(1), 5–15 (2017)
73. de Vasconcelos, J.H., dos Santos, W.P., de Cássia Fernandes de Lima, R.: Analysis of methods of classification of breast thermographic images to determine their viability in the early breast cancer detection. IEEE Lat. Am. Trans. **16**(6), 1631 (2018)
74. Wolpaw, J., Wolpaw, E.W.: Brain-computer interfaces: principles and practice. OUP, USA (2012)
75. Wolpaw, J.R., Birbaumer, N., McFarland, D.J., Pfurtscheller, G., Vaughan, T.M.: Brain-computer interfaces for communication and control. Clin. Neurophysiol. **113**(6), 767–791 (2002)

76. Yuan, Q., Zhou, W., Li, S., Cai, D.: Epileptic EEG classification based on extreme learning machine and nonlinear features. Epilepsy Res. **96**(1), 29–38 (2011)
77. Zander, T.O., Kothe, C.: Towards passive brain–computer interfaces: applying brain–computer interface technology to human–machine systems in general. J. Neural Eng. **8**(2), 025,005 (2011)
78. Zhu, Q.Y., Qin, A.K., Suganthan, P.N., Huang, G.B.: Evolutionary extreme learning machine. Pattern Recognit. **38**(10), 1759–1763 (2005)

Using Artificial Neural Networks on Multi-channel EEG Data to Detect the Effect of Binaural Stimuli in Resting State

Maurício da Silva Júnior, Rafaela Covello de Freitas, Washington Wagner Azevedo da Silva, Marcelo Cairrão Araújo Rodrigues, Erick Francisco Quintas Conde and Wellington Pinheiro dos Santos

Abstract More than 7% of the population of the world is afflicted by anxiety disorders. If related to mood disorders, anxiety can trigger or escalate other symptoms and affects mental diseases, akin depression, and suicidal behavior. Recent works have shown that binaural beats are able to reduce anxiety and modify other psychological conditions, significantly changing cognitive processes and mood states. They can be defined as a low-frequency acoustic stimuli perceived when a given individual is subjected to two marginally different wave frequencies, from 200 to 900 Hz. In the present work, we applied a 5 Hz binaural beat to 6 different subjects, to detect if relevant changes could be noticed in their brainwaves after the stimuli. Twenty minutes stimuli in ten separate sessions were applied. In order to detect these possible differences, we used a single hidden layer Multi-Layer Perceptron neural network and compared its results to non-parametric statistical tests and Low-Resolution Brain Electromagnetic Tomography (eLORETA). Results obtained on eLORETA point to a strong increase in the current distribution, mostly in the Alpha 2 band, at the Anterior Cingulate, pertinent to the recognition and expression of emotions, as well as the monitoring of mistakes regarding social conduct. Many Artificial neural networks models, principally Multi-Layer Perceptron architectures, proved to be able to highlight the main differences with high separability in Delta and Theta spectral bands.

M. da Silva Júnior · W. W. A. da Silva · M. C. A. Rodrigues · W. P. dos Santos (✉)
Universidade Federal de Pernambuco, Recife, Brazil
e-mail: wellington.santos@ufpe.br

R. C. de Freitas
Escola Politécnica de Universidade de Pernambuco, Recife, Brazil
e-mail: rcf@ecomp.poli.br

E. F. Q. Conde
Universidade Federal Fluminense, Campos dos Goytacazes, Brazil
e-mail: psicoerick@yahoo.com.br

G. Naik (ed.), *Biomedical Signal Processing*, Series in BioEngineering,
https://doi.org/10.1007/978-981-13-9097-5_6

1 Introduction

One of the most common mental disorders is anxiety, responsible for bringing several problems to those whom it affects. It can be categorized into social phobia (agoraphobia), panic disorder, generalized anxiety disorder, and obsessive compulsive disorder (OCD) [51]. Usual symptoms range from physical manifestations (palpitations, tremors, trembling, dyspnea), fear of losing control, fear of public places, difficulty concentrating, fear of specifics subjects, such as animals, situations, or natural phenomena [3].

Anxiety disorders afflict almost 7.3% of the planet's population, and recent research suggests that one in 14 people will experience an anxiety event during the given year [4]. It also can trigger or increase other diseases' symptoms and effects, as when associated with mood disorders, such as depression and suicidal behavior [59]. Aiming to alleviate this condition, several treatments have been arising, many of them based on music stimulation.

According to [43], music is an intricate combination of amplitude and frequency patterns that interacts with the human brain, interfering in some of its processes, such as synaptic plasticity, neuronal learning, and world perception [43]. Consequently, different types of music evoke specific physical alterations, such as reduction of pain and blood pressure, and psychological modifications as well, like stress attenuation, relaxation, and good mental moods [36].

Positive results were found on a specific type of acoustic stimulation, which has proven to be able to reduce anxiety as also to attenuate or enhance other psychological conditions and states. It is called a binaural beat [50, 70, 71]. The binaural beat is the cerebral perception of a low-frequency sound originated when the individual is subjected to two slightly different wave frequencies (maximum of 30 Hz), both with frequencies ranging from 200 to 900 Hz [9, 42, 70].

Binaural beats were first perceived and related by *Dove*, before the XIX century, and later detailed by *Oster*, in 1973. For the time being, the binaural beats have been used as an alternative for treatment or manipulation of neuronal activity pattern [9, 18], achieving good results when applied to mental disorders, as is the case of anxiety [50, 70, 71], depression, attention deficit, epilepsy, mood states, vigilance, and concentration states.

The scientific community presents several examples of well-succeeded applications of binaural beats, specifically attending to anxiety problems. Wahbeh et al. [70], for example, was able to show a statistically significant decrease in anxiety self-report (as also a decrease in tension, confusion, and fatigue) of individuals subjected to Theta (4–7 Hz) and Delta (0.5–3.5 Hz). Padmanabhan et al. [50] reported a reduction of 26.3% in anxiety scores, according to *State-Trait Anxiety Inventory* (STA-I) results when applying binaural beats in pre-operatory patients. An analogous approach was taken by Weiland et al. [71], where binaural beats and sound compositions were applied to 170 pre-operatory patients. Their work showed a decrease in anxiety after a 20 min stimulation, based on STA-I answers before and after the intervention. The experiment related by Puzi et al. [53] evinced that stress and anxiety in

students were diminished by 61% after a 10 Hz binaural beat session, according to the *Depression, Anxiety and Stress Scales* test (DASS). Lastly, a pilot study made by Le Scouranec et al. [41] showed the first study related to binaural beats applications, describing positive results after applying the aforementioned stimulus in theta and delta waves. The binaural beat stimulus was applied within 4 weeks, from 1.4 to 2.4 times per week, for approximately 30 min, on each subject. The results were analysed based on STA-I answers, showing that the scored trended toward a reduction in anxiety levels, after the sessions. It is important to emphasize, however, that the results are usually presented based on the questionnaire's responses, being, therefore, subjective [50, 70, 71].

A different and perhaps more objective approach to analyze the impact of those stimuli in the human brain is to acquire and process the electroencephalographic (EEG) signal [64] from each individual, before and after the binaural beats application, in order to find out if a physical change occurred and how it affected the resultant signal. To observe these changes, statistics are often applied, usually relying on methods for feature extraction such as temporal (Hjorth Parameters, Detrended Fluctuation Analysis), spectral (Non-parametrics, Parametrics, Coherence, etc.), time-frequency, and non-linear features [46]. Pre-processing the signal is usually necessary to identify artifacts and clean the signal, using mathematical tools such as Independent Component Analysis (ICA) [68]. Often, many steps are followed in order to extract the signal's attributes, with the aim to analyze it. With the purpose of simplifying this process we propose a novel approach for determining if there were any changes in the EEG signal, using a bandpass Finite Impulse Response (FIR) filter, withdrawing the remaining artifacts after running ICA on the signal and, finally, using a classifier based on Multi-Layer Perceptrons to verify the conditions of the signal before and after the binaural stimuli. The state-of-the-art demonstrates that many architectures of multi-layer perceptrons are capable of differentiating among categories of the same data, with high performance in biomedical applications [2, 16, 17, 19, 20, 55–58, 65]. We then compared the proposed method with a non-parametrical statistical analysis, in order to see the reliability of the emerging results.

The subsequent sections are organized as follows: In Sect. 2, we show the state-of-the-art of the research field, as well as a brief of our proposal; in Sect. 3, we present the materials and methods utilized in this work and Sect. 4, we present the experimental results and discussions. Our conclusions are provided in Sect. 6. This chapter is an extended version of the work presented in [61].

2 Related Works

The effects of auditory beat stimulation have been investigated using monaural and binaural beats [9]. Monaural beats are generated when sine waves of similar frequencies and with the same amplitudes are presented to either both ears simultaneously, while binaural beats are perceived when the waves described previously are presented to each ear separately. For instance, when the 400 Hz tone is presented to the left

ear and the 440 Hz tone to the right one, a beat of 40 Hz is perceived, which appears subjectively to be spatially localized inside the head. This is known as the binaural beat perception. This phenomenon was first registered by H. W. Dove, in 1839, and outlined in detail by Oster [49], who reported that the binaural beats were detected only when the carrier frequency was below 1000 Hz [9]. This finding confirmed an earlier study by Licklider et al. [42], which indicates that beat carrier frequencies have to be low enough to be temporally encoded by the cortex [9, 60].

Oster [49] described binaural beats as "muffled sounds" with an intensity close to 3 dB and also discovered that the acoustic signals responsible for producing the binaural beat must have the same intensity. Other characteristics were pointed out by Oster [49], namely: (1) enhancement of binaural beats by external noise; (2) the proof that the binaural beats are processed differently due to the superior olivary nucleus, due to neurons sensitive to the oscillations of the acoustic signal. Oster [49] also related that some patients were not able to hear the beats or even could not localize the sound produced by the examiner. Coincidentally, people who were unable to localize the generated sounds also suffered from Parkinson's disease [49].

The effects of binaural beats and other types of stimuli are based on the assumption of brainwaves entrainment, also known as Frequency Following Response (FFR) [66]. According to [28], FFR arises from converging inputs of populations of neurons tending to follow a specific external frequency pattern, given the proper stimulation. Consequently, the brainwaves entrainment can be directly influenced by binaural beats. Besides these results, the assumption of FFR is still in discussion, since some works have related no achievements on brainwaves entrainment based on EEG density analysis [25, 66].

Despite the uncertain effect on binaural beats entrainment, there are several works that show a positive influence of this type of stimulation [9, 22, 38, 50, 70]. Applied to areas such as anxiety, depression, creative processes, memory, attention, vigilance, and mood states [9], binaural beats have shown good results. For example, [22] demonstrated that the application of binaural beats of 5 Hz for 15 min twice a day, during 15 days, significantly increased the number of words recalled post-stimulation compared to other techniques. Lane et al. [38] showed that people subjected to binaural beats on Beta 2 range (16–24 Hz), while executing vigilance tasks, presented better performance than when hearing sounds without binaural beats.

There are also reports related to the interference in mood states and the creative process. Wahbeh et al. [70] showed that mood states like depression, fatigue, inertia, and tension were diminished after the application of binaural beats, during 60 days, in Theta, Beta, and Delta frequencies. Lane et al. [38] also showed decreases in depression sub-scales after binaural beat stimulation in Beta, suggesting that stimulation with binaural beats in the given frequencies may be related to a less negative mood. The conditions were assessed using the Profile of Mood States (POMS) questionnaire.

The impact of a binaural beat can also be seen in an EEG analysis. To detect the influence of this sound [35] used the average of the amplitudes of the EEG spectral frequencies allied to statistical analysis, in order to check whether the morphology of the bioelectrical signal had changed after stimuli. Using a 10 Hz binaural beat

stimulus on a sample group of 20 individuals, he observed the FFR effect, finding a component of equivalent frequency to the applied stimulus [35]. The statistical analysis using ANOVA proved the theta wave presented an average increasing amplitude in EEG [35], while there was a significant decrease in the average amplitude of Beta and Alpha brainwaves. Becher et al. [6] recorded the intracranial EEG of a brain under stimulation of 5, 10, 40, and 80 Hz binaural beats, and compared the results with the monoaural beats stimuli. Analyzing power and phase beat synchronization with a Bonferroni-corrected non-parametric label permutation test, results showed that power and phase modulation were statistically and significantly different between the signals, mostly decreasing before and after the stimuli application, at temporo-basal, temporo-lateral, surface sites, and medio-temporal sites [6].

Beauchene et al. [5] applied several EEG signal analysis to perceive statistically significant differences among 6 types of auditory signals (none, pure tone, classical music and 5, 10 and 15 Hz binaural beats), in order to observe its effects on working memory, tested by the delayed match to sample visual task [69]. The metrics used for the analysis were time-frequency synchronization measures using the Phase-Locking Value (PLV), graphical network measures, and Connectivity Ratio (CR). One-way ANOVA was then applied, showing that the theta band had the most significant response among the other bands, and presented the most evident result when the activities were done by 15 Hz binaural beat [5].

Our proposal is based on the identification of binaural beat stimuli using the Independent Component Analysis (ICA) and posterior machine learning techniques over the EEG filtered signals, in order to identify alterations due to binaural beat stimuli. Regarding the EEG signal analysis of binaural using ICA preprocessing, we did not find any works. Nevertheless, several EEG related articles employed similar approaches in order to remove artifacts from signals with significant information. ICA assumes that signals are composed of statistically independent sub-signals [44]. Therefore, after applying ICA to EEG, it is possible to identify the independent data and, consequently, apply some artifact removal techniques, in order to eliminate or, at least, reduce the influence of biosignals originated from the activity of the eyes, breathing, and muscle movements, for example. Jung et al. [34] related that EEG signals collected from normal and autistic subjects demand proper artifact separation, detection, and removal after ICA data analysis. Snyder et al. [63] demonstrated that ICA associated with dipole fitting was able to identify the pure movement artifact in EEG acquired data with an accuracy of up to 99%. However, besides the strong application in EEG data analysis, we did not find any binaural beat related work with such an analysis technique at the pre-processing stage.

In this work, we present the use of artificial neural networks to classify the binaural beats entrainment effects. Despite their regular use on Brain-Controlled Interfaces (BCI) for Motor-Imagery tasks [10, 26] and other applications [23, 47], we did not find works on machine learning applied to binaural beats entrainment detection. Intelligent tools based on machine learning, especially on artificial neural networks, have been successfully applied to process and classify EEG data. For instance, [47] used a Multi-Layer Perceptron (MLP) to classify different emotions based on their EEG data pattern, achieving a considerable accuracy rate of 95.36%.

In summary, we used four different methods to verify every possible change from a different point of view. In the first one, we applied a simple statistical analysis using a non-parametric test for unpaired samples (Friedman test), aiming to find the statistical differences between conditions, regarding EEG amplitude. We then used the *exact-Low Resolution Brain Electromagnetic Tomography* to investigate the spatial changes possibly caused by the binaural beat stimulus, and to compare with already known functionalities of the anatomical structures of the brain. We also aimed to investigate the discrimination capabilities of pattern recognition algorithms in identifying the same changes in amplitude modulation before and after the binaural stimuli. With the latter, the goal was also to investigate, from another perspective, which frequency bands showed the most prominent differences among conditions, and to compare the obtained results with the previous analysis. At last, we applied a self-report questionnaire of the State-Trait Anxiety Inventory and Beck Depression Inventory, looking forward to evaluating the conscious answers of each individual regarding the effects of the binaural beats sessions.

The statistical analysis showed that there were significant differences for almost every condition evaluated, for specific electrodes, regarding Theta, Alpha 1, Alpha 2, Beta 1 and Beta 2, while for Delta, almost every electrode showed different results between conditions. Regarding the eLORETA, our main results suggest a strong increase in the current distribution, mostly in the modulation in Alpha 2, at the Anterior Cingulate. The neural activity of this structure is related, among others, to the monitoring of mistakes regarding social conduct, as also on the recognition and expression of emotions.

Our third analysis showed that pattern recognition algorithms are capable of evincing the main differences among all studied conditions (PRE1 $\times$ POS1, PRE10 $\times$ POS10, and PRE1 $\times$ POS10), with high separability in Delta and, surprisingly, in Theta. Lastly, regarding the self-report questionnaire of the State-Trait Anxiety Inventory and Beck Depression Inventory, significant differences between conditions were not found, although a trend towards diminishing the scores after the tenth session was observed.

EEG analysis is usually handled after the implementation of several preprocessing techniques, including artifact processing and temporal, spectral, frequency, time-frequency and nonlinear feature extraction, used in order to gather information about the data [46].

3 Methods

3.1 Selection and Description of Subjects

A total of 14 volunteers, aging between 18 and 35 years old, all residing in Recife's metropolitan region, State of Pernambuco, Brazil, participated in this research. They were recruited using invitation letters distributed by digital social media networks,

in which they were informed of the experiments purpose, the contact information of the responsible researcher, possible doubts, and the laboratory location where the experiment would be performed.

As eligibility criteria, the participants should be aged between 18 and 35 years old, reporting normal auditory functions, never subjected to binaural beats stimulation, and free of neurological disorders (including epileptic crises). Furthermore, the volunteers should not have ingested caffeine, alcohol, or any drugs 24 hours before EEG recording. The consumption of drugs capable of affecting the nervous system was also prohibited. We excluded subjects in which the recorded signals were compromised by the excessive presence of artifacts or presented pathological traces, such as epileptiform activity, too slow waves, or undesired periodic patterns. These and other aspects of this research were evaluated using three questionnaires: Identification Questionnaire, The State-Trait Anxiety Inventory, and Beck Depression Inventory detailed in Sect. 3.2.

All chosen participants signed a consent form, agreeing on participating in the study. Due to technical problems, the data collected from 8 subjects were lost. The remaining data from 6 subjects (3 males and 3 females) were used in this work. The participants were informed that at any time and for any reason, they could interrupt the session.

3.2 Instruments and Equipment

3.2.1 Identification Questionnaire

This questionnaire was applied to record the subjects' personal information, such as educational degree, age, civil status, and gender. We aimed to collect and evaluate the subjects' experience with binaural beats acoustic stimulation, as well as gather information about possible illnesses or any psychiatric treatment.

3.2.2 The State-Trait Anxiety Inventory—STA-I

STA-I is a tool used to evaluate two different anxiety constructs: trait and state. The test possesses two consecutive scales, one for measuring the state of anxiety and the other for measuring the trait-anxiety, each containing 20 questions, itemized with 4 alternatives. For each item, the candidate should assign, among 4 possible alternatives (1—"almost never"; 2—"sometimes"; 3—"often"; 4—"almost always"), the one that fits the most his/her feelings. The total test score varies between 20 and 80, in which 20–40 points characterize a low anxiety level, 41–60 points a medium anxiety level, and 61–80 points a high anxiety level.

3.2.3 Beck Depression Inventory—BDI

The Beck Depression Inventory is also a self-report test of 21 questions, in which each question has 4 possible answers. The participant is, therefore, instructed to choose the one that better fits his/her feelings about the question. The total test score varies between 0 and 63, where 0 is the lowest score, indicating lack of depression; 10–16 means light to moderate depression state; 17–29 comprises a moderate to a severe depressive state, and 29–63 indicates a severe depressive state.

3.2.4 EEG Acquisition Equipment

For collecting and amplifying the EEG data, we used a Nexus-32 system combined with Biotrace+ software (MinMedia, Roermond-Herten, the Netherlands). Nexus-32 has 32 channels for data acquisition. Biotrace+ can be used to synchronize, store, process, and export the sampled EEG. Its applicability and portability make it suitable for a large range of biofeedback protocols and physiological monitoring.

Nexus-32 is able to use Bluetooth technology to communicate with computers, but the preferable option used in this experiment was the data transference through optic fiber cable and the EEG sampling rate for the acquisition was 256 Hz. EEG is commonly recorded at sampling rates between 250 and 2000 Hz. The EEG acquisition should occur at a minimum sampling rate of three times the high-frequency filter setting. However, higher rates are always preferable. The sample rate needs to be high enough to prevent the aliasing effect.

3.2.5 Binaural Beats Generator

To generate the Binaural Beats, we used the open-source software Gnaural Binaural Beat Audio Generator 2.0. It makes possible the designing of binaural beats based on the parameters described by Oster [49]. This program allows us to create and export the generated data in several different audio and frequency formats. Therefore, using the Gnaural, we created and exported an audio sample containing the 5 Hz binaural beat using carrier waves of 400 and 405 Hz.

The composition of the binaural tones was based on [49], emphasizing that the background around the 400 Hz frequency band is easier to be detected by the subjects. No noises or instrumental sounds were superimposed on the binaural tones.

3.2.6 Earphones

We employed as supra-auricular earphones the Seenheiser HD 220 with frequency response 19–21 kHz, impedance 24 Ω, Sound pressure level (SPL) of 108 dB, and total harmonic distortion $<0.5\%$. The headphone was placed covering the external area of the ear and presenting the possibility of support, and acoustic shells adjust. It

is designed to block the external sound noise and can reproduce 19–21 kHz frequency sounds, reaching a maximum of 108 dB of sound intensity. Its impedance is of 24 Ω.

3.3 Procedural Information

After signing the consent form and answering the proposed questionnaires, the subjects were instructed to schedule sessions to record their EEG (first and tenth sessions) and to receive the binaural beats stimulus (from second to the eighth session). Then, the volunteers were conducted for the first session in the Laboratory of Cognitive Neuroscience at the Federal University of Pernambuco (LNeC-UFPE), Recife, Brazil. There, the volunteers had their foreheads and ears cleaned with an abrasive solution, in order to remove possible skin's dirt and oiliness. Afterward, we placed an EEG cap with 21 electrodes in the subject's head, with 19 electrodes for data acquisition and 2 electrodes for reference on each of the subject's ears.

3.3.1 Data Acquisition

After signing the consent form and answering the proposed questionnaires, the subjects were instructed to schedule sessions to record their EEG (first and tenth sessions) and to receive the binaural beats stimulus (from second to the eighth session). Then, the volunteers were conducted for the first session in the Laboratory of Cognitive Neuroscience at the Federal University of Pernambuco (LNeC-UFPE), Recife, Brazil. There, the volunteers had their foreheads and ears cleaned with an abrasive solution, in order to remove possible skin's dirt and oiliness. Afterward, we placed an EEG cap with 21 electrodes in the subject's head, with 19 electrodes for data acquisition and 2 electrodes for reference on each of the subject's ears.

Nineteen active electrodes were positioned in accordance with the 10–20 system, in the following scalp areas: Prefrontal (Fp1 and Fp2); Frontal (F3 and F4); Front Midline (Fz); Central (C3 and C4); Central Vertex (CZ); Parietal Midline (P3 and P4); Anterior Temporal (F7 and F8); Medial Temporal (T7 and T8); Posterior Temporal (P7 and P8); Posterior Midline (Pz) and Occipital (O1 and O2) in addition to two auricular reference electrodes (A1 and A2). Figure 1 displays a diagram of the used cap for data acquisition.

Each EEG cap was adjusted accordingly to each subject after the circumference of their heads, and the distance between the craniometric points was measured. Once adjusted, a conductive gel was applied to enable better conductivity.

In this situation, the EEG baseline of each participant was acquired and then the binaural stimulus was applied for 20 min. After that, another EEG recording was performed, concluding the first session of the experiment. The EEG was record uninterruptedly during the experiment. However, we only analyze the periods before and after the stimulation. Placed markers in the record were used to separate the

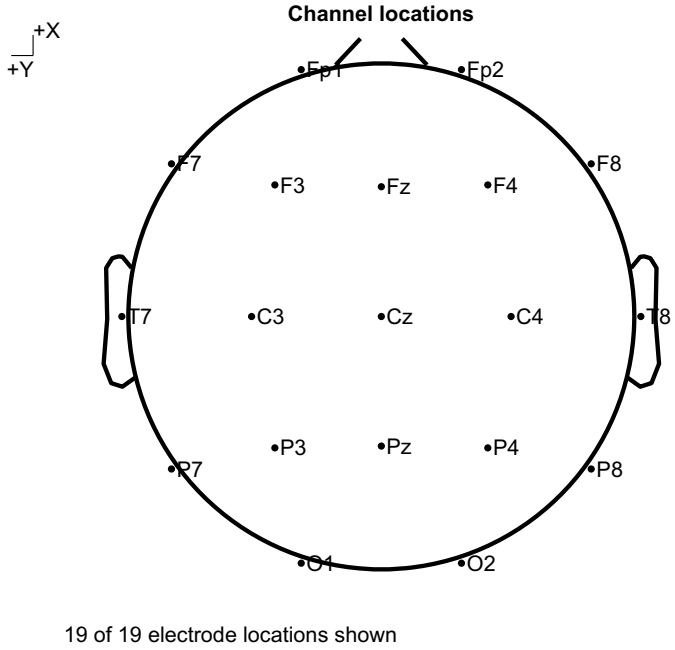

Fig. 1 Cap diagram with 19 electrodes

stimulation section from the others, which started and ended with a delay of 1–2 min for placement and removal of the headset.

Subsequently, the other 8 scheduled sessions were performed, where no EEG recording was performed. In this situation, each participant was accommodated in a chair with arms support, placed in a room with attenuated sound and luminosity, in the LNeC. The binaural stimuli had intensities of 75–80 dB, maintained for 20 min, and the subjects were oriented to keep their eyes closed during the experiment. These intensities were empirical, determined by asking the subjects to return when the signal intensity could be considered comfortable.

As showed in Fig. 3, we used 20 min for the Binaural Beat stimulation and 80 s for the EEG recording time. This temporal dynamic was thought according to [32, 33], that demonstrated a maximum effect of entrainment of the amplitude of the Theta band on the EEG after 10 min of stimulation with binaural beats, decaying into a plateau at 20 min of stimulation and remaining sustained up to at least 30 min.

In the tenth session, the same procedure of session 1 was followed. Once finished, they were told to fill again the psychological inventories, as they did before the first session, detailed in Sect. 3.1. Figure 2 summarizes the whole process for better understanding.

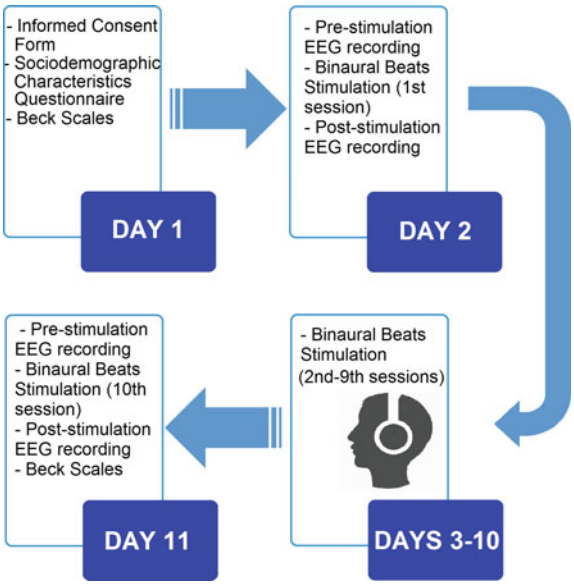

Fig. 2 Timeline of experiment. On the first day, the participants went to the Laboratory of Cognitive Neuroscience (LNeC) to read and sign the informed consent form (ICF). They also completed the sociodemographic characteristics questionnaire and then Beck's Depression (BDI) and Anxiety (BAI) inventories. In the next day, the subjects who filled the inclusion criteria, attended the Laboratory of Applied Neuroscience (NeuroLab BRASIL) to record the EEG, in a rest state, 5 min with open and 5 min with closed eyes, before and after 20 min of stimulation with binaural beats. From the third to the tenth day, the subjects daily experienced one session of binaural beats. On the 11th day, the subjects should return to the NeuroLab BRASIL, when we collected again their EEG, before and after the last session of binaural beats. Lastly, subjects answered again to Beck's scales questionnaire

3.3.2 Data Preprocessing

To obtain the EEG spectrum distribution, 80 s were extracted from each period of records, before and after the 1st and 10th sessions. Artifacts were extracted through visual inspection. The collected data were divided into four conditions, being them: PRE1, POS1, PRE10, and POS10. The PRE1 and POS1 conditions corresponded to the first session when EEG was collected before and after the first binaural stimuli, while PRE10 and POS10 are the EEG records for the tenth session. A pictorial representation of the process for data acquisition concerning epoch, stimulation, and time, is depicted in Fig. 3.

For each volunteer, 40 epochs of 2 s per condition were acquired and saved in Matlab format (.mat), containing 20,480 signal samples and 19 columns for the electrodes. Three types of analysis were performed: statistical, eLORETA, and feature classification analysis. Each of them considered three different conditions: PRE1 × POS1, PRE10 × POS10, PRE1 × POS10. Considering this situation, for each par-

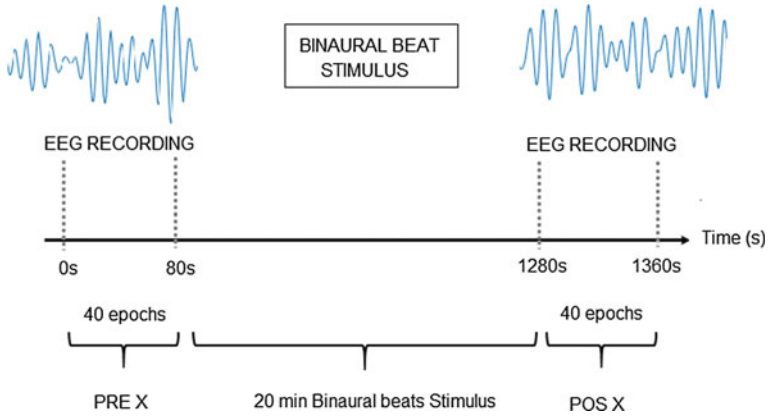

Fig. 3 Pictorial representation of epoch, stimulation and time for data acquisition

ticipant, the data were separated in four .mat files, concerning the conditions PRE1, POS1, PRE10, and POS10, and then individually processed using the EEGLab plugin, installed in Matlab programming environment. Once processed, the files from each subject were concatenated in four main files, one for each condition (PRE1, POS1, PRE10, and POS10). The next topics explain in more detail some of the steps taken for preprocessing the data, and the flowchart, depicted in Fig. 4, provides a general picture of the matter.

1. Filtering
   For filtering, we used a passband Finite Impulse Response (FIR) filter to all the stated conditions in 7 different frequency ranges [7, 13, 37]. Since we chose the default filter order for all the frequency filtering (option provided by EEGLab), it changed based on the cutoff frequencies of each passband window. Their values are detailed in Table 1.
2. Independent Component Analysis—ICA
   The Independent Component Analysis is a method for identifying linear and statistically independent signals superposed in mixed data. Supposing we have two recorded signals, $x_1(t)$ and $x_2(t)$, and assuming that they can be written as a linear combination of two statistically independent signals $s_1(t)$ and $s_2(t)$, as described in Eqs. 1 and 2,

$$x_1(t) = a_{1,1}s_1(t) + a_{1,2}s_2(t) \tag{1}$$

$$x_2(t) = a_{2,1}s_1(t) + a_{2,2}s_2(t) \tag{2}$$

   ICA manages to find the values of the $a_{i,j}$ coefficients, to solve the Eqs. 1 and 2 by classical methods [30]. The aforementioned equations describe the classical illustration of the *Cocktail-Party Problem* [30].
   Therefore, considering ICA's purpose, several applications have emerged, one of

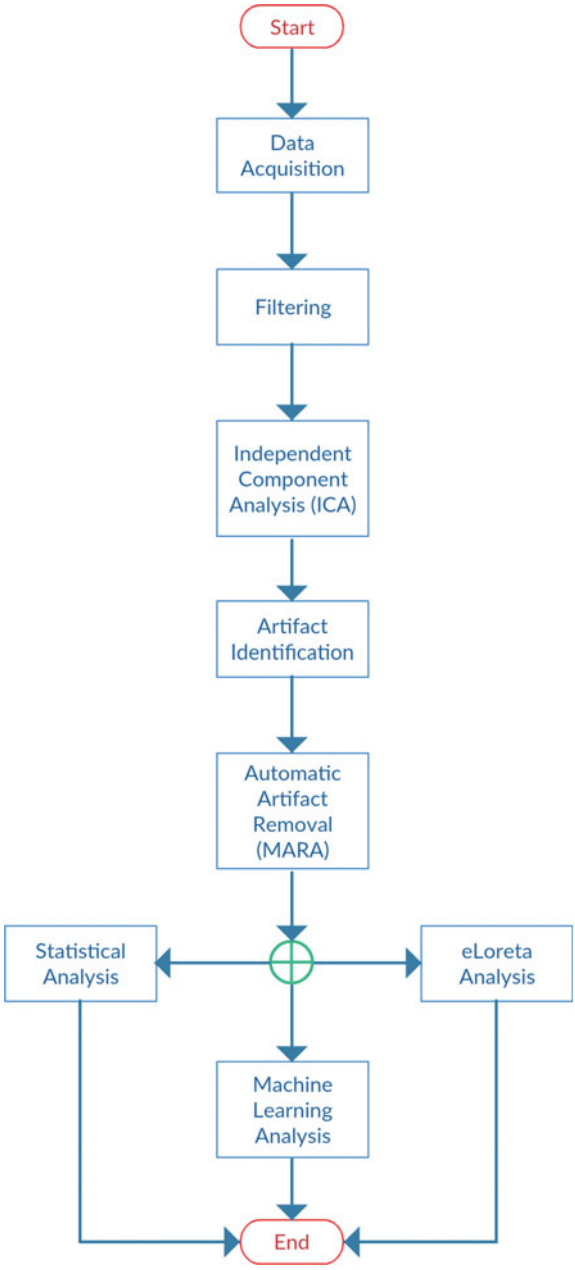

Fig. 4 Flowchart for data acquisition, artifact removal, and data analysis

Table 1 Passband filters and orders [7, 13, 37]

Waves	Ranges (Hz)	Filter order
Broadband*	0.5–35	1690
Delta	0.5–3.5	1690
Theta	4–7	424
Alpha 1	7.5–9.5	424
Alpha 2	10–12.5	339
Beta 1	13–23	261
Beta 2	24–35	143

them being for EEG analysis [30]. In EEGLab, the ICA option is available in MARA [72] plugin, explained on the next topic.

3. Artifacts Identification and Removal using MARA
   Once the independent components were separated, the MARA plugin was used in order to identify the noisy signal's components, such as muscular or breathing artifacts. MARA is an open-source EEGLAB plugin that automatizes the process of hand labeling independent components for artifact rejection [11]. Initially, it uses PCA for reducing the signal dimensionality, and after it applies the TDSEP (Temporal Decorrelation source Separation) algorithm, an ICA method that takes temporal correlations into account for identifying the independent components. Then, 6 features are extracted from the data (*Current Density Norm*, *Range Within Pattern*, *Mean Local Skewness*, λ, *8–13 Hz* and *FitError*) and a Regularized Linear Discriminant Analysis Classifier is used to identify the artifacts. The classifier and features were proven to be the optimal configurations, according to [72], since the trained classifier on unseen data leads to a Mean Square Error of 8.9%, showing a high agreement with the expert's labeling. Once the artifacts were identified and removed from the data, the remaining independent components are projected back to the sensor space, before proceeding with the analysis. MARA is free software distributed under the GNU General Public License.

3.4 eLORETA

The eLORETA (exact-Low Resolution Electromagnetic Tomography) is a method that allows the estimation of probabilistic models of the signals sources within the brain anatomy. It is based on algorithms that report the solution of the inverse problem of the EEG signal with zero error estimation, having, therefore, the property of providing the exact localization for any point source in the brain for any arbitrary distribution [8, 15]. eLORETA is also able to provide the correct localization of sources even in the presence of structured noise. However, low spatial resolution is

provided, in which each voxel presents an anatomical resolution of 5 millimeters for the anatomical model utilized [1].

The algorithms that report the solution of the inverse problem to rely on the differences of electric potentials, measured on the scalp for computing the localization and intensity of the electrically active sources, represented by current density (A/m^2) for each voxel [21]. Also, the brain model used for the anatomical representation of the current sources is based on the cortical model of the Montreal Neurological Institute (MNI), composed of 6239 voxels with 5 mm of resolution [15].

The images generated by eLORETA software (depicted in Figs. 5, 6, and 7) consists of a pictorial representation of the electric activity in the brain. Regions colored in red or blue indicates areas with electrical activity, where red means an elevation of the electric potential in the referred region, and, therefore, more cerebral activity and blue indicates otherwise. The regions colored in gray indicate non-activated regions.

The eLORETA analysis was performed for each experimental condition, where the current density obtained from each situation was compared with a non-parametric statistical analysis, in order to determine if any significant change in the intensity of the current sources had occurred [40].

3.5 Pattern Recognition

3.5.1 Overall Arrangements

In order to analyze the data from another perspective, we performed experiments using pattern recognition. Our hypothesis was that there are differences that are not evident in the usual methods of EEG analysis (such as statistical approaches), but that can be found using common pattern recognition algorithms. Those algorithms have proven to be very efficient for several different areas, such as emotions through speech recognition, gesture identification through image or electromyographic analysis, so on.

However, since those algorithms perform differently, depending on the data, it is wise to test a few of them to find the one with the best performance. For best performance, one must consider the trade-off between the highest discrimination capability possible and the smallest time spent on classification.

It is common to use before discriminating data using a machine learning algorithm to extract features from the raw or original dataset. In our case, however, we used as the input of the classifiers, the raw dataset after filtering and removing artifacts. This means that our features were the amplitude results of the EEG signal for each electrode. It is also important to mention that the original size of the database had a considerable amount of instances (122,880 per class), and the resultant files were too big to be computed in a reasonable time, considering cross-validation and percentage split database's division. Therefore, an elegant solution to this problem was the resampling technique, introduced by Chawla et al. [12]. In summary, it consists of the creation of a new database with the same statistical characteristics of the

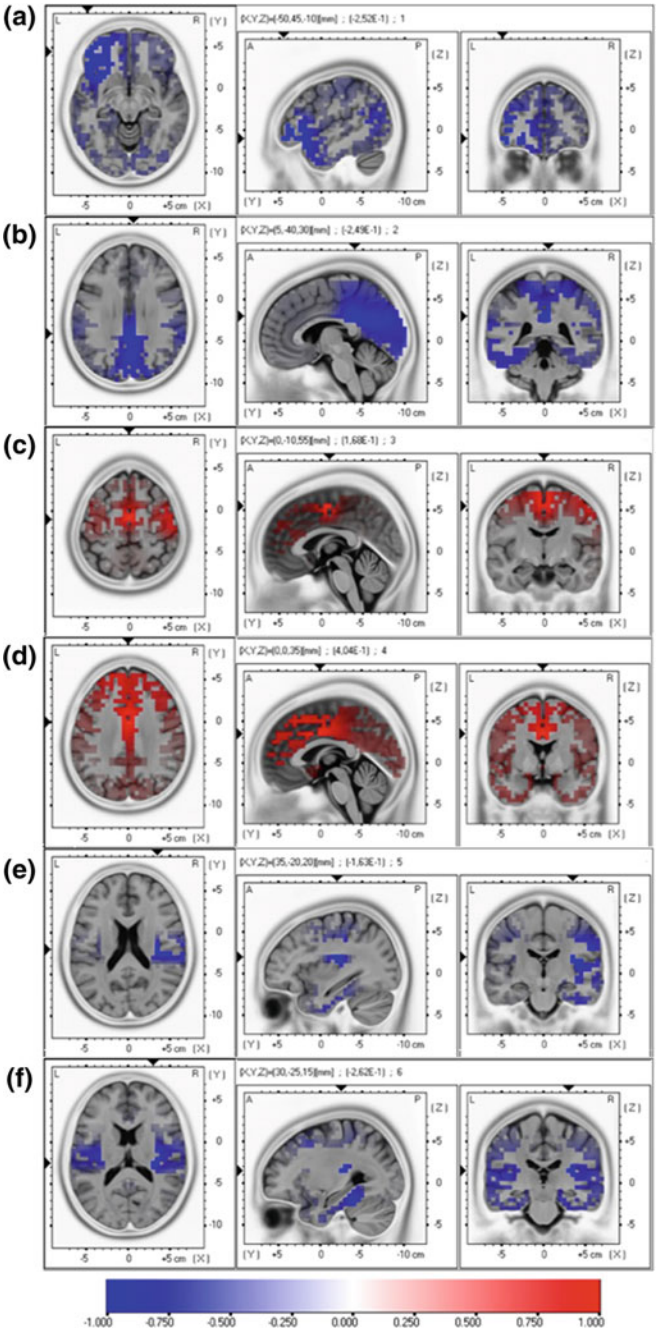
(a)
(b)
(c)
(d)
(e)
(f)
-1.000
-0.750
-0.500
-0.250
0.000
0.250
0.500
0.750
1.000

◄**Fig. 5** Statistical maps of differences between cortical sources computed under the resting state for POS1–PRE1 conditions. The results have been projected onto the MNI152-2009c T2 template. Red color represents ROIs of greatest activity. Blue color indicates ROIs with electrical activity decrease. **a** Oscillations reduction in Delta activity at the left lower Frontal Gyrus; **b** oscillations reduction of theta rhythm at the posterior Cingulate; **c** oscillations increasing within Alpha 1 at the medial Frontal Gyrus; **d** oscillations increasing within Alpha 2 at the anterior Cingulate; **e** oscillation decreasing within Beta 1 and **f** in Beta 2 (**f**) at the right Insula

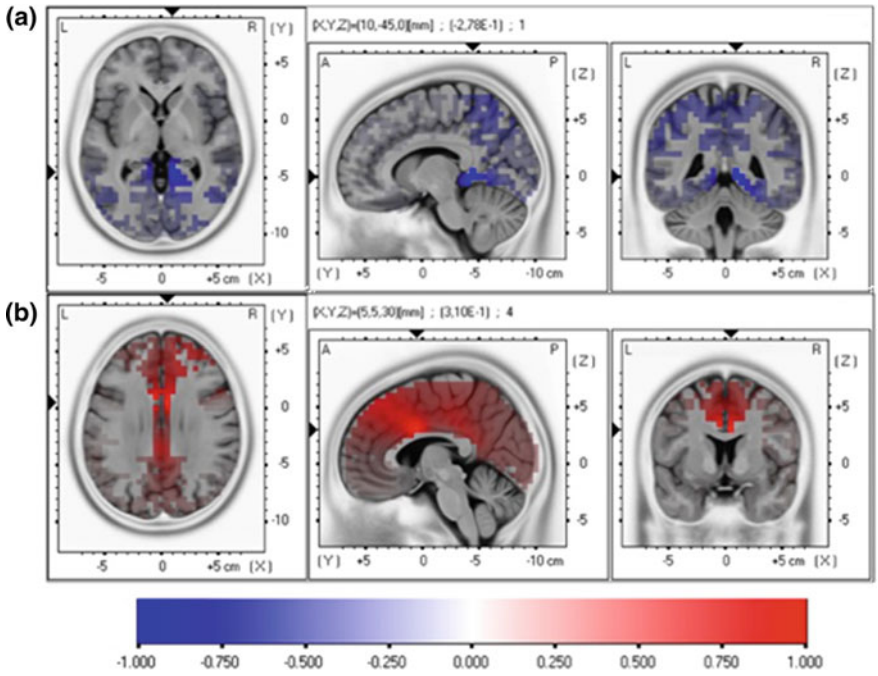

Fig. 6 Statistical maps of differences between cortical sources computed under the resting state for POS10–PRE10 conditions. The results have been projected onto the MNI152-2009c T2 template. Red color represents ROIs of greatest activity. Blue color indicates ROIs with electrical activity decrease. **a** Oscillations reduction in Delta at the Parahippocampal Gyrus; **b** oscillations increasing within alpha 2 in the Anterior Cingulate

original database, but with a reduced number of instances. This procedure diminished considerably the time needed for computing all the classifiers among the classes, and the obtained results were within the expected values (considering classification with the original database).

For those simulations, we employed the free software Weka, a machine learning software with several data preprocessing techniques, classifiers, data visualization, and manipulation tools. Weka uses ARFF files, in which training and testing sets are stored. Therefore, after the preprocessing stage, all the acquired data, i.e., each windowed filtered signal time series, was converted to the aforementioned format in order and resampled using the technique introduced by Chawla et al. [12], to

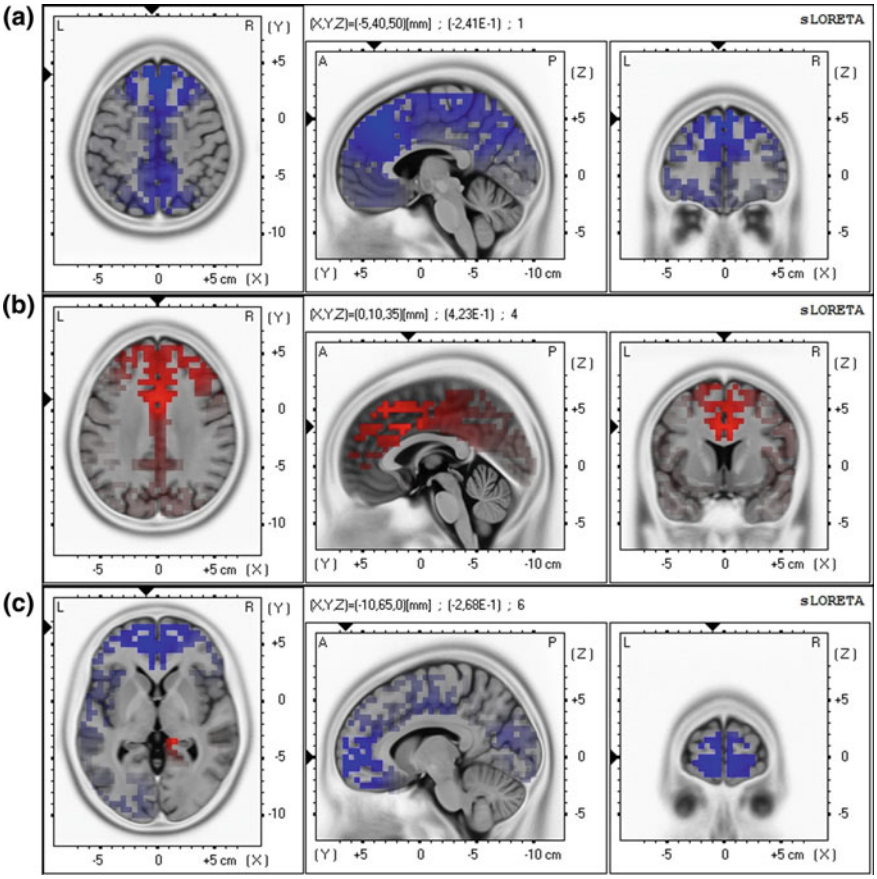

Fig. 7 Statistical maps of differences between cortical sources computed under the resting state for POS10–PRE1 conditions. The results have been projected onto the MNI152-2009c T2 template. Red color represents ROIs of greatest activity. Blue color indicates ROIs with electrical activity decrease. **a** Oscillations reduction in Delta at the Left Lower Frontal Gyrus; **b** increasing oscillations increasing within alpha 2 in the Anterior Cingulate; **c** oscillations increasing and reduction within Beta 2 at the Medial Frontal Gyrus and Parahippocampal Gyrus, respectively

be then classified. The built files were composed of 19 attributes. Each attribute is the representation of one electrode and contains information about the electrode's acquired signal. Each ARFF file contains 2 classes, i.e. condition before and after the stimulus, PREX, and POSX. We built up 21 ARFF files since we considered three different conditions, PRE1 $\times$ POS1, PRE10 $\times$ POS10, and PRE1 $\times$ POS10 and 7 different frequency analysis, Broadband, Delta, Theta, Alpha 1, Alpha 2, Beta 1 and Beta 2.

3.5.2 Classifiers Configuration

In this stage, we tested the database for Multilayer Perceptron (MLP), Support Vector Machine optimized with John Platt's sequential minimal optimization algorithm (SMO) [52], *k*-Nearest Neighbors (*k*NN), J48 decision table classifier and Random Forest (RF). We chose the aforementioned classifiers due to their robustness and good performance in several applications. Also, they are relatively simple and very well studied algorithms, with enough literature to support the choice of near-optimal parameters in little time.

For MLP, SMO, and *k*NN, a few configurations within each classifier were tested. For MLP we changed the values of neurons in the hidden layer between 10, 19, 2, 21, and used the learning rate with values of 0.1 and 0.3. For SMO, we simulated four different configurations by changing its kernel among Radial Basis Function, Linear, Quadratic and Cubic polynomials. Finally, for the *k*NN classifier, we changed the number of neighbors between 1, 3 and 5. For J48 and Random Forest, the default configuration suggested by Weka was applied. The values used here were chosen both empirically and using Weka's predefined parameters.

The results from the classifiers analysis will show that the classifier with best performance is the Multilayer Perceptron, for both percentage split (66% for training and 34% for testing) and 10-fold cross-validation analysis. However, the configurations that presented better results are different between the two simulations, and the one considered for further investigation in the feature classification step was the best result depicted in the cross-validation study.

The chosen MLP uses a sigmoid function as the neuron activation function. The amount of neurons in the input layer equals the number of attributes in the ARFF file, and the amount of neurons in the output layer equals the number of classes in the aforementioned file. Given the best configuration for cross-validation, its hidden layer was set with 2 neurons, with a learning rate and momentum equals to 0.3 and 0.2, respectively.

Once the performance of the classifier was evaluated, and the most suitable algorithm was chosen, we tested the configuration for the reduced database, considering the Kappa Correlation, or Kappa Index. Briefly, the Kappa Index (KI) is one of the most used metrics to measure the performance of a classifier. It is preferred, among others, such as accuracy or sensitivity only since it accounts for the possibility of agreement occurring by chance [45] between observers. The KI is defined as

$$\kappa = \frac{Pr(a) - Pr(e)}{1 - Pr(e)}$$

where κ represents the KI, $Pr(a)$ represents the actual observed agreement and $Pr(e)$ represents the agreement that occurred by chance.

Like any correlation coefficient, the KI range from -1 to $+1$, where -1 indicates a complete systematic disagreement between observers, 0 represents the number of agreement that can be expected from random chance, and 1 represents perfect agreement between observers [45, 67].

4 Results

4.1 Statistical Analysis

This analysis is just an exploratory perspective since it is a single group design [29, 41]. In this research, we also tried to replicate the analyzes of the state-of-the-art [29, 41]. We may in future investigations implement other signal analysis, such as the analysis of signal coherence between Regions of Interest. However, in this case, we performed analysis over amplitude, not phase signals.

Since our samples were not normally distributed, according to the results of a Kolmogorov-Smirnov test [39, 54], non-parametric Wilcoxon test for paired samples were conducted to compare the distribution of the median location of the amplitude of the each EEG frequencies bands, before and after stimulation with binaural beats, position-by-position. The null hypothesis assumed in this statistical analysis is that the amplitude of the EEG frequencies obtained at each pair of electrodes would not differ from the median location when comparing the signal before and after the stimulation, between the following conditions: Cond1—PRE1 $\times$ POS1; Cond2—PRE10 $\times$ POS10; and C3—PRE1 $\times$ POS10. A p-value $p < 0.05$ was established to discriminate statistically different results.

The results are depicted in Tables 2, 3 and 4. They show that there were significant differences among all the EEG frequencies for almost every condition (Cond1, Cond2, and Cond3). However, for Broadband, Theta, Alpha 1, Alpha 2, Beta 1 and Beta 2 frequencies, we observed changes in a few electrodes, while for Delta, every electrode captured, at least, we perceived one significant difference among each condition. More than that, one can also observe that most of the differences were found between conditions PRE1 $\times$ POS1, especially for Delta and Broadband.

Considering the individual variability of the effect of stimulation with a binaural beat of 5 Hz on the cortical electric current distribution, in each EEG recording comparison condition, as described previously, the intraindividual statistical significance of the binaural stimulation effect of 5 Hz was briefly analyzed. To do so, we exported 40 epochs of 2 s for each condition of resting state with closed eyes—PRE1; POS1; PRE10; POS10—were selected for paired statistical analysis of electrophysiological activity, after preprocessing in EEGLab, for the purpose of conduct the intra-group and intra-subject analysis in LORETA. We used the 10/20 system model to adjust the electrode coordinate to the Talairach coordinates, a step necessary to create the transformation matrix, choosing no regularization method and exact low-resolution brain electromagnetic tomography (eLORETA). Thereunto, we compared the cortical electric current sources of each subject between conditions PRE1 $\times$ POS1, PRE10 $\times$ POS10, and PRE1 $\times$ POS10. Only the EEG frequency bands and the regions of interest found during the intra-group analysis were examined, that is, the EEG frequency bands that presented coordinates of voxels with significant statistical values in intra-group analysis.

Then, for each condition, and each intragroup and intrasubject analysis, crossspectral matrices using Fast Fourier Transformation (FFT) were calculated and averaged

Table 2 Electrodes that presented significant statistical differences in the magnitude of the EEG signal compared to their position in three different conditions PRE1 × POS1 (Cond1), PRE10 × POS10 (Cond2) and PRE1 × POS10 (Cond3) in the non-parametric Wilcoxon test with p-value $<$ 0.05

Brainwave	Electrodes	Cond.1	Cond.2	Cond.3
Broadband	FP1	0.02*	0.04*	0.19
	FP2	0.00*	0.02*	0.95
	F8	0.00*	0.15	0.99
	F7	0.04*	0.83	0.02*
	T8	0.00*	0.54	0.08
Delta	FP1	0.00*	0.00*	0.87
	FP2	0.00*	0.41	0.36
	F7	0.00*	0.69	0.00*
	F3	0.00*	0.00*	0.63
	FZ	0.00*	0.00*	0.81
	F4	0.00*	0.00*	0.51
	F8	0.00*	0.00*	0.05*
	T7	0.93	0.00*	0.00*
	C3	0.03*	0.74	0.00*
	CZ	0.00*	0.12	0.05*
	C4	0.00*	0.01*	0.00*
	T8	0.00*	0.00*	0.16
	P7	0.00*	0.01*	0.01*
	P3	0.00*	0.00*	0.59
	PZ	0.01*	0.88	0.71
	P4	0.00*	0.00*	0.00*
	P8	0.00*	0.00*	0.65
	O1	0.00*	0.00*	0.00*
	O2	0.00*	0.00*	0.10
Theta	FP2	0.47	0.04*	0.51
	F7	0.00*	0.36	0.12
	F8	0.95	0.05*	0.15
	C3	0.07	0.03*	0.93
	CZ	0.57	0.02*	0.07
	C4	0.00*	0.69	0.37
	T8	0.01*	0.00*	0.22
	P7	0.01*	0.06	0.16
	P3	0.17	0.03*	0.92
	PZ	0.28	0.00*	0.85
	P8	0.67	0.02*	0.10

Table 3 Electrodes that presented significant statistical differences in the magnitude of the EEG signal compared to their position in three different conditions PRE1 × POS1 (Cond1), PRE10 × POS10 (Cond2) and PRE1 × POS10 (Cond3) in the non-parametric Wilcoxon test with p-value $<$ 0.05

Brainwave	Electrodes	Cond.1	Cond.2	Cond.3
Alpha 1	FP2	0.01*	0.12	0.10
	F7	0.05*	0.89	0.35
	C3	0.02*	0.74	0.30
	CZ	0.00*	0.04*	0.86
	T8	0.06	0.63	0.01*
	P4	0.06	0.02*	0.43
	P8	0.02*	0.58	0.97
	O2	0.01*	0.12	0.74
Alpha 2	F7	0.00*	0.34	0.66
	F3	0.24	0.02*	0.07
	FZ	0.77	0.05*	0.02*
	F4	0.88	0.45	0.75
	F8	0.56	0.37	0.04*
	F7	0.03*	0.33	0.06
	T8	0.00*	0.92	0.00*
	PZ	0.00*	0.01*	0.00*
	O2	0.09	0.92	0.04*

Table 4 Electrodes that presented significant statistical differences in the magnitude of the EEG signal compared to their position in three different conditions PRE1 × POS1 (Cond1), PRE10 × POS10 (Cond2) and PRE1 × POS10 (Cond3) in the non-parametric Wilcoxon test with p-value $<$ 0.05

Brainwave	Electrodes	Cond.1	Cond.2	Cond.3
Beta 1	FP2	0.00*	0.24	0.20
	F8	0.00*	0.61	0.01*
	F7	0.05*	0.95	0.01*
	T8	0.01*	0.08	0.00*
	P3	0.11	0.04*	0.25
	PZ	0.81	0.03*	0.10
	P4	0.03*	0.80	0.42
	O1	0.00*	0.57	0.34
	O2	0.01*	0.88	0.02*
Beta 2	FP1	0.02*	0.65	0.37
	FP2	0.01*	0.87	0.35
	F8	0.01*	0.72	0.18
	T8	0.08*	0.14	0.05*
	P4	0.03*	0.47	0.19
	O1	0.00*	0.82	0.33
	O2	0.03*	0.26	0.03*

for each dataset, converting in one cross-spectral matrix (CRS) for each analysis condition and for each of the discrete frequencies studied: Delta (0.5–3.5 Hz), Theta (4–7 Hz), Alpha-1 (7.5–9.5 Hz), Alpha-2 (10–12.5 Hz), Beta 1 (13–23 Hz) and Beta 2 (24–34 Hz). Next, each CRS file is transformed into eLORETA file for each analysis condition and frequencies band above mentioned. Finally, using the LORETA statistical package, statistical comparisons of the subjects' cortical sources among the condition pairs, via nonparametric mapping approach (SnPM) with randomizations [48], were used to establish the level of significance of each test performed.

4.2 eLoreta Analysis

In this section, we aimed to investigate the differences between conditions before and after the binaural beat stimulus, using the exact Low-Resolution Brain Electromagnetic Tomography method and software. One of state-of-art in literature, invented in 1994, eLORETA solves the inverse problem, localizing the electrical activity within the brain by using the electroencephalographic activity of the individual. The eLORETA analysis allows the investigation of patterns of activation in the brain directly linked to the EEG signal produced, making it possible to cross-reference the obtained results with the functional capabilities of the anatomical regions of the brain.

Considering the individual variability of the effect of stimulation with binaural beat of 5 Hz on the cortical electric current distribution, in each EEG recording comparison condition, as described previously, the intraindividual statistical significance of the binaural stimulation effect of 5 Hz was briefly analyzed.

In order to do so, we compared the cortical electric current distributions of each subject between conditions PRE1 × POS1, PRE10 × POS10, and PRE1 × POS10. Only the EEG frequency bands and the regions of interest found during the intragroup analysis were examined, that is, the EEG frequency bands that presented coordinates of voxels with significant statistical values.

In Table 5, we compare the local electric current density of each individual between the conditions PRE1 × POS1. Note that in the Delta, Alpha 1 and Beta 2 frequency bands, we did not find statistically significant values in the intraindividual comparison for the voxel coordinates identified in the intragroup analysis. However, in these frequency bands, one can see that there is a tendency in the individual effect similar to the group pattern, where all individuals showed local modulation in the electric current density, with a density decrease of Delta and Beta 2 and increase of Alpha 1 brainwaves. In the analysis of the Theta and Alpha 2 current density, besides intraindividual tendency similar to the standard group, we found results with significant values for $p < 0.05$, in subjects 3 and 5 in Theta band and subjects 1, 3, 5 and 6 in Alpha 2 band. That is, in almost all subjects, there is a suggestion, mainly in Alpha 2, as in the intragroup analysis, of a local modulatory effect on the current density of EEG frequency band, with decreased Theta activity and increased activity in Alpha 2. On Beta 1 frequency band, no statistically significant results were found

Table 5 Intraindividual comparison of cortical electric current distribution between the conditions PRE1 × POS1

Subjects	Threshold two-tailed (0.05)	Frequency band					
		Delta	Theta	Alpha 1	Alpha 2	Beta 1	Beta 2
1	0.341	−0.018	−0.175	0.082	0.431*	−0.287	−0.072
2	0.450	0.110	−0.044	0.256	−0.071	0.073	0.087
3	0.344	−0.296	−0.403*	0.103	0.405*	0.203	−0.225
4	0.447	−0.371	−0.084	0.230	0.174	−0.340	−0.406
5	0.503	−0.470	−0.538*	−0.109	1.010*	0.124	−0.160
6	0.413	−0.394	−0.352	0.331	0.443*	−0.261	−0.265

Table 6 Intraindividual comparison of cortical electric current distribution between the conditions PRE10 × POS10. Beta 2 (+) is the superior range of Beta 2 (30–35 Hz), while Beta 2 (−) is the inferior one (24–30 Hz)

Subjects	Threshold two-tailed (0.05)	Frequency band			
		Delta	Alpha 2	Beta 2 (+)	Beta 2 (−)
1	0.549	−0.789*	1.510*	0.107	0.274
2	0.664	−1.040*	1.680*	0.256	0.023
3	0.450	−0.296	0.173	−0.502*	−0.641*
4	0.523	0.797*	−0.935*	0.906*	0.539*
5	0.595	0.047	0.038	−1.060*	−0.389
6	0.479	0.446	−0.274	0.331	−0.331

in the comparison of the local current density between the conditions PRE1 × POS1 conditions. There is no tendency of the intraindividual effect with the binaural beat employed.

In Table 6, one can see the results of the intraindividual comparison of the local electric current density between conditions PRE10 × POS10. In this analysis, considering the current density on frequency bands Delta, Alpha 2, and Beta 2 (+), in most of the subjects occurred the maintenance of the intraindividual tendency of the effect found in the intragroup comparison. In the Delta and Alpha 2 frequency bands we found statistically significant values for $p < 0.05$ in subjects 1, 2, and 3, whereas in Beta 2 (+) we found statistical significance in subjects 2, 3, 4, 5, and 6. These results may indicate that the binaural beat produces a local modulation effect, described in the intragroup analysis, on the current density of the EEG frequency band, with a decrease in delta activity and an increase in Alpha 2 and Beta 2 activity (+). In the Beta 2 frequency band, statistically significant results were found in subjects 3 and 4. However, we did not find an intraindividual tendency of the effect of the binaural beat used. Nevertheless, the results showed that there was again a local effect of modulation of the current density in the voxel coordinates with the max-

Table 7 Intraindividual comparison of cortical electric current distribution between the conditions PRE1 × POS10

Subjects	Threshold two-tailed (0.05)	Frequency band	
		Delta	Alpha 2
1	0.572	−0.927*	0.023
2	0.577	−0.958*	1.380*
3	0.465	0.151	0.320
4	0.514	0.752*	−0.924*
5	0.505	−0.738*	0.794*
6	0.456	0.867*	−0.245

imum statistical value found in the intragroup comparison between the conditions PRE10 × POS10 conditions.

Lastly, the results of the intraindividual comparison of the local electric current density between the conditions PRE1 × POS10 conditions are depicted in Table 7. We found in the Delta frequency band significant statistical values in subjects 1, 2, 4, 5 and 6, and the Alpha 2 frequency band, in subjects 2, 4, and 5. The intraindividual tendency to the effect identified in the intragroup comparison is evidenced in most of these subjects, that is, a decrease in the local density of Delta activity and an increase in Alpha 2 activity. It is observed that the current density in the voxel coordinates with maximum statistical values, in their respective EEG frequency bands, identified in the intragroup analysis, present a local modulatory effect in the intraindividual analysis.

The analysis using eLoreta also provided a pictorial representation of the effects of binaural beats in anatomical areas of the brain. The obtained results for the three studied conditions (PRE1 × POS1, PRE10 × POS10, and PRE1 × POS10) are depicted in Figs. 5, 6, and 7, where are evinced the positions with significant changes in the neural behavior, regarding the studied conditions. For interpretation purposes, one must consider the regions in blue as the ones with a significant decrease in the electrical activity, and the regions in red otherwise. More specifically, Figs. 5, 6 and 7 are pictographic representations in each frequency band and experimental condition, in three planes of perspective—axial, sagittal, and coronal (from left to right).

Our analysis disregards the temporal specificity of when differences in EEG activity began or how long they lasted. Our interest is to describe the differences in the EEG spectrum domain, that is, which EEG frequency bands have activity in the increased or decreased current generating sources and where these EEG current sources are, through the voxel coordinates of the Montreal Neurological Institute brain digital model (MNI). Therefore, the voxels that are shown in Figs. 5, 6, and 7 are in different planes because the location of the differences in current distribution found in the statistical analysis of LORETA is in regions related to the EEG frequencies in each comparison condition.

Regarding Fig. 5, we can observe the effects on the current sources within the first session of the binaural beats application. Also, an acute increasing effect of the neural activity in the regions of the Medial Frontal Gyrus and Anterior Cingulate can be observed, for Alpha 1 and Alpha 2. At last, for Delta, Theta (Left Lower Front Gyrus and Posterior Cingulate, respectively), Beta 1 and Beta 2 frequencies bands (both in the right Insula), a decrease in the neuronal activity is depicted.

The eLORETA analysis of the conditions PRE10 × POS10 on Fig. 6 showed that the dominating effects of the binaural beats stimulation were noticed as an increase in the Alpha 2 neural activity and a diminished neural activity at the Parahippocampal Gyrus, within Delta band.

At last, Fig. 7 suggests a modulation on the signal sources when comparing the conditions before and after the tenth session of the 5 Hz binaural stimulation: an increase of the neural activities at the Alpha 2 and Beta 2 frequency bands, at the Anterior Cingulate and Parahippocampal Gyrus respectively. Also, the Delta frequency displayed an intensity reduction at the Frontal Medial Gyrus.

4.3 Pattern Recognition Results

In this section, we aimed to explore the capabilities of classifiers into finding differences between EEG patterns, before and after an individual was subjected to binaural beats. Our objective with this exploratory study was to investigate the possibility of, while finding these differences, also open a new path for possibly finding the effectiveness of the treatment, duration of the effects, sensitivity to the stimulus, among others.

We divided this subsection into two parts. The first, named Analysis of Classifiers Sect. 4.3.1 concerns the analysis of the results that we obtained with the classifiers we proposed to study, in Sect. 3.5. The second, Multilayer Perceptron Analysis, regards a more profound analysis of the results given by the best configuration of MLP.

4.3.1 Analysis of Classifiers

We analyzed the performance of the algorithms using the cross-validation technique. The obtained results are depicted on boxplots, from Figs. 8, 9, and 10. The results are organized considering the three different conditions (PRE1 × POS1, PRE10 × POS10, PRE1 × POS10) and are detailed and discussed below.

The condition PRE1 × POS1 consists of the brainwaves obtained immediately before and after the first session of binaural beats. The results show the classifiers have different performances, regarding the same EEG frequency. For example, while the Multilayer Perceptron, *k*-Nearest Neighbors, and Random forest had a good performance when classifying Delta, the SMO algorithm showed a relatively bad performance, often showing negative kappa indexes. This suggests that some of those algorithms might be more suitable than others for identifying differences in

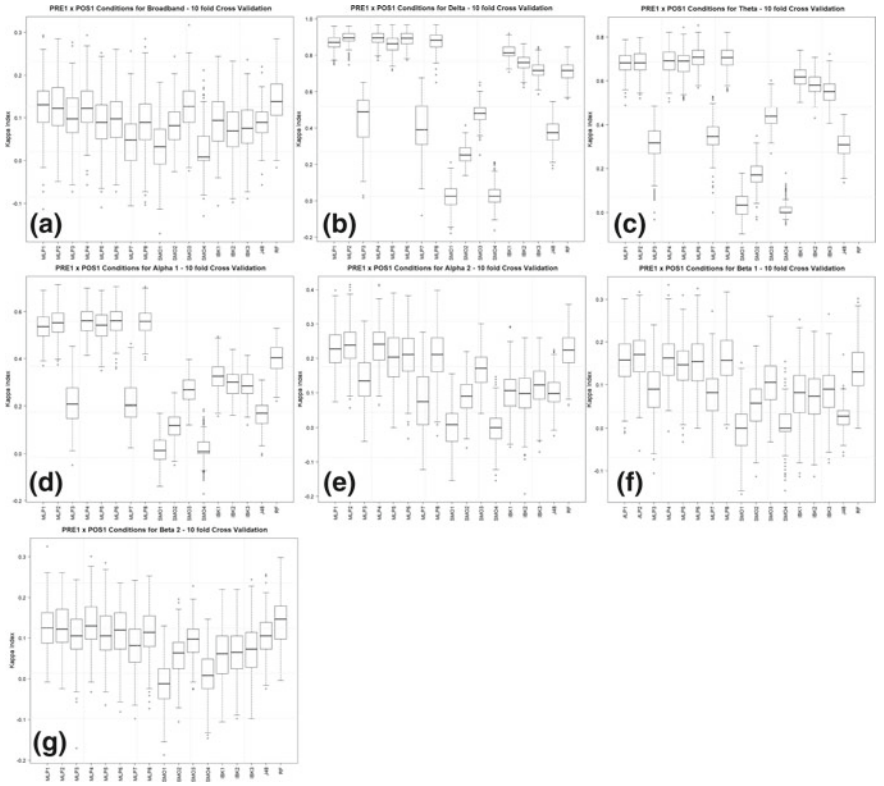

Fig. 8 BoxPlot of the performance of the classifiers from Random Forest (RF), Decision Table J48 (J48), *k*-Nearest Neighbors (IBK), Support Vector Machine (SMO) and Multilayer Perceptron (MLP) algorithms, for PRE1 × POS1 conditions, for PRE10 × POS10 conditions, considering the cross-validation analysis and conditions PRE1 × POS1

the data, which is an expected result, considering that those classifiers rely on different theoretical concepts. The boxplots in Fig. 8 show a detailed view of the performance of the classifiers for each EEG frequency. What one can observe is that the classifiers have similar performance for Broadband, Alpha 2, Beta 1, and Beta 2. However, if we look into Delta, Theta, and Alpha 1, the discrepancies among classifiers are more evident, where almost all MLP configurations performed better (high kappa index and reduced distances between the quartiles and the median) than SMO, *k*NN and Random Forest. This tendency can also be observed in the other frequencies, but, as said before, they are more subtle.

Condition PRE1 × POS1 is one of the three conditions of interest because it shows the immediate effects of binaural beats in subjects with no previous experiences on this type of approach. Our results demonstrate that strong differences can be found on Delta, Theta, and Alpha 1 frequencies, especially if we consider the MLP, *k*NN, and Random Forest. This suggests that the binaural beat has an immediate effect on the

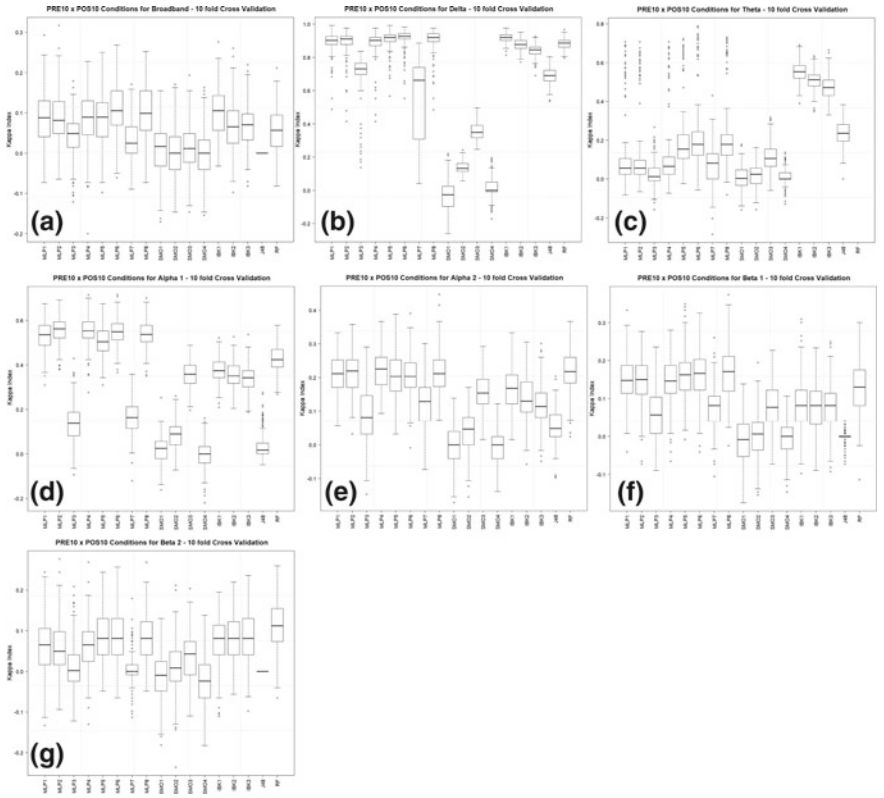

Fig. 9 BoxPlot of the performance of the classifiers from Random Forest (RF), Decision Table J48 (J48), *k*-Nearest Neighbors (IBK), Support Vector Machine (SMO) and Multilayer Perceptron (MLP) algorithms, for PRE1 × POS1 conditions, for PRE10 × POS10 conditions, considering the cross-validation analysis and conditions PRE10 × POS10

modulation of some EEG frequencies, as shown in our previous analysis (Sects. 4.1 and 4.2), with prominent results on Delta and Theta.

Classifiers were also tested among cerebral conditions immediately before and after the tenth session of binaural stimuli, PRE10 × POS10 conditions. As happened concerning the PRE1 × POS1 conditions, most of the classifiers could successfully identify the classes PRE10 and POS10 concerning Delta and Theta brainwaves. It is important to notice, however, that better classification results were obtained for Delta, if we compare the results for Multilayer Perceptron from conditions PRE1 × POS1 and PRE10 × POS10. Also, the performance of MLP, in this condition, dropped considerably, achieving the worst results when comparing the other conditions. This may indicate that after the tenth session, continuous and more prominent modifications still occur regarding the Delta band, but for the Theta frequency, these changes are, somehow, more subtle or nonexistent. The boxplots in Fig. 9 highlights these changes, among conditions. Differences are still easily distinguishable among con-

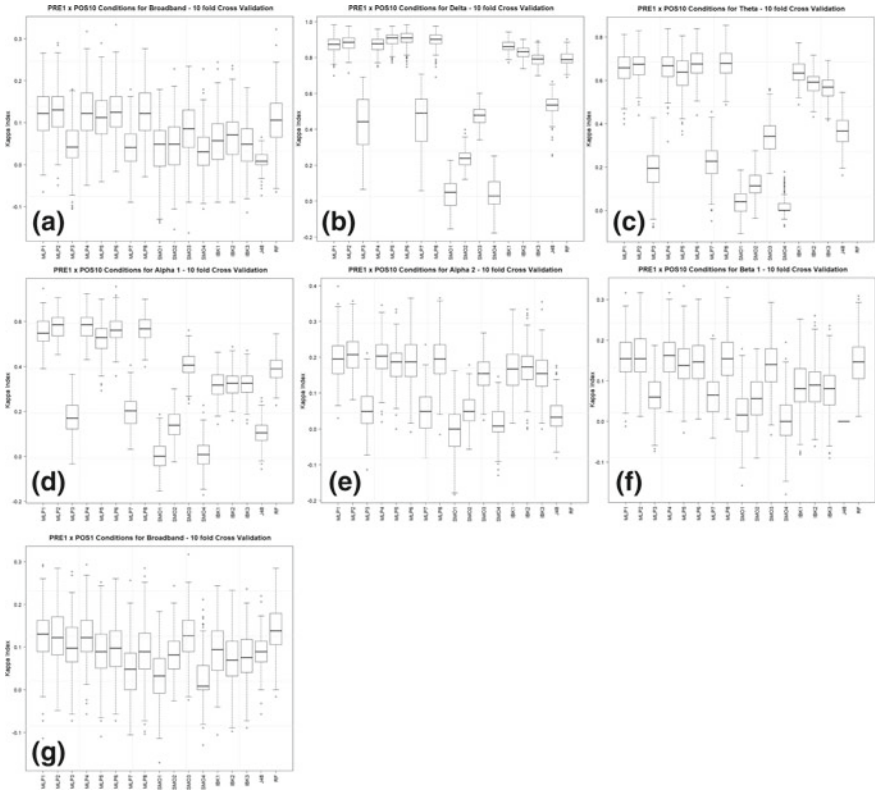

Fig. 10 BoxPlot of the performance of the classifiers from Random Forest (RF), Decision Table J48 (J48), *k*-Nearest Neighbors (IBK), Support Vector Machine (SMO) and Multilayer Perceptron (MLP) algorithms, for PRE1 × POS1 conditions, for PRE10 × POS10 conditions, considering the cross-validation analysis and conditions PRE1 × POS10

ditions for Delta frequency, especially for MLP, *k*-NN, and Random Forest. What is curious, nevertheless, is that *k*-NN and Random Forest had better performance compared to conditions PRE1 × POS1. This and the fact significant differences between conditions (Delta), can indicate that the stimuli still significantly change the EEG modulation from two consecutive sessions, even after 9 sessions of binaural beats.

However, this event is observed in specific frequencies, while in others, it does not happen. It is the case of Theta. From conditions PRE10 to POS10, what we observe, is that there are no significant differences, meaning that the binaural stimuli are not successful in modulating Theta, after 9 sessions of experiments. Those results indicate that an equilibrium state in Theta was achieved after enough number of sessions.

We can also evaluate the performance of the classifiers and the long term effect of the binaural stimulus, observing the conditions before the first session and after the tenth session. The results show that indeed there are differences before the first

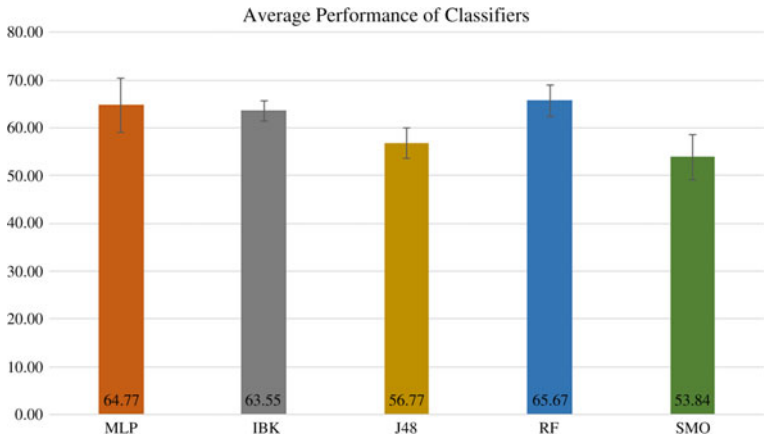

Fig. 11 The general performance of classifiers Random Forest (RF), Decision Table J48 (J48), *k*-Nearest Neighbors (IBK), Support Vector Machine (SMO) and Multilayer Perceptron (MLP) algorithms, considering every condition, PRE1 × POS1, for PRE10 × POS10 and PRE1 × POS10

session and after the tenth session for, especially for Delta, Theta, and Alpha 1. This also means that Theta EEG was modulated on the first session, but stabilized after the tenth session.

Considering the previous results, one can see that there is a trend in which the MLP configurations perform better than the other classifiers. To corroborate this assumption, we run a Wilcoxon test for paired samples, and we calculated the number of classifiers that a specific classifier would outperform. Our results indicated that in 15 of 21 situations (7 band frequencies and 3 different conditions), some MLP configuration outperformed the other classifiers. This means that, while we do not have a specific configuration that has better performance, we have that the MLP, in general, outperforms the other machine learning algorithms. In Fig. 11 we present the general performance of the classifiers we employed.

This result also shows that this dataset is easily generalized. Every MLP configuration had only one hidden layer, meaning that the dataset was separable in a low dimensional space. Therefore, it is possible to conclude that the changes made by binaural beats are almost immediate and easily recognized, opening opportunities for the use of machine learning to identify the EEG modifications after such stimulus.

4.3.2 Self-reporting Results

The assessment of anxiety and depression symptoms in the group was performed using subjective self-reporting instruments, the State-Trait Anxiety Inventory, and the Beck Depression Inventory.

The average anxiety score was 38 ± 6.8 for the Trait factor and 40 ± 8.0 for State factor, before the first binaural session. After the 10th session, the scores were

Table 8 Results for anxiety and depression measures

Instrument	Condition	Mean	Standard deviation	p-value
Anxiety trait	Pre 1st session	38	6.8	0.48
	Post 10th session	37	6.8	
Anxiety state	Pre 1st session	40	8	0.11
	Post 10th session	39	7.6	
Beck depression inventory	Pre 1st session	4.17	3.37	0.52
	Post 10th session	4.5	3.39	

37 ± 6.8 for Trait and 39 ± 7.6 for State. The Wilcoxon test for paired samples indicated that Pre versus Pos comparisons were not significantly different ($p = 0.48$ for Trait $p = 0.11$ for State factors), as shown in Table 8.

For depression, the average score was 4.17 ± 3.37 before the first binaural stimulation. After the 10th session, the scores were 4.5 ± 3.39. The Wilcoxon test for paired samples revealed the absence of significant differences ($p = 0.52$), as shown in Table 8.

These results suggest the absence of depression symptoms in both assessment sessions, showing that the volunteers had no symptoms of depression either before or after the binaural stimulation program.

It is very important to notice that the therapeutic effects of binaural beats in anxiety are related after a more intensive stimulation program. Le Scouranec et al. [41] found differences in anxiety after a month of stimulation, using at least 5 times weekly.

5 Discussion

This chapter aims to investigate the performance of binaural beats in changing the modulation of EEG frequencies after a predefined number of sessions. To perform the experiments, we used EEG data from 6 different individuals, subjected to 10 sessions of binaural beats stimulations. The electroencephalogram was obtained before (PRE1) and after (POS1) the first sessions and before (PRE10) and after (POS10) the tenth session. Therefore, for each volunteer, 40 epochs of 2 s each were obtained, and three different dispositions of the data were analyzed: PRE1 $\times$ POS1, PRE10 $\times$ POS10, PRE1 $\times$ POS10. Each separate condition (PRE1, POS1, PRE10, and POS10) was individually processed using the EEGLab plugin for Matlab, where artifacts were removed using Independent Component Analysis. The remaining data were then filtered in seven different frequency ranges, comprising the Broadband, Delta, Theta, Alpha 1, Alpha 2, Beta 1, and Beta 2.

Considering the frequency bands, we used three different methods to verify every possible change. We first applied a simple statistical analysis using the Wilcoxon

non-parametric test. Then, we used the *exact-Low-Resolution Brain Electromagnetic Tomography* software to investigate the spatial changes caused by the modulations. At last, we considered a novel approach using a pattern recognition algorithm, the Multilayer Perceptron (MLP).

First, the statistical analysis showed that there were significant differences among all EEG frequencies for almost every condition (PRE1 × POS1, PRE10 × POS10, and PRE1 × POS10), and for specific electrodes concerning Theta, Alpha 1, Alpha 2, Beta 1 and Beta 2. For Delta, every electrode captured at least one significant difference among each condition. Finally, more significant differences were observed in condition PRE1 × POS1, especially concerning Delta and Broadband ranges.

In the *eLORETA* study, we performed an intra-subject analysis, due to individual variability. In order to do so, we compared the cortical electric current distributions, considering conditions PRE1×POS1, PRE10 × POS10, and PRE1 × POS10. Considering Table 3, results showed that there is a tendency that appears in both individual and group behavior, where Delta and Beta 2 showed a decrease in local modulation, while an increase was observed for Alpha 1. For Theta and Alpha 2 we found different results for different subjects, meaning that besides the intra-individual tendency, subjects still behaved differently among each other. However, still, almost all subjects presented a local modulation in Alpha 2, while a decrease in Theta activity. Figure 5 displays the locations of local modulations, where, for this condition, and acute effect of the neural activity in the Medial Frontal Gyrus and Anterior Cingulate can be observed, for Alpha 1 and Alpha 2. On the other hand, a decrease in the neuronal activity in the Left Lower Front Gyrus, Posterior Cingulate (Delta and Theta) and right Insula (Beta 1 and Beta 2) is observed. Considering the analysis of PRE10 × POS10 conditions, a decrease in Delta activity and an increase in Alpha 2 and Beta 2 could be observed in specific subjects, but we did not find an intra-individual tendency of the effect of the binaural beat used. Nevertheless, results still corroborated a local modulation in voxels coordinates with maximum statistical values for this condition. Figure 6 depicts these results, where a diminished activity can be observed at the Parahipocampal Gyrus within Delta band. At last, for condition PRE1 × POS10, Delta and Alpha 2 also showed a decrease in Delta modulation and an increase in Alpha 2 activity, and Fig. 7 illustrates these results.

Therefore, comparing the results given by eLORETA, the Alpha 2 band presented a strong increase in the current density distribution, mostly at the Anterior Cingulate. This effect is similar to the ones found in other studies [31]. The neural activity of this structure is related to the monitoring of mistakes regarding social conduct, as also on emotions recognition and expression. Therefore, this region receives information from emotive stimuli and selects the appropriate answer. Also, it adjusts the behavior based on the errors made by one or frustrated expectations [14]. The increase of the Alpha activity in this area is also inversely related with blood oxygenation [24], meaning that the metabolic activity in this region is reduced and the consequent interactions of this nucleus with the Default Mode Network, modulated by binaural beats, can be associated with the cognitive and somatic anxiety symptoms conditioning in clinical populations in training protocols with Neurofeedback [27, 62].

In our third analysis, we considered the classification results provided by machine learning (ML) algorithms. In the first moment, we considered the Random Forest, J48, four configurations of k-Nearest Neighbors, four configurations of Support Vector Machine, and eight configurations of Multilayer Perceptron, in order to obtain the algorithm with the highest discrimination capability. Observing the classification performance depicted in Figs. 8, 9, 10, and 11, we concluded that the MLP algorithm performed better in 15 of 21 situations, meaning that this classifier, in general, outperforms the other ML algorithms. Despite that, most of the classifiers found repeatable results for PRE1 × POS1, PRE10 × POS10, and PRE1 × POS10. In PRE1 × POS1, high separability in frequencies Delta, Theta, and Alpha 1 can be found, especially if we consider MLP, k-NN, and RF algorithms, suggesting that the binaural beats had an immediate effect on EEG modulation. For PRE10 × POS10, Delta and Theta could be successfully identified, but the performance of the ML algorithms dropped considerably for Theta, suggesting that changes in this frequency range after a long program of stimulation are little or non-existent. At last, the performance of the classifiers for PRE1 × POS10 was similar to conditions PRE1 × POS1. In this situation, significant differences could be found in both Delta and Theta, for RF, k-NN and MLP algorithms, meaning that besides little differences occur between consecutive sessions (PRE10 × POS10), they exist if we consider the basal state of EEG, before the binaural stimuli. This study suggested that modulation in theta exists, and this finding could be used to create novel therapeutic solutions towards relaxation and creative states [9].

At last, we considered the self-reporting results of the State-Trait Anxiety Inventory and Beck Depression Inventory, applied before the first session, and after the tenth session of binaural stimuli. Our results were not significantly different between conditions, perhaps because of the short duration of the experiment. Also, subjects did not present depression symptoms in both assessment sessions. Nevertheless, results still showed a trend towards diminishing the scores after the tenth session, and a more intensive stimulation program could show statistically significant differences before and after the binaural beats stimuli [41].

6 Conclusion

In this work, we aimed to explore the effects of a 5 Hz binaural beat stimulation within 10 sessions of the experiment on healthy subjects. For that, we approached the problem using a conventional and a novel approach with MLP, in order to use it as a pilot study for verifying the possible effects of binaural beats on the EEG signal.

Our analysis showed complementary and concordant results. The non-parametric Wilcoxon test for paired data showed a statistically significant difference in the amplitudes of all brainwaves on Tables 2, 3, and 4. The eLORETA analysis, using current sources in order to find the most prominent expressions of neurons groups within different regions showed long term differences among signals before the first experiment session (PRE1) and after the tenth experiment session (POS10) regarding

Delta and Alpha 2 frequencies, with oscillations within Beta 2 when comparing the PRE10 × POS10.

Finally, among several classifiers, we found out that the Multilayer Perceptron is the most suitable machine learning algorithm for the analysis of the effects of binaural beat stimulation. It showed evident changes, mostly in Delta, Theta, and Alpha 1 frequencies. The Theta band was the surprise element in our analysis, since none of the methods used showed a continued modification in the aforementioned frequency, suggesting entrainment, to be further explored. Modifications in the theta range can elicit relaxation and creativity [9].

The statistical analysis showed that there were significant differences for almost every condition evaluated, for specific electrodes, regarding Theta, Alpha 1, Alpha 2, Beta 1 and Beta 2, while for Delta, almost every electrode showed different results between conditions. Our main results on eLORETA indicate a strong increase in the current distribution, mostly in the modulation in Alpha 2, at the Anterior Cingulate. The neural activity of this structure is related to the monitoring of mistakes regarding social conduct, as also on the recognition and expression of emotions. Our third analysis showed that pattern recognition algorithms are able to evince the main differences among all studied conditions (PRE1 × POS1, PRE10 × POS10, and PRE1 × POS10), with high separability in Delta and, surprisingly, in Theta. Lastly, regarding the self-report questionnaire of the State-Trait Anxiety Inventory and Beck Depression Inventory, significant differences between conditions were not found, although a trend towards diminishing the scores after the tenth session was observed.

The lack of a control or placebo group limits our conclusions, though several works deal with just a single group [29, 41]. However, our data also present some important contributions. For further works, the use of a larger sample of subjects must be considered, as well as a control group, providing a bigger quantity of EEG data and questionnaire responses. Furthermore, other classifiers should be tested in order to find a faster and more accurate machine learning algorithm for testing the data. Once the significant relevance of binaural beats is proved, the application of a classifier for identifying the entrainment or EEG amplitude change could be used for biofeedback or for checking if the binaural beats treatment is being effective.

Acknowledgements We would like to express our gratitude to Dr. Marcelo Cairrão and Dr. Sílvia Laurentino for their valuable and constructive suggestions during the development of this research work. We also gratefully acknowledge the Brazilian federal funding agency, CAPES, for partial financial support. Also, this chapter was modified from the paper published by our group in Cognitive Systems Research (Maurício da Silva Junior, Rafaela Covello de Freitas, Wellington Pinheiro dos Santos, Washington Wagner Azevedo da Silva, Marcelo Cairrão Araújo Rodrigues, Erick Francisco Quintas Conde; Available online on 16 of November of 2018; Volume 54; pages 1–20). The related contents are re-used with permission.

References

1. Aoki, Y., Ishii, R., Pascual-Marqui, R.D., Canuet, L., Ikeda, S., Hata, M., Imajo, K., Matsuzaki, H., Musha, T., Asada, T., et al.: Detection of EEG-resting state independent networks by eLORETA-ICA method. Front. Hum. Neurosci. **9**, (2015)
2. Azevedo, W.W., Lima, S.M., Fernandes, I.M., Rocha, A.D., Cordeiro, F.R., da Silva-Filho, A.G., dos Santos, W.P.: Fuzzy Morphological Extreme Learning Machines to detect and classify masses in mammograms. In: 2015 IEEE International Conference on Fuzzy Systems (FUZZ-IEEE), pp. 1–8. IEEE (2015)
3. Bandelow, B., Lichte, T., Rudolf, S., Wiltink, J., Beutel, M.E.: The diagnosis of and treatment recommendations for anxiety disorders. Dtsch Arztebl Int. **111**(27–28), 473–480 (2014)
4. Baxter, A., Scott, K., Vos, T., Whiteford, H.: Global prevalence of anxiety disorders: a systematic review and meta-regression. Psychol. Med. **43**(05), 897–910 (2013)
5. Beauchene, C., Abaid, N., Moran, R., Diana, R.A., Leonessa, A.: The effect of binaural beats on visuospatial working memory and cortical connectivity. PloS One **11**(11), e0166,630 (2016)
6. Becher, A.K., Höhne, M., Axmacher, N., Chaieb, L., Elger, C.E., Fell, J.: Intracranial electroencephalography power and phase synchronization changes during monaural and binaural beat stimulation. Eur. J. Neurosci. **41**(2), 254–263 (2015)
7. Budzynski, T.H., Budzynski, H.K., Evans, J.R., Abarbanel, A.: Introduction to Quantitative EEG and Neurofeedback: Advanced Theory and Applications. Academic Press (2009)
8. Cannon, R.L.: Low resolution brain electromagnetic tomography. Basic Concepts and Clinical Applications. BMED Press (2012) (LORETA)
9. Chaieb, L., Wilpert, E.C., Reber, T.P., Fell, J.: Auditory beat stimulation and its effects on cognition and mood states. Front Psychiatry **6**, (2015)
10. Chatterjee, R., Bandyopadhyay, T.: EEG based motor imagery classification using SVM and MLP. In: 2016 2nd International Conference on Computational Intelligence and Networks (CINE), pp. 84–89. IEEE (2016)
11. Chaumon, M., Bishop, D.V., Busch, N.A.: A practical guide to the selection of independent components of the electroencephalogram for artifact correction. J. Neurosci. Methods **250**, 47–63 (2015)
12. Chawla, N.V., Bowyer, K.W., Hall, L.O., Kegelmeyer, W.P.: SMOTE: synthetic minority oversampling technique. J. Artif. Intell. Res. **16**, 321–357 (2002)
13. Chen, A.C., Feng, W., Zhao, H., Yin, Y., Wang, P.: EEG default mode network in the human brain: spectral regional field powers. NeuroImage **41**(2), 561–574 (2008)
14. Clark, D.L., Boutros, N.N., Mendez, M.F.: The brain and behavior: an introduction to behavioral neuroanatomy. Cambridge University Press (2010)
15. Coben, R., Mohammad-Rezazadeh, I., Cannon, R.L.: Using quantitative and analytic EEG methods in the understanding of connectivity in autism spectrum disorders: a theory of mixed over-and under-connectivity. Front. Hum. Neurosci. **8**, (2014)
16. Cordeiro, F., Santos, W., Silva-Filho, A.: Segmentation of mammography by applying GrowCut for mass detection. Stud. Health Technol. Inform. **192**, 87–91 (2013)
17. Cordeiro, F.R., Santos, W.P., Silva-Filho, A.G.: A semi-supervised fuzzy GrowCut algorithm to segment and classify regions of interest of mammographic images. Expert Syst. Appl. **65**, 116–126 (2016)
18. Crespo, A., Recuero, M., Galvez, G., Begoña, A.: Effect of binaural stimulation on attention and EEG. Arch. Acoust. **38**(4), 517–528 (2013)
19. Cruz, T., Cruz, T., Santos, W.: Detection and classification of lesions in mammographies using neural networks and morphological wavelets. IEEE Lat. Am. Trans. **16**(3), 926–932 (2018)
20. Dos Santos, W.P., De Assis, F.M., De Souza, R.E., Mendes, P.B., de Souza Monteiro, H.S., Alves, H.D.: A dialectical method to classify Alzheimer's magnetic resonance images. In: Evolutionary Computation. InTech (2009)
21. Esslen, M., Pascual-Marqui, R., Hell, D., Kochi, K., Lehmann, D.: Brain areas and time course of emotional processing. Neuroimage **21**(4), 1189–1203 (2004)

22. Fernández, A., Maestu, F., Campo, P., Hornero, R., Escudero, J., Poch, J.: Impact of auditory stimulation at a frequency of 5 Hz in verbal memory. Actas Esp Psiquiatr. **36**(6), 307–313 (2008)
23. de Freitas, R.C., Alves, R., da Silva-Filho, A.G., de Souza, R.E., Bezerra, B.L.D., dos Santos, W.P.: Electromyography-controlled car: a proof of concept based on surface electromyography, extreme learning machines and low-cost open hardware. Comput. Electr. Eng. **73**, 167–179 (2019)
24. Goldman, R.I., Stern, J.M., Engel Jr., J., Cohen, M.S.: Simultaneous EEG and fMRI of the alpha rhythm. Neuroreport **13**(18), 2487 (2002)
25. Goodin, P., Ciorciari, J., Baker, K., Carrey, A.M., Harper, M., Kaufman, J.: A high-density EEG investigation into steady state binaural beat stimulation. PloS One **7**(4), e34,789 (2012)
26. Hamedi, M., Salleh, S.H., Noor, A.M., Mohammad-Rezazadeh, I.: Neural network-based three-class motor imagery classification using time-domain features for BCI applications. In: 2014 IEEE Region 10 Symposium, pp. 204–207. IEEE (2014)
27. Hammond, D.C.: Neurofeedback with anxiety and affective disorders. Child Adolesc. Psychiatr. Clin. N. Am. **14**(1), 105–123 (2005)
28. Hink, R.F., Kodera, K., Yamada, O., Kaga, K., Suzuki, J.: Binaural interaction of a beating frequency-following response. Audiology **19**(1), 36–43 (1980)
29. Huang, S.L., Li, C.M., Yang, C.Y., Chen, J.J.J.: Application of reminiscence treatment on older people with dementia: a case study in Pingtung, Taiwan. J. Nurs. Res. **17**(2), 112–119 (2009)
30. Hyvärinen, A., Oja, E.: Independent component analysis: algorithms and applications. Neural Netw. **13**(4), 411–430 (2000)
31. Ioannou, C.I., Pereda, E., Lindsen, J.P., Bhattacharya, J.: Electrical brain responses to an auditory illusion and the impact of musical expertise. PloS One **10**(6), e0129,486 (2015)
32. Jirakittayakorn, N., Wongsawat, Y.: Brain responses to 40-Hz binaural beat and effects on emotion and memory. Int. J. Psychophysiol. **120**, 96–107 (2017)
33. Jirakittayakorn, N., Wongsawat, Y.: Brain responses to a 6-Hz binaural beat: effects on general theta rhythm and frontal midline theta activity. Front. Neurosci. **11**, 365 (2017)
34. Jung, T.P., Makeig, S., Humphries, C., Lee, T.W., Mckeown, M.J., Iragui, V., Sejnowski, T.J.: Removing electroencephalographic artifacts by blind source separation. Psychophysiology **37**(2), 163–178 (2000)
35. Kasprzak, C.: Influence of binaural beats on EEG signal. Acta Phys. Pol. A **119**(6A), 986–990 (2011)
36. Kemper, K.J., Danhauer, S.C.: Music as therapy. South. Med. J. **98**(3), 282–8 (2005)
37. Kropotov, J.D.: Quantitative EEG, Event-related Potentials and Neurotherapy. Academic Press (2010)
38. Lane, J.D., Kasian, S.J., Owens, J.E., Marsh, G.R.: Binaural auditory beats affect vigilance performance and mood. Physiol. Behav. **63**(2), 249–252 (1998)
39. Larson, R., Farber, B., tradução técnica Patarra, C.: Estatística aplicada. Prentice Hall (2004)
40. Laurentino, S.G.: Tomada de decisão em pacientes deprimidos: estudo eletrofisiológico. Ph.D. thesis, Universidade Federal de Pernambuco (2015)
41. Le Scouranec, R.P., Poirier, R.M., Owens, J.E., Gauthier, J., et al.: Use of binaural beat tapes for treatment of anxiety: a pilot study of tape preference and outcomes. Altern. Ther. Health Med. **7**(1), 58 (2001)
42. Licklider, J.C.R., Webster, J., Hedlun, J.: On the frequency limits of binaural beats. J. Acoust. Soc. Am. **22**(4), 468–473 (1950)
43. Lin, S.T., Yang, P., Lai, C.Y., Su, Y.Y., Yeh, Y.C., Huang, M.F., Chen, C.C.: Mental health implications of music: insight from neuroscientific and clinical studies. Harv. Rev. Psychiatry **19**(1), 34–46 (2011)
44. Makeig, S., Bell, A.J., Jung, T.P., Sejnowski, T.J., et al.: Independent component analysis of electroencephalographic data. Advances in Neural Information Processing Systems, pp. 145–151 (1996)
45. McHugh, M.L.: Interrater reliability: the kappa statistic. Biochem. Med. **22**(3), 276–282 (2012)

46. Motamedi-Fakhr, S., Moshrefi-Torbati, M., Hill, M., Hill, C.M., White, P.R.: Signal processing techniques applied to human sleep EEG signals: a review. Biomed. Signal Process. Control **10**, 21–33 (2014)
47. Nawasalkar, R.K., Butey, P.K.: Analytical and comparative study on effect of Indian classical music on human body using EEG based signals. Int. J. Mod. Eng. Res. (IJMER) **2** (2012)
48. Nichols, T.E., Holmes, A.P.: Nonparametric permutation tests for functional neuroimaging: a primer with examples. Hum. Brain Mapp. **15**(1), 1–25 (2002)
49. Oster, G.: Auditory beats in the brain. Sci. Am. **229**(4), 94–102 (1973)
50. Padmanabhan, R., Hildreth, A., Laws, D.: A prospective, randomised, controlled study examining binaural beat audio and pre-operative anxiety in patients undergoing general anaesthesia for day case surgery. Anaesthesia **60**(9), 874–877 (2005)
51. Pergamin-Hight, L., Naim, R., Bakermans-Kranenburg, M.J., van IJzendoorn, M.H., Bar-Haim, Y.: Content specificity of attention bias to threat in anxiety disorders: a meta-analysis. Clin. Psychol. Rev. **35**, 10–18 (2015)
52. Platt, J.: Fast training of support vector machines using sequential minimal optimization. Advances in Kernel Methods-Support Vector Learning, pp. 185–208 (1999)
53. Puzi, N.M., Jailani, R., Norhazman, H., Zaini, N.M.: Alpha and Beta brainwave characteristics to binaural beat treatment. In: 2013 IEEE 9th International Colloquium on Signal Processing and its Applications (CSPA), pp. 344–348. IEEE (2013)
54. Sani, T.: Experimental Design and Statistics for Psychology: A First Course. Wiley (2006)
55. dos Santos, M.M., da Silva Filho, A.G., dos Santos, W.P.: Deep convolutional extreme learning machines: filters combination and error model validation. Neurocomputing **329**, 359–369 (2019)
56. dos Santos, W.P., de Assis, F.M., de Souza, R.E., dos Santos Filho, P.B.: Evaluation of Alzheimer's disease by analysis of MR images using Objective Dialectical Classifiers as an alternative to ADC maps. In: 30th Annual International Conference of the IEEE Engineering in Medicine and Biology Society, 2008, EMBS 2008, pp. 5506–5509. IEEE (2008)
57. dos Santos, W.P., de Souza, R.E., dos Santos Filho, P.B.: Evaluation of Alzheimer's disease by analysis of MR images using multilayer perceptrons and Kohonen SOM classifiers as an alternative to the ADC maps. In: 29th Annual International Conference of the IEEE Engineering in Medicine and Biology Society, 2007, EMBS 2007, pp. 2118–2121. IEEE (2007)
58. Santos, W.P.d., Assis, F., Souza, R., Santos Filho, P.B., Neto, F.L.: Dialectical multispectral classification of diffusion-weighted magnetic resonance images as an alternative to apparent diffusion coefficients maps to perform anatomical analysis. Comput. Med. Imaging Graph. **33**(6), 442–460 (2009)
59. Sareen, J., Cox, B.J., Afifi, T.O., de Graaf, R., Asmundson, G.J., ten Have, M., Stein, M.B.: Anxiety disorders and risk for suicidal ideation and suicide attempts: a population-based longitudinal study of adults. Arch. Gen. Psychiatry **62**(11), 1249–1257 (2005)
60. Schwarz, D.W., Taylor, P.: Human auditory steady state responses to binaural and monaural beats. Clin. Neurophysiol. **116**(3), 658–668 (2005)
61. da Silva Junior, M., de Freitas, R.C., dos Santos, W.P., Silva, W.W.A., Rodrigues, M.C.A., Conde, E.F.Q.: Exploratory study of the effect of binaural beat stimulation on the EEG activity pattern in resting state using artificial neural networks. Cogn. Syst. Res. **54**, 1–20 (2019)
62. Simkin, D.R., Thatcher, R.W., Lubar, J.: Quantitative EEG and neurofeedback in children and adolescents: anxiety disorders, depressive disorders, comorbid addiction and attention-deficit/hyperactivity disorder, and brain injury. Child Adolesc. Psychiatr. Clin. N. Am. **23**(3), 427–464 (2014)
63. Snyder, K.L., Kline, J.E., Huang, H.J., Ferris, D.P.: Independent component analysis of gait-related movement artifact recorded using EEG electrodes during treadmill walking. Front. Hum. Neurosci. **9**, 639 (2015)
64. Subha, D.P., Joseph, P.K., Acharya, R., Lim, C.M.: EEG signal analysis: a survey. J. Med. Syst. **34**(2), 195–212 (2010)
65. de Vasconcelos, J., dos Santos, W., de Lima, R.: Analysis of methods of classification of breast thermographic images to determine their viability in the early breast cancer detection. IEEE Lat. Am. Trans. **16**(6), 1631 (2018)

66. Vernon, D., Peryer, G., Louch, J., Shaw, M.: Tracking EEG changes in response to alpha and beta binaural beats. Int. J. Psychophysiol. **93**(1), 134–139 (2014)
67. Viera, A.J., Garrett, J.M., et al.: Understanding interobserver agreement: the kappa statistic. Fam. Med. **37**(5), 360–363 (2005)
68. Vigário, R., Sarela, J., Jousmiki, V., Hamalainen, M., Oja, E.: Independent component approach to the analysis of EEG and MEG recordings. IEEE Trans. Biomed. Eng. **47**(5), 589–593 (2000)
69. Vogel, E.K., McCollough, A.W., Machizawa, M.G.: Neural measures reveal individual differences in controlling access to working memory. Nature **438**(7067), 500–503 (2005)
70. Wahbeh, H., Calabrese, C., Zwickey, H., Zajdel, D.: Binaural beat technology in humans: a pilot study to assess neuropsychologic, physiologic, and electroencephalographic effects. J. Altern. Complement. Med. **13**(2), 199–206 (2007)
71. Weiland, T.J., Jelinek, G.A., Macarow, K.E., Samartzis, P., Brown, D.M., Grierson, E.M., Winter, C.: Original sound compositions reduce anxiety in emergency department patients: a randomised controlled trial. Med. J. Aust. **195**(11–12), 694–698 (2011)
72. Winkler, I., Haufe, S., Tangermann, M.: Automatic classification of artifactual ICA-components for artifact removal in EEG signals. Behav. Brain Funct. **7**(1), 30 (2011)

Automated Detection of Seizure and Nonseizure EEG Signals Using Two Band Biorthogonal Wavelet Filter Banks

Dinesh Bhati, Ram Bilas Pachori, Manish Sharma and Vikram M. Gadre

Abstract The automated feature identification and classification of nonseizure and seizure electroencephalogram (EEG) is very useful for the diagnosis of epilepsy. In this chapter two band biorthogonal wavelet filter banks are used for classification of nonseizure and seizure EEG signals, and their classification accuracy has been evaluated. The energy or the bispectral phase entropies of the wavelet subbands can be used to discriminate nonseizure and seizure EEG signals. We compare the performance of energy measure and the bispectral phase entropies to discriminate EEG signals. We compare the classification accuracy of thirty biorthogonal filter banks with respect to the regularity orders of the synthesis and analysis of low pass filters and the number of wavelet decompositions. It is found that the energy measure performs better than the bispectral phase entropy for the cases for which the regularity order is greater than or equal to five independent of the wavelet decomposition level. For the fifth and sixth levels of wavelet decomposition, it is found that the energy measure always performed better than the bispectral phase entropy measure independent of the regularity of the filter bank. For the energy measure, the filter banks with higher regularity orders are found to perform better than the filter banks with lower regularity orders at almost all the decomposition levels. However, for the bispectral phase entropy measure, the filter banks with lower regularity orders are

D. Bhati (✉)
Department of Electronics and Communication Engineering, Acropolis Institute of Technology and Research, Indore, India
e-mail: bhatidinesh@gmail.com

R. B. Pachori
Discipline of Electrical Engineering, Indian Institute of Technology Indore, Indore, India
e-mail: pachori@iiti.ac.in

M. Sharma
Department of Electrical Engineering, Institute of Infrastructure Technology Research and Management Ahmedabad, Ahmedabad, India
e-mail: manishsharma.iitb@gmail.com

V. M. Gadre
Department of Electrical Engineering, Indian Institute of Technology Bombay, Mumbai, India
e-mail: vmgadre@ee.iitb.ac.in

G. Naik (ed.), *Biomedical Signal Processing*, Series in BioEngineering,
https://doi.org/10.1007/978-981-13-9097-5_7

found to perform better than the filter banks with higher regularity orders for most of the decomposition levels. The highest classification accuracies obtained from the bispectral phase entropies and the energy measure is 96.4% and 98.2% respectively.

1 Introduction

In the last two decades, the digital signal processing community has tremendously employed wavelet transform for signal denoising [1], compression [2], and feature extraction [3, 4]. Various authors have proposed different methods for the analysis of biomedical signals such as heart rate variability (HRV) [5] signals, electroencephalogram (EEG) signals [6–10], electrocardiograph (ECG) signals [11, 12] and so on. Epilepsy is characterized by recurrent seizures or the misfirings of the electrical system of the brain. Smart diagnostic systems are required for the automated identification and classification of nonseizure and epileptic seizure EEG signals [3, 13–19]. Researchers have proposed different methods for the automated classification of seizure and nonseizure EEG signals [20–22]. Various authors have proposed EEG signal classification methodologies based on empirical mode decomposition [6, 7, 23, 24], statistical parameters [25, 26], time-frequency analysis [27–29], singular value decomposition [30, 31] and band power and auto regression models [32]. Yol et al. [33] compare the performance of several classifiers such as Linear Discriminant Analysis (LDA), K-Nearest Neighbor classification (KNN) and Naive Bayes classifier for EEG signal classification for several feature extraction methods such as Renyi entropy, Tsallis Entropy and coherent relative entropies of EEG signals. Iftikhar et al. [34] survey various techniques for feature extraction and classification of EEG signals. The method of deep learning is also discussed. Chakole et al. [35] study EEG signal classification in the context of Brain Computer Interface. They extract features from the EEG signals to differentiate several mental tasks. They show that the classification accuracy directly depends on the type of features chosen for the classification and their effectiveness. Subasi et al. [36] study EEG signal classification and flash stimulation in the context of migraine neurological disorder. They have provided guidelines for choosing the effective window length of EEG signals for achieving high classification accuracies. Lu et al. [37] employ hybrid features based on Kraskov entropy and Hilbert Huang Transform. They show that the hybrid features perform very well in the classification of EEG signals. Datta and Chatterjee [38] introduces ensemble architectures and used wavelet based energy and entropy and band power and adaptive auto regressive models. They have shown that good classification accuracies can be obtained with simple classifiers such as K-Nearest Neighbour classifier. In a recent survey by Chakladar and Chakraborty [39], authors compare various methods for EEG signal classification. They classify various methods based on the criteria of low-cost methods or computationally expensive methods. Fasil and Rajesh [40] used exponential energy features and obtained very high classification accuracies for classification EEG signals. EEG signals are nonlinear and nonstationary in nature [41]. Among all the existing signal analysis

transforms, researchers have found that wavelet transform to be the most appropriate choice to capture the dynamics of the signal in time and frequency domain [42]. Two-band wavelet transform has shown outstanding performance in comparison to many other existing methods used for the classification of EEG signals [43, 44].

Orhan et al. [43], Ubeyli et al. [45, 46], Bhati et al. [47] and Sharma et al. [48] study the performance of wavelet filter banks in feature extraction and classification of EEG signals. Patidar et al. [49] use tunable-Q wavelet transform for feature extraction from EEG signals and proposed an empirical alcoholic index for diagnosis of alcoholism. Tapan et al. [50] studied the performance of some specific two band orthogonal as well as the biorthogonal wavelet transform to classify seizure and nonseizure EEG signals. Bhati et al. [47] have shown that time-frequency product optimized three band biorthogonal wavelet filter banks perform very well in classification and identification of nonseizure and seizure EEG signals. Therefore, in this chapter, we evaluate the performance of two-band biorthogonal wavelet filter banks with higher regularity orders in the classification of nonseizure and seizure EEG signals. Bhati et al. [47] use norm of the wavelet subbands to extract the features of the EEG signal. Acharya et al. [4, 51] and [52] use bispectral phase entropies to extract the features of the normal and nonseizure EEG signals. In this work, we present the performance comparison of bispectral phase entropy measures and energy in extracting the features of the EEG signal from its wavelet subband signals extracted from two band biorthogonal wavelet filter banks.

Wavelets are time frequency localized, smooth, oscillating functions used to extract the time and frequency domain features of the nonstationary signals [53]. In this work, we use the wavelet transform to analyze the wavelet components in the nonseizure and seizure EEG signals. The decision of the signal classifier is significantly affected by the wavelet chosen for analyzing the EEG signals. The wavelets form the basis functions of the wavelet transform which are obtained by dilating and shifting a mother wavelet and forms a wavelet multiresolution analysis [53]. Wavelet transform has the advantage that the basis functions not only provide finite resolution in both times as well as a frequency domain, but also the wavelets can be optimized for better resolution simultaneously in time and frequency domain. It is well known that wavelet transform can be implemented using perfect reconstruction orthogonal or biorthogonal filter banks, provided they satisfy certain regularity conditions. Tree structure wavelet filter bank with L level of decompositions divides the input signal in $L + 1$ subband signals. The outputs of the low pass filters are called approximations, and the output of highpass filters are called details. Thus, a wavelet tree with L level of wavelet decomposition yields one approximation signal and L detail signals. The process of feature extraction involves two steps: (1) wavelet decomposition of a signal in wavelet subbands and (2) feature extraction from subband signals. The features of the given EEG signal are obtained by computing a statistical measure for all the $L + 1$ subband signals. Figures 1 and 2 show the seizure (S) and nonseizure (NS) EEG signals and the respective spectra.

Wavelet decomposition of a signal can be obtained either from orthogonal filter banks or biorthogonal filter banks [53]. The regularity orders of synthesis and analysis low pass filters are necessarily the same in case of orthogonal filter banks, which

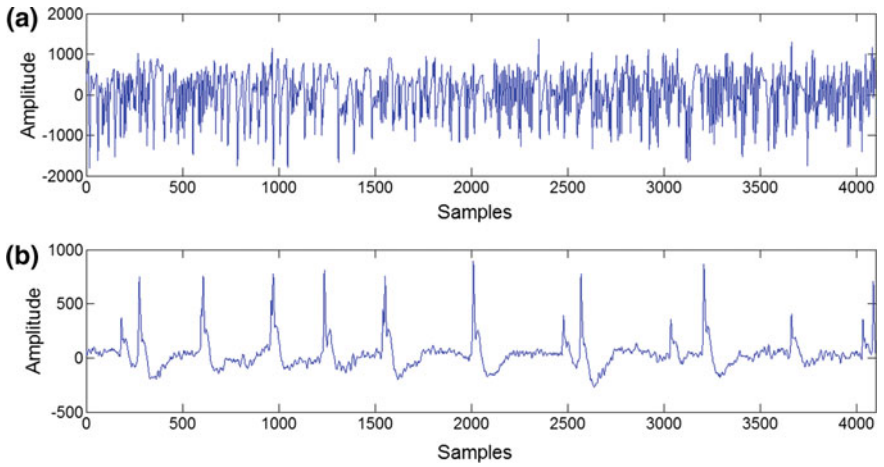

Fig. 1 Plot of **a** seizure EEG signal, **b** nonseizure EEG signal

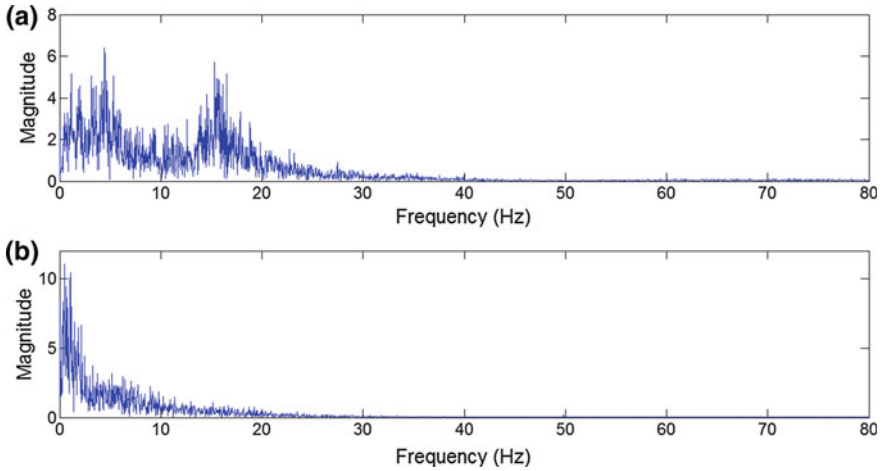

Fig. 2 Magnitude spectrum characteristics of normalized **a** seizure EEG signal, **b** nonseizure EEG signal

is not the case with biorthogonal filter banks [53]. Unlike the design of two-band orthogonal filter banks, more than one filter is designed in two-band biorthogonal filter banks, and therefore degrees of freedom available is more in comparison to orthogonal filter banks. An automated framework for classification of EEG signal comprises a feature extraction unit for dimensionality reduction and a classifier to identify its class as a seizure or nonseizure EEG signal from the extracted features [54]. In this chapter, we use two-band biorthogonal wavelet filter banks to extract features of an EEG signal. To the best of our insight, the comparative study of two-band biorthogonal filter banks with different regularity orders in classification

of nonseizure and seizure, EEG signals are not available in the literature. We study the performance of two-band biorthogonal filter banks with respect to its regularity order and the number of wavelet decompositions in discriminating nonseizure and seizure EEG signals. Since the nonseizure and seizure EEG signals are highly dynamic and nonlinear in nature, we employ higher order spectral measure bispectral phase entropy to extract the features of the EEG signal from its wavelet subband signals.

2 Two-Band Biorthogonal Filter Banks

The nature of EEG signals is highly dynamic and nonstationary [55]. Wavelet filter banks can be used to capture the dynamics of the EEG signals in time and frequency domain. Figure 3 shows the two-band perfect reconstruction filter bank (PRFB) and the wavelet tree structure [53] used to obtain the wavelet decomposition of the given EEG signal at the third level of the wavelet decomposition. The filters $G_0(z)$ and $H_0(z)$ represents the synthesis and analysis of lowpass filters respectively. Similarly, $G_1(z)$ and $H_1(z)$ represents the synthesis and analysis of high pass filters respectively. Alias cancellation can be ensured by choosing [53]:

$$H_1(z) = z^{-1}G_0(-z),\ G_1(z) = zH_0(-z)$$

Wavelets with regularity orders of K_A and K_S can be generated from two-band PRFB, if its low pass filters satisfy the conditions of K_A and K_S zeros on the aliasing frequency $\omega = \pi$. Let

$$H_0(z) = \left(\frac{1+z^{-1}}{2}\right)^{K_A} Q_A(z).$$

and

$$G_0(z) = \left(\frac{1+z^{-1}}{2}\right)^{K_S} Q_S(z).$$

In this work, we evaluate the EEG signal discrimination ability of various biorthogonal filter banks with respect to regularity orders K_A and K_S. It should be noted that

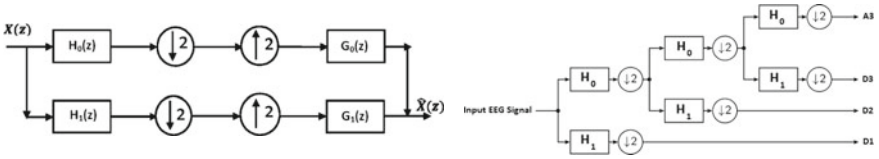

(a) Perfect reconstruction filter bank (b) Wavelet tree filter bank

Fig. 3 Wavelet filter bank. **a** Two-band analysis and synthesis filter bank. **b** Wavelet tree filter bank obtained from iterations of analysis bank on the low pass filter branch

even for the cases $K_A = K_S$ the roles of $Q_A(z)$ and $Q_S(z)$ filters can be interchanged without affecting the perfect reconstruction condition. The energy or the bispectral phase entropy of the wavelet subband signals has been used to compute the features of the given EEG signal.

3 Bispectral Phase Entropy

The bispectrum $\beta(\nu_1, \nu_2)$ of a subband signal $x(t)$ is given by [4, 51]:

$$\beta(\nu_1, \nu_2) = E[X(\nu_1)X(\nu_2)X^*(\nu_1 + \nu_2)]$$

where $X(\nu)$ represents the Fourier transform of the signal $x(t)$. The L_1 and L_2 norm bispectral phase entropies, denoted by H_{en1} and H_{en2} are given by [4, 51]:

$$H_{en1} = -\sum_k p_k \log(p_k)$$

$$H_{en2} = -\sum_i q_i \log(q_i)$$

where,

$$p_k = \frac{|\beta(\nu_1, \nu_2)|}{\sum_\Omega |\beta(\nu_1, \nu_2)|}$$

and

$$q_i = \frac{|\beta(\nu_1, \nu_2)|^2}{\sum_\Omega |\beta(\nu_1, \nu_2)|^2}$$

4 Artificial Neural Network and Classification of Signals

An Artificial neural network (ANN) [56] classifier maps a feature space to discrete class space. It is an interconnection of artificial neurons that simulates a human brain. It takes the features of the signal as an input and identifies its class. A neural network is first trained to learn the different classes to identify. The classification accuracy of an ANN is evaluated using a test set. The class of a given EEG signal is determined using the following three steps:

- Step 1: Wavelet transform of a given EEG signal is computed using two-band biorthogonal filter banks, and subband signals are obtained.
- Step 2: Bispectral phase entropies H_{en1} and H_{en2}, or the energy of each subband signal is computed and features of the EEG signal are obtained. For L level of wavelet decomposition, one approximation and L detail subband signals are available. Thus, L level of wavelet decomposition yields $2(L + 1)$ bispectral phase

entropy features and $(L + 1)$ energy features for the given EEG signal. This step is called dimensionality reduction.

- Step 3: A trained neural network [43, 57] with ten hidden neurons and a single hidden layer is employed to identify the class of a given EEG signal from its features obtained in step 2. The ANN consists of linear activation functions and hyperbolic tangent function in its output and hidden layer respectively [27]. The neural network training algorithm used is Levenberg-Marquardt backpropagation algorithm [43].

In this work, we use ten-fold cross validation to reduce the variance of the estimate of the classification accuracy.

5 Results and Discussion

We evaluate the performance of two-band biorthogonal linear phase wavelet filter banks to classify nonseizure and seizure EEG signals. We compare the performance of energy and the bispectral phase entropy measures in extracting the time and frequency domain features of the EEG signal from its wavelet subband signals and identifying its class. The performance evaluation is done on the EEG signal dataset provided by Bonn University, Germany. The EEG signals are recorded using signal acquisition devices from the epileptic patients, and the healthy persons and a dataset are formed. The samples of the EEG signals of length 4097 are taken at the sampling frequency of 173.61 Hz. The signals are classified into five subclasses and identified by the names A, B, C, D, and E. The sets A, B, C, and D are combined, and a set of nonseizure signal is formed containing 400 signals. Subclass E comprises 100 seizure EEG signals procured from the epileptic patients amid seizure movement [23]. The performance of fifteen biorthogonal filter banks with different K_S and K_A regularity orders of synthesis and analysis of low pass filters is evaluated. Bispectral L_1 and L_2 norm

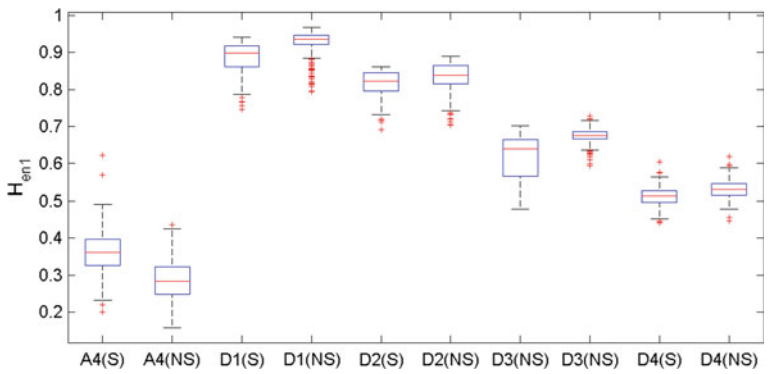

Fig. 4 Entropy H_{en1} of the subband signals obtained at the fourth level of wavelet decomposition using filter bank with $K_A = 3$ and $K_S = 1$

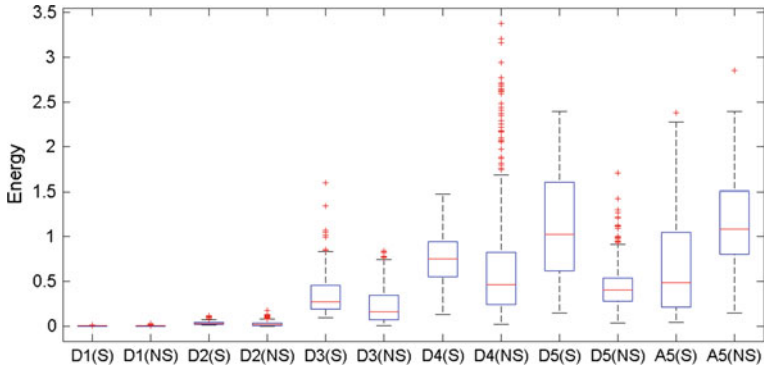

Fig. 5 Energy of subband signals obtained at the fifth level of wavelet decomposition using filter bank with $K_A = 4$ and $K_S = 2$ that yielded the highest classification accuracy of 98.2%

phase entropies H_{en1} and H_{en2}, respectively, and energy measures have been used to extract the features from the subband signals [58]. Figure 4 shows the boxplots of the L_1 norm bispectral phase entropy H_{en1} obtained from the wavelet subbands at the fourth level of wavelet decomposition for 100 seizure (S) and 400 nonseizure (NS) signals from filter bank with $K_A = 3$ and $K_S = 1$. Figure 5 shows the boxplots of the subband energy at the fifth level of wavelet decomposition obtained from filter bank with $K_A = 4$ and $K_S = 2$ and Table 1 shows the corresponding p-values obtained from the Kruskal-Walli's statistical test [47]. It shows that the p-values are very small in the subbands D2–D5 and A5, and thus the filter bank exhibit very high discrimination ability. Figure 6 shows the subband signals of an EEG signal obtained from the same filter bank. Tables 2 and 3 demonstrate the classification accuracy with respect to the regularity orders of the filter banks and the number of wavelet decompositions. Tables 2 and 3 show the classification accuracies when bispectral phase entropies and energy measures are used to extract the features from two-band filter banks, respectively. It shows that the energy measure performs better than the bispectral phase entropies at the fifth and sixth decomposition level independent of the filter bank chosen to compute the wavelet subbands. Figure 7 shows that the energy measure performs better than the bispectral phase entropies for the cases for which the regularity order is greater than or equal to five independent of wavelet decomposition level. Figure 8a, b show that the filter banks with higher regularity orders perform better than the filter banks with lower regularity orders at almost all the decomposition levels when energy measure is used for feature extraction. However, Fig. 8c, d show that the filter banks with lower regularity orders perform better than the filter banks with higher regularity orders for most of the decomposition levels when bispectral phase entropies are used for feature extraction. Tables 2 and 3 show that the highest classification accuracy obtained from bispectral phase entropies is 96.4% from the 8th filter bank at the third level of wavelet decomposition, and that obtained from the energy measure is 98.2% from the 20th filter bank at the fifth level of the wavelet decomposition.

Table 1 Discrimination of normalized seizure and nonseizure EEG signals using subband energy measure and p-values. The results are obtained from biorthogonal filter bank with $K_A = 4$ and $K_S = 2$ at the fifth wavelet decomposition level

Subband	p-value
D1	0.2174
D2	2.2190e–04
D3	5.6470e–09
D4	3.4617e–07
D5	1.8616e–25
A5	3.2407e–13

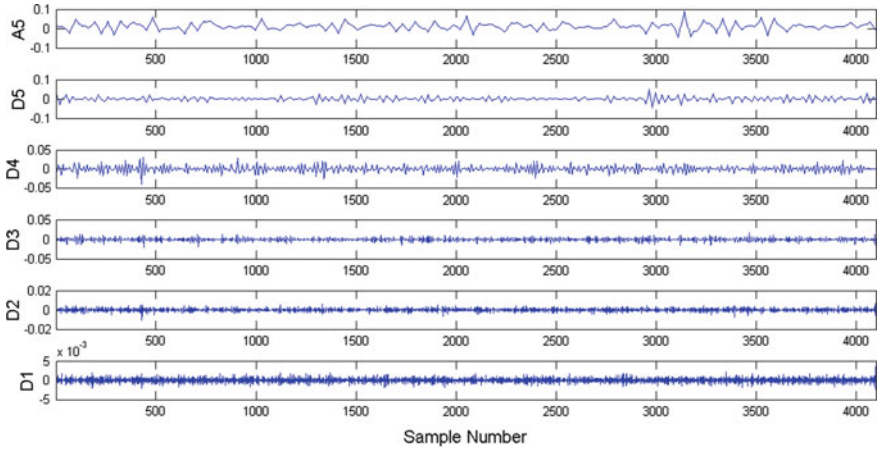

Fig. 6 Wavelet subband signals of the EEG signal

We have further analyzed the nonseizure and seizure EEG signal discrimination ability of bispectral phase entropies and energy measures for the simplest filter bank with $K_A = 1$ and $K_S = 1$ using support vector machine (SVM) [59] at the sixth level of the wavelet decomposition. Thus, there are seven and fourteen features obtained from the energy measurement and the bispectral phase entropies respectively. We used the student's t-test [60] for the selection of significant (M) features and computed the parameters sigma and the box constraint [61, 62] of the SVM that exhibit the highest classification accuracy. Tables 4 and 5 show the classification accuracy when energy measurement and the bispectral phase entropies are used to extract the features from wavelet subbands. We note that the highest number of significant features (M) yields maximum classification accuracy. Thus, we verified that the energy measure perform better than the bispectral phase entropies independent of the classifier chosen for the classification. It should be noted that the energy measure not only yields better classification accuracy than the bispectral phase entropies, the number of features required in case of former is much lesser than that required in case of later.

Table 2 Classification accuracy with respect to number (L) of wavelet decompositions and regularity orders (K_A) and (K_S) when bispectral phase entropies are used to extract the features

FB no.	K_A	K_S	$L = 1$	$L = 2$	$L = 3$	$L = 4$	$L = 5$	$L = 6$
1	1	1	93	92.6	93	94	91.8	89.4
2	1	3	84	90.4	89.4	93.6	91.6	89.8
3	1	5	92	92.8	93.6	94.8	94.2	92.8
4	2	2	85	86.2	88	92.8	90.4	87.2
5	2	4	81.4	85.4	87.4	91.6	92.4	88.6
6	2	6	88.8	91.6	92.2	92.4	92	91
7	2	8	86.2	87.8	88.6	91.2	90.4	89.6
8	3	1	92.2	91.8	96.4	94.8	92.8	91.8
9	3	3	81.4	83.2	87.8	87.4	84.6	85
10	3	5	80.8	83.4	84.6	87.8	85.2	83.6
11	3	7	84.8	84	87	89.4	86.4	87.6
12	3	9	85.8	86	88.4	88.8	87.6	86.8
13	4	4	83.2	88.4	90.6	92.8	92.6	92.8
14	5	5	82.4	88.6	91.2	92.4	92.8	91
15	6	8	86.8	88.4	89.2	91.4	91.8	89.6
16	1	1	92.8	92.4	93.2	93.2	90	88.8
17	3	1	94	94	95	93.8	91.8	91
18	5	1	94.2	94.6	92.8	92.8	92	91.6
19	2	2	83.8	89.2	88.4	92.6	89.4	89
20	4	2	84.6	90.8	88.2	94	91.4	89.6
21	6	2	84	89.6	88	91.6	90.8	89.6
22	8	2	85.2	89.4	91	91.6	90.8	89.4
23	1	3	86.2	89.8	93.8	92.6	91.2	92
24	3	3	86.4	89.8	92	90.8	87.8	88
25	5	3	86.2	89.8	93.4	92	90.2	90.4
26	7	3	87	91	92.2	91.8	89.6	88
27	9	3	86.6	89.4	93.2	92.2	91.4	90.2
28	4	4	87.8	92.6	91.8	94	94.2	94.2
29	5	5	86.4	89.8	90.4	94.2	91.8	89.6
30	8	6	87	89.6	90.2	91.8	91.8	90.4

Table 6 shows the classification accuracy reported by various authors in discriminating nonseizure, and seizure EEG signals. It shows that two-band biorthogonal filter banks with regularity order of $K_A = 4$ and $K_S = 2$ performs better than many other EEG signal classification methods proposed in the literature. It also shows that the energy measure performs better than the bispectral phase entropies to extract the features of the EEG signals when two-band biorthogonal wavelet filter banks are used for the classification of nonseizure and seizure EEG signals.

Table 3 Classification accuracy with respect to number (L) of wavelet decompositions and regularity orders (K_A) and (K_S) when subband energy is used to extract the features

FB no.	K_A	K_S	$L = 1$	$L = 2$	$L = 3$	$L = 4$	$L = 5$	$L = 6$
1	1	1	79.6	86.8	88.6	87.2	95.8	95.8
2	1	3	88.6	90.8	94.2	94	97.6	97.6
3	1	5	89.2	91.8	92.8	95.6	96.6	97.4
4	2	2	87	88.6	96	97	96.4	97.2
5	2	4	88	90.2	95.2	96.4	97.4	96.4
6	2	6	88.2	89.6	94.8	95.8	97	96.8
7	2	8	88.2	90.4	94.6	95.6	96.4	97.4
8	3	1	86.2	86.6	94.2	96.2	97.2	97.2
9	3	3	86.6	89.4	96	96.2	96.4	97
10	3	5	87.4	88.8	95.8	96.6	96.6	96.8
11	3	7	88	89.8	95.8	96.8	96.4	96
12	3	9	87.8	88.6	95.6	96.8	96.8	96.6
13	4	4	87.8	90	95.4	96.2	97	96.8
14	5	5	88.8	90.8	93.4	94.4	96.8	97
15	6	8	88.8	91.6	93.6	93.6	97	96.8
16	1	1	80	87.2	88.6	87.8	96	96.2
17	3	1	88	87.4	90.6	94.2	96.8	96.8
18	5	1	88.4	88.4	90	94.2	97.2	96.6
19	2	2	88	88.6	89.8	97	97.8	97.4
20	4	2	88.2	89.6	91.4	97	98.2	97.6
21	6	2	87.8	88.6	92.6	96.8	97.6	97.8
22	8	2	87.4	89.2	92	96.6	97.2	97.6
23	1	3	87.6	88.8	91	96.8	96.2	96.2
24	3	3	86.8	89.4	91.8	95.8	96.6	97
25	5	3	87.6	88.4	92.6	95.8	96.2	96.8
26	7	3	87	90.6	93	95.6	96.6	96.6
27	9	3	88.4	88.8	92.8	96	97	97
28	4	4	88.6	90	95.6	94.6	97.2	97.4
29	5	5	89.8	90.6	93.8	94.4	96.8	97.8
30	8	6	88.8	91.6	91	94	96.8	97.2

We are analyzing the performance of two-band biorthogonal wavelet filter banks to identify and classify nonseizure and seizure EEG signals with respect to the regularity of filter bank, number of wavelet decompositions, subband energy and bispectral phase entropy feature extraction methods, SVM or ANN classifiers and number of features required to obtain high degree of classification accuracy. Bhati et al. [47] have shown that three-band biorthogonal wavelet filter banks perform very well in the classification of seizure and nonseizure EEG signals. They used subband norms

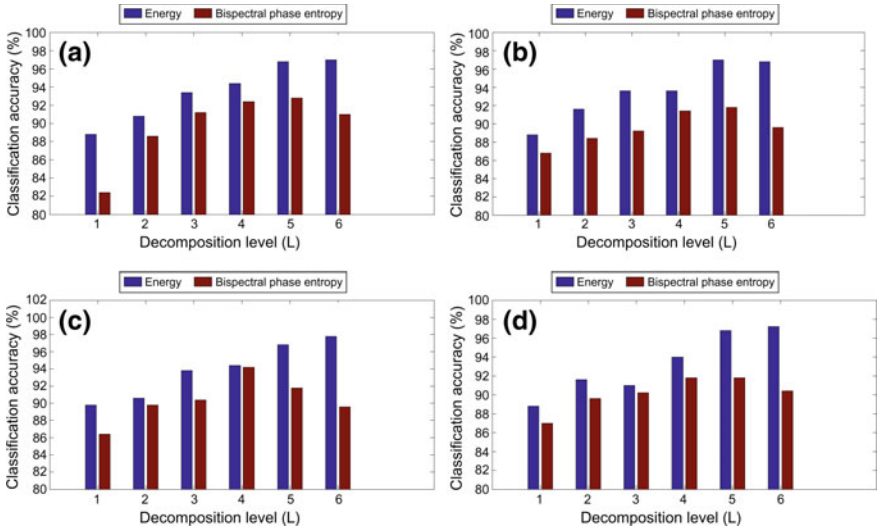

Fig. 7 Classification accuracy with respect to number (L) of wavelet decompositions to compare the performance of subband energy measure and bispectral phase entropy for feature extraction. **a** Classification accuracy obtained from filter bank no. 30 with regularity orders $K_A = 6$ and $K_S = 8$. **b** Classification accuracy obtained from filter bank no. 15 with regularity orders $K_A = 6$ and $K_S = 8$. **c** Classification accuracy obtained from filter bank no. 29 with regularity orders $K_A = 5$ and $K_S = 5$. **d** Classification accuracy obtained from filter bank no. 30 with regularity orders $K_A = 8$ and $K_S = 6$

to extract the features of the EEG signal and obtained a very high classification accuracy. Table 3 shows the classification accuracy obtained when subband energy is used for the classification of nonseizure and seizure EEG signals. The highest classification accuracy obtained from the ANN classifier is 98.2% and found to be better than the many recently reported results in the literature and Fig. 9 shows the corresponding receiver operating characteristic [63]. The subband energy of the signals is the most simple and powerful measure to extract the features of the EEG signals. The results have shown that the subband energy feature extraction measure performs better than the higher order spectral measures in extracting the features of an EEG signal, and the performance comparison of subband energy feature extraction method with other complex feature extraction methods is a nontrivial research problem. It is worth investigating the performance of subband energy feature extraction measure in the classification of signals from various other datasets. There may exist a large class of nonstationary signal datasets wherein subband energy feature extraction measures may perform better than other complex feature extraction measures such as subband entropy [6], frequency variances [7], fractal dimension [48], etc. It should also be noted that the trend of the classification accuracy with respect to number of decomposition levels shown by a given filter bank is a function of the measure used for feature extraction. The results show that the trend for the classification accuracy with respect to the number of the decomposition levels is highly sensitive to the statisti-

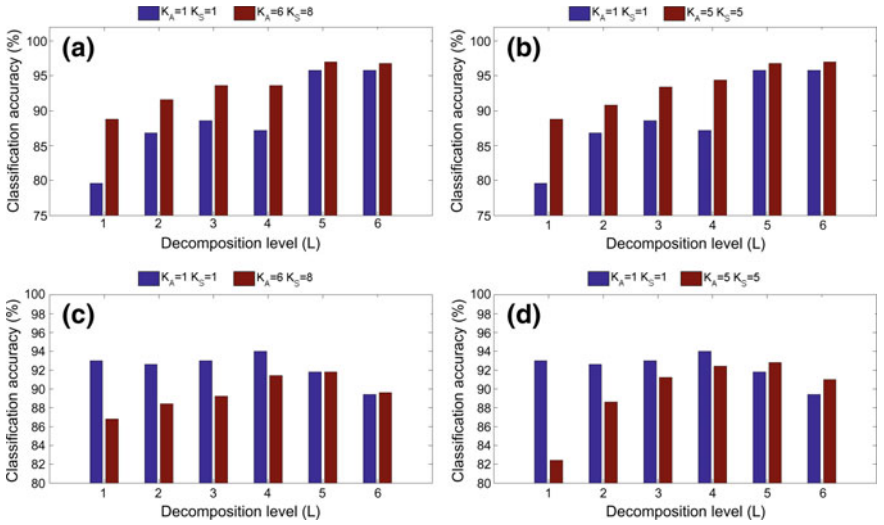

Fig. 8 Classification accuracy with respect to a number (L) of wavelet decompositions. It shows the effect of the regularity of the filter bank on the classification accuracy. **a** and **b** show classification accuracy when subband energy is used to extract features. **c** and **d** show classification accuracy when bispectral phase entropies are used for the classification of signals

cal measure *energy* or the *bispectral phase entropy* used for feature extraction. The results show that, in general, the increase in the the number of decomposition levels increases the classification accuracy when subband energy is used for feature extraction. However, the classification accuracy is found to decrease with the number of decomposition levels at higher decomposition levels when bispectral phase entropies are used for feature extraction. It should be noted that the classification accuracy at the lower decomposition levels is better for filter banks with lower regularity order than the filter banks with higher regularity orders when bispectral phase entropy is used for feature extraction. However, the filter banks with higher regularity order are found to exhibit better performance than the filter banks with lower regularity order at the lower decomposition levels when subband energy is used for feature extraction. It is found that the subband energy feature extraction measure performs better than the bispectral phase entropy measure independent of the ANN or SVM classifier used for EEG signal classification. Subband energy measure is found to yield high classification accuracy even when the number of features is much smaller than required when subband bispectral phase entropy is used for feature extraction.

Table 4 Classification accuracy with respect to a number of significant features (M) and SVM parameters when subband energy is used to extract the features from subbands of filter bank with $K_A = 1$ and $K_S = 1$ at the sixth level of wavelet decomposition

M	Classification accuracy (%)	Sigma	Box constraint
1	0.856	1	0.7
2	0.858	1	0.6
3	0.926	1	0.7
4	0.948	1	0.4
5	0.944	1	0.4
6	0.948	1	0.6
7	0.96	1	0.7

Table 5 Classification accuracy with respect to a number of significant features (M) and SVM parameters when subband bispectral phase entropies are used to extract the features from subbands of filter bank with $K_A = 1$ and $K_S = 1$ at the sixth level of wavelet decomposition

M	Classification accuracy (%)	Sigma	Box constraint
1	0.8	1	0.5
2	0.718	1	0.4
3	0.71	1	0.7
4	0.706	1	0.5
5	0.7	1	0.4
6	0.696	1	0.4
7	0.7	1	0.7
8	0.818	1	0.7
9	0.84	1	0.5
10	0.828	1	0.5
11	0.828	1	0.5
12	0.848	1	0.4
13	0.86	1	0.5
14	0.864	1	0.7

Table 6 Comparison of classification accuracy obtained from the biorthogonal filter banks with recently reported results to classify nonseizure (A, B, C, D) and seizure (E) EEG signals

Authors	Methodology	Year	Classification accuracy (%)
Tzallas et al. [27]	Time-frequency features using ANN	2007	97.73
Guo et al. [64]	DWT and line length feature using ANN	2010	97.77
Gandhi et al. [50]	DWT and energy and entropy features using SVM and Probabilistic neural network	2011	95.44
Nicolaou et al. [65]	Permutation entropy and SVM	2012	86.10
Samiee et al. [66]	Rational discrete short-time Fourier transform using multilayer perceptron	2015	98.10
Swami et al. [67]	DTCWT and energy, Shannon entropy features using general regression neural network	2016	95.24
This work	Two-band biorthogonal filter bank with $K_A = 4$ and $K_S = 2$ and multilayer perceptron	–	98.20

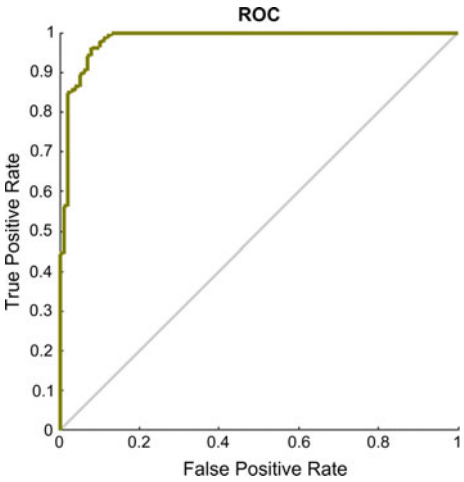

Fig. 9 Receiver operating characteristic for identification of seizure signals for the best case performance obtained with subband energy features and the filter bank no. 20 at the fifth level of wavelet decomposition. Note that corresponding sensitivity and specificity are 99.50% and 95% respectively

6 Conclusion

An automated expert system for the classification and identification of signals consists of a feature extraction unit and a signal classifier to classify the signal based on its features. We modeled an expert system in which a two-band biorthogonal wavelet filter bank is used to compute the wavelet subband signals of nonseizure and seizure EEG signals. Bispectral phase entropies and energy measures are used to extract the features of the EEG signal from its wavelet subband signals. Results show that the energy measure performed better than the bispectral phase entropies for the fifth and sixth levels of wavelet decomposition independent of the regularity of the filter bank. The energy measure performed better than the bispectral phase entropies for all the

decomposition levels if regularity order of the filter bank is greater than five. The filter banks with higher regularity orders are found to perform better than the filter banks with lower regularity orders at almost all the decomposition levels when energy measure is used for feature extraction. The filter banks with lower regularity orders are found to perform better than the higher regularity filter banks for most of the decomposition level when bispectral phase entropies are used for feature extraction. It is found that the energy measure outperforms bispectral phase entropy measure independent of the classifier ANN or SVM was chosen for classification.

References

1. Mamun, M., Al-Kadi, M., Marufuzzaman, M.: Effectiveness of wavelet denoising on electroencephalogram signals. J. Appl. Res. Technol. **11**(1), 156–160 (2013)
2. Sriraam, N.: A high-performance lossless compression scheme for EEG signals using wavelet transform and neural network predictors. Int. J. Telemed. Appl. **2012** (2012) Article ID 302581
3. Acharya, U.R., Sree, S.V., Swapna, G., Martis, R.J., Suri, J.S.: Automated EEG analysis of epilepsy: a review. Knowl. Based Syst. **45**, 147–165 (2013)
4. Acharya, U.R., Sree, S.V., Ang, P.C.A., Yanti, R., Suri, J.S.: Application of non-linear and wavelet based features for the automated identification of epileptic EEG signals. Int. J. Neural Syst. **22**(02), 1250002 (2012)
5. Bozhokin, S., Suslova, I.: Analysis of non-stationary HRV as a frequency modulated signal by double continuous wavelet transformation method. Biomed. Signal Process. Control **10**, 34–40 (2014)
6. Sharma, R., Pachori, R.B., Acharya, U.R.: Application of entropy measures on intrinsic mode functions for the automated identification of focal electroencephalogram signals. Entropy **17**(2), 669–691 (2015)
7. Bajaj, V., Pachori, R.B.: Classification of seizure and nonseizure EEG signals using empirical mode decomposition. IEEE Trans. Inf. Technol. Biomed. **16**(6), 1135–1142 (2012)
8. Tiwari, A., Pachori, R.B., Kanhangad, V., Panigrahi, B.: Automated diagnosis of epilepsy using key-point based local binary pattern of EEG signals. IEEE J. Biomed, Health Inf. (2016)
9. Pachori, R.B., Patidar, S.: Epileptic seizure classification in EEG signals using second-order difference plot of intrinsic mode functions. Comput. Methods Programs Biomed. **113**(2), 494–502 (2014)
10. Joshi, V., Pachori, R.B., Vijesh, A.: Classification of ictal and seizure-free EEG signals using fractional linear prediction. Biomed. Signal Process. Control **9**, 1–5 (2014)
11. Kumar, M., Pachori, R.B., Acharya, U.R.: Characterization of coronary artery disease using flexible analytic wavelet transform applied on ECG signals. Biomed. Signal Process. Control **31**, 301–308 (2017)
12. Karaaslan, O.F., Bilgin, G.: ECG classification with emprical mode decomposition denoised by wavelet transform. In: 22nd Signal Processing and Communications Applications Conference, pp. 694–697, Trabzon, Turkey (2014)
13. Bhattacharyya, A., Pachori, R.B.: A multivariate approach for patient-specific EEG seizure detection using empirical wavelet transform. IEEE Trans. Biomed. Eng. **64**, 2003–2015 (2017)
14. Bhattacharyya, A., Pachori, R.B., Upadhyay, A., Acharya, U.R.: Tunable-q wavelet transform based multiscale entropy measure for automated classification of epileptic EEG signals. Appl. Sci. **7**(4) (2017)
15. Sharma, R., Pachori, R.B.: Classification of epileptic seizures in EEG signals based on phase space representation of intrinsic mode functions. Expert Syst. Appl. **42**(3), 1106–1117 (2015)
16. Kumar, T.S., Kanhangad, V., Pachori, R.B.: Classification of seizure and seizure-free EEG signals using local binary patterns. Biomed. Signal Process. Control **15**, 33–40 (2015)

17. Bajaj, V., Pachori, R.B.: Epileptic seizure detection based on the instantaneous area of analytic intrinsic mode functions of EEG signals. Biomed. Eng. Lett. **3**, 17–21 (2013)
18. Pachori, R.B., Bajaj, V.: Analysis of normal and epileptic seizure EEG signals using empirical mode decomposition. Comput. Methods Programs Biomed. **104**(3), 373–381 (2011)
19. Pachori, R.B., Sharma, R., Patidar, S.: Classification of Normal and Epileptic Seizure EEG Signals Based on Empirical Mode Decomposition, pp. 367–388. Springer International Publishing, Cham (2015)
20. Tzallas, A.T., Tsalikakis, D.G., Karvounis, E.C., Astrakas, L., Tzaphlidou, M., Tsipouras, M.G., Konitsiotis, S.: Automated epileptic seizure detection methods: a review study. INTECH Open Access Publisher (2012)
21. Alotaiby, T.N., Alshebeili, S.A., Alshawi, T., Ahmad, I., El-Samie, F.E.A.: EEG seizure detection and prediction algorithms: a survey. EURASIP J. Adv. Signal Process. **2014**(1), 1–21 (2014)
22. Sharma, M., Pachori, R.B.: A novel approach to detect epileptic seizures using a combination of tunable-q wavelet transform and fractal dimension. J. Mech. Med. Biol. **17**(07), 1740003 (2017)
23. Pachori, R.B.: Discrimination between ictal and seizure-free EEG signals using empirical mode decomposition. Res. Lett. Signal Process. **2008**, 1–5 (2008) Article ID 293056
24. Alam, S.S., TarekShahriar, S.: EEG signal discrimination using non-linear dynamics in the EMD domain. Int. J. Comput. Electr. Eng. **4**(3), 326 (2012)
25. Ebrahimpour, R., Babakhani, K., Asghar Abbaszadeh Arani, S.A., Masoudnia, S.: Epileptic seizure detection using a neural network ensemble method and wavelet transform. Neural Netw. World **22**(3), 291 (2012)
26. Abualsaud, K., Mahmuddin, M., Saleh, M., Mohamed, A.: Ensemble classifier for epileptic seizure detection for imperfect EEG data. Sci, World J (2015)
27. Tzallas, A., Tsipouras, M., Fotiadis, D.: Automatic seizure detection based on time-frequency analysis and artificial neural networks. Comput. Intell. Neurosci. (2007) Article ID 80510
28. Gajic, D., Gligorijevic, J., Djurovic, Z., Di Gennaro, S., Savic-Gajic, I.: Detection of epileptiform activity in EEG signals based on time-frequency and nonlinear analysis. Front. Comput. Neurosci. **9**, 38 (2015)
29. Sharma, R.R., Pachori, R.B.: Time-frequency representation using IEVDHM-HT with application to classification of epileptic EEG signals. IET Sci. Meas. Technol. **12**(1), 72–82 (2018)
30. Vanrumste, B., Jones, R., Bones, P.: Detection of focal epileptiform activity in the EEG: an SVD and dipole model approach. Proc. Eng. Med. Biol. **3**, 2031–2032 (2002)
31. Shahid, A., Kamel, N., Malik, A., Jatoi, M.: Epileptic seizure detection using the singular values of EEG signals. In: International Conference on Complex Medical Engineering, Beijing, China, pp. 652–655, May 2013
32. Parvinnia, E., Sabeti, M., Jahromi, M.Z., Boostani, R.: Classification of EEG signals using adaptive weighted distance nearest neighbor algorithm. J. King Saud Univ. Comput. Inf. Sci. **26**(1), 1–6 (2014)
33. Yol, S., Ozdemir, M.A., Akan, A., Chaparro, L.F.: Detection of epileptic seizures by the analysis of EEG signals using empirical mode decomposition. In: 2018 Medical Technologies National Congress (TIPTEKNO), pp. 1–4, Nov 2018
34. Iftikhar, M., Khan, S.A., Hassan, A.: A survey of deep learning and traditional approaches for EEG signal processing and classification. In: 2018 IEEE 9th Annual Information Technology, Electronics and Mobile Communication Conference (IEMCON), pp. 395–400. IEEE (2018)
35. Chakole, A.R., Barekar, P.V., Ambulkar, R.V., Kamble, S.D.: Review of EEG signal classification. In: Information and Communication Technology for Intelligent Systems, pp. 105–114. Springer (2019)
36. Subasi, A., Ahmed, A., Alickovic, E., Hassan, A.R.: Effect of photic stimulation for migraine detection using random forest and discrete wavelet transform. Biomed. Signal Process. Control **49**, 231–239 (2019)
37. Lu, Y., Ma, Y., Chen, C., Wang, Y.: Classification of single-channel EEG signals for epileptic seizures detection based on hybrid features. Technol. Health Care 1–10 (2018)

38. Datta, A., Chatterjee, R.: Comparative study of different ensemble compositions in EEG signal classification problem. In: Emerging Technologies in Data Mining and Information Security, pp. 145–154. Springer (2019)
39. Chakladar, D.D., Chakraborty, S.: Feature extraction and classification in brain-computer interfacing: future research issues and challenges. In: Natural Computing for Unsupervised Learning, pp. 101–131. Springer (2019)
40. Fasil, O., Rajesh, R.: Time-domain exponential energy for epileptic EEG signal classification. Neurosci. Lett. **694**, 1–8 (2019)
41. Bhattacharyya, A., Singh, L., Pachori, R.B.: Fourier bessel series expansion based empirical wavelet transform for analysis of non-stationary signals. Digital Signal Process. **78**, 185–196 (2018)
42. Bhati, D., Pachori, R.B., Gadre, V.M.: A novel approach for time frequency localization of scaling functions and design of three-band biorthogonal linear phase wavelet filter banks. Digital Signal Process. **69**, 309–322 (2017)
43. Orhan, U., Hekim, M., Ozer, M.: EEG signals classification using the K-means clustering and a multilayer perceptron neural network model. Expert Syst. Appl. **38**(10), 13475–13481 (2011)
44. Guo, L., Rivero, D., Pazos, A.: Epileptic seizure detection using multiwavelet transform based approximate entropy and artificial neural networks. J. Neurosci. Methods **193**(1), 156–163 (2010)
45. Ubeyli, E.D.: Combined neural network model employing wavelet coefficients for EEG signals classification. Digital Signal Process. **19**(2), 297–308 (2009)
46. Ubeyli, E.D., Cvetkovic, D., Cosic, I.: Analysis of human PPG, ECG and EEG signals by eigenvector methods. Digital Signal Process. **20**(3), 956–963 (2010)
47. Bhati, D., Sharma, M., Pachori, R.B., Gadre, V.M.: Time-frequency localized three-band biorthogonal wavelet filter bank using semidefinite relaxation and nonlinear least squares with epileptic seizure EEG signal classification. Digital Signal Process. **62**, 259–273 (2017)
48. Sharma, M., Pachori, R.B., Acharya, U.R.: A new approach to characterize epileptic seizures using analytic time-frequency flexible wavelet transform and fractal dimension. Pattern Recogn. Lett (2017)
49. Patidar, S., Pachori, R.B., Upadhyay, A., Acharya, U.R.: An integrated alcoholic index using tunable-q wavelet transform based features extracted from EEG signals for diagnosis of alcoholism. Appl. Soft Comput. **50**, 71–78 (2017)
50. Gandhi, T., Panigrahi, B.K., Anand, S.: A comparative study of wavelet families for EEG signal classification. Neurocomputing **74**(17), 3051–3057 (2011)
51. Acharya, U.R., Sree, S.V., Suri, J.S.: Automatic detection of epileptic EEG signals using higher order cumulant features. Int. J. Neural Syst. **21**(05), 403–414 (2011)
52. Seijas, C., Caralli, A., Villazana, S.: Neuropathology classifier based on higher order spectra. J. Comput. Commun. **2013** (2013)
53. Vetterli, M., Herley, C.: Wavelets and filter banks: theory and design. IEEE Trans. Signal Process. **40**(9), 2207–2232 (1992)
54. Bhati, D.: Design of time-frequency localized three-band wavelet filter banks and applications in EEG signal analysis. Ph.D. Thesis, Indian Institute of Technology Bombay, Mumbai, India (2017)
55. Pachori, R.B., Sircar, P.: EEG signal analysis using FB expansion and second-order linear TVAR process. Signal Process. **88**(2), 415–420 (2008)
56. Yegnanarayana, B.: Artificial Neural Networks. Prentice-Hall of India Pvt. Ltd. (2004)
57. Valipour, M.: Optimization of neural networks for precipitation analysis in a humid region to detect drought and wet year alarms. Meteorol. Appl. **23**(1), 91–100 (2016)
58. Sharma, R., Pachori, R.B., Acharya, U.R.: An integrated index for the identification of focal electroencephalogram signals using discrete wavelet transform and entropy measures. Entropy **17**(8), 5218–5240 (2015)
59. Andrew, A.M.: An introduction to support vector machines and other kernel-based learning methods by Nello Christianini and John Shawe-Taylor. Cambridge University Press (2000)

60. Boneau, C.A.: The effects of violations of assumptions underlying the t test. Psychol. Bull. **57**(1), 49 (1960)
61. Müller, K.-R., Mika, S., Rätsch, G., Tsuda, K., Schölkopf, B.: An introduction to kernel-based learning algorithms. IEEE Trans. Neural Netw. **12**(2), 181 (2001)
62. Cristianini, N., Shawe-Taylor, J.: An Introduction to Support Vector Machines (2000)
63. Lee, S.-H., Lim, J.S., Kim, J.-K., Yang, J., Lee, Y.: Classification of normal and epileptic seizure EEG signals using wavelet transform, phase-space reconstruction, and euclidean distance. Comput. Methods Programs Biomed. **116**(1), 10–25 (2014)
64. Guo, L., Rivero, D., Dorado, J., Rabual, J.R., Pazos, A.: Automatic epileptic seizure detection in EEGs based on line length feature and artificial neural networks. J. Neurosci. Methods **191**(1), 101–109 (2010)
65. Nicolaou, N., Georgiou, J.: Detection of epileptic electroencephalogram based on permutation entropy and support vector machines. Expert Syst. Appl. **39**(1), 202–209 (2012)
66. Samiee, K., Kovacs, P., Gabbouj, M.: Epileptic seizure classification of EEG time-series using rational discrete short-time fourier transform. IEEE Trans. Biomed. Eng. **62**(2), 541–552 (2015)
67. Swami, P., Gandhi, T.K., Panigrahi, B.K., Tripathi, M., Anand, S.: A novel robust diagnostic model to detect seizures in electroencephalography. Expert Syst. Appl. **56**, 116–130 (2016)

Automated Identification of Epileptic Seizures from EEG Signals Using FBSE-EWT Method

Vipin Gupta, Abhijit Bhattacharyya and Ram Bilas Pachori

Abstract Epilepsy is a neurological disorder that leads to the occurrence of recurrent seizures. The electroencephalogram (EEG) signal is commonly used to record the electrical functioning from the brain. These recorded EEG signals have non-stationary and non-linear characteristics. In this chapter, we have introduced a new methodology based on Fourier-Bessel series expansion (FBSE) and empirical wavelet transform (EWT) for the classification of epileptic seizure EEG signals. The scale-space representation based detection of boundaries has been adapted for the segmentation of the FBSE spectrum obtained with EEG signals, and the EWT is utilized to obtain narrow sub-band signals. Then, the Hilbert marginal spectrum (HMS) of these sub-band signals have been obtained with FBSE-EWT. Afterwards, the line length and entropy features have been computed from obtained HMSs corresponding to different oscillatory levels of the EEG signals. To reduce the feature space, the Kruskal-Wallis test based feature ranking is applied. The selected features after feature ranking are used in random forest (RF) classifier for classifying normal from healthy subjects and seizure from epileptic subjects using EEG signals. The classification is also validated with 10-fold cross-validation and 50% training—50% testing data techniques. In addition to these techniques, the 5-fold cross-validation and 40% training—60% testing data techniques have been also applied on the significant features corresponding to maximum classification accuracies obtained with 10-fold cross-validation and 50% training—50% testing data techniques in order to reduce computational complexity. The assessment of classification performance is also evaluated in terms of classification accuracy for different sample lengths of EEG signals. The obtained maximum classification accuracy in this proposed method is 100%, with 50% training—50% testing data technique. The proposed method may help the neurologists for the identification of healthy and epileptic subjects from EEG signals.

V. Gupta (✉) · A. Bhattacharyya · R. B. Pachori
Indian Institute of Technology Indore, Indore 453552, India
e-mail: vipingupta@iiti.ac.in

A. Bhattacharyya
e-mail: phd1401202001@iiti.ac.in

R. B. Pachori
e-mail: pachori@iiti.ac.in

G. Naik (ed.), *Biomedical Signal Processing*, Series in BioEngineering,
https://doi.org/10.1007/978-981-13-9097-5_8

1 Introduction

Epilepsy is a neurological disease which identifies by the reoccurrence of epileptic seizure [1]. The electroencephalogram (EEG) signals are more often used tool for the identification of epilepsy because these signals contain information about the brain [2]. The recorded EEG signals are non-stationary and non-linear in behaviours [2, 3]. Moreover, the neurologists can have difficulty in visually monitoring for these subtle nature. Therefore, an automated identification system based on non-linear features and non-stationary signal processing techniques are required to identify epileptic seizures.

Several methods depend on non-linear features, and non-stationary signal processing techniques are presented in the literature [4–28]. A method based on second-order difference plot (SODP) of intrinsic mode functions (IMFs) obtained with empirical mode decomposition (EMD) has been proposed in [4] for classification of normal and epileptic seizure EEG signals. The obtained classification accuracy is 100% with this proposed method. The classification of seizure EEG signals based on bandwidth features obtained with EMD is presented in [5]. The achieved minimum and maximum classification accuracies are 99.5 and 100% for this method. In a work [6], the authors proposed a method based on time-frequency localized three-band synthesis wavelet filter bank with sub-band norm used as a feature which achieved a classification accuracy of 99.66% for classifying seizure and non-seizure EEG signals. The instantaneous area of analytic IMFs has also been utilized as features for epileptic seizure detection. The achieved classification accuracy is 90% for this method [7]. A method known as fractional linear prediction (FLP) has been used in research work for the classification of seizure and seizure-free EEG signals. This method gives a classification accuracy of 95.33% [8]. In another work [10], seizure-free and seizure EEG signals have been classified with SODP of IMFs, and 95% confidence ellipse area of SODP were used as features with artificial neural networks (ANN) classifier. The obtained average classification accuracy was 97.75% for this method. The one-dimensional local binary pattern (1D-LBP) based features are used in a method for classifying seizure and seizure-free EEG signals. The classification accuracy obtained in this method is 98.33% [14]. The classification based on phase space representation (PSR) reconstructed with IMFs of EEG signals has been used in work for classifying seizure and seizure-free EEG signals. The classification accuracy achieved in this method is 98.67% [15]. The seizure and seizure-free EEG signals in another work have been classified using three-band orthogonal wavelet filter bank with an achieved classification accuracy of 99.3% [12]. The method based on multiscale radial basis functions (MRBF) and a modified particle swarm optimization (MPSO) have been also used to classify seizure and seizure-free EEG signals with an achieved classification accuracy of 98.7% [13]. The technique for the detection of nonconvulsive seizure detection has been proposed using Hilbert-Haung tensor representation [16]. The time-frequency images of EEG have been proposed for the detection of epileptic seizure in a work with an achieved classification accuracy of 100% [17]. A new approach based on time-frequency localized three-band biorthog-

onal wavelet filter bank has been utilized for the classification of epileptic seizure EEG signals. The obtained classification accuracy is 99.33% for the classification of seizure and seizure-free EEG signals [18]. The tunable-Q wavelet transform (TQWT) with a multiscale entropy method has been also proposed for classification of seizure EEG signals. The obtained classification accuracy was 99% for the classification of seizure and non-seizure EEG signals [19]. An analytic time-frequency flexible wavelet transform based classification of epileptic seizure EEG signals has been proposed in a work. The acquired classification accuracy was 100% for classification of normal and seizure EEG signals [20]. A key-point based LBP method has been proposed for the detection of an epileptic seizure. The achieved classification accuracy was 100% for classifying seizure and normal EEG signals [21]. In another work [22], the authors proposed a different method depends on TQWT with fractal dimension features for the classification of epileptic seizure EEG signals. The obtained highest classification accuracy in this method is 100% for classifying normal and seizure EEG signals. The dynamic mode decomposition (DMD) based methodology has been found significant importance for the detection of epileptic seizures [23]. The classification based on time-frequency domain features has been also proposed using improved eigenvalue decomposition of Hankel matrix and Hilbert transform (IEVDHM-HT). The proposed method has achieved classification accuracy of 100% for classifying seizure and seizure-free EEG signals [24]. The classification based on EMD-TQWT method has been also explored in literature for epileptic EEG signals. This classification method achieved a classification accuracy of 99% for classifying seizure and non-seizure EEG signals [25]. In a recent work [26], the classification based on empirical wavelet transform (EWT) with Hilbert marginal spectrum (HMS) has been proposed for classifying seizure-free and seizure EEG signals. The achieved classification accuracy was 99.33% in this method. The analysis of epileptic EEG signals based on two-dimensional (2D) projection of reconstructed phase space (RPS) has been also proposed in the literature for the discrimination purpose of epileptic seizure EEG signals [27]. A review using various epileptic seizure detection techniques have been published recently. In which, various epilepsy EEG signals databases along with seizure detection methods have been compared [28].

In this chapter, we have proposed a new method for automated classification of epileptic seizure EEG signals based on Fourier-Bessel series expansion (FBSE) [29, 30] and EWT [31]. The FBSE-EWT was proposed in previous work for the time-frequency representation (TFR) of EEG signals [32]. The FBSE is a suitable tool for analysis of non-stationary signals [29], and the analysis of epileptic seizure EEG signals based on FBSE has been presented in [33]. The EWT based studies have a significant contribution to the classification of epileptic EEG signals [34, 35]. In [34], the EWT based multi-variate TFR has been proposed by authors and they have designed models for patient specific EEG seizure detection. In [35], authors separated EEG signal rhythms with filter-bank developed by EWT method and the areas of the 2D RPS have been used in order to classify focal and non-focal EEG signals. Therefore, we have proposed FBSE-EWT based HMS which can be used as a more relevant spectral representation for non-stationary EEG signals. Further, we have evaluated line length and entropy features in the spectral domain from the HMSs

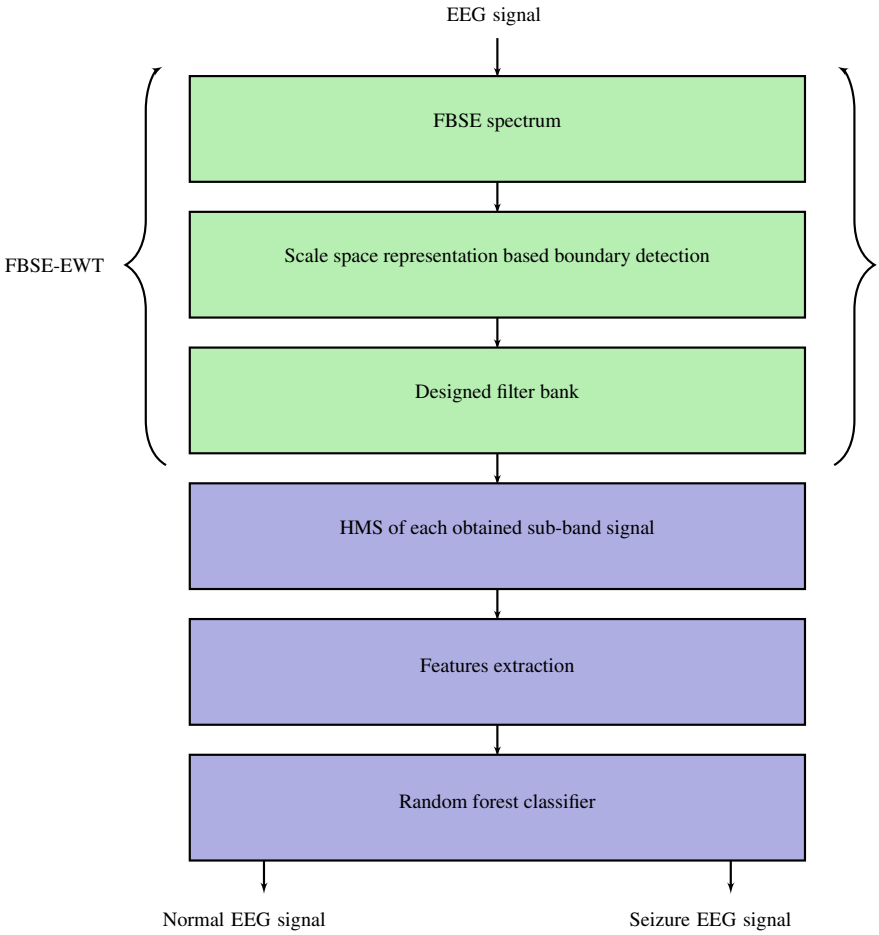

Fig. 1 Block diagram of the proposed method for classification of normal and seizure EEG signals

with different oscillatory levels of EEG signals. Then, we have ranked the evaluated features with the help of Kruskal-Wallis statistical test [36] using their probability (p) values. Finally, the ranked features have fed to random forest (RF) classifier for the classification of normal and seizure EEG signals. In Fig. 1, the block diagram of our proposed method is presented for the classification of epileptic seizure EEG signals.

The organization of the rest book chapter is as follows. Section 2 is briefly discussed about the FBSE-EWT method. The proposed method for automated classification of epileptic seizure based on FBSE-EWT and studied database are described in Sect. 3. Section 4 provides the results with discussions about the effectiveness of the proposed method. Finally, the chapter is concluded in Sect. 5.

2 Overview of the FBSE-EWT Method

The FBSE-EWT is an adaptive method that combines FBSE [29] and EWT [31] signal processing techniques for non-stationary signals analysis [32]. The FBSE uses Bessel functions as bases, which are non-stationary type and this characteristic of FBSE makes it suitable for analysis of signals which have time-varying parameters. On the other hand, the EWT is based on the design of adaptive wavelet based filters. These wavelet filters provide support to localized the analyzed signal in the spectrum. The sub-band signals obtained with EWT method have specific center frequencies with compact support of frequencies. The basic steps involved to implement FBSE-EWT method are described as follows [32]:

1. Firstly, the FBSE method is utilized to get the frequency spectrum of an arbitrary signal $x(n)$ in the range of frequency between $[0, \pi]$. The FBSE of a signal $x(n)$ with the help of zero-order Bessel functions is mathematically expressed as [29, 37–39]:

$$x(n) = \sum_{i=1}^{N} C_i J_0\left(\frac{\beta_i n}{N}\right), \; n = 0, 1, \ldots, N-1 \tag{1}$$

where, C_i are known as the FBSE coefficients of $x(n)$ which can be mathematically written as follows [30, 40, 41]:

$$C_i = \frac{2}{N^2 (J_1(\beta_i))^2} \sum_{n=1}^{N} n x(n) J_0\left(\frac{\beta_i n}{N}\right) \tag{2}$$

where, $J_0(.)$ and $J_1(.)$ represent zero and first-order Bessel functions, respectively. The ascending order positive roots of the zero-order Bessel function ($J_0(\beta) = 0$) are represented by β_i with $i = 1, 2, \ldots N$. The order i of the FBSE coefficients is analogous to peak value of continuous time-frequency f_i (Hz) and it can be expressed by the following equation [29, 30]:

$$\beta_i \approx \frac{2\pi f_i N}{f_s}, \text{ where } \beta_i \approx \beta_{i-1} + \pi \approx i\pi \tag{3}$$

In Eq. (3), f_s represents the sampling frequency and the Eq. (3) can be written as [30, 42],

$$i \approx \frac{2 f_i N}{f_s} \tag{4}$$

Therefore, we can conclude from Eq. (4) that, i should be varied in the range from 1 to N (signal length) in order to capture the entire bandwidth of the signal. Hence, FBSE spectrum is a magnitude plot of the FBSE coefficients ($|C_i|$) versus frequencies (f_i).

2. Secondly, segmenting the obtained FBSE spectrum into U number of contiguous segments using scale-space based boundary detection method [43] in order

to get optimal set of $U + 1$ boundary frequencies denoted as λ_i with first and last boundary frequencies are prefixed to 0 and π, respectively. The rest $U - 1$ intermediate boundary frequencies are obtained using EWT boundary detection method. Therefore, the adaptive segments of FBSE spectrums are expressed as $[0\ \lambda_1]$, $[\lambda_1\ \lambda_2]$, …, and $[\lambda_{U-1}\ \pi]$.

3. In the third step, the empirical scaling and wavelet functions are defined for each adaptive segment of FBSE spectrum as the set of band-pass filters. These wavelet based band-pass filters are constructed with the idea of Littlewood-Paley and Meyer's wavelets [31, 44]. The empirical scaling and wavelet functions of EWT can be mathematically written as [31],

$$\urcorner_i(\lambda) = \begin{cases} 1, & \text{if } |\lambda| \leq (1-\vartheta)\lambda_i. \\ \cos\left(\frac{\pi\Theta(\vartheta,\lambda_i)}{2}\right), & \text{if } (1-\vartheta)\lambda_i \leq |\lambda| \leq (1+\vartheta)\lambda_i. \\ 0, & \text{otherwise.} \end{cases} \tag{5}$$

$$F_i(\lambda) = \begin{cases} 1, & \text{if } (1+\vartheta)\lambda_i \leq |\lambda| \leq (1-\vartheta)\lambda_{i+1}. \\ \cos\left(\frac{\pi\Theta(\vartheta,\lambda_{i+1})}{2}\right), & \text{if } (1-\vartheta)\lambda_{i+1} \leq |\lambda| \leq (1+\vartheta)\lambda_{i+1}. \\ \sin\left(\frac{\pi\Theta(\vartheta,\lambda_i)}{2}\right), & \text{if } (1-\vartheta)\lambda_i \leq |\lambda| \leq (1+\vartheta)\lambda_i. \\ 0, & \text{otherwise.} \end{cases} \tag{6}$$

where,

$$\Theta(\vartheta, \lambda_i) = \kappa\left(\frac{(|\lambda| - (1-\vartheta)\lambda_i)}{2\vartheta\lambda_i}\right) \tag{7}$$

The parameter ϑ generates tight frame in $L^2(\Re)$ with insuring empirical scaling as well as wavelet functions and the function $\kappa(u)$ is defined as [31],

$$\kappa(u) = \begin{cases} 0, & \text{if } u \leq 0. \\ \text{and } \kappa(u) + \kappa(1-u) = 1, & \forall u \in [0\ \ 1]. \\ 1, & \text{if } u \geq 1. \end{cases} \tag{8}$$

The inner product of the wavelet and scaling functions is used to compute detail and approximation coefficients with the analyzed signal $x(n)$.

3 Proposed Method and Studied Database

In the proposed method, we have used FBSE-EWT method in order to obtain HMS of non-stationary EEG signals. The obtained HMSs are considered for feature extraction process, and the classification performance have evaluated with these extracted features in RF classifier. A brief description of the database is also included in this section. The description of these parts is as follows.

3.1 FBSE-EWT Based HMS

In this subsection, the FBSE-EWT method is used to decomposed a signal $x(t)$ into U number of sub-band signals $x_i(t)$; $i = 1, 2, \ldots, U$ as described in the last section. The obtained sub-band signals are narrow-band components. Thus, Hilbert transform function (H) is applied to obtain instantaneous amplitude (IA) and instantaneous frequency (IF) of each sub-band signal then the analytic representation of each sub-band signal is expressed as [45]:

$$x_{+i}(t) = x_i(t) + j\mathrm{H}\left[x_i(t)\right] \tag{9}$$

The same analytic representation which expressed in Eq. (9) can also be written as:

$$x_{+i}(t) = A_i(t)e^{j\phi_i(t)} \tag{10}$$

The IA $A_i(t)$ and instantaneous phase (IP) $\phi_i(t)$ are expressed as [46, 47]:

$$A_i(t) = \sqrt{(x_i(t))^2 + (\mathrm{H}[x_i(t)])^2} \tag{11}$$

$$\phi_i(t) = \arctan\left(\frac{\mathrm{H}[x_i(t)]}{x_i(t)}\right) \tag{12}$$

The IF $f_i(t)$ is expressed as:

$$f_i(t) = \frac{d}{dt}\left[\phi_i(t)\right] \tag{13}$$

Then, the time-frequency coefficients for each decomposition level is written as [48]:

$$\mathrm{Tf}_i(f, t) = A_i(t)\delta[f - f_i(t)] \tag{14}$$

The HMS for each decomposition level is written as:

$$x_i(f) = \int_T \mathrm{Tf}_i(f, t)dt \tag{15}$$

Finally, the TFR with considering all the decomposition levels is mathematically expressed as [48]:

$$\mathrm{Tf}(f, t) = \mathrm{Tf}_i(f, t);\ i = 1, 2, \ldots, U \tag{16}$$

Therefore, the HMS with considering all the decomposition levels is mathematically expressed as:

$$x(f) = \int_T \mathrm{Tf}(f, t)dt \tag{17}$$

3.2 Features Extraction

In this work, we have fixed total number sub-band signals $U = 10$ for each considered EEG signal. In order to differentiate normal and seizure EEG signals, we have computed line length and entropy features from HMS of each sub-band signal in the spectral domain. The description of line length and entropy features are as follows:

3.2.1 Line Length Feature

The line length feature of the HMS is expressed as [49]:

$$\text{LiLe}_i = \frac{1}{K-1} \sum_{k=1}^{K-1} \text{abs}[x_i(k+1) - x_i(k)] \tag{18}$$

Here, x_i represents HMS of ith sub-band signal obtained with EEG signal, k denotes the index of the HMS samples, abs denotes absolute value, and K denotes the total number of samples present in HMS.

3.2.2 Log Energy Entropy

The log energy entropy of HMS for ith sub-band signal is defined as [50, 51]:

$$\text{LgEn}_i = \sum_{k=1}^{K} \log\left([x_i(k)]^2\right) \tag{19}$$

3.2.3 Norm Entropy

The norm entropy of HMS for ith sub-band signal is computed as [51, 52]:

$$\text{NoEn}_i = \sum_{k=1}^{K} [x_i(k)]^{\alpha} \tag{20}$$

where, $1 \leq \alpha < 2$. The LiLe_i, LgEn_i, and NoEn_i denote the features computed with ith sub-band signal.

3.3 *Random Forest Classifier*

The feature values extracted in the last step, are used as the input to a classifier with the aim of obtaining a robust seizure EEG signals classification. In this work. We have used RF classifier for the classification purpose. The RF classifier depends on classification results of many classification trees [53]. These trees are obtained with a random tree technique [54]. After that, each tree is assigned with a random vector. These assigned random vectors have the same distribution, but they are not dependent on each other. Therefore, the training data and assigned random vector provide support to the tree in order to perform classification. In this work, the Waikato environment for knowledge analysis (WEKA) software [55] is used for the classification using RF classifier. The classification performance is also validated using 10-fold cross-validation, 5-fold cross-validation, 50% testing—50% training data, and 40% testing—60% training data techniques [26, 56]. The classification performance parameters named as accuracy, sensitivity, and specificity are used to evaluate the studied method [57].

In this chapter, in order to show the effectiveness of the proposed method based on FBSE-EWT, we have studied publicly available databases by the University of Bonn, Germany [58], which is available online at http://epileptologie-bonn.de/cms/front_content.php?idcat=193&lang=3&changelang=3. This database has five sets (denoted by Z, O, N, F, and S) of EEG signals. The 100 EEG signals in set Z are recorded from the healthy person with eyes open state, and 100 EEG signals available in set O have been obtained from healthy subjects under eyes closed state. The sets N and F have 200 EEG signals, and they are recorded from the epileptic patients during seizure-free conditions. The set S contains 100 EEG signals which are recorded from

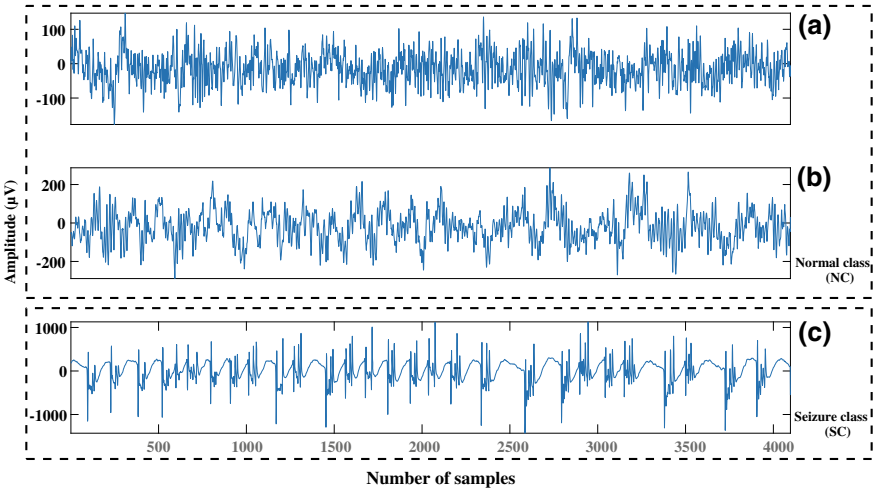

Fig. 2 Plot of EEG signals corresponding to (**a**)–(**b**) NC and (**c**) SC in which **a** normal (eyes open condition), **b** normal (eyes closed condition), and **c** seizure, respectively

the patients during epileptic seizure condition. The sampling rate of these available EEG signals is 173.61 Hz.

In this work, we have studied our proposed framework for the classification of normal class (NC) and seizure class (SC) of EEG signals. The NC has been obtained by combining sets Z and O. The SC is represented by set S. Figure 2 shows NC and SC signals from the described database of EEG signals.

4 Results and Discussions

In this section, the proposed automated classification system has been tested on the Bonn University EEG database [58] to obtain the results in terms of classification accuracy. The publicly available EEG signals are used in FBSE-EWT method to obtain the sub-bands from each EEG signal. Afterward, the HMS is extracted with each extracted sub-band signal. Figures 3, 4, and 5 show the HMSs of normal and seizure EEG signals which are shown in Fig. 2, respectively. It can be observed that HMSs are not overlapped in the frequency domain in different oscillatory levels and the magnitude of HMSs for seizure EEG signal are higher in different oscillatory levels compare to normal EEG signal. Now, we have computed line length, log energy entropy, and norm entropy features from spectral domain of these HMSs. The main motive of using these features in this proposed work because these features found significant importance in classifying epileptic EEG signals [49–52]. The extracted

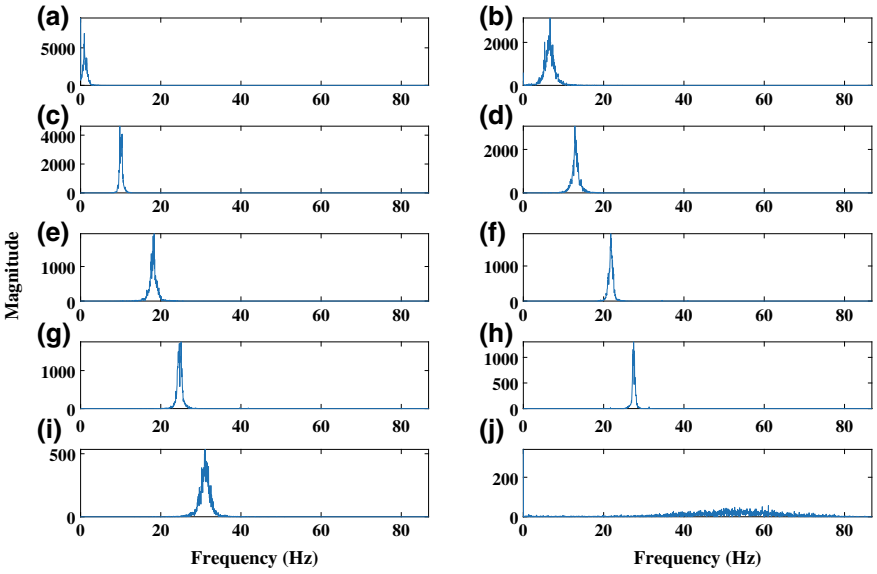

Fig. 3 HMSs of normal EEG signal with eyes open condition

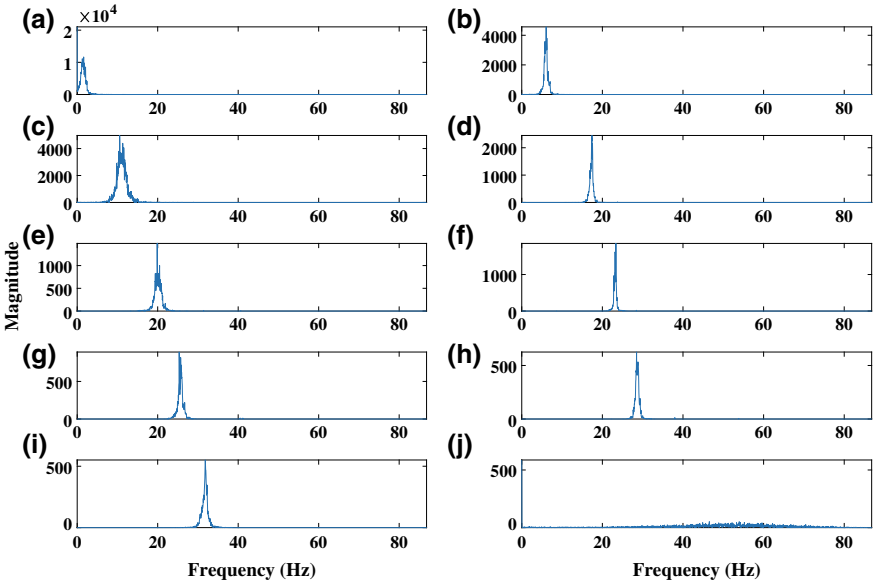

Fig. 4 HMSs of normal EEG signal with eyes closed condition

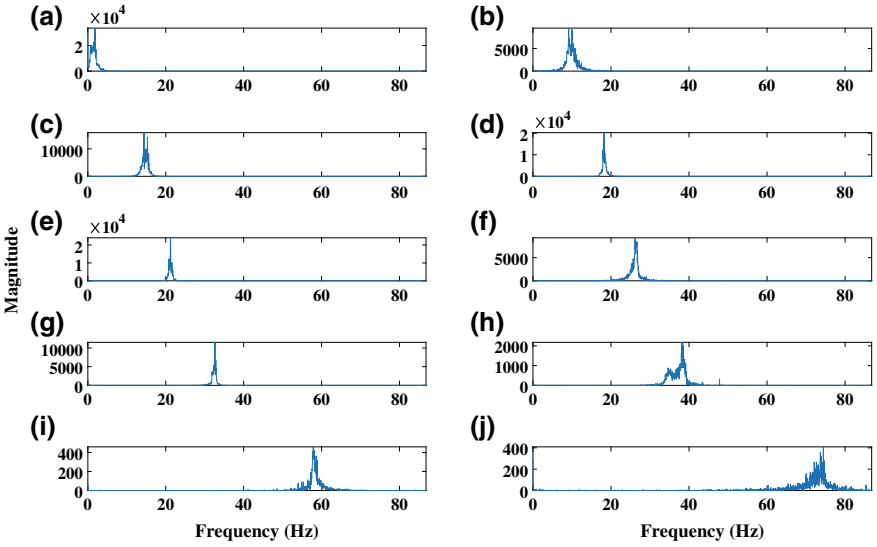

Fig. 5 HMSs of epileptic EEG signal with a seizure condition

features may have redundant and less distinct. To omit these characteristics in feature space, we have implemented Kruskal-Wallis statistical test [36] on obtained features at the various parameter of norm entropy along with line length and log energy entropy features in order to find the statistical significance features which have $p < 0.05$. The

Table 1 Classification accuracy on different norm entropy parameter α along with line length and log energy entropy features using 10-fold cross-validation technique at 4097 sample length of EEG signal

No. of features	Classification accuracy (%)									
	$\alpha = 1$	$\alpha = 1.1$	$\alpha = 1.2$	$\alpha = 1.3$	$\alpha = 1.4$	$\alpha = 1.5$	$\alpha = 1.6$	$\alpha = 1.7$	$\alpha = 1.8$	$\alpha = 1.9$
1	95	96.7	96.3	95.3	95.3	94	96	95.7	95	95.7
2	95.3	96.7	96.3	95.3	97	95.7	96.3	95.7	95.3	96.3
3	97.7	98	97.7	98.3	98.3	98	98	98	97.7	97.7
4	98	98.3	97.7	98.3	98.3	97.7	98.7	98.7	97.3	98
5	98.7	98.3	97.7	97.7	98.3	98	99	98.7	98.3	98
6	98.7	98.3	98	98	98	98.3	98.7	99	98.3	98.3
7	99	98.3	98	98	98.3	98	98.3	98.3	98	98.7
8	98.7	98.3	98	98	98.3	98	98.3	98.7	98.3	98.3
9	99	98.7	97.7	98.7	98	98.3	98.3	98.7	98.3	98
10	98.7	98.7	98.3	98.7	98.3	98.3	98.7	98.3	98.7	98.3
11	99	99	98.3	98.7	98.3	98.7	98.7	98.3	98.3	98.3
12	99	99	98.7	98.7	98.3	98.3	98.7	98.7	98.7	98.7
13	**99.3**	**99.3**	98.3	99	98.7	98.7	98.7	98.7	98.7	98.7
14	**99.3**	99	98.7	98.7	98.7	98.7	98.7	98.7	98.7	98.3
15	99	98.7	98.7	98.7	98.7	98.7	98.7	98.7	98.7	98.7
16	99	99	99	98.7	98.7	98.3	98.7	98.7	98.7	98.7
17	**99.3**	99	98.7	98.7	98.7	98.7	98.7	98.7	98.7	98.7
18	99	99.3	98.7	98.7	98.7	98.7	99	98.7	98.3	98.7
19	**99.3**	98.7	98.7	98.7	99	98.3	98.7	98.7	98.3	98.3
20	99	**99.3**	98.7	95.3	98.7	99	98.7	98.7	98.7	98.7
21	**99.3**	99	98.7	98.3	98.7	98.7	98.7	99	98.7	98.7
22	**99.3**	**99.3**	98.7	98.7	98.7	99	98.7	98.7	98.7	98.7
23	**99.3**	**99.3**	98.7	98.7	98.7	98.3	99	98.7	98.7	98.7
24	**99.3**	99	98.7	99	99	99	98.7	99	98.3	98.7
25	**99.3**	99	98.7	98.7	98.7	98.7	98.3	98.7	98.3	98.7
26	**99.3**	99	99	98.7	99	99	98.7	99	98.7	98.7
27	99	**99.3**	98.7	98.7	98.7	98.7	98.7	98.3	98.3	98.7
28	**99.3**	99	98.3	99	98.3	98.7	98.7	98.7	98.7	99
29	98.7	**99.3**	98.7	99	98.7	98	98.7	99	98.7	98.7
30	99	99	98.7	98.3	98.7	99	98.7	99	98.7	98.7

Kruskal-Wallis statistical test was used for the statistical significance analysis of the EEG signal in [50, 59]. Now, we have ranked the statistically significant features according to their computed p-values and fed them in RF classifier for the classification purpose. The classification of these EEG signals is also validated with 10-fold cross-validation [56] and 50% training—50% testing data [26] techniques. Tables 1 and 2 show the achieved classification accuracies using both validation techniques at different norm entropy parameter α. It can be seen from Tables 1 and 2 that the maximum attain classification accuracy is 100% with thirteen p value based ranked

Table 2 Classification accuracy on different norm entropy parameter α along with line length and log energy entropy features using 50% training—50% testing data at 4097 sample length of EEG signal

No. of features	Classification accuracy (%)									
	$\alpha = 1$	$\alpha = 1.1$	$\alpha = 1.2$	$\alpha = 1.3$	$\alpha = 1.4$	$\alpha = 1.5$	$\alpha = 1.6$	$\alpha = 1.7$	$\alpha = 1.8$	$\alpha = 1.9$
1	93.3	98	96	95.3	97.3	97.3	96	95.3	94.7	93.3
2	96	98	94.7	96	95.3	94.7	97.3	96	95.3	94.7
3	97.3	97.3	98	98	98	98	97.3	97.3	98	96.7
4	98.7	98	97.3	97.3	97.3	97.3	98.7	99.3	98.7	97.3
5	98.7	98.7	98.7	98	98.7	98.7	98.7	98.7	98.7	98.7
6	98.7	98.7	98.7	98.7	98.7	98.7	98.7	98.7	99.3	98
7	98	98.7	98.7	98.7	98.7	98.7	98.7	98.7	98.7	98
8	98.7	98.7	98.7	98.7	98.7	98.7	98.7	98.7	98	98
9	99.3	98.7	98.7	98.7	98.7	98.7	98.7	98.7	98.7	98.7
10	98.7	98.7	98.7	98.7	98.7	98.7	98.7	98.7	98.7	98.7
11	98.7	98.7	98.7	99.3	98.7	98.7	98.7	98.7	98.7	98.7
12	98	98.7	98.7	98.7	98.7	98.7	98.7	98	98.7	98.7
13	**100**	97.3	98.7	98.7	98.7	98.7	98.7	98.7	98.7	98.7
14	98.7	98.7	98.7	99.3	99.3	99.3	98.7	98.7	99.3	98.7
15	97.3	98.7	98	99.3	98.7	98	98.7	98.7	98.7	99.3
16	98.7	98.7	98.7	99.3	98.7	98.7	98.7	98.7	98.7	98.7
17	98	98	98.7	98.7	99.3	98.7	98.7	98.7	98.7	97.3
18	99.3	98.7	98.7	98.7	98.7	98	98.7	98	98.7	98.7
19	98	98.7	98	98.7	98	98	98.7	98.7	99.3	98.7
20	98	98.7	97.3	98	98	98	98.7	98.7	98	98.7
21	97.3	98	96.7	98	98.7	98	98	97.3	98	98.7
22	96.7	98.7	98	98	98	98	98	98.7	99.3	97.3
23	97.3	96.7	98.7	97.3	98.7	98.7	98	98.7	98	98
24	96	96.7	96.7	96	97.3	98.7	98.7	98.7	98.7	97.3
25	97.3	96	97.3	96.7	97.3	98.7	97.3	97.3	96.7	98
26	96.7	96.7	98	96.7	97.3	97.3	97.3	98	97.3	96.7
27	96	97.3	96.7	96.7	97.3	97.3	96.7	97.3	96.7	96.7
28	96	96.7	98.7	97.3	97.3	98.7	97.3	98	96.7	96.7
29	96	96.7	97.3	96	96	97.3	97.3	96	97.3	97.3
30	96	96	96.7	96.7	96	96.7	97.3	98	96	96.7

features using 50% training—50% testing data validation technique. The proposed method is also implemented for the varying samples length of the EEG signals in order to check the robustness of the proposed method in classifying seizure EEG signals. Tables 3 and 4 show the obtained classification accuracies with 3072 and 2048 sample length of EEG signals at the selected value of $\alpha = 1$ which is corresponding to maximum obtain classification accuracy for full length (4097 sample length) EEG signals, respectively. It can be seen from Tables 3 and 4 that the classification accuracies increase for 10-fold cross-validation technique to 99.7% with 3072

Table 3 Classification accuracy on selected norm entropy parameter $\alpha = 1$ along with line length and log energy entropy features at 3072 sample length of EEG signal

No. of features	Classification accuracy (%)	
	10-fold cross-validation technique	50% training—50% testing data
1	95.3	96
2	99	98
3	98.7	98
4	98.7	98
5	**99.7**	98.7
6	**99.7**	98.7
7	99.3	98.7
8	99	98.7
9	**99.7**	98.7
10	99.3	98.7
11	99.3	98.7
12	99.3	98.7
13	99.3	98
14	99.3	98.7
15	**99.7**	98
16	99.3	98.7
17	**99.7**	98.7
18	99.3	97.3
19	99.3	98
20	**99.7**	98
21	99.3	97.3
22	99.3	97.3
23	99.3	96.7
24	99	96.7
25	98.7	98
26	**99.7**	97.3
27	99	97.3
28	99	97.3
29	99.3	97.3
30	99	96.7

sample length of EEG signals, but for 50% training—50% testing data technique, it decreases. The obtained maximum classification accuracies can also be observed by bold entries from Tables 1, 2, 3, and 4. Figures 6 and 7 show the variation of classification accuracy with respect to p value based ranked feature. From Figs. 6 and 7, it can be observed that the obtained highest classification accuracy is 100% with

Table 4 Classification accuracy on selected norm entropy parameter $\alpha = 1$ along with line length and log energy entropy features at 2048 sample length of EEG signal

No. of features	Classification accuracy (%)	
	10-fold cross-validation technique	50% training—50% testing data
1	96.7	98
2	97	98
3	99	98.7
4	99	98.7
5	99	98.7
6	**99.3**	98.7
7	**99.3**	98
8	99	98.7
9	99	98
10	**99.3**	97.3
11	**99.3**	97.3
12	98.7	97.3
13	99	97.3
14	**99.3**	97.3
15	98.7	97.3
16	**99.3**	97.3
17	99	97.3
18	98.7	97.3
19	99	97.3
20	**99.3**	97.3
21	98.7	97.3
22	98.3	97.3
23	98.7	97.3
24	98.3	96.7
25	98.3	96
26	98.3	97.3
27	98.3	96
28	98.3	96.7
29	98.3	96.7
30	98.7	97.3

thirteen most significant p value based ranked features using 50% training—50% testing data technique. The box-plots of thirteen most statistically significant p value based ranked features are shown in Fig. 8. The p value of corresponding box-plots shown in Fig. 8a–m are 2.32×10^{-44}, 4.20×10^{-44}, 3.32×10^{-39}, 6.47×10^{-38}, 8.52×10^{-38}, 1×10^{-37}, 1.02×10^{-36}, 1.09×10^{-36}, 4.58×10^{-36}, 5.23×10^{-34},

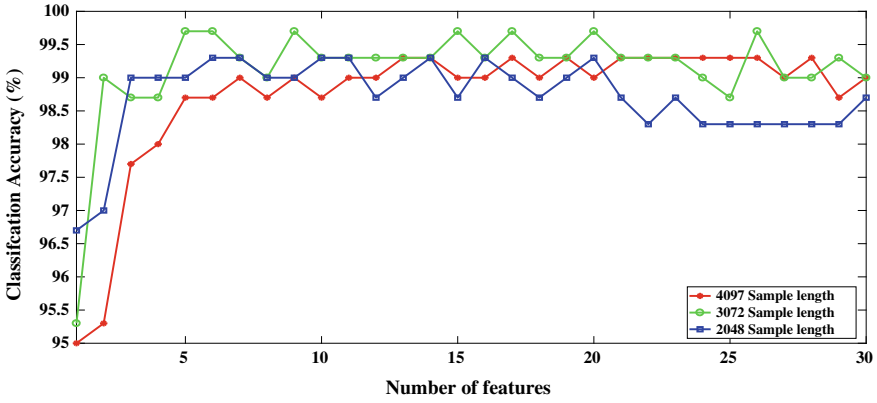

Fig. 6 Classification accuracy variation corresponding to a number of features at $\alpha = 1$ with 10-fold cross-validation technique

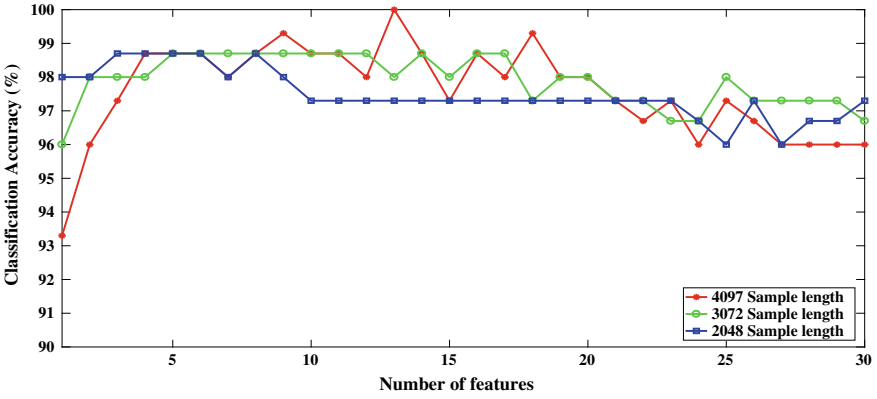

Fig. 7 Classification accuracy variation corresponding to a number of features at $\alpha = 1$ with 50% training—50% testing data

2.07×10^{-33}, 3.40×10^{-33}, and 1.16×10^{-32}, respectively. It can be seen from Fig. 8 that computed features for SC of EEG signals are higher in magnitude compare to NC of EEG signals. Furthermore, we have also applied 5-fold cross-validation and 40% training—60% testing data techniques on 5 and 13 significant features which are corresponding to maximum classification accuracies obtained with 10-fold cross-validation and 50% training—50% testing data techniques in order to reduce the computational complexity of the developed method. However, these 5-fold cross-validation and 40% training—60% testing data techniques provide dip in classification accuracies for both cases, and it can be observed from Table 5. Therefore, we have achieved maximum classification accuracies of 97.7% and 100% using 10-fold cross-validation and 50% training—50% testing data techniques, respectively. The classification sensitivities of 100% are obtained corresponding to these

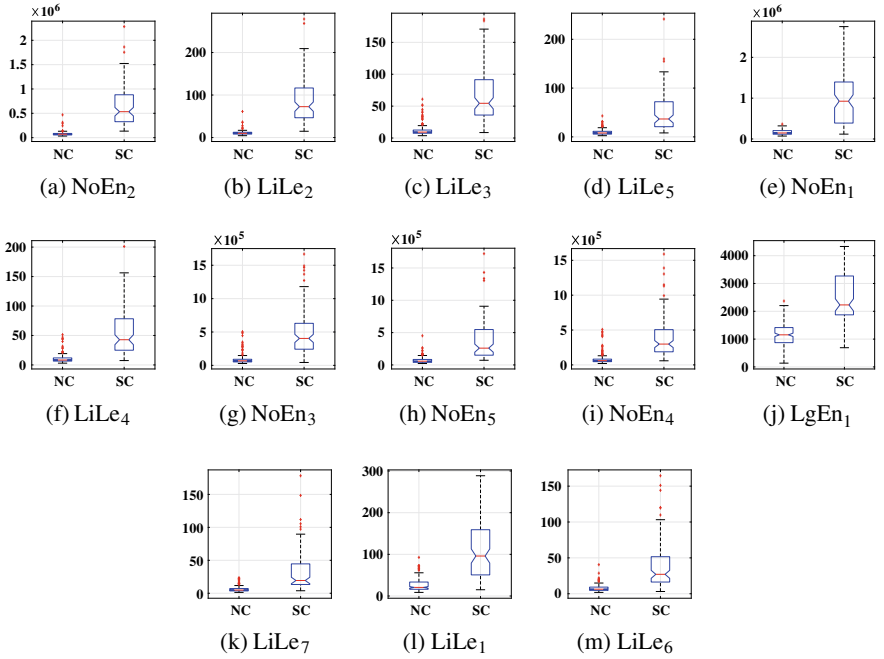

Fig. 8 Box plots of thirteen most significant features corresponding to maximum classification accuracy at $\alpha = 1$ with features description

Table 5 Classification accuracy with different validation techniques applied on significant features corresponding to maximum classification accuracies obtained with 10-fold cross-validation and 50% training—50% testing data techniques

No. of features	Sample length	Validation technique	Classification accuracy (%)
5	3072	5-fold cross-validation	99
13	4097	40% training—60% testing	98.3

achieved maximum classification accuracies for both validation techniques such as 10-fold cross-validation and 50% training—50% testing. Similarly, the classification specificities corresponding to these achieved maximum classification accuracies are 99.5% and 100% for 10-fold cross-validation and 50% training—50% testing data techniques, respectively. The receiver operating characteristic (ROC) curves [60] corresponding to maximum classification accuracies are shown in Fig. 9 using 10-fold cross-validation and 50% training—50% testing data techniques. The ROC curve provides a measure of overall classification performance in which a larger covered area shows better classification accuracy [5]. From Fig. 9, it can be observed that the 50% training—50% testing data technique covered more area as compared to the 10-fold cross-validation technique. In Table 6, we have also compared classification

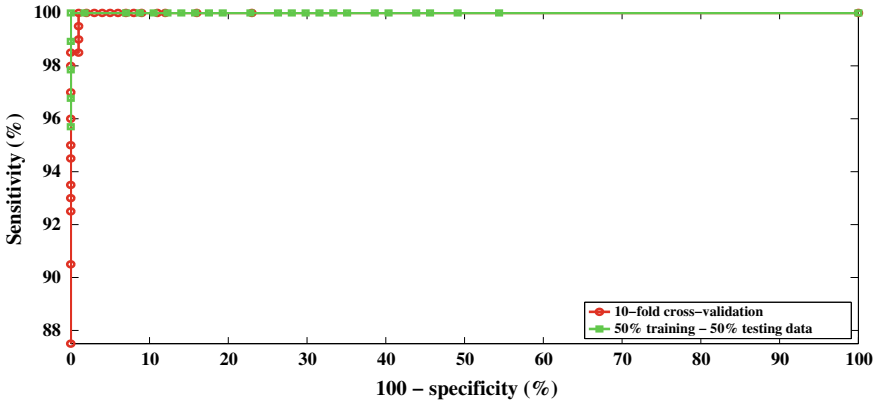

Fig. 9 ROC curves corresponding to maximum classification accuracies obtained with 10-fold cross-validation and 50% training—50% testing data techniques

Table 6 Comparison of our proposed method with existing methods for the classification of NC and SC of EEG signals

Authors	Method	Classification accuracy (%)
Polat and Gunes [61]	FFT and DT	98.7
Lee et al. [62]	WT, PSR, and ED	98.1
Fu et al. [63]	HHT and TFR	99.1
Yuan et al. [64]	KSR	98.6
Kaya et al. [65]	1D-LBP	99.5
Fu et al. [66]	HMS analysis	99.8
Sharmila and Geethanjali [67]	DWT and Naive Bayes	99.2
Yu et al. [71]	KR-PCR	99.3
Mert and Akan [68]	EMD and PSD	97.9
Gupta et al. [69]	DCT, Hurst exponent, and ARMA parameters features	94.8
Sharma et al. [70]	Iterative filtering	99.5
This work	FBSE-EWT based HMS, LiLe, LgEn, and NoEn features	100

accuracy of our proposed method with some other existing epileptic EEG signal classification methods studied on the same EEG database. The classification based on fast Fourier transform (FFT) and decision tree (DT) classifier was obtained a classification accuracy of 98.7% for classifying seizure EEG signals [61]. In another work [62], the authors proposed a method based on wavelet transform (WT), PSR, and Euclidean distance (ED) with a maximum achieved classification accuracy of 98.1% for seizure EEG signals. The Hilbert-Huang transform (HHT) based TFR has been utilized as time-frequency image (TFI) feature in research work with a maximum classification accuracy of 99.1% [63]. A kernel sparse representation (KSR) based

the approach has been also suggested in the literature for classification of epileptic EEG signals with maximum attain classification accuracy of 98.6% [64]. In [65], the classification is based on 1D-LBP method, and the obtained maximum classification accuracy was 99.5% for the classification of seizure EEG signals. The HMS based seizure classification method has been also implemented in [66] with maximum achieved a classification accuracy of 99.8%. The classification of NC and SC EEG signals with discrete wavelet transform (DWT) has been also proposed using two different classifiers, namely, Naive Bayes and k-nearest neighbour (KNN). The highest achieved classification accuracy is 99.2% using Naive Bayes classifier in this method [67]. The EMD and power spectral density (PSD) based work acquired a maximum classification accuracy of 97.9% [68]. The discrete cosine transform (DCT) with Hurst exponent and auto-regressive moving average (ARMA) parameter features gives a classification accuracy of 94.8% [69]. The iterative filtering based automated system has also been proposed for the classification of epileptic seizure EEG signals. The proposed classification system was achieved the highest classification accuracy of 99.50% in classifying NC and SC of EEG signals [70]. A kernel robust probabilistic collaborative representation (KR-PCR) based approach gives a maximum classification accuracy of 99.3% [71]. These existing methods have significant contributions and results in the present literature. Hence, we can conclude that our proposed method gives highest classification accuracy of 100% in comparison to existing methods. It should be noted that the proposed method is based on non-stationary and adaptive signal decomposition techniques.

5 Conclusions

We have proposed a new method for the automated classification of NC and SC of EEG signals. The proposed method is based on the HMS obtained with FBSE-EWT. The FBSE-EWT based HMS provides better spectral representation due to use of non-stationary Bessel basis functions and adaptive wavelet decomposition. The extracted features namely line length and entropies from the HMS along with RF classifier have provided the highest classification accuracy of 100% with utilizing only 50% testing data. The proposed method also found effective for different sample lengths of EEG signals with 10-fold cross-validation technique. Moreover, the proposed method can be used for the clinical purpose and provide help to neurologists in their diagnosis of epilepsy. The proposed method in this chapter needs to be studied on a large number of EEG databases before applying it for the diagnosis of epilepsy. The developed method can also be used with other biomedical signals in order to diagnosed other diseases.

Acknowledgements This work was supported by the Council of Scientific and Industrial Research (CSIR) funded Research Project, Government of India, Grant No. 22/687/15/EMR-II.

References

1. Fisher, R.S., Van Emde Boas, W., Blume, W., Elger, C., Genton, P., Lee, P., Engel, J.: Response: definitions proposed by the international league against epilepsy (ILAE) and the international bureau for epilepsy (IBE). Epilepsia **46**(10), 1701–1702 (2005)
2. Natarajan, K., Acharya, U.R., Alias, F., Tiboleng, T., Puthusserypady, S.K.: Nonlinear analysis of EEG signals at different mental states. Biomed. Eng. OnLine **3**(1), 7 (2004)
3. Barlow, J.S.: Methods of analysis of nonstationary EEGs, with emphasis on segmentation techniques: a comparative review. J. Clin. Neurophysiol. Off. Publ. Am. Electroencephalogr. Soc. **2**(3), 267–304 (1985)
4. Pachori, R.B., Sharma, R., Patidar, S.: Classification of Normal and Epileptic Seizure EEG Signals Based on Empirical Mode Decomposition, pp. 367–388. Springer International Publishing, Cham (2015)
5. Bajaj, V., Pachori, R.B.: Classification of seizure and nonseizure EEG signals using empirical mode decomposition. IEEE Trans. Inf. Technol. Biomed. **16**(6), 1135–1142 (2012)
6. Bhati, D., Pachori, R.B., Gadre, V.M.: A novel approach for time-frequency localization of scaling functions and design of three-band biorthogonal linear phase wavelet filter banks. Digital Signal Process. **69**, 309–322 (2017)
7. Bajaj, V., Pachori, R.B.: Epileptic seizure detection based on the instantaneous area of analytic intrinsic mode functions of EEG signals. Biomed. Eng. Lett. **3**(1), 17–21 (2013)
8. Joshi, V., Pachori, R.B., Vijesh, A.: Classification of ictal and seizure-free EEG signals using fractional linear prediction. Biomed. Signal Process. Control **9**, 1–5 (2014)
9. Bhattacharyya, A., Ranta, R., Le Cam, S., Louis-Dorr, V., Tyvaert, L., Colnat-Coulbois, S., Maillard, L., Pachori, R.B.: A multi-channel approach for cortical stimulation artefact suppression in depth EEG signals using time-frequency and spatial filtering. IEEE Trans. Biomed. Eng. **1–1**, (2018)
10. Pachori, R.B., Patidar, S.: Epileptic seizure classification in EEG signals using second-order difference plot of intrinsic mode functions. Comput. Methods Programs Biomed. **113**(2), 494–502 (2014)
11. Bhattacharyya, A., Singh, L., Pachori, R.B.: Identification of epileptic seizures from scalp EEG signals based on TQWT. In: Tanveer, M., Pachori, R.B. (eds.) Machine Intelligence and Signal Analysis, pp. 209–221. Springer Singapore, Singapore (2019)
12. Bhati, D., Pachori, R.B., Gadre, V.M.: Optimal design of three-band orthogonal wavelet filter bank with stopband energy for identification of epileptic seizure EEG signals. In: Tanveer, M., Pachori, R.B. (eds.) Machine Intelligence and Signal Analysis, pp. 197–207. Springer Singapore, Singapore (2019)
13. Li, Y., Wang, X.D., Luo, M.L., Li, K., Yang, X.F., Guo, Q.: Epileptic seizure classification of EEGs using time-frequency analysis based multiscale radial basis functions. IEEE J. Biomed. Health Inform. **22**(2), 386–397 (2018)
14. Sunil Kumar, T., Kanhangad, V., Pachori, R.B.: Classification of seizure and seizure-free EEG signals using local binary patterns. Biomed. Signal Process. Control **15**, 33–40 (2015)
15. Sharma, R., Pachori, R.B.: Classification of epileptic seizures in EEG signals based on phase space representation of intrinsic mode functions. Expert Syst. Appl. **42**(3), 1106–1117 (2015)
16. Rodriguez Aldana, Y., Hunyadi, B., Maranon Reyes, E.J., Rodriguez Rodriguez, V., Huffel, S.V.: Nonconvulsive epileptic seizure detection in scalp EEG using multiway data analysis. IEEE J. Biomed. Health Inform. **1–1**, (2018)
17. Li, Y., Cui, W., Luo, M., Li, K., Wang, L.: Epileptic seizure detection based on time-frequency images of EEG signals using Gaussian mixture model and gray level co-occurrence matrix features. Int. J. Neural Syst. **28**(07), 1850003 (2018). PMID: 29607682
18. Bhati, D., Sharma, M., Pachori, R.B., Gadre, V.M.: Time-frequency localized three-band biorthogonal wavelet filter bank using semidefinite relaxation and nonlinear least squares with epileptic seizure EEG signal classification. Digital Signal Process. **62**, 259–273 (2017)

19. Bhattacharyya, A., Pachori, R.B., Upadhyay, A., Acharya, U.R.: Tunable-Q wavelet transform based multiscale entropy measure for automated classification of epileptic EEG signals. Appl. Sci. **7**(4), (2017)
20. Sharma, M., Pachori, R.B., Acharya, U.R.: A new approach to characterize epileptic seizures using analytic time-frequency flexible wavelet transform and fractal dimension. Pattern Recogn. Lett. **94**, 172–179 (2017)
21. Tiwari, A.K., Pachori, R.B., Kanhangad, V., Panigrahi, B.K.: Automated diagnosis of epilepsy using key-point-based local binary pattern of EEG signals. IEEE J. Biomed. Health Inform. **21**(4), 888–896 (2017)
22. Sharma, M., Pachori, R.B.: A novel approach to detect epileptic seizures using a combination of tunable-Q wavelet transform and fractal dimension. J. Mech. Med. Biol. **17**(07), 1740003 (2017)
23. Solaija, M.S.J., Saleem, S., Khurshid, K., Hassan, S.A., Kamboh, A.M.: Dynamic mode decomposition based epileptic seizure detection from scalp EEG. IEEE Access **6**, 38683–38692 (2018)
24. Sharma, R.R., Pachori, R.B.: Time-frequency representation using IEVDHM-HT with application to classification of epileptic EEG signals. IET Sci. Meas. Technol. **12**(1), 72–82 (2018)
25. Gupta, V., Bhattacharyya, A., Pachori, R.B.: Classification of seizure and non-seizure EEG signals based on EMD-TQWT method. In: 2017 22nd International Conference on Digital Signal Process (DSP), pp. 1–5, Aug 2017
26. Bhattacharyya, A., Gupta, V., Pachori, R.B.: Automated identification of epileptic seizure EEG signals using empirical wavelet transform based Hilbert marginal spectrum. In: 2017 22nd International Conference on Digital Signal Process (DSP), pp. 1–5, Aug 2017
27. Shah, M., Saurav, S., Sharma, R., Pachori, R.B.: Analysis of epileptic seizure EEG signals using reconstructed phase space of intrinsic mode functions. In: 2014 9th International Conference on Industrial and Information Systems (ICIIS), pp. 1–6, Dec 2014
28. Paul, Y.: Various epileptic seizure detection techniques using biomedical signals: a review. Brain Inform. **5**(2), 6 (2018)
29. Schroeder, J.: Signal processing via Fourier-Bessel series expansion. Digital Signal Process. **3**, 112–124 (1993)
30. Pachori, R.B., Sircar, P.: EEG signal analysis using FB expansion and second-order linear TVAR process. Signal Process. **88**(2), 415–420 (2008)
31. Gilles, J.: Empirical wavelet transform. IEEE Trans. Signal Process. **61**(16), 3999–4010 (2013)
32. Bhattacharyya, A., Singh, L., Pachori, R.B.: Fourier-Bessel series expansion based empirical wavelet transform for analysis of non-stationary signals. Digital Signal Process. **78**, 185–196 (2018)
33. Pachori, R.B.: Discrimination between ictal and seizure-free EEG signals using empirical mode decomposition. Res. Lett. Signal Process. **2008**(1), 5 (2008)
34. Bhattacharyya, A., Pachori, R.B.: A multivariate approach for patient-specific EEG seizure detection using empirical wavelet transform. IEEE Trans. Biomed. Eng. **64**(9), 2003–2015 (2017)
35. Bhattacharyya, A., Sharma, M., Pachori, R.B., Sircar, P., Acharya, U.R.: A novel approach for automated detection of focal EEG signals using empirical wavelet transform. Neural Comput. Appl. **29**(8), 47–57 (2018)
36. Freund, R.J., Wilson, W.J.: Statistical Methods (1993)
37. Jain, P., Pachori, R.B.: Event-based method for instantaneous fundamental frequency estimation from voiced speech based on eigenvalue decomposition of the Hankel matrix. IEEE/ACM Trans. Audio Speech Lang. Process. **22**(10), 1467–1482 (2014)
38. Bansal, M., Sircar, P.: Low bit-rate speech coding based on multicomponent AFM signal model. Int. J, Speech Technol (2018)
39. Hood, A.S., Pachori, R.B., Reddy, V.K., Sircar, P.: Parametric representation of speech employing multi-component AFM signal model. Int. J. Speech Technol. **18**(3), 287–303 (2015)
40. Pachori, R.B., Sircar, P.: Analysis of multicomponent AM-FM signals using FB-DESA method. Digital Signal Process. **20**(1), 42–62 (2010)

41. Pachori, R.B., Sircar, P.: A new technique to reduce cross terms in the Wigner distribution. Digital Signal Process. **17**(2), 466–474 (2007)
42. Pachori, R.B., Sircar, P.: Non-stationary Signal Analysis: Methods Based on Fourier-Bessel Representation. LAP LAMBERT Academic Publishing, Germany (2010)
43. Gilles, J., Heal, K.: A parameterless scale-space approach to find meaningful modes in histograms-application to image and spectrum segmentation. Int. J. Wavelets Multiresolut. Inf. Process. **12**(06), 1450044 (2014)
44. Daubechies, I.: Ten lectures on wavelets. In: CBMS-NSF Regional Conference Series in Applied Mathematics, vol. 61. SIAM, Philadelphia, PA, USA (1991)
45. Huang, N.E., Shen, Z., Long, S.R., Wu, M.C., Shih, H.H., Zheng, Q., Yen, N-C., Tung, C.C., Liu, H.H.: The empirical mode decomposition and the Hilbert spectrum for nonlinear and non-stationary time series analysis. Proc. R. Soc. A Math. Phys. Eng. Sci. (The Royal Society) **454**, 903–995 (1998)
46. Pachori, R.B., Bajaj, V.: Analysis of normal and epileptic seizure EEG signals using empirical mode decomposition. Comput. Methods Programs Biomed. **104**(3), 373–381 (2011)
47. Bajaj, V., Pachori, R.B.: Separation of rhythms of EEG signals based on Hilbert-Huang transformation with application to seizure detection. In: Convergence and Hybrid Information Technology, pp. 493–500. Springer, Berlin, Heidelberg (2012)
48. Ahrabian, A., Looney, D., Stankovic, L., Mandic, D.P.: Synchrosqueezing-based time-frequency analysis of multivariate data. Signal Process. **106**, 331–341 (2015)
49. Guo, L., Rivero, D., Dorado, J., Rabuñal, J.R., Pazos, A.: Automatic epileptic seizure detection in EEGs based on line length feature and artificial neural networks. J. Neurosci. Methods **191**(1), 101–109 (2010)
50. Gupta, V., Priya, T., Yadav, A.K., Pachori, R.B., Acharya, U.R.: Automated detection of focal EEG signals using features extracted from flexible analytic wavelet transform. Pattern Recogn. Lett. **94**, 180–188 (2017)
51. Göksu, H.: EEG based epileptiform pattern recognition inside and outside the seizure states. Biomed. Signal Process. Control **43**, 204–215 (2018)
52. Sert, E., Avci, D.: A new edge detection approach via neutrosophy based on maximum norm entropy. Expert Syst. Appl. **115**, 499–511 (2019)
53. Breiman, L.: Random forests. Mach. Learn. **45**(1), 5–32 (2001)
54. Fraiwan, L., Lweesy, K., Khasawneh, N., Wenz, H., Dickhaus, H.: Automated sleep stage identification system based on time-frequency analysis of a single EEG channel and random forest classifier. Comput. Methods Programs Biomed. **108**(1), 10–19 (2012)
55. Hall, M., Frank, E., Holmes, G., Pfahringer, B., Reutemann, P., Witten, I.H.: The WEKA data mining software: an update. SIGKDD Explor. Newsl. **11**(1), 10–18 (2009)
56. Kohavi, R.: A study of cross-validation and bootstrap for accuracy estimation and model selection. In: Proceedings of the 14th International Joint Conference on Artificial Intelligence, IJCAI'95, vol. 2, pp. 1137–1143 (1995)
57. Azar, A.T., El-Said, S.A.: Performance analysis of support vector machines classifiers in breast cancer mammography recognition. Neural Comput. Appl. **24**(5), 1163–1177 (2014)
58. Andrzejak, R.G., Lehnertz, K., Mormann, F., Rieke, C., David, P., Elger, C.E.: Indications of nonlinear deterministic and finite-dimensional structures in time series of brain electrical activity: dependence on recording region and brain state. Phys. Rev. E **64**(6), 061907 (2001)
59. Bhattacharyya, A., Pachori, R.B., Acharya, U.R.: Tunable-Q wavelet transform based multivariate sub-band fuzzy entropy with application to focal EEG signal analysis. Entropy **19**(3), 99 (2017)
60. Khandoker, A.H., Lai, D.T.H., Begg, R.K., Palaniswami, M.: Wavelet-based feature extraction for support vector machines for screening balance impairments in the elderly. IEEE Trans. Neural Syst. Rehabil. Eng. **15**(4), 587–597 (2007)
61. Polat, K., Güneş, S.: Classification of epileptiform EEG using a hybrid system based on decision tree classifier and fast Fourier transform. Appl. Math. Comput. **187**(2), 1017–1026 (2007)
62. Lee, S.-H., Lim, J.S., Kim, J.-K., Yang, J., Lee, Y.: Classification of normal and epileptic seizure EEG signals using wavelet transform, phase-space reconstruction, and Euclidean distance. Comput. Methods Programs Biomed. **116**(1), 10–25 (2014)

63. Fu, K., Qu, J., Chai, Y., Dong, Y.: Classification of seizure based on the time-frequency image of EEG signals using HHT and SVM. Biomed. Signal Process. Control **13**, 15–22 (2014)
64. Yuan, Q., Zhou, W., Yuan, S., Li, X., Wang, J., Jia, G.: Epileptic EEG classification based on kernel sparse representation. Int. J. Neural Syst. **24**(04), 1450015 (2014)
65. Kaya, Y., Uyar, M., Tekin, R., Yıldırım, S.: 1D-local binary pattern based feature extraction for classification of epileptic EEG signals. Appl. Math. Comput. **243**, 209–219 (2014)
66. Fu, K., Qu, J., Chai, Y., Zou, T.: Hilbert marginal spectrum analysis for automatic seizure detection in EEG signals. Biomed. Signal Process. Control **18**, 179–185 (2015)
67. Sharmila, A., Geethanjali, P.: DWT based detection of epileptic seizure from EEG signals using Naive Bayes and k-NN classifiers. IEEE Access **4**, 7716–7727 (2016)
68. Mert, A., Akan, A.: Seizure onset detection based on frequency domain metric of empirical mode decomposition. Signal Image Video Process. (2018)
69. Gupta, A., Singh, P., Karlekar, M.: A novel signal modeling approach for classification of seizure and seizure-free EEG signals. IEEE Trans. Neural Syst. Rehabil. Eng. **26**(5), 925–935 (2018)
70. Sharma, R.R., Varshney, P., Pachori, R.B., Vishvakarma, S.K.: Automated system for epileptic EEG detection using iterative filtering. IEEE Sens. Lett. **2**(4), 1–4 (2018)
71. Yu, Z., Zhou, W., Zhang, F., Xu, F., Yuan, S., Leng, Y., Li, Y., Yuan, Q.: Automatic seizure detection based on kernel robust probabilistic collaborative representation. Med. Biol. Eng, Comput (2018)

DWT Based Time Domain Features on Detection of Epilepsy Seizures from EEG Signal

A. Sharmila and P. Geethanjali

Abstract In the study of detection of an epileptic seizure using Electroencephalogram (EEG), pattern recognition has been recognized as a valued tool. In this pattern recognition study, the first time the authors have attempted to use time domain (TD) features such as waveform length (WL), number of zero-crossings (ZC) and number of slope sign changes (SSC) derived directly from filtered EEG data and from discrete wavelet transform (DWT) of filtered EEG data for the detection of an epileptic seizure. Further, the authors attempted to study the performance of other time domain features such as mean absolute value (MAV), standard deviation (SD), average power (AVP), which had been attempted by other researchers. The performance of the TD features is studied using naïve Bayes (NB) and support vector machines (SVM) classifiers for the university of Bonn database with fourteen different combinations of set E with set A to D. The proposed scheme was also compared with other existing scheme in the literature. The implementation results showed that the proposed scheme could attain the highest accuracy of 100% for normal eyes open and epileptic data set with direct as well as DWT based TD features. For other data sets, the highest accuracy is obtained with DWT based TD features using SVM. However, no significant difference in the classification of 14 data sets with TD features filtered EEG data and from DWT of filtered EEG data.

Keywords Electroencephalogram (EEG) · Epileptic seizure · Waveform length (WL) · Number of zero-crossing (ZC) · Slope sign change (SSC) · Naïve bayes (NB) · Support vector machine (SVM)

A. Sharmila · P. Geethanjali (✉)
Vellore Institute on Technology, Vellore, India
e-mail: pgeethanjali@vit.ac.in

A. Sharmila
e-mail: asharmila@vit.ac.in

G. Naik (ed.), *Biomedical Signal Processing*, Series in BioEngineering,
https://doi.org/10.1007/978-981-13-9097-5_9

1 Introduction

A tool which is prevalent to study the electrical brain activity is an Electroencephalogram (EEG). Nearly, 1% of the world population grieves from epilepsy, and it is one of the most common neurological disorders [1]. Epilepsy is a condition characterized by transient recurrent seizures [2]. However, detection of epileptic seizures from the recording of the EEG over extensive periods of a few days is tiresome process. Over two decades, attempts have been made to develop an expert system for epileptic seizures detection. In these systems, different techniques have been taken with varying degrees of success. For an automated pattern recognition base seizure detection systems, features such as raw EEG amplitude [3], power spectrum [4], wavelet co-efficient [5], relative spike amplitude, rhythmicity [6], etc., have been utilized to characterize normal and epileptic activity. The extracted features are classified using various techniques such as discriminant analysis [7], nearest neighbor [8], learning vector quantization [7], neural networks [9, 10], etc., for automated seizure detection systems.

Orhan et al. [11] have worked on the kNN classifier and multilayer perceptron neural network model to classify healthy and seizure signals with an accuracy of 100%. Nicolaou and Georgiou [12] have used permutation entropy and SVM classifier to classify healthy and seizure signals, using 82.88%. Sezer et al. [13] have extracted statistical features from wavelet transform and used PCA for feature reduction and ANN classifier to classify between healthy and seizure signals with an accuracy of 100%. Acharya et al. [14] have worked on sample entropy, approximate entropy, phase entropy 1, phase entropy 2, and fuzzy sugeno classifier have classified three class classification to classify healthy patient signal from epileptic patient signal during seizure and non-seizure period with an accuracy of 98.10%. Song and Zhang [15] have worked on wavelet transform and permutation entropy, sample entropy, and Hurst exponent to classify healthy and seizure signals with an accuracy of 94.8%. Hosseini et al. [16] have used discrete wavelet transform and Hurst and Lyupunov exponent to classify healthy and seizure signals with an accuracy of 96.5%. Pachori and Patidar [17] have worked on Epileptic seizure classification in EEG signals using second-order difference plot of intrinsic mode functions with a 95% confidence ellipse area as a feature for discriminating ictal EEG signals from the seizure-free EEG signals using the artificial neural network (ANN) classifier. The maximum classification accuracy obtained using the proposed method is 100%. The average classification accuracy of the proposed method is 97.75%. Kumar et al. [18] have worked on fuzzy approximate entropy and used SVM classifier to classify seven two-class classifications with accuracy ranging from 95.85 to 100%. Chan [19] worked on DTCWT and kNN classifiers to obtain an accuracy of 100% to classify between seizure and healthy signal. Riaz et al. [20] have Empirical mode decomposition-based temporal spectral features and SVM classifier to classify healthy and seizure signals using 100% accuracy. Peker et al. [21] worked on DTCWT and CNN to obtain an accuracy of 98.28% for three class classification. Swami et al. [22] worked on DTCWT and GRNN and obtained 100% accuracy to classify between healthy and

seizure signal. Tiwari et al. [23] have worked on Automated Diagnosis of Epilepsy using Keypoint Based Local Binary Pattern of EEG Signals they achieved to classify between normal and seizure; epileptic seizure and seizure-free; epileptic and non-seizure; normal, epileptic seizure, and seizure classes of EEG signals on two datasets with accuracy ranging from 98.80 to 100%. Sharmila and Geethanjali [24] have worked on DWT Based Detection of Epileptic Seizure from EEG Signals Using Naive Bayes and k-NN Classifiers and were able to obtain accuracy for 14 different classifications with accuracy ranging from 95.1 to 100% using features like Mean absolute value, Standard deviation, and Average power. Also, Sharmila and Geethanjali [25] have worked on Detection of Epileptic Seizure from Electroencephalogram Signals Based on Feature Ranking and Best Feature Subset Using Mutual Information Estimation, they were able to obtain accuracy for 14 different classifications with the help of two features i.e. MAV and standard deviation on sub-bands D3, D4 and D5 with accuracy ranging from 95.08 to 100%. Madan et al. [26] have worked on Discrete Wavelet Transform based Hurst exponent for epilepsy detection and obtained accuracy for 15 classifications resulting from 89.33 to 99% using SVM and KNN classifiers. Sharmila et al. [27] have worked on Epileptic seizure detection using DWT-based approximate entropy, Shannon entropy and support vector machine and have obtained accuracy for 15 different classifications resulting in from 78 to 100%. Chen et al. [28] have worked on A high-performance seizure detection algorithm based on Discrete Wavelet Transform (DWT) and EEG using seven different statistical features. Sharmila and Mahalakshmi [29] have worked on Wavelet-based feature extraction for the classification of epileptic seizure EEG signal, using PCA with Naïve Bayes classifier gave 98.6% accuracy and LDA with Naïve Bayes classifier attained the improved result of 99.8% accuracy. Also, they achieved 98.5 and 100% accuracy by using PCA, LDA with K-NN. Wang et al. [30] have worked on Automatic Epileptic Seizure Detection in EEG Signals Using Multi-Domain Feature Extraction and Nonlinear Analysis. They were able to achieve accuracy of 99.25% using classifiers like KNN, LDA, and Naïve-Bayes. Reddy and Rao [31] have worked on automated identification system for seizure EEG signals using tunable-Q wavelet transform, they were able to classify two categories where the First category is seizure free and seizure (NF-S) classes, and the other one is the normal, seizure free and seizure (ZO-NF-S) classes in which they were able to achieve accuracy of 98.3% and 98.2% respectively. Sharma et al. [32] worked on ATFWT based features and SVM classifier to classify healthy signals and epileptic patient signal during non-seizure period with an accuracy of 92.5%. Further, Ullah et al. [33] have worked on an automated system for epilepsy detection using EEG brain signals based on deep learning approach.

All the pattern recognition methods focused on improving classification accuracy with a varying combination of feature extraction and classification technique in the detection of an epileptic seizure. Therefore, the pattern recognition classification accuracy depends on the type of features, a number of features, and the classifiers [34]. The objective of this study is to identify an efficient pattern recognition method for reliable seizure detection.

The TD features such as waveform length, number of zero crossings, slope sign change are being used for identification of activity in Electromyogram (EMG) signals [35–37]. Recently, these features are used to extract the temporal characteristics hidden in the EMG data [34]. The use of WL, ZC, and SSC in addition to MAV, SD, and AVP features are the main emphasis of this work.

In this proposed scheme, an attempt has been made to obtain good classification accuracy with the individual and combined time domain features extracted directly from filtered EEG data and the discrete wavelet transform for fourteen different combinations of data sets using NB and SVM classifier. The study presented here examines the publicly available five EEG datasets A to E provided by the Department of Epileptology at the University of Bonn, Germany [38]. The performance of WL, SSC, ZC with MAV is studied. Also, the performance of SD, AVP with MAV is studied in the detection of epileptic seizures from EEG signals. Discrete wavelet transform (DWT) has been applied to decompose the signals into sub-bands with various frequencies. The TD features such as WL, ZC, SSC, SD, AVP, and MAV were derived from filtered and from DWT for the sub-bands D3–D5 and A5. The directly derived features and TD features DWT are studied using NB and SVM classifiers to identify the epileptic seizure. It has been found that the NB and SVM perform better with directly derived TD features and from DWT for the normal eyes open and epilepsy data set and gives an accuracy of 100% by considering the features in a different manner.

2 Problem Formulation

In our proposed study, as shown in Fig. 1, the raw EEG data is pre-processed using Butterworth 4th order band-pass filter. The features such as WL, ZC, SSC, MAV, SD, and AVP are extracted directly from the filtered EEG data as well as from DWT of EEG. The equal number of training and testing data sets is chosen to evaluate the performance of the TD features individually and in a combined manner for the fourteen different combinations such as A-E, B-E, C-E, D-E, AB-E, AC-E, AD-E, BC-E, BD-E, CD-E, ABC-E, ACD-E, BCD-E, and ABCD-E.

Fig. 1 Block diagram of the proposed scheme

2.1 Feature Extraction

In Linear methods, the statistical measures of variability which are easy to compute and provide valuable predictive information about patients [39]. Well-known problems of using nonlinear methods for 2-class problems are the non-nutritive nature of such measures, a large amount of data required for reliable parameter estimation including issues of stationarity within these periods, and the high computational requirement. These drawbacks inhibit applications with short latency with regard to recording time and may cause difficulties in real-time applications [40, 41]. So, in our study, we have attempted to work with 2-class problems with short segments of data using the linear method.

Linear methods have been broadly used in epilepsy detection mostly due to their ease and adaptability. Liu et al. [42] used Scored Autocorrelation Moment (SAM) analysis, and distinguished EEG epochs containing seizures even though signals did not exist changes in their spectral properties. The concept of seizure prediction was originally stated in 1975 [43] for the EEG data collected from two electrodes based on spectral analysis. In 1981, Rogowski et al. [44] pole trajectories of an autoregressive model were used to study the preictal periods. Gotman et al. [45] examined rates of interictal spiking as indicators of forthcoming seizures. In order to detect the preictal state, Mormann et al. [46] studied the statistical moment of the EEG amplitudes. The other linear features like power are used in [47], and signal variance is used in [48] to predict seizure onset. Mormann et al. used Hjorth parameters, among others as features for seizure prediction [49]. In various studies of seizure prediction [50, 51], accumulated energy has been used.

Also, seizure onset and offset determination mighty be successful in using linear prediction filters (LPF) [52]. Discrete wavelet transform (DWT) is a transformation extracting scale-frequency components from data that might also be useful in seizure detection. In [53], normal and seizure signals were classified using DWT and a linear classifier. Other linear features, the relative fluctuation index [54], can be used to measure the intensity of the fluctuation of EEG signals. For the period of a seizure, there exists higher fluctuation in the EEG signals than an ictal-free period. Hence, the values of the fluctuation index for the period of a seizure are generally higher than other EEG. In [55], the epileptic seizure from EEG signals is detected using linear least-squares pre-processing.

In this work, the TD features such as WL, ZC, SSC, MAV, SD, and AVP are derived directly and from D3–D5 and A5 coefficients of DWT.

2.2 Classification

The extracted TD features directly and derived from DWT are applied to the classifiers. The purpose of the classifier is to identify epilepsy abnormality in EEG data. In this work, the classifiers used are NB and SVM, to classify epileptic seizure EEG data

for individual and combined TD features for the different combinations of datasets A to D with E. The NB and SVM classifiers can be assessed using the accuracy of the classifier.

3 Results and Discussions

Figures 2 and 3 shows the estimated WL for the entire 23.6 s EEG segments directly and obtained from DWT coefficients D3–D5 and A5 for the data sets A, B, C, D and E. The WL of D3–D5 and A5 coefficients of data set C and D are very lesser than data set A and B. Whereas the WL of D3–D5 and A5 coefficients of data set E is extremely higher than other data sets. It is clear from the graph that WL of an epileptic seizure is higher than other data sets. Figures 4 and 5 show the number of zero crossings (ZC) for the five different data sets, which are derived directly and from DWT coefficients, D3–D5 and A5, and Figs. 6 and 7 show the number of slope sign changes for each EEG segments. Of these newly considered TD features, WL performs better than ZC and SSC, and it showed a wide difference in detecting an epileptic seizure.

In this study, fourteen different classification combinations, such as A-E, B-E, C-E, D-E, AB-E, AC-E, AD-E, BC-E, CD-E, ABC-E, ACD-E, BCD-E and ABCD-E was used in order to identify the epileptic signal from the EEG signal. Of these combinations, the first time we attempted to use the TD features such as WL, ZC, and SSC for dataset combinations AC-E, AD-E, BC-E, BD-E, ABC-E in our study. Tables 1, 2, 3 and 4 presents the performance of the directly derived and DWT based individual and combined TD features for the data sets A to D with E using NB and

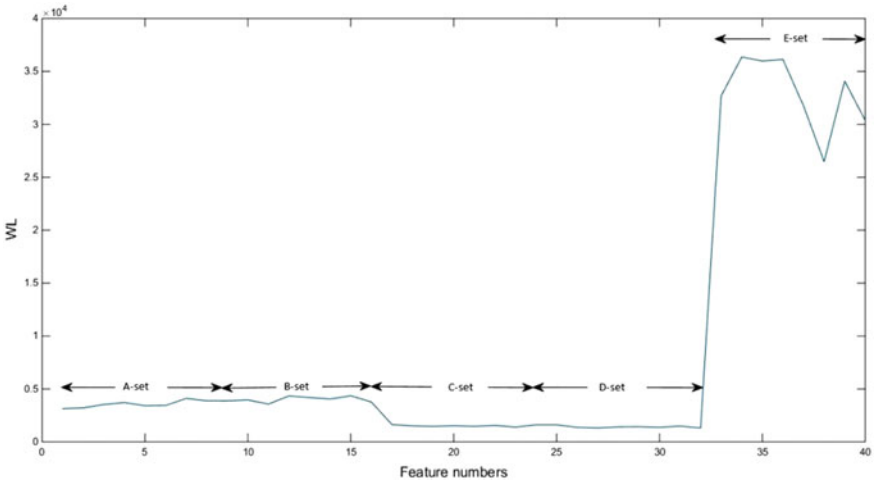

Fig. 2 WL for data set A to E

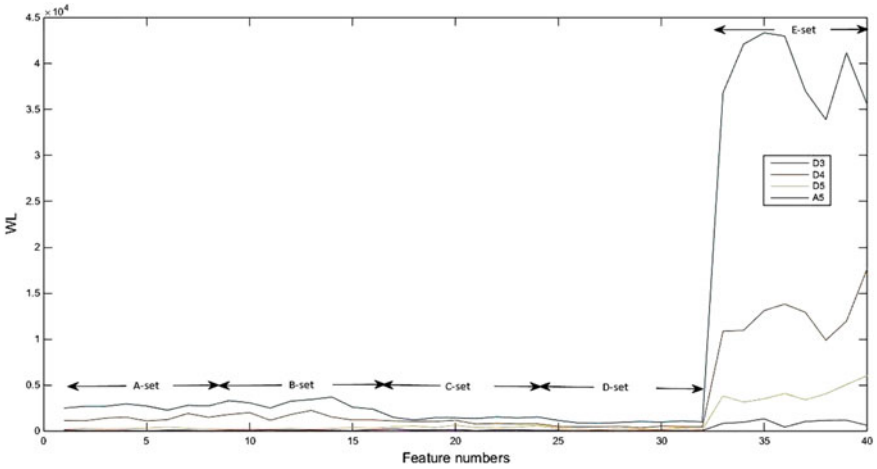

Fig. 3 WL for data set A to E from DWT

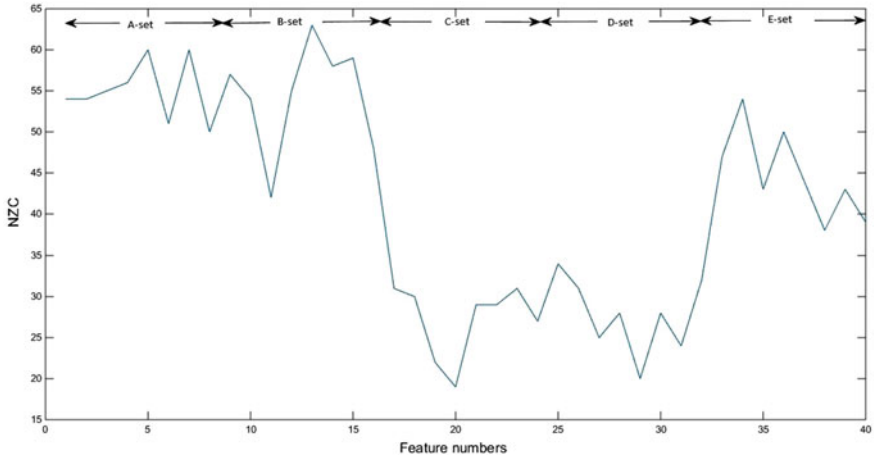

Fig. 4 ZC for data set A to E

SVM classifier. The performance of newly considered TD features and other TD features such as SD and AVP was studied along with MAV.

The average classification accuracy of an individual WL feature is higher than other features ZC and SSC. For the data set D-E, WL derived directly gives the highest accuracy of 97.5% using NB and 97.12% using SVM. The performance of ZC for the B-E data set is higher i.e., 90.37% using NB and 90.12% using SVM classifier. WL extracted after DWT gives an accuracy of 99.87 and 99.37% using NB and SVM for the A-E data set. Further, the performance of SSC is higher for the data set A-E and provides the highest classification accuracy of 94.12% using NB and SVM for direct TD feature extraction and with DWT based feature extraction

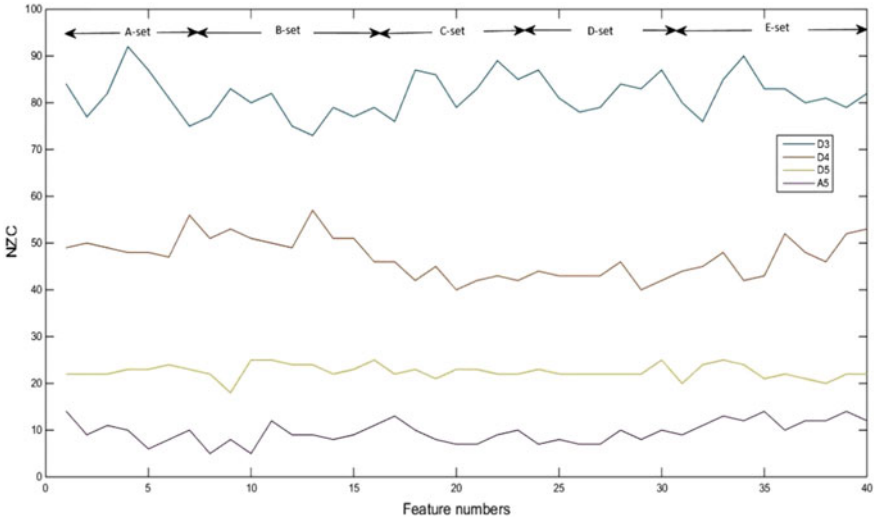

Fig. 5 ZC for data set A to E from DWT

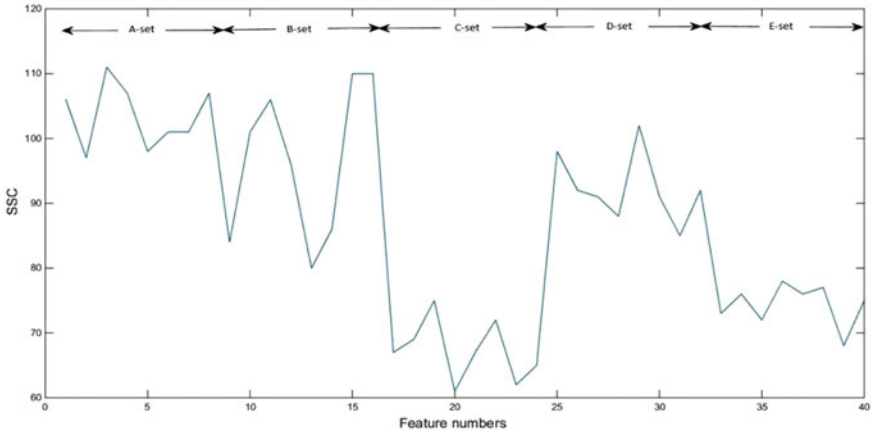

Fig. 6 SSC for data set A to E

it gives an accuracy of 97.15% using NB and 96.5% using SVM. The three TD features if combined with MAV and along with themselves, gives better accuracy than individual features. If WL is directly derived and combined with MAV, ZC, SSC, MAV + ZC, MAV + SSC, and MAV + ZC + SSC, the accuracy for the data set combination A-E is increased to 99, 96.12, 99.12, 99.62, 100, 99.5 and 100% using NB and 99.75, 99.5, 99.37, 100, 99.62, 99.75 and 100% using SVM as shown in Tables 1 and 2. The feature WL extracted after DWT for the coefficients D3–D5 and A5, combined with MAV, ZC, MAV + ZC, MAV + ZC + SSC features gives 100% for data set A-E and WL combined with SSC, ZC + SSC provides an accuracy

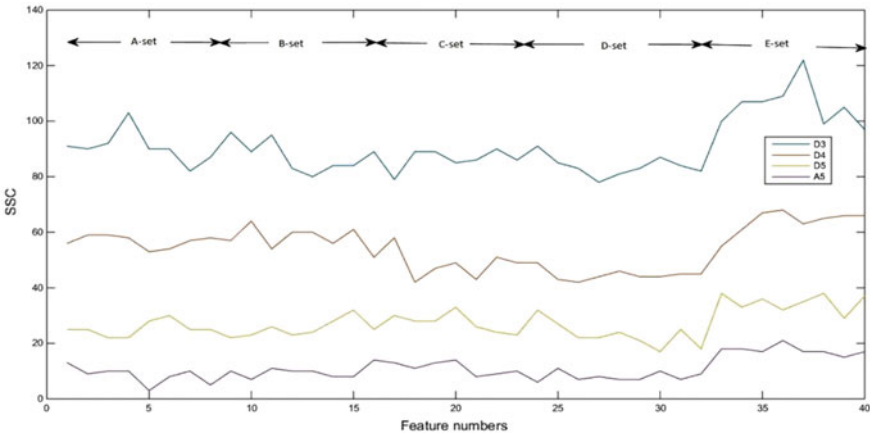

Fig. 7 SSC for data set A to E from DWT

of 99.87% using NB and with SVM, WL combined with MAV + SSC and MAV + ZC gives 100% for the data set A-E. Further, in DWT based TD feature extraction, other features such as ZC, and SSC combined with MAV gives 100% for the data set A-E using both NB and SVM as shown in Tables 3 and 4. Also in direct feature extraction, ZC and SSC, in combination with MAV give 100% accuracy for A-E with SVM classifier, whereas, with NB, SSC in combination with MAV gives 100% for the same data set.

In direct TD feature extraction, the performance of WL in combination with MAV + ZC + SSC is better for all data sets and gives the highest average classification accuracy of 96.08% using NB and the performance of WL in combination with ZC + SSC gives 97.54% using SVM. The performance of MAV + WL + ZC and MAV + ZC + SSC combination gives an average accuracy of 95.93 and 95.72% using NB as mentioned in Table 1. Also, the TD features MAV + WL + ZC, and WL + ZC + SSC combination gives an average accuracy of 97.2 and 97.54% with SVM classifier, and it is shown in Table 2.

In DWT based TD feature extraction, the performance of MAV + ZC + SSC is better and gives the highest average classification accuracy of 97.86% using NB. The other feature combinations such as WL + ZC + SSC and MAV + WL + ZC + SSC are also well performed for all data sets combinations, and give an average accuracy of 97.69% and it is shown in Table 3. From Table 4, it is evident that the performance of WL + ZC + SSC is better for all data sets and provides an average accuracy of 98.28% with SVM. The other features such as MAV + WL + ZC and MAV + WL + ZC + SSC also performed well and give average accuracy of 98.25 and 98.27%.

It is evident from Tables 1, 2, 3 and 4, an individual feature WL performed better and it gives the highest average accuracy, whereas, individual performance of SSC is better for the data set A-E both in direct and DWT based TD feature extraction. Further, the classification accuracy for each data set is increased if either of these

Table 1 Performance of directly derived TD features (WL, ZC and SSC) using NB classifier

Classification accuracy (%) for the datasets A to D with E														
Data sets	WL	ZC	SSC	MAV + WL	MAV + ZC	MAV + SSC	WL + ZC	WL + SSC	ZC + SSC	MAV + WL + ZC	MAV + WL + SSC	MAV + ZC + SSC	WL + ZC + SSC	MAV + WL + ZC + SSC
A-E	88	76	94.12	99	99.62	100	96.12	99.12	89.25	99.62	100	99.75	99.5	100
B-E	84.5	90.37	81.25	91.37	98.12	94.87	96.75	86.62	91	96.62	92.37	97.75	97.25	96.62
C-E	94.37	64	65.62	98.37	97.62	98.25	90.12	97.5	76.12	97.62	98.37	98.87	95.5	96.5
D-E	97.5	65.75	52.12	95.62	87.12	85	97	97.37	70.12	95.5	95.75	87.5	97.75	94.25
AB-E	89.75	88.33	87.41	95.5	98.25	97.33	94.17	91.41	92.67	97	96.25	98.17	97.08	97.75
AC-E	92.91	66.67	77.08	99.08	98.33	98.67	93.33	95.17	74.5	99.25	99.17	98.58	95.67	99.33
AD-E	92.91	66.67	67.58	92.83	91.47	92.75	93.25	94.67	68.08	93.08	93.58	93.17	94.83	93.91
BC-E	90	66.67	72.75	95	97.17	96.58	90.67	90.58	74.83	95.5	95.5	97	91.58	95.75
BD-E	89.41	66.67	67.08	90.5	90	90.25	90.75	90.17	68.67	90.67	90.58	90.58	90.91	90.75
CD-E	90	66.67	72.75	95	97.17	94.56	94.68	95.37	77.43	94.41	94.91	96.33	95.87	95.31
ABC-E	92.5	75	80	96.81	97.81	97.87	93.12	93.12	81	97.25	97.12	98	93.81	97.5
ACD-E	94.56	75	75	94.93	93.75	94.56	94.68	95.37	77.43	95.06	95.37	94.62	95.87	95.31
BCD-E	92.18	75	75	92.75	93.18	93.31	92.93	92.93	76.62	95.31	93.06	93.37	93.06	95.68
ABCD-E	94.15	80	80.4	94.55	94.65	94.85	94.2	93.85	81.1	96.15	94.45	96.45	95.45	96.55
Avg. accuracy	91.62	73.05	74.86	95.09	95.3	94.91	93.69	93.8	78.48	95.93	95.46	95.72	95.29	96.08

Table 2 Performance of directly derived TD features (WL, ZC and SSC) using SVM classifier

Classification accuracy (%) for the datasets A to D with E														
Data sets	WL	ZC	SSC	MAV + WL	MAV + ZC	MAV + SSC	WL + ZC	WL + SSC	ZC + SSC	MAV + WL + ZC	MAV + WL + SSC	MAV + ZC + SSC	WL + ZC + SSC	MAV + WL + ZC +SSC
A-E	88	76.87	94.12	99.75	100	100	99.5	99.37	92.87	100	99.62	100	99.75	100
B-E	84.12	90.12	81.25	94.87	97.87	93.25	98.12	89.12	91	98.37	93.62	96.75	97.5	98.75
C-E	93.25	66.37	64.87	98.5	98.25	97.87	96.62	99.25	78.87	98.37	98.5	98.75	99.25	97.87
D-E	97.12	68.37	51.12	96	93.12	90.25	97.12	96.5	75.12	96.12	96.62	92.87	96.5	97
AB-E	88.67	87.5	89.58	97.25	98.67	96.83	98.67	94.5	93.08	98.83	96.58	98.08	98.58	98.58
AC-E	94.25	56.5	76.08	99	98.58	98.58	97.41	99.5	77.17	98.67	99.33	98.91	99.58	99.41
AD-E	94.75	55.5	70	96.5	96.25	95.25	96.16	97.75	71.5	96.41	97.41	96.58	97.67	97.41
BC-E	86.58	61.67	74.67	96.67	96.67	96.58	96.67	94.08	74.75	96.75	96.25	96.58	96.91	96.91
BD-E	85.67	60.17	66	93.33	93.33	93.25	94.67	92.91	66.67	94.75	93.33	93.41	94.75	94.5
CD-E	94.5	53.75	97.33	88.67	97	96	96	98.18	96.83	95.91	97.08	96.33	98	97.81
ABC-E	89.43	68.31	78.56	97.62	97.37	97.43	97.43	96.37	79.43	97.43	97.25	97.37	97.81	97.62
ACD-E	94.5	53.75	64.62	97.18	97	96	96	98.18	72.75	97.06	97.75	97.25	98	97.81
BCD-E	88.25	47.43	65.81	95.5	95.43	95.18	95.12	95.37	95.25	95.75	95.18	95.18	96.12	94.37
ABCD-E	91	55.45	71.25	96.45	96.05	95.7	95.7	94.6	95.75	96.4	95.7	98.3	95.2	95.25
Avg. accuracy	90.72	64.41	74.66	96.23	96.82	95.86	96.79	96.12	82.93	97.2	96.73	96.88	97.54	97.37

Table 3 Performance of DWT based TD features (WL, ZC, and SSC) using NB classifier

Classification accuracy (%) for the datasets A to D with E														
Data sets	WL	ZC	SSC	MAV + WL	MAV + ZC	MAV + SSC	WL + ZC	WL + SSC	ZC + SSC	MAV + WL + ZC	MAV + WL + SSC	MAV + ZC + SSC	WL + ZC + SSC	MAV + WL + ZC + SSC
A-E	99.87	83.12	97.15	100	100	100	100	99.87	96.62	100	100	100	99.87	100
B-E	97.87	86.25	94.25	97.37	99.12	98.25	99	98.25	96.12	98.37	98.12	99.12	98.62	98.75
C-E	98	78.12	91.87	97.87	97.62	98.12	97.75	98	92.62	97.87	97.75	98	98	97.87
D-E	95.37	73.37	89.62	95.37	95.25	95.87	95	95.12	89.37	95.37	95.87	96	95	95.75
AB-E	98	73.5	88.08	99.83	94.25	98.33	94.66	98.41	96.83	97.66	97.66	97.83	98.25	97.75
AC-E	98.58	80.16	95	98.66	98.58	98.83	98.67	98.75	95.08	98.41	98.83	98.83	98.75	98.75
AD-E	97.41	66.67	92.33	97.33	97.67	97.33	98.08	97.58	94.83	98	97.41	97.83	98.25	98.25
BC-E	98.33	80.58	94.67	98.5	98.58	98.33	98.67	98.25	96.5	98.67	98.41	98.5	98.5	98.5
BD-E	96.58	79	92.25	97	98.58	95.83	97	96.33	94.41	97.41	96.58	97.33	96.91	97.08
CD-E	96.33	79.5	91	96.58	96.75	96.58	96.5	96.5	92.33	96.58	96.58	97	96.58	96.67
ABC-E	97.12	84.12	95.62	96.62	97.37	97.56	97.37	97.37	96	97.06	97.31	97.68	97.5	97.37
ACD-E	97.5	82.93	93.87	97.5	97.62	97.43	97.68	97.43	94.43	97.56	97.5	97.56	97.5	97.56
BCD-E	96.68	75.62	92.87	97.31	97.12	96.12	97.12	96.68	95.37	97.37	97.06	97.43	97.43	97.25
ABCD-E	95.75	85.75	94.55	95.95	96.9	96.8	96.2	96.2	95.4	96.2	96.45	97	96.5	96.2
Avg. accuracy	97.38	79.19	93.08	97.56	97.52	97.52	97.4	97.48	94.7	97.6	97.53	97.86	97.69	97.69

Table 4 Performance of DWT based TD features (WL, ZC, and SSC) using SVM classifier

Classification accuracy (%) for the datasets A to D with E														
Data sets	WL	ZC	SSC	MAV + WL	MAV + ZC	MAV + SSC	WL + ZC	WL + SSC	ZC + SSC	MAV + WL + ZC	MAV + WL + SSC	MAV + ZC + SSC	WL + ZC + SSC	MAV + WL + ZC + SSC
A-E	99.37	83.12	96.5	99.75	100	100	99.75	99.5	98.5	100	100	99.87	99.75	99.87
B-E	98.87	68	95.37	99.5	99.87	99.75	99.62	98.75	98.12	99.87	99.62	99.87	99.62	99.75
C-E	97.75	56.25	92.87	97.75	97.87	97.62	97.62	97.37	95	97.75	97.62	97.37	97.62	97.62
D-E	95.85	74.37	88.25	95.87	96	95.75	97	96.25	91.75	96.25	96	95.87	96.87	96.87
AB-E	99.33	66.67	96.75	99.91	98.41	99.58	97.58	99.08	95.16	99.91	99.75	99.91	99.83	99.83
AC-E	98.58	80.16	95	98.67	98.58	98.83	98.67	98.75	95.08	98.41	98.83	98.83	98.75	98.75
AD-E	97.41	66.67	92.33	97.33	97.67	97.33	98.08	97.58	94.83	98	97.41	97.83	98.25	98.25
BC-E	98.33	80.58	94.67	98.5	98.58	98.33	98.67	98.25	96.5	98.67	98.41	98.5	98.5	98.5
BD-E	96.58	79	92.25	97	98.58	95.83	97	96.33	94.41	97.41	96.58	97.33	96.91	97.08
CD-E	96.58	76.16	91.08	96.75	97.16	96.83	97.17	96.75	95	97.41	96.5	97.33	97.58	97.41
ABC-E	98.75	82.75	95.81	99	98.87	98.68	99	98.5	97.37	99	98.87	98.81	98.87	98.93
ACD-E	97.5	79.31	92.37	97.5	97.75	97.62	98	97.62	95.68	98.06	97.56	98.06	98.18	98.06
BCD-E	96.68	75.62	92.87	97.31	97.12	96.12	97.12	96.68	95.37	97.37	97.06	97.43	97.43	97.25
ABCD-E	97.05	73.9	90.9	97.75	97.8	97.8	97.1	97.6	92.75	97.5	97.9	97.35	97.8	97.7
Avg. accuracy	97.75	74.46	93.35	98.04	98.16	97.86	98.02	97.78	95.39	98.25	98	98.16	98.28	98.27

Table 5 Performance of directly derived TD features (MAV, SD and AVP) using NB classifier

Classification accuracy (%) for the datasets A to D with E							
Data sets	MAV	SD	AVP	MAV + SD	MAV + AVP	SD + AVP	MAV + SD + AVP
A-E	100	100	99.87	100	100	100	100
B-E	94.5	95.25	95.5	94.5	95.12	95.62	95.37
C-E	97.5	98	98.12	97.75	98.25	98.12	98.12
D-E	90.75	90.62	85.75	90.87	88.25	87.87	88.87
AB-E	97	97.91	97.97	95.41	96	95.83	95.75
AC-E	98.83	99	98.91	98.91	98.91	98.91	98.91
AD-E	93.83	93.58	91.83	93.75	93.75	95.41	93.66
BC-E	96	96.33	96.25	96.16	96	96.25	96.08
BD-E	93.91	93.66	91.75	93.91	93.16	93.25	93.91
CD-E	93.91	93.5	91.75	93.58	93.25	93.33	93.75
ABC-E	96.62	97.12	96.75	96.56	96.56	96.5	96.43
ACD-E	95.31	95.12	94.25	95.56	95.31	95.18	95.25
BCD-E	95.37	95.25	94.18	95.25	95.5	95.25	95.37
ABCD-E	96.25	96.1	95.6	96.4	96.35	96.2	96.1
Avg. accuracy	95.69	95.81	94.89	95.61	95.45	95.55	95.54

features or both of these features are combined with other features such as MAV and ZC. Comparing the results obtained from Tables 1 and 2, the performance of WL + ZC + SSC feature combination gives the highest average accuracy of 97.54% using SVM. Similarly, comparing the results of Tables 3 and 4, the performance of WL + ZC + SSC feature combination gives the highest average accuracy of 98.28% using SVM. In both direct and DWT based feature extraction, the WL + ZC + SSC feature combination with SVM classifier. Comparing the direct TD and DWT based TD feature extraction results as presented in Tables 1, 2, 3, and 4, the performance of DWT based WL + ZC + SSC feature extraction with SVM gives better result than direct TD feature extraction.

The performance of directly derived and DWT based TD features such as SD and AVP along with MAV was studied in an individual, and combined manner using NB and SVM classifier and results obtained presented in Tables 5, 6, 7 and 8. The performance of the individual SD feature derived directly is better, and it provides an average accuracy of 95.81% using NB and 94.88% with SVM classifier as presented in Tables 5 and 6. For the data set A-E, NB, and SVM provide 100% for individual features such as MAV and SD, and it also gives 100% with other feature combinations such as MAV + SD, MAV + AVP, SD + AVP and MAV + SD + AVP. The performance of combined TD features MAV + SD + AVP gives an increased average accuracy of 95.88% with SVM as shown in Table 6.

Table 6 Performance of directly derived TD features (MAV, SD and AVP) using SVM classifier

Classification accuracy (%) for the datasets A to D with E							
Data sets	MAV	SD	AVP	MAV + SD	MAV + AVP	SD + AVP	MAV + SD + AVP
A-E	100	100	97.87	100	100	100	100
B-E	94.5	95.5	95	94.62	94.5	95.62	94.62
C-E	97.5	97.62	95	98.25	97.62	97.87	98.25
D-E	83.12	89.37	90.75	92.62	93.75	92.12	92.75
AB-E	97.33	97.83	96.83	95.66	95.5	96	95.83
AC-E	98.91	98.91	97.83	98.91	98.91	98.83	98.91
AD-E	90.41	95.58	90.91	95.75	95.91	93.75	95.75
BC-E	95.08	95.75	96.66	95.5	95.33	96.16	95.5
BD-E	86.91	88	94.25	93.58	93.33	93.58	93.66
CD-E	86.91	90.5	93.25	94.58	95.08	94.33	94.91
ABC-E	96	96.37	97.25	96.31	96.12	96.37	96.25
ACD-E	93.56	92.62	90.93	96.12	96.25	96.12	96.31
BCD-E	93.25	95.31	93.18	94.68	94.37	94.56	94.5
ABCD-E	92.1	95.05	92.7	95.25	95.05	95.2	95.15
Avg. accuracy	93.25	94.88	94.45	95.84	95.83	95.75	95.88

The performance of MAV is better than other features with DWT based TD feature extraction, and it gives an average accuracy of 97.43% with NB and 97.53% with SVM classifier. For the data set A-E, all individual and combined features give 100% accuracy with NB as presented in Table 7. The performance of MAV and MAV + AVP provides 100% for A-E data set using SVM classifier, and the performance of MAV + AVP affords an increased average accuracy of 98.11% with SVM as stated in Table 8. Comparing the results obtained in Tables 5 and 6, the performance of MAV + SD + AVP feature combination is better with SVM, and it gives an average accuracy of 95.88% and the performance of the SD feature is better with NB and affords an accuracy of 95.81%. In the DWT based TD feature extraction, the feature MAV performs well, and it gives an average accuracy of 97.43% using NB. Further, the performance of MAV + AVP feature combination is better with SVM and provides an average accuracy of 98.11%. Comparing the results in Tables 5 and 6, the MAV + SD + AVP feature combination with SVM is performed well, and similarly, comparing the results in Tables 7 and 8, the MAV + AVP feature combination with SVM is best performed. Comparing the direct TD and DWT based TD feature extraction results as presented in Tables 5, 6, 7, and 8, the performance of DWT based MAV + AVP TD feature extraction with SVM gives better results than direct TD feature extraction.

Comparing the results obtained from Tables 1 to 4 with Tables 5 to 8, in general, the performance of DWT based WL + ZC + SSC feature combination with SVM

Table 7 Performance of DWT based TD features (MAV, SD, and AVP) using NB classifier

Classification accuracy (%) for the datasets A to D with E							
Data sets	MAV	SD	AVP	MAV + SD	MAV + AVP	SD + AVP	MAV + SD + AVP
A-E	100	100	100	100	100	100	100
B-E	97.62	97.62	97.75	97.62	97.62	97.62	97.62
C-E	97.87	98	97.87	97.87	98	98	98
D-E	95.37	93.62	90.37	94.75	92.5	91.25	92.75
AB-E	99.66	97.33	97.58	97	97.41	97.33	97.25
AC-E	98.66	98.58	98.58	98.58	98.66	98.75	96.83
AD-E	97.33	96.83	94.41	97.25	96.33	96.16	96.83
BC-E	96.83	96.66	96.41	96.75	96.66	96.41	96.33
BD-E	97.82	94.16	92.33	94.66	93	93.16	93.41
CD-E	96.66	96.41	94.41	96.66	96	95.83	96.58
ABC-E	97	97	96.81	96.62	96.81	96.68	96.62
ACD-E	97.62	97.25	96.62	97.62	97.43	97.37	97.5
BCD-E	95.5	95.37	94.25	95.18	95.06	94.93	95.06
ABCD-E	96.2	95.9	95.35	95.85	95.85	95.65	95.75
Avg. accuracy	97.43	96.76	95.91	96.88	96.52	96.36	96.46

classifier affords highest average accuracy of 98.27%, and its classification accuracy ranges from 97.43 to 99.75% for the fourteen different combinations of data sets A to D with E. So, it is the most appropriate pattern recognition approach to detect the epileptic seizure.

In this work the TD features already attempted by other researchers [5, 16] such as SD and AVP along with MAV are also studied and compared with WL, ZC, and SSC along with MAV, both in direct and DWT based feature extraction. It has been found that the newly attempted features are best performed for fourteen different combinations such as A to D with E. The accuracy of classification with individual TD features is less with SVM. However, the performance of classification increases when used in combination with other TD features. Though the feature ZC does not contribute good accuracy individually and improves accuracy when used in combination with other features MAV, WL, and SSC. Further, the features SD and AVP show good accuracy individually. However, the performance of features in combination with other features does not improve significantly as compared to the combination of ZC and WL.

Similarly the performance of TD features is studied with D3–D5 and A5 co-efficients. It has been found that SVM classifier performs well with individual as well as with a combination of features. It has been found that WL + ZC + SSC performs well in direct extraction as well as extraction from DWT co-efficient. The performance of WL + ZC + SSC is the best presented for the data sets C-E, D-E,

Table 8 Performance of DWT based TD features (MAV, SD, and AVP) using SVM classifier

Classification accuracy (%) for the datasets A to D with E							
Data sets	MAV	SD	AVP	MAV + SD	MAV + AVP	SD + AVP	MAV + SD + AVP
A-E	100	99.75	99.37	99.75	100	99.75	99.75
B-E	99.12	99.25	98.75	99.12	99.12	99.25	99.12
C-E	97.75	97.75	96.62	97.75	97.75	97.75	97.75
D-E	95.75	94.87	91.75	96	96.5	96.25	96.75
AB-E	99.66	99.41	99.08	99.58	99.41	99.5	99.58
AC-E	98.5	98.5	98.5	98.5	98.75	98.5	98.08
AD-E	97.5	97.58	96.41	97.75	98.16	98	98.08
BC-E	98.16	97.75	97.5	98.16	98.41	97.91	98.16
BD-E	95.58	95	95	95.83	96.75	94.58	95.83
CD-E	97	97.08	95.66	97	97.41	97.25	97.33
ABC-E	98.12	98.12	97.68	98	98.93	98.12	98.06
ACD-E	97.62	97.5	97.56	97.81	98	97.93	98.06
BCD-E	95.06	94.5	95.18	95.06	96.87	94.62	96.06
ABCD-E	95.6	94.9	95.1	95.3	97.5	94.75	95.4
Avg. accuracy	97.53	97.28	96.72	97.54	98.11	97.44	97.71

ACD-E, BCD-E, AC-E, and AD-E. The other data sets also performed well when WL is in combination with MAV, ZC or SSC. The combination of WL features shows a significant role in obtaining better classification accuracy.

4 Conclusions

In this study, first time the TD features waveform length (WL), number of zero crossings (ZC) and number of slope sign changes (SSC) extracted directly and from DWT coefficients have been employed for the detection of epileptic seizure using Naïve Bayes (NB) and support vector machine (SVM). Also, for the first time, the data sets such as AC-E, AD-E, BC-E, BD-E, and ABC-E have been considered and obtained better classification accuracy for these data sets as well as for all fourteen different combinations. In this proposed scheme, the observation of WL is very high during epileptic seizures. The classification accuracy of 100% is obtained using NB and SVM for the data set A-E. The achievement of the proposed scheme is confirmed by comparing the performance of classification problems as addressed by other researchers. It can be concluded that DWT based TD features achieve more satisfactory results to distinguish the EEG signals in comparison to other methods.

Since these features WL, ZC, and SSC afford the best presented along with MAV, they are employed for automatic detection of epileptic seizures from EEG signals.

References

1. Lehnertz, K.: Epilepsy and nonlinear dynamics. J. Biol. Phys. **34**, 253–266 (2008)
2. Duncan, J.S., Sander, J.W., Sisodiya, S.M., Walker, M.C.: Adult epilepsy. Lancet 367, 1087 (2006)
3. Pradhan, N., Sadasivan, P.K., Arunodaya, G.R.: Detection of seizure activity in EEG by an artificial neural network: a preliminary study. Comput. Biomed. Res. **29**, 303–313 (1996)
4. Kiymik, V.P., Subasi, A., Ozcalik, H.R.: Neural networks with periodogram and autoregressive spectral analysis methods in detection of epileptic seizures. J. Med. Syst. **28**, 511–522 (2004) Klinik für Epileptologie, Universität Bonn. In
5. Subasi, A.: Epileptic seizure detection using dynamic wavelet network. Expert Syst. Appl. **29**, 343–355 (2005)
6. Srinivasan, V., Eswaran, C., Sriraam, N.: Artificial neural network based epileptic detection using time-domain and frequency-domain features. J. Med. Syst. **29**, 647–660 (2005)
7. Murro, A.M., King, D.W., Smith, J.R., Gallagher, B.B., Flanigin, H.F., Meador, K.: Computerized seizure detection of complex partial seizures. Electroencephalogr. Clin. Neurophysiol. **79** (1991)
8. Qu, H., Gotman, J.: A patient-specific algorithm for the detection of seizure onset in long-term EEG monitoring: possible use as a warning device. IEEE Trans. Biomed. Eng. **44**, 115–122 (1997)
9. Gabor, A.J., Leach, R.R., Dowla, F.U.: Automated seizure detection using a self-organizing neural network. Electroencephalogr. Clin. Neurophysiol. **99**, 257–266 (1996)
10. Webber, W.R.S., Lesser, R.P., Richardson, R.T., Wilson, K.: An approach to seizure detection using an artificial neural network (ANN). Electroencephalogr. Clin. Neurophysiol. **98**, 250–272 (1996)
11. Orhan, U., Hekim, M., Ozer, M.: EEG signals classification using the K-means clustering and a multilayer perceptron neural network model. Expert Syst. Appl. **38**(10), 13475–13481 (2011)
12. Nicolaou, N., Georgiou, J.: Detection of epileptic electroencephalogram based on permutation entropy and support vector machines. Expert Syst. Appl. **39**(1), 202–209 (2012)
13. Sezer, E., Işik, H., Saracoğlu, E.: Employment and comparison of different artificial neural networks for epilepsy diagnosis from EEG signals. J. Med. Syst. **36**(1), 347–362 (2012)
14. Acharya, U.R., Sree, S.V., Alvin, A.P.C., Suri, J.S.: Use of principal component analysis for automatic classification of epileptic EEG activities in wavelet framework. Expert Syst. Appl. **39**(10), 9072–9078 (2012)
15. Song, Y., Zhang, J.: Automatic recognition of epileptic EEG patterns via extreme learning machine and multiresolution feature extraction. Expert Syst. Appl. **40**(14), 5477–5489 (2013)
16. Hosseini, S.A., Akbarzadeh-T, M.-R., Naghibi-Sistani, M.-B.: Methodology for epilepsy and epileptic seizure recognition using chaos analysis of brain signals. In: Computational Intelligence in Multi-agent Systems: Theory and Practice, pp. 20–36 (2013)
17. Pachori, R.B., Patidar, S.: Epileptic seizure classification in EEG signals using second-order difference plot of intrinsic modefunctions. Comput. Methods Programs Biomed. **113**, 494–502 (2013)
18. Kumar, Y., Dewal, M.L., Anand, R.S.: Epileptic seizures detection in EEG using DWT-based ApEn and artificial neural network. Signal, Image Video Process. **8**(7), 1323–1334 (2014)
19. Chen, G.: Automatic EEG seizure detection using dual-tree complex wavelet-fourier features. Expert Syst. Appl. **41**, 2391–2394 (2014)
20. Riaz, F., Hassan, A., Rehman, S., Niazi, I.K., Dremstrup, K.: EMD-based temporal and spectral features for the classification of EEG signals using supervised learning. IEEE Trans. Neural Syst. Rehabil. Eng. **24**(1), 28–35 (2016)

21. Peker, M., Sen, B., Delen, D.: A novel method for automated diagnosis of epilepsy using complex-valued classifiers. IEEE J. Biomed. Health Inform. **20**(1), 108–118 (2016)
22. Swami, P., Gandhi, T.K., Panigrahi, B.K., Tripathi, M., Anand, S.: A novel robust diagnostic model to detect seizures in electroencephalography. Expert Syst. Appl. **56**, 116–130 (2016)
23. Tiwari, A.K., Pachori, R.B., Kanhangad, V., Panigrahi, B.K.: Automated diagnosis of epilepsy using key-point-based local binary pattern of EEG signals. IEEE J. Biomed. Health Inform. **21**(4), 888–896 (2017)
24. Sharmila, A., Geethanjali, P.: Detection of epileptic seizure from electroencephalogram signals based on feature ranking and best feature subset using mutual information estimation. J. Med. Imag. Health Inform. **6**(8), 1850–1864 (2016)
25. Sharmila, A., Geethanjali, P.: DWT based detection of epileptic seizure from EEG signals using naive Bayes and k-NN classifiers. IEEE Access **4**, 7716–7727 (2016)
26. Madan, S., Srivastava, K., Sharmila, A., Mahalakshmi, P.: A case study on discrete wavelet transform based hurst exponent for epilepsy detection. J. Med. Eng. Technol. **42**(1), 9–17 (2018)
27. Sharmila, A., Aman Raj, S., Shashank, P., Mahalakshmi, P.: Epileptic seizure detection using DWT-based approximate entropy, Shannon entropy and support vector machine: a case study. J. Med. Eng. Technol. **42**(1), 1–8 (2018)
28. Chen, D., Wan, S., Xiang, J., Bao, F.S.: A high-performance seizure detection algorithm based on discrete wavelet transform (DWT) and EEG. PLoS ONE **12**(3), e0173138 (2017)
29. Sharmila, A., Mahalakshmi, P.: Wavelet-based feature extraction for classification of epileptic seizure EEG signal. J. Med. Eng. Technol. **41**(8), 670–680 (2017)
30. Wang, L., Xue, W., Li, Y., Luo, M., Huang, J., Cui, W., Huang, C.: Automatic epileptic seizure detection in EEG signals using multi-domain feature extraction and nonlinear analysis. Entropy **19**(6), 222 (2017)
31. Reddy, G.R.S., Rao, R.: Automated identification system for seizure EEG signals using tunable-Q wavelet transform. Eng. Sci. Tech. Int. J. **20**(5), 1486–1493 (2017)
32. Sharma, M., Pachori, R.B., Acharya, U.R.: A new approach to characterize epileptic seizures using analytic time-frequency flexible wavelet transform and fractal dimension. Pattern Recogn. Lett. **94**, 172–179 (2017)
33. Ullah, I., Hussain, M., Aboalsamh, H.: An automated system for epilepsy detection using EEG brain signals based on deep learning approach. Expert Syst. Appl. **107**, 61–71 (2018)
34. Geethanjali, P., Ray, K.K.: A low-cost real-time research platform for EMG pattern recognition-based prosthetic hand. IEEE/ASME Trans. Mechatron. **20**(4), 1948–1955 (2015)
35. Englehart, K., Hudgins, B.: A robust, real-time control scheme for multifunction myoelectric control. IEEE Trans. Biomed. Eng. **50**(7), 848–854 (2003)
36. Oskoei, M.A., Hu, H.: Support vector machine-based classification scheme for myoelectric control applied to upper limb. IEEE Trans. Biomed. Eng. **55**(8), 1956–1965 (2008)
37. Huang, H.P., Chen, C.Y.: Development of a myoelectric discrimination system for a multi-degree prosthetic hand. In: Proceedings 1999 IEEE International Conference on Robotics and Automation, vol. 3, pp. 2392–2397 (1999)
38. EEG Database From University of Bonn, June 2013. http://www.epileptologiebonn.de
39. Subasi, A., Gursoy, M.I.: EEG signal classification using PCA, ICA, LDA and support vector machines. Expert Syst. Appl. **37**(12), 8659–8666 (2010)
40. Subha, D.P., Joseph, P.K., Acharya, R., Lim, C.M.: EEG signal analysis: a survey. J. Med. Syst. **34**(2), 195–212 (2010)
41. Meier, R., Dittrich, H., Schulze-Bonhage, A., Aertsen, A.: Detecting epileptic seizures in long-term human EEG: a new approach to automatic online and real-time detection and classification of polymorphic seizure patterns. J. Clin. Neurophysiol. **25**(3), 119–131 (2008)
42. Liu, A., Hahn, J.S., Heldt, G.P., Coen, R.W.: Detection of neonatal seizures through computerized EEG analysis. Electroencephalogr. Clin. Neurophysiol. **82**(1), 30–37 (1992)
43. Viglione, S.S., Walsh, G.O.: Proceedings: epileptic seizure prediction. Electroencephalogr. Clin. Neurophysiol. **39**(4), 435–436 (1975)

44. Rogowski, Z., Gath, I., Bental, E.: On the prediction of epileptic seizures. Biol. Cybern. **42**(1), 9–15 (1981)
45. Gotman, J.: Changes in interictal EEG spiking and seizure occurrence in humans. Epilepsia **23**, 432–433 (1982)
46. Mormann, F., Kreuz, T., Rieke, C., Andrzejak, R.G., Kraskov, A., David, P., Elger, C.E., Lehnertz, K.: On the predictability of epileptic seizures. Clin. Neurophysiol. **116**(3), 569–587 (2005)
47. Van Drongelen, W., Nayak, S., Frim, D.M., Kohrman, M.H., Towle, V.L., Lee, H.C., Hecox, K.E.: Seizure anticipation in pediatric epilepsy: use of Kolmogorov entropy. Pediatr. Neurol. **29**(3), 207–213 (2003)
48. McSharry, P.E., Smith, L.A., Tarassenko, L.: Comparison of predictability of epileptic seizures by a linear and a nonlinear method. IEEE Trans. Biomed. Eng. **50**(5), 628–633 (2003)
49. Litt, B., Esteller, R., Echauz, J., D'Alessandro, M., Shor, R., Henry, T., Vachtsevanos, G.: Epileptic seizures may begin hours in advance of clinical onset: a report of five patients. In: Applications of Intelligent Control to Engineering Systems, pp. 225–245. Springer, Dordrecht (2009)
50. Maiwald, T., Winterhalder, M., Aschenbrenner-Scheibe, R., Voss, H.U., Schulze-Bonhage, A., Timmer, J.: Comparison of three nonlinear seizure prediction methods by means of the seizure prediction characteristic. Physica D **194**(3–4), 357–368 (2004)
51. Gigola, S., Ortiz, F., D'attellis, C.E., Silva, W., Kochen, S.: Prediction of epileptic seizures using accumulated energy in a multiresolution framework. J. Neurosci. Methods **138**(1–2), 107–111 (2004)
52. Altunay, S., Telatar, Z., Erogul, O.: Epileptic EEG detection using the linear prediction error energy. Expert Syst. Appl. **37**(8), 5661–5665 (2010)
53. Fathima, T., Bedeeuzzaman, M., Farooq, O., Khan, Y.U.: Wavelet based features for epileptic seizure detection. MES J. Technol. Manag. **2**(1), 108–112 (2011)
54. Yuan, Q., Zhou, W., Liu, Y., Wang, J.: Epileptic seizure detection with linear and nonlinear features. Epilepsy Behav. **24**(4), 415–421 (2012)
55. Zamir, Z.R.: Detection of epileptic seizure in EEG signals using linear least squares preprocessing. Comput. Methods Programs Biomed. **133**, 95–109 (2016)

ECG and Cardiac Signal Processing Applications

Unipolar Cardiac Leads Between History and Science

Hossein Moeinzadeh, Joseph Assad, Paolo Bifulco, Mario Cesarelli, Alistair L. McEwan, Aiden O'Loughlin, Ibrahim M. Shugman, Jonathan C. Tapson, Aravinda Thiagalingam and Gaetano D. Gargiulo

Abstract The surface electrocardiography (ECG) uses a virtual reference point to measure the potential of chest electrodes. This reference potential is known as *Wilson central terminal (WCT)* and is assumed negligible (near zero) in amplitude. Consequently, the precordial leads have been named as the *unipolar leads*. Although this assumption was found incorrect immediate after this reference potential was introduced, it was difficult to measure its real amplitude. We recently introduced a 15-lead electrocardiography device that can record the traditional ECG leads in combination with the raw potential of limbs and chest electrodes directly referred to the circuit grounding. Consequently, we are able to record the potential of the raw chest electrodes, which we named as *true unipolar chest leads*. The aim of this study is to have

H. Moeinzadeh (✉) · J. C. Tapson · G. D. Gargiulo
MARCS Institute for Brain, Behaviour and Development, Western Sydney University, Sydney, Australia
e-mail: h.moeinzadeh@westernsydney.edu.au

J. Assad
Department of Cardiology, Liverpool Hospital, Liverpool, NSW, Australia

P. Bifulco · M. Cesarelli
Department of Biomedical Engineering, "Federico II" The University of Naples, Naples, Italy

A. L. McEwan
School of Electrical and Information Engineering, University of Sydney, Sydney, NSW, Australia

A. O'Loughlin
School of Medicine, Western Sydney University, Campbelltown, NSW, Australia

I. M. Shugman
Cardiology Department, Campbelltown Hospital, Campbelltown, NSW, Australia

A. Thiagalingam
School of Medicine, The University of Sydney, Sydney, NSW, Australia

Cardiology Department, Westmead Hospital, Westmead, NSW, Australia

Westmead Institute for Medical Research, Westmead, NSW, Australia

G. D. Gargiulo
School of Computing, Engineering and Mathematics, Western Sydney University, Penrith, Australia

G. Naik (ed.), *Biomedical Signal Processing*, Series in BioEngineering,
https://doi.org/10.1007/978-981-13-9097-5_10

a clear understanding of the WCT potential and its influence on the chest leads. Our records show that the true unipolar leads may be more sensitive for detecting cardiac diseases in the left anterior descending coronary artery in patients with non-ST elevation reported on chest leads.

Keywords Electrocardiography · Wilson central terminal · Unipolar leads · Limb potential · Left anterior descending · Electrocardiography database

1 Introduction

The heart impresses an electrical current that flows from the heart through the limbs, which can be used for examining the cardiac function [1, 2]. First, Waller used two electrodes on the body and found changes in electrometer by heartbeat [3, 4]. He applied electrodes on limbs to show the electrical activity of the heart. However, Einthoven made a major breakthrough in Electrocardiography by using the string galvanometer in 1901 [4]. He used a silver-coated quartz filament (or string) in a strong magnetic field to measure the strength and direction of the *current* of the heart [5]. The string was moved in the magnetic field when the current of the heart moved through it [5]. The Einthoven's device was very bulky and far from the hospital, hence, he used the telephone wire to receive the patients' heart impulse from the hospital [2, 5]. Later, Einthoven introduced the mathematics relations between three limb leads, which has been known as *Einthoven Triangle* hypothesis [6]. The vertices of the Einthoven Triangle are electrodes placed on the right hand, left hand, and left leg which are used to measure the limb leads, known as the lead I, lead II, and lead III [4, 6]. In this theory, the human body is characterized as a two dimensional, homogeneous conductor and part of infinity with the heart located in the centroid of the triangle [2, 4].

$$\begin{aligned} \text{Lead I} &= \Phi_L - \Phi_R \\ \text{Lead II} &= \Phi_F - \Phi_R \\ \text{Lead III} &= \Phi_F - \Phi_L \end{aligned} \tag{1}$$

As the three limb leads to construct a closed loop (Fig. 1), the Kirchhoff's voltage law can show the relationship between the limbs (Eq. 2) [2].

$$I + III = II \tag{2}$$

Although some researchers suggested a different system to record the heart activity [2, 3, 7], only the Einthoven limb leads had clinically used for three decades [2, 5, 8]. Wilson highlighted the fact that the limb electrodes are far from the heart, and introduced the *unipolar lead* concept [5, 8–10]. In *Wilson hypothesis,* the electrical activity of the heart can be measured by the potential difference between six exploring

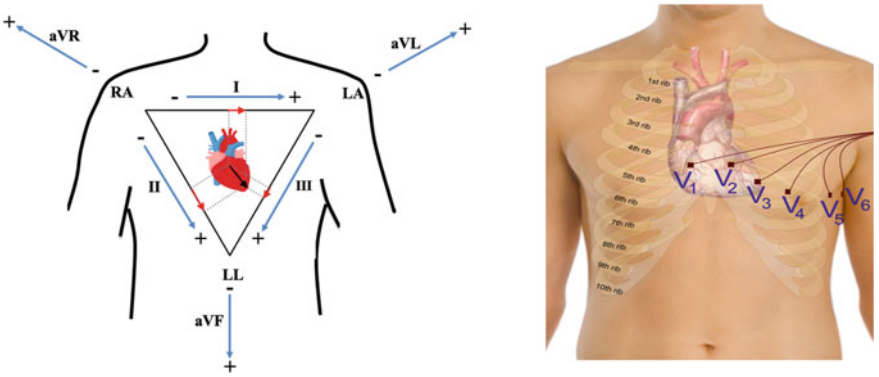

Fig. 1 Twelve lead electrocardiography

electrodes on the chest and an *indifferent electrode* of zero potential, which is known as Wilson Central Terminal (WCT) [10]. These six leads are designated as unipolar precordial leads (V1:V6) as he assumed the WCT amplitude is equal to zero [2, 10]. The Wilson Central Terminal is measured by the average potential of the right arm (Φ_R), left arm (Φ_L) and left leg (Φ_F) [9, 10].

$$\Phi_{WCT} = \frac{1}{3}(\Phi_L + \Phi_R + \Phi_F) \tag{3}$$

$$V_1 : V_6 = \Phi_{V1} : \Phi_{V6} - \Phi_{WCT} \tag{4}$$

Wilson also proposed to use three unipolar limb leads (VR, VL, and VF), which were measured by the difference potential of limbs' electrode and the WCT reference point [10].

$$\begin{aligned} VL &= \Phi_L - \Phi_{WCT} \\ VR &= \Phi_R - \Phi_{WCT} \\ VF &= \Phi_F - \Phi_{WCT} \end{aligned} \tag{5}$$

Because the three unipolar limb leads had a small amplitude, Goldberger [11] modified the WCT to increase these leads' amplitude by 50%. The new leads are measured as the potential difference between each limb potential and the average of the other two limb potentials. These leads are known as augmented leads and named as aVR, aVL, and aVF [11].

$$\begin{aligned} aVL &= \Phi_L - \frac{1}{2}(\Phi_R + \Phi_F) \\ aVR &= \Phi_R - \frac{1}{2}(\Phi_L + \Phi_F) \end{aligned}$$

$$aVF = \Phi_F - \frac{1}{2}(\Phi_R + \Phi_L) \tag{6}$$

The augmented leads were suggested in 1942 finalizing the development of the ECG lead system. The current ECG lead system consists of three Einthoven limb leads, three augmented leads, and six precordial leads (Fig. 1) [4].

Currently, Electrocardiography is the most wide-spread non-invasive tool for diagnosis of cardiac diseases, currently in use in every clinical center. However, some of the aforementioned fundamental ECG hypotheses have been challenged either during the development of the Electrocardiography [1901–1942], or afterward. Therefore, we discuss two of these fundamental ECG hypotheses: the Einthoven equilateral Triangle hypothesis, and the Wilson hypothesis in order to make a tangible picture of the Wilson central terminal and its influence on the precordial leads.

1.1 Wilson Central Terminal

Wilson hypothesized that a neutral reference point of the human body could be measured by averaging the limb potentials. This reference point was introduced having null amplitude, being steady, and locating in the center of the Einthoven triangle [10]. The potential in the infinite medium has a null amplitude, which could be considered as the ideal reference point. In physics, we can only measure the potential difference between two points. However, we can have the potential of one point in case the second point is located in the far distance (infinity) from the first [12]. Thus, Wilson used three large resistors through which a negligible current would pass (based on Ohm's law), and consequently, he was able to measure the limbs' potential (Fig. 2, panel a) [10]. This assumption was found incorrect and absorbed immediate interests among researchers to measure this systematic error in the Electrocardiography. The proposed methods can be categorized into three different perspectives.

In the first approach, the human body is immersed in large homogeneous conductor to measure the potential difference between the WCT and the assumed zero potential (the water itself). In 1938, Eckey and Frohlich immersed a human body into a full bathtub and determined the WCT amplitude to be into a range of 0.2–0.3 [mV] [13]. A year later, Burger conducted the same experiment and immersed five men into a bathtub filled by water and reported the WCT amplitude was 0.26 mV [14]. In 1946, Wilson submerged a human in the Lake Michigan and found that the average absolute amplitude of the WCT could be as large as 0.15 mV [9]. Dolgin repeated the same experiment with different adjustments and confirmed the previous finding [15]. In 1954, Bayley et al. and Bayley and Kinard encased the body of volunteers inside a metal structure and immersed it in water for the duration of the recording [16, 17]. They determined that the WCT is not steady and its amplitude could be as large as 0.4 of Einthoven's leads during the cardiac cycle [16–18]. Thus, they used three rheostats to adjust the weights of the three WCT components in order

to minimize the WCT amplitude [17]. The legitimacy of the first approach was undermined by a variety of factors, including the effect of water pressure on ECG recording and degree of the conductivity of surrounding water [19]. Additionally, the zero potential of surrounding water [9, 20] and the widespread use of this method [21] have been questioned.

In the second approach, the *zero potential* of the human body was measured using numerical methods [2, 22–24] or surface potential mapping [25–27]. In these methods, the zero potential is not exactly aligned with the WCT definition; however, they referred to it as Wilson Center Terminal. The numerical methods are developed based on the theory that the summation of the electrical potential at the body surface should be zero [2]. Miyamoto et al. used 128 electrodes placed on the thorax and averaged their potential to estimate the amplitude of the human reference point. They reported the average value of the WCT as −0.169 mV in 10 normal volunteers, and −0.051 mV in all 60 subjects including controls and patients [19, 25, 26,].

In a third approach, the potential of the right arm left arm and left leg directly measured using the right leg as a reference point (Fig. 2, panel b) [28]. We recently developed a new Electrocardiography device that can measure nine unipolar leads including three limbs' potential and six true unipolar limb leads, in addition to 12 lead ECG [28–32, 33, 28]. Our results confirm the previous findings that the WCT is not steady and null, and we found out the WCT amplitude could exceed the amplitude of lead II (up to 247% of lead II).

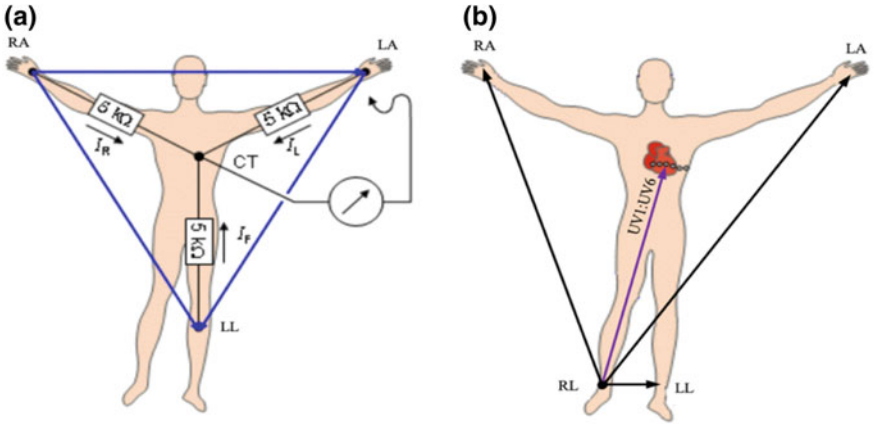

Fig. 2 Traditional approach (panel **a**) in comparison with our approach (panel **b**) to measure the WCT. In our approach, the limb potential and unipolar chest lead are measured with respect to the right leg

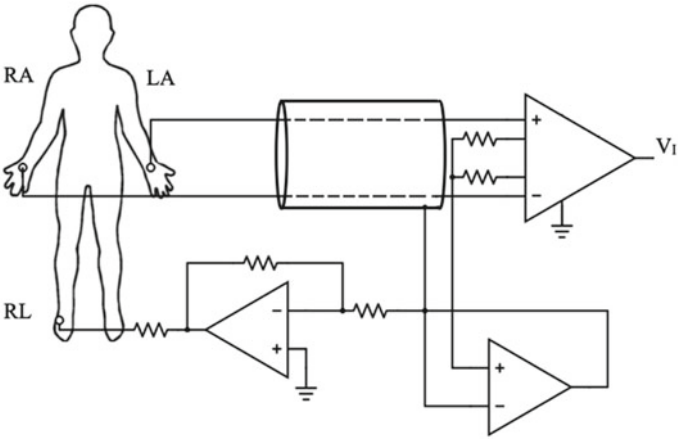

Fig. 3 ECG amplifier using right leg driver (lead I)

2 True Unipolar ECG Recording Device

Our ECG device is designed to record traditional ECG signals in addition to the nine true unipolar leads including three limb potentials and six unipolar chest leads. The true unipolar leads are the raw biopotential measured from the exploring electrodes directly referred to the *right leg* (RL). Although the right leg was not included in the original ECG montage, it was added as necessary return grounding for voltage amplifier as well as a way to reduce the interference from external electric fields [33]. Reduction of interference from external electrical fields is usually achieved with a technique known as a *driven right leg* or *right leg driver*, which usually implies an injection of a small current into the body (via the right leg electrode) and measuring amplifier circuits (via their reference terminal). In some specific biopotentials applications, the right leg driver is avoided using a technique known as voltage reference bootstrap that might result in an advantage to reduce common noise capture [2, 4, 33].

Driven right leg circuitries (DRLs) are widely used for the majority of the designs. Using the DRL increases patient safety because the human body is not directly grounded [4, 33, 34]. Figure 3 shows an example of the DRL application. As can be seen, the human body is driven by a measure of the common mode signal at the measuring electrodes while the amplifier is directly grounded. The technical documentation of the INA118 can be found in [35].

Our hardware system is developed around the INA116 instrumentation amplifier [36] from Texas Instruments (Burr-Brown series). This chip has typically a bias current of the only handful of femto-Amperes, and it incorporates a specialized guard ring amplifier which is primarily used to preserve the signal to noise ratio (SNR). The guard ring amplifier is used to measure the WCT components, as it generates a replica of the input signal [28, 29, 31, 32, 37,]. Therefore, the WCT components' voltages are directly measured by using the guard buffer of the limb electrodes. The

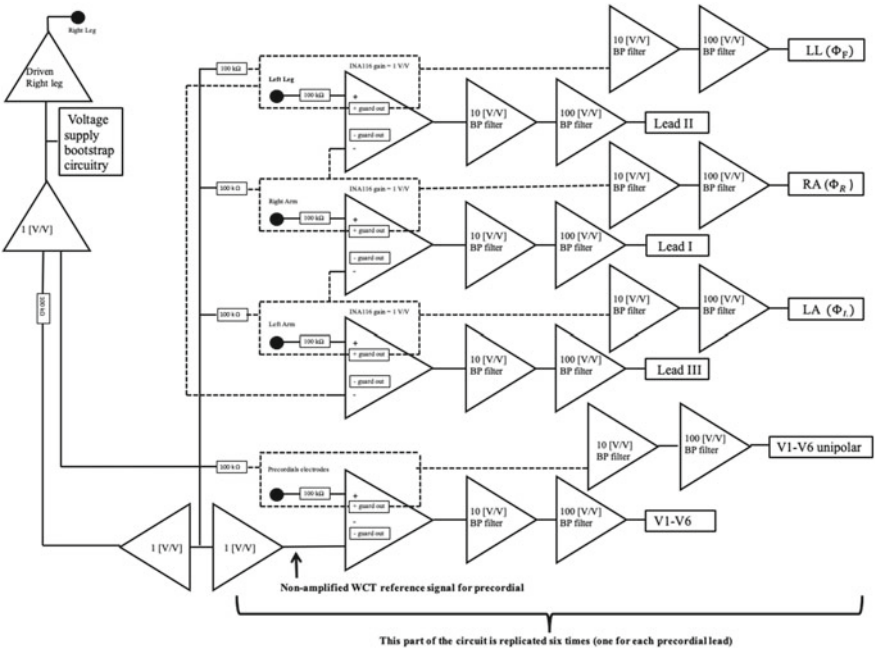

Fig. 4 Block diagram of the employed hardware (adapted from [28])

INA116 chips have a gain set of 1 V/V; two AC coupled active non-inverting low pass filters with gains of 10 V/V and 100 V/V are used to provide the required gain and bandpass filtering.

To ensure that the SNR of the measured signals is sufficient, specialized grounding circuitry is designed utilizing a combination of the right leg circuitry and a modified voltage bootstrap circuitry [9, 29, 37–39]. The non-amplified average of the measurement electrodes is directly inputted to the driven right leg circuitry, which is designed to drive 20 μA [40–42].

This circuitry is battery powered, and the necessary analogue to digital conversion and data logging is operated by the BIOADC [43], which samples data with a 16-bit over a range of ±5 V with a sampling rate of 800 Hz. The BIODAC is directly (galvanically insulated USB HUB) connected to a battery-powered laptop, and it comprises an anti-aliasing low-pass filter operating at the Nyquist frequency. Finally, a specialized importing script including a zero-phase lag 50th order bandpass filter (0.05–150 Hz), a zero-phase lag 50th order 50 Hz and harmonics notch IIR filters are used to normalize the frequency components to the diagnostic ECG bandwidth of the acquired signal. Complete details can be found in our recent publication [28] (Fig. 4).

3 True Unipolar Leads

We are able to record the three Einthoven unipolar limb lead (the voltage of right arm, left arm, and left leg) and six true unipolar precordial leads for the first time. We have recorded data from more than 100 patients at the Campbelltown hospital (NSW) over two years (2016–2018). All the patients volunteered for this study and gave written consent (this study was approved by the Ethics Committee of the South West Sydney Health District on 23rd September 2015 with the protocol number HREC/15/LPOOL/302). Some recordings have been removed from the dataset due to poor signal to noise ratio or because of abrupt interruption of the recording (emergency or patient being transferred to another department for an intervention/procedure). The published dataset[1] [44] contains 92 patients (27 were female) with an average age of 65.23 years and a standard deviation of 12.12 years. The majority of the patients had a history of cardiac disease and were admitted to the hospital from the emergency department because of difficulties in breathing and/or chest pain.

3.1 Einthoven Unipolar Limb Lead

We are able to measure the amplitude of Wilson Central Terminal by averaging the voltage of Einthoven limbs. In this part, we are trying to answer the question of *what is the Wilson Central Terminal?* We investigate the legitimacy of two hypotheses:

1. *The WCT is null and steady during the cardiac cycle.*
2. *The WCT and aVF are inversely proportional.*

The first hypothesis is the Wilson assumption to measure the precordial leads, which has been proved incorrect by many researchers. However, their approaches were cumbersome, usually having a small test case population, and more importantly, their validity has been questioned [9, 20, 21]. The second hypothesis assumes that the left leg potential has the smallest amplitude among the Einthoven limb potentials, as it has the longest distance from the heart. Hence, considering the assumption that the left leg has near zero amplitude ($\Phi_F \cong 0$), the WCT can obtain using the right arm, and left arm. Consequently, WCT and aVF are inversely proportional.

$$\begin{matrix} \Phi_{WCT} = \frac{1}{3}(\Phi_R + \Phi_L) \\ aVF = -\frac{1}{2}(\Phi_R + \Phi_L) \end{matrix} \overset{yields}{\rightarrow} \Phi_{WCT} = -\frac{2}{3}aVF \tag{6}$$

To assess the credibility of these two theories, we calculated the average peak to peak amplitude of three beats for all patients. In Fig. 5, We report the relative amplitude of the WCT, RA, LA, and LL with respect to lead II. As it is shown in

[1] Our dataset name is WCTECGdb, and was published in the Physionet website (https://alpha.physionet.org/content/wctecgdb/).

Fig. 5 (panel a), the minimum, maximum and average amplitude of the WCT in relation to lead II among all 92 patients are 0.11, 2.47, and 0.78 respectively. The left arm expected to have a higher potential than the right arm, as it is closer to the heart (Fig. 5 panels b, c). The left arm with respect to lead II has an average of 1.61 (within range of [0.038 6.41]), while right arm average is 0.88 (within range of [0.01 2.79]) for all 92 patients. Figure 5 (panel d) demonstrates the amplitude of the left leg with respect to lead II. Although the left leg has a small amplitude in comparison with the right and left arms' potentials, it does not have zero amplitude. The left leg potential in relation to lead II is in the range of [0.007 1.78] with an average of 0.22 for all patients.

Our recording shows that the WCT does not have a small amplitude and has ECG lead characteristics such as p-wave or QRS complex. The WCT has neutral (Figs. 6 and 8), negative (Fig. 7), or positive (Fig. 9) deflection during the cardiac cycle. Figure 6 is an example of the WCT with a large amplitude. The WCT signal is as large as 2.41 of lead II, and it exhibits all the characteristics of the ECG trace.

Figure 7 is an example of WCT with negative deflection. The left arm, right arm, and left leg show ECG features. Furthermore, the left leg has relatively small potential in comparison with the right arm and left arm.

As it can be referred from Eq. 6, the WCT and aVF are highly correlated in case the left leg potential has near zero amplitude. It can be understood from Fig. 5 (panel d) that the left leg has a small amplitude for most of the patients, however, it also has a relatively big amplitude for some patients. Figures 8 and 9 are an example of the WCT and aVF lead having a low and high correlation. As can be seen in these figures, the RA, LA, and LL signals have ECG characteristics. Figure 8, shows a low correlation between the aVF lead and the WCT signal, as the LL amplitude is as large as 0.22 of lead II. In contrast, the LL has a negligible amplitude in Fig. 9, consequently the WCT and the aVF lead are highly correlated.

3.2 True Unipolar Precordial Leads

The true unipolar leads and precordial leads are referred to like the same concept in the literature. However, it has been known that this terminology is incorrect. The precordial leads initially represent the difference potential between the electrodes placed on the chest and the WCT. Since Wilson assumed the WCT is null, the precordial leads have been referred to as unipolar leads. However, our ECG device is able to record the potential of electrodes placed on the chest without using the WCT signal [29–32]. Therefore, we recorded the traditional precordial leads (V1:V6) and what we address as the true unipolar leads (UV1:UV6) at the same time for all patients.

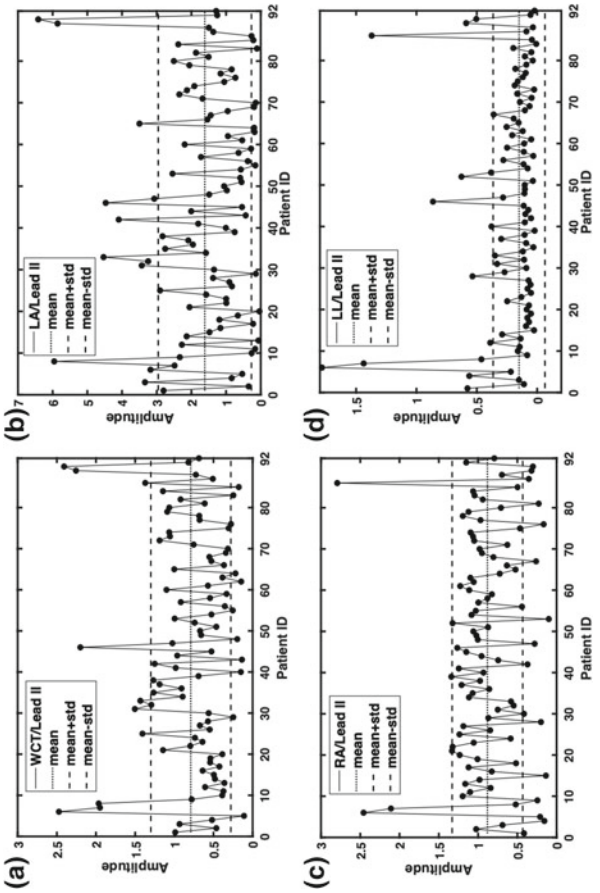

Fig. 5 The amplitude of the WCT, right arm, left arm and left leg with respect with Lead II

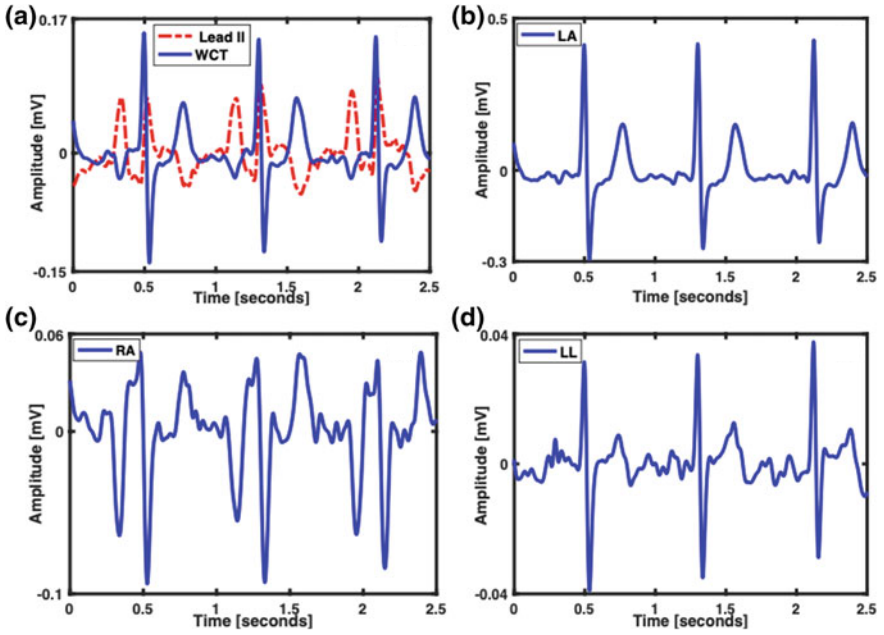

Fig. 6 Example of neutral WCT. The WCT is 2.41 of lead II amplitude (average); the recording is from a 80-year-old male patient admitted from the emergency department with NSTEMI diagnosis

Our recording shows that the WCT is highly individual and has medically relevant amplitude, which impacts the precordial leads' shape and resulting to lose important information in the precordial leads.

We investigated the clinical features of true unipolar leads in comparison with precordial leads for all 92 patients. In this paper, we selected four patients from the WCTECGdb [44] with Non-ST Elevation Myocardial Infarction (NSTEMI) diagnosis to show the influence of the WCT on precordial leads. Our records show that the unipolar ECG may be more sensitive for detecting disease in the left anterior descending (LAD) coronary artery in patients presenting with NSTEMI. We are currently recording more data to show the validity of this hypotheses. As the WCT has no effect on the limb leads and augmented leads, we do not include them in the Figs. 10, 11, 12 and 13.

- Patient75: He presented with a non-ST segment elevation myocardial infarction. In this type of myocardial infarction, the mechanism of injury is subendocardial myocardial infarction. As it can be referred from Fig. 10 (panel a), the t-waves are biphasic in leads V2:V4, while they are inverted in leads UV1:UV6. Consequently, the unipolar ECG may be more sensitive at detecting this type of injury than the standard ECG. As the only difference between unipolar chest lead, and precordial

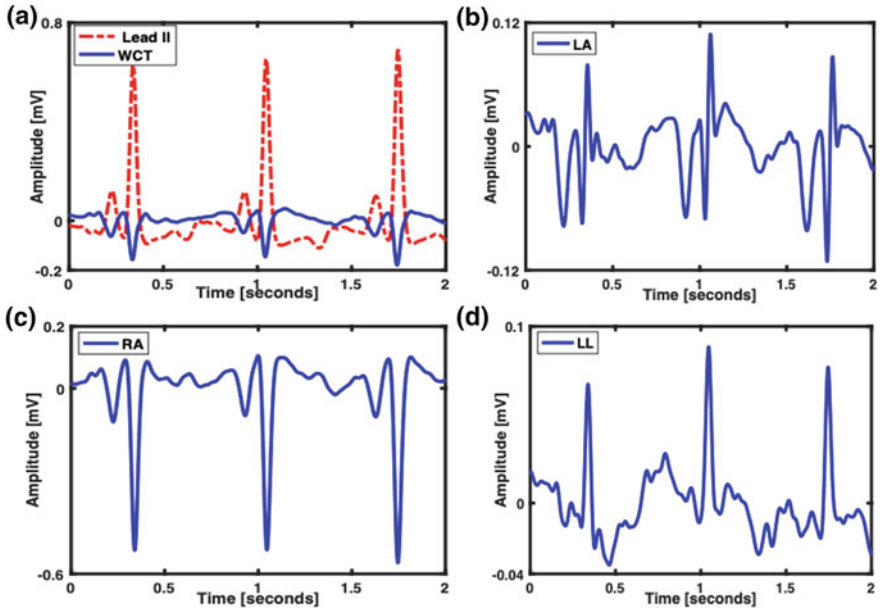

Fig. 7 Example of negative WCT. The WCT is 0.32 of lead II amplitude (average); the recording is from a 54-year-old male patient admitted from the emergency department with ischemic cardiomyopathy diagnosis

lead is the WCT signal (Eq. 4), the influence of the WCT on UV1 can be clearly seen in Fig. 10 (panel b).

- Patient46: His angiography showed focal severe mid LAD stenosis, which supplied a large collateral to a distal dominant right coronary artery (the native right coronary artery being completely occluded). The patient subsequently underwent coronary artery bypass surgery. As can be seen in Fig. 11, the true unipolar leads show loss of clear T waves, which is suggestive of ischemia.
- Patient85: His angiography showed proximal to mid LAD stenosis, which was subsequently stented (after optical coherent tomography (OCT) imaging). As seen in Fig. 12, the true unipolar leads show more markedly biphasic T waves UV1:UV3. In other words, biphasic T waves in VU1–UV3 typically suggest proximal LAD disease which is known as Wellens Syndrome. This was not apparent on the precordial leads but was predictive of the underlying culprit lesion.
- Patient66: His angiography showed focal severe stenosis in distal RCA and proximal large diagonal branch stenosis of the LAD (both of which were stented). As it can be referred from Fig. 13, the true unipolar leads show T wave inversion UV4:UV6 consistent with diagonal branch territory problem/ischemia.

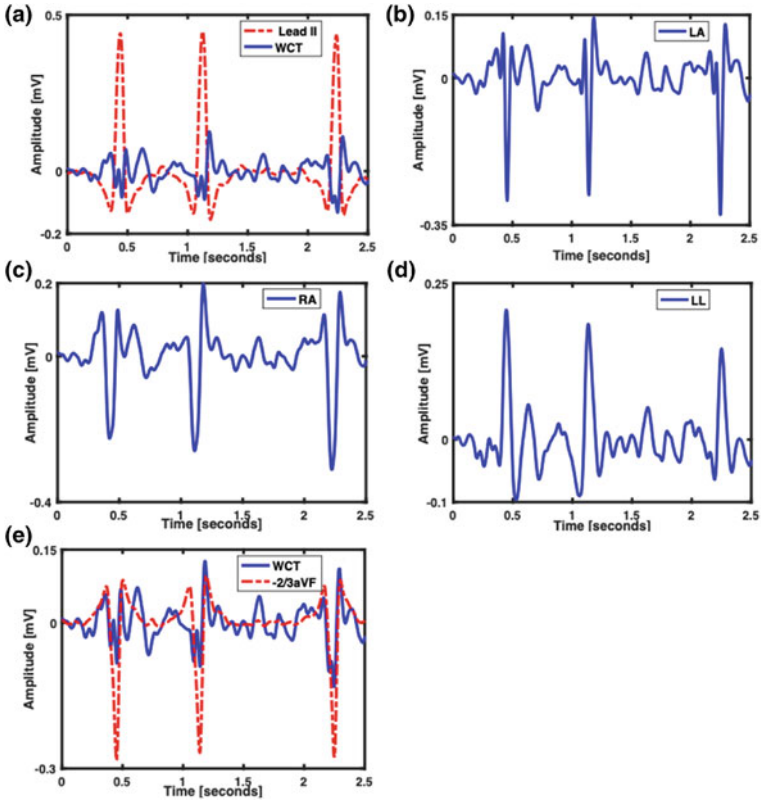

Fig. 8 Example of neutral WCT that mutates into positive and neutral. There is low a correlation (45%) between the WCT and aVF lead. The LL amplitude is as large as 0.22 of lead II

4 The WCT Location

In theory, the WCT is located in the centroid of the Einthoven triangle. However, research conducted in 2005 shows that many cardiologists do not have a clear understanding of unipolar leads and the WCT concept [45]. As mentioned earlier, although there was an initial wave of interest working on the fault in the WCT assumption after Wilson hypothesized its concept, this error has been widely accepted, and the topic received scant research attention. Furthermore, there is no consensus understanding of the Einthoven triangle, as its edges have been considered differently in the literature. Hence, a clear view of the Einthoven triangle hypothesis may lead to a more precise answer to the question, *where is Wilson central terminal?*

Einthoven assumed the human body is two-dimensional conducting homogeneous medium with the shape of a triangle. The heart is regarded as a single dipole in the center of the triangle. The dipole changes its magnitude and direction in every moment, which causes it to change its electrical field. Considering these assumptions,

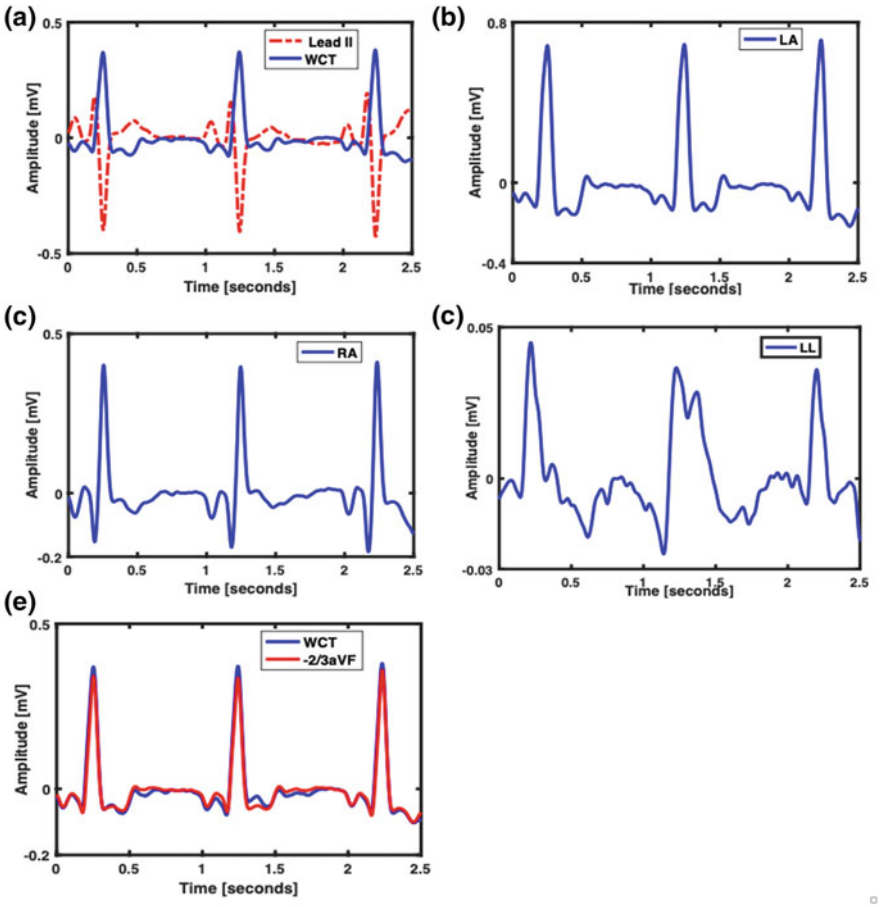

Fig. 9 Example of positive WCT with small LL amplitude (0.032 of Lead II). The WCT and aVF are highly correlated (98%) as the amplitude of WCT is negligible

the potential of every point in the body measured by Eq. 7 [1], which Φ is the potential of a single current dipole $\vec{p}$ (with strength p) in infinite homogenous medium with a conductivity of (σ):

$$\Phi = \frac{1}{4\pi\sigma}\frac{p\cos\theta}{R^2} + c \tag{7}$$

R is the length of the vector $\vec{R}$ directed from dipole source location to the target point, and θ is the angle between vectors $\vec{p}$ and $\vec{R}$.

As Goldberger discussed [46], the distance between the limb electrodes and the dipole are equivalent; therefore the difference between the limb potential amplitudes is only dependent to angles θ_1, $\theta_2(\theta_1 + 120)$ and $\theta_3(\theta_1 + 240)$. It could be easily

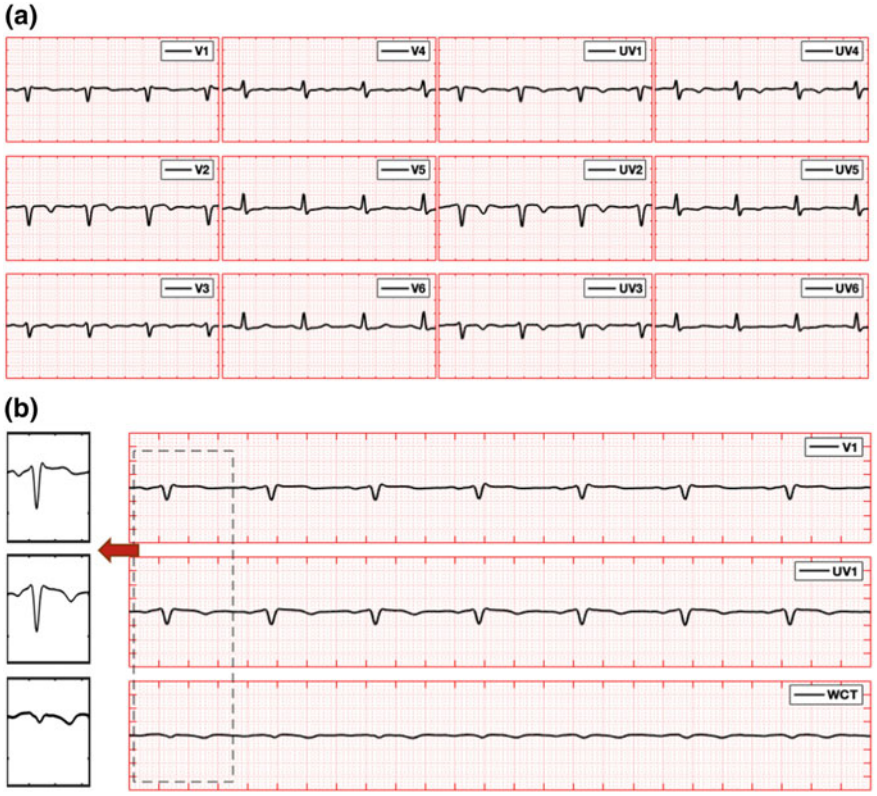

Fig. 10 Panel **a**: comparison of unipolar chest lead (UV1:UV6) with precordial leads (V1:V6). Panel **b**: the influence of the WCT on V1; top panel is standard V1 precordial; middle is true unipolar UV1; bottom panel is the WCT signal. The t-wave is inverted in UV1. Recorded from 70 years old male, admitted to a hospital for NSTEMI (patient75)

Fig. 11 Comparison of unipolar chest lead (UV1:UV6) with precordial leads (V1:V6). Recorded from 69 years old male, admitted to a hospital for NSTEMI (patient46)

Fig. 12 Comparison of unipolar chest lead (UV1:UV6) with precordial leads (V1:V6). Recorded from 52 years old male, admitted to a hospital for NSTEMI (patient85)

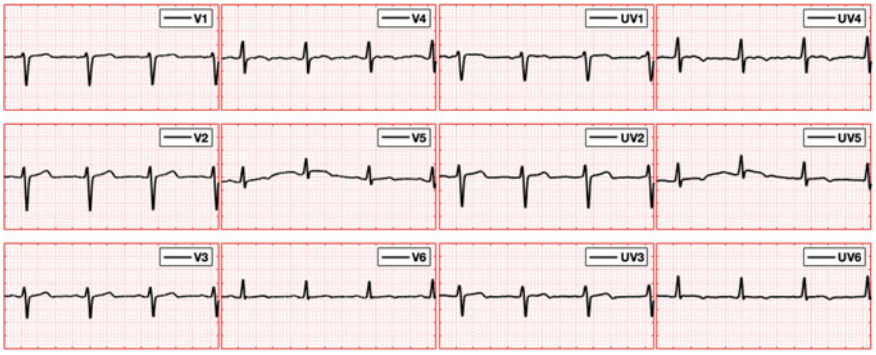

Fig. 13 Comparison of unipolar chest lead (UV1:UV6) with precordial leads (V1:V6). Recorded from 41 years old male, admitted to a hospital for NSTEMI (patient66)

shown that for every direction of the heart vector, the sum of the limb potential is equal to zero [46] (Fig. 14).

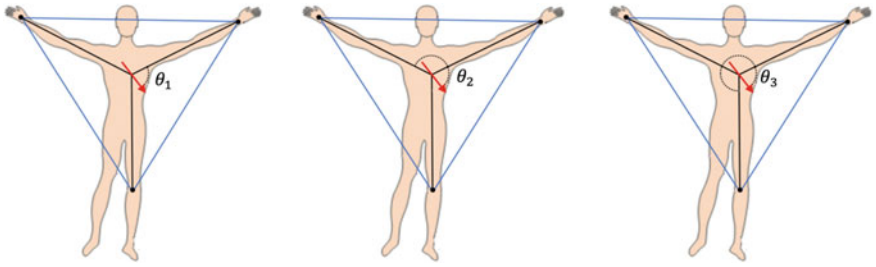

Fig. 14 Einthoven assumed the potential of each limb only depends on the angle between $\vec{p}$ and $\vec{R}$ vectors

The geometrical position of the limb electrodes shaped the Einthoven triangle [46–48,]. Wilson assumed the symmetrical orientation of the heart vector with respect to the electrodes on the limbs [17] and hypothesized that the potential of the dipole (heart) is equal to zero and calculated by the average of the Einthoven limb potentials. Although the Einthoven hypothesis is the major breakthrough in electrocardiography, it has been known his assumptions are oversimplifying the human body, and the heart activity. The same argument can be made for the Wilson hypothesis.

> The WCT located in the centroid of Einthoven triangle, represents the potential of the single dipole, and its potential is equal to zero in case three electrodes are placed in the same distance from the heart, and all Einthoven assumptions are correct.

However, as it can be referred from Eq. 7, in case the imaginary line between limb electrodes do not build up the equilateral triangle, the limb potentials depend on the R amplitude and the angle (θ). Consequently, the centroid of the triangle cannot represent the dipole anymore. Furthermore, the other assumptions (the electrical activity of the heart is a single dipole located in the center of the body, and the human body is a homogeneous conductor) are ill-posed models of the human body [46].

In some literature, there is also a misunderstanding between geometrical space and electrical space. As an example, in the standard surface ECG representation, it is possible to see that limb leads are the edges of the Einthoven triangle, this can be easily shown incorrectly. The Einthoven law (Eq. 2) contradicts the fact that equilateral triangle edges are in the same length, and more importantly, three limb leads could only construct a triangle (not equilateral) for less than 50% of the cardiac cycle [49].

5 Discussion

Originally, the heart was theorized to act as a current source, and the electrocardiography model measured bio-currents using a very sensitive galvanometer (string galvanometer). As there is no obvious current pathway that includes the heart when the instrument is connected between the two legs and the right leg is the most distant limb from the heart, Einthoven did not include the right leg in the cardiac conduction model. In other words, ECG recordings were intended as a measure of the net current impressed by the heart circulating into an external circuit closed by the measurement instrument. Therefore, it was possible for Wilson to complete the transformation from the equilateral triangle (Einthoven's triangle) to the equivalent star circuit (originating the augmented leads) when he faced the problem of finding a reference for precordials. In theory, if each of the Einthoven leads measures the net current impressed by the heart between the two limbs, averaging all the electrodes

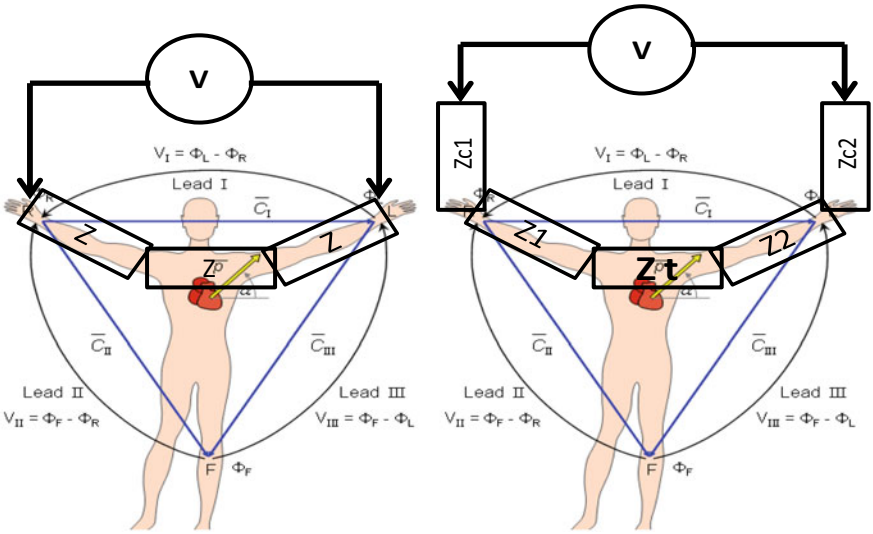

Fig. 15 Ideal measurement of lead I versus real measurement of lead I. Left panel shows an idealized measurement of lead I as voltage; right panel refers to real measurements of lead I in which includes contact impedances (Zc1 and Zc2) and variable impedance of torso (Zt)

together should give the best approximation of the point of origin, the neutral point of the cardiac electrical activity.

Impractical use of current measurement devices and the link between current and voltage resulted in the replacement of all ECG current measurements with voltage, neglecting that measuring voltage instead of current requires dealing with the different impedances of body sections. In fact, each lead is interpreted as the voltage drop across a composed resistance (impedance, as a matter of fact) due to the net current impressed by the heart to the points of measurement based on Ohm's law (Voltage = Resistance * Current]). For example, lead I (Fig. 15) can be interpreted as the drop of voltage across the sum of the contact impedance at both electrodes that includes the impedance of the two arms and the impedance of the chest across the shoulders that changes with respiration.

Of course, current and voltage measurements are perfectly interchangeable if the body is simply considered as a homogeneous volume conductor (constant resistance) with the limb electrodes placed at equal distance with no or negligible contact impedance. However, in real life recording the contact impedance imbalance between the ECG electrodes is often not verified. Additionally, the limb leads are measured across different sections of the chest, which are different in shape, and their resistance changes with respiration and body posture resulting in adding a frequency-dependent delay and a phase difference between voltage and current. The modified phase relationship between voltage and current may also affect the limbs' potential and consequently, the WCT. Moreover, as the voltage potential difference between the reference point (RL) and the other limb electrodes are used to measure the RA, LA, and LL

potentials, different body and contact impedances may impose different delays upon the limb potentials resulting in an unpredictable alteration of WCT [29, 32].

Based on the Einthoven theory, if the limb electrodes placed on the same distance from the heart, the WCT presents the potential of the dipole. However, it is not the case in practice. The WCT amplitude is highly dependent on where the limb electrodes are placed (Eq. 7). Hence, it is obvious not to have a negligible amplitude in averaging the limbs' potential. On the other hand, the location of the limb electrodes influences the shape and amplitude of precordial leads [50]. As our device uses the right leg as a reference point to measure the potential of the electrodes on the chest, the WCT variation does not affect the true unipolar leads. On the other hand, the true unipolar leads are robust and independent from the limb electrodes' displacement.

6 Conclusion

The electrocardiography is the most common tool in the diagnosis of cardiac diseases. In this paper, we discussed two important hypotheses proposed by Einthoven and Wilson, which shapes the currently in use electrocardiography tool. It has been known that these two theories simplify heart activity, and do not provide a precise model for the human body. However, no one can measure the influence of these false assumptions on the leads. As our ECG device can record the potential of the Einthoven limb electrodes and chest electrodes, we were able to show the impact of the WCT on precordial leads. Furthermore, we depicted a clear picture of the WCT concept by answering the questions *what is the Wilson central terminal*? and *where is the Wilson central terminal?* Our records show that the WCT is not null, and it has ECG features such as p-wave and QRS complex with clinically relevant amplitude (as high as 2.47 of lead II). We also compared the limb potential amplitudes. Our records show that the left arm has a high amplitude as it is closer to the heart, and the left leg has a small amplitude for most of the patients. However, the left leg potential is not negligible for all the patients, and its amplitude with respect to lead II is in a range of [0.007 1.78] and with an average of 0.22 for all patients.

We used two terminologies to address the chest leads, first, precordial leads (V1:V6) referring to the current approach used for recording the chest leads, second, the true unipolar leads (UV1:UV6) addressing our approach used for recording the chest electrodes' potential. We show that the WCT signal is clinically relevant, and has an impact on precordial leads' shape and amplitude. Our preliminary results show that the true unipolar leads may be more sensitive for detecting cardiac diseases in the left anterior descending coronary artery in patients with NSTEMI.

References

1. Webster, J.G.: Medical instrumentation-application and design. J. Clin. Eng. **3**(3), 306 (1978)
2. Macfarlane, P.W., van Oosterom, A., Janse, M.: Comprehensive Electrocardiology (2010)
3. Waller, A.D.: A demonstration on man of electromotive changes accompanying the heart's beat. J. Physiol. **8**(5), 229–234 (1887)
4. Malmivuo, J., Plonsey, R.: Bioelectromagnetism Principles and Applications of Bioelectric and Biomagnetic Fields. Oxford University Press (1995). http://www.oxfordscholarship.com/view/10.1093/acprof:oso/9780195058239.001.0001/acprof-9780195058239
5. Fye, W.B.: A history of the origin, evolution, and impact of electrocardiography. Am. J. Cardiol. **73**(13), 937–949 (1994). http://linkinghub.elsevier.com/retrieve/pii/000291499490135X
6. Einthoven, W., Fahr, G., de Waart, A.: Über die Richtung und die manifeste Grösse der Potentialschwankungen im menschlichen Herzen und über den Einfluss der Herzlage auf die Form des Elektrokardiogramms. Pflüger's Archiv für die gesamte Physiologie des Menschen und der Tiere **150**(6–8), 275–315 (1913). http://link.springer.com/10.1007/BF01697566
7. Anon: The mechanism and graphic registration of the heart beat. JAMA: J. Am. Med. Assoc. **85**(23), 1832 (1925). http://jama.jamanetwork.com/article.aspx?doi=10.1001/jama.1925.02670230064033
8. Kossmann, C.E.: Unipolar electrocardiography of Wilson: a half century later. Am. Heart J. **110**(4), 901–904 (1985). http://linkinghub.elsevier.com/retrieve/pii/0002870385904843
9. Wilson, F.N., et al.: Electrocardiograms that represent the potential variations of a single electrode. Am. Heart J. **9**(4), 447–458 (1934). http://linkinghub.elsevier.com/retrieve/pii/S0002870334900934
10. Wilson, F.N., et al.: On Einthoven's triangle, the theory of unipolar electrocardiographic leads, and the interpretation of the precordial electrocardiogram. Am. Heart J. **32**(3), 277–310 (1946). http://doi.wiley.com/10.1111/j.1365-2818.1858.tb04542.x
11. Goldberger, E.: A simple, indifferent, electrocardiographic electrode of zero potential and a technique of obtaining augmented, unipolar, extremity leads. Am. Heart J. **23**(4), 483–492 (1942). http://linkinghub.elsevier.com/retrieve/pii/S000287034290293X
12. Burger, H.C.: The zero of potential: a persistent error. Am. Heart J. **49**(4), 581–586 (1955). http://linkinghub.elsevier.com/retrieve/pii/0002870355900764
13. Eckey, P., Fröhlich, R.: Archiv für Kreislaufforschung, pp. 349–356 (1938)
14. Burger, R.: Ueber das elektrische Feld des Herzens. Cardiology **3**(1–2), 56–138 (1939). https://www.karger.com/Article/FullText/164634
15. Dolgin, M., Grau, S., Katz, L.N.: Experimental studies on the validity of the central terminal of Wilson as an indifferent reference point. Am. Heart J. **37**(6), 868–880 (1949)
16. Bayley, R.H., et al.: The zero of potential of the electric field produced by the heart beat; the problem with reference to homogenous volume conductors. Circ. Res. **2**(1), 4–13 (1954). http://www.ncbi.nlm.nih.gov/pubmed/13116387
17. Bayley, R.H., Kinard, C.L.: The zero of potential of the electrical field produced by the heart beat; the problem with reference to the living human subject. Circ. Res. **2**(2), 104–111 (1954). http://www.ncbi.nlm.nih.gov/pubmed/13141373
18. Bayley, R.H., Schmidt, A.E.: The problem of adjusting the Wilson central terminal to a zero of potential in the living human subject. Circ. Res. **3**(1), 94–102 (1955). http://circres.ahajournals.org/cgi/doi/10.1161/01.RES.3.1.94
19. Okamoto, Y., Mashima, S.: The zero potential and Wilson's central terminal in electrocardiography. Bioelectrochem. Bioenerg. **47**, 291–295 (1998)
20. Wolferth, C.C., Livezey, M.M.: A study of methods of making so-called unipolar electrocardiograms. Am. Heart J. **27**(6), 764–782 (1944). https://www.sciencedirect.com/science/article/pii/S000287034490311X. Accessed 8 Feb 2019
21. Dower, G.E., Osborne, J.A., Moore, A.D.: Measurement of the error in Wilson's central terminal: an accurate definition of unipolar leads. Br. Heart J. **21**, 352–60 (1959). http://www.ncbi.nlm.nih.gov/pubmed/13817890

22. Fischer, G., et al.: On modeling the Wilson terminal in the boundary and finite element method. IEEE Trans. Biomed. Eng. **49**(3), 217–224 (2002)
23. Lynn, M.S., Timlake, W.P.: The use of multiple deflations in the numerical solution of singular systems of equations, with applications to potential theory. SIAM J. Numer. Anal. **5**(2), 303–322 (1968). http://epubs.siam.org/doi/10.1137/0705027
24. Wach, P., et al.: Magnetic source imaging in the human heart: estimating cardiac electrical sources from simulated and measured magnetocardiogram data. Med. Biol. Eng. Comput. **35**(3), 157–166 (1997). http://link.springer.com/10.1007/BF02530031
25. Miyamoto, N., et al.: The absolute voltage and the lead vector of Wilson's central terminal. Jpn. Heart J. **37**(2), 203–214 (1996). http://www.ncbi.nlm.nih.gov/pubmed/8676547
26. Miyamoto, N., et al.: On the potential of the Wilson central terminal with respect to an ideal reference for unipolar electrocardiography. J. Electrocardiol. **28**(4), 336–337 (1995). http://linkinghub.elsevier.com/retrieve/pii/S0022073605800548
27. Hoekema, R., Uijen, G.J., van Oosterom, A.: On selecting a body surface mapping procedure. J. Electrocardiol. **32**(2), 93–101 (1999). https://linkinghub.elsevier.com/retrieve/pii/S0022073699900882
28. Gargiulo, G.D.G., et al.: On the "zero of potential of the electric field produced by the heart beat". A machine capable of estimating this underlying persistent error in electrocardiography. Machines **4**(4), 18 (2016). http://www.mdpi.com/2075-1702/4/4/18
29. Gargiulo, G.D.: True unipolar ECG machine for Wilson central terminal measurements. BioMed Res. Int. **2015**, 586397 (2015). http://www.ncbi.nlm.nih.gov/pubmed/26495303
30. Gargiulo, G.D., et al.: Towards true unipolar bio-potential recording: a preliminary result for ECG. Physiol. Meas. **34**(1), N1–N7 (2013). http://www.ncbi.nlm.nih.gov/pubmed/23248178
31. Gargiulo, G.D., et al.: Unipolar ECG circuits: towards more precise cardiac event identification. In: 2013 IEEE International Symposium on Circuits and Systems (ISCAS2013), pp. 662–665. IEEE (2013). http://ieeexplore.ieee.org/lpdocs/epic03/wrapper.htm?arnumber=6571932
32. Gargiulo, G.D., et al.: A 9-independent-leads ECG system from 10 electrodes: a practice preserving WCT-less true unipolar ECG system. In: 2015 IEEE Biomedical Circuits and Systems Conference (BioCAS), pp. 1–4. IEEE (2015). http://ieeexplore.ieee.org/document/7348300/
33. Webster, J.G.: Medical Instrumentation Application and Design. Wiley (2009)
34. Winter, B.B., Webster, J.G.: Reductionl of interference due to common mode voltage in biopotential amplifiers. IEEE Trans. Biomed. Eng. **30**(1), 58–62 (1983)
35. BurrBrown: INA 118 Precision low power Instrumentation Amplifier. Technical data. http://www.ti.com/lit/ds/symlink/ina118.pdf (2000)
36. BurrBrown: INA116. Technical data. http://www.burbrown.com (2008)
37. Gargiulo, G., et al.: True unipolar ECG leads recording (without the use of WCT). Heart Lung Circ. **22**, S102 (2013)
38. Gargiulo, G., Bifulco, P., et al.: Problems in assessment of novel biopotential front-end with dry electrode: a brief review. Machines **2**(1), 87–98 (2014). http://www.mdpi.com/2075-1702/2/1/87/
39. Gargiulo, G.D., et al.: Towards true unipolar ECG recording without the Wilson central terminal (preliminary results). Physiol. Meas. **34**(9), 991–1012 (2013). http://stacks.iop.org/0967-3334/34/i=9/a=991?key=crossref.3ee57f77157cc5fa56247c2775f2317d
40. Fisher, W., et al.: Event-related potentials in impulsively aggressive juveniles: a retrospective chart-review study. Psychiatry Res. **187**(3), 409–413 (2011). http://linkinghub.elsevier.com/retrieve/pii/S0165178111001661
41. Madias, J.E.: On recording the unipolar ECG limb leads via the Wilson's vs the Goldberger's terminals: aVR, aVL, and aVF revisited. Indian Pacing Electrophysiol. J. **8**(4), 292–297 (2008). http://www.ncbi.nlm.nih.gov/pmc/articles/PMC2572021/
42. Undar, A., Calhoon, J.H., da Rocha, A.: Medical instrumentation: application and design. Control Eng. Pract. **5**(2), 295–296 (1997). http://linkinghub.elsevier.com/retrieve/pii/S0967066197900307
43. Gargiulo, G., Bifulco, P., et al.: Open platform, 32-channel, portable, data-logger with 32 PGA control lines for wearable medical device development. Electr. Lett. **50**(16), 1127–1129 (2014). https://digital-library.theiet.org/content/journals/10.1049/el.2014.1791

44. Gargiulo, G., Moeinzadeh, H.: Wilson central terminal ECG database. PhysioNet. https://alpha.physionet.org/content/wctecgdb/ (2019)
45. Bacharova, L., et al.: Where is the central terminal located? In search of understanding the use of the Wilson central terminal for production of 9 of the standard 12 electrocardiogram leads. J. Electrocardiol. **38**(2), 119–127 (2005). http://www.ncbi.nlm.nih.gov/pubmed/15892021
46. Goldberger, E.: The validity of the Einthoven triangle hypothesis. Am. Heart J. **29**(3), 369–377 (1945). https://www.sciencedirect.com/science/article/pii/0002870345903383. Accessed 4 Mar 2019
47. Burger, H.C., van Brummelen, A.G.W., van Herpen, G.: Heart-vector and leads. Am. Heart J. **61**(3), 317–323 (1961). http://linkinghub.elsevier.com/retrieve/pii/0002870361906019
48. Einthoven, W.: Die galvanometrische Registrirung des menschlichen Elektrokardiogramms, zugleich eine Beurtheilung der Anwendung des Capillar-Elektrometers in der Physiologie. Pflüger, Archiv für die Gesammte Physiologie des Menschen und der Thiere **99**(9–10), 472–480 (1938). http://link.springer.com/10.1007/BF01811855
49. Gargiulo, G.D.G., et al.: On the Einthoven triangle: a critical analysis of the single rotating dipole hypothesis. Sensors **18**(7), 2353 (2018). http://www.mdpi.com/1424-8220/18/7/2353
50. Farrell, R.M., et al.: Effects of limb electrode placement on the 12- and 16-lead electrocardiogram. J. Electrocardiol. **41**(6), 536–545 (2008). http://dx.doi.org/10.1016/j.jelectrocard.2008.07.023

Novel Methodology for Cardiac Arrhythmias Classification Based on Long-Duration ECG Signal Fragments Analysis

Paweł Pławiak and Moloud Abdar

Abstract According to the reports published by various organizations, it can be seen that about 50 million people are at risk of cardiovascular diseases (CVDs) around the world. Moreover, different types of heart diseases are the most common causes of mortality. This chapter, therefore, investigates a cardiac disorders database (ECG) with 17 classes (normal sinus rhythm, the rhythm of the pacemaker, and fifteen arrhythmias) using a novel classification methodology. The data set is based on long-duration ECG signal fragments. The Electrocardiography (ECG) is a very popular process to record the electrical activity of the heart during specific time. Even though there are a lot of studies in the literature, however, there are many other open issues in the topic. The main objective of the current study is to present a new and efficient methods in order to do automatic recognition of myocardium dysfunctions. The proposed methods are introduced that can be used in different situations such as mobile devices, telemedicine, cloud computing, and finally supporting preventive and supportive treatment of CVDs. Since the performance of proposed algorithms is very important, the time duration, as an additional criterion, is also analyzed in real time. The obtained outcomes demonstrate that our methodology has outstanding performance compared to the methods presented in the literature. This study uses 744 fragments of ECG signal database related to 29 patients from the MIH-BIH Arrhythmia database (only for one lead—MLII). By using Welch's method and a discrete Fourier transform, the spectral power density is predicted in order to increase the characteristic features of the ECG signals. The research presents a new evolutionary-neural system, based on the SVM classifier. The proposed method shows good performance with high sensitivity (90.19%), specificity (99.39%), and accuracy (98.85%).

P. Pławiak (✉)
Faculty of Physics, Mathematics and Computer Science, Cracow University of Technology, Warszawska 24 st., 31-155 Krakow, Poland
e-mail: plawiak@pk.edu.pl; plawiak.pawel@gmail.com

M. Abdar
Département d'Informatique, Université du Québec a Montréal, Montréal, QC, Canada
e-mail: abdar.moloud@courrier.uqam.ca; m.abdar1987@gmail.com

G. Naik (ed.), *Biomedical Signal Processing*, Series in BioEngineering,
https://doi.org/10.1007/978-981-13-9097-5_11

1 Introduction

The Electrocardiography (ECG) is a very popular diagnostic tool for diagnosis of heart disease, which is an inexpensive and non-invasive tool [7, 65, 69]. For this reason, the extensive range of applications of ECG signal analysis can be observed. The ECG signals can reveal very important information about the rhythm and function of the heart. This is a very important point about ECG because it reveals very essential information while it is not expensive. In other words, the ECG tool benefits both physicians (with valuable information) and patients (with low cost). Thus, ECG records can be considered as a good resource for doing research on heart diseases.

The statistics published by accredited organizations (e. g., World Health Organization: WHO) clearly indicate that cardiovascular diseases are the number one reason for death in the globe [3, 7]. According to the reports published by WHO, about 17.7 million people annually die, which means 31% of all global deaths happened because of CVDs in 2015 [2]. The significant point is that about 80% of CVDs deaths are occurred because of heart attacks and/or strokes. Another point is that above 75% of CVD mortalities happen in middle-income and low-income countries. Based on these statistics, the estimation of CVDs patients may reach up to approximately 23.6 million in 2030 [61, 88]. Moreover, the American Heart Association (AHA) expressed that different kinds of heart diseases are the number one killer for all American individuals [1]. This constitutes an alarm for governments and researchers to find some solution to reduce the negative and destructive effects of this disease. In recent decades, computer-aided diagnostic systems (CADSs) have been significantly applied to different types of heart diseases.

The computer-aided diagnostic system (CADS) uses different machine learning (ML) and data mining (DM) techniques to improve the quality of diagnosis of different medical subjects (heart disease [8, 60, 66, 71], Parkinson's disease [5, 39, 48, 89], bioinformatics [20, 23, 78, 79], breast cancer [12, 34, 35, 50], liver disease [4, 6, 41, 45], hepatocellular carcinoma [46] etc.). In each of these subjects, various methods have been applied and these methods showed different performances in each case study. This means that the performance of ML algorithms depends on various circumstances and also data types. For this reason, attention to different aspects of medical databases can be helpful in reaching a better point of outcomes. There are many works in the litterateur applied different algorithms on ECG data sets.

Sannino and Pietro [69] proposed a classification-based approach to address the problem related to ECG beat classification. To this end, a Deep Neural Network (DNN) method with 7 hidden layers is applied to the MIT-BIH Arrhythmia data set. The best accuracy using the proposed method was 99.09% for testing set whereas in whole data was 99.68%. Due to the importance of coronary artery disease (CAD), authors in [2] used the decomposition of ECG signals to provide an automated characterization and classification approach. In this regard, Empirical Mode Decomposition (EMD), Discrete Wavelet Transform (DWT), and Discrete Cosine Transform (DCT) were chosen and compared. Moreover, they used the highly ranked coefficients into the K-Nearest Neighbor (KNN) algorithm. The proposed methodology showed very

good performance with 99.7% sensitivity, 98.5% specificity, and 98.5% accuracy. Varatharajan et al. [80] applied the Linear Discriminant Analysis (LDA) technique to decrease the features in ECG data. In addition, to improve the performance of traditional SVM, a weighted kernel function approach was used with SVM. This new model was classified as various heartbeat levels, such as Premature Ventricular Contraction (PVC), Premature Atrial Contractions (PACs). Left Bundle Branch Block (LBBB), and Right Bundle Branch Block (RBBB).

Similarly, authors in [22] investigated the ECG data set authentication and also gender recognition. In this regard, several algorithms were used. The highest accuracy for ECG data set authentication was about 98%, whereas the best accuracy for gender recognition was 94%. In another research [26], studied compressive sensing (CS) due to its importance in the long-term ECG telemonitoring. Based on subspace-based representation, the low-complexity framework of Privacy-Preserving Compressive Analysis (PPCA) is proposed. The accuracy of the model was 96.05%. The ECG heartbeat signal clustering approach is proposed by Rodríguez-Sotelo et al. [67]. The proposed approach showed good results with a specificity of 98.69%, sensitivity of 85.88%, and a general clustering performance of 95.04%. Yildirim [85] studied ECG signals using a novel Long-short term memory network (LSTM). The research introduced a deep bidirectional LSTM network-based wavelet sequence named DBLSTM-WS method. The proposed model was applied to the Ventricular Premature Contraction (VPC), Left Bundle Branch Block (LBBB), Normal Sinus Rhythm (NSR), Right Bundle Branch Block (RBBB), and Paced Beat (PB) heartbeats. The best accuracy of the model was 99.39.

Luz et al. [29] proposed a new methodology for cardiac arrhythmia signal data. The optimum-path forest (OPF) algorithm was applied to the ECG signals. The performance of OPF was compared with a multilayer artificial neural network (MLP), support vector machine (SVM), and Bayesian network. Their outcomes indicated that OPF classifier yielded better classification results compared with other methods applied in the research. In [30] reviewed several studies in the literature about the ECG signal preprocessing approaches and also the heartbeat segmentation methods. By using the Association for the Advancement of Medical Instrumentation (AAMI), they explained some of the databases applied for evaluation of techniques. The evidence indicated that the MIT-BIH data set (also called as MIT-BIH ARR DB) utilized in most of the studies, was an imbalance. This is very important to have balance data since majority class/classes can affect the results. This means that since we have imbalance data the results are not trustable. Alickovic and Subasi [11] examined the design of an efficient recognition approach for ECG database in order to diagnose heart disease. To this end, the multiscale principal component analysis (MSPCA) and the autoregressive (AR) modeling were applied for noise reduction of the ECG signals and for extracting features, respectively. It should be noted that the Burg Method was applied with for AR parameter estimation which named AR Burg. The model showed very high performance with 99.93% when SMO-SVM method was used with MSPCA and AR Burg.

Banerjee and Mitra [16] investigated ECG signals using machine learning techniques. They, therefore, used the cross wavelet transform (XWT) analysis approach.

After using XWT, wavelet cross spectrum (WCS) and wavelet coherence (WCOH) were yielded. Their results demonstrated that combining these three approaches can show very good outcomes with 97.6% accuracy, 97.3% sensitivity, and 98.8% specificity. Authors in [25] proposed a novel machine learning approach by using a combination of projected and dynamic features. Then, using the discrete cosine transform (DCT) each row was transformed. The study used the support vector machine (SVM) as a classifier to cluster heartbeats either into one of 15 or 5 classes. The best accuracy for "class-based" assessment strategy was 98.46% while the highest accuracy for the "subject-based" assessment strategy was 93.1%. A Study [10] applied a Gaussian mixture modeling (GMM) to coordinate the possibility density function of heartbeats. Moreover, the expectation maximization (EM) approach was also used. The overall accuracy for the "class-oriented" scheme was 99.70% whereas the accuracy for "subject-oriented" scheme was 96.15%. Kalgotra et al. [44] presented an algorithm for automatic recognition of 5 classes (Normal, Atrial Fibrillation, Atrioventricular Block, Sinus Bradycardia and Sinus Tachycardia) with 91% accuracy. The presented solution is used in a commercial mobile device to control the heart condition of users.

The most popular topic of ECG signal analysis in the diagnosis of cardiac arrhythmia based on the MIT-BIH arrhythmia database. The works on this subject are presented below. Yildirim [86] proposed recognition system for detection and classification of heartbeats in ECG signals. The new method is based on detection (wavelet transform) and segmentation of QRS complexes. Then the Online Sequential Extreme Learning Machine classifier was used to recognize the heartbeats. The trained model achieved an accuracy of 98.51% in recognition of 5 AAMI classes from MIT-BIH arrhythmia data set. Martis et al. [54] described a method for automatic detection of 3 classes of arrhythmia: normal, AF and AFL of ECG signal. Four methods of feature extraction were compared: the principal components (PCs) of discrete wavelet transform (DWT) coefficients, the independent components (ICs) of DWT coefficients, the PCs of discrete cosine transform (DCT) coefficients, and the ICs of DCT coefficients. Three classifiers have also been tested in this paper: K-nearest neighbor (KNN), decision tree (DT), and artificial neural network (ANN). MIT-BIH arrhythmia and atrial fibrillation databases were used. The best result, 99.45% accuracy, was obtained for DCT with ICA and kNN and 10-fold cross validation. de Chazal et al. [31] presented an automated method for classifying 5 AAMI heart beats classes (normal beat, ventricular ectopic beat (VEB), supraventricular ectopic beat (SVEB), fusion of a normal and a VEB, or unknown beat type). The MIT-BIH arrhythmia database was used in the study, which was divided according to the subject-oriented validation scheme (inter-patient paradigm). The work focuses on the extraction of features based on ECG morphology, heartbeat intervals, and RR-intervals. The authors achieved an accuracy of 83%, obtained with linear discriminant analysis. Acharya et al. [9] applied a novel method of deep learning to classify heartbeats. They obtained an accuracy of 94.03% in recognition 5 AAMI classes from the MIT-BIH arrhythmia database using the 9-layer deep convolutional neural network (CNN). Oh et al. [58] introduced the Novel modified U-net model for automated arrhythmia diagnosis. They proposed autoencoder to diagnose 5 classes: normal sinus beats, atrial premature beats (APB),

premature ventricular contractions (PVC), left bundle branch block (LBBB) and right bundle branch block (RBBB) from the MIT-BIH arrhythmia database. They have achieved accuracy equal to 97.32% using a 10-fold cross-validation strategy. Llamedo and Martinez [51] proposed a simple heart beat classifier based on ECG feature models selected. The authors have considered features from the RR series, the ECG samples, and different scales of the wavelet transform. In the research, they used 3 databases: the MIT-BIH Arrhythmia, the MIT-BIH Supraventricular Arrhythmia, and the St. Petersburg Institute of Cardiological Technics (INCART). A floating feature selection algorithm achieved an accuracy of 93%. Ye et al. presented in paper [84] a new algorithm for heartbeat classification based on morphological and dynamic features. Wavelet transform, independent component analysis (ICA) and RR interval information were used to extract the features. Data from the MIT-BIH arrhythmia database were used. Support vector machine classifier achieved outcomes equal to 86.4% in classifying 5 AAMI classes, for subject-oriented evaluation. Yang et al. described in the paper [82] novel heartbeat recognition method. MIT-BIH arrhythmia database with 5 AAMI classes was used in the research. The main contribution was to apply principal component analysis network (PCANet) for feature extraction. Linear support vector machine (SVM) achieved a score of 97.08% accuracy. Bazi et al. in study [17] used 2 kinds of features: (a) ECG morphology features and (b) ECG wavelet features with QRS complexes. The authors used MIT-BIH arrhythmia database. For SVM, they achieved an accuracy of 91.8%, for 5 AAMI classes and subject-oriented scheme. Zhang and Luo described in [91] multi-lead fused classification schema. The ECG features adopted include inter-beat and intra-beat intervals, amplitude morphology, area morphology, morphological distance, and wavelet coefficients. MIT-BIH arrhythmia database with 5 AAMI classes was used. The proposed method has obtained an accuracy of 87.88%. Elhaj et al. [36] proposed support vector machine and neural network methods with radial basis function to arrhythmia recognition and classification. In this work they were combined nonlinear and linear features (high order statistics, cumulants, independent component analysis, principal component analysis of discrete wavelet transform coefficients). Combined SVM and radial basis function method achieved 98.91% accuracy based on the MIT-BIH arrhythmia database and 10-fold cross-validation in classifying 5 AAMI classes. Zubair et al. [92] introduced an ECG beat classification system using convolutional neural networks (CNN). In this work MIT-BIH arrhythmia database was used, and 5 AAMI classes were recognized. An accuracy of 92.7% was obtained.

This research studies a cardiac disorders database (ECG) with 17 classes (normal sinus rhythm, the rhythm of the pacemaker, and fifteen cardiac arrhythmias). The data set includes 744 fragments of ECG signals related to 29 patients from the MIH-BIH Arrhythmia database, MLII. This study, therefore, has three main aims that we will explain in the following of the research. The first aim to propose an accurate and efficient recognition method to classify myocardium dysfunctions based on ECG signals. Secondly, the proposed method can be used in tele-medicine and mobile devices. Finally, the new method is universal, which means that it can be used for general population not only for individuals. To this end, the major contributions, as our novelties, of the study can be expressed as follows. The first innovative element

is related to the genetic training and optimization of classifiers which means the methods will have better training step by using GA. Moreover, current research optimized feature extraction using the Welch method and the discrete Fourier transform approach. These approaches strengthen the characteristic features of ECG signals by predicting the power spectral density. It should be expressed that data analysis in the frequency domain is analyzed for several Hamming window widths. As a point, the described research in this chapter was continued in some of our prior papers [60–62, 87], which will be explained in the following of the research briefly.

2 Data Set Used

As discussed earlier, we used the MIH-BIH Arrhythmia data set [56], which publicly available at the PhysioNet [40]. The database includes the information of 29 patients which 15 were female, and 14 of them were male. The range of age for female is 23–89 while the range of males is 32–89 years old. The ECG data is categorized into 17 classes in which one class is related to normal sinus rhythm, one class is related to pacemaker rhythm, and the rest of classes (15 classes) are related to 15 different types of cardiac arrhythmias. The sampling frequency of 360 [Hz] and also a gain of 200 [adu/mV] were used for all ECG signals. Moreover, the database consists of randomly chosen signals (744 ECG signal fragments) which have 10 s long, 3600 samples as well as the do not have an overlapping issue. Additionally, all of these ECG signal fragments are derived from one lead (MLII).

A description of the collected signals (number of ECG signal fragments for all classes from 1.34 to 25.94%, Imbalance Ratio (IR) = 19) is given in Table 1, which presents the analyzed heart disorders, number of signal fragments collected for each disorder, number of patients from whom the ECG data were derived. Moreover, division of signal fragments into training and test sets for 2 types of stratified cross-validation.

An important aspect is the appropriate balance of data. The number of signal fragments corresponding to physiological heart evolutions should not be significantly greater than the number of ECG signals for the other classes. This may cause an artificial increase in the recognition efficiency of cardiac disorders.

Obtaining a greater number of suitable ECG signal fragments for the rarest disorders (10 or 11 ECG signal fragments in Table 1) from the MIT-BIH Arrhythmia database for the MLII lead was not possible.

Collected data from all 48 records is not possible because of records no. 102 and 104 do not have signals from MLII lead. In record no. 232, the entire signal containing rhythm “Sinus bradycardia” (not recognized in the article).

Table 1 A description of the database with the selected ECG signals along with the allocation of signals to the training and testing sets related to 4-fold and 10-fold cross-validation

No.	Class	Fragments number	Patients number	4-fold cross validation				10-fold cross-validation			
				Groups 1–3		Group 4		Groups 1–9		Group 10	
				Training set	Test set	Training set	Test set	Training set	Test set	Training set	Test set
1	Normal sinus rhythm	193	14	135	58	174	19	174	19	171	22
2	Atrial premature beat	58	8	41	17	51	7	53	5	45	13
3	Atrial flutter	17	2	12	5	15	2	16	1	9	8
4	Atrial fibrillation	93	3	65	28	84	9	84	9	81	12
5	Supraventricular tachyarrhythmia	11	3	8	3	9	2	10	1	9	2
6	Pre-excitation (WPW)	21	1	15	6	18	3	19	2	18	3
7	Premature ventricular contraction	78	9	55	23	69	9	71	7	63	15
8	Ventricular bigeminy	44	4	31	13	39	5	40	4	36	8
9	Ventricular trigeminy	13	4	9	4	12	1	12	1	9	4
10	Ventricular tachycardia	10	3	7	3	9	1	9	1	9	1
11	Idioventricular rhythm	10	1	7	3	9	1	9	1	9	1
12	Ventricular flutter	10	1	7	3	9	1	9	1	9	1
13	Fusion of ventricular and normal beat	11	3	8	3	9	2	10	1	9	2
14	Left bundle branch block beat	88	2	62	26	78	10	80	8	72	16
15	Right bundle branch block beat	47	2	33	14	42	5	43	4	36	11
16	Second-degree heart block	10	1	7	3	9	1	9	1	9	1
17	Pacemaker rhythm	30	1	21	9	27	3	27	3	27	3
Sum		744	29	523	221	663	81	675	69	621	123

3 Methods

This section presents the subsequent stages of processing and analysis of the ECG signals along with the methods utilized.

3.1 Step I—Preprocessing with Normalization

The aim of this stage was to unify the data from various ECG devices (gain reduction, frequency uniformity, and constant component reduction) and from different patients (normalization of signal amplitude).

In the research, the data were properly organized, and three preprocessing (normalization) paths were tested:

- **no normalization**:
  - reduce the gain
  - reduce the constant component (mean signal value)
- **rescaling**:
  - reduce the gain
  - reduce the constant component
  - rescale the signal to the range of $[-1, 1]$
  - reduce the constant component
- **standardization**:
  - reduce the gain
  - reduce the constant component
  - standardize the signal (mean signal value = 0 and signal standard deviation = 1)

Rescaling was performed on all the ECG signal fragments for a given disorder for a given patient.

Therefore, the following techniques were applied in order to attain fulfill favorable impacts. The reduction of gain can be calculated by using Eq. 1.

Reduction of gain:

$$S = \frac{S_g}{g} \tag{1}$$

where:

S represents the value of ECG after gain reduction,
S_g represents the value of ECG before gain reduction,
g represents the value of gain of device that ECG signal was recorded.

Moreover, the reduction of a constant component can be computed by Eq. 2.

Reduction of constant component:

$$\mu = \frac{1}{n} \cdot \sum_{i=1}^{n} x_j(i) \tag{2}$$

where:

n the number of ECG signal samples j,
i represents the index of consecutive ECG signal samples,
j represents the index of consecutive ECG signals.

Rescaling to the range $[-1, 1]$ is another preprocessing approach used which Eq. 3 shows how it can be calculated:
Rescaling to the range $[-1, 1]$:

$$\bar{x}_j(i) = 2 \cdot \left(\frac{x_j(i) - min(x_j)}{max(x_j) - min(x_j)} \right) - 1 \tag{3}$$

where:

i indicates the index of consecutive ECG signal samples,
j indicates the index of consecutive ECG signals,
$min(x_j)$ indicates the minimum signal amplitude value,
$max(x_j)$ indicates the maximum signal amplitude value.

Similarly, we used standardization approach as shown in Eqs. 4 and 5
Standardization:

$$\hat{x}_j(i) = \frac{x_j(i) - \mu}{\sigma} \tag{4}$$

$$\sigma = \sqrt{\frac{1}{n-1} \sum_{i=1}^{n} (x_j(i) - \mu)^2} \tag{5}$$

where:

i is the index of consecutive ECG signal samples,
j is the index of consecutive ECG signals,
μ is the mean signal value j, which can be calculated by Eq. 2,
σ is the standard deviation of the signal j, which can be calculated by Eq. 5.

3.2 Step II—Feature Extraction

The aim of this stage was to extract and strengthen the characteristic features of the signal and thereby increase the recognition efficiency for the dysfunctions.

Due to the periodic nature of the ECG signal, the extraction of features based on the estimation of the power spectral density [72] of the ECG signal was performed using the Welsh method [81] and the discrete Fourier transform (DFT) [72]. Then, to normalize the frequency components of the power spectral density, the transformed signal was logarithmized.

To this end, the following techniques were selected for this phase of research.

Power spectral density (PSD) The PSD of the signal is a solution to explain the power present in the signal as a frequency function. In other words, the PSD explains how much signal arises per unit bandwidth. Generally, the PSD can be commonly represented in watts [$power$] per hertz (W/Hz), which can be obtained by using the Fourier transform.

Welch's method This is one of the approaches to predict the PSD function of the signals at different frequencies. The periodogram is computed by calculating the discrete Fourier transform and after that, calculating the squared magnitude of the outcome. Finally, the individual periodograms are averaged, that decreases the variance related to the individual power measurements.

Periodogram is a diagram that represents the most important periodic regularities in different signals. The periodogram, as one of the nonparametric techniques, helps to find out the estimation of the power spectral density of a signal. The diagrams have peaks that correspond to periods (cycles). It should be noted that the closest correlate with the data.

Fourier discrete transform The Fourier transform is a very important function of time (a signal) that is used in order to present different signal distribution into sinusoidal and cosine waveforms. Therefore, it transforms the signals from the time domains to the frequency domains. It should be explained that a discrete Fourier transform is a result of using the counterpart of the Fourier transform related to the discrete (digital) signals and periodic signals. The Fourier transform can be calculated according to Eq. 6

$$X(k) = \sum_{n=0}^{N-1} x(n) \cdot e^{-j \cdot \frac{2 \cdot \pi \cdot n \cdot k}{N}} \tag{6}$$

where:

- $x(n)$ represents the nth sample of the discrete signal,
- k represents the line number (in other words: frequency component number); $k = 0, ..., N - 1$,
- N represents the number of signal samples.

Hamming window is a function to describe the time window in order to determine the manner of sampling from the signal data.

Series of logarithms of signals This is a form in order to normalize different features and/or attributes of the signals which are used as inputs for various classifiers. It can be calculated by Eq. 7:

$$x(n) = 10 \cdot log_{10}(P_{xx}(n)) \tag{7}$$

where:

n represents the index of consecutive ECG signal samples,
$x(n)$ represents the series of logarithms of ECG signal,
$P_{xx}(n)$ represents the power spectral density.

To calculate the power spectral density, 3 Hamming window widths (Experiment No. 1: 128, 256, and 512 samples) or 4 Hamming window widths (Experiments No. 2 and No. 3: 128, 256, 512, and 1024 samples) were applied. The Hamming window widths were selected experimentally, with 6 tested widths, therein rejecting windows with 768 and 1536 sample widths. The subsequent values of the tested Hamming window widths were determined using a geometric string (multiples of 2).

In all experiments, as a result of the feature extraction, from a single fragment of the ECG signal, a feature vector with a length of 4001 frequency components was obtained.

To estimate the power spectral density (in all experiments), the following parameters were used: the number of common samples for 2 adjacent signal fragments equal to half of the width of the adopted Hamming window and a DFT vector length equal to 8000 as well as a sampling frequency equal to 360 [Hz].

3.3 Step III—Feature Selection

The aim of this stage was to reduce the data (and thus accelerate the computations) and both extract and strengthen the characteristic features of the signal by reducing the features that carry redundant and erroneous information.

In order to solve and optimize different real problems, different types of Genetic algorithms (GA) [42, 68] can be used which are based on natural evolution. Generally, the procedure of GAs is based on two mechanisms, including natural selection and inheritance. Gas Belong to a larger family of methods called evolutionary algorithms. Indeed, GAs benefit from the evolutionary principle of survival of the best adapted individuals.

In the research, a genetic algorithm (GA) [68] was used for the feature selection. The genes in the population of individuals represented subsequent single features/attributes of the signal entered as input for the classifiers.

Genes could take on the following values:

- 0—means that reject a given feature or
- 1—means that accept a given feature.

The genetic algorithm creates subsequent populations of individuals based on the fitness function and optimizes the efficiency of the classifiers through the selection of the most valuable features of the ECG signal.

3.4 Step IV—Cross-Validation

The aim of this stage was to eliminate the effect of over-fitting the designed classifiers, thereby increasing the effect of generalizing knowledge and increasing the reliability of the obtained results.

A study [47] mentioned there are different types of approaches for choosing training and testing sets: k-fold cross-validation, hold-out, leave-one-out cross-validation, bootstrap, and resubstitution.

In this study, we use stratified k-fold cross-validation (CV) [47] in order to choose the elements for the training and testing sets. Two types of cross-validation were used to create the training and testing sets: stratified 4-fold cross-validation (4 CV) and stratified 10-fold cross-validation (10 CV).

Applying a stratified 10-fold and stratified 4-fold cross-validation method that is more consistent with the subject-oriented validation scheme (inter-patient paradigm) than class-oriented validation scheme (intra-patient paradigm) [10, 30, 31]. Table 1 shows the allocation of ECG signal fragments (divided into disorders) to training and test sets for both types of validation. The reference matrices with the expected responses were created to enable a comparison of the final results. They contained the required outputs of the classifiers. The reference matrices for both variants of the cross-validation are not shown in this article because of their known form.

3.5 Step V—Machine Learning Algorithms

This main aim of current research is to present an efficient and accurate approach to investigate heart disorders based on ECG signal fragments. In order to reach this point, some cases have a remarkable impact on the final results, such as the design and selection of appropriate parameters and subsequently retraining and testing the systems using machine learning algorithms [13, 19, 37]. For this research, 4 well-known classifiers were chosen which are: Probabilistic Neural Network (PNN), Radial Basis Function Neural Network (RBFNN), Support Vector Machine (SVM, nu-SVC), and k-Nearest Neighbor (kNN).

It should be mentioned that some other classifiers such as Decision Trees (DTs) [64], Discriminant Analysis [55], the Takagi-Sugeno Fuzzy System [76], Multi-Layer Perceptron (MLP) and Recurrent Neural Networks (RNN) [63, 77]) were also tested. These algorithms had worse results and are not presented in this article due to space limitations.

The classification of the samples with the machine learning methods used in the present research was based on the Winner-Takes-All (WTA) rule. This means that the classification algorithm, depending on the value of certain algorithm-dependent response parameters, always assigns exactly one class identifier to a test sample, independent of the number of classes.

3.5.1 Probabilistic Neural Network (PNN)

The Probabilistic Neural Network (PNN) [63, 77], as an artificial neural network, is one of the well-known machine learning classifiers developed by Specht [75]. The PNN can be applied to unravel different classification problems. The algorithm utilizes the kernel approximation approach in order to predict the probability density function for various categories (classes). Mainly, the PNN includes at least three major layers including an input layer, radial layer and finally output layer. Neurons in the radial layer have several parameters that are copied from the training data directly. Each of them corresponds to only one item. Accordingly, neurons in the output layer are responsible, to sum up, the values generated by radial neurons. It should be noted that there is a proportional relationship between output values, kernel estimators and also probability density functions for various classes in which can predict the probability of each class accordingly. The smoothing factor is the only parameter that has an impact on the learning procedure of the PNN.

3.5.2 Radial Basis Function Neural Network (RBFNN)

The Radial Basis Function Neural Network (RBFNN) algorithm is another type of artificial neural network that initially introduced by Broom head and Lowe [21]. Generally, the RBFNN has only one hidden layer which consists of several radial neurons. By using hyperspheres, which can be determined by their centers and radii, separates the space related to the input signals. A Gaussian function is the response surface of a single radial neuron which includes a vertex placed above the center as well as a decreasing value of the function along with the distance from this point. The slope of the Gaussian function can be modified. The radial neuron is defined by two things: its center and a parameter named “radius”. By using N numbers a point in an N-dimensional space can be defined that is entirely relevant to the number of neuron weights.

3.5.3 Support Vector Machines (SVMs)

The Support Vector Machines (SVMs) have different types that the first type of SVM was developed by Vapnik [27]. The LIBSVM [24] is used as a library for MATLAB which is an open source tool for using different types of SVMs which we used nu-SVC method. The original SVM was applied to solve binary classification problems. In other words, SVM originally tries to find out an appropriate hyperplane to recognize two classes as the simplest problem. Indeed, there are many hyperplanes to fulfill this matter, however, to achieve the best results, the optimal hyperplanes should be found. As mentioned above, there are several types of SVMs such as C-SVC, nu-SVC, epsilon-SVR, nu-SVR. As studies [28, 70] showed, the effectiveness and performance of the SVM depend on two factors: type of SVM and also type of the kernel function. Some of the most important kernel functions are as follows:

linear, polynomial, Radial Basis Function (RBF—radial), Gaussian RBF (GRBF), and sigmoid. Different types of support Vector machines have been successfully applied in different subjects [15, 52, 57].

3.5.4 k-Nearest Neighbor (kNN)

The k-Nearest Neighbor (kNN) algorithm is a non-parametric technique used for classification and regression [14]. The kNN needs a distance metric in which the most well-known distance metric is the minimum-distance classifier (MDC). The MDC attempts to assign a classified variable to the most common category (class) amongst its neighbors, which means that it measures the distance from neighbors and classify them. There are different distance measures but Euclideandistance or Manhattandistance measures are the most commonly used distance measures. There are other measure metrics such as Chebyshev or Mahalonobis, however, less often used because of their higher computational cost. The learning process of the kNN includes choosing appropriate parameter k. Even though various approaches to select this parameter have been previously applied, but however, the cross-validation is the simplest approach and most commonly utilized technique.

3.5.5 Step VI—Optimization of Parameters

In order to improve the performance and also the efficiency of the proposed methodology, we aim to optimize the parameters using the following two techniques:

- Grid search [18]: hyperparameter optimization group is an approach that includes different methods. The Grid search is one of the hyperparameter optimization techniques, which includes a whole search of a specific subset of the space. The method optimizes the parameters of the classifiers.
- Genetic Algorithm: as it is previously explained in Sect. 3.3, this is a very well-known algorithm that can be used to optimize the parameters [42, 68].

3.6 Assumptions

The major assumptions of current research are listed as follows:

Assumption 1 Analysis of longer (10-s) ECG signal fragments, which contain multiple heart evolutions.

Assumption 2 Not applying signal filtering due to both the use of Welch's method and the genetic selection of features.

Assumption 3 Not applying the QRS complex detection and segmentation of the ECG signal.

Assumption 4 Applying stratified 10-fold and 4-fold cross-validation method that is more consistent with the subject-oriented validation scheme (inter-patient paradigm) than class-oriented validation scheme (intra-patient paradigm) [10, 30, 31]—the selection of elements for training and test sets based on signals from other patients.

Assumption 5 The classification of the samples was based on the Winner-Takes-All (WTA) rule.

Assumption 6 Investigating ECG signals fragments that include only one type of class but except for those normal sinus rhythm.

4 Experiments

Three experiments were conducted based on the analysis of the ECG signal according to the assumptions from the previous section.

4.1 First Experiment

The first experiment was characterized by the following:

- Applied feature extraction for 3 widths of the Hamming window (128, 256, and 512 samples).
- Applied the 4-fold cross-validation method.
- Applied the grid search method to optimize the classifier parameters.

4.2 Second Experiment

The second experiment was characterized by the following:

- Applied feature extraction for 4 widths of the Hamming window (128, 256, 512, and 1024 samples).
- Applied and compared two types of cross-validation methods: 4-fold and 10-fold cross-validation.
- Applied the genetic algorithm to optimize the classifier parameters.

4.3 Third Experiment

The third experiment was characterized by the following:

- Applied feature extraction for 4 widths of the Hamming window (128, 256, 512, and 1024 samples).
- Applied the 10-fold cross-validation method.
- Applied the genetic algorithm to optimize the classifier parameters.
- Applied the genetic algorithm for feature selection.

Experiment No. 3 obtained the highest recognition sensitivity for heart disorders (Table 4). Figure 1 shows the scheme of Experiment No. 3. Table 2 contains detailed information about the genetic algorithm and optimum values of parameters. Section 4.4 shows the procedure for the evolutionary-neural system from Experiment No. 3.

4.4 Evolutionary-Neural System

Experiment No. 3 designed an evolutionary-neural system that consisted of a classifier (e.g., SVM) trained by a genetic algorithm. The genetic algorithm, coupled with 10-fold cross-validation was used to select signal features and optimize the parameters of the classifier.

Procedure No. 1 presented the evolutionary-neural system algorithm.

4.5 Evaluation Criteria

In different subjects, evaluation of the proposed methods is highly recommended. This solution allows us to check the performance of the proposed methodology and compare its effectiveness with previous methods. This is also quite common in machine learning area to evaluate the performance of algorithms. This study, therefore, computes several coefficients (metrics) including [38, 73]: accuracy (ACC), sensitivity (SEN), specificity (SPE), k coefficient (or called Fleiss' κ), sum of errors (ERR_sum), acceptance feature coefficient (C_F), Optimization time (T_o), Training time (T_t), as well as Classification time (T_c). The metrics can be computed using Eqs. 9, 10, 11, 12 and 13.

The definitions of the calculated coefficients are as follows:

- **Accuracy**

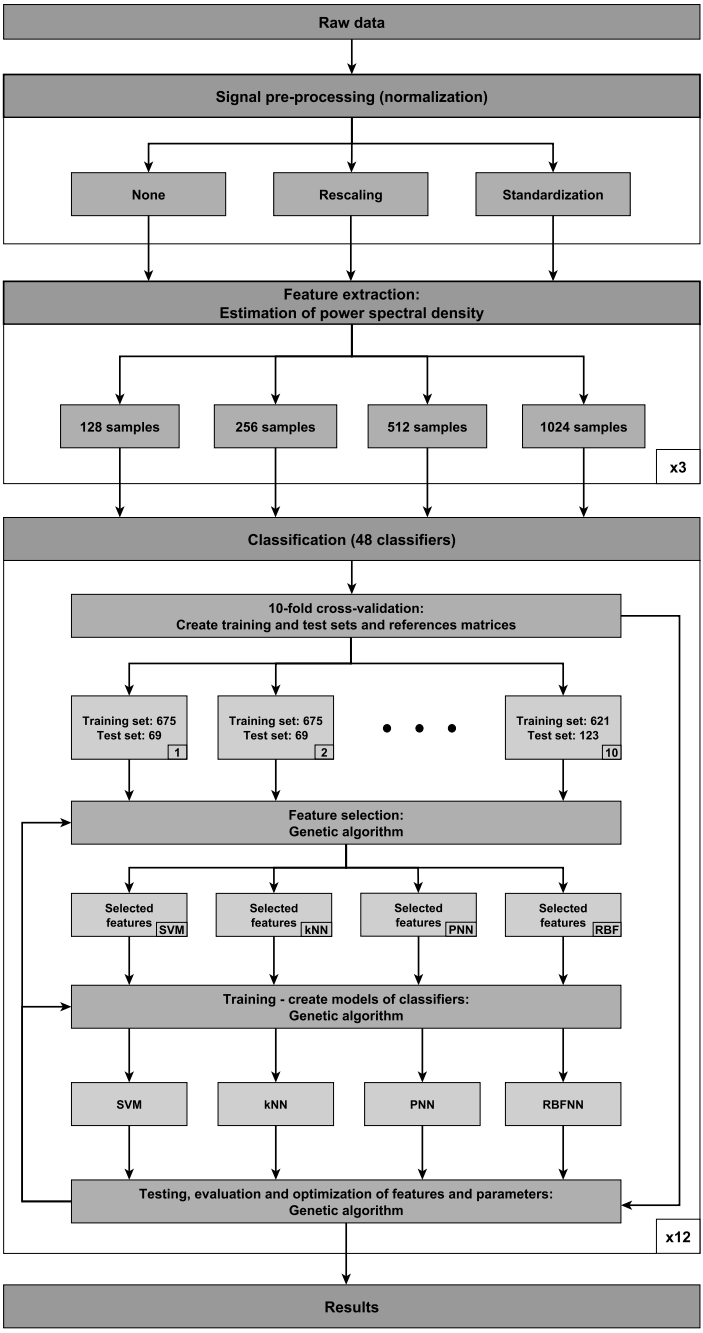

Fig. 1 Scheme of Experiment No. 3—genetic feature selection [61]

Table 2 Detailed information about Experiment No. 3 [61]

Feature selection and classifier parameter optimization

The *genetic algorithm* coupled with the 10-fold cross-validation method was used for feature selection and classifier parameter optimization

Genetic algorithm	• Number of individuals in the population: 50: • Type of gene representation: floating-point vectors • Chromosome construction of individual: Floating point vector of the form $[g_1, g_2, c_1, ..., f_{4001}]$ for SVM, where g_1—the first gene, which determines the value of the first parameter, γ, g_2—the second gene, which determines the value of the second parameter, ν, and $f_1, ..., f_{4001}$—4001 genes, with values in the range of [0, 1], which determine the feature selection, rounded to the values 1—acceptance of a feature—or 0—rejection of a feature. For the other classifiers (*kNN*, *PNN*, and *RBFNN*), the chromosome consists of one gene, g, which determines the value of one optimized parameter • Initial population: random, uniform • Range of the gene values for the initial population: the local range of gene values for each classifier parameter, consistent with the information given in the line *Optimized parameters*, experimentally selected based on the global (broader) range. For feature selection, the range is [0, 1] • Target value of fitness function: 0 • Maximum number of generations: 20 $\vee$ 30 • Type of crossover: intermediate; Probability of crossover: 0.7 • Type of mutation: uniform; Probability of mutation: 0.3 • Number of individuals in the current generation that are guaranteed to survive to the next generation: 3 • Method of scaling the value of the fitness function: ranking • Method of parent selection: tournament • Fitness function of individuals calculated based on the following formula: $ERR = w_l \cdot err_{Lsum} + w_t \cdot err_{Tsum} + w_f \cdot \frac{F_a}{F}$ (8) where: $w_l = 1$ weight for errors from the training set $w_t = 1$ weight for errors from the test sets $w_f = 1$ weight for acceptance feature coefficient err_{Lsum} total number of errors in the 10 training sets err_{Tsum} total number of errors in the 10 test sets $\frac{F_a}{F}$ acceptance feature coefficient: the ratio of the number of accepted features, F_a, to the total number of features, F • As a result of the feature selection, the length of the feature vector was on average reduced twice to approximately 2000 features (frequency components of the ECG signal)—Table 3

(continued)

Table 2 (continued)

Classifiers	
48 trained, tested and optimized classifiers:	
4 classifier types · 4 Hamming window widths · 3 signal pre-processing types · 1 cross-validation type	
Basic parameters	
SVM	• Type: nu-SVC • Kernel function type: RBF (radial, Gaussian type) • Number of outputs = 1, from the set: {1, ..., 17}
kNN	• Number of nearest neighbors = 1 • Metric of distance calculation: *Minkowski* • Number of outputs = 1, from the set: {1, ..., 17}
PNN	• Activation function: radial (Gaussian type)—competition • Training algorithm: mapping of training set based on distance • Method of calculating the objective function: sse • Topology (neurons): length of the feature vector –675 ∨ 621 –17; Biases: 1 –0 • Number of outputs = 17, from the set: {0, 1}
RBFNN	• Activation function: radial (Gaussian type)—linear • Training algorithm: mapping of training set based on distance • Method of calculating the objective function: sse • Topology (neurons): length of the feature vector –675 ∨ 621 –17; Biases: 1 –1 • Number of outputs = 17, from the set: {0, 1}. Value of "1" assigned to the output (class) with the highest stimulus
Optimized parameters	
The final parameter ranges were selected experimentally based on a broader range	
SVM	• The parameter γ $(-g)$ determines the spread of the radial basis function (RBF) of the kernel from the range $[2 \cdot 10^{-6}; 2 \cdot 10^{-4}]$, with resolution 10^{-14}, $50 \cdot 30 = 1500$ values • The parameter ν $(-n)$ determines the width of the margins from the range [0.001; 0.05], with resolution 10^{-14}, $50 \cdot 30 = 1500$ values
kNN	• The parameter *exponent* affects the calculation of the Minkowski distance from the range [0.01; 100], with resolution 10^{-14}, $50 \cdot 20 = 1000$ values
PNN	• The parameter *spread* determines the spread of the radial basis function (RBF) of the network kernel from the range [1; 100], with resolution 10^{-14}, $50 \cdot 20 = 1000$ values
RBFNN	• The parameter *spread* determines the spread of the radial function (RBF) of the network kernel from the range [1; 300], with resolution 10^{-14}, $50 \cdot 20 = 1000$ values

Algorithm 1: Evolutionary-neural system.

Data:
X –matrix with raw data;
R –matrix with reference answers;
$svm_{type} \leftarrow 1$ –defining the type of SVM on $\nu - SVC$;
$kernel_{type} \leftarrow 2$ –defining the type of kernel function on RBF;

Result:

B – vector of the form $[f_p, g_1, g_2, c_1, ..., c_{4001}]$, with associated values of the fitness function (f_p); the determined optimal parameters of the SVM classifier, γ and ν; and the selected features;
O_L and O_T – matrices with the classifier responses of the SVM;
CF – confusion matrix with the classifier responses of the SVM; and
E – vector with the calculated evaluation coefficients of the SVM;

```
Perform one type of signal pre-processing based on X
Perform one type of feature extraction
Create training and test sets and reference matrices based on R
Set genetic algorithm parameters (Table 2);
GENETIC ALGORITHM:
Create an initial population of individuals
for i ← 1 to 20 (number of generations) do
    for j ← 1 to 50 (number of individuals) do
        Perform feature selection
        Save the value of the basic and optimized parameters of the SVM classifier.
        for c ← 1 to 10 (number of set combinations) do
            Create the model of the SVM classifier
            Determine the SVM classifier responses
            Determine the number of errors
        end
        Calculate the sum of the errors for the training and test sets
        Determine the value of the fitness function (f_f)
        Save the related values B for the fitness function (f_f), classifier parameters and selected features
        as well as the matrices with classifier responses: O_L and O_T
    end
    if f_f == 0 then
        Lead out the "best" individual with the corresponding response matrices
        break
    else
        Perform the selection of individuals
        Apply the genetic operators: crossover and mutation
        Create a new population of individuals
    end
end
(   /* End of GA */) Lead out the "best" individual with the corresponding response matrices
Create the confusion matrix CF
Calculate the evaluation coefficients E for the SVM classifier
```

$$ACC = \left(\sum_{i=1}^{N} \frac{TP + TN}{TP + FP + TN + FN} \right) \cdot 100\% \Big/ N \tag{9}$$

- **Sensitivity**

$$SEN = \left(\sum_{i=1}^{N} \frac{TP}{TP + FN} \right) \cdot 100\% \Big/ N \tag{10}$$

- **Specificity**

$$SPE = \left(\sum_{i=1}^{N} \frac{TN}{FP + TN} \right) \cdot 100\% \Big/ N \tag{11}$$

where:

N represents the number of different sets utilized in the cross-validation (either 4-fold or 10-fold validation),
TP represents True Positive,
TN represents True Negative,
FP represents False Positive, and
FN represents False Negative.

- Additionally, in order to evaluate the efficiency and usefulness of the proposed method, ***k* coefficient** can be applied which can be evaluated using the following equation:

$$\kappa = \left(\sum_{i=1}^{N} \frac{M \sum_{j=1}^{n} m_{j,j} - \sum_{j=1}^{n} (G_j C_j)}{M^2 - \sum_{j=1}^{n} (G_j C_j)} \right) \cdot 100\% \Big/ N \tag{12}$$

where:

N represents the number of different sets utilized in the cross-validation (either 4-fold or 10-fold validation),
j is the class index,
n represents the total number of classes (in this study, we have 17 classes),
M represents the total number of categorized variables which compared to the ground truth,
$m_{j,j}$ shows the number of samples related to the ground truth class j which have been truly categorized with a class j (for example various values detected along the diagonal of the generated confusion matrix),
C_j represents the whole number of classified variables related to the class j, and finally
G_j represents the whole number of ground truth variables related to the class j.

It should be noted that this metric should be used for multi-class problems. Another point is that the higher value of k coefficient shows better performance and outcome.

- The **sum of errors** (ERR_{sum}): Based on the confusion matrix and the total number of erroneous classifications, the sum of errors (ERR_{sum}) can be calculated. The sum of errors (ERR_{sum}) is equal to the totality of the off-diagonal entrances of the confusion matrix for all classifications (744 classifications).
- **Acceptance feature coefficient** (C_F): This is another metric used in this research which shows the ratio of the total number of accepted features (F_a) towards the whole number of features (F). The C_F was determined when the genetic feature selection was used. The C_F can be computed by Eq. 13:

$$C_F = \frac{F_a}{F} \cdot 100\% \tag{13}$$

where:

F_a—shows the total number of accepted features, and
F—indicates the whole number of features.

- **Optimization time** (T_o): This is a metric to show the required time for optimization of the method which was used after pre-processing and feature extraction stages on the ECG signal data. For a given algorithm, the optimization time (T_o) is computed for all training and testing sets in the classification step for both cross-validation values (4-fold and 10-fold). This time indicates the time needed for finding the optimal parameter configuration related to the given method or the optimal vector of input features related to the feature selection stage.
- **Training time** (T_t): The training time (T_t) is used to compute the sum of the training times related to both cross-validation values (4-fold and 10-fold). As the same with the optimization time (T_o), the training time (T_t) is also used after pre-processing and feature extraction and selection stages on the ECG signal data.
- **Classification time** (T_c): For a 10-s fragment of an ECG signal, the classification time (T_c) is used to calculate the average time for a single classification required from a given method after pre-processing and feature extraction and selection stages on the ECG signal data.

We would argue that all listed metrics listed above were used to evaluate the overall performance and efficiency of the different machine learning techniques for different classes of ECG signal fragments. In order to verify the performance of individual classes in terms of recognition, the same metrics for class S were computed. In this regard, we calculated different values for each class including $TP(S)$, $TN(S)$, $FP(S)$, and $FN(S)$. First, these values were computed by using the classical approach (based on the confusion matrix). After that, based on these generated values, the coefficients of $ACC(S)$, $SEN(S)$, and $SPE(S)$ were computed.

It should be mentioned that in this research, the SEN (see Table 5) is equal to the *overallAcc* from the literature [30, 31]. The reason is that the WTA (Winner-Takes-All) approach was applied for the methods.

5 Results

The methods applied in the current research were implemented in the MATLAB R2014b environment and used the LIBSVM library with MATLAB [24]. The computations were performed on an Intel Core i7-6700K 4.0 GHz machine with 32 GB of RAM (only a single core was used). The total computation times, consisting of the training, testing, and optimization phases, are shown in Tables 4, 3, 6, and 7.

We would argue that sensitivity (SEN) and the sum of errors (ERRsum) metrics are the most important coefficients because of using the WTA approach and also the recognition of 17 classes (see Table 3). As Table 3 shows, the accuracy (ACC) and specificity (SPE) coefficients have very good performances and very high values (ACC> 98% and SPE > 99%). Optimizing the time needed to extract results can be much shorter by using the parallelization of the computation.

5.1 Raw Data

Figure 2 presents an example of single fragments (10 s) of raw ECG signals corresponding to all 17 analyzed classes. Before the visualization, the raw ECG signal fragments were processed by a reduction in the gain and constant component. For certain disorders, Fig. 2 denotes their characteristic fragments (features) by a black dashed line.

5.2 Preprocessing with Normalization

Figure 3 presents a comparison of ECG signals for all 17 classes following normalization (rescaling the signal to the range [−1, 1]), reducing the constant component, and feature extraction based on the applied DFT with a Hamming window width of 512 samples. The presented visualizations for each class include all 10-s fragments of the ECG signals. The other colors represent the signals from other patients.

Figure 4 presents a visualization of the subsequent ECG signal processing stages for the optimal combination (with the highest efficiency in the recognition of heart disorders; Table 3): classifier: *SVM*, signal pre-processing: *rescaling*, feature extraction: *512 samples* and feature selection. Figure 4 presents an example of a single fragment (10 seconds) of an ECG signal for *normal sinus rhythm* from patient No. 100 from the MIT-BIH Arrhythmia Database.

In Fig. 5, a comparison of the following ECG signal fragments is presented: **A**—concentration within the classes: normal sinus rhythm (all fragments of the ECG signal, where other colors represent signals from other patients); **B**—separation between all 17 classes (only the first fragments of the ECG signal for each class, where other colors represent the signals from other classes). The graphs show the

Table 3 The results of *Experiment No. 3* for 10-fold cross-validation [62]. In all training sets, in all cases, the sum of the errors equals zero

Normalization:	Window width:	Classifiers			
		SVM	kNN	PNN	RBFNN
No normalization	128 samples	$-g = 9.89e-5$ $-n = 0.0087$	*exponent* = 2.38	*spread* = 13.94	*spread* = 70.28
		$\boldsymbol{ERR_{sum} = 99}$	$\boldsymbol{ERR_{sum} = 125}$	$\boldsymbol{ERR_{sum} = 116}$	$\boldsymbol{ERR_{sum} = 101}$
		$ACC = 98.44\%$	$ACC = 98.02\%$	$ACC = 98.17\%$	$ACC = 98.40\%$
		$\boldsymbol{SEN = 86.69\%}$	$\boldsymbol{SEN = 83.20\%}$	$\boldsymbol{SEN = 84.41\%}$	$\boldsymbol{SEN = 86.43\%}$
		$SPE = 99.17\%$	$SPE = 98.95\%$	$SPE = 99.03\%$	$SPE = 99.15\%$
		$\boldsymbol{\kappa = 84.67\%}$	$\boldsymbol{\kappa = 80.71\%}$	$\boldsymbol{\kappa = 82.11\%}$	$\boldsymbol{\kappa = 84.40\%}$
		$C_F = 49.29\%$	$C_F = 49.16\%$	$C_F = 47.99\%$	$C_F = 48.76\%$
		$T_t = 12.5594$ [s]	$T_t = 0.1074$ [s]	$T_t = 0.4257$ [s]	$T_t = 57.4693$ [s]
		$\boldsymbol{T_c = 0.0018}$ [$\boldsymbol{s}$]	$\boldsymbol{T_c = 0.0511}$ [$\boldsymbol{s}$]	$\boldsymbol{T_c = 0.0060}$ [$\boldsymbol{s}$]	$\boldsymbol{T_c = 0.0080}$ [$\boldsymbol{s}$]
	256 samples	$-g = 4.24e-5$ $-n = 0.0167$	*exponent* = 2.00	*spread* = 13.22	*spread* = 115.96
		$\boldsymbol{ERR_{sum} = 98}$	$\boldsymbol{ERR_{sum} = 109}$	$\boldsymbol{ERR_{sum} = 104}$	$\boldsymbol{ERR_{sum} = 109}$
		$ACC = 98.45\%$	$ACC = 98.28\%$	$ACC = 98.36\%$	$ACC = 98.28\%$
		$\boldsymbol{SEN = 86.83\%}$	$\boldsymbol{SEN = 85.35\%}$	$\boldsymbol{SEN = 86.02\%}$	$\boldsymbol{SEN = 85.35\%}$
		$SPE = 99.18\%$	$SPE = 99.08\%$	$SPE = 99.13\%$	$SPE = 99.08\%$
		$\boldsymbol{\kappa = 84.84\%}$	$\boldsymbol{\kappa = 83.20\%}$	$\boldsymbol{\kappa = 83.96\%}$	$\boldsymbol{\kappa = 83.16\%}$
		$C_F = 50.61\%$	$C_F = 72.31\%$	$C_F = 50.94\%$	$C_F = 50.94\%$
		$T_t = 11.9220$ [s]	$T_t = 0.1163$ [s]	$T_t = 0.4521$ [s]	$T_t = 56.6089$ [s]
		$\boldsymbol{T_c = 0.0020}$ [$\boldsymbol{s}$]	$\boldsymbol{T_c = 0.0747}$ [$\boldsymbol{s}$]	$\boldsymbol{T_c = 0.0065}$ [$\boldsymbol{s}$]	$\boldsymbol{T_c = 0.0076}$ [$\boldsymbol{s}$]
	512 samples	$-g = 3.74e-5$ $-n = 0.0051$	*exponent* = 3.70	*spread* = 20.56	*spread* = 79.55
		$\boldsymbol{ERR_{sum} = 83}$	$\boldsymbol{ERR_{sum} = 103}$	$\boldsymbol{ERR_{sum} = 97}$	$\boldsymbol{ERR_{sum} = 97}$
		$ACC = 98.69\%$	$ACC = 98.37\%$	$ACC = 98.47\%$	$ACC = 98.47\%$
		$\boldsymbol{SEN = 88.84\%}$	$\boldsymbol{SEN = 86.16\%}$	$\boldsymbol{SEN = 86.96\%}$	$\boldsymbol{SEN = 86.96\%}$
		$SPE = 99.30\%$	$SPE = 99.14\%$	$SPE = 99.19\%$	$SPE = 99.19\%$
		$\boldsymbol{\kappa = 87.14\%}$	$\boldsymbol{\kappa = 84.14\%}$	$\boldsymbol{\kappa = 85.03\%}$	$\boldsymbol{\kappa = 84.99\%}$
		$C_F = 49.24\%$	$C_F = 50.04\%$	$C_F = 49.09\%$	$C_F = 49.11\%$
		$T_t = 12.4013$ [s]	$T_t = 0.1074$ [s]	$T_t = 0.5083$ [s]	$T_t = 46.8782$ [s]
		$\boldsymbol{T_c = 0.0020}$ [$\boldsymbol{s}$]	$\boldsymbol{T_c = 0.0518}$ [$\boldsymbol{s}$]	$\boldsymbol{T_c = 0.0061}$ [$\boldsymbol{s}$]	$\boldsymbol{T_c = 0.0061}$ [$\boldsymbol{s}$]
	1024 samples	$-g = 2.08e-5$ $-n = 0.0122$	*exponent* = 2.95	*spread* = 26.88	*spread* = 140.02
		$\boldsymbol{ERR_{sum} = 85}$	$\boldsymbol{ERR_{sum} = 92}$	$\boldsymbol{ERR_{sum} = 83}$	$\boldsymbol{ERR_{sum} = 94}$
		$ACC = 98.66\%$	$ACC = 98.55\%$	$ACC = 98.69\%$	$ACC = 98.51\%$
		$\boldsymbol{SEN = 88.58\%}$	$\boldsymbol{SEN = 87.63\%}$	$\boldsymbol{SEN = 88.84\%}$	$\boldsymbol{SEN = 87.37\%}$
		$SPE = 99.29\%$	$SPE = 99.23\%$	$SPE = 99.30\%$	$SPE = 99.21\%$
		$\boldsymbol{\kappa = 86.84\%}$	$\boldsymbol{\kappa = 85.84\%}$	$\boldsymbol{\kappa = 87.19\%}$	$\boldsymbol{\kappa = 85.40\%}$
		$C_F = 48.34\%$	$C_F = 49.39\%$	$C_F = 49.49\%$	$C_F = 50.24\%$
		$T_t = 14.7607$ [s]	$T_t = 0.1130$ [s]	$T_t = 0.4349$ [s]	$T_t = 41.1444$ [s]
		$\boldsymbol{T_c = 0.0021}$ [$\boldsymbol{s}$]	$\boldsymbol{T_c = 0.0503}$ [$\boldsymbol{s}$]	$\boldsymbol{T_c = 0.0061}$ [$\boldsymbol{s}$]	$\boldsymbol{T_c = 0.0057}$ [$\boldsymbol{s}$]

Table 3 (continued)

Rescaling+ reduction of constant component	128 samples	$-g = 8.04e-5$ $-n = 0.0114$	*exponent* = 3.35	*spread* = 15.78	*spread* = 71.94
		$\boldsymbol{ERR_{sum} = 91}$	$\boldsymbol{ERR_{sum} = 93}$	$\boldsymbol{ERR_{sum} = 98}$	$\boldsymbol{ERR_{sum} = 93}$
		$ACC = 98.56\%$	$ACC = 98.53\%$	$ACC = 98.45\%$	$ACC = 98.53\%$
		$\boldsymbol{SEN = 87.77\%}$	$\boldsymbol{SEN = 87.50\%}$	$\boldsymbol{SEN = 86.83\%}$	$\boldsymbol{SEN = 87.50\%}$
		$SPE = 99.24\%$	$SPE = 99.22\%$	$SPE = 99.18\%$	$SPE = 99.22\%$
		$\boldsymbol{\kappa = 85.94\%}$	$\boldsymbol{\kappa = 85.68\%}$	$\boldsymbol{\kappa = 84.89\%}$	$\boldsymbol{\kappa = 85.57\%}$
		$C_F = 46.74\%$	$C_F = 48.21\%$	$C_F = 48.46\%$	$C_F = 49.89\%$
		$T_t = 9.7303$ [s]	$T_t = 0.1142$ [s]	$T_t = 0.4301$ [s]	$T_t = 60.9248$ [s]
		$\boldsymbol{T_c = 0.0016}$ **[s]**	$\boldsymbol{T_c = 0.0492}$ **[s]**	$\boldsymbol{T_c = 0.0060}$ **[s]**	$\boldsymbol{T_c = 0.0084}$ **[s]**
	256 samples	$-g = 4.81e-5$ $-n = 0.0125$	*exponent* = 3.47	*spread* = 11.19	*spread* = 136.77
		$\boldsymbol{ERR_{sum} = 87}$	$\boldsymbol{ERR_{sum} = 90}$	$\boldsymbol{ERR_{sum} = 92}$	$\boldsymbol{ERR_{sum} = 86}$
		$ACC = 98.62\%$	$ACC = 98.58\%$	$ACC = 98.55\%$	$ACC = 98.64\%$
		$\boldsymbol{SEN = 88.31\%}$	$\boldsymbol{SEN = 87.90\%}$	$\boldsymbol{SEN = 87.63\%}$	$\boldsymbol{SEN = 88.44\%}$
		$SPE = 99.27\%$	$SPE = 99.24\%$	$SPE = 99.23\%$	$SPE = 99.28\%$
		$\boldsymbol{\kappa = 86.53\%}$	$\boldsymbol{\kappa = 86.13\%}$	$\boldsymbol{\kappa = 85.83\%}$	$\boldsymbol{\kappa = 86.70\%}$
		$C_F = 49.39\%$	$C_F = 49.99\%$	$C_F = 50.21\%$	$C_F = 49.59\%$
		$T_t = 10.6013$ [s]	$T_t = 0.1356$ [s]	$T_t = 0.3270$ [s]	$T_t = 59.0492$ [s]
		$\boldsymbol{T_c = 0.0018}$ **[s]**	$\boldsymbol{T_c = 0.0541}$ **[s]**	$\boldsymbol{T_c = 0.0055}$ **[s]**	$\boldsymbol{T_c = 0.0076}$ **[s]**
	512 samples	$-g = 2.64e-5$ $-n = 0.0183$	*exponent* = 3.61	*spread* = 18.85	*spread* = 117.89
		$\boldsymbol{ERR_{sum} = 73}$	$\boldsymbol{ERR_{sum} = 87}$	$\boldsymbol{ERR_{sum} = 80}$	$\boldsymbol{ERR_{sum} = 80}$
		$ACC = 98.85\%$	$ACC = 98.62\%$	$ACC = 98.74\%$	$ACC = 98.74\%$
		$\boldsymbol{SEN = 90.19\%}$	$\boldsymbol{SEN = 88.31\%}$	$\boldsymbol{SEN = 89.25\%}$	$\boldsymbol{SEN = 89.25\%}$
		$SPE = 99.39\%$	$SPE = 99.27\%$	$SPE = 99.33\%$	$SPE = 99.33\%$
		$\boldsymbol{\kappa = 88.70\%}$	$\boldsymbol{\kappa = 86.60\%}$	$\boldsymbol{\kappa = 87.65\%}$	$\boldsymbol{\kappa = 87.63\%}$
		$C_F = 49.09\%$	$C_F = 49.59\%$	$C_F = 49.76\%$	$C_F = 50.81\%$
		$T_t = 11.3537$ [s]	$T_t = 0.1192$ [s]	$T_t = 0.3194$ [s]	$T_t = 56.8192$ [s]
		$\boldsymbol{T_c = 0.0018}$ **[s]**	$\boldsymbol{T_c = 0.0597}$ **[s]**	$\boldsymbol{T_c = 0.0055}$ **[s]**	$\boldsymbol{T_c = 0.0076}$ **[s]**
	1024 samples	$-g = 7.69e-6$ $-n = 0.0105$	*exponent* = 2.34	*spread* = 20.11	*spread* = 148.12
		$\boldsymbol{ERR_{sum} = 74}$	$\boldsymbol{ERR_{sum} = 79}$	$\boldsymbol{ERR_{sum} = 77}$	$\boldsymbol{ERR_{sum} = 79}$
		$ACC = 98.83\%$	$ACC = 98.75\%$	$ACC = 98.78\%$	$ACC = 98.75\%$
		$\boldsymbol{SEN = 90.05\%}$	$\boldsymbol{SEN = 89.38\%}$	$\boldsymbol{SEN = 89.65\%}$	$\boldsymbol{SEN = 89.38\%}$
		$SPE = 99.38\%$	$SPE = 99.34\%$	$SPE = 99.35\%$	$SPE = 99.34\%$
		$\boldsymbol{\kappa = 88.53\%}$	$\boldsymbol{\kappa = 87.84\%}$	$\boldsymbol{\kappa = 88.14\%}$	$\boldsymbol{\kappa = 87.73\%}$
		$C_F = 47.91\%$	$C_F = 78.26\%$	$C_F = 49.51\%$	$C_F = 47.86\%$
		$T_t = 10.4768$ [s]	$T_t = 0.1432$ [s]	$T_t = 0.3316$ [s]	$T_t = 54.0503$ [s]
		$\boldsymbol{T_c = 0.0019}$ **[s]**	$\boldsymbol{T_c = 0.0853}$ **[s]**	$\boldsymbol{T_c = 0.0055}$ **[s]**	$\boldsymbol{T_c = 0.0077}$ **[s]**

Table 3 (continued)

Standardization	128 samples	$-g = 1.59e-4$ $-n = 0.0290$	*exponent* = 5.55	*spread* = 17.95	*spread* = 88.52
		$\boldsymbol{ERR_{sum} = 103}$	$\boldsymbol{ERR_{sum} = 123}$	$\boldsymbol{ERR_{sum} = 120}$	$\boldsymbol{ERR_{sum} = 107}$
		$ACC = 98.37\%$	$ACC = 98.06\%$	$ACC = 98.10\%$	$ACC = 98.31\%$
		$\boldsymbol{SEN = 86.16\%}$	$\boldsymbol{SEN = 83.47\%}$	$\boldsymbol{SEN = 83.87\%}$	$\boldsymbol{SEN = 85.62\%}$
		$SPE = 99.14\%$	$SPE = 98.97\%$	$SPE = 98.99\%$	$SPE = 99.10\%$
		$\boldsymbol{\kappa = 84.04\%}$	$\boldsymbol{\kappa = 81.03\%}$	$\boldsymbol{\kappa = 81.47\%}$	$\boldsymbol{\kappa = 83.44\%}$
		$C_F = 48.84\%$	$C_F = 47.69\%$	$C_F = 48.59\%$	$C_F = 49.34\%$
		$T_t = 16.9512$ [s]	$T_t = 0.1331$ [s]	$T_t = 0.3458$ [s]	$T_t = 64.2180$ [s]
		$\boldsymbol{T_c = 0.0018}$ [$\boldsymbol{s}$]	$\boldsymbol{T_c = 0.0525}$ [$\boldsymbol{s}$]	$\boldsymbol{T_c = 0.0054}$ [$\boldsymbol{s}$]	$\boldsymbol{T_c = 0.0089}$ [$\boldsymbol{s}$]
	256 samples	$-g = 4.80e-5$ $-n = 0.0126$	*exponent* = 2.64	*spread* = 14.98	*spread* = 77.97
		$\boldsymbol{ERR_{sum} = 97}$	$\boldsymbol{ERR_{sum} = 122}$	$\boldsymbol{ERR_{sum} = 121}$	$\boldsymbol{ERR_{sum} = 110}$
		$ACC = 98.47\%$	$ACC = 98.07\%$	$ACC = 98.09\%$	$ACC = 98.26\%$
		$\boldsymbol{SEN = 86.96\%}$	$\boldsymbol{SEN = 83.60\%}$	$\boldsymbol{SEN = 83.74\%}$	$\boldsymbol{SEN = 85.22\%}$
		$SPE = 99.19\%$	$SPE = 98.98\%$	$SPE = 98.98\%$	$SPE = 99.08\%$
		$\boldsymbol{\kappa = 85.02\%}$	$\boldsymbol{\kappa = 81.22\%}$	$\boldsymbol{\kappa = 81.33\%}$	$\boldsymbol{\kappa = 83.00\%}$
		$C_F = 50.56\%$	$C_F = 49.01\%$	$C_F = 49.16\%$	$C_F = 49.11\%$
		$T_t = 9.8686$ [s]	$T_t = 0.1586$ [s]	$T_t = 0.3504$ [s]	$T_t = 58.4766$ [s]
		$\boldsymbol{T_c = 0.0016}$ [$\boldsymbol{s}$]	$\boldsymbol{T_c = 0.0590}$ [$\boldsymbol{s}$]	$\boldsymbol{T_c = 0.0054}$ [$\boldsymbol{s}$]	$\boldsymbol{T_c = 0.0077}$ [$\boldsymbol{s}$]
	512 samples	$-g = 1.46e-5$ $-n = 0.0129$	*exponent* = 3.61	*spread* = 24.35	*spread* = 193.28
		$\boldsymbol{ERR_{sum} = 83}$	$\boldsymbol{ERR_{sum} = 115}$	$\boldsymbol{ERR_{sum} = 101}$	$\boldsymbol{ERR_{sum} = 112}$
		$ACC = 98.69\%$	$ACC = 98.18\%$	$ACC = 98.40\%$	$ACC = 98.23\%$
		$\boldsymbol{SEN = 88.84\%}$	$\boldsymbol{SEN = 84.54\%}$	$\boldsymbol{SEN = 86.43\%}$	$\boldsymbol{SEN = 84.95\%}$
		$SPE = 99.30\%$	$SPE = 99.03\%$	$SPE = 99.15\%$	$SPE = 99.06\%$
		$\boldsymbol{\kappa = 87.16\%}$	$\boldsymbol{\kappa = 82.33\%}$	$\boldsymbol{\kappa = 84.38\%}$	$\boldsymbol{\kappa = 82.65\%}$
		$C_F = 48.94\%$	$C_F = 48.61\%$	$C_F = 49.11\%$	$C_F = 50.14\%$
		$T_t = 9.2840$ [s]	$T_t = 0.1537$ [s]	$T_t = 0.3000$ [s]	$T_t = 58.8405$ [s]
		$\boldsymbol{T_c = 0.0017}$ [$\boldsymbol{s}$]	$\boldsymbol{T_c = 0.0583}$ [$\boldsymbol{s}$]	$\boldsymbol{T_c = 0.0052}$ [$\boldsymbol{s}$]	$\boldsymbol{T_c = 0.0077}$ [$\boldsymbol{s}$]
	1024 samples	$-g = 1.59e-5$ $-n = 0.0202$	*exponent* = 14.08	*spread* = 25.90	*spread* = 171.45
		$\boldsymbol{ERR_{sum} = 81}$	$\boldsymbol{ERR_{sum} = 98}$	$\boldsymbol{ERR_{sum} = 81}$	$\boldsymbol{ERR_{sum} = 92}$
		$ACC = 98.72\%$	$ACC = 98.45\%$	$ACC = 98.72\%$	$ACC = 98.55\%$
		$\boldsymbol{SEN = 89.11\%}$	$\boldsymbol{SEN = 86.83\%}$	$\boldsymbol{SEN = 89.11\%}$	$\boldsymbol{SEN = 87.63\%}$
		$SPE = 99.32\%$	$SPE = 99.18\%$	$SPE = 99.32\%$	$SPE = 99.23\%$
		$\boldsymbol{\kappa = 87.45\%}$	$\boldsymbol{\kappa = 84.87\%}$	$\boldsymbol{\kappa = 87.53\%}$	$\boldsymbol{\kappa = 85.74\%}$
		$C_F = 48.46\%$	$C_F = 51.26\%$	$C_F = 48.84\%$	$C_F = 48.64\%$
		$T_t = 12.9148$ [s]	$T_t = 0.1016$ [s]	$T_t = 0.2981$ [s]	$T_t = 58.0527$ [s]
		$\boldsymbol{T_c = 0.0020}$ [$\boldsymbol{s}$]	$\boldsymbol{T_c = 0.0469}$ [$\boldsymbol{s}$]	$\boldsymbol{T_c = 0.0052}$ [$\boldsymbol{s}$]	$\boldsymbol{T_c = 0.0079}$ [$\boldsymbol{s}$]

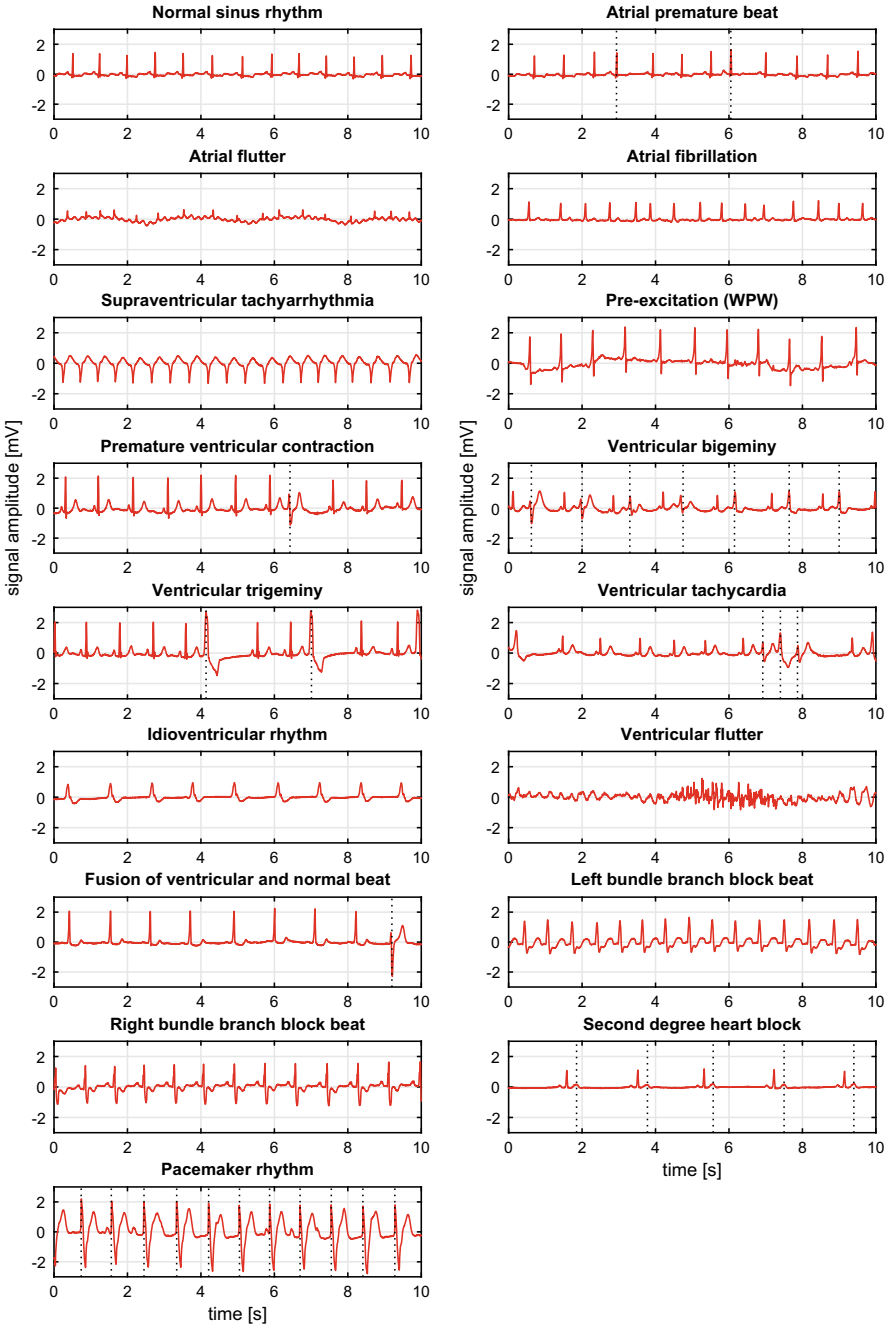

Fig. 2 Visualizations of the raw data for each analyzed class. For each class, an example single fragment (10 s) of raw ECG signals is presented

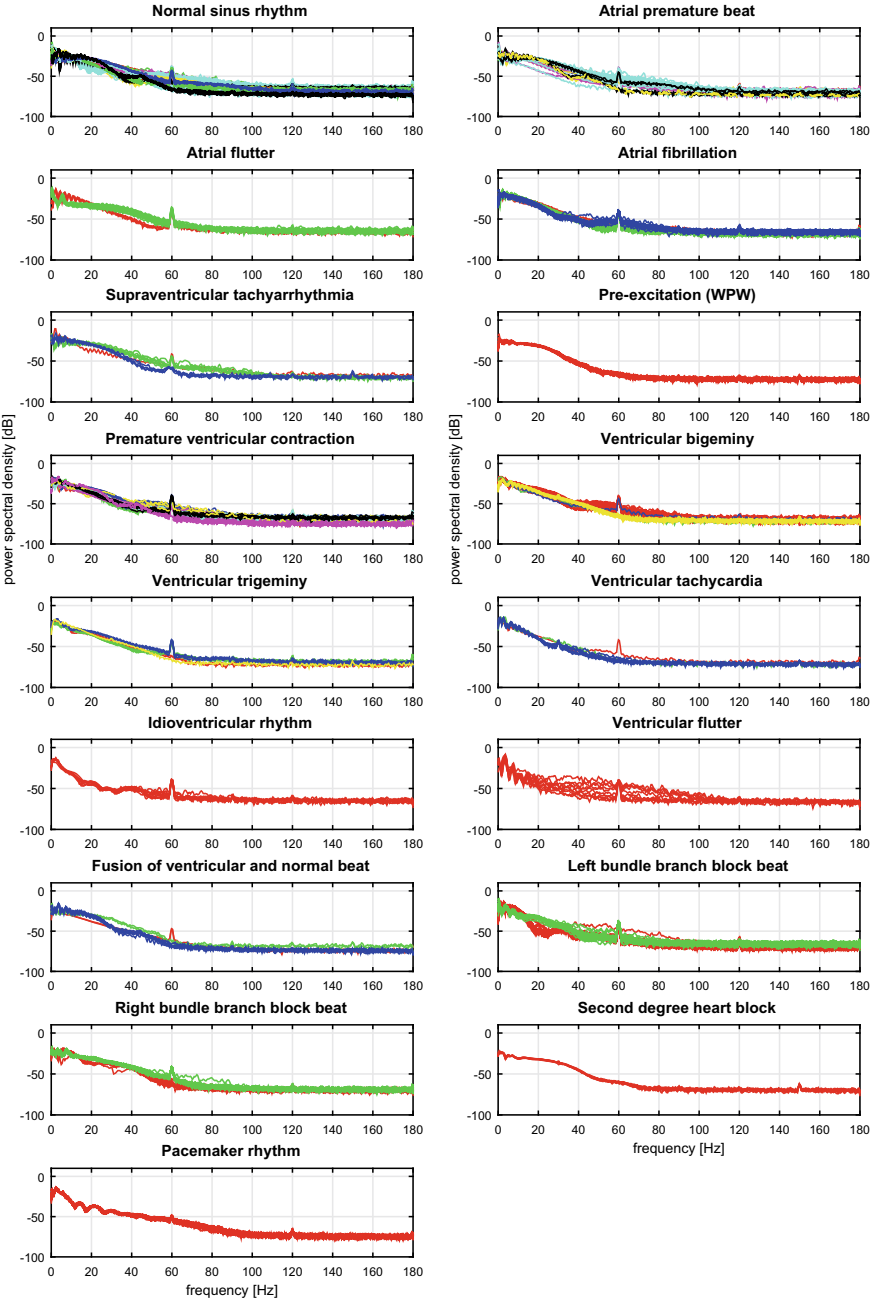

Fig. 3 A comparison of the analyzed classes after the DFT is applied. The presented visualizations for each class include all 10-s fragments of the ECG signals. The other colors represent the signals from the other patients

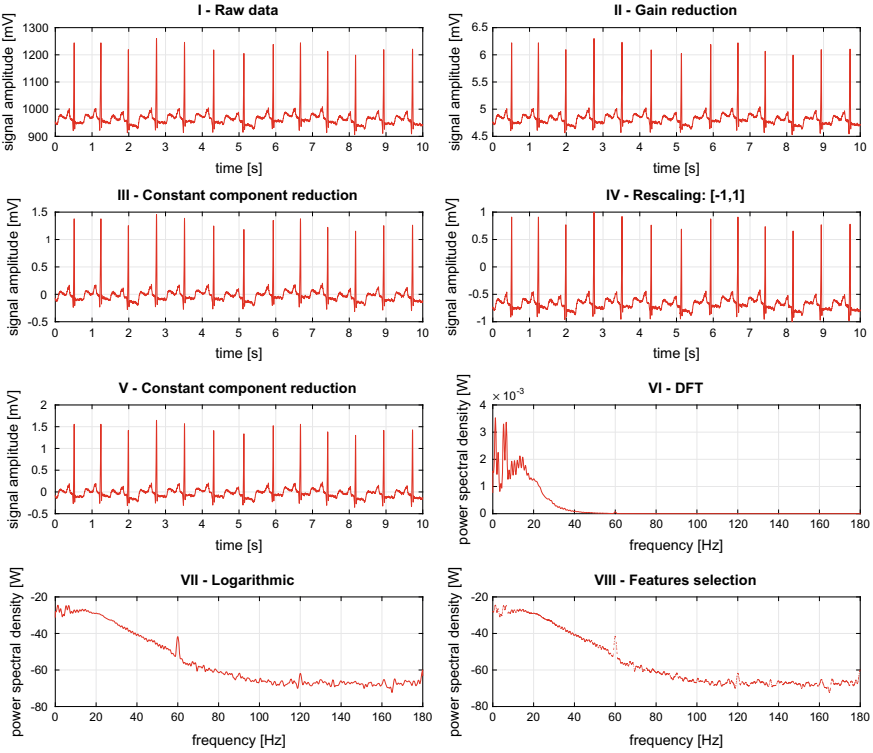

Fig. 4 A visualization of the subsequent ECG signal processing stages for the optimal method combination. All graphs present an example of a single fragment (10 s) of an ECG signal for *normal sinus rhythm* from patient No. 100 from the MIT-BIH Arrhythmia database

10-second fragments of the ECG signals after normalization based on rescaling the signal to the range $[-1, 1]$, reducing the constant component, and performing feature extraction based on the DFT with a Hamming window with a width of 512 samples.

5.3 Experiments

This section presents the results of Experiment No. 3, which achieved the highest recognition sensitivity for heart disorders. On all the training sets, the obtained recognition sensitivity (*SEN*) of myocardium dysfunctions was 100% (zero errors). The ERR_{sum} coefficient equals the sum of the errors on all training and test sets per 744 classifications (in the training sets, in all cases, the sum of the errors equals zero).

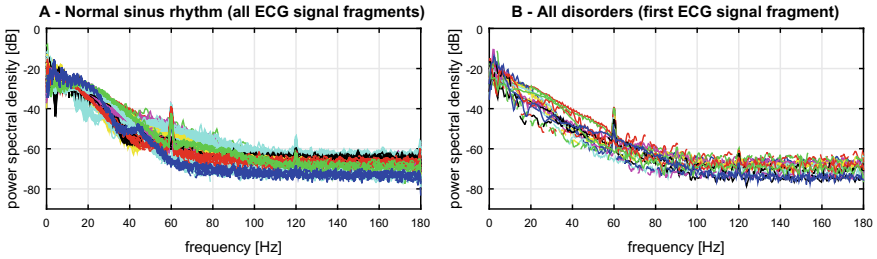

Fig. 5 Comparison of the analyzed classes after applying the DFT and logarithm procedure: **A**—concentration within the classes: normal sinus rhythm (all fragments of the ECG signal, where the other colors represent signals from other patients); **B**—separation between all 17 classes (only the first fragments of the ECG signal for each class, where the other colors represent the signals from other classes)

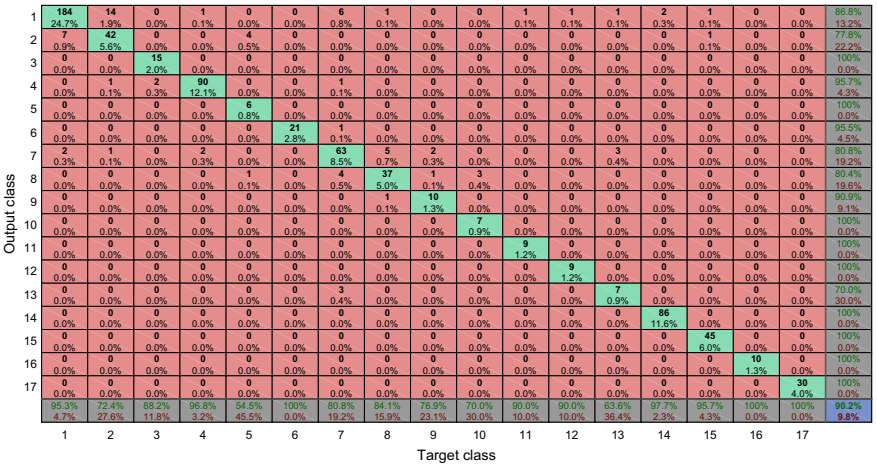

Fig. 6 Confusion matrix

Table 3 presents detailed results on 4 types of classifiers (SVM, kNN, PNN and RBFNN), 3 types of signal pre-processing methods (no normalization, rescaling + reduction in constant component, and standardization) and 4 types of feature extraction (4 widths of the Hamming window: 128, 256, 512 and 1024 samples) for one variant of the cross-validation method—10-fold cross-validation.

In Figs. 6, 7, and 8, the detailed results for the best classifier—*SVM* from Table 3—are presented. In Fig. 6, the confusion matrix, under the 10-fold cross-validation method, is presented. In Fig. 7, the following coefficient values are presented: the sum of errors (*ERR*), accuracy (*ACC*), sensitivity (*SEN*), and specificity (*SPE*) for each class. Figure 8 presents the coefficient value comparison of the sum of errors (*ERR*), accuracy (*ACC*), sensitivity (*SEN*), specificity (*SPE*), and κ coefficient for the recognition of 17, 15, and 12 classes.

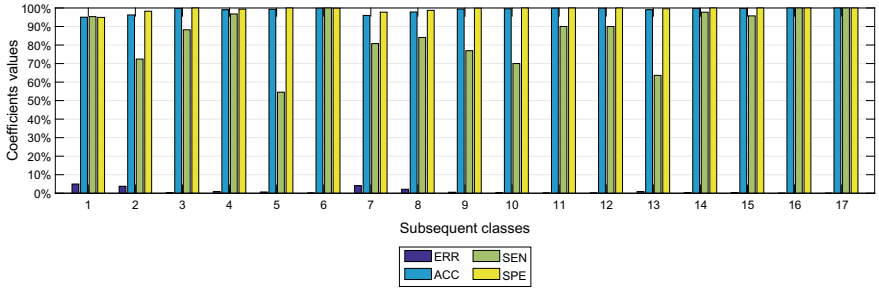

Fig. 7 Comparison of coefficient values for each class

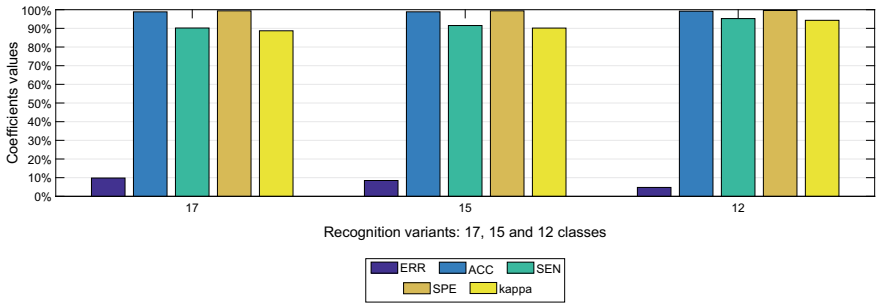

Fig. 8 Comparison of coefficient values for the recognition of 17, 15, and 12 classes

In Table 4, a comparison of the obtained results for all 3 conducted experiments is presented. T_{sum} coefficient—the total optimization time for all classifiers for a given experiment.

In Table 5, a summary of the results (with the highest overall accuracy/sensitivity in the recognition of cardiac disorders) from the current scientific literature together with the results obtained by the author is presented. The summary is based on the more objective subject-oriented validation scheme [10, 30] and includes information about the applied ECG signal analysis methods.

Table 6 presents a comparison of the results obtained with 4 types of classifiers, SVM, kNN, PNN, and RBFNN, calculated based on Experiment Nos. 1, 2, and 3.

Table 6 presents a comparison of the results obtained for 2 variants of the cross-validation method, 4-fold and 10-fold cross-validation, calculated based on Experiment No. 2.

Table 7 presents a comparison of the results obtained for 3 types of normalization methods (signal pre-processing), no normalization, rescaling and standardization, calculated based on Experiment Nos. 1, 2 and 3.

Table 4 A comparison of the obtained results for all 3 conducted experiments, where the T_{sum} coefficient is the total optimization time for all classifiers for a given experiment. In all training sets, in all cases, the sum of the errors equals zero

Coefficients	Experiments			
	E1	E2a	E2b	E3
Validation	*4-fold*	*4-fold*	*10-fold*	*10-fold*
Optimization	*Grid*	*Genetic*	*Genetic*	*Genetic*
Selection	*No*	*No*	*No*	*Yes*
Results obtained for the best case (combination of classifier + normalization + window width)				
Classifier	*SVM*	*SVM*	*SVM*	*SVM*
Normalization	*Rescaling*	*Rescaling*	*Rescaling*	*Rescaling*
Window	128	512	512	512
ERR_{sum}	**106**	**97**	**81**	**73**
ACC	98.32%	98.47%	98.72%	98.85%
SEN	**85.75%**	**86.96%**	**89.11%**	**90.19%**
SPE	99.11%	99.19%	99.32%	99.39%
κ	**83.65%**	**85.05%**	**87.45%**	**88.70%**
C_F	–	–	–	49.09%
T_t [*s*]	8.2920	8.21	30.1079	11.3537
T_c [*s*]	**0.0029**	**0.0034**	**0.0041**	**0.0018**
T_o [*h*]	15	10	20	100
Average result for all cases of a given experiment				
ERR_{sum}	**131.28**	**121.02**	**104.65**	**96.25**
ACC	97.92%	98.09%	98.35%	98.48%
SEN	**82.36%**	**83.73%**	**85.93%**	**87.06%**
SPE	98.90%	98.98%	99.12%	99.19%
κ	–	**81.40%**	**83.83%**	**85.13%**
C_F	–	–	–	50.34%
T_t [*s*]	7.7012	10.1802	35.7554	17.1122
T_c [*s*]	**0.0260**	**0.0250**	**0.0297**	**0.0182**
T_o [*h*]	5.5	12	24	110
Summary				
T_{sum} [*days*]	8	24	48	220

Table 7 presents a comparison of the results obtained for 4 widths of the Hamming window (feature extraction), 128, 256, 512 and 1024 samples, calculated based on Experiment Nos. 2 and 3 and for 3 widths of the Hamming window (feature extraction), 128, 256 and 512 samples, calculated based on Experiment No. 1.

Table 5 A comparison of the results under the methods based on the subject-oriented validation scheme [30]

No.	Work	Year	# of classes	Feature set	Classifier	Acc = SEN (%)
1.	Huang et al. [43]	2014	5	Random projection, RR-intervals	Ensemble of SVM	94
2.	Llamedo and Martinez [51]	2011	5	Wavelet, VCG + SFFS	Weighted LD	93
3.	Lin and Yang [49]	2014	5	Normalized RR-interval	Weighted LD	93
4.	Bazi et al. [17]	2013	5	Morphological, Wavelet	SVM, IWKLR, DTSVM	92
5.	Soria and Martinez [74]	2009	5	RR-intervals, VCG, morphological + FFS	Weighted LD	90
6.	Mar et al. [53]	2011	5	Temporal features, morphological, statistical features + SFFS	Weighted LD, MLP	89
7.	Zhang and Luo [91]	2014	5	RR-intervals, morph. features, ECG-inter. and segments, wavelet coeff.	Combined SVM	87
8.	Zhang et al. [90]	2014	5	RR-intervals, morphological features, ECG-intervals and segments	Combined SVM	86
9.	Ye et al. [83]	2012	5	Morphological, wavelet, RR interval, ICA, PCA	SVM	86
10.	Park et al. [59]	2008	5	HOS, HBF	Hierarchical SVM	85
11.	de Lannoy et al. [33]	2012	5	RR-intervals, ECG-segments, morphological, HBF, HOS	Weighted CRF	85
12.	de Chazal et al. [31]	2004	5	ECG-intervals, morphological	Weighted LD	83
13.	de Lannoy et al. [32]	2010	5	ECG-intervals, morphological, HOS, HBF coefficients	Weighted SVM	83
Proposed method			12	Frequency components of the power spectral density of the ECG signal	Evolutionary-Neural System (based on SVM)	95
			15			92
			17			90

Table 6 Comparison of the results obtained for 4 types of classifiers and 2 variants of cross-validation calculated based on the results obtained for Experiment Nos. 1, 2 and 3. In all training sets, in all cases, the sum of the errors equals zero

Coefficients	Classifiers				Cross-validation	
	SVM	kNN	PNN	RBFNN	4-fold	10-fold
Experiment No. 1						
The results obtained for the best case (combination: classifier + normalization + window width)						
ERR_{sum}	**106**	**122**	**107**	**120**	**106**	–
ACC	98.32%	98.07%	98.31%	98.10%	98.32%	–
SEN	**85.75%**	**83.60%**	**85.62%**	**83.87%**	**85.75%**	–
SPE	99.11%	98.98%	99.10%	98.99%	99.11%	–
T_t $[s]$	8.2920	0.0368	0.1597	25.0262	–	–
T_c $[s]$	**0.0029**	**0.0844**	**0.0082**	**0.0090**	–	–
T_o $[h]$	15	5	0.5	1	–	–
Average results for all cases of the given experiment						
ERR_{sum}	**121.89**	**137.89**	129.22	**136.11**	**131.28**	–
ACC	98, 07%	97, 82%	97, 96%	97, 85%	97, 92%	–
SEN	**83, 62%**	**81, 47%**	**82, 63%**	**81, 71%**	**82, 36%**	–
SPE	98, 98%	98, 84%	98, 91%	98, 86%	98, 90%	–
T_t $[s]$	6.3159	0.0360	0.1781	24.2748	7.7012	–
T_c $[s]$	**0.0024**	**0.0838**	**0.0089**	**0.0089**	0.0260	–
T_o $[h]$	15	5	0.5	1	5.5	–
Experiment No. 2						
4-fold cross-validation/10-fold cross-validation						
The results obtained for the best case (combination: classifier + normalization + window width)						
ERR_{sum}	97	102	**98**	**108**	97	**81**
	81	**85**	**85**	**92**		
ACC	98.47%	98.39%	98.45%	98.29%	98.47%	98.72%
	98.72%	98.66%	98.66%	98.55%		
SEN	**86.96%**	**86.29%**	**86.83%**	**85.48%**	**86.96%**	**89.11%**
	89.11%	**88.58%**	**88.58%**	**87.63%**		
SPE	99.19%	99.14%	99.18%	99.09%	99.19%	99.32%
	99.32%	99.29%	99.29%	99.23%		
κ	**85.05%**	**84.37%**	**84.98%**	**85.48%**	**85.05%**	**87.46%**
	87.46%	**86.92%**	**86.91%**	**85.73%**		
T_t $[s]$	8.21	0.0685	0.3327	36.8604	–	–
	30.1079	0.1280	0.4455	115.8806		
T_c $[s]$	**0.0034**	**0.0840**	**0.0106**	**0.0099**	–	–
	0.0041	**0.1083**	**0.0116**	**0.0127**		
T_o $[h]$	10	15	10	12.5	–	–
	20	30	20	25		

(continued)

Table 6 (continued)

Coefficients	Classifiers				Cross-validation	
	SVM	kNN	PNN	RBFNN	4-fold	10-fold
Average results for all cases of the given experiment						
ERR_{sum}	**109, 67**	**125, 92**	**123, 42**	**125, 08**	**121, 02**	**104, 65**
	92, 25	**110, 58**	**104, 92**	**110, 83**		
ACC	98, 27%	98, 01%	98, 05%	98, 02%	98.09%	98.35%
	98, 54%	98, 25%	98, 34%	98, 25%		
SEN	**85, 26%**	**83, 08%**	**83, 41%**	**83, 19%**	**83, 73%**	**85, 93%**
	87, 60%	**85, 14%**	**85, 90%**	**85, 10%**		
SPE	99, 08%	98, 94%	98, 96%	98, 95%	98, 98%	99, 12%
	99, 23%	99, 07%	99, 12%	99, 07%		
κ	**83, 12%**	**80, 73%**	**81, 08%**	**80, 69%**	**81, 40%**	**83, 83%**
	85, 71%	**82, 96%**	**83, 82%**	**82, 83%**		
T_t $[s]$	7.0025	0.0673	0.2421	33.409	10.1802	35.7554
	23.1446	0.1263	0.4785	119.2722		
T_c $[s]$	**0.0026**	**0.0790**	**0.0092**	**0.0093**	**0.0250**	**0.0297**
	0.0036	**0.0903**	**0.0120**	**0.0128**		
T_o $[h]$	10	15	10	12.5	12	24
	20	30	20	25		
Experiment No. 3						
The results obtained for the best case (combination: classifier + normalization + window width)						
ERR_{sum}	**73**	**79**	**77**	**79**	–	**73**
ACC	98.85%	98.75%	98.78%	98.75%	–	98.85%
SEN	**90.19%**	**89.38%**	**89.65%**	**89.38%**	–	**90.19%**
SPE	99.39%	99.34%	99.35%	99.34%	–	99.39%
κ	**88.70%**	**87.84%**	**88.14%**	**87.73%**	–	**88.70%**
C_F	49.09%	78.26%	49.51%	47.86%	–	49.09%
T_t $[s]$	11.3537	0.1432	0.3316	54.0503	–	–
T_c $[s]$	**0.0018**	**0.0853**	**0.0055**	**0.0077**	–	–
T_o $[h]$	100	125	100	115	–	–
Average results for all cases of the given experiment						
ERR_{sum}	**87.83**	**103.00**	97.50	**96.67**	–	**96.25**
ACC	98.61%	98.37%	98.46%	98.47%	–	98.48%
SEN	**88.19%**	**86.16%**	**86.90%**	**87.01%**	–	**87.06%**
SPE	99.26%	99.13%	99.18%	99.19%	–	99.19%
κ	**86.41%**	**84.13%**	**84.96%**	**85.03%**	–	**85.13%**
C_F	48.95%	53.63%	49.26%	49.54%	–	50.35%
T_t $[s]$	11.9020	0.1253	0.3770	56.0443	–	17.1122
T_c $[s]$	**0.0018**	**0.0577**	**0.0057**	**0.0076**	–	**0.0182**
T_o $[h]$	100	125	100	115	–	110

Table 7 Comparison of the results obtained for 3 types of normalization methods and 4 widths of the Hamming window calculated based on the results obtained for Experiment Nos. 1, 2 and 3. In all training sets, in all cases, the sum of the errors equals zero

Coefficient	Normalization			Extraction			
	No normalization	Rescaling	Standardization	128 samples	256 samples	512 samples	1024 samples
Experiment No. 1							
The results obtained for the best case (combination: classifier + normalization + window width)							
ERR_{sum}	**118**	**106**	**126**	**106**	**112**	**107**	–
ACC	98.13%	98.32%	98.01%	98.32%	98.23%	98.31%	–
SEN	**84.14%**	**85.75%**	**83.06%**	**85.75%**	**84.95%**	**85.62%**	–
SPE	99.01%	99.11%	98.94%	99.11%	99.06%	99.10%	–
Average results for all cases of the given experiment							
ERR_{sum}	**134, 83**	**119, 83**	**139, 17**	**134, 17**	**134, 25**	**125, 42**	–
ACC	97, 87%	98, 11%	97, 80%	97, 88%	97, 88%	98, 02%	–
SEN	**81, 88%**	**83, 89%**	**81, 29%**	**81, 97%**	**81, 96%**	**83, 14%**	–
SPE	98, 87%	98, 99%	98, 83%	98, 87%	98, 87%	98, 95%	–
T_t $[s]$	7, 5405	8, 1127	7, 4504	7, 7549	7, 6641	7, 6847	–
T_c $[s]$	**0, 0260**	**0, 0261**	**0, 0259**	**0, 0260**	**0, 0260**	**0, 0260**	–
T_o $[h]$	5, 5	5, 5	5, 5	5, 5	5, 5	5, 5	–
Experiment No. 2							
4-fold cross-validation/10-fold cross-validation							
The results obtained for the best case (combination: classifier + normalization + window width)							
ERR_{sum}	**108**	**97**	**109**	**99**	**104**	**97**	**98**
	85	**81**	**87**	**92**	**89**	**81**	**85**
ACC	98.29%	98.47%	98.28%	98.43%	98.36%	98.47%	98.45%
	98.66%	98.72%	98.62%	98.55%	98.59%	98.72%	98.66%
SEN	**85.48%**	**86.96%**	**85.35%**	**86.69%**	**86.02%**	**86.96%**	**86.83%**
	88.58%	**89.11%**	**88.31%**	**87.63%**	**88.04%**	**89.11%**	**88.58%**
SPE	99.09%	99.19%	99.08%	99.17%	99.13%	99.19%	99.18%
	99.29%	99.32%	99.27%	99.23%	99.25%	99.32%	99.29%
κ	**83.42%**	**85.05%**	**83.27%**	**84.81%**	**83.97%**	**85.05%**	84.98%
	86.82%	**87.46%**	**86.51%**	**85.80%**	**86.20%**	**87.46%**	**86.92%**
Average results for all cases of given experiment							
ERR_{sum}	**125, 56**	**108, 94**	**128, 56**	**126, 17**	**127, 50**	**118, 17**	**112, 25**
	109, 38	**92, 63**	**111, 94**	**110, 25**	**108, 83**	**102, 25**	**97, 25**
ACC	98, 01%	98, 28%	97, 97%	98, 00%	97, 98%	98, 13%	98, 23%
	98, 27%	98, 54%	98, 23%	98, 26%	98, 28%	98, 38%	98, 46%
SEN	**83, 12%**	**85, 36%**	**82, 72%**	**83, 04%**	**82, 86%**	**84, 12%**	**84, 91%**
	85, 30%	**87, 55%**	**84, 95%**	**85, 18%**	**85, 37%**	**86, 26%**	**86, 93%**
SPE	98, 95%	99, 08%	98, 92%	98, 94%	98, 93%	99, 01%	99, 06%
	99, 08%	99, 22%	99, 06%	99, 07%	99, 09%	99, 14%	99, 18%

(continued)

Table 7 (continued)

Coefficient	Normalization			Extraction			
	No normalization	Rescaling	Standardization	128 samples	256 samples	512 samples	1024 samples
κ	**80, 70%**	**83, 28%**	**80, 24%**	**80, 65%**	**80, 43%**	**81, 82%**	**82, 72%**
	83, 10%	**85, 68%**	**82, 70%**	**82, 97%**	**83, 20%**	**84, 18%**	**84, 97%**
T_t [s]	10, 6200	10, 1902	9, 7305	9, 9812	10, 0230	10, 7484	9, 9684
	38, 7735	34, 4454	34, 0473	34, 9725	36, 5018	35, 5818	35, 9654
T_c [s]	**0, 0217**	**0, 0264**	**0, 0275**	**0, 0264**	**0, 0197**	**0, 0270**	**0, 0272**
	0, 0204	**0, 0343**	**0, 0343**	**0, 0252**	**0, 0253**	**0, 0343**	**0, 0339**
T_o [h]	12	12	12	12	12	12	12
	24	24	24	24	24	24	24
Experiment No. 3							
The results obtained for the best case (combination: classifier + normalization + window width)							
ERR_{sum}	**83**	**73**	**81**	**91**	**86**	**73**	**74**
ACC	98.69%	98.85%	98.72%	98.56%	98.64%	98.85%	98.83%
SEN	**88.84%**	**90.19%**	**89.11%**	**87.77%**	**88.44%**	**90.19%**	**90.05%**
SPE	99.30%	99.39%	99.32%	99.24%	99.28%	99.39%	99.38%
κ	**87.19%**	**88.70%**	**87.53%**	**85.94%**	**86.70%**	**88.70%**	**88.53%**
C_F	49.49%	49.09%	48.84%	46.74%	49.59%	49.09%	47.91%
Average results for all cases of the given experiment							
ERR_{sum}	**99.69**	**84.94**	**104.13**	**105.75**	**102.08**	**92.58**	**84.58**
ACC	98.42%	98.66%	98.35%	98.33%	98.39%	98.54%	98.66%
SEN	**86.60%**	**88.58%**	**86.00%**	**85.79%**	**86.28%**	**87.56%**	88.63%
SPE	99.16%	99.29%	99.13%	99.11%	99.14%	99.22%	99.29%
κ	**84.60%**	**86.88%**	**83.92%**	**83.66%**	**84.24%**	**85.70%**	**86.93%**
C_F	50.93%	50.94%	49.14%	48.58%	51.82%	49.46%	51.52%
T_t [s]	16.0006	17.1829	18.1530	18.6174	17.3389	16.4237	16.0685
T_c [s]	**0.0180**	**0.0193**	**0.0173**	**0.0167**	**0.0195**	**0.0178**	**0.0189**
T_o [h]	110	110	110	110	110	110	110

6 Discussion

6.1 Hypothesis

The results obtained in all experiments confirmed the thesis: the application of the proposed methodology will enable the automatic, efficient, universal, low computational complexity and fast recognition of heart disorders based on ECG signal analysis and the evolutionary-neural system.

The confirmation of this statement is given by the obtained results, summarized in Tables 3, 4, and 5. The presented results show that the recognition **sensitivity** of

the 17 classes for the best evolutionary-neural system based on the *SVM* classifier (rescaling + 512 samples) is ***SEN* = 90.19%** (*ACC* = 98.85%, *SPE* = 99.39%). This result is better than the average sensitivity of the results presented in the current scientific literature, which is **88.86%** (Table 5). The obtained result is one of the best in the scientific literature, where the three best results are **94%** [43] and **93%** [49, 51] (Table 5). It should be noted that the results obtained by the author include the recognition of 17 classes (a recognition sensitivity for 15 and 12 classes of 92 and 95%; Fig. 8). In contrast, the results presented in the scientific literature include the recognition of only 5 classes (for the subject-oriented validation scheme [30]).

The obtained classification time for the ECG signal fragments, $\boldsymbol{C_k}$ **= 0.0018 [*s*]**, for the best evolutionary-neural system based on the *SVM* classifier is also very important.

6.2 Machine Learning Algorithms

Based on the results obtained in Experiment No. 3 and presented in Table 3 and Table 4, we find that the best classifier was the **SVM** classifier (ERR_{sum} = 73 errors and average = 87.83 errors; *SEN* = 90.19% and average = 88.19%); the other classifiers obtained worse results: **PNN** (ERR_{sum} = 77 errors and average = 97.50 errors; *SEN* = 89.65% and average = 86.90%), **RBFNN** (ERR_{sum} = 79 errors and average = 96.67 errors; *SEN* = 89.38% and average = 87.01%) and **kNN** (ERR_{sum} = 79 errors and average = 103.00 errors; *SEN* = 89.38% and average = 86.16%).

Analogous results were obtained for Experiment Nos. 1, 2a, and 2b, which are presented in Tables 6 and 4.

6.3 Preprocessing with Normalization

Based on the results obtained in Experiment No. 3 and presented in Table 3 and Table 4, we find that the best signal normalization method was the **rescaling** method (ERR_{sum} = 73 errors and average = 84.94 errors; *SEN* = 90.19% and average = 88.58%); the other methods obtained worse results: **standardization** (ERR_{sum} = 81 errors and average = 104.13 errors; *SEN* = 89.11% and average = 86.00%) and **no normalization** (ERR_{sum} = 83 errors and average = 99.69 errors; *SEN* = 88.84% and average = 86.60%).

Analogous results were obtained for Experiment Nos. 1, 2a and 2b, which are presented in Table 7 and Table 4.

6.4 Feature Extraction

Based on the results obtained in No. 3 and presented in Tables 3 and 4, we find that the greatest efficiency for feature extraction was based on Hamming windows with widths of **512 samples** (ERR_{sum} = 73 and average = 92.58 errors; *SEN* = 90.19% and average = 87.56%) and **1024 samples** (ERR_{sum} = 74 and average = 84.58 errors; *SEN* = 90.05% and average = 88.63%); other Hamming window widths obtained worse results: **256 samples** (ERR_{sum} = 86 errors and average = 102.08 errors; *SEN* = 88.44% and average = 86.28%) and **128 samples** (ERR_{sum} = 91 errors and average = 105.75; *SEN* = 87.77% and average = 85.79%).

Analogous results were obtained for Experiment Nos. 1, 2a and 2b, which are presented in Tables 4 and 7.

The obtained result indicates that the best result was achieved under one of the widest Hamming windows: 512 samples. This width corresponds to an analysis window with a duration of approximately 1.25 [s] (approximately 2 heart evolutions), assuming that one evolution of the heart corresponds to approximately 310 samples of the ECG signal. The obtained result confirms the validity of the research methodology based on the analysis of longer (10-s) fragments of the ECG signal because the results for the narrower Hamming windows (256 samples) corresponding to a single evolution of the heart were characterized by lower recognition efficiency for heart disorders.

6.5 Feature Selection

Experiment No. 3 tested the effect of the applied genetic selection of the features. The applied feature selection increased the recognition sensitivity of heart pathology due to the removal of redundant or misleading information. Another positive effect of its utilization was the reduction in the length of the input feature vector. This resulted in an increased effect of the knowledge generalization achieved by the classifiers, reduced effect of over-fitting and reduced training, optimization, and classification times. The aim of the genetic selection of features was to eliminate the frequency components corresponding to noise, measurement errors, network voltage components, baseline wandering, and redundant information.

The confirmation of the presented findings is given by the obtained results, presented in Tables 3 and 4. From the results, it follows that the applied feature selection increased the recognition accuracy of heart dysfunctions (average *SEN* higher by about 1.0%) and decreased the sample training and classification times about 2-fold.

The results obtained for **Experiment No. 3** are as follows: $\boldsymbol{ERR_{sum}}$ **= 73 errors**; **average** $\boldsymbol{ERR_{sum}}$ **= 96 errors**; ***SEN*** **= 90.19%**, **average *SEN* = 87.06%**, $\boldsymbol{T_t}$ **= 11.35 [*s*]**, **average** $\boldsymbol{T_t}$ **= 17.11 [*s*]**, $\boldsymbol{T_c}$ **= 0.0018 [*s*]**, and **average** $\boldsymbol{T_c}$ **= 0.0182 [*s*]**. For comparison, for **Experiment No. 2b** (10-fold cross-validation), the results are as follows: ERR_{sum} = 81 errors; average ERR_{sum} = 105 errors; *SEN* = 89.11% and

average SEN = 85.93%, T_t = 30.11, average T_t = 35.76 [s], T_c = 0.0041 [s], and average T_c = 0.0297 [s].

Based on the obtained results presented in Tables 3 and 4, it can be observed that the average number of accepted features for Experiment No. 3 is $\boldsymbol{C_F}$ = **50.34%**. This means that the optimal results (highest sensitivity) were obtained after rejecting more than half of the features (the frequency components of the ECG signal power spectral density) from the input vector.

6.6 Cross-Validation

Based on the obtained results presented in Tables 4 and 6, it can be stated that better results were achieved under **10-fold cross-validation**. The respective obtained results for 4-fold and 10-fold cross-validation (based on Experiment No. 2) were the following: $\boldsymbol{ERR_{sum}}$ = 97 errors and **81 errors**; **average** $\boldsymbol{ERR_{sum}}$ = 121 errors and **105 errors**; $\boldsymbol{SEN}$ = 86.96 and **89.11%**, **average** $\boldsymbol{SEN}$ = 83.73 and **85.93%**.

The 4-fold cross-validation method is less computationally complex but based on the obtained results, the method achieves a lower efficiency. Because fewer classifiers models were created based on this method and because the created models learned on fewer elements of the training set, the models produced a worse fit for the recognition classes.

6.7 Parameter Optimization

Based on the obtained results presented in Table 4, it can be stated that better results were obtained under the **genetic algorithm**. The respective obtained results for the grid search method and the genetic algorithm (based on Experiment Nos. 1 and 2 for 4-fold cross-validation) were as follows: $\boldsymbol{ERR_{sum}}$ = 106 errors and **97 errors**; **average** $\boldsymbol{ERR_{sum}}$ = 131 errors and **121 errors**; $\boldsymbol{SEN}$ = 85.75 and **86.96%**, **average** $\boldsymbol{SEN}$ = 82.36 and **83.73%**.

The obtained result is as expected. Using a genetic algorithm, it was possible to search a much larger solution space compared to the grid search method. Another advantage was the much higher resolution (smaller step size) for the tested parameters. These two features resulted in a substantially better GA score.

6.8 Dysfunctions/Classes

One of the biggest difficulties in analyzing the ECG signal observed during this research is the variability of the morphological and dynamic features within a given class (disorder) for different patients. This problem was presented for the *normal*

sinus rhythm class for 14 different patients in Fig. 5 for ECG signals after the DFT was applied. The variability of the signals within one class for different patients is very large and comparable to the variability of the shapes of the ECG signals for different classes, as presented in Fig. 5b. This problem is presented in greater detail in Fig. 3.

In Fig. 7, the recognition efficiency for each class is presented with the best classifier from Experiment No. 3 - *SVM*. Based on this, we can observe a high recognition efficiency for practically all classes: ***SEN* over 70%**. The worst results were obtained for *supraventricular tachyarrhythmia* (*SEN* over 50%) and *fusion of ventricular and normal beat* (*SEN* over 60%).

Based on the obtained results presented in Fig. 7, we removed dysfunctions with the smallest value of the *SEN* coefficient. As a result, two other recognition cases were considered: **15 classes** (after removing the *supraventricular tachyarrhythmia* and *fusion of ventricular and normal beat* classes) and **12 classes** (after removing the *premature ventricular contraction*, *supraventricular tachyarrhythmia*, *ventricular trigeminy*, *Ventricular tachycardia* and *fusion of ventricular and normal beat* classes). The best classifier, *SVM*, obtained the following sensitivity for heart dysfunction recognition for **17, 15 and 12 classes**, respectively: ***SEN* = 90.19**, **91.52**, and **95.23%** and κ = **88.70**, **90.15**, and **94.31%**.

6.9 Times

6.9.1 Experiments

Based on Table 4, we can state that under **both methods for parameter optimization**, the grid search and the genetic algorithm (*Experiment No. 1* and *Experiment No. 2*) **obtained comparable optimization times**: $T_o[h]$ = 15 and 10 (for *SVM*, 2 parameters) and average $T_o[h]$ = 5.5 and 12. This confirms the superiority of the genetic algorithm, which achieved better results in a comparable amount of time. It should also be noted that the **training and classification times were significantly shortened** when applying **feature selection**. The algorithm without feature selection (*Experiment No. E2b*) and with feature selection (*Experiment No. 3*) obtained the following respective times: $T_t[s]$ = 30.11 and 11.35; $T_c[s]$ = 0.0041 and 0.0018 and average $T_t[s]$ = 35.76 and 17.11; $T_c[s]$ = 0.0297 and 0.0182.

Based on the optimization time (T_o), we can state that for *Experiment No. 3*, the classifier optimization required the most time: 220 days. The shortest time, 8 days, was required by *Experiment No. 1*.

6.9.2 Classifiers

According to Table 6, we can state that the **training of the kNN classifier was the fastest** and that the **training of the RBFNN classifier was the slowest** for *Experi-*

ment No. 3: average T_t [s] = 0.1253 and 56.0443, respectively. The **classification** of the ECG signal fragments by the **SVM classifier was the fastest**, and the **classification by the kNN classifier was the slowest** for *Experiment No. 3*: average T_c [s] = 0.0018 and 0.0577. **The optimization of the SVM and PNN classifiers was the fastest**, and the **optimization of the kNN classifier was the slowest** for *Experiment No. 3*: average T_o [h] = 100 and 125.

6.9.3 Cross-Validation

According to Table 6, we can state that, as expected, training, classification, and optimization **lasted much longer under 10-fold cross-validation** than under 4-fold cross-validation. The following results were respectively obtained for *Experiment No. 2* for 4-fold cross-validation and 10-fold cross-validation: average: T_t [s] = 10.18 and 35.76; T_c [s] = 0.0250 and 0.0297; T_o [h] = 12 and 24.

6.10 Computational Complexity

Our proposed methodology has a valuable benefit, which is **low computational complexity**. The investigation of longer segments of ECG signals (10-s), the proposed method could reduce the number of classifications when heart rate was 80 beats per minute, we had an **average of 13 times fewer classifications**. This advantage eliminated the need for both detections as well as the segmentation of QRS complexes. We would argue that training and optimization steps have computational complexity whereas the classification step has much less computationally complex compared to the traditional approach based on QRS complex detection. The proposed approach can be considered as a practical solution in mobile devices with less CPU and memory load, lower power consumption, and also longer battery life.

6.11 Advantages and Limitations

The proposed methodology (analysis of longer-duration ECG signal fragments) has the following advantages:

- reduced number (an average of 13 times) of classifications (analysis),
- no need to detect and segment QRS complexes,
- no need to filter the ECG signal,
- possibility to use the new methodology in tele-medicine (real-time signal processing) through implement designed solution in mobile devices or cloud computing (one lead, low computational complexity, and low cost),
- recognition of 17 cardiac arrhythmias (classes),

- high performance (high accuracy/sensitivity),
- more accurate classification for some diseases that are more likely to have time-varying ECG signal changes, e.g. pre-excitation syndromes, atrio-ventricular conduction blocks.

In turn, the main limitations can be included:

- a low number of ECG signal fragments (744 from 29 patients) in the analysed data set,
- no possibility to classification fragments of ECG signal containing more than one class (except normal sinus rhythm),
- not applying a completely subject-oriented validation scheme (inter-patient paradigm), due to an insufficient number of appropriate ECG signals in MIT-BIH database.

7 Conclusion

The major aim of this research was to present an efficient machine learning-based methodology to classify ECG signals. Therefore, an efficient and new recognition system of myocardium dysfunctions was applied to the data set with **17 classes** including normal sinus rhythm, pacemaker rhythm, as well as 15 arrhythmias. An evolutionary-neural system was applied to the **10-s fragments of ECG signals**. The data set included 744 fragments of ECG signals, which was related to 29 patients that collected from the MIH-BIH Arrhythmia data set (for one lead—MLII). The analysis of longer fragments (10-s) of the ECG signal was considered to conduct this research. By using Welch's method and a discrete Fourier transform approach the spectral power density was predicted in order to improve the characteristic features of the ECG signal. We conducted the research via three main experiments. Basic analysis of ECG signals was investigated. Therefore, genetic optimization of parameters and genetic selection of features were studied. The main three experiments were as follows: pre-processing, normalization, feature extraction, and selection, stratified cross-validation, machine learning algorithms (SVM, kNN, PNN, and RBFNN). It should be noted that obtained parameter optimizations outcomes were used. The proposed methodology showed remarkable performance with **high sensitivity (90.19%)**, specificity (99.39%), and accuracy (98.85%). It should be expressed that the **time for classification of one sample was 0.0018 (s)**, and there were 73 errors per 744 classifications. The novel methodology can be implemented in mobile devices or applied in cloud computing to diagnosis cardiac health immediately with highest accuracy.

There are several research topics for further investigation in the future. The first research in the future can be done about wavelet analysis in feature extraction. It is also worth to apply different ensemble learning techniques [60] and also deep learning methods [61, 87]. In addition, since current research used fragments of ECG signals only from one lead, future works can be concentrated on the more leads

(e. g., 2–12). Moreover, doing research on ECG signals fragments with more than one class type can also be considered. Finally, the methods can be applied to more number of appropriate ECG signal fragments [60, 87].

References

1. American Heart Association (AHA): What is cardiovascular disease? http://www.heart.org/en/health-topics/consumer-healthcare/what-is-cardiovascular-disease. Accessed 17 Sept 2018
2. World Health Organization WHO: Cardiovascular diseases. http://www.who.int/cardiovascular_diseases/en/. Accessed 17 Sept 2018
3. World Health Organization WHO: Cardiovascular diseases (CVDs). http://www.who.int/news-room/fact-sheets/detail/cardiovascular-diseases-(cvds). Accessed 17 Sept 2018
4. Abdar, M., Yen, N.Y., Hung, J.C.-S.: Improving the diagnosis of liver disease using multilayer perceptron neural network and boosted decision trees. J. Med. Biol. Eng. (2017)
5. Abdar, M., Zomorodi-Moghadam, M.: Impact of patients' gender on parkinson's disease using classification algorithms. J. AI Data Min. **6**(2), 277–285 (2018)
6. Abdar, M., Zomorodi-Moghadam, M., Das, R., Ting, I.-H.: Performance analysis of classification algorithms on early detection of liver disease. Expert Syst. Appl. **67**, 239–251 (2017)
7. Acharya, U.R., Fujita, H., Adam, M., Lih, O.S., Sudarshan, V.K., Hong, T.J., Koh, J.E., Hagiwara, Y., Chua, C.K., Poo, C.K., San, T.R.: Automated characterization and classification of coronary artery disease and myocardial infarction by decomposition of ECG signals: a comparative study. Inf. Sci. **377**, 17–29 (2017)
8. Acharya, U.R., Hagiwara, Y., Koh, J.E.W., Oh, S.L., Tan, J.H., Adam, M., Tan, R.S.: Entropies for automated detection of coronary artery disease using ECG signals: a review. Biocybern. Biomed. Eng. **38**(2), 373–384 (2018)
9. Acharya, U.R., Oh, S.L., Hagiwara, Y., Tan, J.H., Adam, M., Gertych, A., Tan, R.S.: A deep convolutional neural network model to classify heartbeats. Comput. Biol. Med. **89**, 389–396 (2017)
10. Afkhami, R.G., Azarnia, G., Tinati, M.A.: Cardiac arrhythmia classification using statistical and mixture modeling features of ECG signals. Pattern Recognit. Lett. **70**, 45–51 (2016)
11. Alickovic, E., Subasi, A.: Effect of multiscale PCA de-noising in ECG beat classification for diagnosis of cardiovascular diseases. Circuits Syst. Signal Process. **34**(2), 513–533 (2015)
12. Aličković, E., Subasi, A.: Breast cancer diagnosis using GA feature selection and rotation forest. Neural Comput. Appl. **28**(4), 753–763 (2017)
13. Alpaydin, E.: Introduction to Machine Learning. MIT Press (2014)
14. Altman, N.S.: An introduction to kernel and nearest-neighbor nonparametric regression. Am. Stat. **46**(3), 175–185 (1992)
15. Arjunan, S.P., Kumar, D.K., Naik, G.R.: A machine learning based method for classification of fractal features of forearm sEMG using twin support vector machines. In: 2010 Annual International Conference of the IEEE Engineering in Medicine and Biology, Aug 2010, pp. 4821–4824
16. Banerjee, S., Mitra, M.: Application of cross wavelet transform for ECG pattern analysis and classification. IEEE Trans. Instrum. Meas. **63**(2), 326–333 (2014)
17. Bazi, Y., Alajlan, N., AlHichri, H., Malek, S.: Domain adaptation methods for ECG classification. In: 2013 International Conference on Computer Medical Applications (ICCMA), Jan 2013, pp. 1–4
18. Bergstra, J., Bengio, Y.: Random search for hyper-parameter optimization. J. Mach. Learn. Res. **13**(1), 281–305 (2012)
19. Bishop, C.: Pattern Recognition and Machine Learning, 1st edn. Springer (2006)
20. Boc, A., Makarenkov, V.: Towards an accurate identification of mosaic genes and partial horizontal gene transfers. Nucl. Acids Res. **39**(21), e144 (2011)

21. Broomhead, D.S., Lowe, D.: Radial basis functions, multi-variable functional interpolation and adaptive networks. Complex Syst. **2** (1988)
22. Cabra, J.-L., Mendez, D., Trujillo, L.C.: Wide machine learning algorithms evaluation applied to ECG authentication and gender recognition. In: Proceedings of the 2018 2nd International Conference on Biometric Engineering and Applications, ICBEA '18, New York, NY, USA, 2018. ACM, pp. 58–64
23. Caraus, I., Mazoure, B., Nadon, R., Makarenkov, V.: Detecting and removing multiplicative spatial bias in high-throughput screening technologies. Bioinformatics **33**(20), 3258–3267 (2017)
24. Chang, C.-C., Lin, C.-J.: LIBSVM: a library for support vector machines. ACM Trans. Intell. Syst. Technol. **2**, 27:1–27:27 (2011). http://www.csie.ntu.edu.tw/~cjlin/libsvm
25. Chen, S., Hua, W., Li, Z., Li, J., Gao, X.: Heartbeat classification using projected and dynamic features of ECG signal. Biomed. Signal Process. Control. **31**, 165–173 (2017)
26. Chou, C., Chang, E., Li, H., Wu, A.: Low-complexity privacy-preserving compressive analysis using subspace-based dictionary for ECG telemonitoring system. IEEE Trans. Biomed. Circuits Syst. **12**(4), 801–811 (2018)
27. Cortes, C., Vapnik, V.: Support-vector networks. Mach. Learn. **20**(3), 273–297 (1995)
28. Cristianini, N., Schölkopf, B.: Support vector machines and kernel methods: the new generation of learning machines. AI Mag. **23**(3), 31–41 (2002)
29. da S. Luz, E.J., Nunes, T.M., de Albuquerque, V.H.C., Papa, J.P., Menotti, D.: ECG arrhythmia classification based on optimum-path forest. Expert Syst. Appl. **40**(9), 3561–3573 (2013)
30. da S. Luz, E.J., Schwartz, W.R., Cámara-Chávez, G., Menotti, D.: ECG-based heartbeat classification for arrhythmia detection: a survey. Comput. Methods Program Biomed. **127**, 144–164 (2016)
31. de Chazal, P., O'Dwyer, M., Reilly, R.B.: Automatic classification of heartbeats using ECG morphology and heartbeat interval features. IEEE Trans. Biomed. Eng. **51**(7), 1196–1206 (2004)
32. de Lammoy, G., Francois, D., Delbeke, J., Verleysen, M.: Weighted SVMs and feature relevance assessment in supervised heart beat classification. Communications in Computer and Information Science, vol. 127. Springer, pp. 212–223 (2010) (ch. Biomedical Engineering Systems and Technologies)
33. de Lannoy, G., Francois, D., Delbeke, J., Verleysen, M.: Weighted conditional random fields for supervised interpatient heartbeat classification. IEEE Trans. Biomed. Eng. **59**(1), 241–247 (2012)
34. Delen, D., Walker, G., Kadam, A.: Predicting breast cancer survivability: a comparison of three data mining methods. Artif. Intell. Med. **34**(2), 113–127 (2005)
35. Dora, L., Agrawal, S., Panda, R., Abraham, A.: Optimal breast cancer classification using Gauss-Newton representation based algorithm. Expert. Syst. Appl. **85**, 134–145 (2017)
36. Elhaj, F.A., Salim, N., Harris, A.R., Swee, T.T., Ahmed, T.: Arrhythmia recognition and classification using combined linear and nonlinear features of ECG signals. Comput. Methods Programs Biomed. **127**, 52–63 (2016)
37. Engelbrecht, A.P.: Computational Intelligence: An Introduction, 2nd edn. Wiley (2007)
38. Fawcett, T.: An introduction to ROC analysis. Pattern Recogn. Lett. **27**(8), 861–874 (2006)
39. Gao, C., Sun, H., Wang, T., Tang, M., Bohnen, N.I., Müller, M.L.T.M., Herman, T., Giladi, N., Kalinin, A., Spino, C., Dauer, W., Hausdorff, J.M., Dinov, I.D.: Model-based and model-free machine learning techniques for diagnostic prediction and classification of clinical outcomes in parkinson's disease. Sci. Rep. **8**(1), 7129 (2018)
40. Goldberger, A.L., Amaral, L.A.N., Glass, L., Hausdorff, J.M., Ivanov, P.C., Mark, R.G., Mietus, J.E., Moody, G.B., Peng, C.-K., Stanley, H.E.: PhysioBank, PhysioToolkit, and PhysioNet: components of a new research resource for complex physiologic signals. Circulation **101**(23), e215–e220 (2000). Circulation Electronic Pages: http://circ.ahajournals.org/content/101/23/e215.fullPMID:1085218. https://doi.org/10.1161/01.CIR.101.23.e215.
41. Hassoon, M., Kouhi, M.S., Zomorodi-Moghadam, M., Abdar, M.: Rule optimization of boosted c5.0 classification using genetic algorithm for liver disease prediction. In: 2017 International Conference on Computer and Applications (ICCA), Sept 2017, pp. 299–305

42. Holland, J.H.: Adaptation in Natural and Artificial Systems. MIT Press, Cambridge, MA, USA (1992)
43. Huang, H., Liu, J., Zhu, Q., Wang, R., Hu, G.: A new hierarchicalmethod for inter-patient heartbeat classification usingrandom projections and RR intervals. Biomed. Eng. Online **13**, 1–26 (2014)
44. Kalgotra, P., Sharda, R., Hammer, B., Albert, D.E.: Sensor analytics for interpretation of EKG signals. Expert. Syst. Appl. **123**, 377–385 (2019)
45. Kawaguchi, T., Tokushige, K., Hyogo, H., Aikata, H., Nakajima, T., Ono, M., Kawanaka, M., Sawada, K., Imajo, K., Honda, K., Takahashi, H., Mori, K., Tanaka, S., Seko, Y., Nozaki, Y., Kamada, Y., Fujii, H., Kawaguchi, A., Takehara, T., Yanase, M., Sumida, Y., Eguchi, Y., Seike, M., Yoneda, M., Suzuki, Y., Saibara, T., Karino, Y., Chayama, K., Hashimoto, E., George, J., Torimura, T.: A data mining-based prognostic algorithm for NAFLD-related hepatoma patients: a nationwide study by the Japan study group of NAFLD. Sci. Rep. **8**(1), 10434 (2018)
46. Książek, W., Abdar, M., Acharya, U.R., Pławiak, P.: A novel machine learning approach for early detection of hepatocellular carcinoma patients. Cogn. Syst. Res. **54**, 116–127 (2019)
47. Kuncheva, L.I.: Combining Pattern Classifiers: Methods and Algorithms. Wiley-Interscience (2004)
48. Lacy, S.E., Smith, S.L., Lones, M.A.: Using echo state networks for classification: a case study in parkinson's disease diagnosis. Artif. Intell. Med. **86**, 53–59 (2018)
49. Lin, C.C., Yang, C.M.: Heartbeat classification using normalized RR intervals and wavelet features. In: 2014 International Symposium on Computer, Consumer and Control (IS3C), June 2014, pp. 650–653
50. Liu, K., Kang, G., Zhang, N., Hou, B.: Breast cancer classification based on fully-connected layer first convolutional neural networks. IEEE Access **6**, 23722–23732 (2018)
51. Llamedo, M., Martinez, J.P.: Heartbeat classification using feature selection driven by database generalization criteria. IEEE Trans. Biomed. Eng. **58**(3), 616–625 (2011)
52. Ly, Q.T., Handojoseno, A.M.A., Gilat, M., Chai, R., Martens, K.A.E., Georgiades, M., Naik, G.R., Tran, Y., Lewis, S. J.G., Nguyen, H.T.: Detection of gait initiation failure in parkinson's disease based on wavelet transform and support vector machine. In: 2017 39th Annual International Conference of the IEEE Engineering in Medicine and Biology Society (EMBC), July 2017, pp. 3048–3051
53. Mar, T., Zaunseder, S., Martineznez, J.P., Llamedo, M., Poll, R.: Optimization of ECG classification by means of feature selection. IEEE Trans. Biomed. Eng. **58**(8), 2168–2177 (2011)
54. Martis, R.J., Acharya, U.R., Adeli, H., Prasad, H., Tan, J.H., Chua, K.C., Too, C.L., Yeo, S.W.J., Tong, L.: Computer aided diagnosis of atrial arrhythmia using dimensionality reduction methods on transform domain representation. Biomed. Signal Process. Control **13**, 295–305 (2014)
55. Mclachlan, G.J.: Discriminant Analysis and Statistical Pattern Recognition (Wiley Series in Probability and Statistics). Wiley-Interscience (2004)
56. Moody, G.B., Mark, R.G.: The impact of the MIT-BIH arrhythmia database. IEEE Eng. Med. Biol. Mag. **20**(3), 45–50 (2001)
57. Naik, G.R., Kumar, D.K., Jayadeva: Hybrid independent component analysis and twin support vector machine learning scheme for subtle gesture recognition. Biomedizinische Technik/Biomed. Eng. **55**(5), 301–307 (2010)
58. Oh, S.L., Ng, E.Y., Tan, R.S., Acharya, U.R.: Automated beat-wise arrhythmia diagnosis using modified U-net on extended electrocardiographic recordings with heterogeneous arrhythmia types. Comput. Biol. Med. **105**, 92–101 (2019)
59. Park, K.S., Cho, B.H., Lee, D.H., Song, S.H., Lee, J.S., Chee, Y.J., Kim, I.Y., Kim, S.I.: Hierarchical support vector machine based heartbeat classification using higher order statistics and hermite basis function. Comput. Cardiol. **2008**, 229–232 (2008)
60. Pławiak, P.: Novel genetic ensembles of classifiers applied to myocardium dysfunction recognition based on ECG signals. Swarm Evol. Comput. **39**, 192–208 (2018)
61. Pławiak, P.: Novel methodology of cardiac health recognition based on ECG signals and evolutionary-neural system. Expert Syst. Appl. **92**, 334–349 (2018)

62. Pławiak, P., Acharya, U.R.: Novel deep genetic ensemble of classifiers for arrhythmia detection using ECG signals. Springer Neural Comput. Appl. (2019)
63. Prieto, A., Prieto, B., Ortigosa, E.M., Ros, E., Pelayo, F., Ortega, J., Rojas, I.: Neural networks: an overview of early research, current frameworks and new challenges. Neurocomputing **214**, 242–268 (2016)
64. Quinlan, J.: Induction of decision trees. Mach. Learn. **1**(1), 81–106 (1986)
65. Rad, A.B., Eftestol, T., Engan, K., Irusta, U., Kvaloy, J.T., Kramer-Johansen, J., Wik, L., Katsaggelos, A.K.: ECG-based classification of resuscitation cardiac rhythms for retrospective data analysis. IEEE Trans. Biomed. Eng. **64**(10), 2411–2418 (2017)
66. Rajesh, K.N., Dhuli, R.: Classification of imbalanced ECG beats using re-sampling techniques and adaboost ensemble classifier. Biomed. Signal Process. Control **41**, 242–254 (2018)
67. Rodriguez-Sotelo, J., Peluffo-Ordonez, D., Cuesta-Frau, D., Castellanos-Domínguez, G.: Unsupervised feature relevance analysis applied to improve ECG heartbeat clustering. Comput. Methods Programs Biomed. **108**(1), 250–261 (2012)
68. Rutkowski, L.: Computational Intelligence: Methods and Techniques. Springer (2008)
69. Sannino, G., Pietro, G.D.: A deep learning approach for ECG-based heartbeat classification for arrhythmia detection. Future Gener. Comput. Syst. **86**, 446–455 (2018)
70. Scholkopf, B., Smola, A.J.: Learning with Kernels: Support Vector Machines, Regularization, Optimization, and Beyond. MIT Press, Cambridge, MA, USA (2001)
71. Sharma, M., Deb, D., Acharya, U.R.: A novel three-band orthogonal wavelet filter bank method for an automated identification of alcoholic EEG signals. Appl. Intell. **48**(5), 1368–1378 (2018)
72. Smith, S.: Digital Signal Processing: A Practical Guide for Engineers and Scientists. Newnes (2002)
73. Sokolova, M., Lapalme, G.: A systematic analysis of performance measures for classification tasks. Inf. Process. Manag. **45**(4), 427–437 (2009)
74. Soria, M.L., Martinez, J.: Analysis of multidomain features for ECG classification. Comput. Cardiol. **2009**, 561–564 (2009)
75. Specht, D.F.: Probabilistic neural networks. Neural Netw. **3**(1), 109–118 (1990)
76. Sugeno, M.: Industrial Applications of Fuzzy Control. Elsevier Science Pub. Co. (1985)
77. Tadeusiewicz, R.: Neural networks as a tool for modeling of biological systems. Bio-Algorithms Med-Syst. **11**(3), 135–144 (2015)
78. Tahiri, N., Willems, M., Makarenkov, V.: A new fast method for inferring multiple consensus trees using k-medoids. BMC Evol. Biol. **18**(1), 48 (2018)
79. Tverskoi, D., Makarenkov, V., Aleskerov, F.: Modeling functional specialization of a cell colony under different fecundity and viability rates and resource constraint. PLOS One **13**(8), 1–27 (2018)
80. Varatharajan, R., Manogaran, G., Priyan, M.K.: A big data classification approach using LDA with an enhanced SVM method for ECG signals in cloud computing. Multimed. Tools Appl. **77**(8), 10195–10215 (2018)
81. Welch, P.: The use of fast fourier transform for the estimation of power spectra: a method based on time averaging over short, modified periodograms. IEEE Trans. Audio Electroacoust. **15**(2), 70–73 (1967)
82. Yang, W., Si, Y., Wang, D., Guo, B.: Automatic recognition of arrhythmia based on principal component analysis network and linear support vector machine. Comput. Biol. Med. **101**, 22–32 (2018)
83. Ye, C., Kumar, B.V.K.V., Coimbra, M.T.: Combining general multi-class and specific two-class classifiers for improved customized ECG heartbeat classification. In: 2012 21st International Conference on Pattern Recognition (ICPR), Nov 2012, pp. 2428–2431
84. Ye, C., Kumar, B.V.K.V., Coimbra, M.T.: Heartbeat classification using morphological and dynamic features of ECG signals. IEEE Trans. Biomed. Eng. **59**(10), 2930–2941 (2012)
85. Yildirim, O.: A novel wavelet sequence based on deep bidirectional ISTM network model for ECG signal classification. Comput. Biol. Med. **96**, 189–202 (2018)
86. Yildirim, O.: ECG beat detection and classification system using wavelet transform and online sequential ELM. J. Mech. Med. Biol. **19**, 1940008 (2019)

87. Yildirim, O., Pławiak, P., Tan, R.-S., Acharya, U.R.: Arrhythmia detection using deep convolutional neural network with long duration ECG signals. Comput. Biol. Med. **102**, 411–420 (2018)
88. Yu, M.-L., Li, S.-M., Gao, X., Li, J.-G., Xu, H., Chen, K.-J.: Sodium tanshinone II a sulfonate for coronary heart disease: a systematic review of randomized controlled trials. Chin. J. Integr. Med. (2018)
89. Zham, P., Arjunan, S.P., Raghav, S., Kumar, D.K.: Efficacy of guided spiral drawing in the classification of parkinson's disease. IEEE J. Biomed. Health Inform. **22**(5), 1648–1652 (2018)
90. Zhang, Z., Dong, J., Luo, X., Choi, K.-S., Wu, X.: Heartbeat classification using disease-specific feature selection. Comput. Biol. Med. **46**, 79–89 (2014)
91. Zhang, Z., Luo, X.: Heartbeat classification using decision level fusion. Biomed. Eng. Lett. **4**(4), 388–395 (2014)
92. Zubair, M., Kim, J., Yoon, C.: An automated ECG beat classification system using convolutional neural networks. In: 2016 6th International Conference on IT Convergence and Security (ICITCS), Sept 2016, pp. 1–5

Artificial Intelligence-Enabled ECG Big Data Mining for Pervasive Heart Health Monitoring

Qingxue Zhang

Abstract The ECG signal is a gold standard physiological signal to reflect heart health and has been studied for many decades. It can not only be leveraged to generate real-time emergency alarms before a heart attack but also be mined in a long-term manner for risk pattern discovery. ECG signal has specific characteristics in multiple domain, such as the temporal, frequency, statistical, and phase domains, each of which can reveal some interesting medical hints related to the mechanical and electrical behaviors of the heart. Traditionally, ECG signals are acquired in clinics or hospitals, where very high signal quality can be guaranteed. However, along with the advance of wearable computers and mobile computing platforms, there are many emerging ECG-based heart disease management possibilities, i.e., possibly, we can monitor the ECG signal in our daily lives and effectively track our heart health without going to medical facilities. However, it is very challenging to deal with motion artifacts during people's physical activates. Many researchers have proposed a large number of ECG signal processing algorithms and studied a bunch of potential applications. We have introduced artificial intelligence into wearable ECG-based heart rate monitoring during severe human activities, which greatly outperform previous studies. We have also studied novel ECG applications, which can capture single-arm-ECG for 24-hour heart disease monitoring. The goal in this work is to eliminate the uncomfortableness and inconvenience induced by traditional ECG configurations, i.e., the 12-lead ECG placement methods. Especially, previously, people put the ECG electrodes on the chest, which requires a chest strap to fix the electrodes. Leveraging advanced signal sensing and artificial intelligence algorithms, we have successfully demonstrated the potential of this highly wearable arm-worn heart rate monitor. This chapter will systematically introduce the current advancement of ECG signal processing algorithms and applications, including previous works and our research progress. The readers from both academia and industry can benefit from the chapter by understanding the advancement, challenges, and future opportunities from this chapter.

Q. Zhang (✉)
Indiana University-Purdue University Indianapolis, Indianapolis, USA
e-mail: qxzhang@iu.edu

G. Naik (ed.), *Biomedical Signal Processing*, Series in BioEngineering,
https://doi.org/10.1007/978-981-13-9097-5_12

1 Introduction

Cardiac health monitoring is of significant value to effectively manage people's heart health, due to the fact that heart disease is the leading cause of death worldwide [59]. To monitor cardiac health, it is essential to find out a vital signal that can reflect rich information during the cardiac cycles. Electrocardiogram (ECG) [13, 39, 51], has been used as the gold standard signal to monitor cardiac health. ECG signal is of many medical relevant characteristics and has been used by physicians for decades in heart disease diagnosis. Unfortunately, ECG measurements are usually performed in the medical facilities, such as the clinical and hospital. This poses lots of inconvenience for cardiac health monitoring since the patients need to make the appointments, go to the facilities, get the measurement, and then return home. Moreover, it also induces a high medical cost, since both medical facilities and physicians/nurses need to be involved in this frequency and checkups.

The advancement of the internet of things (IoT) [62] and artificial intelligence (AI) [34, 56] have been paving a promising way for smart health [5, 6, 30, 45, 57, 58]. The former one, IoT, actually includes many technologies, such as wearable sensing, wireless transmission, and mobile edge computing, which make the body worn sensor network (BSN) more and more promising in pervasive health monitoring [9, 22, 49, 52, 67]. The latter one, AI, makes the signal processing much more powerful, in terms of signal characteristic extraction and high-level medical insights learning [2, 20, 31, 41, 47]. We take a special interest in the wearable daily cardiac health monitoring application and highlight the advanced artificial intelligence methods in smart health applications [17, 29, 37]. The AI will be new electricity for the whole society and is reshaping many areas now, including the healthcare area.

In this chapter, the advancement of ECG-based cardiac health monitoring, visualized in Fig. 1, will be deeply analyzed and summarized. Especially, the AI-enabled signal processing methods will be highlighted and compared with traditional signal processing methods. In wearable daily heart health monitoring, people are randomly performing different physical activities, which greatly impact the ECG signal quality and pose huge challenges to its signal processing [23, 28, 46, 64]. As we know, the sensor-skin contact is randomly impacted by the human motions, which make the bio-sensing suffer a lot from the unstable and poor signal propagation path. The ECG signal may be contaminated or even highly corrupted during diver human motions. We have proposed multiple AI-enabled algorithms to identify the heartbeat from highly noisy ECG signals, which are expected to advance the pervasive ECG-based cardiac health monitoring. Meanwhile, traditional algorithms in terms of wearable heart rate monitoring are also summarized, and the limitations are also given. Furthermore, the opportunities and future directions of AI-enabled ECG heart health monitoring are given, which are expected to greatly benefit both academic and industrial communities.

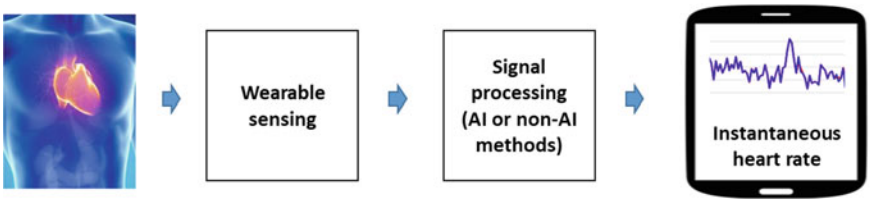

Fig. 1 Pervasive ECG-based AI-enabled cardiac health monitoring

2 Cardiac ECG Bio-potential

The cardiac movement can be effectively monitored by the standard ECG signal. Here the cardiac movements, cardiac bio-potential, and cardiac ECG will be detailed.

2.1 Cardiac Movements

A cardiac cycle corresponds to two phases of the heart muscle movements: the contraction and the expansion, each of which has very complicated mechanisms. During the contraction, the heart pumps the blood out of the heart and empty the heart, and immediately the heart relaxes and receives the blood returning from other systems of the human body. So these two periods, the contraction and the expansion, repeat, and quasi-periodically control the blood flow [18, 21, 68].

In the heart, there are two atrial and ventricle chambers, which play irreplaceable roles in each cardiac cycle. In the left heart, there are the left atrium and the left ventricle, and in the right, there are the right atrium and the right ventricle. Each component of the heart needs to coordinate with each other and work continuously to finish a cardiac cycle, which is be quantitatively represented as the heart rate (number of cardiac cycles per minute).

The heart rate reveals many valuable indicators of heart movement conditions. Many heart movement abnormalities can be reflected in the abnormal heart rate. That's why the heart rate has been used in doctor visits as a routine cardiac health measurement approach. The cardiac movements all contribute to the heart rate measurements. Therefore, many medical investigations have shown a strong relationship between the heart rate and many cardiac malfunctions. Since here, we focus on the ECG-based heart rate monitoring; we will further demonstrate how the cardiac movements relate to the cardiac bio-potential behaviors, and how the bio-potential is finally measured as ECG.

2.2 Cardiac Bio-potential

In a healthy heart, the sinus node in the heart is triggered by the electrical impulse from the nerve connected with the brain. After this triggering event, the sinus node stimulated the heart muscle to contract and expand, to pump out the blood and to receive the blood consecutively. More specifically, one cardiac cycle includes four stages: atrial systole, ventricular systole, atrial diastole, and ventricular diastole [15, 33, 54].

During atrial systole, both atria contract and push the blood into the ventricles, lasting about 0.1 s; during ventricular systole, both ventricles contract to push the blood through the pulmonary trunk to both lungs and other systems of the body through the aorta, lasting 0.3 s; during atrial diastole, both atria expand and thus receive the blood from large veins—the vena cava; and finally during ventricular diastole, both ventricles expand and receive blood from the atria passively, lasting about 0.5 s.

The electrical behaviors of all the heart elements need to coordinate with each other, to generate a normal heart rhythm. The sinus node is like a cardiac pacemaker and is situated in the upper wall of the right atrium. This node quasi-periodically stimulates the atria and then another node, the atrioventricular (AV) node, located in the lower wall between the atrium and the ventricle, is triggered. The two nodes control the contraction of the atria and ventricles, respectively. There is a delay between activation of these two nodes, to allow the blood to flow from atria to the ventricles, before pumping the blood to the lungs and other systems of the body.

2.3 Cardiac ECG

The muscle movements of different heart elements correspond to different electrical behaviors, which can be measured on the body surface in terms of the ECG signal. ECG signal has been used as a gold standard for decades, to reflect cardiac internal behaviors. The ECG morphology includes several key segments: P wave, QRS complex, and T wave [3, 12, 13]. The P wave corresponds to the atrial depolarization (contraction), the QRS complex corresponds to the ventricular depolarization (contraction), and the T wave corresponds to the ventricular repolarization (expansion).

Malfunction of each element of the heart may yield different heart rhythms, such as fast heartbeat, slow heartbeat, and irregular heartbeat, which all result in abnormal heart rate information. That is why the heart rate information reflects the electrical behaviors of the heart and corresponding mechanical behaviors. Many research findings reveal more and more relations between heart rate information and cardiac diseases.

Traditionally, ECG is measured by the 12-lead ECG configuration methods [13, 32, 39, 50]. Six electrodes are placed on the chest, surrounding the heart to yield v1 to v6—six leads. Besides, electrodes are placed on two wrists, left leg, yielding

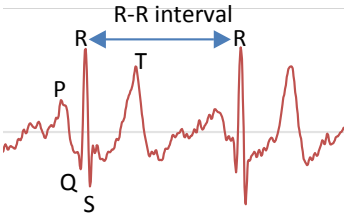

Fig. 2 ECG heartbeat morphology

three leads (selecting any two electrodes, with one as the signal electrode, and the other as the reference electrode). Another three leads are yielded as generating virtual reference electrodes, for example, the average of the right wrist and the left leg is regarded as the virtual reference, and the left wrist is regarded as the signal electrode. To enhance the signal quality, a bias electrode is usually placed on the right leg, named as the 'Driving Right Leg' (DRL) electrode. These 12-lead ECG signals can provide very strong signal strength, and spatially reflect the electrical/mechanical behaviors of the whole heart (Fig. 2).

Nowadays, people are interested in measuring heart rate information from wearable ECG monitors. This is of tremendous potential towards pervasive heart health monitoring. Some works still put the electrodes on the chest or two wrists—traditional lead configurations, to get the wearable ECG. When the wearer is performing different physical activities, the sensor-skin contact is randomly impacted and thus highly lower the ECG signal quality.

In this chapter, as mentioned above, we mainly focus on how to robustly process the highly noisy ECG signals to advance daily heart rate monitoring during body movements. One thing worth noting is that wearable heart rate monitoring also paves a way for continuous heart rate monitoring. That means the instantaneous heart rate information can be continuously estimated and visualized/stored on the cellphone, for long-term high-resolution heart health monitoring. This cannot be imagined using traditional medical facilities, due to the fact that patients are unable to and unwilling to stay in clinics/hospitals all the time to get continuous heart health monitoring.

3 Traditional Cardiac Health Signal Processing

Many investigations have been made to deal with the noisy ECG signal, to estimate the heart rate information, including the wavelet de-noising, Kalman filtering, weighted regularized least square, and so on. Here, we mainly focus on these three representative methods and details their technical foundations, advantages, and limitations. An example of the clean and noisy ECG signals is given in Fig. 3

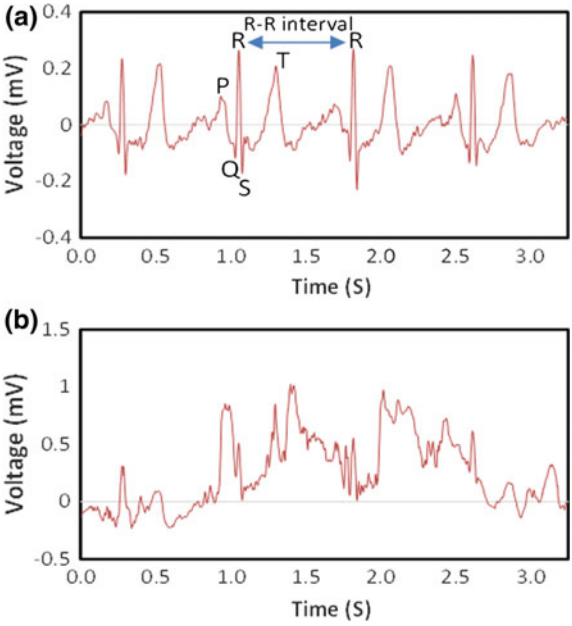

Fig. 3 An example of the clean and motion artifact-corrupted ECG signals

3.1 Kalman Filtering

The Kalman filtering method aims to enhance the measurement robustness by firstly predicting and then refining each measurement. Given a series of measurements that are observed over time, Kalman Filtering tends to produce estimates that are more robust than a single measurement itself. More specifically, Kalman Filtering predicts the measurement with the process model, and then refine it using the measurement model [26, 43, 55].

In the former step, i.e., prediction, Kalman Filtering generates estimates of the current state variables and their uncertainties, and in the latter step, i.e., refinement, it leverages the next measurement that is contaminated with noise and error, to update the prediction using a weighted average. With the weighted average, more weight will be given to the measurement that owns higher certainty. The whole process is recursive and can work in real-time.

During heart rate estimation, the sequence of the instantaneous heart rate is the output of the filter. For each heart rate estimate, the process model predicts a guess, and then the measurement model updates this guess with new measured information. If the new measurement is of higher certainty, then the new measurement contributes more to update the guess. Otherwise, the new measurements may have very little impact the guess. The certainty can be generated using a detector, such as an impulse rejection filter, which applies some rules to check whether the new measurement may be an outlier or not.

During the Kalman Filtering, the noise covariance matrix is usually chosen to be 0.1, and the noise covariance matrix is updated based on $M = M_0 \cdot \exp\left(1/w^2 - 1\right)$, where w is a weighting factor representing the certainty of the measurement ($w = 10^{-5}$ for outliers detected by the rejection filter, and $w = 1$ for non-outliers), and M_0 is a parameter to be tuned.

The advantage of Kalman Filtering is that is can apply more weight on the prediction when the measurement is suspected to be of much uncertainty, and vice verse. However, the limitation is also obvious since it needs to assume the noise model. Considering the motion artifacts are very difficult to be modeled, Kalman Filtering may not be able to well predict and refine the estimates during random and severe motion artifacts.

3.2 Wavelet De-noising

The wavelet method decomposes the ECG signal to multiple signal components, usually using the QRS complex-mimic mother wavelet—Daubechies6 wavelet, and then reconstruct the ECG signal using selected signal components and discard components that are more likely due to noise. So this method is somehow like a noise filtering method. In previous studies [4, 11, 19, 25, 35, 42, 61], the wavelet methods usually include the following key steps:

Step 1. Select the ECG signal
Step 2. Decompose the signal to multiple signal elements, corresponding to different detail coefficients
Step 3. Select specific detail coefficients, which include most energy of the QRS complex
Step 4. Reconstruct the ECG signal using these selected components

After wavelet-based signal de-noising, usually, a threshold-based method is applied to detect the R peaks of the ECG heartbeats. Consequently, the instantaneous heart rate can be estimated.

The advantage of this method is that it can suppress the motion artifacts during slight human body movements. However, during severe human body movements, the frequency spectrum of motion artifacts usually overlap with the ECG heartbeat, making the reconstructed signal still include lots of motion artifacts. This is the major limitation of this method. The quantitative comparison will be given later to illustrate more details on the heartbeat distinguishing capability of wave de-noising.

3.3 Weighted Regularized Least Square

The weighted regularized least square (WRLS) method [16, 66], assumes the heart rate estimation task to be an optimization problem. It tries to minimize the cost function as shown in (1):

$$\|A \cdot W \cdot RRI_{OLS} - A \cdot W \cdot RRI_{WRLS}\|^2 + \lambda^2 \cdot \|L \cdot RRI_{WRLS}\|^2 \quad (1)$$

where,

- RRI_{OLS}: the R peak-to-R peak interval (RRI) estimates generated by an ordinary least square problem (ORS)
- RRI_{WRLS}: the target RRI estimates to be found
- A: a lower triangular integration matrix, with a dimension of $N \times N$
- W: a diagonal weighting matrix, with a dimension of $N \times N$
- L: a smoothing matrix, with a dimension of $(N - 2) \times N$
- λ: a parameter to be tuned to regularize the objective function, in terms of the smoothness of the target RRI sequence

With the weighted regularized least square (WRLS) method, the heart rate estimation sequence may be well smoothed during motion artifacts. Nevertheless, when motion artifacts are severe, a heavy smoothing operation is required, which may cause a large drift between the estimated sequence and the ground truth sequence.

4 Artificial Intelligence-Empowered Cardiac Health Mining

Artificial intelligence (AI) methods [8, 10, 34, 38, 53, 56] are paving a promising way towards robust cardiac health monitoring. As analyzed above, although traditional non-artificial intelligence-based methods own different advantages in heart rate estimation from noisy ECG signals, they cannot work well during severe random motion artifacts.

Here we will introduce the new advancements in AI-based methods, especially the AI frameworks we have proposed, in terms of robust ECG-based heart rate monitoring. Furthermore, a detailed quantitative comparison between the traditional and AI-based methods will be illustrated to show the competitiveness of the AI techniques.

4.1 Pattern Recognition

Pattern recognition techniques recognize the patterns from the signal [1, 7, 14, 24, 36, 40, 66]. Broadly speaking, pattern recognition can also be grouped into machine learning techniques. However, these techniques usually more focus on capturing patterns from the signal. Given patterns or regularities in the data, pattern recognition techniques are concerned with how to automatically discover them in the data.

The ECG heartbeat is a typical pattern in the ECG data since a heartbeat is composed of several segments that repeat every cardiac cycle. That's why we have introduced a famous pattern recognition technique, dynamic time warping (DTW) to the ECG heartbeat recognition task, and achieved promising performance boosting compared with traditional approaches mentioned above [66]. Later, we will also show how we applied novel methods to enhance the DTW to be multi-view DTW, which highly boosted the heart rate estimation performance. The general pattern recognition framework is shown in Fig. 4, where the ECG signal is usually pre-processed by a band-pass filter, screened by a DTW template, and finally recognized from the DTW matching paths. A purification step can also be added to smooth the heart rate estimation curve.

More specifically, DTW builds two matrices during the pattern (heartbeat) recognition process, a local distance matrix, and a path distance matrix [66]. Given an ECG sequence X as (2), and a pre-defined heartbeat template Y as (3), where N and M are a number of sample in X and Y, respectively.

$$X = [x_i | 0 \leq i \leq N - 1] \tag{2}$$

$$Y = [y_j | 0 \leq j \leq M - 1] \tag{3}$$

When building the local distance matrix, DTW calculates the sample to sample distance between X and Y, as (4), where $d_{i,j}$ is the local distance element.

$$d_{i,j} = \left| x_i - y_j \right|, \forall i, \forall j \tag{4}$$

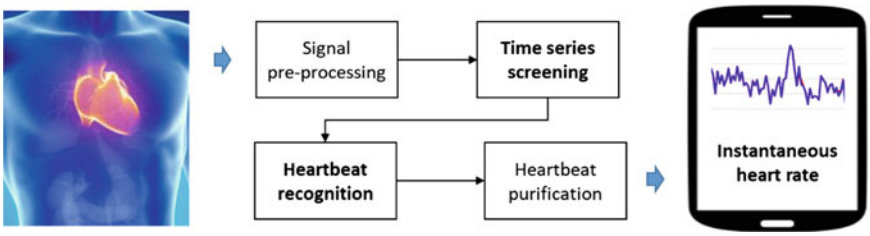

Fig. 4 The ECG heartbeat pattern recognition for wearable heart rate monitoring

When building the path distance matrix, a dynamic programming strategy is applied, as shown in (5), where $D_{i,j}$ is the path distance element. To determine $D_{i,j}$, three surrounding candidate paths are evaluated, and the shortest one is chosen to extend the path. After this dynamic path searching process, multiple paths can be generated.

$$D_{i,j} = \begin{cases} d_{i,j} + \min \begin{cases} D_{i-1,j} \\ D_{i-1,j-1} \\ D_{i,j-1} \end{cases} & \forall i > 0, \forall j > 0 \\ d_{i,j} & \forall i, j = 0 \\ inf & i = 0, \forall j > 0 \end{cases} \tag{5}$$

To determine which paths correspond to actually heartbeat pattern in the signal, a threshold is required, and it can be obtained from the training data. Once this threshold is determined, the DTW paths can be subsequently selected out, each of which corresponds to a heartbeat pattern found in the signal sequence.

Since the R peak location in the template signal is known, we can determine the corresponding matched sample in the DTW path that will be a heartbeat R peak. We have introduced this powerful method to the heartbeat recognition task and further enhance the DTW to be multi-view DTW. In multi-view DTW, we have increased the dimension of the signal and template sequences from one to three.

The advantage of this high-dimensional data representation is that the so-called phase loop, as shown in Fig. 5, are more tolerant of motion artifacts. Figure 5d4 shows heartbeat trajectories, which are more distinguishable than the time-domain ECG heartbeats in Fig. 5b. On the left side, the clean ECG signal is also visualized in the original time-domain and the new high-dimensional domain for comparison purpose. The multi-view ECG sequence is fed into the multi-view DTW, and the corresponding heartbeats will be recognized more robustly.

Multiple high-dimensional spaces have been evaluated, as shown in Fig. 6. It is clearly shown that the introduced dimensions have successfully suppressed the motion artifacts, and yielded much more robust heart rate estimation results (e.g., Fig. 6d, which includes three dimensions).

4.2 Machine Learning

The machine learning techniques, mainly the classification approaches, attracting intensive attention these days to differentiate different objects [27, 34, 44, 48, 60]. In the heartbeat identification task, the classification methods can be applied to differentiate the real heartbeats from faking heartbeats due to the motion artifacts. As shown in Fig. 7, the major difference between it and the pattern recognition methods, are the steps between pre-processing and purification. Here, the heartbeat candidates need to be firstly generated from the noisy signal sequence, which will be fed into

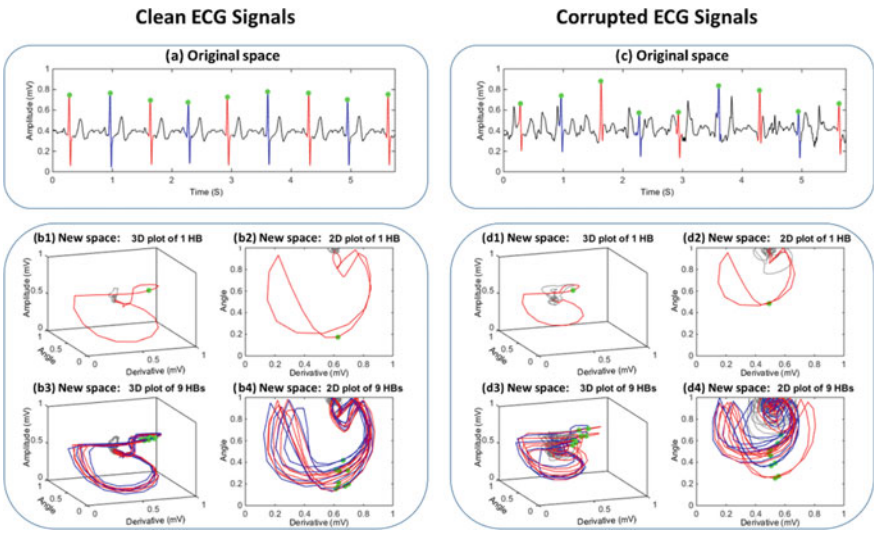

Fig. 5 Multi-view ECG phase loops to be fed into the multi-view DTW, for heartbeat recognition purpose, which shows that with sever

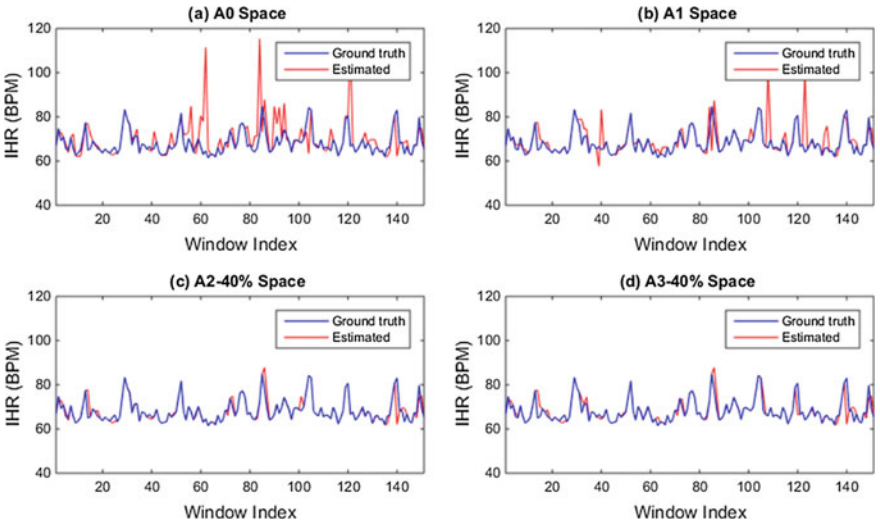

Fig. 6 Pattern recognition-based heart rate estimation results. A0 space: the original time-domain; A1 space: both amplitude and derivative dimensions are included; A2-40% space: both amplitude and angle dimensions are included; A3-40% space: amplitude, derivative and angle dimensions are all includes; 40%: 40% of the length of the QRS complex is used to determine the left/right angle boundaries

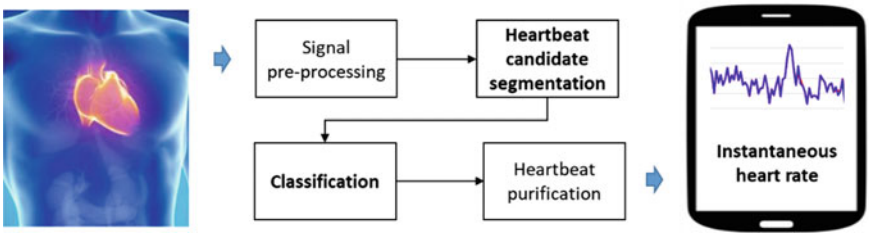

Fig. 7 The heartbeat identification framework using machine learning techniques

the machine learning classifier to generate the class labels—either real heartbeat or faking heartbeat.

We have proposed a novel machine learning framework, including a powerful machine learning classifier, support vector machine (SVM), and advanced feature extraction techniques. The proposed framework has been validated on the motion-tolerant heartbeat identification task [63, 64, 65], and greatly outperforms traditional signal processing methods. More specifically, SVM tries to find out a hyper plane to separate two classes, during optimizing the cost function defined in (6–8),

$$\min_{w,b} \frac{1}{2}\left\|w^2\right\| + C\sum_{i=1}^{M}\xi_i \tag{6}$$

$$s.t.\quad y_i\left(w^T \cdot \Phi(x_i) + b\right) \geq 1 - \xi_i,\ \forall x_i \tag{7}$$

$$\xi_i \geq 0 \tag{8}$$

where,

- $\frac{1}{2}w^2$: the regularization part
- $C\sum_i^M \xi_i$: the loss due to misclassified instances
- w: a weighting factor to be determined
- C: a parameter to tradeoff between the separation margin and the classification error
- ξ_i: the nonnegative slave variables for misclassification penalization
- y_i: class label
- x_i: instance
- $\Phi(x_i)$: kernel function
- b: bias to be determined

After applying the Lagrange multipliers α_i, the above optimization problem can be solved and finally yields a classification function as (9), where $K\left(x_i, x_j\right) = \Phi(x_i) \cdot \Phi\left(x_j\right)$ is the inner product between two instances in the kernel space.

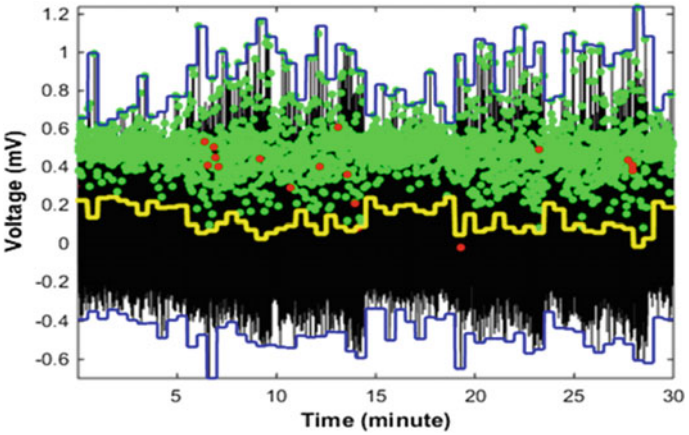

Fig. 8 Heartbeat candidates generated by a threshold-based method. Green dots: selected real heartbeats; red dots: missing heartbeats; large amounts of faking heartbeats are also selected but not visualized; yellow line: adaptive threshold; blue lines: signal envelope

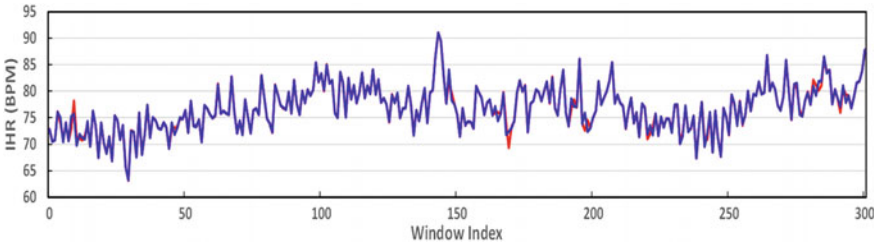

Fig. 9 The machine learning-based heart rate estimation curve. Blue curve: ground truth; red curve: the estimated heart rate trend

$$\bar{y} = sign\left(\sum_{i=1}^{M} \alpha_i y_i K\left(x_i^T, x\right) + b\right) \tag{9}$$

The heartbeat candidates generated by the threshold-based methods are shown in Fig. 8, which will be fed into the SVM classifier to generate the class labels. One thing worth noting is that large amounts of faking heartbeats are also selected but not visualized in Fig. 8.

After identifying the heartbeats and applying an outlier removal filter, the heart rate estimation curve is shown in Fig. 9, showing that the heart rate is robustly estimated and almost overlap with the ground truth heart rate curve.

To enhance the wearability, we have studied a non-traditional sensing method—sensing the ECG signal from the left upper-arm, not from the chest or two wrists. The sensing signal is pretty weak, only around 10% of the traditional chest ECG, in terms of the signal strength. However, it paves a way towards unobtrusive sensing

and pervasive heart health monitoring because people can wear the device and forget about it. Also using the machine learning algorithm—the SVM, and unsupervised purification methods, we have achieved very robust heart rate estimation results from this single-arm ECG signal. The root means square error and the mean absolute error are 1.2 and 0.2 beats per minute, respectively.

5 Conclusion and Future Directions

5.1 Conclusion

Smart cardiac health monitoring is attracting more and more intentions nowadays. To thoroughly compare traditional signal processing approaches and advanced artificial intelligence-based approaches, we have quantitatively compared them using two databases. The results are shown in Table 1, which clearly shows that advanced AI-enabled methods greatly outperform the traditional non-AI-based signal processing methods.

The AI techniques are capable of capturing more signal characteristics from the corrupted information. Therefore, we conclude that AI has been paving a promising way for noisy cardiac ECG learning, and our studies have demonstrated that AI techniques have greatly boosted the ECG-based heart rate estimation performance. These advancements are expected to contribute to pervasive heart health management.

Table 1 Quantitative comparison among multiple traditional and advanced artificial intelligence-enabled approaches

Databases	KLMF	WRLS	DWT	DTW	MDTW	SVM
WECG_SNRm1	4.2/6.8	4.6/6.1	3.1/4.8	1.2/4.2	0.2/1.4	0.1/0.6
WECG_SNRm7	63.1/68.0	39.0/43.2	7.1/12.8	6.7/14.1	1.6/5.3	1.4/6.5
FECG_SNRm1	2.2/5.0	2.8/4.4	2.0/3.6	1.8/6.6	0.5/2.6	0.4/1.6
FECG_SNRm7	69.6/76.7	44/8.50.0	4.5/9.2	7.1/16.0	1.4/4.9	1.4/5.8

Notes KLMF Kalman Filtering; *WRLS* weighted regularized least square; *DWT* discrete wavelet transform; *DTW* dynamic time warping; *MDTW* multi-view dynamic time warping; *SVM* support vector machine; two numbers in the format x/y: x is the mean absolute error, and y is the root mean square error, both with the same unit—beats per minute; WECG_SNRm1: a wrist ECG database acquired from 22 subjects, and corrupted by motion artifacts to be −1 dB (the signal to noise ratio); m7: −7 dB; FECG: another database called Fantasia ECG database

5.2 Future Directions

In the future, there are several promising research directions, focusing on current challenges in cardiac health monitoring. Firstly, it will be promising to explore more motion tolerant features, considering the motion artifacts are highly random and may be very severe during intensive body movement. The current features extracted have been validated on a few databases. However, when dealing with noisy or corrupted ECG signals under diverse motion scenarios, it is still very necessary to explore more motion tolerant features. Moreover, it is necessary to lower the computation complexity of the algorithms. Since the wearable health monitoring applications usually have a strict power budget, the corresponding signal processing algorithms need to be tailored sometimes to accommodate this constraint. Many new technologies such as sparse signal processing and down-sampling techniques, are of great potentials to lower the power consumption of the algorithms. How to balance the performance and the power consumption is highly important, since the complicated algorithm may greatly increase the power requirements when bringing better performance. This chapter is expected to provide the readers with advancements, limitations, and future directions, in terms of ECG signal processing for pervasive cardiac health monitoring in the era of smart health.

References

1. Al-Jawad, A., Adame, M.R., Romanovas, M., Hobert, M., Maetzler, W., Traechtler, M., et al.: Using multi-dimensional dynamic time warping for tug test instrumentation with inertial sensors. In: 2012 IEEE Conference on Multisensor Fusion and Integration for Intelligent Systems (MFI), pp. 212–218. IEEE (2012)
2. Alemdar, H., Tunca, C., Ersoy, C.: Daily life behaviour monitoring for health assessment using machine learning: bridging the gap between domains. Pers. Ubiquitous Comput. **19**(2), 303–315 (2015)
3. AlGhatrif, M., Lindsay, J.: A brief review: history to understand fundamentals of electrocardiography. J. Community Hosp. Intern. Med. Perspect. **2**(1), 14383 (2012)
4. Awal, M.A., Mostafa, S.S., Ahmad, M., Rashid, M.A.: An adaptive level dependent wavelet thresholding for ECG denoising. Biocybern. Biomed. Eng. **34**(4), 238–249 (2014)
5. Baig, M.M., Gholamhosseini, H.: Smart health monitoring systems: an overview of design and modeling. J. Med. Syst. **37**(2), 9898 (2013)
6. Baig, M.M., Gholamhosseini, H.: Smart health monitoring systems: an overview of design and modeling. J. Med. Syst. **37**(2), 1–14 (2013)
7. Birjandtalab, J., Zhang, Q., Jafari, R.: A case study on minimum energy operation for dynamic time warping signal processing in wearable computers. In: 2015 IEEE International Conference on Pervasive Computing and Communication Workshops (PerCom Workshops), pp. 415–420. IEEE (2015)
8. Chai, R., Naik, G.R., Ling, S.H., Nguyen, H.T.: Hybrid brain–computer interface for biomedical cyber-physical system application using wireless embedded EEG systems. Biomed. Eng. Online **16**(1), 5 (2017)
9. Clark, S.L., Hamilton, E.F., Garite, T.J., Timmins, A., Warrick, P.A., Smith, S., et al.: The limits of electronic fetal heart rate monitoring in the prevention of neonatal metabolic acidemia. Am. J. Obstet. Gynecol. **216**(2), 163, e1–163, e6 (2017)

10. Clifford, G., McSharry, P., Tarassenko, L.: Characterizing artefact in the normal human 24-hour RR time series to aid identification and artificial replication of circadian variations in human beat to beat heart rate using a simple threshold. In: Computers in Cardiology, 2002, pp. 129–132. IEEE (2002)
11. da Silva, M.J.: Characterization of QRS complex in ecg signals applying wavelet transform. In: 2015 International Conference on Mechatronics, Electronics and Automotive Engineering (ICMEAE), pp. 86–89. IEEE (2015)
12. Das, M.K., Saha, C., El Masry, H., Peng, J., Dandamudi, G., Mahenthiran, J., et al.: Fragmented QRS on a 12-lead ECG: a predictor of mortality and cardiac events in patients with coronary artery disease. Heart Rhythm **4**(11), 1385–1392 (2007)
13. Das, M.K., Suradi, H., Maskoun, W., Michael, M.A., Shen, C., Peng, J., et al.: Fragmented wide QRS on a 12-lead ECG: a sign of myocardial scar and poor prognosis. Circ.: Arrhythmia Electrophysiol. **1**(4), 258–268 (2008)
14. Di Brina, C., Niels, R., Overvelde, A., Levi, G., Hulstijn, W.: Dynamic time warping: a new method in the study of poor handwriting. Hum. Mov. Sci. **27**(2), 242–255 (2008)
15. Freyermuth, F., Rau, F., Kokunai, Y., Linke, T., Sellier, C., Nakamori, M., et al.: Splicing misregulation of SCN5A contributes to cardiac-conduction delay and heart arrhythmia in myotonic dystrophy. Nat. Commun. **7**, 11067 (2016)
16. Gribok, A.V., Chen, X., Reifman, J.: A robust method to estimate instantaneous heart rate from noisy electrocardiogram waveforms. Ann. Biomed. Eng. **39**(2), 824–834 (2011)
17. Guo, Y., Naik, G.R., Huang, S., Abraham, A., Nguyen, H.T.: Nonlinear multiscale maximal Lyapunov exponent for accurate myoelectric signal classification. Appl. Soft Comput. **36**, 633–640 (2015)
18. Hall, J.E.: Guyton and Hall Textbook of Medical Physiology E-BOOK. Elsevier Health Sciences (2015)
19. He, H., Wang, Z., Tan, Y.: Noise reduction of ECG signals through genetic optimized wavelet threshold filtering. In: 2015 IEEE International Conference on Computational Intelligence and Virtual Environments for Measurement Systems and Applications (CIVEMSA), pp. 1–6. IEEE (2015)
20. Hijazi, S., Page, A., Kantarci, B., Soyata, T.: Machine learning in cardiac health monitoring and decision support. Computer **49**(11), 38–48 (2016)
21. Kern, M.J., Sorajja, P., Lim, M.J.: Cardiac Catheterization Handbook E-Book. Elsevier Health Sciences (2015)
22. Khan, E., Al Hossain, F., Uddin, S.Z., Alam, S.K., Hasan, M.K.: A robust heart rate monitoring scheme using photoplethysmographic signals corrupted by intense motion artifacts. IEEE Trans. Biomed. Eng. **63**(3), 550–562 (2016)
23. Kim, H., Kim, S., Van Helleputte, N., Berset, T., Geng, D., Romero, I., et al.: Motion artifact removal using cascade adaptive filtering for ambulatory ECG monitoring system. In: 2012 IEEE Biomedical Circuits and Systems Conference (BioCAS), pp. 160–163. IEEE (2012)
24. Kotas, M.: Application of dynamic time warping to ECG processing. In: Proceedings of the International Conference on MIT, Poland, IX, pp. 169–175 (2006)
25. Li, C., Zheng, C., Tai, C.: Detection of ECG characteristic points using wavelet transforms. IEEE Trans. Biomed. Eng. **42**(1), 21–28 (1995)
26. Li, Q., Mark, R.G., Clifford, G.D.: Robust heart rate estimation from multiple asynchronous noisy sources using signal quality indices and a Kalman filter. Physiol. Meas. **29**(1), 15 (2008)
27. Li, Q., Rajagopalan, C., Clifford, G.D.: A machine learning approach to multi-level ECG signal quality classification. Comput. Methods Programs Biomed. **117**(3), 435–447 (2014)
28. Liu, S.-H.: Motion artifact reduction in electrocardiogram using adaptive filter. J. Med. Biol. Eng. **31**(1), 67–72 (2011)
29. Ly, Q.T., Handojoseno, A.A., Gilat, M., Chai, R., Martens, K.A.E., Georgiades, M., et al.: Detection of turning freeze in Parkinson's disease based on S-transform decomposition of EEG signals. In: 2017 39th Annual International Conference of the IEEE Engineering in Medicine and Biology Society (EMBC), pp. 3044–3047. IEEE (2017)

30. Lymberis, A.: Smart wearable systems for personalised health management: current R&D and future challenges In: Proceedings of the 25th Annual International Conference of the IEEE Engineering in Medicine and Biology Society, 2003, pp. 3716–3719. IEEE (2003)
31. Mahdavinejad, M.S., Rezvan, M., Barekatain, M., Adibi, P., Barnaghi, P., Sheth, A.P., et al.: Machine learning for internet of things data analysis: a survey. Digit. Commun. Netw. **4**(3), 161–175 (2018)
32. Maron, B.J., Friedman, R.A., Kligfield, P., Levine, B.D., Viskin, S., Chaitman, B.R., et al.: Assessment of the 12-Lead ECG as a screening test for detection of cardiovascular disease in healthy general populations of young people (12–25 years of age). Circulation **130**(15), 1303–1334 (2014)
33. Marraffa, J., Holland, M., Sullivan, R., Morgan, B., Oakes, J., Wiegand, T., et al.: Cardiac conduction disturbance after loperamide abuse. Clin. Toxicol. **52**(9), 952–957 (2014)
34. Michalski, R.S., Carbonell, J.G., Mitchell, T.M.: Machine Learning: An Artificial Intelligence Approach. Springer Science & Business Media (2013)
35. Mukhopadhyay, S., Biswas, S., Roy, A.B., Dey, N.: Wavelet based qrs complex detection of ECG signal. Int. J. Eng. Res. Appl. **2**(3), 2361–2365 (2012)
36. Myers, C., Rabiner, L.R., Rosenberg, A.E.: Performance tradeoffs in dynamic time warping algorithms for isolated word recognition. IEEE Trans. Acoust., Speech Signal Process. **28**(6), 623–635 (1980)
37. Naik, G.R., Baker, K.G., Nguyen, H.T.: Dependence independence measure for posterior and anterior EMG sensors used in simple and complex finger flexion movements: evaluation using SDICA. IEEE J. Biomed. Health Inform. **19**(5), 1689–1696 (2015)
38. Naik, G.R., Selvan, S.E., Gobbo, M., Acharyya, A., Nguyen, H.T.: Principle component analysis applied to surface electromyography: a comprehensive review. IEEE Access (2016)
39. Perlman, O., Katz, A., Weissman, N., Amit, G., Zigel, Y.: Atrial electrical activity detection using linear combination of 12-lead ECG signals. IEEE Trans. Biomed. Eng. **61**(4), 1034–1043 (2014)
40. Phinyomark, A., Limsakul, C., Phukpattaranont, P.: A novel feature extraction for robust EMG pattern recognition. arXiv preprint: arXiv:0912.3973 (2009)
41. Pramanik, M.I., Lau, R.Y., Demirkan, H., Azad, M.A.K.: Smart health: big data enabled health paradigm within smart cities. Expert. Syst. Appl. **87**, 370–383 (2017)
42. Sayadi, O., & Shamsollahi, M.B.: ECG denoising with adaptive bionic wavelet transform. In: Conference proceedings: … Annual International Conference of the IEEE Engineering in Medicine and Biology Society. IEEE Engineering in Medicine and Biology Society. Annual Conference, pp. 6597–6600 (2005)
43. Sayadi, O., Shamsollahi, M.B.: ECG denoising and compression using a modified extended Kalman filter structure. IEEE Trans. Biomed. Eng. **55**(9), 2240–2248 (2008)
44. Shalev-Shwartz, S., Ben-David, S.: Understanding Machine Learning: From Theory to Algorithms. Cambridge University Press (2014)
45. Solanas, A., Patsakis, C., Conti, M., Vlachos, I.S., Ramos, V., Falcone, F., et al.: Smart health: a context-aware health paradigm within smart cities. IEEE Commun. Mag. **52**(8), 74–81 (2014)
46. Song, J., Shan, T., Zhu, S., Chiu, Y.: A motion-artifact tracking and compensation technique for dry-contact EEG monitoring system In: 2014 IEEE Signal Processing in Medicine and Biology Symposium (SPMB), pp. 1–4. IEEE (2014)
47. Sprint, G., Cook, D., Fritz, R., Schmitter-Edgecombe, M.: Detecting health and behavior change by analyzing smart home sensor data. In: 2016 IEEE International Conference on Smart Computing (SMARTCOMP), pp. 1–3. IEEE (2016)
48. Sra, S., Nowozin, S., Wright, S.J.: Optimization for Machine Learning. Mit Press (2012)
49. Sun, B., Zhang, Z.: Photoplethysmography-based heart rate monitoring using asymmetric least squares spectrum subtraction and bayesian decision theory. IEEE Sens. J. **15**(12), 7161–7168 (2015)
50. Tomašić, I., Trobec, R.: Electrocardiographic systems with reduced numbers of leads—synthesis of the 12-Lead ECG. IEEE Rev. Biomed. Eng. **7**, 126–142 (2014)

51. Tsouri, G.R., Ostertag, M.H.: Patient-specific 12-lead ECG reconstruction from sparse electrodes using independent component analysis. IEEE J. Biomed. Health Inform. **18**(2), 476–482 (2014)
52. van Andel, J., Ungureanu, C., Aarts, R., Leijten, F., Arends, J.: Using photoplethysmography in heart rate monitoring of patients with epilepsy. Epilepsy & Behav. **45**, 142–145 (2015)
53. Varon, C., Caicedo, A., Testelmans, D., Buyse, B., Huffel, S.V.: A novel algorithm for the automatic detection of sleep apnea from single-lead ECG (2015)
54. Veeraraghavan, R., Gourdie, R.G., Poelzing, S.: Mechanisms of cardiac conduction: a history of revisions. Am. J. Physiol.-Hear. Circ. Physiol. **306**(5), H619–H627 (2014)
55. Vullings, R., De Vries, B., Bergmans, J.W.: An adaptive Kalman filter for ECG signal enhancement. IEEE Trans. Biomed. Eng. **58**(4), 1094–1103 (2011)
56. Vyas, N.: Biomedical Signal Processing. Pinnacle Technology (2011)
57. Wang, B.R., Park, J.-Y., Chung, K., Choi, I.Y.: Influential factors of smart health users according to usage experience and intention to use. Wireless Pers. Commun. **79**(4), 2671–2683 (2014)
58. Warren, S., Craft, R.L., Bosma, B.: Designing smart health care technology into the home of the future. In: Workshops on Future Medical Devices: Home Care Technologies for the 21st Century, p. 667 (1999)
59. WHO: The 10 leading causes of death in the world. http://www.who.int/mediacentre/factsheets/fs310/en/ (2014)
60. Witten, I.H., Frank, E., Hall, M.A., Pal, C.J.: Data Mining: Practical Machine Learning Tools and Techniques. Morgan Kaufmann (2016)
61. Yadav, T., Mehra, R.: Denoising and SNR improvement of ECG signals using wavelet based techniques. In: 2016 2nd International Conference on Next Generation Computing Technologies (NGCT), pp. 678–682. IEEE (2016)
62. Zhang, Q.: Deep learning of electrocardiography dynamics for biometric human identification in era of IoT. In: 2018 IEEE 9th Annual Ubiquitous Computing, Electronics and Mobile Communication Conference (UEMCON). IEEE (in press) (2018)
63. Zhang, Q., Zeng, X., Hu, W., Zhou, D.: A machine learning-empowered system for long-term motion-tolerant wearable monitoring of blood pressure and heart rate with ear-ECG/PPG. IEEE Access **5**, 10547–10561 (2017)
64. Zhang, Q., Zhou, D., Zeng, X.: A novel machine learning-enabled framework for instantaneous heart rate monitoring from motion-artifact-corrupted electrocardiogram signals. Physiol. Meas. **37**(11), 1945 (2016)
65. Zhang, Q., Zhou, D., Zeng, X.: Highly wearable cuff-less blood pressure and heart rate monitoring with single-arm electrocardiogram and photoplethysmogram signals. Biomed. Eng. Online **16**(1), 23 (2017)
66. Zhang, Q., Zhou, D., Zeng, X.: A novel framework for motion-tolerant instantaneous heart rate estimation by phase-domain multi-view dynamic time warping. IEEE Trans. Biomed. Eng. **64**(11), 2562–2574 (2017)
67. Zhang, Z., Pi, Z., Liu, B.:. TROIKA: a general framework for heart rate monitoring using wrist-type photoplethysmographic signals during intensive physical exercise. IEEE Trans. Biomed. Eng. **62**(2), 522–531 (2015)
68. Zipes, D.P., Libby, P., Bonow, R.O., Mann, D.L., Tomaselli, G.F.: Braunwald's Heart Disease E-Book: A Textbook of Cardiovascular Medicine. Elsevier Health Sciences (2018)

The Power of Tensor-Based Approaches in Cardiac Applications

Sibasankar Padhy, Griet Goovaerts, Martijn Boussé, Lieven De Lathauwer and Sabine Van Huffel

Abstract The electrocardiogram (ECG) is a biomedical signal that is widely used to monitor the heart and diagnose cardiac problems. Depending on the clinical need, the ECG is recorded with one or multiple leads (or channels) from different body locations. The signals from different ECG leads represent the cardiac activity in different spatial directions and are thus complementary to each other. In traditional methods, the ECG signal is represented as a vector or a matrix and processed to analyze temporal information. When multiple leads are present, most methods process each lead individually and combine decisions from all leads in a later stage. While this approach is popular, it fails to exploit the structural information captured by the different leads. Recently, there is a trend towards the use of tensor-based methods in biomedical signal processing. These methods represent the signals by tensors, which are higher-order generalizations of vectors and matrices that allow the analysis of multiple modes simultaneously. In the past years, tensor decomposition methods

The first two authors have equal contribution for the work.

S. Padhy (✉) · G. Goovaerts · M. Boussé · L. De Lathauwer · S. Van Huffel
Department of Electrical Engineering (ESAT), STADIUS Center for Dynamical Systems, Signal Processing and Data Analytics, KU Leuven, Leuven, Belgium
e-mail: sibasankar.padhy@kuleuven.be; sibasankar.padhy@vit.ac.in

G. Goovaerts
e-mail: griet.goovaerts@kuleuven.be

M. Boussé
e-mail: martijn.bousse@kuleuven.be

L. De Lathauwer
e-mail: lieven.delathauwer@kuleuven.be

S. Van Huffel
e-mail: sabine.vanhuffel@kuleuven.be

S. Padhy · G. Goovaerts · S. Van Huffel
imec, Leuven, Belgium

S. Padhy
School of Electronics (SENSE), Vellore Institute of Technology, Vellore, India

L. De Lathauwer
Group Science, Engineering and Technology, KU Leuven Kulak, Kortrijk, Belgium

G. Naik (ed.), *Biomedical Signal Processing*, Series in BioEngineering,
https://doi.org/10.1007/978-981-13-9097-5_13

have been applied to ECG signals to solve different clinical challenges. This chapter discusses the power of different tensor decompositions with a focus on typical ECG problems that can be solved using tensors.

1 Introduction

The electrocardiogram (ECG) is a well-known diagnostic tool and one of the most preferred tests in every day clinical practice. It is widely-used in both hospitals and ambulatory environments because it is easy to measure and contains a large amount of information about the condition of the heart. Moreover, its associated cost is relatively low compared to imaging techniques such as echocardiography or magnetic resonance imaging.

In recent years, advances in sensor techniques and the introduction of wireless technologies have led to the development of various new ECG technologies, including wearable devices and smart phone set-ups. The rise of these novel technologies has introduced both opportunities and challenges in the field of ECG monitoring. Improvements in digital filters led to more accurate noise removal methods and increased signal qualities, which allow the detection and analysis of more refined ECG characteristics. Expansions of computing power and storage capacity permit the use of more advanced signal processing techniques, and advances in material sciences have to lead to the development of sensors that can be worn for many days in a row. Manual analysis of these large-scale ECG data sets has become tedious, time-consuming, and expensive, leveraging the need for automated ECG processing methods that can analyze the data in a computationally efficient way.

In a clinical context, ECG signals are mostly recorded with different channels or leads, where each lead corresponds to the cardiac electrical signal viewed from a different spatial angle. The combination of these channels gives a global view from the heart in three dimensions. While matrices could technically be used to analyze these multidimensional signals by constructing multiple matrices for each spatial angle and concatenating them in one big matrix, there is no reason why the original multidimensionality of the data should not be preserved and exploited maximally. This way the information that is shared over all dimensions can be analyzed simultaneously. This can be done in a straightforward way through the use of tensors. Mathematically speaking, tensors are higher-order generalizations of vectors (first-order) and matrices (second-order). Tensor tools have been applied extensively in various applications within signal processing, data mining, object recognition, and machine learning [8, 19, 26, 52, 53, 63, 64, 84, 93]. In biomedical signal processing, they have also gained popularity in neuroscience applications such as gait recognition, epilepsy monitoring, brain tissue segmentation, neuroimaging, magnetic resonance imaging, and EEG processing [9, 10, 22, 43, 51, 58, 60, 86, 88, 92, 97, 99].

In the context of tensor-based ECG signal processing, tensors are first used in blind source separation to separate the fetal ECG (FECG) from the maternal ECG. In the PhysioNet/Computing in Cardiology (CinC) Challenge 2013 with a topic

Noninvasive Fetal ECG, a number of methods have been developed for solving the FECG separation problem. Niknazar et al. [72] reshaped the measured signals in a three-way tensor which was then decomposed with canonical polyadic decomposition (CPD), separating the maternal and fetal ECG signals. In a similar approach by Akhbari et al. [4], a weighted CPD version was used in order to improve the robustness of the method. Debals et al. [24] and Boussé et al. [14] both used tensorization techniques, Löwnerization and segmentation in the respective methods, for blind source separation and showed the effectiveness for the FECG separation problem. Other tensor decomposition methods used for FECG separation are PARAFAC2 [1], which extends the CPD by allowing variations in one mode, and the periodic Tucker Decomposition [5].

The literature also includes a few tensor-based studies on various cardiac abnormality detection problems. One such study is irregular heartbeat classification where the objective is to discriminate different types of heartbeats affected by arrhythmia from normal sinus beats. Li et al. [59] and Huang and Zhang [46] both proposed tensor-based methods on 12-lead ECG with the objective to maximally exploit spatial information of the different ECG leads and extract more robust features. Spectral information using the short-time Fourier transform has been used to construct tensors, which were then decomposed with higher-order variations of Principal Component Analysis (PCA) and Linear Discriminant Analysis (LDA) in the respective methods. Another abnormal heart rhythm is atrial fibrillation (AF). Block term decomposition has been applied to analyze the atrial activity [81, 98] and automatically extract atrial sources [73] in multilead ECG signals of patients with AF. A multiscale tensor-based approach combining wavelet decompositions and multilinear Singular Value Decomposition have also been proposed for the following two ECG applications: detection and localization of myocardial infarction [77], and T-wave alternans analysis [79]. Finally, other ECG application areas in which tensors were used are ECG denoising [54] and compression [75]. Recently, He et al. developed a new feature extraction approach in tensor space by combining the discrete wavelet packet transform and multilinear PCA [42].

The purpose of this chapter is to focus on five representative applications in ECG processing where tensors have been successfully used to process multilead ECG signals. Since tensors are a rather novel concept in ECG processing, the next section first gives motivation for the use of tensor methods in ECG processing. In Sect. 3, the main concepts and methods related to tensors are summarized. We encourage interested readers to refer to the overview articles and references therein for a more comprehensive overview of tensor methods and their applications [8, 19, 52, 84]. Section 4 discusses the use of tensor methods in five specific ECG applications, where we highlight the flexible way tensors can be used to deal with specific ECG characteristics. Here, we discuss the tensor-based approaches to the third-order tensor. Finally, Sect. 5 concludes the chapter by suggesting possible directions for future research. The work described in this chapter, especially Sects. 2 and 3 and the CPD-based methods, is largely based on [38].

2 Motivation

ECG signals can be measured with one or more leads, but multilead recordings are considered as the gold standard, especially in clinical contexts. Also, long-term recordings are often performed using Holter monitors, which typically have a minimum of two channels. Each lead records the cardiac electrical activity from a different spatial angle, complementing each other and enabling a comprehensive three-dimensional view of the electrical activity of the heart.

Most methods that deal with multilead ECG data employ a late-integration approach, which means that they process each lead *separately* and afterward combine the results of all channels [41, 55, 95]. This obviously fails to exploit the correlations *between* the different spatial angles, leading to a loss of available information. Tensor methods allow one to simultaneously analyze all channels, enabling exploitation of all the available information at once in contrast to late-integration methods. Hence, a tensor-based approach is clearly advantageous for applications that require the assessment of the global behavior of the heart.

While matrix-based decomposition methods have been used successfully in many applications, they often put constraints on the signals in order to obtain unique and thus interpretable solutions. For example, Principal Component Analysis (PCA) requires the different components to be orthogonal to each other, and Independent Component Analysis enforces independence between the different components. These assumptions are, however not necessarily met in real-life conditions. However, in contrast to low-rank matrix models, low-rank tensor models are unique under mild conditions.

Finally, when dealing with biomedical signal processing problems, interpretability of the final outcome is paramount, especially when the results need to be communicated with clinicians and patients. Nowadays, deep learning methods such as artificial neural networks are rapidly gaining popularity. Although these models have been shown to give accurate results, they are *black box* models, meaning it is not straightforward to interpret how the outcome is calculated from the input. In contrast to artificial neural networks, tensor methods can lead to physiologically interpretable results. Tensor methods, on the other hand, can lead to interpretable components which can be physiologically interpreted.

3 Tensors and Tensor Tools

3.1 Basic Concepts and Notations

Appropriate data representation is an important step that helps gain insight and process the data in an effective way. Generally speaking, data with N modes are represented by a Nth-order tensor $\mathcal{X} \in \mathbb{R}^{I_1 \times I_2 \times \cdots \times I_N}$. The number of modes of a tensor is equal to the order, e.g. a tensor with three modes is a third-order tensor. Within this

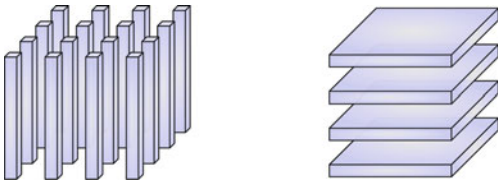

(a) Mode-1 vectors or fibers. (b) Mode-(2,3) slices.

Fig. 1 The mode-1 or column vectors and mode-(2, 3) or horizontal slices of a $4 \times 4 \times 4$-tensor. The other mode-n vectors and mode-(m, n) slices can be constructed in a similar way

framework, it is also possible to define scalars ($N = 0$), vectors ($N = 1$), and matrices ($N = 2$).

Scalars, vectors, and matrices are all commonly encountered in biomedical signal processing. A single observation or sample is represented by a scalar. Any signal recorded from a single source over a period of time can be described by a vector. The observations from acquisition with multiple sensors or electrodes are expressed in matrix-format. Data obtained from multiple subjects or due to repeated measurements can provide much more information, and these types of data can effectively be represented by a higher-order array or tensor.

From hereon, we refer to scalars with italic lower-case letters x, vectors with bold lower-case letters $\mathbf{x} \in \mathbb{R}^{I_1}$, and matrices with bold upper-case letters $\mathbf{X} \in \mathbb{R}^{I_1 \times I_2}$. Finally, tensors are written as calligraphic letters $\mathcal{X}$. For example, a third-order tensor is denoted by $\mathcal{X} \in \mathbb{R}^{I \times J \times K}$ and its elements as x_{ijk} with $i = 1, \ldots, I$, $j = 1, \ldots, J$ and $k = 1, \ldots, K$.

A matrix $\mathbf{X}$ consists of row- and column vectors. In a similar way, *mode-n vectors* or *fibers* are defined for tensors. A mode-n tensor fiber is a vector that is the result of fixing all indices except the nth index. For example, the mode-1 fiber of a third-order tensor is analogue to a column vector and is denoted by $\mathbf{x}_{:jk}$. The mode-2 and the mode-3 fibers are the row and the tube vectors and are denoted by $\mathbf{x}_{i:k}$ and $\mathbf{x}_{ij:}$, respectively. Figure 1a shows an example of the mode-1 or column vectors of a third-order tensor. The mode-2 and mode-3 vectors can be visualized similarly.

Slices are defined in the same way. A mode-(m, n) slice of a tensor is the matrix that is the result of fixing all indices except the mth and nth index. In a third-order tensor, the different types of slices are typically named after their corresponding directions: this way, horizontal (mode-(2, 3)), vertical (mode-(1, 3)), and frontal (mode-(1, 2)) slices are defined. Figure 1b shows the horizontal slices of a third-order tensor. The other slices can be visualized in a similar way.

The rank of a tensor is defined as the minimal number of rank-1 tensors that generate the tensor as their sum. A rank-1 tensor is defined as the outer product of nonzero vectors.

Finally, the *Frobenius-norm* of a tensor $\mathcal{X} \in \mathbb{R}^{I_1 \times I_2 \times \cdots \times I_N}$ is given by

$$||\mathcal{X}||_F = \sqrt{\langle \mathcal{X}, \mathcal{X} \rangle} = \sqrt{\sum_{i_1=1}^{I_1} \sum_{i_2=1}^{I_2} \cdots \sum_{i_N=1}^{I_N} x_{i_1 i_2 \cdots i_N}^2}. \tag{1}$$

with $\langle \mathcal{A}, \mathcal{B} \rangle$ the representation of the inner product between two tensors. The Frobenius norm is analogous to the matrix Frobenius-norm and is essentially the multilinear generalization of the L_2-norm commonly used in vectors.

3.2 Tensor Operations

In many applications, tensors are converted to matrices and vice versa. The transformation from a tensor to a matrix is referred to as tensor unfolding or flattening, a process where the elements of the tensor are reformatted in a lower-order structure [52]. One way of transforming tensors to matrices is the case of mode-n unfolding or matricization, which places the mode-n fibers of a tensor $\mathcal{X}$ as column-vectors in the matrix $\mathbf{X}^{(n)}$. The different unfoldings of a third-order tensor are presented in Fig. 2.

When data or signals are naturally collected in matrix-format, they have to be transformed into tensors in order to be able to apply tensor methods. This is done through tensorization, where a vector or a matrix is mapped onto a tensor by creating additional modes. Many different tensorization methods exist, and the choice of method is dependent on both the data and the application. An overview of the most well-known deterministic and statistical techniques can be found in [23].

In the applications discussed in the remainder of the chapter, tensorization will be mainly done through segmentation, e.g., by dividing the signals into equal-length segments and stacking these in the frontal slices of a third-order tensor. The main advantage of ECG signals is that they contain 'natural' segments in the form of heartbeats or individual ECG waves, where the temporal profile of a beat is simi-

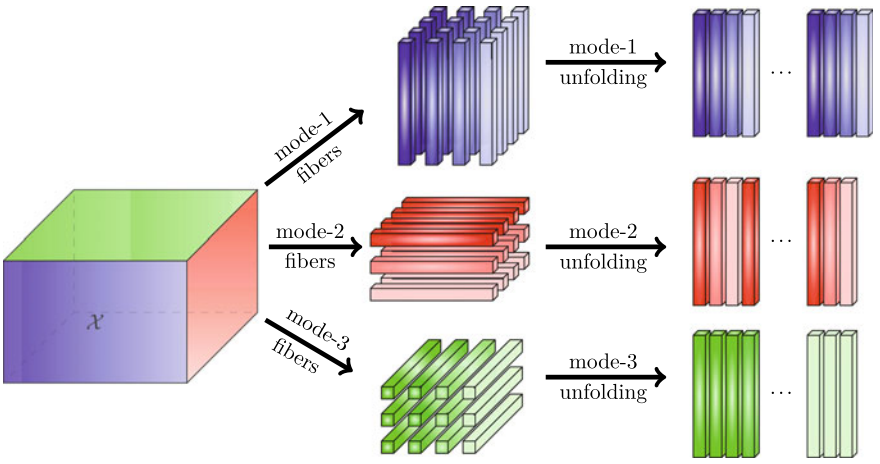

Fig. 2 Mode-1, mode-2, and mode-3 matricizations or flattenings or unfoldings of a 3rd-order ($3 \times 4 \times 4$) tensor

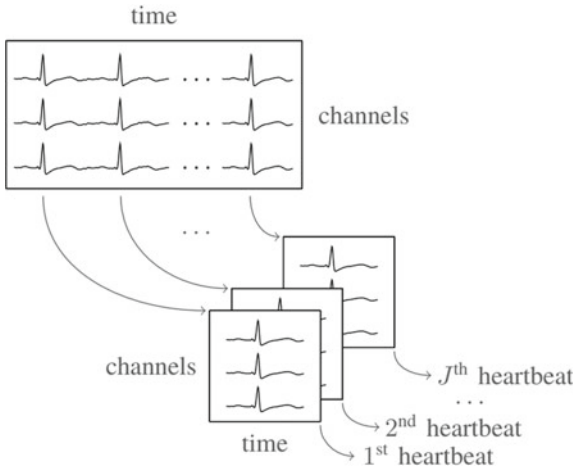

Fig. 3 Tensorization techniques create a tensor from a data matrix in a meaningful way, enabling tensor tools that allow one to extract more information [25]. Here, we apply a technique called *segmentation* to a multilead ECG data matrix, obtaining a third-order tensor with modes *channels* × *time* × *beats* (Figure reproduced from [11].)

lar across all channels of the signal. Tensorizing them in such manner transforms ECG signals with modes *time* × *channels* to third-order tensors with modes *time* × *channels* × *heartbeats*, where each mode-2 vector contains the temporal profile of one heartbeat in one channel. The resulting tensor allows studying the variations in ECG waveforms of consecutive heartbeats in all channels simultaneously, which is the goal in many ECG applications. Figure 3 illustrates the tensorization process: the two-dimensional multilead ECG signal that contains J beats is transformed into a higher-order tensor.

An important tensor-matrix multiplication is the mode-n product between a tensor $\mathcal{X} \in \mathbb{R}^{I_1 \times I_2 \times \cdots \times I_N}$ and a matrix $\mathbf{A} \in \mathbb{R}^{J \times I_n}$. It is represented as:

$$(\mathcal{X} \cdot_n \mathbf{A})_{i_1 i_2 \cdots j \cdots i_N} = \sum_{i_n=1}^{I_n} x_{i_1 i_2 \cdots i_n \cdots i_N} a_{j i_n}. \tag{2}$$

In practice, the mode-n product multiplies each mode-n vector of $\mathcal{X}$ with $\mathbf{A}$.

3.3 Tensor Decompositions

Tensor decompositions are powerful tools that have been used successfully in various applications within signal processing and machine learning [84]. In this chapter, we will focus on the canonical polyadic decomposition (CPD) and multilinear singular value decomposition (MLSVD), which have become popular tools in biomedical signal processing in recent years.

3.3.1 Multilinear Singular Value Decomposition (MLSVD)

The MLSVD is a powerful tensor tool in applications such as compression and dimensionality reduction in different fields; see [27, 52]. Recently, it has been applied for different ECG applications such as data compression and feature extraction for myocardial infarction classification, and irregular heartbeat classification [11, 75, 77], which will be discussed in Sect. 4.

The key idea behind the MLSVD is to find the components that best capture the variations in each mode individually, while not considering the other modes at this point in time [52]. The MLSVD is the multilinear generalization of the singular value decomposition (SVD) for matrices [26].

As a recap, the SVD of a matrix $\mathbf{X} \in \mathbb{R}^{I \times J}$ can be written as:

$$\mathbf{X} = \mathbf{U}\Sigma\mathbf{V}^T = \sum_{i=1}^{R} \mathbf{u}_i \sigma_i \mathbf{v}_i^T \tag{3}$$

where $\mathbf{U} \in \mathbb{R}^{I \times I}$ and $\mathbf{V} \in \mathbb{R}^{J \times J}$ are orthogonal matrices whose columns are respectively called the left and the right singular vectors of $\mathbf{X}$. $\Sigma \in \mathbb{R}^{I \times IJ}$ is a non-negative diagonal matrix that contains the ordered singular values σ_i on the diagonal. The rank of the matrix R is defined as the number of non-zero singular values. The SVD of a matrix $\mathbf{X}$ is often used when one wants to compute a low-rank approximation of $\mathbf{X}$, since it can be proven (in the *Eckhart-Young theorem*) that the optimal rank-r approximation of $\mathbf{X}$ is calculated by taking the singular vectors corresponding to the r largest singular values of $\mathbf{X}$ (Fig. 4) [26, 52, 57].

The MLSVD of a third-order tensor $\mathcal{X} \in \mathbb{R}^{I \times J \times K}$ is defined as follows [26]:

$$\mathcal{X} = \mathcal{S} \cdot_1 \mathbf{U} \cdot_2 \mathbf{V} \cdot_3 \mathbf{W} \tag{4}$$

with $\mathbf{U} \in R^{I \times I}$, $\mathbf{V} \in R^{J \times J}$ and $\mathbf{W} \in R^{K \times K}$ orthogonal factor matrices that contain the mode-n left singular vectors. The core tensor $\mathcal{S} \in \mathbb{R}^{I \times J \times K}$ governs the interaction between the different modes. It has the following properties:

- *All-orthogonality*: any two slices in a fixed mode are orthogonal.

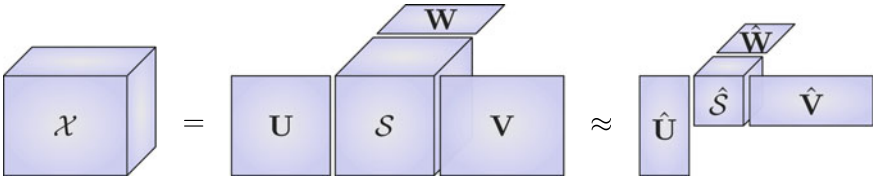

Fig. 4 The MLSVD and LMLRA of a third-order tensor $\mathcal{X}$. The column spaces of $\mathbf{U}$, $\mathbf{V}$, and $\mathbf{W}$ represent the signal subspaces along the three modes. The core tensor is non-diagonal, governing the interaction between the different modes

- *Ordering*: the norms of the slices along any mode are ordered in a decreasing manner

The Frobenius norms of the core tensor are called the multilinear or mode-n singular values (MSVs) of $\mathcal{X}$ and are denoted as $\sigma_i^{(n)}$. The values I, J, and K correspond to the ranks of the different matrix unfoldings of $\mathcal{X}$ along with the different modes.

The MLSVD can also be used to calculate a low multilinear rank approximation (LMLRA) of a tensor $\mathcal{X}$, but contrary to the matrix case, it is not necessarily the optimal approximation [19, 26, 84]. Truncation can be done in a similar way as the matrix case, e.g. by only keeping the mode-n singular vectors corresponding to the highest mode-n singular values. While the LMLRA calculated in this way is not perfect, it is usually a good approximation since the multilinear singular values are ordered, meaning that most 'energy' is concentrated in the vectors corresponding to the first singular values (the part that is kept in the LMLRA). It is therefore considered a suitable solution for most applications, which can be refined by iterative algorithms if necessary [48].

To have the core tensor $\mathcal{S}$ as a compressed form of $\mathcal{X}$, reduced dimensions of different modes can be chosen as $R_1 \ll I$, $R_2 \ll J$ and $R_3 \ll K$. Hence, $\mathcal{X}$ can be approximated as

$$\mathcal{X} \approx \hat{\mathcal{S}} \cdot_1 \hat{\mathbf{U}} \cdot_2 \hat{\mathbf{V}} \cdot_3 \hat{\mathbf{W}} \tag{5}$$

where $\hat{\mathcal{S}} \in \mathbb{R}^{R_1 \times R_2 \times R_3}$, $\hat{\mathbf{U}} \in \mathbb{R}^{I \times R_1}$, $\hat{\mathbf{V}} \in \mathbb{R}^{J \times R_2}$ and $\hat{\mathbf{W}} \in \mathbb{R}^{K \times R_3}$, respectively.

3.3.2 Canonical Polyadic Decomposition (CPD)

The CPD is also an important tensor tool in many applications within the signal processing, biomedical sciences, data mining, and machine learning; see [19, 52, 84]. The decomposition is unique under mild conditions [6, 14] which is a powerful advantage of tensors over matrices in many applications [3].

A polyadic decomposition (PD) expresses a tensor as a sum of rank-one components. If the number of components is the minimal number of components necessary to exactly decompose the tensor, then the PD is called the canonical polyadic decomposition (CPD). For a third-order tensor $\mathcal{X} \in \mathbb{R}^{I \times J \times K}$, it is expressed as:

$$\mathcal{X} = \sum_{r=1}^{R} \mathbf{a}_r \otimes \mathbf{b}_r \otimes \mathbf{c}_r \tag{6}$$

with R the total number of components or rank of the decomposition and $\mathbf{a}_r \in \mathbb{R}^I$, $\mathbf{b}_r \in \mathbb{R}^J$ and $\mathbf{c}_r \in \mathbb{R}^K$ for $r = 1, \ldots, R$ the factor vectors. CPD is also known as PARAFAC (Parallel Factor Analysis) or CANDECOMP (Canonical Decomposition) [52]. A schematic presentation of CPD for a third-order tensor is shown in Fig. 5.

While the definition of tensor rank is straightforward, its determination is a NP-hard [40, 45]. Different approaches for automatic rank estimation exist such as the core consistency diagnostic [16] or Rankest available in Tensorlab [89]. Both

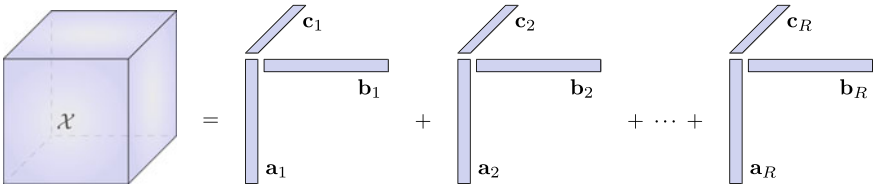

Fig. 5 Schematic representation of the Canonical Polyadic Decomposition of a third-order tensor in the individual factor vectors $\mathbf{a}_r$, $\mathbf{b}_r$ and $\mathbf{c}_r$ for $r = 1, \ldots, R$. The different factor vectors can be used in various ways depending on the application

approaches gradually increase the tensor rank and compare the results of the decomposition with the original tensor. They, however, lead to an overestimation of the tensor rank for noisy signals [20] and are therefore less suitable for biomedical signals that inherently contain noise. In practice, visual inspection of the obtained components for different ranks is very informative for evaluating the results and determining suitable rank values. Another starting point is the multilinear singular values, which can provide a lower-bound for determining the rank [19].

One of the main advantages of tensor decompositions compared to matrix-based methods is that the resulting components are unique under mild conditions (up to trivial permutation and scaling indeterminacies). A general framework for the uniqueness properties of third-order tensors is presented in [28–30]. This means that no additional constraints have to be imposed on the data or factor matrices, which is required for matrix decompositions such as orthogonality in case of PCA or independence in ICA.

While many other tensor decomposition methods exist, CPD can be considered one of the most accessible approaches. Generally, it generates components which can be easily visualized and interpreted. Furthermore, different computation methods have been developed that deal with practical issues such as missing data [94] or noisy signals [12]. In the next section, these methods will be applied to identify different ECG features, highlighting the power of these tensor decompositions in cardiac applications.

4 Applications of Tensors in ECG Processing

Multilead ECG signals are described by two parameters: time and space. In contrast to other biomedical signals, such as EEG, ECG is relatively noise-free and exhibit intrinsic structure, making this type of data a prime candidate for tensor-based analysis. In the last few years, tensor methods have been used in a limited number of ECG applications.

This section gives an overview of five typical problems in ECG processing where tensors have been used successfully to obtain relevant results:

1. ECG data compression [75],
2. Detection and localization of myocardial infarction [77],
3. Irregular heartbeat classification [11, 34],
4. Detection and quantification of T-wave alternans [33, 35, 36, 79],
5. Analysis of changes in heartbeat morphology [37].

The goal of this section is to highlight the flexible nature in which tensor tools can be used in various important use-cases. We also show how the tensor decompositions can be adapted to different typical characteristics of ECG signals in order to deal with real-life problems such as noisy signals or changes in heart rate. For a more comprehensive explanation of the methods, we refer to the dedicated papers of each method.

Many different tensor decompositions exist, each with specific advantages and disadvantages. The applications discussed here all make use of either the MLSVD or CPD to decompose the ECG signal. The first two applications combine the MLSVD with the discrete wavelet transform to exploit different types of correlations in the ECG signal. For the next two applications, e.g. irregular heartbeat classification and detection of T wave alternans, we present and compare a CPD- and MLSVD-approach. Both approaches have their own strengths and are preferred in different cases. Finally, the last application is tackled using another variant of the CPD.

4.1 ECG Data Compression

Diagnosis of heart diseases often requires long-term multilead ECG recordings in order to accurately determine the extent of cardiac abnormalities. When dealing with many patients in a hospital setting, this quickly leads to large-scale datasets: a 24-hour ECG signal measured with 12 leads with a sampling frequency of 250 Hz, digitized at 11 bits/sample, for example, requires a storage capacity of 2.88 Gb. There is a growing need to store these datasets as compactly as possible without distorting the ECG signals since this might lead to the loss of important clinical information.

For this purpose, many ECG compression methods have been developed that reduce the number of samples required to store the signal. They mostly start from the idea that there are different types of correlations present in ECG signals [49]:

1. intra-beat: correlations between the different samples in a heartbeat,
2. inter-beat: correlations among different heartbeats in a long-term signal,
3. inter-lead: correlations between different leads in a multilead signal.

Different methods exploit one or more type(s) of correlations in order to efficiently reduce the required storage capacity. Vector-based methods utilize intra-beat correlations by means of sampling or interpolation [2, 21, 49, 69]. Matrix-based methods can handle up to two types of correlations simultaneously. Different matrix decompositions, such as the Karhunen-Loève transform (KLT) or PCA [82] and SVD have been used for ECG compression [76, 96]. The use of tensor methods allows an

analysis of all three correlations types at the same time, making optimal use of all information present in the signal.

In the remainder of this section, we will describe a multiscale tensor-based ECG compression method that uses the discrete wavelet transform (DWT) to represent the signal. It starts from an ECG signal that has been tensorized by segmenting the signal in different heartbeats, as described in Sect. 3 and shown in Fig. 3. A full description of the method can be found in [77].

The ECG signal is a low-frequency signal where most of the physiological activity is contained in the frequency band between 1 and 40 Hz. It furthermore has different morphological components (in the form of the different ECG waves) that vary both in duration and frequency. The multilevel decomposition using DWT can grossly segment the different components into different subbands while preserving the information in an effective way [66]. An $L-$level wavelet decomposition splits up the ECG signal in $L+1$ subbands of different dimensions. Here, a decomposition of $L=7$ levels is applied on the mode-2 fibers $\mathbf{x}_{i:k}$ of the original tensor ($\mathcal{X} \in \mathbb{R}^{I\times J\times K}$) with modes *channels* $\times$ *time* $\times$ *beats*. Each mode-2 fiber represents one heartbeat in one channel. The result is eight subband tensors: one approximation subband tensor $\mathcal{A}_L$ containing the approximation coefficients in mode-2, and L detail subbands tensors $\mathcal{D}_l$, $l=L,\ldots,1$ that contain the detail coefficients in mode-2 of respective levels. The dimensions of these tensors, $\mathcal{A}_L$ and $\mathcal{D}_l$, $l=L,\ldots 1$, are given as $I\times J/2^L\times K$ and $I\times J/2^l\times K$, respectively, and we say now each subband tensor has modes *channels* $\times$ *wavelet coefficients* $\times$ *beats*. Because the different heartbeats in the ECG signal are related in time and in space (due to *inter-beat* and *inter-lead*) correlations, the wavelet coefficients show a high correlation in the different subbands [78]. Therefore they can be represented in a more efficient way with the truncated MLSVD.

Following (4), the MLSVD of each subband tensor can be expressed as

$$\begin{aligned}\mathcal{A}_L &= \mathcal{S}_{A_L}\cdot_1 \mathbf{U}_{A_L}\cdot_2 \mathbf{V}_{A_L}\cdot_3 \mathbf{W}_{A_L}\\ \mathcal{D}_l &= \mathcal{S}_{D_l}\cdot_1 \mathbf{U}_{D_l}\cdot_2 \mathbf{V}_{D_l}\cdot_3 \mathbf{W}_{D_l}\end{aligned} \tag{7}$$

where $\mathbf{U}_{A_L}$, $\mathbf{V}_{A_L}$, and $\mathbf{W}_{A_L}$ are orthonormal matrices of approximation subband tensors, and $\mathbf{U}_{D_l}$, $\mathbf{V}_{D_l}$, and $\mathbf{W}_{D_l}$ are that of each detail subband tensor, along with different modes. The orthonormal column vectors of $\mathbf{U}_{A_L}$ and $\mathbf{U}_{D_l}$ span the channel space of each subband. Similarly, the column vectors of $\mathbf{V}_{A_L}$, $\mathbf{V}_{D_l}$ and $\mathbf{W}_{A_L}$, $\mathbf{W}_{D_l}$ span the coefficient space and heartbeat space.

The ECG signal is then compressed by truncating the MLSVDs of the subband tensors that contain the detail coefficients. The truncation is done such that 95% of the energy contained in the multilinear singular values in each mode is kept. This means that for each subband tensor $\mathcal{D}_i$ we will define a multilinear rank (R_1, R_2, R_3) such that:

$$\frac{\sum_{i=1}^{R_n}(\sigma_i^{(n)})^2}{||\mathcal{S}_{D_l}||_F^2}\geq 0.95,\quad n=1,\ 2,\ \text{and } 3. \tag{8}$$

where $||\mathcal{S}_{D_l}||_F$ is the Frobenius norm of each detail subband tensor. Note that the multilinear rank of the truncated MLSVD (R_1, R_2, R_3) is defined separately for each subband tensor $\mathcal{D}_l$. Since the multilinear singular values typically decrease rapidly for most subbands, values for R_n can be kept relatively low, resulting in an efficient compression. While it is known that the truncated MLSVD, in general, does not result in the optimal low-rank approximation of the original tensor, the results are however considered good enough for most applications.

In order to compare different vector-, matrix- and tensor-based approaches we use standard measures such as the compression ratio (CR), which is defined as

$$CR = \frac{\text{bits in the input signal}}{\text{bits in the compressed signal}}.$$

The higher the CR, the better the compression performance. However, as mentioned before, this should not come at the cost of reduced signal accuracy. To control this trade-off, we, therefore, use additional quality measures such as the percentage of root-mean-square difference (PRD). The PRD is defined as

$$PRD = \sqrt{\frac{\sum_{n=1}^{N}(x(n) - \tilde{x}(n))^2}{\sum_{n=1}^{N} x(n)^2}} \times 100$$

where N is the total number of samples and $x(n)$ and $\tilde{x}(n)$ are, respectively, the original and the reconstructed signals. The quality of the reconstructed signal is 'very good' and 'good' if the PRD (%) value is between 0 and 9. Analysis of different compression algorithms, however, suggests keeping the PRD value as small as possible (under 3%) [67].

Table 1 shows CR and PRD values for several of the methods mentioned in the first part of this section, together with the results for the proposed tensor-based method. In order to make a fair comparison possible, all methods were performed in the same environment and on the same database, the PTB database available on Physionet [32]. From Table 1 it is clear that increasing the number of correlation types that

Table 1 Comparison of tensor-based ECG compression method with vector- and matrix-based methods using the PTB database [32]. The tensor-based method using multilevel DWT and MLSVD in [77] exploits all three types of correlations and leads to the best results. Adapted from [75]

Decomposition	Correlation type	CR	PRD (%)
KLT [18]	Intra-beat	7.25	3.18
DWT + PCA [82]	Inter-lead	12.61	2.66
SVD [96]	Intra- and inter-beat	15.70	2.83
DWT + SVD [75]	Intra-beat, inter-lead	19.34	3.05
DWT + MLSVD [77]	Intra- and inter-beat, inter-lead	45.00	2.71

are exploited by the decomposition results in a better compression ratio: the lowest CR values are obtained by methods using only one type of correlation. Adding a correlation type immediately improves the compression ratio with minimal impact on the PRD. The proposed tensor-based method that combines DWT and MLSVD results in the highest compression ratio with PRD <3.

Here, the combination of multiscale DWT and truncated MLSVD was used solely for data compression. The technique could, however also be used for feature extraction, since the singular values and singular vectors inherently contain valuable information about the underlying ECG signal.

4.2 Myocardial Infarction Classification

Myocardial infarction (MI) occurs when the flow of oxygen-rich blood to the heart muscle is halted, which causes cell death and tissue damage. It can be diagnosed through blood tests or imaging techniques [90]. However, since MI is also known to cause alterations in the electrical conduction pattern of the heart, efficient detection can also be done by examining changes in the ECG signal (such as ST-segment deviations or T wave inversions). MI detection should be done as early as possible, so accurate treatment can start, and damage to the heart muscle can be kept minimal. Therefore there is a clear advantage over using ECG analysis over other techniques since results can be processed and analyzed in real-time.

A second objective is often MI localization, where the goal is to indicate the location on the heart wall that is affected by the infarction. This can be done by making use of the fact that each ECG lead represents cardiac activity from a different spatial angle, as discussed earlier. Clinically, we make the distinction between lateral leads (I, aVL, V5, and V6), anterior leads (V3–V4), septal leads (V1–V2), and inferior leads (II, III, aVF). When a patient experiences an anterior MI, for example, it will mainly be characterized by changes in the anterior leads. This way, we can define four major MI types: anterior MI (AMI), inferior MI (IMI), posterior MI (PMI), and lateral MI (LMI). Additional subtypes are possible when the MI can be detected in more than one region, such as for example antero-lateral MI (ALMI), antero-septal MI (ASMI), or infero-lateral MI (ILMI).

Since MI detection and localization is an important clinical task, a large number of automated methods have been developed for this purpose. Their goal is to identify discriminative features that can characterize the different MI subtypes compared to ECG signals of healthy subjects. Many methods aim to detect and quantify specific ECG changes such as ST-segment deviations [7, 62, 87] or alterations in the QRS complex [80]. While these features are known to change after MI, they are difficult to accurately measure in the presence of noise, which may affect the final performance. A second class of methods, therefore, transforms the ECG signal to the frequency- or wavelet domain before feature extraction. Examples can be found in [50, 83], where the DWT is used to represent the signal and extract more robust features. This way

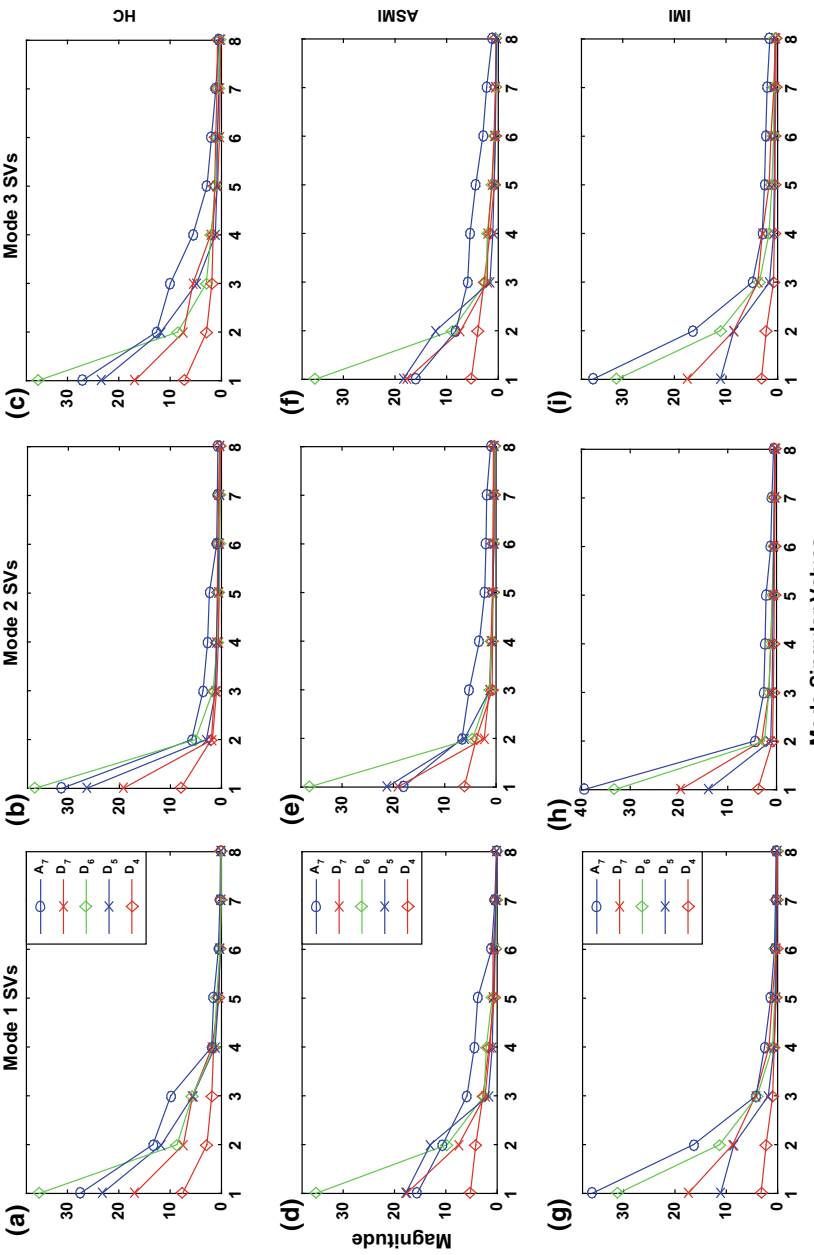

Fig. 6 The multilinear singular values for a healthy subject (top row), a subject with an ASMI (middle row) and an IMI (bottom row). The myocardial infarction causes changes in the frequency content of the ECG signal and induces changes in the MSVs of the different subband tensors. Reproduced from [77]

detection and localization accuracies of >95% can be achieved. A comprehensive view of recent advances in the field can be found in [3].

Similar to ECG compression, tensor decompositions can exploit spatial and temporal correlations in the signal simultaneously to detect and localize the MI in an even more efficient way. The method described here is a multiscale approach that starts from an ECG signal that has been converted to the multiscale domain and compressed with the method described earlier. Here, however, features are extracted from the MLSVD to detect and localize MI.

MI induces morphological changes in the ECG signal, which are captured by the multilinear singular values (MSVs) of the subtensors corresponding to the different wavelet bands. An illustration is shown in Fig. 6, which shows the MSVs for a healthy subject (top row), a patient with an ASMI (middle row), and a patient with an IMI (bottom row), respectively. In a healthy subject, most of the energy is contained in the $\mathcal{D}_6$ subband tensor, followed by $\mathcal{A}_7$, $\mathcal{D}_5$, and $\mathcal{D}_7$. This pattern is visible in all three modes. The explanation can be found in the QRS complex, which is the most dominant wave in healthy ECG signals and which is mainly segmented in $\mathcal{D}_6$. ASMI introduces pathological Q-waves in the ECG signal, which changes the frequency content in different wavelet bands. In the MSVs, this corresponds to a large drop in the values for $\mathcal{D}_5$ and $\mathcal{A}_7$. Similarly, an ISMI causes ST-elevation which increases the MSVs for the $\mathcal{A}_7$ subband. The significant MSVs of modes 1 and 2 were therefore used as features for MI *detection*, whereas the mode 3 MSVs are used to *localize* the MI. Additionally, normalized multiscale wavelet energy features were also extracted to make MI localization more accurate. A more comprehensive explanation of the different features can be found in [77].

The features are then used as input to a support vector machine classifier with χ^2-kernel, to do the classification in a supervised way. The SVM parameters (both the regularization parameters and kernel parameters) are optimized using a grid-search algorithm and 5-fold cross-validation on the training set. The final performance is calculated on an independent test set. The performance of the proposed method is evaluated on a subset of the PTB database [32]. The full dataset considered here consists of 390 records: 78 healthy controls and 312 records of subjects with different types of MI. 89 records were used as a training set, the remainder as a test set.

The results of the methods mentioned in Table 2 are rather similar for all three methods. The proposed tensor-based approach, however, has several advantages. First

Table 2 Comparison of MI detection and localization performance with existing methods. Adapted from [77]

Method	Decomposition	Detection			Localization
		Sen (%)	Spe (%)	Acc (%)	Acc (%)
Arif [7]	N.a.	97.2	99.6	NA	98.8
Sharma [83]	DWT + PCA	93.0	99.0	96.0	99.6
Proposed	DWT + MLSVD	94.6	96.0	95.3	98.1

of all, the results on the first two methods were not obtained with an independent test set (e.g. which does not contain signals of patients in the training set). There is, therefore, a significant risk of over-fitting, meaning that the methods are not capable of generalizing and will lead to inferior results on different datasets. Second, the matrix-based features are calculated for each lead individually, which is computationally not very efficient, while the proposed tensor-based approach processes all leads simultaneously. The tensor-based method, on an average, takes 0.23 and 0.021 s for detection and localization, respectively, during testing compared to 0.44 and 0.025 s of [83].

4.3 Heartbeat Classification

Cardiac arrhythmias affect millions of people and are the main cause of many cases of sudden cardiac death. A large number of people could benefit from a better and more reliable detection of cardiac dysfunction. An arrhythmia is defined as any disturbance of the normal sinus rhythm. This can be a perturbation or abnormality in the rate, the regularity, the site of origin, or the conduction of the electrical impulses of the heart. In general, they can be divided into two main groups: the first group, morphological arrhythmia, contains arrhythmia that consists of only one heartbeat; the second group consists of arrhythmia formed by a group of heartbeats and is called rhythmic arrhythmia [61]. The focus of this section lies in the automatic detection of the first class, e.g. morphological arrhythmia. Various types of morphological arrhythmia exist, each differing in the origin and/or electrical pathway of the abnormal beat. In general, we make the distinction between three types of abnormal beats: Normal beats, atrial or supraventricular beats, and ventricular beats. Normal beats refer to beats that originate during normal sinus rhythm. Atrial and ventricular beats respectively arise in the atria or ventricles.

Classification of heartbeats in different classes is important for two main reasons. Firstly, heart rate variability studies, which are useful in many clinical and non-clinical scenarios require a series of normal RR-intervals. The presence of ectopic beats or other abnormalities introduces abrupt changes in the RR time series which can seriously disturb the values of HRV indices. Secondly, the most ventricular arrhythmia, which is potentially lethal, is initiated by premature ventricular beats. Their frequency and complexity have been shown to be predictive for predicting SCD in certain patient groups and have been used as stratification tools in large clinical trials.

Here we present two different tensor-based approaches to irregular heartbeat detection. The first method detects irregular heartbeats in an unsupervised manner using the CPD. A full explanation can be found in Goovaerts et al. [34]. The second method uses the MLSVD to perform a supervised classification and is described in Boussé et al. [11]. For both methods, the multilead ECG signal is first preprocessed to remove major noise sources such as baseline wander and high-frequency noise. The signal is then transformed into a third-order tensor in the same way as shown in

Fig. 5. First, we segment the signals in individual heartbeats of equal lengths. Next, all heartbeats are stacked in the third mode, resulting in a third-order tensor $\mathcal{T}$ with dimensions *channel* $\times$ *time* $\times$ *heartbeat*. Tensorizing the signals in this way allows us to study the differences between the heartbeats in a signal in a straightforward way by studying the variation in the third mode.

4.3.1 CPD

We explained in Sect. 3 that the CPD can be used to decompose a tensor in a sum of rank-1 components. In this case, R, the rank of the decomposition, is fixed to one since we are interested in the *main* variation between different heartbeats. The result is 1 rank-one tensor consisting of three loading vectors $\mathbf{a}_1$, $\mathbf{b}_1$ and $\mathbf{c}_1$.

An example of the CPD result for a 12-lead ECG signal with five abnormal heartbeats are shown in Fig. 7. The feature vectors have a straightforward physiological interpretation, especially for the temporal and heartbeat mode. The first loading vector, $\mathbf{a}_1$, corresponding to the channel mode, is associated with the differences in heartbeat morphologies over different channels. The second loading vector $\mathbf{b}_1$ (time) shows the temporal profile of the component and is a representation of the average heartbeat in the signal. It is easily recognizable as a normal (regular) heartbeat, which is expected since the majority of heartbeats are by definition normal. Furthermore, the morphology of a normal heartbeat is similar over all channels, making it suitable to capture in a rank-one component. Finally, the factor vector of the heartbeat dimension is the most important for irregular heartbeat detection since it shows the changes in the ECG over different heartbeats. The values of this loading vector for normal heartbeats vary around -0.1. The abnormal heartbeats are easily distinguishable by their higher values, and they can be detected by simple thresholding or clustering methods.

4.3.2 MLSVD

The second approach uses the MLSVD to detect heartbeats in a supervised way, e.g. by making use of a training set of heartbeats with a known label. We first collect all

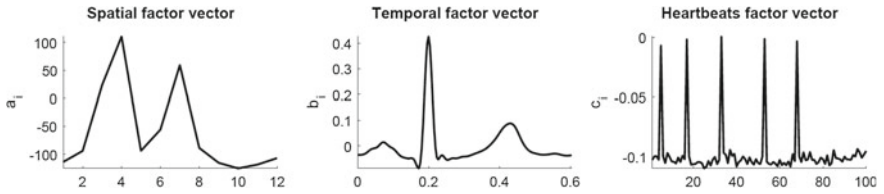

Fig. 7 The factor vectors for the different modes obtained by CPD. The irregular heartbeats are clearly distinguishable in the third factor vector and can be detected by thresholding or clustering. Reproduced from [38]

labeled training beats in a tensor $\mathcal{T}$. The (truncated) MLSVD of this tensor is given by:

$$\mathcal{T} = \mathcal{S} \cdot_1 \mathbf{U}_c \cdot_2 \mathbf{U}_t \cdot_3 \mathbf{U}_3 \tag{9}$$

where $\mathbf{U}_c$, $\mathbf{U}_t$ and $\mathbf{U}_h$ form an orthonormal basis for the spatial, temporal and heartbeats components respectively. Every heartbeat in a particular channel $\mathbf{t}$ can be written as:

$$\mathbf{t}^{\mathrm{T}} = \mathcal{S} \cdot_1 \mathbf{C}_c^T \cdot_2 \mathbf{U}_t \cdot_3 \mathbf{c}_h^T \tag{10}$$

The mode-2 unfolding of this Equation is a so-called Kronecker-product equation (KPE), which is a linear system with a solution that has a Kronecker product structure. It expresses each heartbeat in the column space $\mathbf{U}_t$ and an unfolded interaction tensor $\mathcal{S}$:

$$\mathbf{t} = \mathbf{U}_t \mathbf{S}_{(2)} (\mathbf{c}_h \otimes \mathbf{c}_c) \tag{11}$$

We can solve this system in an efficient way to obtain coefficient vectors $\mathbf{c}_h$ and $\mathbf{c}_c$ using nonlinear least squares algorithms [12].

A new heartbeat without a known label, that is thus not included in $\mathcal{T}$, can now be classified by solving (10) as such:

$$\mathbf{U}_t \mathbf{S}_{(2)} (\mathbf{c}_h^{(\text{new})} \otimes \mathbf{c}_c^{(\text{new})}) = \mathbf{t}^{(\text{new})} \tag{12}$$

to obtain estimates $\hat{\mathbf{c}}_h^{(\text{new})}$ and $\hat{\mathbf{c}}_c^{(\text{new})}$. The new heartbeat can then be classified by comparing $\hat{\mathbf{c}}_h^{(\text{new})}$ with the rows of $\mathbf{U}_h$, after normalizing all vectors to correct for scaling and sign differences. Since each row of $\mathbf{U}_h$ corresponds to a heartbeat from the training set with a known label, we can assign the new heartbeat the label corresponding to the closest match.

Note that while the data of *all* channels are used to compute the MLSVD, classification is only done using the signal from a *single* channel. In practice, however, the MLSVD model holds only approximately, and incorrect classification can possibly occur. It is, therefore, possible to make the classification more robust by using heartbeats from multiple channels, which can be solved using a *coupled* KPE. More information can be found in [11].

To compare both approaches with each other and with alternative matrix-based approaches, they were both applied on the first ten signals of the INCART database, which is a publicly available multilead database that contains heartbeat annotations. The unsupervised CPD-based method obtains a mean F_1-score of 79%. Further inspection of the results, however, revealed that the method distinguishes normal and ventricular beats almost perfectly but lacks performance for atrial beat classification. The MLSVD-based method reaches a mean F_1-score of 94.2% which is better than the best performance (92%) of traditional techniques [61]. The results could be improved further by using all channels to perform the classification. Furthermore, because of the generic nature of the method [12], the same concept can be applied to other classification problems with minimal alterations, which shows the flexibility

of the method. Examples of recently developed applications in biomedical signal processing are atrial fibrillation detection [31] and EEG classification [92].

The CPD-based approach is clearly not suitable as a general irregular heartbeat detection method but could be used to automatically detect ventricular beats. Since most lethal arrhythmias are initiated by premature ventricular contractions, a type of ventricular beats, this class is more important in a clinical context, so this would be a practically useful result. It is furthermore an unsupervised detection method, meaning that no annotations are required to perform the analysis, which is an advantage in clinical practice. Similarly to the proposed MLSVD-based approach, the CPD-based method can be used to analyze other abnormal ECG patterns with minimal alterations. In the next section, for example, we present a similar algorithm to analyze T wave alternans.

4.4 T-Wave Alternans Detection and Estimation

T wave alternans (TWA) is an abnormal ECG pattern where the amplitude of the T wave shows a beat-to-beat change in a characteristic ABABAB-pattern [70]. It can be detected in healthy hearts at high heart rates, but if it also appears at lower heart rates ($<$110 beats per minute) it is a sign of electrically unstable tissue and associated with increased mortality [47]. When the variation between subsequent T waves is large enough, TWA can be detected by visually inspecting the ECG signal. In cases where the difference is only a few microvolts or when dealing with long ECG signals, this is however not feasible. Therefore (semi-)automatic methods are used that can reliably detect TWA in the ECG signal.

Martínez and Olmos [65] gave an overview of commonly used algorithms for (semi-)automatic T Wave Alternans detection. Most methods start with a preprocessing stage followed by the actual TWA detection. Examples of commonly used methods are the modified moving average method [71] or the spectral method [85]. Most methods decompose the ECG signal to a beat-to-beat time series that contains the T wave characteristics. The actual detection of T wave alternans is then done on this decomposed signal. Most TWA detection and quantification methods have been designed for use with single lead ECG signals. They can be applied to multilead signals by processing each lead individually and combining the results of different leads in a second stage; however it has been shown that this might not be optimal [17]. Analyzing all leads simultaneously can be done in a straightforward way through the use of tensors, as we already showed in the previous examples. Here, we present two different tensor-based approaches for TWA detection and quantification. Similarly to the previous section, the first method starts from the CPD [33, 35, 36] and the second uses the MLSVD as the main building block [79].

CPD and PARAFAC2

In a similar way as before, the ECG signal was transformed into a tensor before applying tensor decompositions. Since the objective is TWA detection, the tensor should be constructed in such a way that the changes in T waves over different

heartbeats are maximally emphasized. Therefore we constructed a T wave tensor $\mathcal{T}$: a third-order tensor that consists of the T waves of all channels and heartbeats.

There is an important difference between the tensorization in the previous section and here: before, the individual heartbeats were segmented by selecting a window *around* the R peaks. When these heartbeats are placed in the tensor, the different heartbeats are automatically synchronized at the R peak location (which is always at the same time location in the segmentation window). Here, segmentation is done by taking a fixed-size window *after* the R peak that contains the T wave. When for example the heart rate changes within a signal, it is possible that the timing of the T wave with respect to the R peak changes, and that the T waves of different beats are thus not strictly aligned in the third mode.

Similarly to the approach for irregular heartbeat detection, CPD was the first decomposition method used to break down the tensor in different factors. Since here the interest lies in the main variation between subsequent T waves, only one component was extracted and therefore R was restricted to one. If the tensor is low-rank, the CPD model is accurate, and the three factor vectors will capture the main variations present in the tensor. When the ECG signal is relatively noise-free and the T waves are perfectly aligned in the third mode, this assumption is met and CPD will lead to correct results. When there is however a variation in, for example, the timing of subsequent T waves (as can be the case with a changing heart rate), the tensor cannot be decomposed in rank-1 components, and CPD will lead to inaccurate results. In those cases, it is better to use a more general tensor decomposition method such as PARAFAC2. PARAFAC2 is a tensor decomposition method that is a variation of the standard CPD [15]. The main difference is that PARAFAC2 is less restrictive than CPD in the sense that it allows variations in the factor vectors of one mode. This is especially useful when one of the factors contains a time shift. PARAFAC2 models an individual loading vector $\mathbf{b}_{1,m}$ for each frontal slice of the tensor, effectively making $\mathbf{B}_1$ a loading matrix that contains the collection of loading vectors for each heartbeat. Each row of this loading matrix corresponds to the temporal profile of a T wave in one heartbeat, taking into account the possible time shifts in T waves due to heart rate changes.

The result of the tensor decomposition is a collection of three factor vectors (or two factor vectors and one matrix in the case of PARAFAC2), which give information about the structure of the signal in the three tensor modes. All three components give valuable information about the T wave characteristics in time and space, but since the mode-3 factor vector expresses the differences in the T wave in subsequent heartbeats, only this vector was used for the actual detection of T wave alternans. If a signal contains TWA, the typical ABABAB-pattern that is present in the T wave amplitude will be captured by the tensor decomposition as an alternating time series in the third dimension. To detect and quantify TWA, the number of consecutive turning points of $\mathbf{c_r}$, the loading vector of the heartbeat dimension, was first detected. The total TWA level in a signal is then defined as the mean amplitude difference between all consecutive turning points.

To illustrate the difference between the decomposition methods, Fig. 8 shows the CPD and PARAFAC2 results for three signals with respectively no TWA, with TWA

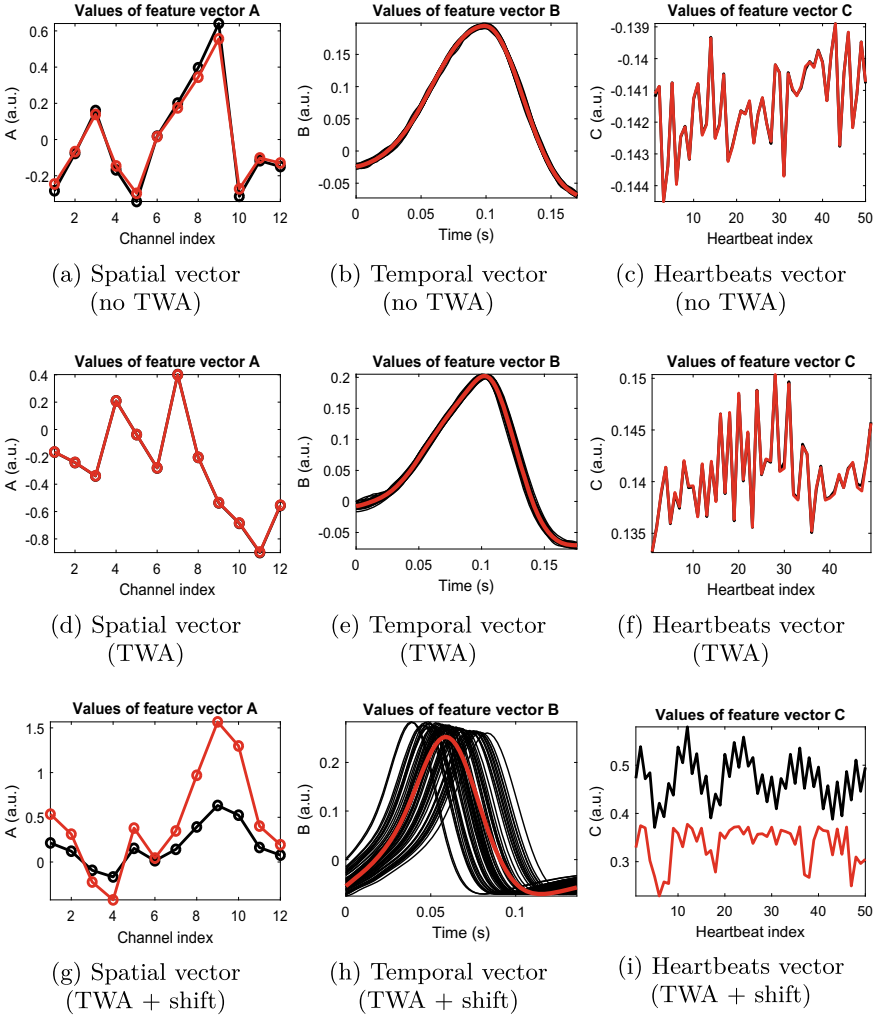

(a) Spatial vector (no TWA) (b) Temporal vector (no TWA) (c) Heartbeats vector (no TWA)

(d) Spatial vector (TWA) (e) Temporal vector (TWA) (f) Heartbeats vector (TWA)

(g) Spatial vector (TWA + shift) (h) Temporal vector (TWA + shift) (i) Heartbeats vector (TWA + shift)

Fig. 8 Vectors **a**, **b** and **c** for signal without TWA (top row), a signal with TWA (middle row) and a signal with TWA and shifted T waves (bottom row). The results for CPD are plotted in red, the results for PARAFAC2 in black. The three different columns show respectively the spatial, temporal and heartbeats feature vectors. PARAFAC2 is better able to capture dynamic changes in the ECG signal caused by changes in heart rate. When such differences are present, CPD fails to accurately extract TWA activity. Reproduced from [36]

and with TWA and T wave shifts in the different rows. The columns show the factor vectors for all tensor modes. Figures 8a, d, g show the spatial vector for the signal without TWA, with TWA and with TWA and T wave shift respectively, which show the sign and magnitude of the T wave in different channels. From Fig. 8a we can, for example, conclude that T waves in channel 9 had a larger amplitude than those in

channel 12. The temporal vectors, shown in Fig. 8b, e, h correspond to the shape of the T wave in time. Here the difference between CPD and PARAFAC2 is obvious, especially in Fig. 8h. The result for PARAFAC2 is a matrix, and each row of the matrix (corresponding to the temporal profile for each heartbeat) is plotted on top of each other. The presence of a large T wave shift in the third signal is evident. While CPD succeeded in capturing the mean shape of the T wave, the difference in the timing of the subsequent waves was discarded. This information is contained in the feature matrix obtained by PARAFAC2. The other signals did not contain a large shift, as is demonstrated by the small variation in the PARAFAC2 results of Fig. 8b, e. Hence, the results of CPD and PARAFAC2 were much more similar.

TWA can be detected by analyzing the third loading vector. Figures 8c, f, i show this loading vector for all analyzed signals. In Fig. 8c we see that, although there is a certain variation in the T wave magnitude over different heartbeats, no clear pattern is visible. The typical ABABAB-pattern is, however, clearly visible in Fig. 8f, i. Note that in Fig. 8f, there is only T wave alternans present in the first part of the signal. The results for PARAFAC2 and CPD are almost identical in Fig. 8c, f, while the results in Fig. 8i differ significantly. This is caused by the large T wave shift (see Fig. 8i).

MLSVD

Apart from using CPD and PARAFAC2, TWA can also be detected using the MLSVD as the main building block. Furthermore, since noise can seriously alter the ECG signal in the time domain, we first transform the signal to the multiscale wavelet domain using DWT to perform a more robust detection. The first aim is to extract the only T-wave morphology from the ECG signal. Multiscale analysis, as discussed earlier, alleviates this problem by grossly segmenting the ECG morphological features where the signal of interest (T-wave with/without TWA) and noise are placed into different subbands. To get back the time-domain signal from the wavelet coefficients in a subband, these coefficients are synthesized in that subband, which is the same as applying inverse DWT to that subband. This process collectively is termed as multiscale analysis-by-synthesis (MAS). Since the objective is to extract the only T-wave morphology whose frequency is concentrated in between 0.3 and 15 Hz [44], synthesized signals of low-frequency (A_6, D_6, and D_5) subbands are added (here, $L^1 = 6$ as the sampling frequency of the signal is 500 Hz). The maximum frequency of these subbands is 3.906, 7.812, 15.624 Hz, respectively. Hence, the T-wave information is retained in these three subbands.

After obtaining $L + 1$ subband tensors (ref, Sect. 4.1), the T-wave tensor is obtained as follows:

Reconstruct the subband tensors using multiscale synthesis on mode-2 fibers of $\mathcal{A}_6$, $\mathcal{D}_6$ and $\mathcal{D}_5$.

Add the reconstructed samples to get the T-wave tensor,

$$\mathcal{R} = \mathbf{r}_{i:k} = \mathbf{a}_{6i:k} + \mathbf{d}_{6i:k} + \mathbf{d}_{5i:k}, \quad i = 1{:}I, k = 1{:}K \tag{13}$$

[1] $L = \lfloor \log_2 F_s - 2.96 \rfloor = \lfloor \log_2 500 - 2.96 \rfloor = 6$ [6].

where $\mathbf{a}_{6i:k}$, $\mathbf{d}_{6i:k}$, and $\mathbf{d}_{5i:k}$ is the reconstructed fibers. Similarly to [68] where PCA was applied to improve the TWA analysis performance by exploiting the spatial redundancy, here, MLSVD is employed on the T-wave tensor $\mathcal{R}$ for the same purpose by exploiting both spatial and temporal redundancy.

For comparison purposes of the MAS-MLSVD method over the multi-PCA (a matrix-based) method [68], we discuss here the results on a semi-synthetic database. It is created by adding different TWA amplitude levels ranging from 0 to 100 μVs to every other T-wave of ECG signals. The signals are considered from 52 records of healthy subjects' in the PTB database [32]. The addition of alternate waveforms is carried out with selected but randomly chosen leads rather than with all 8-leads. Further, to experience a high degree of realism, four types of noise, namely Gaussian, Laplacian, electrode motion, and muscular activity are considered and with different noise levels ranging from 0 to 50 dB. Figure 9 shows the mean and standard deviation of the estimated alternans level for each input alternans level for these two methods, and also in the presence of *laplacian* noise of 20 dB. Noise is added to verify the robustness of the proposed method. For input alternans levels ranging from 10 to 50 μV, difference between the mean estimated alternans level, and input alternans level in case of multi-PCA method is significantly higher than the MAS-MLSVD method (for instance, 16.56 versus 0.48 μV and 14.93 versus 0.07 μV when input alternans levels are 20 μV and 50 μV, respectively). In the presence of noise, the estimation

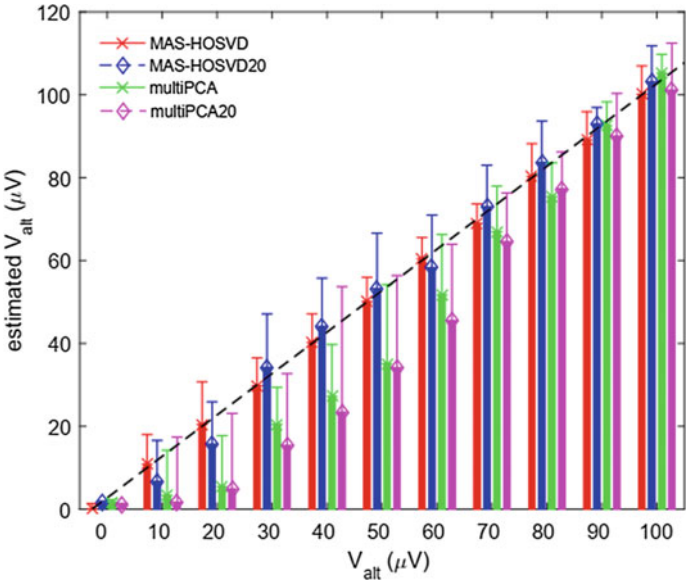

Fig. 9 Variation of estimated versus input alternans level in semi-synthetic datasets with *lp* noise of SNR = 20 dB for the multi-PCA and MAS-MLSVD techniques. Markers and bars represent the mean and standard deviation of the estimated TWA amplitude, respectively. The dashed straight line represents the would-be (perfect) estimated alternans levels. Adapted from [79]

Table 3 Kendall coefficient scores obtained by comparing the rankings from different methods found in literature and the two proposed tensor-based methods with the reference ranking for the Physionet database. The tensor-based approaches reach the highest scores

Method	Kendall coefficient
CPD	0.79
PARAFAC2	0.87
MLSVD	0.81
Periodic component analysis [68]	0.77
Modified moving average method [71]	0.73
Spectral method [85]	0.42

accuracy of the multi-PCA degrades comparatively more than the MAS-MLSVD method. Additionally, for input alternans levels from 10 to 60 μV, the standard deviations observed are 15–30 μV. This indicates the inconsistency in estimation accuracy results of the multi-PCA scheme in the presence of noise.

To our knowledge, the Physionet TWA database is the only publicly accessible labeled TWA database. This makes it ideal for use as a benchmarking tool to make a comparison with existing methods possible. It consists of 100 multilead ECG signals that are ranked based on their TWA level. Comparing different methods can be done by ranking the results from the TWA detection in order of magnitude, and comparing this ranking with the reference ranking by calculating the Kendall rank correlation coefficient between the two. The results for the three tensor-based approaches and some of the most well-known methods from literature can be found in Table 3. It is clear that all tensor methods outperform the matrix-based alternatives. This could be expected since it was already proven that combining information from all leads increased results for TWA detection [17]. The method that used PARAFAC2 obtains the best result overall, while the results for CPD and MLSVD are comparable. Using a more general tensor decomposition method thus has clear added value in this application. The advantage of the MLSVD-based approach is however that it can also be used to assess TWA in each lead individually, and can thus be used to differentiate between different locations of TWA similarly to the MI detection method discussed earlier.

4.5 Analysis of Changes in Heartbeat Morphology

The final application discussed in this chapter is the analysis of changes in heartbeat morphology prior to cardiorespiratory arrest in the intensive care unit, explained in [37, 39]. For this study, a dataset with long-term patients in the intensive care unit was collected. The data were however characterized by large amounts of noise, diminishing the signal quality and possibly affecting the analysis results. While the

corrupted portions could be removed prior to the analysis; this seriously reduces the amount of information available. Furthermore, since often, not all leads are contaminated by noise, removing the corrupted portions also eliminates a clean ECG signal that contains valuable information. The method proposed here introduces the use of weighted tensor decompositions, which allow us to incorporate prior knowledge about the signal quality in the tensor decomposition in the form of a weight tensor [74]. When choosing the weights properly, they can automatically deal with the noise that is inherent to biomedical signals, leading to more accurate analysis and making them better suited to work with real-life signals. The method used in this study furthermore uses a computationally efficient weighting scheme [13], which is essential for real-time processing.

As explained before, CPD writes a tensor $\mathcal{T}$ as a sum of rank-one terms. Here, we used an alternative way to compute the CPD, namely Weighted CPD (WCPD), which uses weighted least-squares instead of regular least-squares. WCPD permits the incorporation of prior knowledge about the signal quality in the tensor decomposition, giving lower weight to entries with higher noise levels. This is done by introducing a weight tensor $\mathcal{W}$ with the same dimensions as $\mathcal{T}$ into the standard CPD optimization problem. Each entry of $\mathcal{W}$ contains the weight for the corresponding entry of $\mathcal{T}$. A detailed explanation of the weight tensor construction follows in the next paragraph. The new optimization problem is then:

$$\min_{\mathbf{A},\mathbf{B},\mathbf{C}} \frac{1}{2} ||\mathcal{W} * (\mathcal{T} - [\mathbf{A}, \mathbf{B}, \mathbf{C}])||_F^2 \tag{14}$$

The optimization problem can be solved using a novel Weighted Least Squares (WLS) approach, where the weight tensor is modeled by a polyadic decomposition, enabling efficient weighting. The computational details of the WLS algorithm can be found in [13].

The weight tensor $\mathcal{W}$ contains information about the signal quality, e.g. entries with higher quality receive higher weights. The quality of ECG signals is reduced by artifacts, which are technical or physiological. Technical artifacts can be caused by equipment malfunctioning or electrode loosening. During a technical artifact, no ECG signal is measured; the corresponding entries in $\mathcal{T}$, therefore, receive a weight of 0, effectively eliminating them from further analysis. Physiological artifacts are caused by for example muscle contractions and are superimposed onto the ECG signal, reducing the Signal-to-Noise Ratio (SNR). For signals which do not contain technical artifacts an estimate of the SNR was therefore used as a weight. We calculated one weight for each complete mode-2 fiber, e.g. each full heartbeat in each channel. It was thus assumed that the signal quality was the same during the time course of one heartbeat but could differ from channel to channel or between different heartbeats. Hence, the resulting weight tensor $\mathcal{W}$ has rank M, by construction, with M equal to the number of channels in the ECG signal.

The result of the WCPD with rank 1 is three factor vectors that are identical to the ones shown in Fig. 7. For this application, the second factor vector, which contains the temporal profile of the main heartbeat in the signal, is analyzed and processed further.

Standard techniques [56] can be used to detect fiducial points on the P wave, QRS complex, and T wave from which interval- and amplitude-parameters can be derived. By applying the tensor decomposition with a sliding window of 100 heartbeats, we could track and analyze the changes of these parameters in time.

From these analyses, explained in more detail in [37, 39], it could be concluded that changes in interval lengths are more significant between groups of patients with different causes of cardiac arrest than changes in amplitude. Changes in amplitude, especially for P wave and T wave amplitude, are however, more prevalent overall and might thus be useful to monitor overall patient deterioration. To confirm this, it would be beneficial to collect data from a group of control patients that do not experience a code blue to verify the normal physiological variations in different parameters.

The Weighted Least-Squares approach used to compute the WCPD optimization problem is computationally much more efficient than previous weighted tensor decomposition methods. This is extremely beneficial for use in continuous patient monitoring, where the delay between the physiological change and the algorithmic output should be minimal. The current method gives an output for each sliding window of 100 heartbeats (1–1.5 min), resulting in a quasi-real-time monitoring of ECG morphology. Recent advances in tensor methodology, however, focus on the development of efficient tensor updating methods [91]. This class of methods calculates a new tensor decomposition every time new data arrives (for example after every heartbeat) in a time- and memory-efficient way. Their use would lead to an improvement in the time resolution of the results, which could help gain a deeper understanding of the timing of the changes in ECG morphology before cardiac arrest.

5 Conclusions and Future Directions

Tensors are a novel concept in ECG signal processing. This chapter gave an overview of different applications where tensors have been used to solve problems in cardiac processing. As such we have shown that tensor-based methods are very suitable to represent data with multiple modes and lead to improved results compared to matrix-based methods when multiple leads need to be processed simultaneously.

We gave an overview of five typical ECG applications: data compression, myocardial infarction detection and localization, irregular heartbeat classification, TWA detection and quantification, and analysis of changes in heartbeat morphology. Most of the methods presented are, however, highly flexible and can be used in different applications with minimal changes. This can be done by either including different segments of the ECG signal in the tensor or by extracting different features from the decomposition results.

The popularity of tensor-based algorithms has increased in the past years, and it is expected that this increase will continue in the near future. We can, therefore, define possible future directions for the use of tensors in ECG applications.

The use of tensor decompositions for single-lead ECG signal is a first future direction that has a lot of potentials. As more and more wearable devices are equipped with

ECG recording devices, the amount of single-lead ECG signals is expected to increase drastically in the next years. Single lead ECG signals require an extra tensorization step prior to tensor decomposition methods, but since many tensorization techniques have been developed [25], this should not be a large bottleneck. The use of tensor updating was briefly explored in the previous section. It is a promising approach for most real-time monitoring methods, where an immediate output is required. Here, tensor updating was applied in a very straightforward way, by updating the result of the tensor decomposition for each new heartbeat. The updating could, however, be taken even further, by for example, not only updating the results of the tensor decomposition but also updating the rank of the decomposition as the signals are changing over the course of time. Tensors can also be applied for data fusion, where signals from different sources are analyzed simultaneously. While joint analysis of measurements from different signal types has not been explored in this chapter, it has the potential to reveal additional features that describe the interaction *between* different biosignals. It is for example known that cardiorespiratory coupling, which describes the influences of respiration on heart rate and blood pressure, is different for healthy and sick people. Using data fusion approaches on the combination of ECG and respiration or blood pressure would open the door to the development of algorithms to analyze a whole new class of biomarkers.

Acknowledgements This research was supported by: imec funds 2017, Belgian Foreign Affairs Development Cooperation: VLIR-UOS programs (20132019), Fonds de la Recherche Scientifique—FNRS and Fonds Wetenschappelijk Onderzoek—Vlaanderen under EOS Project no 30468160 (SeLMA), Research Council KU Leuven: C1 project C16/15/059-nD, European Research Council: The research leading to these results has received funding from the European Research Council under the European Unions Seventh Framework Programme (FP7/2007–2013)/ERC Advanced Grant: BIOTENSORS (no. 339804). This paper reflects only the authors' views and the Union is not liable for any use that may be made of the contained information. Griet Goovaerts is a SB Ph.D. fellow at Fonds voor Wetenschappelijk Onderzoek (FWO), Vlaanderen, supported by the Flemish government.

References

1. Abadi, B.M., Jarchi, D., Sanei, S.: Simultaneous localization and separation of biomedical signals by tensor factorization. In: 15th IEEE Workshop on Statistical Signal Processing, pp. 497–500. Cardiff, UK (2015)
2. Abenstein, J.P., Tompkins, W.J.: A new data-reduction algorithm for real-time ECG analysis. IEEE Trans. Biomed. Eng. BME **29**(1), 43–48 (1982)
3. Ansari, S., Farzaneh, N., Duda, M., Horan, K., Andersson, H.B., Goldberger, Z.D., Nallamothu, B.K., Najarian, K.: A review of automated methods for detection of myocardial ischemia and infarction using electrocardiogram and electronic health records. IEEE Rev. Biomed. Eng. **10**, 264–298 (2017)
4. Akhbari, M., Niknazar, M., Jutten, C., Shamsollahi, M., Rivet, B.: Fetal electrocardiogram R-peak detection using robust tensor decomposition and extended kalman filtering. In: Computing in Cardiology, Spain 2013, pp. 189–192 (2013)

5. Akbari, H., Shamsollahi, M.B., Phlypo, R.: Fetal ECG extraction using π tucker decomposition. In: 2015 International Conference on Systems, Signals and Image Processing (IWSSIP), Sept 2015, pp. 174–178 (2015)
6. Al-Fahoum, A.S.: Quality assessment of ECG compression techniques using a wavelet-based diagnostic measure. IEEE Trans. Inf. Technol. Biomed. **10**(1), 182–191 (2006)
7. Arif, M., Malagore, I., Afsar, F.: Detection and localization of myocardial infarction using k-nearest neighbor classifier. J. Med. Syst. **36**(1), 279–289 (2012)
8. Bergqvist, G., Larsson, E.G.: The higher-order singular value decomposition: theory and an application. IEEE Signal Process. Mag. **27**(3), 151–154 (2010)
9. Bharath, H.N., Sauwen, N., Sima, D.M., Himmelreich, U., De Lathauwer, L., Van Huffel, S.: Canonical polyadic decomposition for tissue type differentiation using multi-parametric MRI in high-grade gliomas. In: 24th European Signal Processing Conference (EUSIPCO), Budapest, 2016, pp. 547–551 (2016)
10. Bharath, H.N., Sima, D.M., Sauwen, N., Himmelreich, U., De Lathauwer, L., Van Huffel, S.: Non-negative canonical polyadic decomposition for tissue type differentiation in gliomas. IEEE J. Biomed. Health Inform. **21**(4), 1124–1132 (2017)
11. Boussé, M., Goovaerts, G., Vervliet, N., Debals, O., Van Huffel, S., De Lathauwer, L.: Irregular heartbeat classification using Kronecker product equations. In: 39th Annual International Conference of the IEEE Engineering in Medicine and Biology Society (EMBC 2017), July 2017, pp. 438–441 (2017)
12. Boussé, M., Vervliet, N., Domanov, I., Debals, O., De Lathauwer, L.: Linear systems with a canonical polyadic decomposition constrained solution: algorithms and applications. Numerical Linear Algebra with Applications 2018, p. e2190 (2018)
13. Boussé, M., De Lathauwer, L.: Nonlinear least squares algorithm for canonical polyadic decomposition using low-rank weights. In: 7th IEEE International Workshop on Computational Advances in Multi-Sensor Adaptive Processing, pp. 1–5. CAMSAP, Curaçao, Dutch Antilles (2017)
14. Boussé, M., Debals, O., De Lathauwer, L.: A tensor-based method for large-scale blind source separation using segmentation. IEEE Trans. Signal Process. **65**(2), 346–358 (2017)
15. Bro, R., Andersson, C., Kiers, H.: PARAFAC2-Part II. Modeling chromatographic data with retention time shifts. J. Chemom. **309**, 295–309 (1999)
16. Bro, R., Kiers, H.A.L.: A new efficient method for determining the number of components in PARAFAC models. J. Chemom. **17**, 274–286 (2003)
17. Burattini, L., Man, S., Burattini, R., Swenne, C.A.: Comparison of standard versus orthogonal ecg leads for t-wave alternans identification. Ann. Noninvasive Electrocardiol. **17**(2), 130–140 (2012)
18. Cetin, A.E., Koymen, H., Aydin, M.C.: Multichannel ECG data compression by multirate signal processing and transform domain coding techniques. IEEE Trans. Biomed. Eng. **40**(5), 495–499 (1993)
19. Cichocki, A., Mandic, D.P., De Lathauwer, L., Zhou, G., Zhao, Q., Caiafa, C.F., Phan, A.H.: Tensor decompositions for signal processing applications: from two-way to multiway component analysis. IEEE Signal Process. Mag. **32**(2), 145–163 (2015)
20. Cong, F., Nandi, A.K., He, Z., Cichocki, A., Ristaniemi, T.: Fast and effective model order selection to determine the number of sources in a linear transformation model. In: Proceedings of the 20th European Signal Processing Conference (EUSIPCO), Bucharest, Romania, 2012, pp. 1870–1874 (2012)
21. Cox, J.R., Nolle, F.M., Fozzard, H.A., Oliver, G.C.: AZTEC: a preprocessing scheme for real-time ECG rhythm analysis. IEEE Trans. Biomed. Eng. BME **15**, 128–129 (1968)
22. Dauwels, J., Srinivasan, K., Reddy, M.R., Cichocki, A.: Near-lossless multichannel EEG compression based on matrix and tensor decompositions. IEEE J. of Biomed. Health Info. **17**(3), 708–714 (2013)
23. Debals, O., De Lathauwer, L.: Stochastic and deterministic tensorization for blind signal separation. In: Latent Variable Analysis and Signal Separation, pp. 3–13 (2015)

24. Debals, O., Van Barel, M., De Lathauwer, L.: Blind signal separation of rational functions using Löwner-based tensorization. In: International Conference on Acoustics, Speech, Signal Processing (ICASSP), Brisbane, Australia Apr 2015, pp. 4145–4149 (2015)
25. Debals, O., De Lathauwer, L.: The concept of tensorization. Technical Report 17-99, ESAT-STADIUS, KU Leuven, Leuven, Belgium (2017)
26. De Lathauwer, L., De Moor, B., Vandewalle, J.: A multilinear singular value decomposition. SIAM J. Matrix Anal. Appl. **21**(4), 1253–1278 (2000)
27. De Lathauwer, L., Vandewalle, J.: Dimensionality reduction in higher-order signal processing and rank-$(R_1, R_2, \ldots, R_N)$ reduction in multilinear algebra. Linear Algebr. Its Appl. **391**, 31–55 (2004)
28. Domanov, I., De Lathauwer, L.: On the uniqueness of the canonical polyadic decomposition of third-order tensors—Part II: uniqueness of the overall decomposition. SIAM J. Matrix Anal. Appl. **34**(3), 876–903 (2013)
29. Domanov, I., De Lathauwer, L.: Generic uniqueness conditions for the canonical polyadic decomposition and INDSCAL. SIAM J. Matrix Anal. Appl. **36**(4), 1567–1589 (2015)
30. Domanov, I., De Lathauwer, L.: Canonical polyadic decomposition of third-order tensors: relaxed uniqueness conditions and algebraic algorithm. Linear Algebr. Its Appl. **513**, 342–375 (2017)
31. Geirnaert, S., Goovaerts, G., Padhy, S., Boussé, M., De Lathauwer, L., Van Huffel, S.: Tensor-based ECG signal processing applied to atrial fibrillation detection. In: Proceedings of the 52th IEEE Asilomar conference, Pacific Grove, CA, USA (2018)
32. Goldberger, A.L., et al.: Physiobank, physiotoolkit, and physionet: components of a new research resource for complex physiologic signals. Circulation **101**(23), e215–e220 (2000)
33. Goovaerts, G., Varon, C., Vandenberk, B., Willems, R., Van Huffel, S.: Tensor-based detection of T wave alternans in multilead ECG signals. In: Computing in Cardiology Conference, pp. 185–188 (2014)
34. Goovaerts, G., De Wel, O., Vandenberk, B., Willems, R., Van Huffel, S.: Detection of irregular heartbeats using tensors. In: 42nd Annual Conference of Computing in Cardiology, Sept 2015 (2015)
35. Goovaerts, G., Vandenberk, B., Willems, R., Van Huffel, S.: Tensor-based detection of T wave alternans using ECG. In: Proceedings of the 37th Annual International Conference of the IEEE Engineering in Medicine and Biology Society of the IEEE (EMBC), Milan, Italy, Aug 2015, pp. 6991–6994 (2015)
36. Goovaerts, G., Vandenberk, B., Willems, R., Van Huffel, S.: Automatic detection of T wave alternans using tensor decompositions in multilead ECG signals. Physiol. Meas. **38**(8), 1513–1528 (2017)
37. Goovaerts, G., Van Huffel, S., Hu, X.: Tensor-based analysis of ECG changes prior to in-hospital cardiac arrest. In: Proceedings of the 44rd Annual Computing in Cardiology (CinC 2017). CinC, Rennes, France, Sept (2017)
38. Goovaerts, G., Willems, R., Van Huffel, S.: Tensor-based ECG analysis in sudden cardiac death. Ph.D. thesis, Department of Electrical Engineering, KU Leuven, Dec 2018 (2018)
39. Goovaerts, G., Boussé, M., Do, D., De Lathauwer, L., Van Huffel, S., Hu, X.: Analysis of changes in ECG morphology prior to in-hospital cardiac arrest using weighted tensor decompositions. Submitted for publication
40. Håstad, J.: Tensor rank is NP-complete. J. Algorithms **11**(4), 644–654 (1990)
41. Hayn, D., Kollmann, A., Schreier, G.: Automated QT interval measurement from multilead ECG signals. In: Computing in Cardiology, Valencia, Spain, 2006, pp. 381–384 (2006)
42. He, H., Tan, Y., Xing, J.: Unsupervised classification of 12-lead ECG signals using wavelet tensor decomposition and two-dimensional Gaussian spectral clustering. Knowl.-Based Syst. **163**, 392–403 (2019)
43. He, J., Liu, Q., Christodoulou, A.G., Ma, C., Lam, F., Liang, Z.: Accelerated high-dimensional MR imaging with sparse sampling using low-rank tensors. IEEE Trans. Med. Imaging **35**(9), 2119–2129 (2016)

44. Hearing, B.D., Stone, P.H., Verrier, R.L.: Frequency response characteristics required for detection of T-wave alternans during ambulatory ECG monitoring. Ann. Noninvasive Electrocardiol. **1**(2), 103–112 (1996)
45. Hillar, C.J., Lim, L.H.: Most tensor problems are NP-hard. Technical Report, Eprint arXiv:0911.1393v4 (2009)
46. Huang, K., Zhang, L.: Cardiology knowledge free ECG feature extraction using generalized tensor rank one discriminant analysis. EURASIP J. Adv. Signal Process. (1) (2014)
47. Ikeda, T., Saito, H., Tanno, K., Shimizu, H., Watanabe, J., Ohnishi, Y., Kasamaki, Y., Ozawa, Y.: T-wave alternans as a predictor for sudden cardiac after myocardial infarction. Am. J. Cardiol. **89**(1), 79–82 (2002)
48. Ishteva, M., Absil, P.A., Van Huffel, S., De Lathauwer, L.: Best low multilinear rank approximation of higher-order tensors, based on the riemannian trust-region scheme. SIAM J. Matrix Anal. Appl. **32**(1), 115–135 (2011)
49. Jalaleddine, S., Hutchens, C., Stratran, R., Coberly, W.: ECG data compression techniques—a unified approach. IEEE Trans. Biomed. Eng. **37**(4), 329–343 (1990)
50. Jayachandran, E., Joseph, K.P., Acharya, U.R.: Analysis of myocardial infarction using discrete wavelet transform. J. Med. Syst. **34**(6), 985–992 (2010)
51. Kargas, N., Weingartner, S., Sidiropoulos, N.D., Akcakaya, M.: Low-rank tensor regularization for improved dynamic quantitative magnetic resonance imaging. In: SPARS 2017, Lisbon, Portugal, pp. 1–2 (2017)
52. Kolda, T.G., Bader, B.W.: Tensor decompositions and applications. SIAM Rev. **51**(3), 455–500 (2009)
53. Kuang, L., Hao, F., Yang, L., Lin, M., Luo, C., Min, G.: A tensor-based approach for big data representation and dimensionality reduction. IEEE Trans. Emerg. Top. Comput. **2**(3), 280–291 (2014)
54. Kuzilek, J., Kremen, V., Lhotska, L.: Comparison of JADE and canonical correlation analysis for ECG de-noising. In: Annual International Conference of the IEEE Engineering in Medicine and Biology Society, Chicago, USA, pp. 3857–3860 (2014)
55. Laguna, P., Jane, R., Caminal, P.: Automatic detection of wave boundaries in multilead ECG signals: validation with the CSE database. Comput. Biomed. Res. **27**, 45–60 (1994)
56. Laguna, P., Martinez Cortes, J.P., Pueyo, E.: Techniques for ventricular repolarization instability assessment from the ECG. Proc. IEEE **104**(2), 392–415 (2016)
57. Lee, H., Buckley, K.M.: ECG data compression using cut and align beats approach and 2-D transforms. IEEE Trans. Biomed. Eng. **46**(5), 556–564 (1999)
58. Li, J., Zhang, L., Tao, D., Sun, H., Zhao, Q.: Aprior neurophysiologic knowledge free tensor-based scheme for single trial EEG classification. IEEE Trans. Neural Syst. Rehabil. Eng. **17**(2), 107–115 (2009)
59. Li, D., Huang, K., Zhang, H., Zhang, L.: UMPCA based feature extraction for ECG. ISNN2013 Advances in Neural Networks, pp. 383–390. Springer, Berlin, Heidelberg (2013)
60. Li, X., Zhou, H., Li, L.: Tucker tensor regression and neuroimaging analysis. arXiv:1304.5637 pp. 1–28 (2013)
61. Llamedo, M., Khawaja, A., Martínez, J.: Analysis of 12-lead classification models for ECG classification. In: Computing in Cardiology, Sept 2010, pp. 673–676 (2010)
62. Lu, H.L., Ong, K., Chia, P.: An automated ECG classification system based on a neuro-fuzzy system. Comput. Cardiol. 387–390 (2000)
63. Lu, H., Plataniotis, K.N., Venetsanopoulos, A.N.: MPCA: multilinear principal component analysis of tensor objects. IEEE Trans. Neural Netw. **19**(1), 18–39 (2008)
64. Lu, H., Plataniotis, K.N., Venetsanopoulos, A.N.: Uncorrelated multilinear principal component analysis for unsupervised multilinear subspace learning. IEEE Trans. Neural Netw. **20**(11), 1820–1836 (2009)
65. Martinez, J., Olmos, S.: Methodological principles of T wave alternans analysis: a unified framework. IEEE Trans. Biomed. Eng. **52**(4), 599–613 (2005)
66. Manikandan, M.S., Dandapat, S.: Wavelet energy based diagnostic distortion measure for ECG. Biomed. Signal Process. Control., Elsevier **2**, 80–96 (2007)

67. Manikandan, M.S., Dandapat, S.: Wavelet threshold based TDL and TDR algorithms for real-time ECG signal compression. Biomed. Signal Process. Control., Elsevier **3**, 44–66 (2008)
68. Monasterio, V., Laguna, P., Martinez, J.: Multilead analysis of T-wave alternans in the ECG using principal component analysis. IEEE Trans. Biomed. Eng. **56**(7), 1880–1890 (2009)
69. Mueller, W.: Arrhythmia detection program for an ambulatory ECG monitor. Biomed. Sci. Instrum. **14**, 81–85 (1978)
70. Narayan, S.M., Smith, J.M.: Spectral analysis of periodic fluctuations in electrocardiographic repolarization. IEEE Trans. Biomed. Eng. **46**(2), 203–212 (1999)
71. Nearing, B.D., Verrier, R.L.: Modified moving average analysis of T-wave alternans to predict ventricular fibrillation with high accuracy. J. Appl. Physiol. **92**(2), 541–549 (2002) (Bethesda, Md.: 1985)
72. Niknazar, M., Rivet, B., Jutten, C.: Fetal QRS complex detection based on three-way tensor decomposition. Comput. Cardiol., Spain, 185–188 (2013)
73. Oliveira, P.M.R., de, Zarzoso, V.: Source analysis and selection using block term decomposition in Atrial fibrillation. In: Latent Variable Analysis and Signal Separation, pp. 46–56. Springer (2018)
74. Paatero, P.: A weighted non-negative least squares algorithm for three-way 'PARAFAC' factor analysis. Chemom. Intell. Lab. Syst. **38**(2), 223–242 (1997)
75. Padhy, S., Dandapat, S.: Exploiting multi-lead electrocardiogram correlations using robust third-order tensor decomposition. Healthc. Technol. Lett. **2**(5), 112–117 (2015)
76. Padhy, S., Sharma, L., Dandapat, S.: Multilead ECG data compression using SVD in multiresolution domain. Biomed. Signal Process. Control., Elsevier **23**, 10–18 (2016)
77. Padhy, S., Dandapat, S.: Third-order tensor based analysis of multilead ECG for classification of myocardial infarction. Biomed. Signal Process. Control., Elsevier **31**, 71–78 (2017)
78. Padhy, S., Multilead, E.C.G.: Data analysis using SVD and higher-order SVD. Ph.D. thesis, Indian Institute of Technology Guwahati, India, March 2017. http://gyan.iitg.ernet.in/handle/123456789/1006 (2017)
79. Padhy, S., Dandapat, S.: Validation of μ-volt T-wave alternans analysis using multiscale analysis-by-synthesis and higher-order SVD. Biomed. Signal Process. Control., Elsevier **40**, 171–179 (2018)
80. Reddy, M.R.S., Edenbrandt, L., Svensson, J., Haisty, W.K., Pahlm, O.: Neural network versus electrocardiographer and conventional computer criteria in diagnosing anterior infarct from the ECG. In: Computers in Cardiology, Oct 1992, pp. 667–670 (1992)
81. Ribeiro, L.N., Hidalgo-Muñoz, A.R., Favier, G., Mota, J.C.M., De Almeida, A.L.F., Zarzoso, V.: A tensor decomposition approach to noninvasive atrial activity extraction in atrial fibrillation ecg. In: 23rd European Signal Processing Conference (EUSIPCO-2015), Aug 2015, pp. 2576–2580 (2015)
82. Sharma, L.N., Dandapat, S., Mahanta, A.: Multichannel ECG data compression based on multiscale principal component analysis. IEEE Trans. Inf. Technol. Biomed. **16**(4), 730–736 (2012)
83. Sharma, L.N., Tripathy, R., Dandapat, S.: Multiscale energy and eigenspace approach to detection and localization of myocardial infarction. IEEE Trans. Biomed. Eng. **62**(7), 1827–1837 (2015)
84. Sidiropoulos, N., De Lathauwer, L., Fu, X., Huang, K., Papalexakis, E., Faloutsos, C.: Tensor decomposition for signal processing and machine learning. IEEE Trans. Signal Process. **65**(13), 3551–3582 (2017)
85. Smith, J.M., Clancy, E.A., Valeri, C.R., Ruskin, J.N., Cohen, R.J.: Electrical alternans and cardiac electrical instability. Circulation **77**(1), 110–121 (1988)
86. Srinivasan, K., Dauwels, J., Reddy, M.R.: Multichannel EEG compression: Wavelet-based image and volumetric coding approach. IEEE J. Biomed. Health Inform. **17**(1), 113–120 (2013)
87. Sun, L., Lu, Y., Yang, K., Li, S.: ECG analysis using multiple instance learning for myocardial infarction detection. IEEE Trans. Biomed. Eng. **59**(12), 3348–3356 (2012)

88. Tao, D., Li, X., Wu, X., Maybank, S.J.: General tensor discriminant analysis and Gabor features for gait recognition. IEEE Trans. Pattern Anal. Mach. Intell. **29**(10), 1700–1715 (2007)
89. Vervliet, N., Debals, O., De Lathauwer, L.: Tensorlab 3.0—Numerical optimization strategies for large-scale constrained and coupled matrix/tensor factorization. In: 50th Asilomar Conference on Signals, Systems and Computers, pp. 1733–1738. IEEE (2016)
90. Thygesen, K., Alpert, J.S., Jaffe, A.S., Simoons, M.L., Chaitman, B.R., White, H.D.: Third universal definition of myocardial infarction. Circulation **126**(16), 2020–2035 (2012)
91. Vandecappelle, M., Boussé, M., Vervliet, N., De Lathauwer, L.: CPD updating using low-rank weights. In: 25th European Signal Processing Conference (EUSIPCO), pp. 557–663. Kos, Greece (2017)
92. Van Eyndhoven, S., Boussé, M., Hunyadi, B., De Lathauwer, L., Van Huffel, S.: Single-channel EEG classification by multi-channel tensor subspace learning and regression. In: Proceedings of the 28th IEEE International Workshop on Machine Learning for Signal Processing (MLSP 2018), Sept (2018)
93. Vasilescu, M., Terzopoulos, D.: Multilinear (tensor) image synthesis, analysis, and recognition [exploratory dsp]. IEEE Signal Process. Mag. **24**(6), 118–123 (2007)
94. Vervliet, N., Debals, O., Sorber, L., De Lathauwer, L.: Breaking the curse of dimensionality using decompositions of incomplete tensors: tensor-based scientific computing in big data analysis. IEEE Signal Process. Mag. **31**(5), 71–79 (2014)
95. Vítek, M., Hrubeš, J., Kozumplík, J.: A wavelet-based ECG delineation in multilead ECG signals: evaluation on the CSE database. In: World Congress on Medical Physics and Biomedical Engineering, pp. 177–180. Springer, Berlin, Heidelberg (2009)
96. Wei, J., Chang, C., Chou, N., Jan, G.: ECG data compression using truncated singular value decomposition. IEEE Trans. Inf. Technol. Biomed. **5**(4), 290–299 (2001)
97. Yaman, B., Weingärtner, S., Kargas, N., Sidiropoulos, N.D., Akcakaya, M.: Locally low-rank tensor regularization for high-resolution quantitative dynamic MRI. In: 7th IEEE International Workshop on Computational Advances in Multi-Sensor Adaptive Processing, pp. 1–5. CAMSAP, Curaçao, Dutch Antilles (2017)
98. Zarzoso, V.: Parameter estimation in block term decomposition for noninvasive atrial fibrillation analysis. In: 7th IEEE International Workshop on Computational Advances in Multi-Sensor Adaptive Processing, pp. 1–5. CAMSAP, Curaçao, Dutch Antilles (2017)
99. Zhou, H., Li, L., Zhu, H.: Tensor regression with applications in neuroimaging data analysis. J. Am. Stat. Assoc. **108**(502), 540–552 (2013)

Syntactic Methods for ECG Signal Diagnosis and QRS Complexes Recognition

Salah Hamdi, Asma Ben Abdallah and Mohamed Hedi Bedoui

Abstract Grammar and the theory of language have been around for a long time. So far, grammar formalism has been used for programming and formal languages to describe natural languages and software engineering. However, the grammatical discipline can be extended to join other areas of applications such as ECG signal analysis. Thus, this chapter will provide an overview of the related methods and show that syntactic methods and regular grammar can be supported for ECG analysis and especially for the recognition of QRS complexes. A comparative study with a huge number of known methods will be presented.

1 Introduction

The processing of 1D medical data is a very active subject, and several approaches have been proposed. The Electrocardiogram (ECG) signal is widely used in the field of cardiology. This signal represents the electrical activity of the heart and constitutes a crucial clinical added value to diagnose one of the different types of arrhythmias. Generally, cardiac pathologies are indicated by disorders of the electrical activities of the heart. In this chapter, we address the problem of automatic ECG signal processing and the extraction of QRS complexes through type 3 and type 2 grammar. Grammar is a formalism designed to describe languages and recognize all learned words. However, syntactic approaches can powerfully represent signal structures and therefore make information retrieval easier. The input data appears to be a structured scene with a hierarchical order because grammar can represent hierarchical structures using non-terminal and terminal nodes. In addition, syntactic approaches can

S. Hamdi (✉) · A. Ben Abdallah · M. H. Bedoui
Laboratory of Technology and Medical Imaging (LTIM), Faculty of Medicine of Monastir, University of Monastir, Monastir, Tunisia
e-mail: salah.hamdi@isffs.u-sousse.tn

A. Ben Abdallah
e-mail: asma.benabdallah@cristal.rnu.tn

M. H. Bedoui
e-mail: medhedi.bedoui@fmm.rnu.tn

G. Naik (ed.), *Biomedical Signal Processing*, Series in BioEngineering,
https://doi.org/10.1007/978-981-13-9097-5_14

describe a large set of complex objects using small sets of simple primitives and grammatical rules [38]. A set of grammar-based approaches were proposed for ECG signal processing [22, 29, 42–44, 50]. The main advantage of these methods was the representation of available ECG signal elements. In this chapter, we focus first on related techniques. Then a syntactic method [43, 44] will be applied in real ECG signals representing different patients issued from the standard MIT-BIH arrhythmia database. For all input records, QRS complexes, RR distances, and Q, R and S peaks are detected. A comparative study with a large number of known methods [3, 4, 7, 9, 16, 17, 19, 20, 30, 31, 40, 47, 49] is presented in terms of accuracy rate. In the ECG feature extraction 1D module, an algorithm for detecting QRS complexes from the ECG signal using a regular grammar-based approach is developed. It allows extracting representative parameters of each heart-beat. We expand the ECG signal database to apply the standard MIT-BIH method to have a balanced number of signal types, to encompass other types and varieties of signals and to increase the quality of learning. This chapter is organized as follows: Sect. 2 lists several application areas of grammar formalism. Section 3 sheds the light on the state of the art and the methods based on context-free grammars. Section 4 discusses the results of the related techniques. Section 5 presents a method based on regular grammar [43, 44] which gives better results. Section 6 concludes this chapter.

2 Application Areas of Grammar

Grammar is a key step that facilitates data compression [27, 28], video scene interpretation [8], pattern recognition [11, 15], image segmentation [10, 13, 18, 48, 53, 54] and medical data analysis [35, 36, 51, 52]. In [32], the author put a set of production rules governing the use of similarity criteria to judge the similarity between objects. The goal was to design a smart perception system based on pattern retrieval from a database. The system had to retrieve the closest match in terms of similarity to a request image entered by the user. In [12], the author used grammar for syntactic recognition of cheese. The main idea was to represent a model as a structure of strings, trees, or graphs. Then a set of structures was considered as a formal language that could be analyzed with a PLC. The process of syntactic recognition of forms consisted of three main phases: preprocessing the image (filtering, improvement …), generating structural presentations and analyzing structural representations (parsing). In [8], the author utilized grammar to direct a vision system for the interpretation of dynamic scenes. The system was implemented based on production rules for the interpretation of a scenario of putting a cup on a saucer and then on a table. Once the functionality (f_i) was detected and given the current state (q_i), a production rule (P_i) would be invoked resulting in a new state (q_j). The transition from state (q_i) to state (q_j) indicated a stage scene. Therefore, each transition in (P_i) had an associated semantic description which described the observed phenomena. According to [39], as books had chapters, sections, paragraphs, and sentences, videos also had an inherent hierarchical structure. The author focused on recent research in the areas of

scene extraction. The first step was the detection of firing transitions with separate detectors for difficult cuts. After that, complex cuts were segmented into semantically meaningful units called sub-slices. Finally, the results were used to extract the scenes. The author proposed to utilize transition to improve scene detection results. The suggested algorithm was robust to the distortions and artifacts founded in the video. The grammar-based lossless coding theory was put forward by Kieffer et al. [27, 28]. First, the encoding transformed the original data sequence into an irreducible grammar, which was then compressed using arithmetic coding. It was shown that grammar-based coding could specifically predict good performances on files that had multimedia features. The proposed process applied the reduction rules in order to reduce grammar G into irreducible grammar G'. Therefore, the role of reduction rules was to ensure that a grammar G was irreducible. The code-based grammar then used a zero-order arithmetic code to compress the irreducible grammar G to the high compression ratio. Once the final irreducible grammar G was obtained, it was compressed using a zero-order arithmetic code of a dynamic alphabet. Alex et al. [1, 34] demonstrated that stochastic context-free grammars (SCFGs) were adequate for signal processing. The grammar was applied for MFR signal processing using stochastic syntactic models by a Markov chain representing radars policy of operation. The timing of the emitter was dictated by word. The words occur serially in the pulse train so that one word starts as the previous word is ending.

Ogiela et al. [36] presented a method to obtain a bone description of the wrist in the form of a graph. First, the images were subjected to a preprocessing step to indicate the contours of the bone. Subsequently, the terminal symbols of the grammar were represented by the gravity centers of each bone of the hand. The application of the proposed techniques achieved a recognition rate of approximately 93%. The grammar was aimed at the automatic construction and the semantic and topological interpretation of the wrist bones. Trzupek et al. [51, 52] presented an approach for medical image interpretation and the recognition of cardiac diseases from 3D images of coronary arteries. After a phase of skeletonization, a grammatical description in the form of a graph represented the spatial relationships between the arteries. This operation determined the starting point and the point of arrival of each branch of the arteries. Then, each point was tagged to identify the type of each branch based mostly on the coordinates of the points. The set of these points constitute the nodes of the generated graph, which represented a semantic model for the spatial reconstruction of the coronary arteries. The coordinates of the branches represented the terminal vocabulary of the grammar used, whereas the non-terminal vocabulary represented the different possibilities of distribution of the arteries and thus the different types of stenosis. The proposed method showed a classification rate of 85%. In Salah et al. [41], a method to segment a cardiac image and to estimate the area using regular grammars was presented. An image was defined as a set of words based on an alphabet, and an object, similar to a word, was recognized by an automaton. The image was divided into small blocks, each having a predefined structure that represented the terminal node of a grammar. Then, each block was associated with a number that performed the mapping of the represented structure in such a way as to create a numeric matrix, which represented the image. The next step created a regular expression rep-

Table 1 Synthesis of application domains based on syntactic methods

Application domain	Primitives	Results
Data compression	The axiom is the sequence to be compressed; the transitions are trying to reduce the sequence size	Lossless coding based on grammar. The coding transforms the original sequence of data into an irreducible grammar
Video scene interpretation	The transition from one state to another indicates a stage in the scene	An associated semantic description describes the observed phenomena
Pattern recognition	Patterns and dictionary of basic shapes from a database	Using similarity criteria to judge the similarity between objects in an image
Image segmentation	Set of pixels in a specific format	Presentation of the generated image
Medical image analysis	The terminal symbols of grammar were represented by the gravity centers of each organ	Spatial relationship and classification rate

resenting a closed contour. The automaton equivalent to this regular expression was used to analyze the matrix in order to search sub-matrix with these contours, performing the image segmentation. The authors conducted tests with cardiac images and indicated an accuracy of 93.22% to estimate the segmented areas. Lluis-Pere et al. [23] presented a stochastic grammar to represent the structural, hierarchical, and semantic relations between floor plan elements. A Bottom-Up/Top-Down parser has been used for floor plan recognition. The method was able to represent examples of the corpus supposing idealistic component extraction techniques. Kasemsumran et al. [25] developed a face recognition system with a string grammar nearest neighbor (sgNN). The method was tested on AT&T, MIT-CBCL, and Georgia Tech face databases ant it provided 88.25%, 87.50%, and 70.71% recognition rates respectively.

Table 1 synthetizes the application domains of grammar. We presented succinctly many fields with the application domains, primitives, and results.

The exploitation of syntactic methods for ECG signal processing will be described in detail in the following sections. A large part of QRS complex recognition and waves extraction will be devoted.

3 Context-Free Grammar for ECG Signal Analysis

In this section, all the methods that use context-free grammar to analyze ECG signals are listed. Trahanias et al. [50] presented an application of a syntax method for ECG signal recognition and the measurement of associated parameters. The work was composed of two parts: the extraction of peaks and their grammatical analysis. Each peak was characterized by three points: the two left and right limit points plus one

energy value. One peak could be either linear or parabolic. The extraction of peaks was done by scanning the signal interval by interval to exclude erroneous peaks which appeared as adjacent peaks satisfying a set of criteria. The suggested method recognized all peaks and then rejected false peaks. Each peak was characterized by three points: the two left and right limit points plus one energy value. A peak could be either linear or parabolic. The extraction of peaks and endpoints was done by scanning the signal interval by interval. In [50], a method for recognizing erroneous peaks or false peaks in an ECG signal was presented. The erroneous peaks appeared as adjacent peaks satisfying a set of criteria. Direct methods recognized all peaks $P_1, P_2, \ldots, P_i$ and rejected false peaks based on a set of criteria. Each peak Pi was characterized by time P_{xi} and amplitude P_{yi}. The criteria were applied to each of the five consecutive peaks $P_{i-3}, P_{i-2}, P_{i-1}, P_i, P_{i+1}$, as shown in Fig. 1. The peak evaluation criteria were based on the amplitudes and durations of the following five peaks:

$$Py_{i-3} \leq Py_{i-1}\ AND\ Py_{i-1} \geq Py_{i-2} \tag{1}$$

$$|Py_{i-2} - Py_{i-1}| \leq s1 \tag{2}$$

$$\Delta t_m \leq s2 \tag{3}$$

$$if\ \Delta t_m \leq s3\ so\ skip\ (5) \tag{4}$$

$$\Delta t_m \geq \Delta t_g\ AND\ \Delta t_m \geq \Delta t_d \tag{5}$$

$i \leftarrow 0$
$P0 \leftarrow$ *the first peak of the signal*
Step1: find the next peak
if *there are no subsequent peaks* **then**
  END
end if
Step 2: $i \leftarrow i + 1$
if $i \leq 3$ **then**
  Goto Step 1
end if
Step3:
if the peer (Pi-2, Pi-1) is not noisy **then**
  Goto Step1
end if
$Pi - 2 \leftarrow Pi$
$i \leftarrow i - 2$
if $i \leq 3$ **then**
  Goto Step 1
end if
Goto Step 3

Algorithm 1: Peaks detection

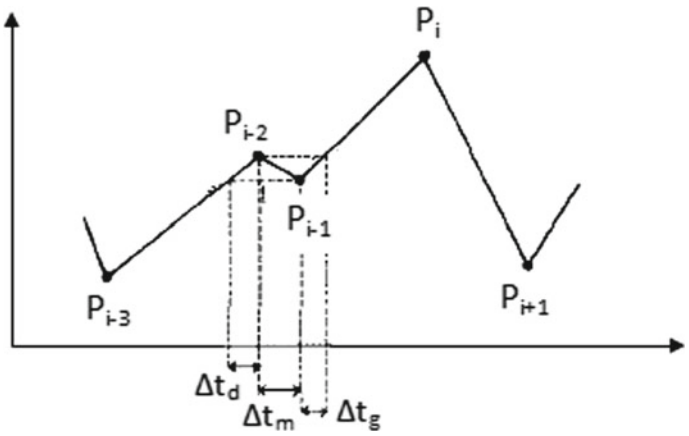

Fig. 1 Application on each group of five peaks and detection of false peaks

Peaks with amplitudes above a fixed threshold were not considered false peaks. Peaks with durations above a fixed threshold were not considered as false peaks. The false peak detection algorithm applied to a group of five consecutive peaks.

A sequence of n peaks would be considered a QRS complex if they satisfied both of the following conditions: The sum of energies of the n peaks was greater than a threshold $s1$:

$$\sum_{i=1}^{n} e_i \geq s1 \tag{6}$$

The angle θ between the two consecutive peaks, pic_i, and pic_{i+1}, was less than a threshold $s2$:

$$\theta(pic_i, pic_{i+1}) \leq s2 \tag{7}$$

The angle concept made it possible to avoid confusion between the QRS complexes and the P and T waves. The recognition of the P and T waves was based on the measurement of the amplitude and the wavelength compared to thresholds $s3$ and $s4$. One or two consecutive peaks were recognized as being a P or T wave, setting their width and amplitude according to the evaluated syntactic rule. They were discriminated from other peaks by comparing their energies. Noisy peaks in a region between two QRS complexes had to have less energy than the energy of the P and T complexes in this region. The alternative of the syntactic rule that corresponded to a P or T wave would specify its morphology. It was noted that the P and T waves that had occurred before the first and after the last found QRS complex was not recognized. This would make grammar easier. In [50], the author used the alphabet Σ = K+, K−, rest, wave knowing that: K+ described a positive peak and K− described a negative one. An ECG signal was assimilated into a sequence of symbols of Σ. Each symbol was assigned corresponding values. After that, the author used a context-free

grammar G = (VT, VN, S, P) to describe an ECG signal where VT represented the terminal vocabulary, VN represented the non-terminal vocabulary, S was the axiom, and P represented the production rules where the character '.' is a concatenation operator:

Grammar G = (VT, VN, S, P) where:
VT={K+, K−, rest, wave}
VN={ECG, Beginning, End, Cardiac_Cycles, QRS, Peak, Rest, Segment, Remaining, Non_QRS, QS, Q, R, S, P, T, R', S', R", S", SR, ST, TR, SP, PR, TP, A, B, C, D, E, F}
S = {ECG}
P is the following rules:
ECG → Beginning.Cardiac_Cycles.End
Beginning → ϵ | Segment.Beginning | Peak.Beginning
Segment → Rest | wave
Pic → K+ | K−
End → QRS.Remaining
Remaining → ϵ | Segment.Remaining | Peak.Remaining
Cardiac_Cycles → Cardiac_Cycle.Cardiac_Cycles
QRS → [Q]?.R.S.R'.S'.R".[S"]? | [Q]?.R.S.R'.[S']? | [Q]?R.[S]? | Q.S
Non_QRS → SR | ST.T.TR | SP.P.PR | ST.T.A
A → B | C | D | E
B → ϵ | P . B
C → TP.P.PR.P.PR
D → TP.P.PR
E → ϵ | Pic.E | Segment.E
ST → F
TP → F
PR → F
TR → F
SP → F
PP → F
SR → Segment.F | Peak.F
F → ϵ | Segment.F | Peak.F
T → K+.K− | K−.K+ | K+ | K−
P → K+.K− | K−.K+ | K+ | K−
R → K+
R' → K+
R" → K+
Q → K−
QS → K−
S → K−
S' → K−
S" → K−

In [50], the QRS complex classification was performed by the nearest neighborhood classification algorithm (KNN). The distance between a given QRS complex and a given class of QRS complexes was calculated as the average of the distances between the given QRS complex and each QRS complex in the given class of QRS complexes. The morphological (structural) and quantitative (statistical) characteristics were taken into account when calculating the distance. Normalized duration and normalized amplitude were the statistical characteristics used. Morphological characteristics, when calculating the distance between two complexes, were taken into account by aligning the complexes so that they would correspond best. Kokai et al. [29] used grammar rules to recognize QRS complexes and distinguish between QRS and non-QRS data. The authors relied on context-free grammar G = (VT, VN, S, P) where VT was a terminal vocabulary, VN was a non-terminal vocabulary, S was the ECG, and P was a set of the production rules. A QRS complex had to satisfy the following 3 conditions:

The value of a peak had to be greater than a threshold $s1$. The angle between the right segment of peak i and the left segment of peak $i + 1$ had to be less than a threshold $s2$. The angle of each peak was less than a threshold $s3$.

The author used grammar G = (VT, VN, S, P), where:
VT={K+, K−, Line, Parabola}
K+ is a positive peak.
K− is a negative peak.
VN={ CARDIAC_CYCLES, CARDIAC_CYCLE, PEAK, PEAKS, QRS, NON_QRS, SEGMENT, INTERWAVE_SEGMENT, SR, T_OR_P, P, T}
S = {ECG}
P represents the following production rules:
CARDIAC_CYCLES → CARDIAC_CYCLE.CARDIAC_CYCLES
CARDIAC_CYCLES → ϵ
CARDIAC_CYCLE → QRS.NON_QRS
QRS → PEAK.PEAKS
PEAKS → PEAK.PEAKS
PEAKS → ϵ
PEAK → K+ | K−
NON_QRS → SR|INTERWAVE_SEGMENT.T.INTERWAVE_SEGMENT|
INTERWAVE_SEGMENT.P.INTERWAVE_SEGMENT|
INTERWAVE_SEGMENT.T.INTERWAVE_SEGMENT.P.INTERWAVE_SEGMENT
SR → SEGMENT.INTERWAVE_SEGMENT|PEAK.INTERWAVE_SEGMENT
INTERWAVE_SEGMENT→ | SEGMENT.INTERWAVE_SEGMENT|PEAK.
INTERWAVE_SEGMENT
T → T_OR_P
P → T_OR_P
T _OR_P→ K+|K-|K+.K-| K−.K+
SEGMENT → Line|Parabola

Hanieh et al. [22] proposed a method for ECG signal segmentation separating P, QRS complex, and T waves from the electrocardiogram signal. The ECG was first normalized in order to be prepared for the next stage. The segmentation of each wave was based on its time interval and waveform. A context-free grammar was used to

extract the cardiac disease, which contains atrial fibrillation arrhythmia modeled by regular expressions and DFA corresponding to each patient. The segmented ECG signal was compared with the grammars generated by each DFA, and the disease was confirmed if it matches the arrhythmia DFA. Otherwise, if it is not a match for any arrhythmia DFA, it enters the comparison phase. Algorithm 2 presents the proposed algorithm. In order to transform the ECG signal and generate its model based on

```
ecgSignal ← ECGrecorder(20s)
denoisedECG ← Filtering(ecgSignal)
ecgCharSequence ← Segmentation(denoisedECG)
inEcgSentence ← Optimize(ecgCharSequence)
for dfa ∈ ECG.DFA do
  return dfa.associatedDesease
  if dfa.accept(inEcgSentence) then
    return dfa.associatedDesease
  else
    ecgSents ← dfa.Generate(|inEcgSentence|)
    AT ← proposedMatch(ecgSents, inEcgSentence)
  end if
end for
return AT
```

Algorithm 2: Arythmy Recognizer

regular expressions or form a corresponding DFA, the model was first formed from the signal using a sequence of alphabets. This sequence was ((PQRTS)U*)* for a normal waveform and (P*QRSTU)* for an atrial fibrillation arrhythmia. This model was created based on the features of normal and arrhythmia waveforms, and the DFA corresponding to the normal and arrhythmia waveforms was then delineated, which is presented in Fig. 2 where the character '∼' means that the element has not been observed.

Salah et al. [42] described an entire normal ECG signal using a context-free grammar. QRS complexes, RR distances, PR, and QT intervals were calculated. First, the aim of the analyzers was to classify the input signal in the case of an ECG signal or not and then to determine the number of cardiac cycles and the various indicators.

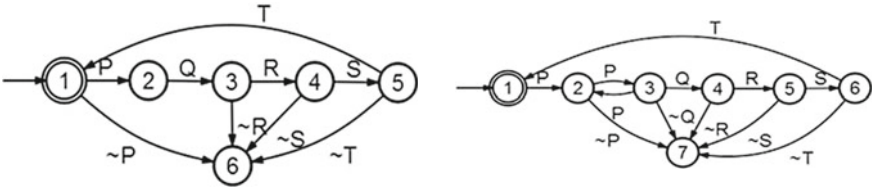

(a) A normal ECG pattern

(b) ECG of a kind of atrial fibrillation disease

Fig. 2 DFA of two different ECG patterns

The author was based on the following grammar G to describe the signal. VT was the terminal vocabulary of the grammar. VN was the non-terminal vocabulary. S was the axiom and P was the set of production rules. The proposed grammar G could describe a normal ECG and could automate the detection of deviations from the norm.

G = (VT, VN, S, P) where:
VT = {0, 1, 2, 3, 4, 5, 6, 7, 8, 9, −, ., }
VN = {ECG, Col, Palier, Coda, Rest, End}
S = {ECG}
P is the set of the following rules:
ECG → Rest.P.Col | P.Col
Col → Q.R.Palier
Palier → S.Coda
Coda → Rest.T.End | T.End
End → ECG | ϵ

4 Discussion

Although the syntactic methods seem to be suitable for ECG signal recognition and parameter measurement, little progress has been made up to date. In the reported attempts, only specific aspects of this problem have been addressed. Context-free grammar for peak recognition in ECGs has been described. Grammar has been proposed for the detection of QRS complexes. Context-free grammar has been used for the detection of certain ventricular arrhythmias. An attempt to analyze arrhythmia using the finite state automata model has been described and the filtering of ECG waveforms by the syntactic method has also been studied. The application of the syntactical approaches to ECG signal recognition and parameter measurement described in this document have yielded results inferior to those reported by some implementations using the non-syntactic approach. However, the non-syntactic approach has been quite mature in this particular problem after a considerable body of research work. Syntactic approaches may improve the results by further refinement of the method. We have observed that the primitive pattern extractor does not always accurately delineate the limits of the peaks. This type of error spreads in the following steps, and is responsible for many inaccurate results. Removing this deficiency will critically improve the overall performance of the approach. Hanieh et al. [22] applied their method on the MIT-BIH arrhythmias database, and the algorithm has shown an average sensitivity rate that does not exceed 96.3%. In [29], no information was given on the database used, and the sensitivity rate reached. The methods mentioned above are all context-free grammar used mainly for the spatial interpretation of peaks. In addition, they are very sensitive to noise and the choice of intra and inter peak energy thresholds. Context-free grammar demands polynomial time parsing process. The main goal of [43, 44] was to reach regular grammar with the addition of some criteria. The author used a regular grammar and deterministic automata for the recognition of QRS complexes which will be detailed in the following section.

Although the syntactic method seems to be suitable for the problem of ECG signal recognition and parameter measurement, little progress has been made so far. In the reported attempts, only specific aspects of this problem were addressed. Context-free grammar for peak recognition in ECGs was described. Grammar was proposed for the detection of QRS complexes. Context-free grammar was used for the detection of certain ventricular arrhythmias. An attempt to analyze arrhythmia using the finite state machine model was described, and even the filtering of ECG waveforms by the syntactic method was also studied. The application of the syntactical approach to ECG signal recognition and parameter measurement that has been described in this document has yielded results inferior to those reported by some implementations using the non-syntactic approach.

However, the latter is quite mature in this particular problem after a considerable amount of research work for many years. In the syntactic approach, there is a lot of room for improving the results by further refining the method. We have observed that the primitive pattern extractor does not always accurately delineate the limits of peaks. This type of error spreads in the following steps and is responsible for many inaccurate results. Removing this deficiency will greatly improve the overall performance of the approach. Hanieh et al. [22] applied their method on the MIT-BIH arrhythmias data-base. The author formed an appropriate grammar for the atrial fibrillation disease based on the performed segmentation. Common detection algorithms of ECG signal waves used time interval length and range (width and height) of the QRS combinations. Although these parameters are essential, they are not sufficient for accurate detection. Therefore, the algorithm showed an average sensitivity rate that did not exceed 96.3%.

Salah et al. [42] presented a context-free grammar to describe an entire ECG signal. Nevertheless, this could not represent all the various types of signals. The author focused only on normal cases, and the method was applied on very short signal durations. Besides, the author compared his approach with old techniques adopted by Holsinger [24], and Fraden and Neuman [14]. In [29], no information was given about the database used, and the sensitivity rate reached. In addition, the methods mentioned above are very sensitive to noise. Because of noise, several morphologies can be found and thus interfere with the grammatical description of the signal and generate erroneous peaks. Indeed, grammar has become able to classify several signal types as ECG signals. On the other hand, the grammatical formalism has been used only at level 3 (Fig. 3) to make the spatial interpretation of the elements of the signal. In other words, researchers have not exploited the formalism of grammar during the peak extraction phase at level 2 (Fig. 3).

The syntactic methods mentioned above are sensitive to the choice of energy thresholds (amplitudes) and to intra and inter peak thresholds. Peak recognition was carried out using another method, regardless of grammar. Indeed, our goal is to extend the level of use of grammar and utilize grammar to extract shapes (level 2) and spatial interpretation of shapes (level 3) with an addition of other criteria of standard deviations and durations. We will use grammar type 3 for extracting QRS complexes from an ECG signal and grammar type 2 for ECG signal recognition.

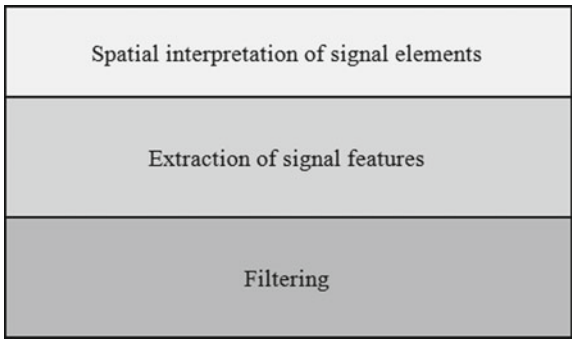

Fig. 3 Signal processing levels

The next section presents the work carried out in applying the syntax method to the whole problem of ECG pattern recognition and parameter measurement. Solutions to the sub-problems of primitive pattern selection, primitive pattern extraction, linguistic representation, and pattern grammar formulation will be described.

5 Regular Grammar for QRS Complex Detection

The QRS complex represents the ventricular depolarization curve. All these three peaks have durations between 0.06 and 0.1 s [2, 5, 6, 21, 26, 33, 45, 46]. In this section, we will describe in detail the method of [43, 44]. A normalized QRS complex is assimilated as a sequence of peaks, and very short rests based on a specific vocabulary with constraints. We show that regular grammar and deterministic automata are useful for the recognition of QRS complexes. They are used to represent a normalized QRS complex as a sequence of positive and negative peaks based on the regular grammar. This method is applied to the ECG records of the standard MIT-BIH database. Several parameters are determined, such as QRS durations, RR distances, and peak amplitudes. In other words, the ECG is likened to a language where a QRS complex represents a sequence of words.

In the final version of the chapter, the method described above will be implemented to extract QRS complexes. True Positive (TP), False Positive (FP), False Negative (FN), Sensitivity (Se), Positive Predictivity (+P), False Detection Rate (FDR), and FN Rate (FNR) will be computed.

5.1 Signal Preprocessing

Practically, an ECG signal is too noisy and contains many artifacts, hence the need for pretreatment phases to reduce noise and facilitate lexical analysis afterwards. A band pass filter reduces the influence of muscular noise, 60 Hz interference, and T-wave

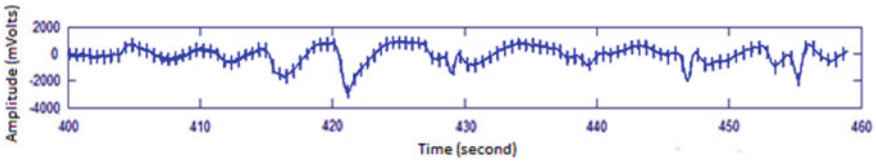

(a) Input ECG

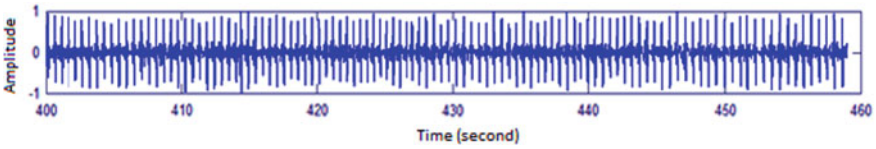

(b) Output ECG

Fig. 4 ECG signal preprocessing: filtering, centering and normalization

interference, and promotes the baseline. The desirable bandwidth for maximizing the QRS energy is about 5–15 Hz [37].

The following mathematical equations describe the different steps of the preprocessing phase: band-pass filtering, centralization, and normalization of the signal amplitude. An example is shown later in Fig. 4 where an ECG signal representing tachycardia is filtered by a band-pass filter, normalized and centered.

S[n] is the signal, and H[n] is the band pass filter where the cut-off frequency is 5–15 Hz. m is the signal length.

$$S1[n] = S[n] * H[n] \tag{8}$$

$$S2[n] = S1[n] - \frac{\sum_{n=1}^{m} S1[n]}{m} \tag{9}$$

$$S2[n] = \frac{S2[n] - Mean(S2[n])}{Max(S2[n] - Mean(S2[n]))} \tag{10}$$

Figure 4 provides an example of a real ECG signal before and after the filtering process. The input signal is derived from a patient who presents with tachycardia. The preprocessing process eliminates the artifacts and centralizes the signal.

5.2 Variation in Standard Deviations of Peaks and Waves

Mathematically, a positive peak or a negative peak must have a standard deviation σ very large compared to that of a wave and greater than a predefined threshold $\sigma 1$ for a very short duration Δ below a predefined threshold $\Delta 1$.

Given the sampling frequency Fs, a peak (positive or negative), a wave or a rest phase, is formed of a series of n normalized amplitudes $a1, a2, \ldots, an$. The calculation of the standard deviation σ and the duration Δ is as follows:

$$\sigma = \sqrt{\sum_{i=1}^{n} \frac{(ai - \sum_{i=1}^{n} \frac{ai}{n})}{n}} \tag{11}$$

$$\Delta = \frac{n}{Fs} \tag{12}$$

Figure 5 illustrates the standard deviation values of the many Q, R and S peaks and the different P and T waves. This figure confirms that the two R and S peaks show very large standard deviations greater than 0.2. Peak Q has standard deviations greater than 0.1, while both P and T waves have very low values of standard deviations below 0.05.

According to Fig. 5, we can designate $\sigma 1 = 0.1$. From this value, we may distinguish between peaks and waves. In fact, a QRS complex is equated with a pair of adjacent peaks that satisfy standard deviation criteria.

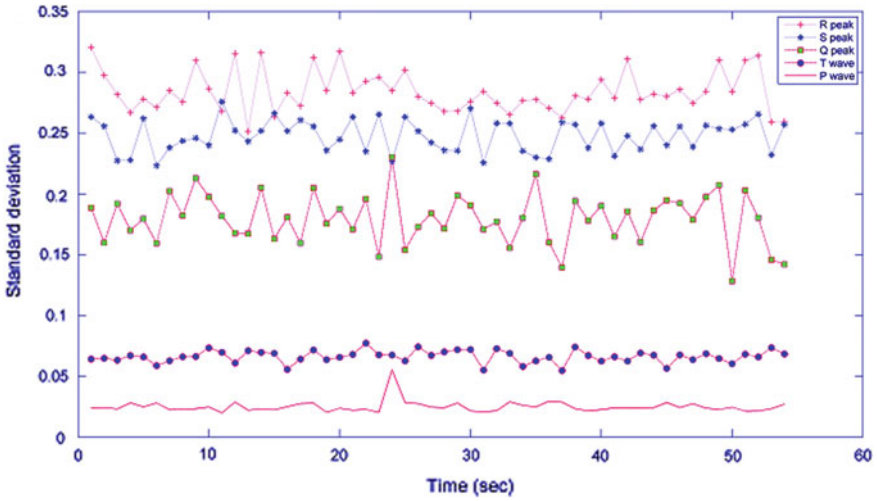

Fig. 5 Variation in standard deviations of peaks and waves

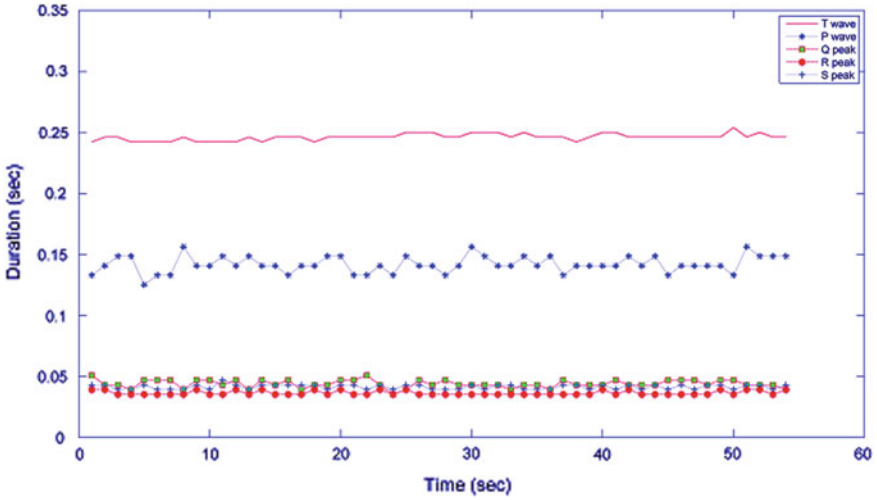

Fig. 6 Variation in duration of peaks and waves

5.3 Variation in Duration of Peaks and Waves

Figure 6 depicts the values of the duration of the numerous Q, R and S peaks and the different P and T waves. This figure confirms that the three Q, R and S peaks indicate very short durations of less than 0.1 s whereas, the two P and T waves have very important value durations that exceed 0.1 s.

According to Fig. 6, we can designate $\Delta 1 = 0.1$ s. From this value, we may distinguish between peaks and waves. In fact, a QRS complex is referred to as a pair of adjacent peaks that satisfy criteria for standard deviations and durations.

5.4 Grammatical Analysis of Signal

A finite deterministic automaton (FDA) consists of a finite set of states (often denoted Q), a finite set Σ of symbols (alphabet), a transition function which takes as argument a state and a symbol and returns a state (often noted δ), a start state often denoted as q0, and a set of final states (often denoted F). Always q0 $\in$ Q and F $\subseteq$ Q.

DFA is a quintuplet (Q, Σ, δ, q0, F), where Σ is an alphabet, Q is a finite set of states, $\delta : Q * \Sigma \rightarrow$ Q is the transition function, q0 is the initial state, and F is a set of final states.

Here, the amplitude of the signal is processed as a sequence of values belonging to the bounded interval $[-1, 1]$. The normalized amplitude is described as a sequence of almost near zeros, as well as negative and positive values. In other words, the signal is likened to a language where a QRS complex represents a sequence of

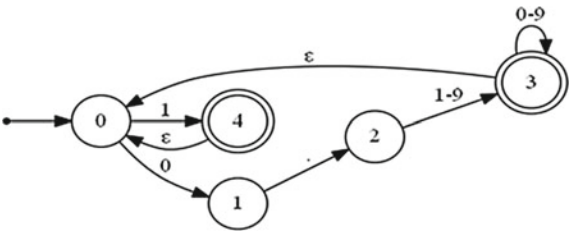

Fig. 7 DFA representing a normalized R peak

words. The Σ alphabet contains all the symbols that can represent the normalized amplitude belonging to the bounded interval $[-1, 1]$. Then regular expressions allow the lexical analysis of the signal. In fact, DFA and regular expressions represent the rest phase, the positive peak, and the negative peak. These form the QRS complex besides the standard deviation constraints.

Grammatically, character 'ϵ' is an empty word having a zero length. Character '*' means 'zero or more times', character '+' means 'one or more times', and '?' means 'zero or one time'. Often, the initial state is marked by an incoming arrow, the states are symbolized by simple circles and the final states are marked by double circles.

The DFA above (Fig. 7) and the following regular expressions describe a normalized R peak:

- The initial state q0 = {0}.
- The finite set of states Q = {0, 1, 2, 3, 4}.
- The set of finite states F = {3, 4}.
- The finite set of symbols $\Sigma = \{0, 1, 2, 3, 4, 5, 6, 7, 8, 9, -, .\}$.
- The transition functions are:
  $\delta(0, 0) = 1$
  $\delta(1, .) = 2$
  $\delta(2, 1-9) = 3$
  $\delta(3, 0-9) = 3$
  $\delta(3, \epsilon) = 0$
  $\delta(0, 1) = 4$
  $\delta(4, \epsilon) = 0$

$$R = \{0.[1-9][0-9] * |1\}+ \tag{13}$$

$$\sigma R > \sigma 1 \tag{14}$$

$$\Delta R < \Delta 1 \tag{15}$$

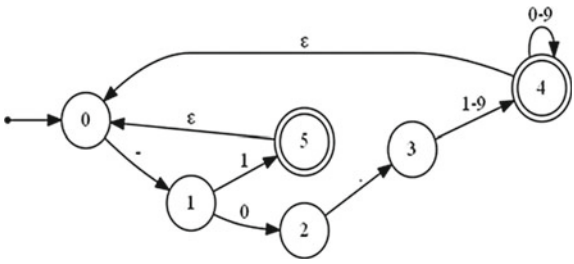

Fig. 8 DFA representing a normalized negative peak (Q or S peak)

DFA (Fig. 8), as well as the regular expressions describing a normalized negative peak, are as follows:

$$Q = \{-0.[1-9][0-9]*|-1\}+ \tag{16}$$

$$\delta Q > \frac{\delta 1}{2} \tag{17}$$

$$\Delta Q < \Delta 1 \tag{18}$$

$$S = \{-0.[1-9][0-9]*|-1.0\}+ \tag{19}$$

$$\delta S > \delta 1 \tag{20}$$

$$\Delta S < \Delta 1 \tag{21}$$

- The initial state q0 = {0}.
- The finite set of states Q = {0, 1, 2, 3, 4, 5}.
- The set of finite states F = {4, 5}.
- The finite set of symbols $\Sigma = \{0, 1, 2, 3, 4, 5, 6, 7, 8, 9, -, .\}$.
- The transition functions are:
  $\delta(0, -) = 1$
  $\delta(1, 0) = 2$
  $\delta(2, .) = 3$
  $\delta(3, 1-9) = 4$
  $\delta(4, 0-9) = 4$
  $\delta(4, \epsilon) = 0$
  $\delta(1, 1) = 5$
  $\delta(5, \epsilon) = 0$

Practically, the Q, R and S peaks are separated possibly by very short rest phases. The following regular expression describes a standard rest phase:

$$rest = \{\{-\}0.0[0-9]*\}+ \tag{22}$$

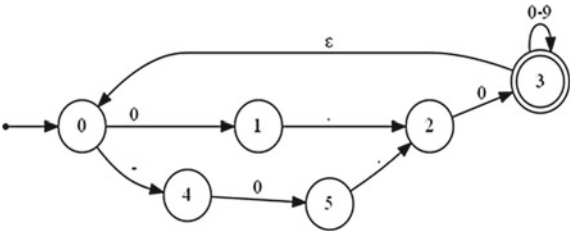

Fig. 9 DFA representing a normalized rest phase

$$\Delta rest < \frac{\Delta 1}{2} \tag{23}$$

The following DFA (Fig. 9) describes a normal rest phase where:

- The initial state q0 = {0}.
- The finite set of states Q = {0, 1, 2, 3, 4, 5}.
- The final state F = {3}.
- The finite set of symbols $\Sigma = \{0, 1, 2, 3, 4, 5, 6, 7, 8, 9, -, .\}$.
- The transition functions are:
  $\delta(0, 0) = 1$
  $\delta(1, .) = 2$
  $\delta(2, 0) = 3$
  $\delta(3, 0 - 9) = 3$
  $\delta(3, \epsilon) = 0$
  $\delta(0, -) = 4$
  $\delta(4, 0) = 5$
  $\delta(5, .) = 2$

Grammatically, the QRS complex is likened to a series of negative and positive peaks that are eventually separated by a very short resting phase. The regular expressions as well as the deterministic automata below (Figs. 10 and 11) assume that Q peaks and rest phases may be absent.

The regular expression below and Fig. 10 describe a whole standardized QRS complex. Q is the first peak down, which is always visible in the field. Peak R is the second one; it has a high amplitude and is directed upwards. Peak S is the last one; it is directed downwards.

$$QRS = \{Q\}?\{rest\}?\{R\}\{rest\}?\{S\} \tag{24}$$

- The initial state q0 = {0}.
- The finite set of states Q = {0, 1, 2, 3, …, 23, 24}.
- The set of finite states F = {23, 24}.
- The finite set of symbols $\Sigma = \{0, 1, 2, 3, 4, 5, 6, 7, 8, 9, -, .\}$.
- The transition functions are:
  $\delta(0, -) = 1$

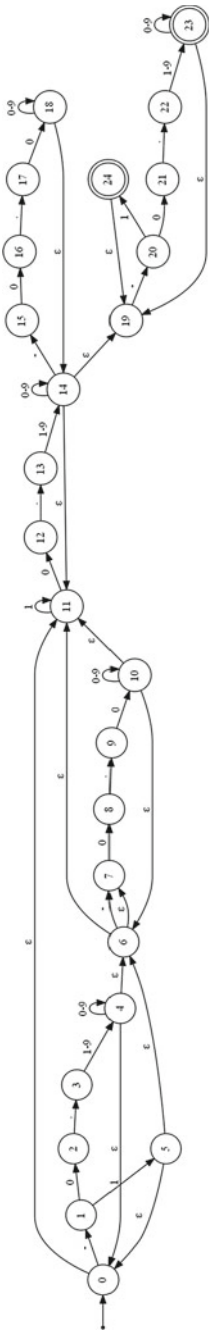

Fig. 10 DFA representing normalized QRS complex

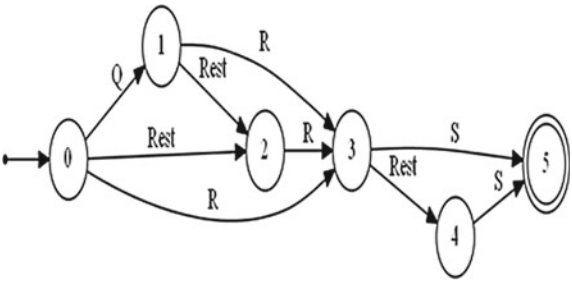

Fig. 11 DFA representing QRS complex

$\delta(1, 0) = 2$
$\delta(2, .) = 3$
$\delta(3, 1 - 9) = 4$
$\delta(4, 0 - 9) = 4$
$\delta(4, \epsilon) = 6$
$\delta(1, 1) = 5$
$\delta(4, \epsilon) = 0$
$\delta(5, \epsilon) = 6$
$\delta(5, \epsilon) = 0$
$\delta(6, \epsilon) = 7$
$\delta(6, -) = 7$
$\delta(6, \epsilon) = 11$
$\delta(7, 0) = 8$
$\delta(8, .) = 9$
$\delta(9, 0) = 10$
$\delta(10, 0 - 9) = 10$
$\delta(10, \epsilon) = 11$
$\delta(10, \epsilon) = 6$
$\delta(11, 1) = 11$
$\delta(11, 0) = 12$
$\delta(12, .) = 13$
$\delta(13, 1 - 9) = 14$
$\delta(14, 0 - 9) = 14$
$\delta(14, \epsilon) = 11$
$\delta(14, -) = 15$
$\delta(15, 0) = 16$
$\delta(16, .) = 17$
$\delta(17, 0) = 18$
$\delta(18, 0 - 9) = 18$
$\delta(18, \epsilon) = 14$
$\delta(14, \epsilon) = 19$
$\delta(19, -) = 20$
$\delta(20, 0) = 21$
$\delta(21, .) = 22$

$\delta(22, 1-9) = 23$
$\delta(23, \epsilon) = 19$
$\delta(23, 0-9) = 23$
$\delta(20, 1) = 24$
$\delta(24, \epsilon) = 19$

To better represent the automaton describing an entire QRS complex in a simpler way, the next automaton (Fig. 11) describes an entire QRS complex where we have modified and minimized the finite set of symbols, the finite set of states and the set of finite states.

- The initial state q0 = {0}.
- The finite set of states Q = {0, 1, 2, 3, 4, 5}.
- The set of finite states F = {5}.
- The finite set of symbols Σ = {Q, R, S, Rest}.
- The transition functions are:
  $\delta(0, Q) = 1$
  $\delta(0, Rest) = 2$
  $\delta(0, R) = 3$
  $\delta(1, R) = 3$
  $\delta(2, R) = 3$
  $\delta(3, Rest) = 4$
  $\delta(4, S) = 5$
  $\delta(3, S) = 5$

5.5 Results

In this section, the method described above is applied to several real ECG signals representing different patients and derived from the standard MIT-BIH arrhythmia database. For all input signals, Q, R and S peaks, RR distances, and QRS complexes are detected. The RR distance is the duration between two successive R peaks. It is the most important indicator of the frequency of the ventricles. In addition, a comparison study with a large number of methods [3, 4, 7, 9, 16, 17, 19, 20, 30, 31, 37, 40, 47, 49] is applied in terms of QRS complex detection.

Table 2 presents an application on several real ECG signals to extract QRS complexes. TP, FP, FN, Se, +P, FDR and FNR are determined, where TP represents the correctly identified QRS, FP represents the incorrectly identified QRS and FN represents the incorrectly rejected QRS.

$$Se\ (\%) = \frac{TP}{TP + FN} * 100 \tag{25}$$

$$+P\ (\%) = \frac{TP}{TP + FP} * 100 \tag{26}$$

Table 2 Application on MIT-BIH standard database. Extraction of QRS complexes and determination of Se and +P rates

Record	Record length	Real number of QRS	TP	FN	FP	Se (%)	+P (%)	FDR (%)	FNR(%)	$\overline{RR}$	$\overline{QRS}$
100	1805	2273	2272	1	0	99.96	100.00	0.00	0.04	0.79	0.05
101	1805	1865	1864	1	0	99.95	100.00	0.00	0.05	0.96	0.06
102	1805	2187	2183	4	2	99.82	99.91	0.09	0.18	0.83	0.14
103	1805	2084	2082	2	2	99.90	99.90	0.10	0.10	0.86	0.05
104	1805	2230	2211	19	24	99.15	98.93	1.07	0.85	0.81	0.04
105	1805	2572	2571	1	0	99.96	100.00	0.00	0.04	0.70	0.07
106	60	67	67	0	0	100.00	100.00	0.00	0.00	0.88	0.06
107	60	70	70	0	2	100.00	97.22	2.78	0.00	0.82	0.12
108	1805	1763	1761	2	0	99.89	100.00	0.00	0.11	1.02	0.09
109	1805	2532	2526	6	2	99.76	99.92	0.08	0.24	0.71	0.09
111	60	69	69	0	0	100.00	100.00	0.00	0.00	0.89	0.05
112	1805	2539	2537	2	6	99.92	99.76	0.24	0.08	0.71	0.06
113	1805	1794	1794	0	1	100.00	99.94	0.06	0.00	1.00	0.05
114	60	54	54	0	0	100.00	100.00	0.00	0.00	1.10	0.03
115	1805	1953	1953	0	0	100.00	100.00	0.00	0.00	0.92	0.05
116	60	78	78	0	0	100.00	100.00	0.00	0.00	0.76	0.06
117	1805	1535	1534	1	1	99.93	99.93	0.07	0.07	1.17	0.06
118	1805	2275	2275	0	12	100.00	99.48	0.52	0.00	0.78	0.07
119	1805	1987	1987	0	0	100.00	100.00	0.00	0.00	0.90	0.07
121	1805	1863	1861	2	3	99.89	99.84	0.16	0.11	0.96	0.08
122	1805	2476	2475	1	2	99.96	99.92	0.08	0.04	0.72	0.07
123	1805	1518	1517	1	4	99.93	99.74	0.26	0.07	1.18	0.06
124	60	49	49	0	0	100.00	100.00	0.00	0.00	1.21	0.07
200	60	87	87	0	0	100.00	100.00	0.00	0.00	0.72	0.09
201	60	90	90	0	0	100.00	100.00	0.00	0.00	0.66	0.06
202	1805	2136	2111	25	0	98.83	100.00	0.00	1.17	0.85	0.07
203	60	97	97	0	0	100.00	100.00	0.00	0.00	0.61	0.08
205	60	89	89	0	0	100.00	100.00	0.00	0.00	0.66	0.05
207	1805	1862	1859	3	0	99.84	100.00	0.00	0.16	0.96	0.07
208	60	87	87	0	0	100.00	100.00	0.00	0.00	0.69	0.07
209	1805	3004	3002	2	7	99.93	99.77	0.23	0.07	0.59	0.05
210	1805	2647	2606	41	9	98.45	99.66	0.34	1.55	0.69	0.07
212	1805	2748	2748	0	5	100.00	99.82	0.18	0.00	0.65	0.06
213	1805	3251	3243	8	2	99.75	99.94	0.06	0.25	0.55	0.06
214	1805	2262	2229	33	0	98.54	100.00	0.00	1.46	0.81	0.07

(continued)

Table 2 (continued)

Record	Record length	Real number of QRS	TP	FN	FP	Se (%)	+P (%)	FDR (%)	FNR(%)	$\overline{RR}$	$\overline{QRS}$
215	1805	3363	3337	26	0	99.23	100.00	0.00	0.77	0.54	0.06
217	1805	2208	2206	2	0	99.91	100.00	0.00	0.09	0.88	0.10
219	1805	2154	2152	2	0	99.91	100.00	0.00	0.09	0.83	0.06
220	1805	2048	2047	1	4	99.95	99.80	0.20	0.05	0.88	0.05
221	1805	2427	2400	27	0	98.89	100.00	0.00	1.11	0.75	0.06
222	60	75	75	0	0	100.00	100.00	0.00	0.00	0.81	0.05
223	60	80	80	0	0	100.00	100.00	0.00	0.00	0.75	0.07
228	60	68	68	0	0	100.00	100.00	0.00	0.00	0.86	0.07
230	1805	2256	2219	37	0	98.36	100.00	0.00	1.64	0.81	0.06
231	60	63	63	0	0	100.00	100.00	0.00	0.00	0.94	0.06
232	1805	1780	1747	33	4	98.15	99.77	0.23	1.85	1.03	0.06
233	60	94	94	0	0	100.00	100.00	0.00	0.00	0.58	0.07
234	1805	2753	2752	1	0	99.96	100.00	0.00	0.04	0.65	0.06
Total	58,720	73,562	73,278	284	92	99.74	99.86	0.14	0.26	0.82	0.07

$$FDR\ (\%) = \frac{FP}{TP + FP} * 100 \tag{27}$$

$$FNR\ (\%) = \frac{FN}{TP + FN} * 100 \tag{28}$$

Table 2 shows an application of the proposed method on different types of ECG signals from the MIT-BIH arrhythmia database to extract the QRS complex. The sampling frequency is 360 Hz, the gain is 200, and the base is 1024 mV.

For an input signal, several parameters are determined, such as the QRS number, the RR distances, the QRS duration, and the standard deviation of RR distances.

Figure 12 shows the Se an +P rates of the proposed method. The mean Se rate is 99.74% and the average rate of +P is 99.86%. The average FDR is 0.14%, and the average FNR is 0.26%.

5.6 Noise Se

Table 3 provides the noise Se, where the method is applied to different ECG recordings. Table 3 shows the sensitivity variation and the positive Signal-to-Noise Ratio (SNR) prediction rates.

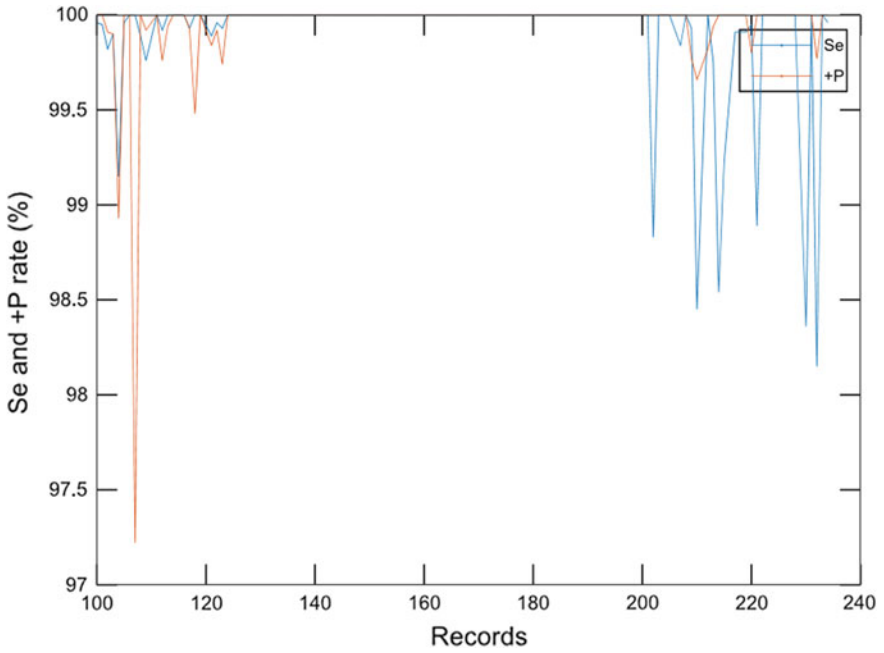

Fig. 12 Se and +P rates according to MIT-BIH records

For SNR values greater than 40dB, the method provides high Se values that exceed 99%. For SNR values above 30 dB, the method gives Se values that exceed 97%. For low SNR values that are less than 24 dB, the Se value decreases by 90%.

Figure 13 illustrates the SNR Se rate variation for different ECG recordings (100, 101, 102, 103, and 105) from the MIT-BIH standard database. For low SNR values below 20 dB, the method provides Se rates that are less than 50%. However, Se becomes increasingly important when the SNR values are greater than 30 dB. For SNR values that are greater than 30 dB, the method gives Se rates that exceed 97%. If the SNR is greater than 40 dB, the method provides high Se values that exceed 99%.

5.7 R Peak Accuracy Detection

In this part, we determine the exact time of the first two R peaks present in records 100–110. Next, we compare the exact time of each peak R to that automatically detected, and we calculate the RR distance. Thus, we can determine the value of accuracy for each peak. From the values presented in Table 4, the precision values are very small and vary from 0.000 to 0.010 s. As an average, the accuracy value is 0.002 s for R peak detection and 0.003 for RR distance calculation.

Table 3 Noise Se study of proposed method. Application on ECG signals with different SNR values

Record	SNR (dB)	90	70	50	30	25	24	23	22	21	20
100	Se (%)	99.96	99.96	99.96	99.96	93.27	90.32	85.97	79.94	63.57	55.52
	+P (%)	100.0	100.0	100.0	99.91	83.73	80.29	76.99	72.80	62.72	57.52
101	Se (%)	99.95	99.95	99.95	99.79	95.28	86.27	84.13	81.88	87.56	48.04
	+P (%)	100.0	100.0	100.0	99.95	84.86	69.44	66.65	65.37	69.05	39.54
102	Se (%)	99.82	99.82	99.82	91.13	83.36	79.84	74.67	66.03	57.80	43.80
	+P (%)	99.91	99.91	99.91	88.90	83.51	75.52	68.84	58.87	51.34	40.47
103	Se (%)	99.90	99.90	99.90	99.86	97.46	95.30	88.58	83.25	70.59	54.89
	+P (%)	99.90	99.90	99.90	99.90	95.85	92.07	81.75	74.95	60.46	45.52
105	Se (%)	99.96	99.96	99.96	97.51	93.58	90.90	81.22	73.21	73.13	53.30
	+P (%)	100.0	100.0	100.0	99.09	95.90	92.56	79.61	73.15	73.04	61.01
Total	Se (%)	99.92	99.92	99.92	97.65	92.59	88.53	82.91	76.86	70.53	51.11
	+P (%)	99.97	99.97	99.97	97.95	88.12	79.89	73.42	68.42	64.28	47.27

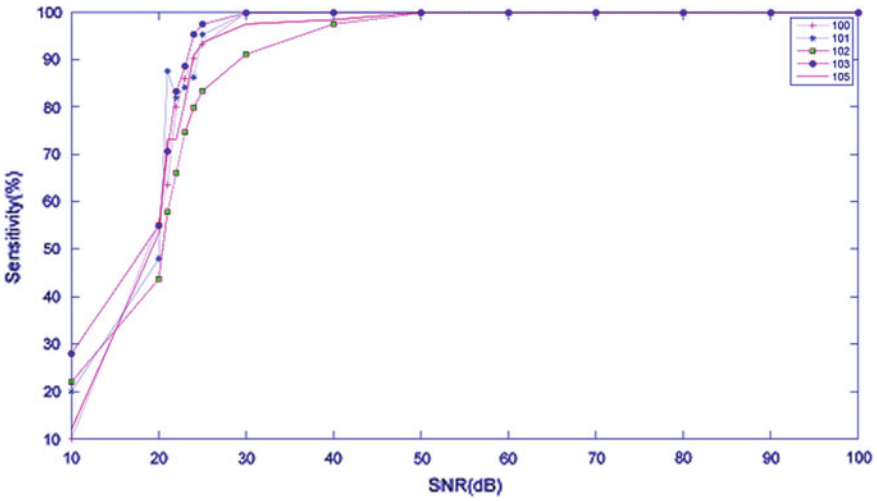

Fig. 13 Variation in Se rate according to SNR. Application on records 100, 101, 102, 103 and 105

Table 4 Precision of proposed method for R peaks detection and calculating RR distance

ECG	R peak order	Exact time of R peak (s)	Detected time of R peak (s)	Precision (s)	Exact distance of RR (s)	Detected RR distance (s)	Precision (s)
100	1	0.171	0.172	0.001	–	–	–
	2	0.985	0.986	0.001	0.814	0.814	0.000
101	1	0.189	0.186	0.003	–	–	–
	2	1.060	1.050	0.010	0.871	0.864	0.007
102	1	0.269	0.269	0.000	–	–	–
	2	1.090	1.088	0.002	0.821	0.819	0.002
103	1	0.693	0.694	0.001	–	–	–
	2	1.56	1.555	0.005	0.867	0.861	0.006
105	1	0.502	0.502	0.000	–	–	–
	2	1.230	1.230	0.000	0.728	0.728	0.000
106	1	0.933	0.933	0.000	–	–	–
	2	1.970	1.972	0.002	1.037	1.039	0.002
107	1	0.712	0.708	0.004	–	–	–
	2	1.530	1.533	0.003	0.818	0.825	0.007
108	1	0.140	0.141	0.001	–	–	–
	2	0.978	0.977	0.001	0.838	0.836	0.002
109	1	0.261	0.261	0.000	–	–	–
	2	0.906	0.905	0.001	0.645	0.644	0.001
110	1	0.507	0.507	0.000	–	–	–
	2	1.320	1.317	0.003	0.813	0.810	0.003
AVG precision rate	–	0.002	–	–	–	–	0.003

5.8 Performance Comparison

In order to compare the QRS complex detection algorithm with other algorithms in the literature, the quality of performance detection is compared with several algorithms tested and validated on the MIT-BIH database. These algorithms are varied, and each of them is based on an appropriate technique.

Table 5 shows a comparative study with a large number of methods applied to the same MIT-BIH database in terms of sensitivity rates. Based on the results presented in Table 5, all QRS complex detection algorithms have good detection rates with Se exceeding 99%. Similarly, the proposed method provides satisfactory and competitive results with Se (99.74%) and can be considered as a powerful tool for detecting the QRS complex in ECG signals.

Table 5 Comparison of performances of several QRS detection algorithms cited in the literature

Method	Description	Sensitivity (%)
[37]	A derivative approach based on filtering and slope analysis	99.30
[20]	A derivative approach based on filtering and optimized decision rule process technique based on recursive temporal prediction	99.46
[30]	Neural network based on adaptive filtering	99.00
[47]	An approach based on mathematical morphology	99.50
[49]	Support Vector Machine (SVM) based approach	99.38
[16]	A mathematical model based on continuous wavelet transform	99.91
[17]	Transformation based on duration and energy	99.26
[9]	Use of adaptive thresholding	99.65
[7]	Multi decomposition in wavelet packet	99.14
[31]	SVM-based approach	99.75
[4]	Approach based on discrete wavelet decomposition and energy calculation	99.39
[19]	Empirical modal decomposition	99.92
[40]	Use of Euclidean metric distance with K-nearest neighbor algorithm (KNN)	99.81
[44]	Regular grammar-based approach and calculation of standard deviations	99.74

6 Conclusion

This chapter has delivered an overview of ECG signal processing techniques, QRS complex detection approaches, and waveform delineation based on syntactic methods. We have mentioned related context-free and regular grammar. We have deliberately relied on regular grammar, which has shown better results in improving the accuracy rate. Deterministic automata have proved useful for the recognition of QRS complexes. ECG signals have been observed as structured sections with a hierarchical order and proved that their representation is still more flexible. A comparison study with a huge number of statistic methods has been established as regards the accuracy rates.

In this chapter, regular grammar and deterministic automata have been found to be useful for the recognition of QRS complexes and cardiac cycles and the interpretation of ECG signals. An ECG is referred to as a pair of adjacent waves and peaks that meet certain criteria for standard deviations and durations.

Context-free grammar has proven to be useful for the recognition of normal ECG signals. The results of the experiments have shown that the application of our approach to several parts of a real ECG signal allows us to calculate the durations of QRS complexes and the RR distances. Furthermore, a comparative study with the literature methods has been established in terms of Se rate.

However, type 2 grammatical formalism has been applied only to normal ECGs. Context-free grammar is unable to describe any ECG signals. The use of context-free grammar was insufficient due to the varieties of ECG signals and the different types of wave morphologies.

Indeed, type 3 grammar and deterministic automata have proved useful for the recognition of peaks and QRS complexes and different morphologies of cardiac cycles. These have been described using deterministic automata and regular expressions. For an input signal, all the indicators have been deduced, such as QRS durations and RR distances. This work is intended to help with medical diagnosis and clinical decision support.

Compared to statistical methods, the use of grammar provides more flexibility in applications. Grammatical rigor has been extended to include other areas of application such as signal and medical imaging. The main advantage of these methods is the representation that it can provide. Syntactic approaches can powerfully represent object structures and therefore can easily retrieve information. Finally, the grammatical formalism has proved its effectiveness for the processing and interpretation of 1D and 2D medical data. This type of work is aimed at helping with a medical diagnosis. Although the concise representation and the space economy provided by the syntactic representation, it is important to highlight some limitations. The processing cost can be high. As observed in this chapter, there are a dozen methods, several objectives, and different types of possible representations.

Another limitation perceived in most use of the grammars. More complex morphologies often require greater representation power and, therefore, higher time complexity recognition. Especially, when the method needs a training phase, the processing can request additional high computational time, depending on the morphology to be represented and the type of grammar to be used.

Other very important restrictions can be observed concerning the high dependence to preprocessing steps. Some of the mentioned articles in this chapter discussed this level and used techniques to smooth noises, to enhance structures, and to segment signals. It is very important to note that failures in this preprocessing step can lead to failure in the use of grammars.

In future work, two fundamental and applicative perspectives will be dealt with. Fundamentally, we can improve the preprocessing part and the accuracy rate. Besides, we can propose other grammatical rules to represent distinct pathological cases. At the application level, we can broaden the base of ECG signals and treat other pathological cases such as those of the standard American Heart Association (AHA). We will be able to extend our validation bases, carry out a preliminary preprocessing, measure other indicators, and compare the method to those of references.

References

1. Alex, W., Vikram, K.: Signal interpretation of multifunction radars: modeling and statistical signal processing with stochastic context free grammar. IEEE Trans. Signal Process. **56**(3), 1106–1119 (2008)
2. Aytemir, K., Maarouf, N., Gallagher, M.M., Yap, Y.G., Waktare, J.E.P., Malik, M.: Comparison of formula for heart rate correction of QT interval in exercise electrocardiograms. Pacing Clin. Electrophysiol. **22**(9), 1397–1401 (1999)
3. Benali R., Dib N., Reguig B.F.: Cardiac arrhythmia diagnosis using a neuro-fuzzy approach. J. Mech. Med. Biol. **10**(3), 417–429 (2010)
4. Benali, R., Reguig, B.F., Hadj Slimane, Z.: Automatic classification of heartbeats using wavelet neural network. J. Med. Syst. **36**(2), 883–892 (2012)
5. Chalabi Z., Boudjzmaoui A., Saadia L., Berrached N.: Détection et Classification Automatiques d'arythmies Cardiaques, 5th Sciences of Electronic, Technologies of Information and Telecommunications (2009)
6. Chen, S.W., Chen, C.H., Chan, H.L.: A real-time QRS detection method based on moving-averaging incorporating with wavelet denoising. Comput. Methods Programs Biomed. **82**(3), 187–195 (2006)
7. Chouhan S., Mehta S.S.: Total removal of baseline drift from ECG signal. In: International Conference on Computer: Theory and Application (2007)
8. Christensen, H.I., Matas, J., Kittler, J.: Using grammars for scene interpretation. IEEE Trans. Image Process. **3**(1), 793–796 (1996)
9. Christov, I., Herrero, G.G., Krasteva, V., Jekova, I., Gotchev, A., Egiazarian, K.: Comparative study of morphological and time frequency ECG descriptors for heartbeat classification. Med. Eng. Phys. **28**(9), 876–887 (2006)
10. Chuang, K.S., Tzeng, H.L., Wu, J., Chen, S., Chen, T.J.: Fuzzy c-means clustering with spatial information for image segmentation. Comput. Med. Imaging Graph. **30**(1), 9–15 (2006)
11. Eiichi, T.: Theoretical aspects of syntactic pattern recognition. Pattern Recognit. **28**(7), 1053–1061 (1995)
12. Flasinski, M., Jureket, J., Myslinski, S.: Parallel computing scheme for graph grammar-based syntactic pattern recognition. Parallel Process. Appl. Math. **8**, 156–165 (2010)
13. Flasinsk, P.: Syntactic pattern recognition of ECG for diagnostic justification. Mach. Graph. Vis. **24**, 43–55 (2014)
14. Fraden, J., Neumann, M.R.: QRS wave detection. Med. Biol. Eng. Comput. **18**(2), 125–132 (1980)
15. Gao, J., Ding, X., Zheng, J.: Image Pattern Recognition Based on Examples—A Combined Statistical and Structural-Syntactic Approach. Lecture Notes in Computer Science, vol. 1876, pp. 57–66 (2000)
16. Ghaffari, A., Golbayani, H., Ghasemi, M.: A new mathematical based QRS detector using continuous wavelet transform. Comput. Electr. Eng. **34**(2), 81–91 (2008)
17. Gritzali, F.: Towards a generalized scheme for QRS detection in ECG waveforms. Signal Process **15**(2), 183–192 (1998)
18. Guowei, W., Andrei, S.: Grammar-based 3D facade segmentation and reconstruction. Comput. Graph. **36**(4), 216–223 (2012)
19. Hadj, S.Z., Nait, A.A.: QRS complex detection using empirical mode decomposition. Elsevier J. Digit. Signal Process. **20**(4), 1221–1228 (2010)
20. Hamilton, P.S., Tompkin, W.J.: Quantitative investigation of QRS detection rules using MIT/BIH Arrhythmia database. IEEE Trans. Biomed. Eng. **33**(12), 1157–1165 (1986)
21. Hampton, J.R.: L'ECG Facile, 6th edn. EDISEM, Maloine (2004)
22. Hanieh, L.M., Fardin, A.M., Abdolhossein, F.: A novel grammar-based approach to atrial fibrillation arrhythmia detection for pervasive healthcare environments. J. Comput. Secur. **2**(2), 155–163 (2015)

23. Heras, L., Gemma, S.: And-Or graph grammar for architectural floor plan representation, learning and recognition. In: A Semantic, Structural and Hierarchical Model. Lecture Notes in Computer Science, vol. 6669, pp. 17–24 (2011)
24. Holsinger, W.P., Kempner, K.M., Miller, M.H.: A QRS preprocessor based on digital differentiation. IEEE Trans. Biomed. Eng. **18**(3), 212–217 (1971)
25. Kasemsumran, P., Auephanwiriyakul, S., Theera-Umpon, N.: Face recognition using string grammar nearest neighbor technique. J. Image Graph. **3**(1), 6–10 (2015)
26. Khandoker, A.H., Palaniswami, M., Karmakar, C.K.: Support vector machines for automated recognition of obstructive sleep apnea syndrome from ECG recordings. IEEE Trans. Inf. Technol. Biomed. **13**(1), 37–48 (2009)
27. Kieffer, J.C., Yang, E.H.: Grammar based codes: a new class of universal lossless source codes. IEEE Trans. Inf. Theory **46**(3), 737–754 (1999)
28. Kieffer, J.C., Yang, E.H.: Efficient universal lossless data compression algorithms based on a greedy sequential grammar transform. IEEE Trans. Inf. Theory **49**(11), 2874–2894 (2003)
29. Kkai, G., Csirik, J., Gyimthy, T.: Learning the Syntax and Semantic Rules of an ECG Grammar. Lecture Notes in Computer Science, vol. 1321, pp. 171–182 (1997)
30. Kyrkos, A., Giakoumakis, E.A., Carayannis, G.: QRS detection through time recursive prediction technique. Signal Process. **15**(4), 429–436 (1988)
31. Mehta, S.S., Lingayat, N.S.: Development of SVM based classification techniques for the delineation of wave components in 12-lead electrocardiogram. Biomed. Signal Process. Control **3**(4), 341–349 (2008)
32. Mojsilovic, A.: Matching and retrieval based on vocabulary and grammar of color patterns. IEEE Trans. Image Process. **9**(1), 38–54 (2000)
33. Moody, G.B., Mark, R.G.: The impact of the MIT-BIH arrhythmia database. IEEE Eng. Med. Biol. Mag. **20**(3), 45–50 (2001)
34. Nikita, V., Vikram, K., Alex, W., Simon, H.: Syntactic modeling and signal processing of multifunction radars: a stochastic context-free grammar approach. Proc. IEEE **95**(5), 1000–1025 (2007)
35. Ogiela, L., Tadeusiewicz, R., Ogiela, M.R.: Cognitive modeling in medical pattern semantic understanding. In: 8th International Conference on Multimedia and Ubiquitous Engineering, pp. 15–18 (2008)
36. Ogiela, L., Ogiela, M.R., Tadeusiewicz, R.: Mathematical linguistics in cognitive medical image interpretation systems. J. Math. Imaging Vis. **34**(3), 328–340 (2009)
37. Pan, J., Tompkins, W.J.: A real-time QRS detection algorithm. IEEE Trans. Biomed. Eng. **32**(3), 230–236 (1985)
38. Pedro, R.W.D., Nunes, F.L.S., Lima, A.M.: Using grammars for pattern recognition in images: a systematic review. ACM Comput. Surv. **46**(2), 1–34 (2013)
39. Petersohn, C.: Temporal video structuring for preservation and annotation of video content. In: IEEE International Conference on Image Processing, vol. 16, pp. 93–96 (2009)
40. Saini, I., Singhb, D., Khoslaa, A.: QRS detection using K-Nearest Neighbor algorithm (KNN) and evaluation on standard ECG databases. J. Adv. Res. **4**(4), 331–344 (2012)
41. Salah, H., Asma, B.A., Mohamed, H.B.: Grammar-based image segmentation and automatic area estimation. In: 16th IEEE Mediterranean Electro-technical Conference, pp. 356–359 (2012)
42. Salah, H., Asma, B.A., Mohamed, H.B.: Grammar formalism for ECG signal interpretation and classification. Appl. Med. Inform. **35**(4), 21–26 (2015)
43. Salah, H., Asma, B.A., Mohamed, H.B.: Real time QRS complex detection using DFA and regular grammar. BioMed. Eng. Online **16**(31), 1–20 (2017)
44. Salah, H., Asma, B.A., Mohamed, H.B.: A robust QRS complex detection using regular grammar and deterministic automata. Biomed. Signal Process. Control **40**, 263–274 (2018)
45. Su, L., Zhao, G.: De-noising of ECG signal using translation-invariant wavelet de-noising method with improved thresholding. IEEE Eng. Med. Biol. **6**(1), 5946–5949 (2005)
46. Sumathi, S., Sanavullah, M.Y.: Comparative study of QRS complex detection in ECG based on discrete wavelet. Int. J. Recent Trends Eng. **2**(5), 273–277 (2009)

47. Szu, H.: Neural network adaptive wavelets for signal representation and classification. Opt. Eng. **31**(9), 1907–1916 (1992)
48. Teboul, O., Simon, L., Koutsourakis, P., Paragios, N.: Segmentation of building facades using procedural shape priors. In: 23rd IEEE Computer Society Conference on Computer Vision and Pattern Recognition, pp. 3105–3112 (2010)
49. Trahanias, P.: An approach to QRS-complex detection using mathematical morphology. IEEE Trans. Biomed. Eng. **40**(2), 201–205 (1993)
50. Trahanias, P., Skordalakis, E.: Syntactic pattern recognition of the ECG. IEEE Trans. Pattern Anal. Mach. Intell. **12**(7), 648–657 (1990)
51. Trzupek, M., Ogiela, M.R., Tadeusiewicz, R.: Image Content Analysis for Cardiac 3D Visualizations. Lecture Notes in Computer Science, vol. 5711, pp. 192–199 (2009)
52. Trzupek, M., Ogiela, M.R., Tadeusiewicz, R.: Intelligent Image Content Description and Analysis for 3D Visualizations of Coronary Vessels. Lecture Notes in Computer Science, vol. 6592, pp. 193–202 (2011)
53. Wang, W., Pollak, I., Bouman, C.A., Harper, M.P.: Classification of images using spatial random trees. In: IEEE Workshop on Statistical Signal Processing, vol. 13, pp. 449–452 (2005)
54. Wang, W., Pollak, I., Wong, T.S., Bouman, C.A., Harper, M.P., Siskind, J.M.: Hierarchical stochastic image grammars for classification and segmentation. IEEE Trans. Image Process. **15**(10), 3033–3052 (2006)

Extraction of ECG Significant Features for Remote CVD Monitoring

V. Naresh and Amit Acharyya

Abstract Remote healthcare monitoring for Cardiovascular Diseases (CVD) in the present lifestyle is of the utmost importance throughout the world because of high mortality rate, around 30% of deaths all over the world are due to the CVD as per the World Health Organization (WHO) statistics. With the advancement of medical industry and huge growth in IoT technology is gradually making the remote CVD monitoring a reality. During the real-time Electrocardiography (ECG) acquisition, proper detection of individual ECG beats, and the extraction of essential features from each ECG beat is crucial to automate the diagnosis process of CVD remotely. Therefore, it is necessary to explore various techniques for the detection of CVD and the complexity involved in it. This chapter does the review and covers various methods to process the ECG signal and focuses on the low complexity algorithms to extract the significant clinical features of ECG.

Keywords ECG · Boundary detection · Feature extraction · Discrete wavelet transform · Fragmented QRS · Cardiovascular diseases

1 Introduction

Electrocardiogram (ECG) is an interpretation of the electrical activity of the heart over a certain period, which can be acquired by placing the electrodes on the chest and limbs. It is an effective means of knowing the functional aspects of cardiovascular system, ECG is the graphical representation of direction and magnitude of the electrical activity of the heart which leads to the diagnosis of various Cardiovascular Diseases (CVD) [1]. ECG is comprised of different characteristic waves (P, Q, R, S,

V. Naresh · A. Acharyya (✉)
Department of Electrical Engineering, IIT Hyderabad, Kandi, Sangareddy 502285, Telangana, India
e-mail: amit_acharyya@iith.ac.in

V. Naresh
e-mail: ee14resch01003@iith.ac.in

G. Naik (ed.), *Biomedical Signal Processing*, Series in BioEngineering,
https://doi.org/10.1007/978-981-13-9097-5_15

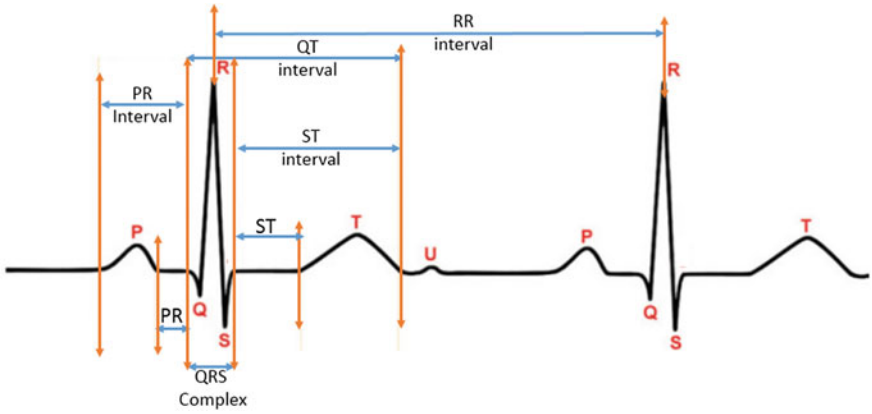

Fig. 1 Standard ECG wave with its characteristic points and intervals

T) represents the depolarization and repolarization of the atria and ventricles of the heart [2, 3] as shown in Fig. 1.

Among the various non-communicable diseases, CVD has become one of the prominent reasons behind the agony of a large section of people all over the world, resulting in millions of deaths every year throughout the globe [4]. There is an abrupt increment in the human mortality rate due to CVD; the reasons could be due to the delayed diagnosis or lack of proper distribution of health care facilities in the vicinity. Thus, there is a tremendous necessity of developing a personalized CVD monitoring device powered by battery backup and with a very low form factor to achieve unobtrusiveness that works under the emerging Internet of Things (IoT) system setup [5–8]. The device should be affordable and also should be reliable enough to extract the essential features from the continuous ECG signal in a low complex fashion. To achieve this, many challenges [9] imposed on such devices development viz., low power consuming system design [6, 7], the complexity of analog front end circuit design [10–12] and the processing algorithms [13–17] should remain at a minimum level to prolong the battery life. As a part of processing, the acquired continuous ECG data from the sensor need to be filtered and segregate into individual beats for further analysis, reliable and accurate evaluation of ECG takes place by observing the morphological features (including, amplitude, duration, polarity, and shape) of characteristic waves such as P-wave, QRS-complex, T-wave, and the interval features between the characteristic waves. [17]. During the acquisition in the real-time, ECG signals are often corrupted with different types of noises such as baseline wandering (electrode contact noise and motion artifacts), Power Line Interference (PLI), Electromyogram (EMG) noise, and instrumentation noise which leads to the change of original signal morphology [18–22]. Therefore, automatic assessment of ECG signal is highly demanded in reducing false CVD detection due to the presence of an unacceptable level of noises. ECG signal consists of very low-frequency components of about 0.5–100 Hz, digital filters [23–25], are very effective for noise removal of

such low-frequency signals. Methods of noise filtering have a decisive influence on the performance of all ECG signal processing systems. Tremendous and elaborative research regarding the processing of ECG is done by various researchers, Empirical mode decomposition [26], Pan-Tompkins based method for estimating the wave boundaries [27], wavelets based boundaries extraction [5], hidden Markov models proposed in [28], spline representation [29], and template methods [30]. Approaches like time-domain feature termed as randomly selected signal pair difference (RSSPD) [31], wavelet-based multi-scale derivative estimators [32, 33], feature extractions using the steep slope of characteristic waves [34], time domain morphology and gradient based methodology for the ECG feature extraction [17] have been used for the detection of individual ECG beats and extraction of essential features from ECG to detect the CVD. However, the major drawback of these methods is that they are computationally intensive while implementing the whole system for the remote CVD monitoring which contains feature extraction, compression, and other classification techniques along with a communication module. Thus, optimization and robustness of algorithms play a significant role when modeling the portable remote CVD monitoring system. Therefore, this chapter covers processing algorithms for the application of ECG, which are low-complex by sharing the resources between the algorithms and efficient enough to extract the essential features of ECG to detect the CVD. By exploring the advantages of both Discrete Wavelet Transform (DWT) and Time Domain Morphology (TDM) analysis [5, 13, 35], this book chapter covers three topics and provides an insight into the computation of each topic. Firstly, the Boundary Detection (BD) followed by Feature Extraction (FE) and the Fragmented QRS (f-QRS) complex.

2 Application of DWT for CVD Monitoring

An ECG signal is susceptible to noise and a high degree of variability can be observed in the signal due to various physiological conditions. Various ECG denoising methods have been presented based on the moving average and median filters [36], frequency-selective filters, adaptive filters, Discrete Cosine Transform (DCT) [37], nonlinear Bayesian filter, mathematical morphological operators, independent component analysis (ICA) [38]. Several transformation techniques like Short Time Fourier Transform (STFT) [39] and Discrete Time Fourier transform (DTFT) [40] were used, but they were restricted due to the limitation of signal analysis either in time or frequency domain. Fourier transform provides the information of spectral components existing in the signal but does not provide the information regarding the occurrence of the components at the specific time intervals. The alternative approach is based on the DWT, which interprets the signal in time-scale domain that represents the timescale of the input signal and also its corresponding frequency at that instant. Because of time-scale analysis, DWT can separate the noise and artifacts at its different resolution levels [41]. Due to the periodic occurrence of ECG waves with different frequency components, DWT will be a helpful tool for the analysis. DWT has been

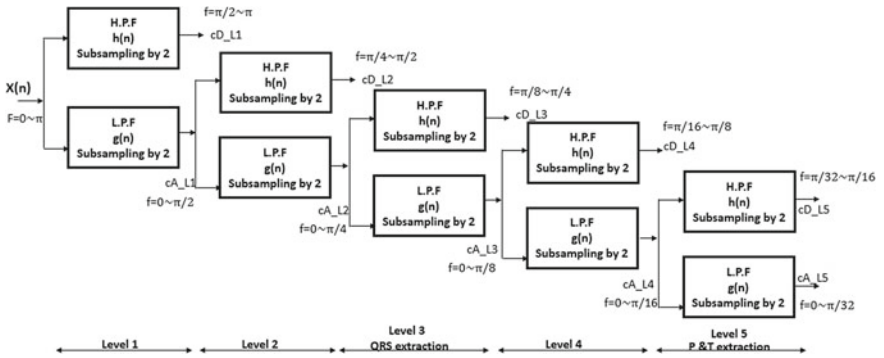

Fig. 2 DWT flow diagram (H.P.F: High Pass Filter h(n), L.P.F: Low Pass Filter g(n), filter co-efficient cD_Lx represents Detailed coefficients of level 'x', similarly cA_Lx: Approximation coefficients of level 'x')

used in the past for several applications including ECG where the basis function used is quadratic spine wavelet [33], which is computationally intensive.

Discrete wavelet transform decomposes the discrete time signals by passing through a series of high pass and low pass filters; the filtering operation changes the resolution of the signal, which reflects the degree of information contained in the signal, also changing the scale by the down sampling operation [42]. Decomposition process halves the time resolution of the signal since half the number of samples of the original signal characterizes the present signal, and on the other hand it doubles the frequency resolution since the frequency band represents half of the original frequency band. This procedure is performed several times, i.e. decomposing the original signal at various levels as shown in Fig. 2. The original signal X(n) is decomposed by passing through a series of high pass and low pass filters and subsampled by two at each level, the frequency at each level is represented in radians since it is a discrete signal. The output of the high pass filter has half the time resolution but doubles the frequency resolution as compared to the original signal at each level.

The output of the high pass filter is known as detailed coefficients, and the output of the low pass filter is known as the approximation co-efficient, which is passed onto the successive levels for further decomposition. This procedure eliminates the less prominent frequency bands from the original signal having low amplitudes thus, in effect, aiding in data compression. This technique is suitable for filtering out the unwanted components like noise and artifacts from the original ECG signal and thus helps in getting a clean ECG signal. The selection of the type of the wavelet to be implemented is of utmost importance as it determines the accuracy of ECG feature extraction and complexity since the output of low pass or a high pass filter is basically a convolution of the incoming signal with the corresponding filter co-efficient. In this chapter, HAAR wavelet transform is taken for the analysis of ECG signal, because it involves minimal filter coefficients and is computationally efficient and thus makes it more suitable for the purpose of being implemented compared to other conventional

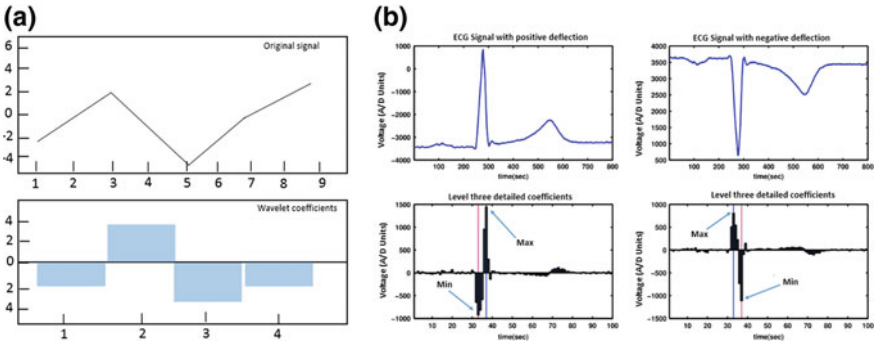

Fig. 3 (Case **a**) Observation of DWT coefficients on the occurrence of discontinuities, (Case **b**) level three detailed coefficients pattern w.r.t the ECG wave deflections

wavelet transform like quadratic spline wavelets. The equations of the high pass (h(n)) and low pass (g(n)) [43] shown in Eqs. (1) and (2) are used to compute the detailed and approximate coefficients for a generalized signal.

$$h(n) = \frac{1}{\sqrt{2}}\left(\sum_{n=0}^{n/2}(X_i[2n+1] - X_i[2n+2])\right) \tag{1}$$

$$g(n) = \frac{1}{\sqrt{2}}\left(\sum_{n=0}^{n/2}(X_i[2n+1] + X_i[2n+2])\right) \tag{2}$$

The morphology of the ECG samples remains unchanged even if the multiplication the factor is removed from the equation; hence $1/\sqrt{2}$ in the equation can be eliminated during the processing of the ECG signal to reduce the complexity of the algorithm. The detailed coefficients of DWT filter banks will follow a particular manner whenever there is any discontinuity in the original signal, maximum or minimum peaks or any changes like notches in the signal can be easily detected by the zero crossing of the wavelet coefficients as shown in Fig. 3a, it can be noticed that the increasing part of the original signal results in negative wavelet coefficients, and the decreasing slope gives the positive wavelet coefficients, the amplitude of the coefficients depends on the slope value of the signal at that index. This analysis is helpful to find the positive deflections and negative deflections of the ECG wave w.r.t the isoelectric line and also helps to detect the local maximum and minimum in the QRS complex to find the discontinuities. For the positive deflection of the ECG wave, minimum followed by maximum coefficients are observed in the third level detailed coefficients and vice versa for the negative deflection, as shown in Fig. 3b. DWT acts as a basic building block that will be shared by BD, FE and f-QRS modules as shown in Fig. 4 to reduce the complexity of the system and maintain the accuracy level of classification.

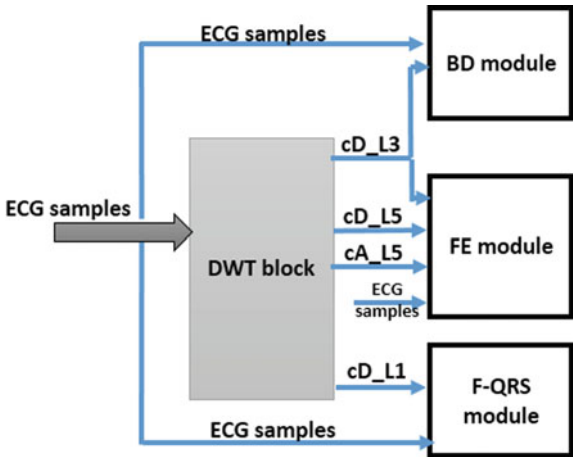

Fig. 4 DWT block shared by ECG processing blocks. *(cD_Lx, cA_Lx represents level 'x' detailed and approximation coefficients respectively)

3 Boundary Detection

After placing the electrodes on the body, the ECG device start sensing from any point within P, Q, R, S, T. Since the starting point is unknown, and the real challenge exists in segregating each ECG beat accurately from the continuous waveform and feed them to other processing blocks as shown in Fig. 5. Three steps are involved in detecting the boundaries of each beat from the continuous ECG wave, firstly minimum and maximum estimation of coefficients in the level three detailed coefficients, secondly R-peak estimation and boundary calculation is the final step of BD block.

3.1 Maximum and Minimum Calculation of Detailed Coefficients

To achieve the accurate boundaries from the continuous ECG wave, the analysis has to be done on the third level detailed coefficients, where the noise components are

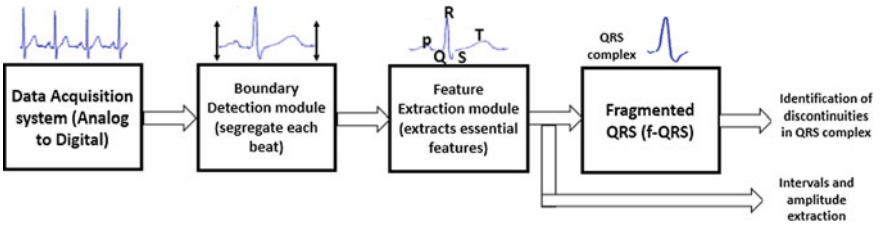

Fig. 5 Block level diagram of the processing steps

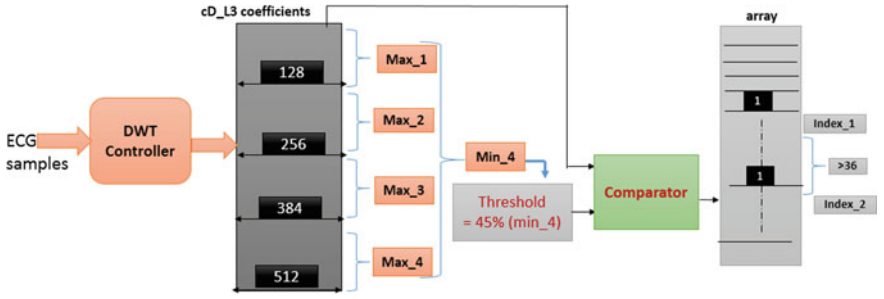

Fig. 6 Block level representation of BD flow

suppressed in the first two levels of DWT, and the noise-free representation starts from the third level. To begin the discussion of BD, consider 'X' number of ECG samples are applied as an input to the DWT, with the effect of down sampling, every stage of filter gives $X/2^L$ number of coefficients as the output. 'L' represents the resolution level of the DWT performed, the number of coefficients obtained at the third level are $X/2^3$. Since the analysis should be performed on the third level, we concentrate on the third level detailed coefficients. To obtain boundaries, level three coefficients are divided into 'k' number of sub frames, where k = X/1024(sampling rate), each frame holds $X/(2^L \times k)$ a number of coefficients. If X = 4096 ECG samples, then the number of sub frames would be '4', and each sub frame has 128 number of level three detailed coefficients, as shown in Fig. 6. Algorithm 1 shows the pseudo code for extracting the boundaries of the ECG wave, detecting the boundary of ECG beats depends on the R-peak index location, which in turn depends on the minimum and maximum index locations of level three detailed coefficients. For a better understanding of the BD module, it would be good to consider the fixed number of input ECG samples and explain the flow. Considering the number of input ECG samples X = 4096 applied to DWT module as shown in Fig. 6, the number of detailed coefficients obtained at third (cD_L3) and fifth (cD_L5) level of DWT are 512 and 128 respectively. cD_L3 coefficients are used to extract the R-peak indexes and cD_L5 are used to extract the P and T waves respectively. Split the cD_L3 into four sub frames as shown in Fig. 6 and refer line number 6 of Algorithm 1. The index of minimum and maximum value in each sub frame corresponds to R-peak of each ECG beat as shown in Fig. 7b, hence the exact R-peak indexes of all the beats can be found if the minimum and maximum index values of the cD_L3 coefficients in each sub frame are known. Hence, further analysis has to be done to find the index of maximum and minimum value in each sub frame, to find the indexes take the minimum value (min_of_max) from all the maximums as described in line number 6 of Algorithm 1.

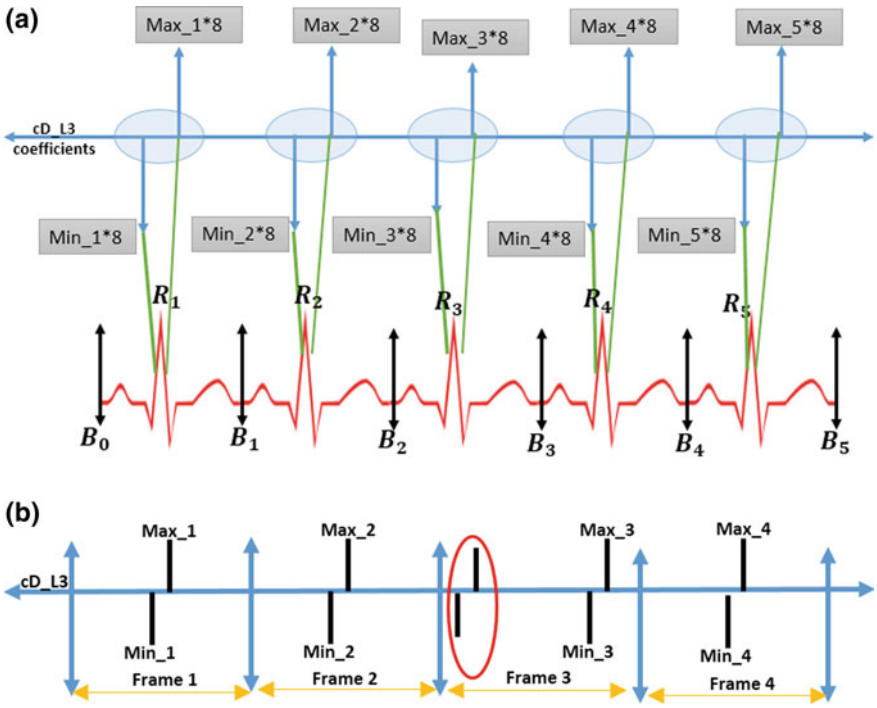

Fig. 7 (Case **a**) Projections of cD_L3 coefficients on original ECG signal, (Case **b**) maximum and minimum of cD_L3 coefficients present in each sub frame

3.2 R-Peak Estimation

Based on the index of the maximum value in each sub frame of cD_L3 R-peak can be extracted, but there would be a chance of missing the ECG beat due to lesser R-peak amplitude and its corresponding coefficients compared to other beats as shown in Fig. 7b highlighted with oval shape in the third frame. In order to find the missing ECG beat, threshold calculation is performed by taking the minimum value of all the maximums as shown in Fig. 6. Based on the rigorous testing during the development of algorithm on various healthy and unhealthy ECG test cases, the threshold has been fixed to 45% of the minimum value ('min_of_max'). To find the R-peak index, the threshold value and all the cD_L3 coefficients are passed to the comparator as shown in Fig. 6, the output of the comparator produces '1' if the cD_L3 value is greater than the threshold value else it produces '0'. The output '1' from the comparator indicates that there would be a possibility of R-peak corresponding to that index. The sequence of 1's and 0's comes as the output from the comparator and stored in an array as shown in Fig. 6, search for the indexes which are having '1' and note them if the difference between the index is greater than 36, the fixed value '36' is proven to give accurate results based on the statistical analysis for the ECG sampling

of 1 kHz, the fixed value will alter if there is any change in the sampling frequency of the ECG signal. The index of all '1's obtained corresponds to the index of maximum values of the cD_L3 coefficients of each sub frame, with the above procedure the index of missing coefficient present in the third frame is obtained along with the index of other maximum coefficients.

Generally, the R-peak (positive deflection) in the ECG signal is decomposed as the minimum followed by a maximum in the cD_L3 coefficients, since the index of maximum values is obtained, index of minimum values need to be found. To calculate these indexes, search for the index of minimum value with the range 10 samples towards the left and right side of the maximum index as explained in line number 40 of Algorithm 1. The R-peak index is calculated by projecting the obtained and minimum index (min_1, min_2 min_3, min_4, min_5) and maximum index (max_1, max_2 max_3, max_4, max_5) to the original signal as shown in Fig. 7a, since the analysis is done on the third level decomposition, the obtained maximum and minimum index values of cD_L3 has to be multiplied by 8 (min_1 $\times$ 2^3, max_1 $\times$ 2^3) to project the original signal. If the ECG wave has positive deflection, then the index of absolute value within the indexes will be the R-peak index, whereas if the ECG wave has negative deflection, then search for the positive value towards the left from the index of absolute value.

Algorithm 1 Pseudo code for Boundary Detection

1: $ECG\_data = load(.matfile\ of\ ECG)$ {X=4096 ECG samples}
2: **for** $k = 1$ *to* N **do**
3: $cD\_L3 = Third\_level\_haar\_dwt(ECG\_data)$
4: $cD\_L5 = Fifth\_level\_haar\_dwt(ECG\_data)$ {cD_L3, cD_L5 results 512 & 128 coefficients respectively }
5: **end for**
6: $min\_of\_max = min(max(cD\_L3(1:128), max(cD\_L3(129:256), max(cD\_L3(257:384), max(cD\_L3(385:512))$
7: $Th = 45\%(min\_of\_max)$
8: **for** $k = 1$ *to* $length(Third\_level\_haar\_dwt)$ **do**
9: **if** $(cD\_L3(k) > Th)$ **then**
10: $Comp\_mem[k] = 1$
11: **else**
12: $Comp\_mem[k] = 0$
13: **end if**
14: **end for**
15: **for** $k = 1$ *to* $length(Third\_level\_haar\_dwt)$ **do**
16: **if** Comp_mem (k) ==1 & Comp_mem (k+1)==1) **then**
17: $Comp\_mem(k) = 0$
18: $k = k + 1$
19: **else**
20: $Comp\_mem(k) = Comp\_mem(k)$
21: $k = k + 1$
22: **end if**
23: **end for**

```
for k = 1 to length(Third_level_haar_dwt) do
  if (Comp_mem == 1) then
    Comp_mem = k
    k = k + 1
  end if
end for
for l = 1 to length(cd_3_logic_location) do
  if ((Comp_mem_location(j + 1) − Comp_mem_location(l)) > 36) then
    store_index(j) = Comp_mem_location(l)
    l = l + 1
  else
    store_index(l) = cd_3_logic_location(l + 1)
    l = l + 1
  end if
end for
for k = 1 to length(store_index) do
  R_Peak[k]=abs(ECG_data(((min((cD_L3(store_index(k)-
  10)):(cD_L3(store_index (k)+10)))*8):((store_index (k)+10)*8)))
end for
if ((R_Peak(1) − 1 >= (R_Peak(1) + R_Peak(2))/2)) then
  first_Boundary = (R_Peak(1) − (R_Peak(1) + R_Peak(2))/2))
else
  first_Boundary = first_Boundary
end if
if length(ECG_data) − R_Peak(end) >= (R_Peak(end) − R_Peak(end −
1))/2 then
  last_Boundary = (R_Peak(end) − (R_Peak(end) + R_Peak(end − 1))/2))
else
  last_Boundary = last_Boundary
end if
```

3.3 Boundary Calculation of ECG Beats

Start and end boundary of each ECG beat can be obtained by taking the average of two successive R-peak index values noted as B0–B5 as shown in Fig. 7a, the average calculation of R-peak index may not give the exact boundary index values for every ECG beat, particularly at the time of abnormal heart rhythm. For few ECG test cases, the boundary index resulted from the average of R-peak indexes may occur on the previous T-wave of ECG beat or it may be on the P-wave of its own beat, hence few conditions based on the RR interval and checking the amplitude of the index obtained to be followed to get the accurate boundary index, since the boundary of the ECG beat should be on the isoelectric line, the value of the obtained boundary index should be close to the zero value. In some cases, the first and last ECG beat is neglected if the

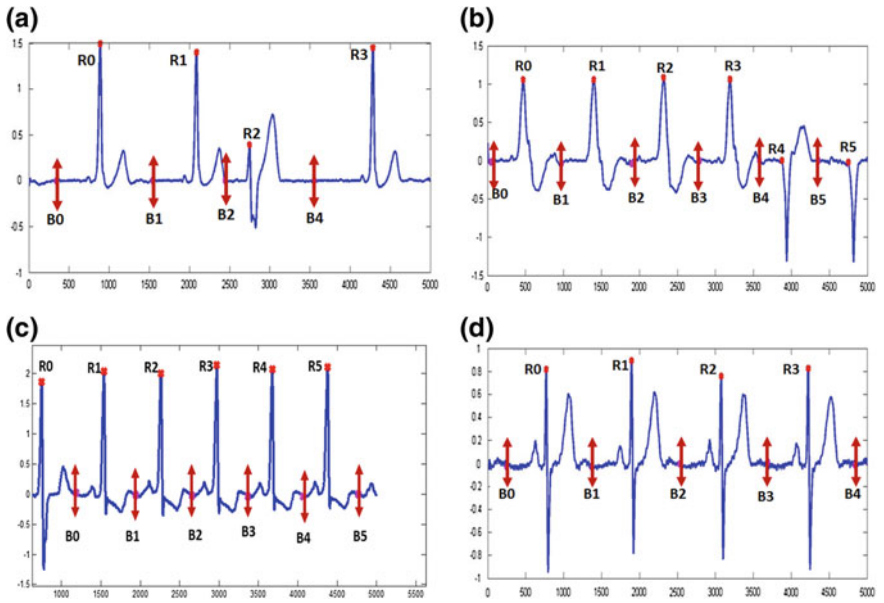

Fig. 8 Different ECG test cases extracting R-peaks and boundaries, (Case **a**: First degree AV block, Case **b**: Left BBB, Case **c**: Right BBB, Case **d**: Normal signal)

entire beat information (P, Q, R, S, T) is not present within the 'X' number of ECG samples, the condition for these types of cases are shown in line number 43 and 48 of Algorithm 1. BD uses the DWT module and extracts the start and end boundaries of each ECG beat along with the R-peak index and amplitude information. Heart Rate Variability (HRV) and Heart Rate (HR) can be calculated with the help of R-peak index values. HRV is the index difference between the successive R-peaks, whereas HR is calculated by counting the number of R-peaks for one minute and used to find the condition of the patient, such as bradycardia (HR < 50) and tachycardia (HR > 100). The BD has been analyzed by applying various ECG test cases, which start with different characteristic points (P, Q, R, S, and T) as shown in Fig. 8.

4 Feature Extraction

The time interval between the characteristic waves follows a standard time duration and amplitude (voltage) if any deviation from the normal tracing represents pathological. The process of extracting the clinically important fiducial points like onset and offset index of P-wave, QRS complex, T-wave as well as the amplitudes of characteristic waves (P, Q, R, S, T) from the ECG beat is termed as FE, extracting these feature points of ECG beats and categorizing them as normal and abnormal is termed

as classification. The detection of each ECG beat from the BD module is fed to the FE block to extract these fiducial points. Finding QRS complex and P/T characteristic waves are possible by applying Modulus-Maxima Analysis (MMA) on cD_L3 and cD_L5 coefficients, respectively, time domain morphology is used to refine the findings that occurred using MMA. Since the analysis employs both frequency and time analysis, this method is called a Hybrid Feature Extraction Algorithm (HFEA) [13]. For the explanation of the FE algorithm, a single isolated heart beat with all the characteristic waves is considered. The onset and offset of the characteristic waves are calculated based on MMA principle, and they are localized by a Modulus-Maximum Pair (MMP) on the coefficients of DWT. With respect to the isoelectric line, the ECG wave can have positive or negative deflection, the index locations corresponding to the pair of extrema in the cD_L3 coefficients will behave minimum followed by maximum for the positive deflection and vice versa for the negative deflection of ECG wave. The complete flow of HFEA has been shown in the form of pseudo-code shown in Algorithm 2.

Using MMA, the global extrema pair, which is having the temporal positions (t_1, t_2) in the cD_L3 can be obtained, these positions exhibit the highest separation from the isoelectric line, as shown in Fig. 3b. The extraction of QRS onset is calculated as the preceding extrema from the MMP of the search window $[t_1 - 4, t_1]$, likewise, the QRS offset is estimated using the succeeding extrema of the MMP of search window $[t_2, t_2 + 4]$. The temporal resolution of level three coefficients is reduced by a factor of '8' compared to the input given original timescale, this leads to the less accurate localization of the deflections either Q-peak, S-peak, and QRS boundaries as shown in Fig. 9a To avoid this, time domain morphology is employed for the refinement of the extracted values to achieve an accurate estimation of the fiducial points. For the refinement of the QRS complex, exploiting the characteristic signal of the QRS complex by using the derivative signal is performed on Level three approximation (cA_L3) coefficients for the analysis. The initial QRS boundaries are extended in time by 64 ms before to the initial QRS onset $[t'_3 = t_3 - 8]$ and 120 ms after the initial QRS offset $[t'_6 = t_6 + 15]$. An approximation of the derivative $f'[n]$ for $n \in [t'_3, t'_6]$ is calculated as the backward difference between two successive samples of cA_L3 coefficients. The derivative signal is compared with the threshold values as shown in the line number 24 of Algorithm 2, the point where the value of the gradient is more than the predefined threshold leads to the amendment of the QRS boundary. To find the QRS onset, the derivative signal is taken from the beginning up to the R-peak index [t'_3, R-peak], whereas for the QRS offset, the gradient signal is taken from its end toward s R-peak [R-peak, t'_6]. The threshold value is ascertained based on the computation of applied ECG signal; the initial approximation produced by DWT is improved with the execution of TDM, as shown in Fig. 9b.

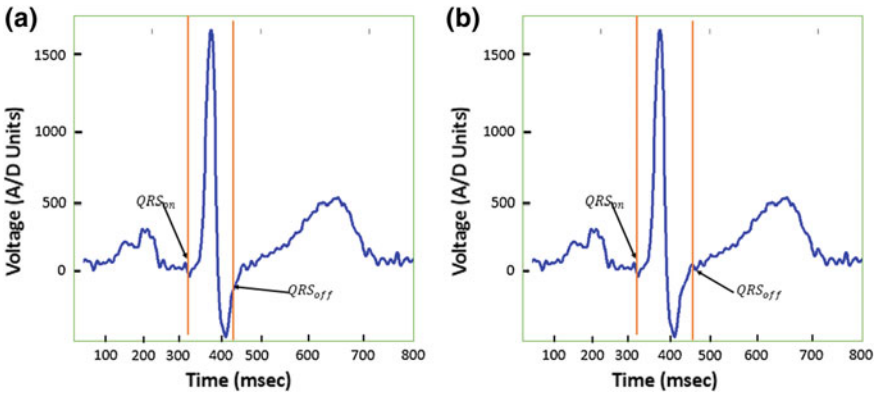

Fig. 9 Case **a**: Interpretation of initial QRS boundaries using MMA, Case **b** final QRS boundaries using TDM refinement

Algorithm 2 Pseudo code for feature extraction of ECG beat

The index of boundaries (B_0 B_1) *and R_peak of ECG beat are fed from BD block.*
B_cD_L3 = cD_L3(X($B_0 : B_1$)) (*'X' hold continuous ECG samples*)
B_cA_L3 = cA_L3(X($B_0 : B_1$))
B_cD_L5 = cD_L5(X($B_0 : B_1$))
QRS extraction begins
Applying MMA on B_cD_L3
$t_1 = min\_index(B\_cD\_L3)$
$t_2 = max\_index(B\_cD\_L3)$
Finding the positions (t_3, t_4) *of MMP in cD_L3 for* $k \in [t_1 - 4, t_1]$ *and* (t_5, t_6) *for* $k \in [t_2, t_2 + 4]$
Initial $QRS_{on} = t_3 \times 2^3$
Initial $QRS_{off} = t_6 \times 2^3$
Refinement process: Time Domain Refinement (TDM)
$X_{max} = max(B\_cD\_L3)$
$X_{min} = min(B\_cD\_L3)$
Set diff_abs = abs($X_{max} - X_{min}$)
Threshold calculation

17: **if** $diff\_abs > 4000$ **then**
$\text{Thr}_1 = diff\_abs/16$
$\text{Thr}_2 = diff\_abs/32$
18: **else**
If $diff\_abs > 2000$
$\text{Thr}_1 = diff\_abs/8$
$\text{Thr}_2 = diff\_abs/16$
19: **else**
$\text{Thr}_1 = diff\_abs/8$
$\text{Thr}_2 = diff\_abs/8$
20: **end if**
21: Expand $t_3^1 = t_3 - 8$
22: Expand $t_6^1 = t_6 + 15$
23: Analysis on Approximation coefficients
24: $d_n = [B\_cA\_L3[m] - B\_cA\_L3[m-1]], m \in [t_3^1, t_6^1]$
25: Final $\text{QRS}_{on} = first\ m \in [t_3^1, R - peak], d_n > Thr_1$
26: Final $\text{QRS}_{off} = last\ m \in [R - peak, t_6^1,], d_n > Thr_2$
27: Q-Peak and S-Peak calculation
28: $\text{Q}_{peak} = min(X[m]), m \in [QRS_{on} \times 2^3, R - peak]$
29: $\text{S}_{peak} = min(X[m]), m \in [R - peak, QRS_{off} \times 2^3]$
30: P and T wave extraction
31: for P-wave
32: $t_7 = min(cD\_L5[m]), m \in [1, QRS_{on}/32]$
33: $t_8 = max(cD\_L5[m]), m \in [1, QRS_{on}/32]$
34: $\text{P}_{onset} = t_7 \times 2$
35: $\text{P}_{offset} = t_8 \times 2^5$
36: P-peak= abs (X[$\text{P}_{onset}, P_{offset}$])
37: Repeat the P-wave process with m $\in [QRS_{on}, cD_L5_end] for the T_{onset}, T_{offset}, T-peak extraction.$

Finding the Q-peak and S-peak indexes is the final step of the QRS refinement, the Q-peak can be obtained by finding the minimum value between the QRS onset to the R-peak and the S-peak index is calculated by finding the minimum value between the R-peak to QRS offset. After finalizing the QRS boundaries using the TDM refinement process, a similar procedure modulus-maxima analysis is applied on the cD_L5 coefficients within the portion of the signal that precedes and succeeds the QRS complex to identify the onset and offset of P and T waves and its corresponding peaks indexes. P and T waves follow the positive or negative deflection based on the leads considered and the condition of the patient, hence the modulus-maxima pair in cD_L5 that localize the P and T waves helps to determine the deflections and the peak value by projecting the maximum and minimum values to the original signal by multiplying with a factor of '32' as shown in the line number 34 of Algorithm 2. The following explanation of Algorithm 2 is for one ECG beat, and the same applies to all other ECG beats extracted from the BD algorithm. Various ECG abnormalities can be identified using the extracted features from the FE algorithm. For example, P-wave follows a positive deflection in most of the leads except in the case of avR, in unusual cases, P-wave can be of negative deflected or produce long duration

which indicates an ectopic pacemaker and atrial enlargement, respectively. Using the FE algorithm, the deflection and the duration of the P-wave can be identified by searching the absolute value and the interval difference between the P onset and P offset respectively, and the obtained values are compared to the standard P-wave amplitude and the duration to detect CVD. Typically, the P wave interval should less than 80 ms, if the duration is higher it indicates an abnormality. Likewise, other features from the FE give the information of intervals and amplitudes and compared to the standard values to detect the abnormalities like first degree atrioventricular block (PR > 200 ms), LBBB, RBBB (QRS complex interval > 120 ms), left ventricular hypertrophy (high QRS amplitudes), hyperkalemia (peaked T-waves), ventricular tachycardia (prolonged QT interval), etc. [1]. The validation of BD and FE is done using various healthy and unhealthy cases of ECG taken from publically available ECG database PhysioNet's PTB Database (PTBDB), CSEDB and IITHDB sampled at 1 kHz to show the HFEA performance is very close to the state of the art ECG delineators.

The performance evaluation of BD and FE are shown in Tables 1 and 2 respectively in-terms of the mean and standard deviation of the error between the algorithm and the annotation result for each record. Overall mean and the standard deviation are calculated by taking the average of mean and the standard deviation error of all the records. The BD and FE algorithms have been analyzed by customizing the continuous ECG wave starting index with different case points (P, Q, R, S, and T) and resulted in achieving 99% accuracy in detecting the boundary of ECG beat and extracting the features from each ECG beat. The use of DWT with the Haar function as the basis allows for a significant reduction in the computational complexity compared to other DWT based approaches, which is beneficial in terms of the overall energy consumption. Taking these concepts from the algorithm level to hardware system level perspective will reduce the complexity and can be integrated with other intellectual properties like compression and communication blocks for the CVD monitoring device.

5 Fragmented QRS

The f-QRS is an indicator of myocardial scar, due to which abnormalities within the QRS complex can be observed. Due to the intraventricular conduction defect, a notch in the QRS complex can be noticed in the patients with left ventricular hypertrophy [44]. RsR′ pattern of the QRS complex can be seen due to the injured tissue around the infarct scar [45]. Das et al. [46] have proved that the patients with coronary artery disease and were associated with myocardial conduction block has f-QRS complex, which is defined by a notch or an additional R wave within the QRS complex as shown in the Fig. 10 [44]. Haukilahti et al. [47] defined that if the QRS complex has more than one R wave or any notch in the nadir of the R wave or the S wave can be defined as f-QRS complex. On a 12 lead ECG, f-QRS is defined as narrow QRS complex duration which maintains an interval of less than 120 ms for healthy cases.

Table 1 Performance details of boundary detection algorithm [5]

Database	Performance metric	Start boundary	End boundary
CSE DB	# ann beats	10,500	10,500
	u ± S (ms)	4 ± 5.2	3 ± 4.7
	Sigma (samples)	5	4
	% Error FBD	0.03%	
PTBDB	# ann beats	1950	1950
	u ± s (ms)	3 ± 4.5	3.5 ± 3.8
	sigma (samples)	4	7
	% Error FBD	0.03%	
IITH database	# ann beats	750	750
	u ± s (ms)	7 ± 9.1	5 ± 7.2
	Sigma (samples)	9	10
	% Error FBD	0.06%	

Several investigations [48–50] have been published and proven the effectiveness of f-QRS over conventional biomarkers in the detection of myocardial infarction, cardiac sarcoidosis and various other diseases which fields it on a path to become a potential bio-marker.

Automated detection of f-QRS followed by identification of its various morphologies in addition to the conventional ECG feature (e.g. P, QRS, T amplitude, and duration, etc.) extraction will lead to a more reliable diagnosis and disease prognosis than the state-of-the-art approaches and thereby will be of significant clinical importance for both hospital-based and emerging remote health monitoring environments. Hence, this topic gives an insight into the automatic detection of f-QRS and identifying its different morphologies and termed as Fragmentation Detection and Morphology Identification (FDMI) [35]. QRS complex of the ECG beat is extracted from the FE block as explained in the earlier section since the index of QRS complex is known, the corresponding level one detailed coefficient can be taken from the DWT block to find the irregularities. FDMI uses the detailed wavelet coefficients of QRS to find the discontinuities along with the position of its occurrence and frame the classification rules for different types of fragmentation. There are two subsections in FDMI viz. Fragmentation Detection (FD) and Morphology Identification (MI).

5.1 Fragmentation Detection

As discussed in the earlier section, DWT helps to find the discontinuities that occur in the original signal. DWT generates zero crossing points whenever there is any peak or nadir in the signal [35] as shown in Fig. 3b, this analysis can be used to model the FD. A peak in the QRS complex is identified as a sudden change in sign and

Table 2 Performance details of feature extraction algorithm [5]

DB	PM	Pon	Ppeak	Poff	QRSon	Rpeak	QRSoff	Ton	Tpeak	Toff
PTBDB	ann beats	1950	1950	1950	1950	1950	1950	1950	1950	1950
	u ± s (ms)	1.8 ± 7.8	4.2 ± 8.4	−5.2 ± 9.9	4 ± 10.3	1 ± 2.4	3.4 ± 7	−7.8 ± 11.1	−7.5 ± 11.3	−6.9 ± 8.8
CSEDB	ann beats	10,500	10,500	10,500	10,500	10,500	10,500	10,500	10,500	10,500
	u ± s (ms)	−3.8 ± 7.5	4.1 ± 7.8	2.1 ± 5	1 ± 5.9	1 ± 2.2	4.9 ± 8.8	−8.3 ± 10.7	−10.1 ± 12.4	3.1 ± 11.9
IITHDB	ann beats	750	750	750	750	750	750	750	750	750
	u ± s (ms)	7.8 ± 9.9	5.3 ± 9.3	−4.2 ± 10.2	3.5 ± 11.3	1 ± 3.4	7 ± 10.9	−5.3 ± 11.2	−7.1 ± 10.3	4.4 ± 13.2
Mazomcnos [3] PTBDB	ann beats	422	–	422	450	–	450	–	–	432
	u ± s (ms)	1.1 ± 9.5	–	−6 ± 11	3.8 ± 10.8	–	3.7 ± 6.8	–	–	−8 ± 10.8
CSE [21]	2 sigma	10.2	–	12.7	6.5	–	11.6	–	–	30.6

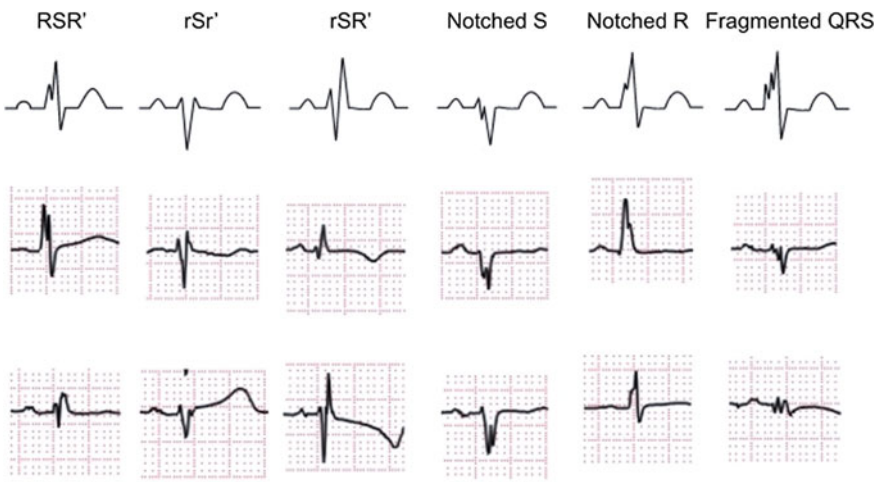

Fig. 10 Discontinuities associated within the QRS complex [46]

follow the wavelet coefficients with the same sign, whereas the behavior of notches is identified by the frequent change in the sign of detailed coefficients.

To detect the local extrema and the notches in the QRS complex accurately, linear interpolation is performed on the QRS complex to increase the time resolution by a factor of 2, interpolation is performed based on the observational interpretations during the development of FDMI algorithm [35]. Interpolation is performed by taking the mean of two consecutive samples and insert in between them to increase the number of samples applied to FDMI, and this process doesn't affect the morphology of extrema and the notches. The Fig. 3b shows the bar plots of detailed wavelet coefficients corresponding to the QRS complex, noticing the change in coefficients and correlating them w.r.t to applied QRS complex helps to formulate the rules for identifying the notches and extrema. The coefficient values represented as bars may not seem to align because the scale of the x-axis of the original signal and the bar plot of detailed coefficients are different. The number of detailed coefficients obtained is half the number of samples applied at the input of DWT, in Fig. 3b, the number of samples applied to DWT is 9, and the obtained coefficients are 5, the value of the last coefficient is zero. After analyzing several test cases of healthy and unhealthy QRS complexes, the criteria shown in Fig. 11 has been formulated [35] and it is refined to capture all sorts of discontinuities like local extrema and notches in the QRS complex. The FD algorithm starts by observing the leftmost side of the detailed coefficients of DWT and proceeds towards the right while moving through the coefficients, patterns are spotted and if any of the patterns match with the rules mentioned in the Fig. 11, then the corresponding discontinuity is recognized. Algorithm pointer (k) is used to point out the detailed coefficients, if any discontinuity occurs, 'k' pointing at a particular point of the wavelet coefficients is incremented as per the rules mentioned in Fig. 11, else it increments by one. In the pattern A1 shown in Fig. 11, there are two

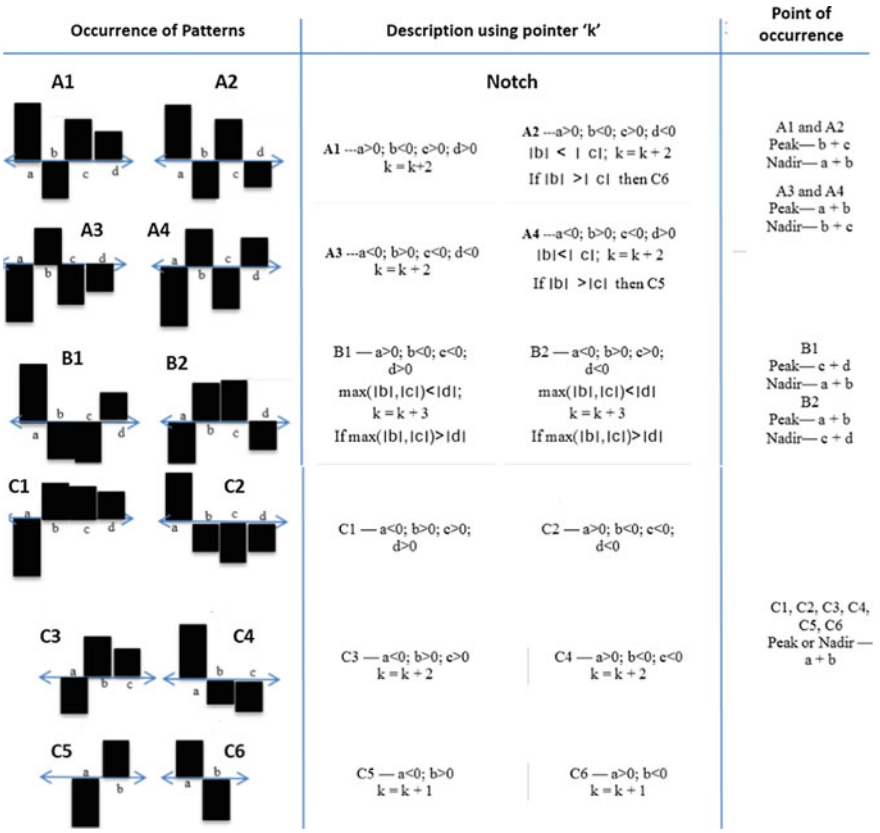

Fig. 11 Rules for the identification of discontinuities, ('a', 'b', 'c', 'd' are the successive detailed coefficients in the bar plot. Pointer 'k' starts from 'a' and its increment shifts from 'a' to 'b')

successive sign changes in the value of detailed coefficients which says that there is an occurrence of a local extreme pair in its vicinity and hence it can be assumed as the presence of a notch. Likewise, in pattern A2, there are three consecutive sign changes in the coefficients and implies that there are three extrema and the identification of notch depends on the magnitude of the coefficients, and the other is identified as extrema. Similarly, Fig. 11 describes the rules for the identification of other patterns having notch or extrema. FD algorithm makes use of the rules and gives the number of notches, maxima, and minima present in the QRS complex as the output.

5.2 Morphology Identification

There exist several various RSR′ patterns, and six fundamental morphologies of f-QRS, [35] had covered various other possible morphologies in RSR′ patterns to increase the robustness of the algorithm. Figure 12 shows the necessary criteria for the identification of various QRS morphologies whose interval is $\leq$120 ms. Information on the number of notches, maxima, and minima from the FD module is given to MI module to get the details of a point of occurrence, which can be the positive or negative side of the reference axis, height, and depth of the R and S waves in the QRS complex. A clear attempt has been made to maintain the difference between a notch and extrema pair to find the locations of discontinuities. In Fig. 12, morphology A, C, E, and I are considered to be dominant over the presence of notches so as to prevent the morphologies from being identified as f-QRS. The criteria formulated for the MI are more robust, where it is able distinctively to identify all the morphologies without any conflict.

To measure the performance of FDMI in terms of accuracy, PTBDB [51] from PhysioNet has been used, this database has 15 lead ECG data comprising conventional 12 lead and 3 orthogonal Frank lead which are sampled at 1 kHz. ECG database is categorized based on cardiac disorders, to design and model the FDMI algorithm ECG data from various diagnostic classes viz. cardiomyopathy, BBB, dysrhythmia, myocardial hypertrophy, valvular heart disease, myocarditis, healthy controls, myocardial infarction, and other miscellaneous conditions have been considered. Based on the criteria shown in Figs. 12 and 13 the output from the FDMI results in the number of notches extrema points (maxima, minima), the time instant at which they occur and the magnitude of the extrema. To explain the insight of algorithm, four different test cases of f-QRS are taken shown in Fig. 13, in all the cases, explained plot 'a' shows the QRS complex and the plot 'b' shows the bar plot of detailed wavelet coefficients and the notches are indicated with circles, extreme are indicated with rectangles in the QRS complex.

Case 1: The QRS morphology shown in Fig. 13 case 1a is a notched R (rsR′), it shows that there are two minima's both are less than zero which indicates a negative value, one maxima with a positive value and single positive notch. Case 1(b) shows the detailed coefficients of the QRS complex and applied as an input to the FDMI module, the algorithm detects all the points by using the rules shown in Fig. 12.

Case 2: In this case, the morphology is RsR′ without ST elevation as shown in Fig. 13 case 2a, the corresponding wavelet coefficients shown in Fig. 13 case b applied to FDMI and resulted in two maxima, two minima and zero notches in the original signal as the output.

Case 3: The morphology shown here is Rsr′, the number of maxima, minima, and notches are 1, 2, and 1 respectively will be the outcome from the FDMI as shown in Fig. 13 case b.

Case 4: Fragmented QRS has been shown in this case, where the number of maxima, minima, and notches is 2, 3 and 0 respectively as shown in Fig. 13 cases a.

Morphology	Name	Criteria	Conflict
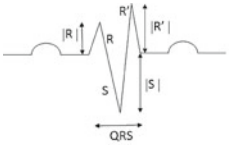	(A) **rSr'**	(A) max($P_{maxv}(1,2)$) <$\|P_{minv}(1)\|$ N_{max} = 2 N_{min} = 1 $P_{maxv}(1,2)>0$ $P_{minv}(1)<0$ N_{notch} = NF	When this morphology is encountered, the presence of notches on R, R' or S wave will not lead it to be termed as fragmented QRS
B1  B2 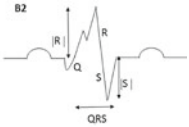	(B) Notched R (**rsR'**) (B1) Without Q (B2) WithQ	N_{max}=1; N_{notch}=1 $P_{maxv}(1)>0$;$P_{notchv}(1)>0$ $P_{notchh}(1)<P_{maxh}(1)$ (B1) N_{min}=1; $P_{minv}(1)<0$ (B2) N_{min}=2; $P_{minv}(1,2)<0$	When N_{notch}>1 then the morphology resembles Fragmented QRS
C1 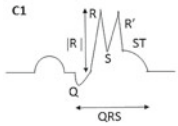 C2 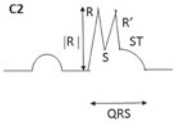	(C) **RsR'** with ST elevation (C1) With Q (C2) Without Q	N_{max}=2; N_{notch}=0 $P_{maxv}(1,2)>0$; End of QRS complex must lie above horizontal axis. (C1) N_{min}=2; $P_{minv}(1)<0$; $P_{minv}(2)>0$ (C2) N_{min}=1; $P_{minv}(1)>0$	Case may arise when sR' is identified as a notch instead of a minima-maxima pair. Then all the cases arising are captured by morphology (F). For an extremum to be **R** it has to be identified as a maximum.
D1 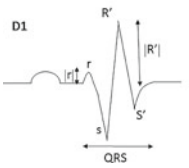 D2 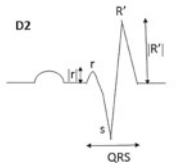	(D) **rsR'** (D1) With S' (D2) Without S'	N_{max}=2;$P_{maxv}(1,2)>0$; $P_{maxh}(1)<P_{minh}(1)$. (D1) N_{min}=2; $P_{minv}(1,2)<0$ (D2) N_{min}=1; $P_{minv}(1)<0$; $P_{maxv}(1)<P_{minv}(1)$; $P_{minv}(1)<P_{maxv}(2)$;	Presence of notches will not affect the morphology.

Fig. 12 Various QRS morphologies. *(NF, number and the presence of notches not fixed, N_{max}: Number of maxima, N_{min}: Number of minima, N_{notch}: Number of notches, $P_{max}(i)$: position at which i_{th} maxima occurs on the vertical axis (magnitude along with sign); $P_{maxh}(i)$, position at which i_{th} maxima occurs on the horizontal axis; $P_{minv}(i)$, position at which i_{th} minima occurs on the vertical axis; $P_{minh}(i)$, position at which i_{th} minima occurs on the horizontal axis; $P_{notchv}(i)$, position at which i_{th} notch occurs on the vertical axis; $P_{notchh}(i)$, position at which i_{th} notch occurs on the horizontal axis)

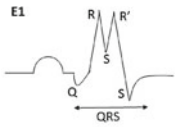	**(E) RsR' without ST elevation**	**N_{max}=2;N_{notch}=0; $P_{maxv}(1,2)>0$;**	
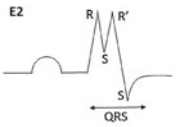	**(E1) With Q and S**	**(E1) N_{min}=3;$P_{minv}(1,3)<0$; $P_{minv}(2)>0$**	**If $N_{notch}\geq1$ then the morphology resembles Fragmented QRS. R' or R must be etected as a maxima and not a notch for its morphology to be RsR'.**
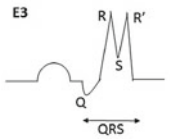	**(E2) S without Q**	**(E2) N_{min}=2;$P_{minv}(1)>0$; $P_{minv}(2)<0$**	
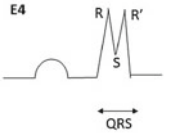	**(E3) Q without S**	**(E3) N_{min}=2;$P_{minv}(1)<0$; $P_{minv}(2)>0$;$P_{minh}(1)<P_{maxh}(1)$**	
	(E4) Without Q and S	**(E4) N_{min}=1;$P_{minv}(1)>0$**	
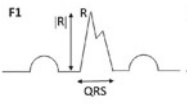	(F) **Rsr'**	N_{max}=1;N_{notch}=1; $P_{maxv}(1)>0$; $P_{notchh}(1)>P_{maxh}(1)$; $P_{notchv}>0$	sr' must be identified as a notch and not an extremum pair. If more than one notch occurs the morphology resembles Fragmented QRS
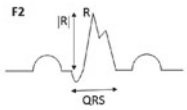	(F1) Without Q and S wave	(F1) N_{min}=0	
	(F2) Only Q	(F2) N_{min}=1;$P_{minv}(1)<0$; $P_{minh}(1)<P_{maxh}(1)$	
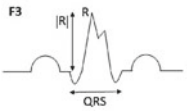	(F3) Q and S both present	(F3) N_{min}=2;$P_{minv}(1,2)<0$; $P_{minh}(1)< P_{maxh}(1)$; $P_{minh}(2)>P_{maxh}(1)$	
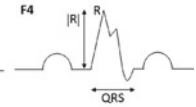	(F4) Only S	(F4) N_{min}=1;$P_{minv}(1)<0$; $P_{minh}(1)>P_{maxh}(1)$	
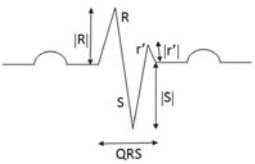	(G) **RSr'**	N_{max}=2;N_{notch}=UD N_{min}=1;$P_{maxv}(1,2)>0$ $P_{minv}(1)<0$ $P_{maxv}(1)>\|P_{minv}(1)\|$ $P_{maxv}(2)<\|P_{minv}(1)\|$	Presence of notches will not affect the morphology.

Fig. 12 (continued)

In Fig. 13 case b a minima (<0) is encountered first followed by maxima (>0), minima (<0), maxima (>0) and minima (<0). A four-point star shown does not lead to discontinuity but, represents the sudden changes in the gradient of the wave.

For the evaluation of FDMI, several ECG test cases were taken from the database, the QRS complexes extracted from FE were examined by two cardiologists who are referred to cardiologist's status (CS). The results obtained from the FDMI were compared with the CS, the sensitivity and specificity values are calculated.

True Positive (TP): The cardiologists detected fragmentation in a particular lead of the patient, and the algorithm reported correctly.

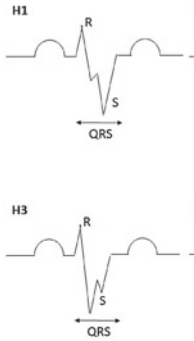	**(H) Notched S** **(H1 and H3) Notch in downstroke and upstroke of S wave. Q not present** **(H2 and H4) Notch in downstroke and upstroke of S wave. Q present.** **(H5 and H6) If notch is detected as extremum pair in any of the cases.**	**(H1 and H3)** $N_{max}=1; N_{notch}=1;$ $N_{min}=1; P_{minv}(1)<0;$ $P_{maxv}(1)>0; P_{notchv}<0$ $P_{notchh}(1)< P_{maxh}(1);$ **(H2 and H4)** $N_{max}=1; N_{notch}=1;$ $N_{min}=2; P_{minv}(1,2)<0;$ $P_{maxv}(1)>0; P_{notchv}<0$ $P_{notchh}(1)> P_{maxh}(1);$ **(H5)** $N_{max}=2; N_{min}=2;$ $N_{notch}=1;$ $P_{maxv}(1)>0; P_{maxv}(2)<0$ $P_{minv}(1,2)<0$ **(H6)** $N_{max}=2; N_{min}=3;$ $N_{notch}=1;$ $P_{maxv}(1)>0; P_{maxv}(2)<0$ $P_{minv}(1,2,3)<0$	**If more than one notch is present then the morphology will be termed as Fragmented QRS. Notch may be discovered as a extremum pair but still the morphology resembles Notched S.**
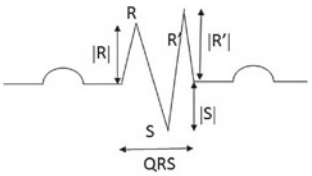	(I) **RSR'**	(I) $Min(P_{maxv}(1,2))>\|P_{minv}(1)\|$ $N_{max}=2; N_{min}=1$ $P_{maxv}(1,2)>0$ $P_{minv}(1)<0$ $N_{notch}=NF$	Presence of notch doesn't affect the morphology.
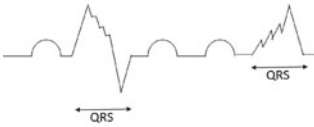	(J) **Fragmented QRS**	(J) If none of the aforementioned morphologies are detected and $N_{notch}>=1;$ Or $N_{max}>=2; N_{min}>=2$	Visually identified notch may be detected as an extremum pair. If so, then such morphology will be termed as Fragmented QRS. Notches may occur in R and/or S wave.

Fig. 12 (continued)

False Positive (FP): The cardiologists did not detect fragmentation, but the algorithm reported the presence of fragmentation in a particular lead.

True Negative (TN): The cardiologists did not detect fragmentation and the algorithm reported correctly.

False Negative (FN): The cardiologists detected fragmentation in a particular lead but the algorithm could not detect

The sensitivity and specificity were calculated using Eqs. (3) and (4)

$$\text{Sensitivity} = \text{TP}/(\text{TP} + \text{FN}) \tag{3}$$

$$\text{Specificity} = \text{TN}/(\text{TN} + \text{FP}) \tag{4}$$

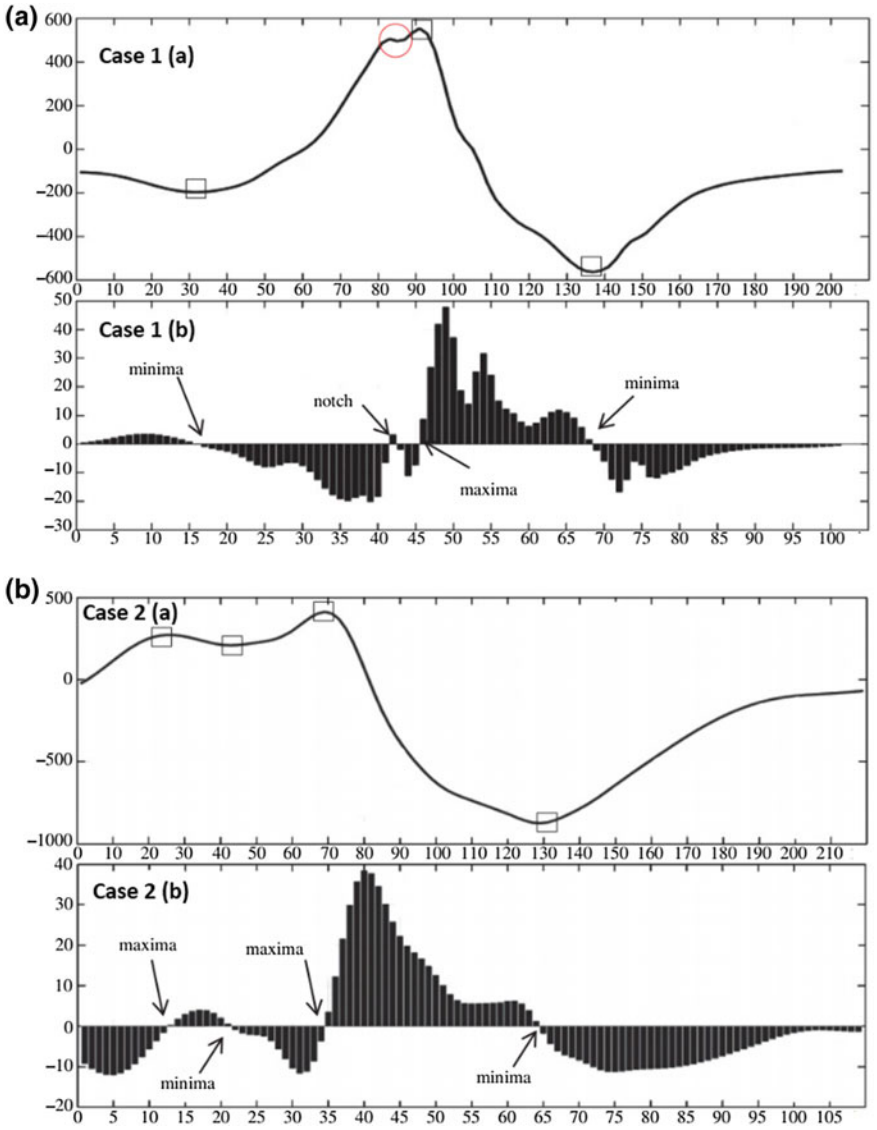

Fig. 13 Different cases of QRS complex and their corresponding detailed coefficients [35] (Notches and extrema are denoted by circle and rectangle, respectively.)

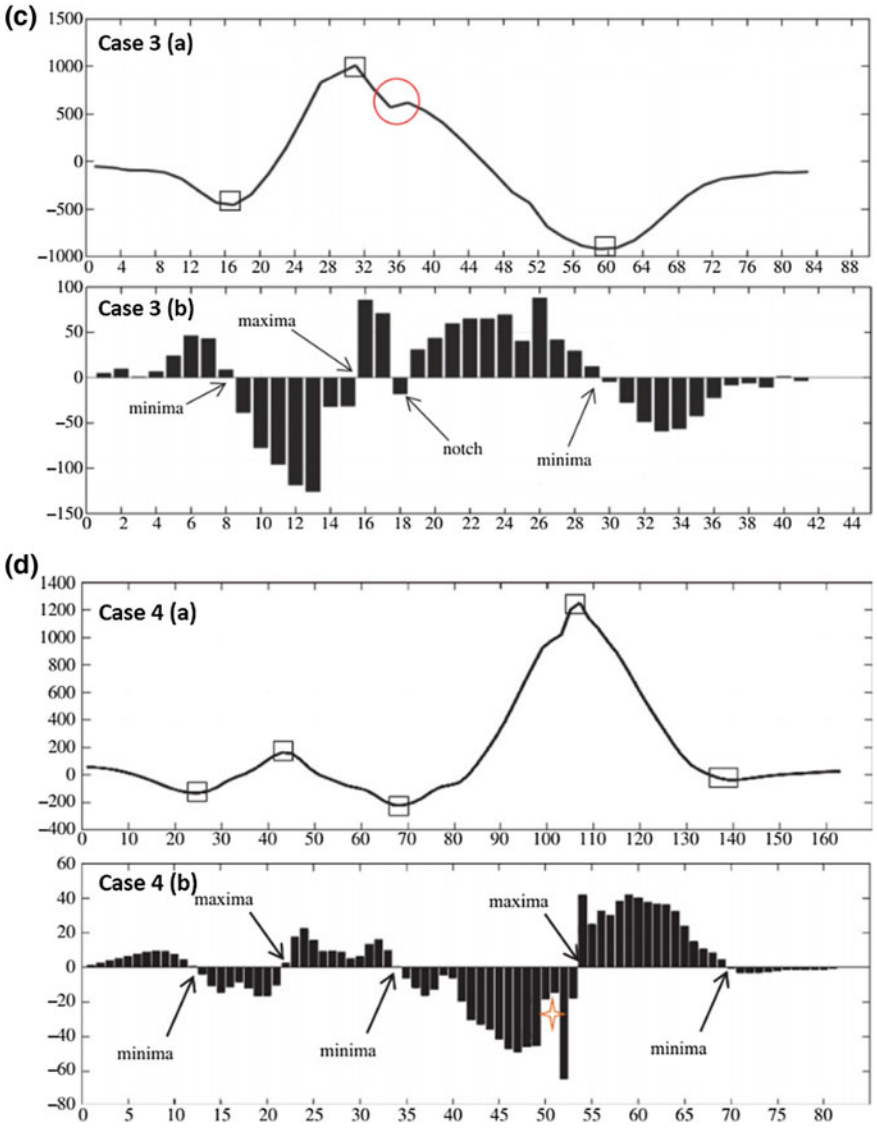

Fig. 13 (continued)

To know the performance of the algorithm, 372 leads from thirty-one test cases neglecting the frank lead the result obtained is 89.8%, it says that the sensitivity and specificity values obtained are 0.897 and 0.899 respectively. Most of the cardiologist show interest to check for fragmentation in Bundle Branch Block (BBB) cases, for the test cases which are having BBB alone, the sensitivity and specificity are found to be 0.932 and 0.933, respectively.

In the test cases shown in Fig. 13 case 4b, it is observed that whenever the gradient is high, the magnitude of the detailed coefficients is also high in value. FDMI algorithm also captures the sudden changes in gradient which do not result in the extremum pair, this can be seen clearly in the case 4, a sudden gradient change in the gradient before the occurrence of final maxima (case 4(b)) can be seen (denoted by a four-point orange star) with the magnitude of detailed coefficients suddenly decreasing and then increasing. This highlights the sensitivity of the detailed coefficients to sudden changes in the ECG, thus, it is significant to denoise the raw ECG before applying to the FDMI blocks otherwise a noisy part in the QRS complex may be detected as a notch. Hence, baseline wandering removal and denoising is essential for the accurate detection of morphology in the QRS complex.

The sampling rate of the ECG signal is crucial while performing the f-QRS detection, if the sampling rate of ECG is low, then the probability of detecting the discontinuities in the QRS complex will be less due to its low time resolution. Sampling frequency of 2 kHz will be suitable for the FDMI algorithm implementation.

The importance of sampling frequency can be observed with an example, Fig. 14a (i) (ii) shows the interpolated QRS complex and the original QRS, which have high and less time resolution respectively, Fig. 14a (iii) (iv) shows the bar plot of detailed coefficients corresponding to interpolated and original QRS complex respectively. From the figures, it can be observed that the increasing number of samples helps to identify the undetectable notches. The undetectable notch will lead to an inaccurate count of notches; hence morphology will lead to an improper diagnosis. Figure 14b (iii) Follow the patterns shown in Fig. 11, when patterns of A1 and A3 are found, it identifies the presence of notch but, if the patterns like A2 and A4 are found, it is tough to interpret whether this pattern should be considered as a notch or an extremum pair. If magnitude criteria are not considered, then the maximum would be identified as a notch, and its peak is identified as maxima. Hence, it is necessary to have the magnitude criteria to find the difference between the notch and the extrema.

6 Conclusion

This chapter emphasis processing the ECG signal to extract the essential clinical features in low-complex fashion and detect cardiovascular diseases. The topics covered in this chapter are three-folded. Firstly, detecting boundaries of individual ECG beats from the continuous ECG signal using the BD algorithm. Secondly, a low-complex ECG feature extraction algorithm is performed on each ECG beat to extract the morphological features (including, amplitude, duration, polarity, and shape) of

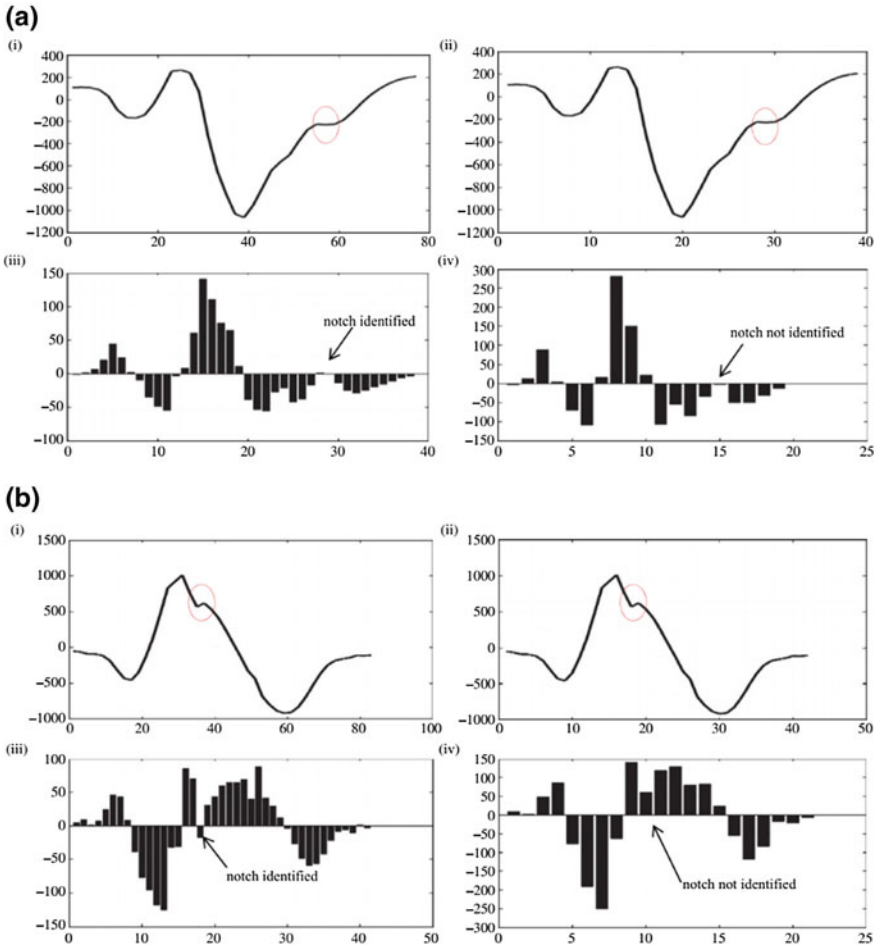

Fig. 14 Importance of QRS complex interpolation and magnitude criteria

characteristic waves such as P-wave, QRS-complex, T-wave, and the interval features between the characteristic waves by reusing the same module present in the proposed BD methodology. Thirdly, fragmented QRS (f-QRS) complex reuses the module present in the BD and acts as an efficient bio-marker to detect the ECG abnormalities occurring due to the discontinuities present in the QRS complex, FD module gives the details of the number of notches, maximas and minimas present, this count is applied as input to MI module to identify the morphology of the QRS complex by extracting the time instance of discontinuities. Low-complexity is achieved by reusing the DWT module with Haar function as the basis allows for a significant reduction in the computational complexity compared to other DWT based approaches. Several test cases of healthy and unhealthy from PTBDB, MIT-DB,

IITHDB are considered to validate the algorithms and achieved the accuracy levels suitable for clinical relevance.

References

1. Wikipedia Contributors: 'Electrocardiography', Wikipedia, The Free Encyclopedia. https://en.wikipedia.org/w/index.php?title=Electrocardiography&oldid=875817847 (2018)
2. Baltazar, R.: Basic and Bedside Electrocardiography. Lippincott Williams & Wilkins (2009)
3. Willems, I., CSE Working Party: Recommendations for measurement standards in quantitative. ECG Eur. Hear. J. **6**, 815–825 (1985)
4. World Health Organization: Cardiovascular Diseases (CVDs), World Health Organization, 26 Sept. www.who.int/cardiovascular_diseases/en/ (2018)
5. Vemishetty, N., et al.: Low power personalized ECG based system design methodology for remote cardiac health monitoring. IEEE Access **4**, 8407–8417 (2016)
6. Van Helleputte, N., et al.: A 345 μW multi-sensor biomedical SoC with bio-impedance, 3-channel ECG, motion artifact reduction, and integrated DSP. IEEE J. Solid-State Circuits **50**(1), 230–244 (2015)
7. Yan, L., Harpe, P., Pamula, V.R., Osawa, M., Harada, Y., Tamiya, K., Van Hoof, C., Yazicioglu, R.F.: A 680 nA ECG acquisition IC for leadless pacemaker applications. IEEE Trans. Biomed. Circuits Syst. **8**(6), 779–786 (2014)
8. Naresh, V., et al.: An on-chip robust real-time automated non-invasive cardiac remote health monitoring methodology. In: 41st Annual International Scientific Conference on Computing in Cardiology (CinC 2014), pp. 249–252. Cambridge, Massachusetts (2014)
9. Myers, J., Prabhat, P., Savanth, A., Yang, S., Gaddh, R.: Design challenges for near and sub-threshold operation: a case study with an ARM Cortex-M0 + based WSN subsystem. In: 2016 26th International Workshop on Power and Timing Modeling, Optimization and Simulation (PATMOS), pp. 56–63. IEEE (2016)
10. Tsai, T., Hong, J., Wang, L., Lee, S.: Low-power analog integrated circuits for wireless ECG acquisition systems. IEEE Trans. Inf Technol. Biomed. **16**(5), 907–917 (2012)
11. Ng, K.A., Chan, P.K.: A CMOS analog front-end IC for portable EEG/ECG monitoring applications. IEEE Trans. Circuits Syst. I Regul. Pap. **52**(11), 2335–2347 (2005)
12. Hsu, Y., Liu, Z., Hella, M.M.: A 1.8 μW −65 dB THD ECG acquisition front-end ic using a bandpass instrumentation amplifier with class-ab output configuration. IEEE Trans. Circuits Syst. II: Express Briefs **65**(12), 1859–1863 (2018)
13. Mazomenos, E.B., Biswas, D., Acharyya, A., Chen, T., Maharatna, K., Rosengarten, J., Morgan, J., Curzen, N.: A low complexity ECG feature extraction algorithm for mobile health care applications. IEEE Trans Biomed. Health Inform. **17**, 459–469 (2013)
14. Chen, T., Mazomenos, E.B., Maharatna, K., Dasmahapatra, S., Niranjan, M.: Design of a low-power on-body ECG classifier for remote cardiovascular monitoring systems. IEEE J. Emerg. Sel. Top. Circuits Syst. **3**(1), 75–85 (2013)
15. Vemishetty, N., Jain, A., Amber, A., Acharyya, A.: A low complexity architecture for online on-chip detection and identification of f-QRS feature for remote personalized health care applications. In: Fifth International Symposium on Electronic System Design (ISED), pp. 120–124. Surathkal (2014)
16. Vemishetty, N., Jadhav, P., Adapa, B., Acharyya, A., Pachamuthu, R., Naik, G.R.: Affordable low complexity heart/brain monitoring methodology for remote health care. In: 37th Annual International Conference of the IEEE Engineering in Medicine and Biology Society (EMBC), pp. 5082–5085. Milan (2015)
17. Mazomenos, E., Chen, T., Acharyya, A., Bhattacharya, A., Rosengarten, J., Maharatna, K.: A time-domain morphology and gradient based algorithm for ECG feature extraction. In: IEEE International Conference on Industrial Technology, pp. 117–122 (2012)

18. Satija, U., Ramkumar, B., Manikandan, M.S.: Real-time signal quality-aware ECG telemetry system for IoT-based health care monitoring. IEEE Internet Things J. **4**(3), 815–823 (2017)
19. Satija, U., Ramkumar, B., Manikandan, M.S.: Automated ECG noise detection and classification system for unsupervised healthcare monitoring. IEEE J. Biomed. Health Inform. **22**(3), 722–732 (2018)
20. Friesen, G.M., et al.: A comparison of the noise sensitivity of nine QRS detection algorithms. IEEE Trans. Biomed. Eng. **37**(1), 85–98 (1990)
21. Clifford, G.D.: ECG statistics, noise, artifacts, and missing data. In: Advanced Methods and Tools for ECG Data Analysis, pp. 55–99. Artech House, Norwood, MA, USA (2006)
22. Van Alste, J.A., Schilder, T.S.: Removal of base-line wander and power-line interference from the ECG by an efficient FIR filter with a reduced number of taps. In: IEEE Trans. Biomed. Eng., BME **32**(12), 1052–1060 (1985)
23. Maharatna, K., Bonfiglio, S.: Systems Design for Remote Healthcare. Springer Science & Business Media (2013)
24. Weng, B., Velasco, M.B., Barner, K.E.: ECG denoising based on the empirical mode decomposition. In: Proceedings of the 28th IEEE EMBS Annual International Conference New York City, USA, pp. 1–4 (2006)
25. Sayadi, O., Shamsollahi, M.B.: ECG denoising with adaptive bionic wavelet transform. In: 28th Annual International Conference of the IEEE Engineering in Medicine and Biology Society. EMBS '06, pp. 6597–6600 (2006)
26. Arafat, M.A., Hasan, M.K.: Automatic detection of ECG wave boundaries using empirical mode decomposition. In: IEEE International Conference on Acoustics, Speech and Signal Processing, ICASSP 2009, pp. 461–464. IEEE (2009)
27. Pan, J., Tompkins, W.J.: A real-time qrs detection algorithm. IEEE Trans. Biomed. Eng. **32**(3), 230–236 (1985)
28. Andreão, R.V., Dorizzi, B., Boudy, J.: ECG signal analysis through hidden Markov models. IEEE Trans. Biomed. Eng. **53**(8), 1541–1549 (2006)
29. Guilak, F.G., McNames, J.: A Bayesian-optimized spline representation of the electrocardiogram. Physiol. Meas. **34**(11), 1467 (2013)
30. Homaeinezhad, M.R., ErfanianMoshiri-Nejad, M., Naseri, H.: A correlation analysis-based detection and delineation of ECG characteristic events using template waveforms extracted by ensemble averaging of clustered heart cycles. Comput. Biol. Med. **2014**(44), 66–75 (2014)
31. Gao, P., Zhao, J., Wang, G., Guo, H.: Real time ECG characteristic point detection with randomly selected signal pair difference (RSSPD) feature and random forest classifier. In: 2016 IEEE 38th Annual International Conference of the Engineering in Medicine and Biology Society (EMBC), pp. 732–735 (2016)
32. Li, C., Zheng, C., Tai, C.: Detection of ECG characteristic points using wavelet transforms. IEEE Trans. Biomed. Eng., **42**, 21–28 (1995)
33. Martinez, J., Almeida, R., Olmos, S.: A wavelet-based ECG delineator: evaluation on standard database. IEEE Trans. Biomed. Eng., **51**, 570–581 (2004)
34. Hamilton, P.S., Tompkins, W.J.: Quantitative investigation of QRS detection rules using the MITIBIH arrhythmia database. IEEE Trans. Biomed. Eng. **33**(12), 1157–1165 (1986)
35. Maheshwari, S., Acharyya, A., Puddu, P.E., Mazomenos, E.B., Leekha, G., Maharatna, K., Schiariti, M.: An automated algorithm for online detection of fragmented QRS and identification of its various morphologies. J. R. Soc. Interface **10**(89), 20130761 (2013)
36. Chen, H.C., Chen, S.W.: A moving average based filtering system with its application to real-time QRS detection. In: Computers in Cardiology, 2003, pp. 585–588. Thessaloniki Chalkidiki, Greece (2003)
37. Gad, M.M.A.: Feature extraction of electrocardiogram signals using discrete sinc transform. In: 9th Biomedical Engineering International Conference (BMEiCON), pp. 1–4. Laung Prabang (2016)
38. Kuzilek, J., Kremen, V., Soucek, F., Lhotska, L.: Independent component analysis and decision trees for ECG holter recording de-noising. PLoS ONE **9**(6), e98450 (2014)

39. Wiklund, U., Akay, M., Niklasson, U.: Short-term analysis of heart-rate variability of adapted wavelet transforms. IEEE Eng. Med. Biol. Mag. **16**(5), 113–118 (1997)
40. Mishra, S., Das, D., Kumar, R., Sumathi, P.: A power-line interference canceler based on sliding DFT phase locking scheme for ECG signals. IEEE Trans. Instrum. Meas. **64**(1), 132–142 (2015)
41. Velchev, Y., Boumbarov, O.: Wavelet transform based ECG characteristic points detector. In: International Scientific Conference Computer Science, vol. 1, pp. 22–25 (2008)
42. Rincon, F., Recas, J., Khaled, N., Atienza, D.: Development and evaluation of multilead wavelet-based ECG delineation algorithms for embedded wireless sensor nodes. IEEE Trans. Inf Technol. Biomed. **15**(6), 854–863 (2011)
43. Chivukula, K.B., Vemishetty, N., Jagirdar, A., Acharyya, A.: A low-complexity on chip real-time automated ECG frame identification methodology targeting remote health care. In: 2014 Fifth International Symposium on Electronic System Design (ISED), pp. 125–129 (2014)
44. Take, Y., Morita, H.: Fragmented QRS: what is the meaning? Indian Pacing Electrophysiol. J. **12**(5), 213–225 (2012)
45. Varriale, P., Chryssos, B.E.: The RSR′ complex not related to right bundle branch block: diagnostic value as a sign of myocardial infarction scar. Am. Heart J. **123**(2), 369–376 (1992)
46. Das, M.K., Michael, M.A., Suradi, H., Peng, J., Sinha, A., Shen, C., Mahenthiran, J., Kovacs, R.J.: Usefulness of fragmented QRS on a 12-lead electrocardiogram in acute coronary syndrome for predicting mortality. Am. J. Cardiol. **104**(12), 1631–1637 (2009)
47. Haukilahti, M.A.E., Eranti, A., Kentta, T., Huikuri, H.V.: QRS fragmentation patterns representing myocardial scar need to be separated from benign normal variants: hypotheses and proposal for morphology based classification. Front. Physiol. **7**, 653 (2016)
48. Das, M.K., Khan, B., Jacob, S., Kumar, A., Mahenthiran, J.: Significance of a fragmented QRS complex versus a Q wave in patients with coronary artery disease. Circulation **113**, 2495–2501 (2006)
49. Pietrasik, G., Goldenberg, I., Zdzienicka, J., Moss, A.J., Zareba, W.: Prognostic significance of fragmented QRS complex for predicting the risk of recurrent cardiac events in patients with Q-wave myocardial infarction. Am. J. Cardiol. **100**(4), 583–586 (2007b)
50. Pietrasik, G., Goldenberg, I., Zdzienicka, J., Moss, A.J., Zareba, W.: Prognostic significance of fragmented QRS complex for predicting the risk of recurrent cardiac events in patients with Q-wave myocardial infarction. Am. J. Cardiol. **100**(4), 583–586 (2007a)
51. Pietrasik, G., Goldenberg, I., Zdzienicka, J., Moss, A.J., Zareba, W.: Prognostic significance of fragmented QRS complex for predicting the risk of recurrent cardiac events in patients with Q-wave myocardial infarction. Am. J. Cardiol. **100**(4), 583–586 (2007c)

Other Applications

An Accelerated Computational Approach in Proteomics

Swati Bhardwaj, Venkateshwarlu Yellaswamy Gudur and Amit Acharyya

Abstract The advent of new technologies and research in the field of computational bioinformatics has revolutionized the rate of biological data generation. As a result, the contribution of data from proteomics and genomics has increased by many folds, doubling every 18 months. Thereby, the operations involved in proteomics study have become significantly compute intensive. Protein identification, a fundamental process in proteomics study, requires identification of one or more proteins from a large database of proteins. It is rigorously used for disease diagnosis and prognosis by assisting in biomarker identification and discovery for the futuristic medical prescription. Now a days, mass spectrometry is a widely used analytical tool in proteomics studies which includes peak detection and database searching as essential steps. To cope up with the ever increasing growth of biological data in the domain of proteomics, protein identification requires accelerated and efficient solutions. This chapter mainly focuses on the review of various hardware accelerated methodologies for peak detection in mass spectrometry data and database searching for strings from an algorithmic and architectural perspective in the context of protein identification.

1 Proteomics: A Generic Overview

A biological molecule or biomolecule is the generic term for molecules and ions in living organisms. Macromolecules are large biomolecules including nucleic acids, proteins, carbohydrates, and lipids. Proteins are the most abundant macromolecules

Swati Bhardwaj and Venkateshwarlu Yellaswamy Gudur have contributed equally to this chapter.

S. Bhardwaj · V. Y. Gudur · A. Acharyya (✉)
Department of Electrical Engineering, Indian Institute of Technology, Hyderabad 502285, India
e-mail: amit_acharyya@iith.ac.in

S. Bhardwaj
e-mail: ee14resch11018@iith.ac.in

V. Y. Gudur
e-mail: ee15resch02009@iith.ac.in

G. Naik (ed.), *Biomedical Signal Processing*, Series in BioEngineering,
https://doi.org/10.1007/978-981-13-9097-5_16

in the human body. They are indispensable agents serving crucial functions in all the biological processes [1, 2]. They play an integral role in several physiological functions, including metabolism, immunity, growth control, tissue repair, transportation and storage of other molecules like oxygen, etc. They also function as catalysts, membranes, enzymes, and play crucial structural and functional roles.

Amino acids are the basic building blocks of proteins, and the immense diversity and properties of proteins are substantiated by the unique characteristics of these amino acids. Proteins are also called linear polymers of amino acids. There are 20 amino acids in human body, and every protein is composed of these amino acids. The amino acids in proteins are linked together by chemical bonds called peptide bond. The peptide bond is formed when the carboxyl group of one amino acid reacts with the amino group of another amino acid. A short chain of two or more amino acids is called peptide, and a chain of a large number of amino acids is called polypeptide. Protein consists of one or more polypeptide chains. Therefore, proteins are long chains of amino acids held together by peptide bonds [1, 2].

Proteomics is a generic term used for the large-scale study of proteins, especially their structure and physiological roles or functions. The term proteome was coined by Marc R. Wilkins in 1994, an Australian scientist, and the term proteomics first appeared in 1997. The human blood serum and plasma contain a mixture of various proteins. These proteins and their constituents in the blood are directly related to the physiological and functional features of the body. Their relative abundance and modification may precisely reflect the disease or infection status of different organs inside the human body. Therefore, the systematic analysis and study of the proteins are useful for prediction, diagnosis, prognosis, treatment, and prevention for a variety of diseases [3–5].

The basis for disease diagnosis using clinical chemistry is bestowed by the concept that many diseases manifest themselves by changes in human physiology [6]. It has been established that the presence of various pathologies is substantiated by misregulations in proteins [7]. The protein signatures acting as biomarkers can directly reflect the status of a disease. Thus, protein identification and a comprehensive examination of various changes in the proteins is the key to the diagnosis of various health disorders.

In disease diagnosis using proteomics study, protein identification is an integral part. Protein identification is the process to identify and characterize the protein in the given serum sample. In layman terms, it identifies the sequence of amino acids of the protein. As described earlier, protein identification leads to a comprehensive study of the protein by understanding its sequence, structure, and functionality. It is widely being used for clinical studies of various domains including cancer, cardiovascular diseases, organ transplant, neuromuscular disease, etc. [8–10]. In addition, it is also being used for early detection of diseases, disease-tailored therapeutic targets, personalized therapy and genetic medicine [3–6, 8, 11, 12].

In this chapter, we briefly introduce proteomics followed by protein identification involving mass spectrometry. In Sect. 2, preprocessing of mass spectrometry data using Independent Component Analysis (ICA) and string matching in protein databases are discussed. The need for accelerated approaches in proteomics is dis-

cussed in Sect. 3. In Sect. 4, accelerated solutions with detailed hardware architectures for ICA and string matching are discussed followed by the respective computational analysis in Sect. 5.

2 Mass Spectrometery Analysis for Protein Identification

Proteomic research and protein identification require the analysis of large-volume of protein data with high-throughput methodologies. Mass spectrometry (MS) has emerged as a powerful tool for proteomic research enabling high-speed analysis, sensitivity, and selectivity [13]. It is a widely used technique for detecting proteins or peptides in mixtures obtained from biological samples like serum or plasma. It provides immense potential for the proteomic study of disease detection and helps to identify the targeted drugs at the protein or peptide level [6, 8, 11, 13]. MS is used over a wide range of applications involving various biomolecules. It is extensively used in the domain of tissue biopsy, disease-tailored therapeutic targets, food adulteration, environmental observation, diagnosis and treatment of cancer, etc [5–8].

In the proteomics studies, proteins are digested into peptides and later analyzed by mass spectrometry. Proteins can be identified either by a single stage of mass spectrometry, called peptide mass fingerprinting (PMF) or by using two stages, called tandem MS or MS/MS. The analysis of MS data can be done using two approaches, peptide mass fingerprinting (PMF) and MS/MS followed by de novo sequencing. In PMF followed by database searching, generally, a protein is digested using enzymes like trypsin, chymotrypsin, etc. and the generated pattern of peptide masses is correlated with the peptide sequences that are obtained from the in-silico digestion of the database proteins. This approach is applicable only when the peptides corresponding to the m/z values of the unknown peptides are pre-existing in the database. In de novo sequencing the amino acid sequence of the unknown peptides is determined from the mass spectrum. In this approach, a purified sample is subjected to proteolytic digestion using enzymes like trypsin, chymotrypsin, Lys-C, etc. The peptides obtained after digestion undergoes through MALDI and tandem MS analysis. The isolated peptide ions in the first MALDI MS stage are further subjected to MS analysis to determine the amino acid sequence. The amino acid sequences are searched in protein databases using string matching operation to identify proteins or to obtain relevant information from databases [13–15].

Mass to charge (m/z) ratios of the peptides is determined using MS. In the proteomic analysis using MS, one of the essential steps is to extract peptide peaks from the raw MS spectra. Peak detection is a feature extraction step which further leads to protein identification, and discovery of biomarkers for disease detection [16, 17]. Initially, the raw data obtained must be converted to discrete peaks that can be used in a database search. However, it is a very challenging process to detect the peak from the raw data collected from MS and to finally conclude the peptide or protein identification. The acquired spectra from MS have complex features, as they are composed of a number of overlapping peaks having different amplitudes that quantify the abun-

dance of the peptides. Usually, MS spectra are contaminated by biological or physical artifacts, including the background noise and the baseline trend [16]. Peak-detection methods with high accuracy and sensitivity are needed to separate peptide signals from the noise and artifacts. Therefore, various algorithms facilitating the identification of the peaks corresponding to the true peptide signals have been proposed in the literature for analyzing MALDI-TOF data [16–21]. However, the problem of the potential detection of noise peaks as desired signals was not completely resolved, which is a bottleneck for the development of reliable tools for biomarker discovery using proteomics analysis and early disease diagnosis [22].

An Independent Component Analysis (ICA) based approach for the processing of proteomic signals and extracting the protein profiles from MALDI-TOF MS data was proposed in [23]. In the context of ICA, the mass spectra are considered as the observed mixed signals where the protein profiles are assumed to be independent of each other and correspond to the independent source signal components. Each independent source signal should contain a single peak or multiple peaks that are up-scaled or down-scaled by the same factor across the mass spectra. As a basic requirement for the ICA problem, the number of mass spectra needed for the ICA decomposition should be at least equal to the number of expected peptides. Therefore, ICA with high dimensions is used for proteomic data analysis, for separating the artifacts and for direct resolution of the protein signals. This ICA based method was validated by Mantini et. al. on simulated data for separating protein peaks, without significant signal distortion in [23]. ICA based protein identification method was found more reliable and reduced the false discovery rate of protein peak masses than the state-of-the-art classical methods in terms of peak detection [23].

String matching is a versatile operation employed at various stages of the bioinformatics pipelines including searching genome databases and mass spectrometry based proteomics study where database search parameters are controlled for searching of peptide tags. Online data analysis is a part of hypotheses-driven tandem mass spectrometry (hdMS/MS). HdMS/MS need to perform data analysis under a strict real-time limits [24, 25]. In LC-MS/MS based shotgun proteomics, the precursor ion selection is an important task to reduce the number of MS/MS peaks in the analysis. The peptide sequences are used to avoid redundant computations and searches and thereby reducing the time consumption. In these applications, peptides derived from the mass spectrometry data are either searched in protein databases or proteins obtained from genome translated in all six reading frames. There is a need for accelerated solutions to analyse the evergrowing proteomic and genomic databases, as discussed in the next section.

3 Need for Accelerated Approaches in Proteomics

Recent technological advancements and research in high-throughput next-generation sequencing methods have contributed a large amount of genomics data to the life science society, and it is growing at an exponential rate doubling every 18 months,

surpassing Moore's law in electronics [26]. Furthermore, due to the advancements in liquid chromatography and mass spectrometry, mass spectra data in proteomics is also growing at a very high rate [27]. As a result of the increasing growth of data in genomics and proteomics, various operations of bioinformatics involving this data have become computationally intensive and time consuming. As discussed in the previous section, the operations for MS data analysis like independent component analysis and string matching need immediate attention for designing efficient methodologies addressing the problems arising as a result of the huge data growth [23, 28].

In the field of computational bioinformatics various computationally intensive algorithms are accelerated using high-performance computing solutions including multiprocessors, multicore CPUs, clusters, cloud and grid computing, etc. These solutions involve a large computational infrastructure and thereby making their management very costly [29]. Hence, research is emphasized on cost-effective hardware accelerators including field programmable gate arrays (FPGAs). In literature, high-density FPGAs are reported to employ for efficient implementation and acceleration of various computationally intensive algorithms in bioinformatics [30, 31]. Hardware acceleration using FPGAs is achieved in numerous domains like signal preprocessing using ICA, pairwise sequence alignment, resequencing, gene-sequence analysis, multiple sequence alignment, read assembly in genomics, the study of homologous sequences, DNA sequencing, database searching, etc. [30, 31].

In mass spectrometry based proteomic data analysis, peak detection is an essential step for subsequent analysis. ICA forms an integral part of proteomics using mass spectrometry. The aforementioned applications, require hand-held devices that perform the necessary computations on-the-fly. ICA has wide-ranging applications across multiple domains like biomedical signal separation for EEG, ECG, EMG [32–37], fetal heart sound extraction [38, 39], speech and audio processing [40, 41] and protein identification [23] to name a few. The need for unobtrusiveness, portability, speed, and power-efficiency demanded by these devices have imposed speed, area and power constraints on the design. Various algorithms for ICA have been proposed over a period of time. FastICA (FICA) algorithm proposed in [42] is the most commonly used algorithm as it is faster than the other state-of-the-art ICA algorithms [43, 44] in terms of convergence speed.

FICA involves various complex arithmetic operations such as square root, matrix multiplications, and division operations. It comprises two steps—Preprocessing and fixed-point Iteration. A low complex algorithm-architecture optimization approach to eliminate the computationally complex operations using COordinate Rotation DIgital Computer (CORDIC) was presented in [45]. This makes use of a single 2D CORDIC engine recursively to perform nD FICA, resulting in hardware saving and thereby makes it suitable for resource constrained applications. The method illustrated in [45] uses entirely sequential operations for computing each fixed point Iteration step iteratively for all the n vector, hence drastically increasing the overall computation time. So, there is a need to explore the possibilities for accelerating the FICA algorithm by reducing the number of computation steps required by removing the redundant steps on the architectural-algorithmic level.

Hardware acceleration in string matching is useful in various disciplines including biomarker discovery, basic local alignment search tool, proteogenomic mapping, homologous series detection, sequence alignment and sequence similarity in homology, etc. [14, 46, 47]. Aho-Corasick algorithm (ACA) is one of the most popular multi-pattern string matching algorithms [28]. In the literature, various research groups have reported the applications of Aho-Corasick algorithm in computational bioinformatics. Brudno et al. (2003) used a simplified version of ACA in the fast alignment of large genomic sequences [48]. The SITEBLAST algorithm by Michael et al. (2004), uses ACA for local alignment of genomic sequences [49]. Hyyrö et al. (2005) have reported that ACA performs best from various string matching algorithms to locate unique oligonucleotides from DNA databases [46]. In the protein identification pipeline, Alex et al. (2005) used ACA for matching peptides obtained using mass spectrometry in DNA databases [50]. Parallelly, Dandass et al. used ACA in genome annotation using proteomics data called proteogenomic mapping where peptides obtained in mass spectrometry are matched in a genome database translated in all six reading frames [51].

In bioinformatics, very often there is a need for completing string matching in strict time constraints. These include various domains like searching genome databases for nucleotide sequences, proteome databases for amino acid sequences, hypotheses-driven tandem mass spectrometry (hdMS/MS), LC-MS/MS based shotgun proteomics, etc. where the search operation has to be completed in stipulated time to avoid data pile up and match with the rate of data generation [15, 24, 25, 48, 49, 52]. In conventional FPGA based hardware accelerators design for string matching, the design-steps involve commercial tools and require hundreds of seconds for executing synthesis, implementation, and configuration file generation [53–55]. This approach is limited with drawbacks at instances where the patterns are generated at a higher rate than the reconfiguration time of FPGAs [24, 25, 50]. The reconfiguration of FPGAs is a time-consuming task and involves dedicated computer systems and technical expertise to handle sophisticated proprietary tools. To match with the data rate of high-throughput technologies and to provide an efficient solution for the computationally intensive string matching operation there is an utmost requirement for alternate accelerated methodologies.

4 Hardware Acceleration in Protein Identification

Mass spectrometry (MS/MS) analysis of a substantial proteomic study can generate hundreds of gigabytes of raw mass spectrometry data. In order to effectively address the bottlenecks of huge data analysis for proteomic studies, high-performance and accelerated computing resources are essential. In the previous section, we have seen that there is a need for a hardware accelerator for ICA and string matching architecture and algorithms to facilitate low-cost, high speed solution for protein identification. In this section, we will study the accelerated approaches at the algorithmic and architectural level to meet the evergrowing need for high throughput technologies in the field of proteomics.

4.1 Independent Component Analysis for Proteomics

Mass spectrometry analysis is based on the measurement of mass to charge (m/z) values, present in the MS spectra. As briefly explained in Sect. 2, for reliable protein identification the raw MS data is preprocessed using methods like baseline removal, denoising, normalization, and peak detection [16] as various artifacts are also mixed with the MS data. These artifacts may be the result of other peptides and chemicals eluting from the chromatographic column, degradation (i.e., mass reduction) of peptides in the mass analyzer and airborne contaminants. The analyzed MS spectra have multiple overlapping peaks with a large variation that makes them difficult to be solved with the typically available methods. Proteomic studies using MS require data analysis where little or no prior information on the composition of a sample is available, resulting in a typical case of a Blind Source Separation (BSS) problem. The use of BSS for mass spectra separation using Principal Component Analysis (PCA) [56, 57] and Independent Component Analysis (ICA) [23, 58, 59] have been well explored in the literature. The components estimated by PCA may contain negative values as PCA does not impose any constraints on non-negativity. However, the components of the real mass spectra are non-negative, which makes PCA non-effective for MS data analysis [56, 57]. The protein identification method based on ICA was found to be more reliable than the state-of-the-art classical methods in terms of peak detection [23].

As discussed in Sect. 3, ICA has many applications in the biomedical signal processing, genomics, and protein profiling [23, 58, 59]. ICA can separate the statistically independent source signals in the domain of protein identification. To meet the need for high-throughput technologies and the ever-growing proteomic data, low complex hardware accelerators are needed for peak detection and protein identification without sacrificing accuracy. This motivated the researchers to develop the architectural-algorithmic holistic approach for hardware accelerators using CORDIC and Vector cross product [60, 61]. In continuation to the CORDIC based methodology proposed for *n*D FICA by Acharyya et. al. in [45], Bhardwaj et al. proposed an accelerated yet low complex FICA methodology termed as Hybrid FICA [60, 61].

4.1.1 Mathematical Overview of Independent Component Analysis

FICA attempts to solve the basic problem of BSS comprising of a system of n independent sources, where n is the number of expected peptides found in the protein mixture in context to proteomics. The basic representation of FICA can be expresses is as follows:

$$\mathbf{X} = \mathbf{AS} \tag{1}$$

where $\mathbf{X}$ is a matrix with n mixed signal vectors or MS spectra in context to proteomics, $\mathbf{S}$ is a matrix with n statistically independent source signal vectors or independent peptide signals in context to proteomics, out of which no more than one is

Gaussian distributed, and $\mathbf{A}$ is the $n \times n$ mixing matrix used to obtain $\mathbf{X}$ from $\mathbf{S}$ [62]. $\mathbf{X}$ and $\mathbf{S}$ are $n \times L$ matrix with each row denoted by $\mathbf{x_i}$ and $\mathbf{s_i}$ respectively and can be expressed as $\mathbf{X} = \{\mathbf{x_i}\}$ and $\mathbf{S} = \{\mathbf{s_i}\}$, $i \in [1, n]$. $\mathbf{x_i}$ and $\mathbf{s_i}$ in turn can be expressed as $\mathbf{x_i} = \{x_{i,j}\}$ and $\mathbf{s_i} = \{s_{i,j}\}$, $j \in [1, L]$, where L is the frame-length of each signal.

As mentioned earlier, FICA consists of Preprocessing and Iteration steps [62]. The aim of the preprocessing is to do centering and whitening of the mixed signals. The mixed signals with zero mean and unit variance are obtained after preprocessing by using centering, covarience and EVD which can be implemented using CORDIC [44, 63]. For the sake of brevity, the discussion about preprocessing is omitted here as the focus is on FICA Iteration, the inputs to which are available after preprocessing. The Iteration step takes the centered and whitened signals ($\mathbf{Z}$) and computes an estimate ($\mathbf{S^{est}}$) of the original sources by finding an $n \times n$ unmixing matrix $\mathbf{W}$. This is expressed as:

$$\mathbf{S^{est}} = \mathbf{W^T Z} \tag{2}$$

$$\mathbf{W} = \begin{bmatrix} w_{1,1} & w_{2,1} & \cdots & w_{n,1} \\ w_{1,2} & w_{2,2} & \cdots & w_{n,2} \\ \vdots & \vdots & & \vdots \\ w_{1,n} & w_{2,n} & \cdots & w_{n,n} \end{bmatrix} \tag{3}$$

The ith column of $\mathbf{W}$ represents the weight vector $\mathbf{w_i}$ used to estimate the ith independent component ($i \in [1, n]$). The fixed-point FICA Iteration introduces a contrast function to maximize the non-Gaussianity and hence maximizing the independence of the sources. Considering Kurtosis-based contrast function, $\mathbf{w_i}$ is updated at the end of every iteration as shown [62]:

$$\mathbf{w_i}^{new} = E\{\mathbf{Z}(\mathbf{w_i}^T \mathbf{Z})^3\} - 3\mathbf{w_i} \tag{4}$$

The vector update step is followed by orthogonalization of $\mathbf{w_i}$ with respect to all the previously computed unit vectors $\underline{\mathbf{w}}_\mathbf{j}^c$, $\forall i \in [2, n]$, $j \in [1, i-1]$ (where c stands for the converged vector), in order to ensure that different $\mathbf{w_i}$ do not converge to the same maxima. This can be achieved by Gram Schmidt Orthogonalization which is expressed as:

$$\mathbf{w_i}^{orth} = \mathbf{w_i}^{new} - \sum_{j=0}^{i-1} (\mathbf{w_i}.\mathbf{w_j}^c)\underline{\mathbf{w}}_\mathbf{j}^c \tag{5}$$

where "_" indicates *normalized value* henceforth. Orthogonalization is followed by normalization of the vector as shown:

$$\underline{\mathbf{w}}_\mathbf{i}^{new} = \frac{\mathbf{w_i}^{orth}}{\|\mathbf{w_i}^{orth}\|} \tag{6}$$

After normalization, a convergence check is performed to ascertain if $\mathbf{w_i}^{orth}$ is in the same direction as $\mathbf{w_i}$. If not, the entire process (4)–(6) is repeated. The FICA Iteration procedure is carried out until $i = n$, following which $\mathbf{S_{est}}$ can be computed using $\mathbf{W}$ as shown in (2).

The computationally expensive nature of the arithmetic operations in (2), (4), and (6) prompted the introduction of CORDIC to provide a low-complex hardware mapping for 2D FICA in [45]. Considering clockwise rotation, the fundamental CORDIC expressions can be given as follows:

$$\begin{bmatrix} x_f \\ y_f \end{bmatrix} = \begin{bmatrix} \cos\theta & \sin\theta \\ -\sin\theta & \cos\theta \end{bmatrix} \begin{bmatrix} x_0 \\ y_0 \end{bmatrix} \tag{7}$$

where the initial vector (x_0, y_0) is rotated by an angle θ to obtain the final vector (x_f, y_f) [64–68]. This fundamental 2D CORDIC can be used iteratively in the Rotation and Vectoring modes of operation to perform generic nD FICA. This section summarizes the aforementioned procedure in terms of its mathematical formulation that is essential for understanding the proposed methodology. Interested readers can refer to [45] for a detailed description of the architecture.

The following concise notations for x_f, y_f, and θ in (7) were introduced in [45] for brevity: $x_f = Rot_x(x_0, y_0, \theta)$, $y_f = Rot_y(x_0, y_0, \theta)$, $\theta = Vec_\theta(x_0, y_0)$ and $\|(x_0, y_0)\| = Vec_x(x_0, y_0)$. Expanding (4) for n dimensions, we get:

$$w_{i,k}^{new} = E\left[z_{k,j} \left(\sum_{p=1}^{p=n} z_{p,j} \underline{w}_{i,p} \right)^3 \right] - 3\underline{w}_{i,k} \tag{8}$$

where $w_{i,k}^{new}$ is the kth component of $\mathbf{w_i}^{new}$, $\underline{w}_{i,k}$ is the kth component of the unit vector $\underline{\mathbf{w}}_\mathbf{i}$ $(i, k \in [1, n])$, and $j \in [1, L]$. Expressing $\underline{\mathbf{w}}_\mathbf{i}$ in polar form gives rise to the following terms:

$$\begin{aligned} R_{x,j}^{2D} &= Rot_x(z_{1,j}, z_{2,j}, Vec_\theta(w_{1,1}, w_{1,2})) \\ V_\theta^{2D} &= Vec_\theta(\underline{w}_{1,1}, \underline{w}_{1,2}),\ V_x^{2D} = Vec_x(\underline{w}_{1,1}, \underline{w}_{1,2}) \\ R_{x,j}^{nD} &= Rot_x(z_{1,j}, R_{x,j}^{(n-1)D}, Vec_\theta(w_{1,n}, V_x^{(n-1)D})) \\ V_\theta^{nD} &= Vec_\theta(\underline{w}_{1,n}, V_x^{(n-1)D}),\ V_x^{nD} = Vec_x(\underline{w}_{1,n}, V_x^{(n-1)D}) \end{aligned} \tag{9}$$

The vector update step in (4) can now be performed by recursive use of the fundamental 2D CORDIC as follows:

$$w_{i,k}^{new} = E\left[z_{k,j} \{R_{x,j}^{nD}\}^3 \right] - 3\underline{w}_{i,k} \tag{10}$$

To map the normalization step in (6) onto the same CORDIC, $[x_0 \ \ y_0]$ in (7) were replaced with $[0 \ \ 1]$. The outputs $\begin{bmatrix} x_f & y_f \end{bmatrix}$, therefore, become $[\sin\theta \ \ \cos\theta]$, which are the normalized components of $[x_0 \ \ y_0]$.

The following terms were defined to obtain generalized expressions for nD normalization.

$$\begin{aligned} V_x^{2D} &= Vec_x(w_{i,1}^{orth}, w_{i,2}^{orth}),\ V_x^{kD} = Vec_x(w_{i,k}^{orth}, V_x^{(k-1)D}) \\ V_\theta^{2D} &= Vec_\theta(w_{i,1}^{orth}, w_{i,2}^{orth}),\ V_\theta^{kD} = Vec_\theta(w_{i,k}^{orth}, V_x^{(k-1)D}) \\ R_x^{(k-1)D} &= Rot_x(0, R_x^{kD}, V_\theta^{kD}),\ R_x^{nD} = Rot_x(0, 1, V_\theta^{nD}) \\ R_y^{(k-1)D} &= Rot_y(0, R_x^{kD}, V_\theta^{kD}),\ R_y^{nD} = Rot_y(0, 1, V_\theta^{nD}) \end{aligned} \tag{11}$$

where $k \in [3, n]$. The normalized vector $\underline{\mathbf{w}}_\mathbf{i}^{new}$ of an nD vector $\mathbf{w_i}^{orth}$ can now be obtained as follows:

$$\underline{w}_{i,k}^{new} = \begin{cases} Rot_y(0, R_x^{3D}, V_\theta^{2D}) & \text{if } k = 1 \\ Rot_x(0, R_x^{3D}, V_\theta^{2D}) & \text{if } k = 2 \\ Rot_y(0, R_x^{(k+1)D}, V_\theta^{kD}) & \text{if } k \in [3, n-1] \\ Rot_y(0, 1, V_\theta^{nD}) & \text{if } k = n \end{cases} \tag{12}$$

Finally, the estimation step in (2) was expressed in terms of CORDIC operations by replacing $\underline{\mathbf{w}}_\mathbf{i}$ in (9) with the converged ith weight vector $\underline{\mathbf{w}}_\mathbf{i}^c$. The estimation of the ith independent component $\mathbf{s_i^{est}} = \{s_{i,j}^{est}\}$ $(j \in [1, L])$ is given by:

$$s_{i,j}^{est} = Rot_x(z_{n,j}, R_{x,j}^{(n-1)D}, Vec_\theta(\underline{w}_{i,n}^c, V_x^{(n-1)D})) \tag{13}$$

4.1.2 Acceleration by Exploiting Algorithmic Redundancies for Independent Component Analysis

The procedure for CORDIC-based nD FICA illustrated in the previous subsection based on [45] computes the weight vectors in an entirely sequential manner, reusing the same 2D CORDIC engine over multiple levels to realize the highly complex operations involved in each stage of FICA Iteration. The iterative use of a single unit of CORDIC contributes to the overall low complexity of the architecture. Each stage of FICA Iteration still involves a significant number of clock cycles to compute the expressions in (4)–(6). The number of clock cycles taken by one level of CORDIC rotation will depend on the frame-length L, as the samples of each signal $\mathbf{z_i}$ have to be fed sequentially to the CORDIC block. As there are $(n-1)$ levels of CORDIC Rotation Mode (CRM) for nD FICA according to (10), one vector update step requires $(L(n-1) + N_{cordic})$ cycles, where N_{cordic} is the CORDIC latency. In addition, each Iteration stage involves Gram Schmidt orthogonalization, CORDIC-based normalization, and convergence check, each of which further contributes to the total computation time [45].

As proposed in [61], reducing the computation time of FICA needs observation of all the steps involved. FICA Iteration requires orthogonalization of each $\mathbf{w_i}$ after every update step to ensure maximum de-correlation between the computed vectors

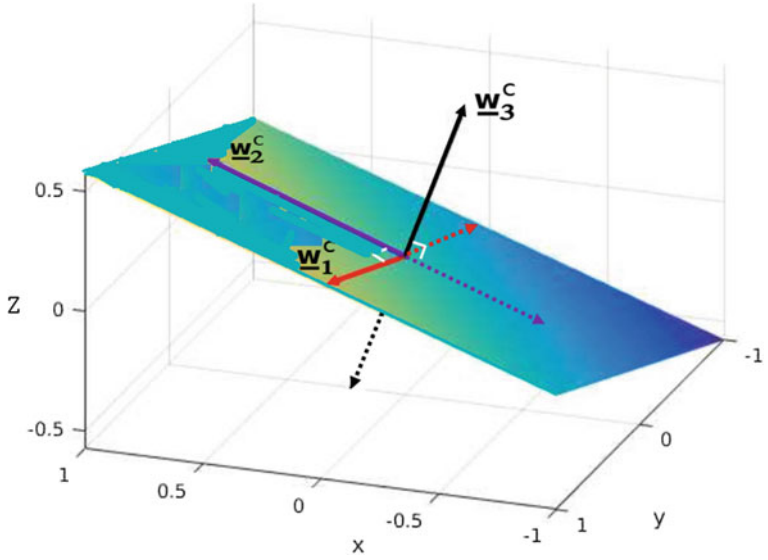

Fig. 1 The results obtained by performing conventional FICA on mixtures of three independent signals generated in Matlab

as evident from (5) and (6). Figure1 shows the unmixing vectors obtained after performing conventional 3D FICA in Matlab. It can be inferred from this figure that $\underline{\mathbf{w}}_3^c$ is perpendicular to the plane containing $\underline{\mathbf{w}}_1^c$ and $\underline{\mathbf{w}}_2^c$. We know that, a cross product operation performed on two vectors $\mathbf{v_1}$ and $\mathbf{v_2}$ in $\mathbf{R}^3$, results in a vector that is mutually perpendicular to both $\mathbf{v_1}$ and $\mathbf{v_2}$ [69, 70]. The direction of $\underline{\mathbf{w}}_3^c$ can be directly obtained by performing a cross product operation on $\underline{\mathbf{w}}_1^c$ and $\underline{\mathbf{w}}_2^c$. Also, the orthogonalization in FICA is always followed by the normalization, so the converged vectors $\underline{\mathbf{w}}_1^c$ and $\underline{\mathbf{w}}_2^c$ in Fig. 1 are of unit magnitude. Therefore, the magnitude of the result obtained by taking the cross product of $\underline{\mathbf{w}}_1^c$ and $\underline{\mathbf{w}}_2^c$ can be expressed as:

$$\begin{aligned} \|\underline{\mathbf{w}}_1^c \times \underline{\mathbf{w}}_2^c\| &= \|\underline{\mathbf{w}}_1^c\| \cdot \|\underline{\mathbf{w}}_2^c\| \cdot \sin \pi/2 \\ &= \|\underline{\mathbf{w}}_1^c\| \cdot \|\underline{\mathbf{w}}_2^c\| = 1 \end{aligned} \tag{14}$$

This signifies that a cross product operation on $\underline{\mathbf{w}}_1^c$ and $\underline{\mathbf{w}}_2^c$ results in not only the direction but also the exact value of the required unit vector $\underline{\mathbf{w}}_3^c$ without having to perform normalization separately. Extending the same concept to n dimensions, it can be inferred that a cross product operation on the orthonormal vectors $\underline{\mathbf{w}}_1^c, \underline{\mathbf{w}}_2^c, \ldots, \underline{\mathbf{w}}_{\mathbf{n-1}}^c$ will directly yield the final vector $\underline{\mathbf{w}}_\mathbf{n}^c$ [69, 70] as shown:

$$\underline{\mathbf{w}}_{\mathbf{n}}^{c} = \begin{vmatrix} \mathbf{e_1} & \mathbf{e_2} & \cdots & \mathbf{e_n} \\ \underline{w}_{1,1}^{c} & \underline{w}_{1,2}^{c} & \cdots & \underline{w}_{1,n}^{c} \\ \underline{w}_{2,1}^{c} & \underline{w}_{2,2}^{c} & \cdots & \underline{w}_{2,n}^{c} \\ \vdots & \vdots & & \vdots \\ \underline{w}_{n-1,1}^{c} & \underline{w}_{n-1,2}^{c} & \cdots & \underline{w}_{n-1,n}^{c} \end{vmatrix} \tag{15}$$

where $|.|$ represents **determinant** operation, $\mathbf{e_1}, \ldots, \mathbf{e_n}$ represent the unit vectors in $\mathbf{R^n}$, and $\underline{w}_{i,j}^{c}$ represents the jth component of the ith converged vector $\underline{\mathbf{w}}_{\mathbf{i}}^{c}$, $\forall i \in [1, n-1]$, $j \in [1, n]$.

Obtaining $\underline{\mathbf{w}}_{\mathbf{n}}^{c}$ through cross product requires only the $(n-1)$ previously converged vectors as opposed to the entire mixed signal matrix $\mathbf{Z}$ that is required in (4) and (10). This eliminates the process of feeding L inputs sequentially to $(n-1)$ levels of 2D CORDIC, and can substantially reduce the overall time required for computing $\underline{\mathbf{w}}_{\mathbf{n}}^{c}$. In addition, there is now no need to perform orthogonalization, normalization, and convergence check, as $\underline{\mathbf{w}}_{\mathbf{n}}^{c}$ is already orthonormal to all the other vectors by virtue of the mathematical rules governing cross product. In other words, eliminating the nD hybrid FICA algorithmic redundancy proposed in [61], the result of carrying out the operations in (4)–(6) over multiple iterations can now be attained by simply computing a vector cross product, thereby eliminating the entire stage of FICA Iteration required for computing $\underline{\mathbf{w}}_{\mathbf{n}}^{c}$. The architecture details to Hybrid FICA will be discussed in the next subsection.

Although, [61] provides acceleration, but vector cross product requires huge area corresponding to the extra hardware resulting in area overhead for higher dimension Hybrid FICA, adding to the hardware complexity. In [71] paper, the authors tried to explore the algorithmic redundancies without adding any extra architectural hardware complexity, resulting in low complex and accelerated nD FICA architectural design methodology termed as Simplex FICA. Motivated by this fact, as part of preliminary study, Bhardwaj et al. introduced the basic concept of Simplex FICA in [72] and extended the work further to [71] to propose an nD Simplex FICA methodology, in which a significant gain in computation time without adding any area overhead to the CORDIC-based FICA presented in [45]. It is to be noted, that the scope of nD Simplex FICA methodology is not limited only to the CORDIC based FICA implementation proposed in [45], but it can be easily adopted by any FICA implementation techniques resulting in significant acceleration.

Simplex FICA uses a different approach to compute nth weight vector [71]. It is illustrated as follows.

Let us consider the case of 3D FICA as shown in Fig. 1. To ensure that there is maximum de-correlation between the vectors, the update step in FICA Iteration stage should be followed by orthogonalization of each $\mathbf{w_i}$ as observed from (5) and (6). If the three unmixing vectors are given by $\underline{\mathbf{w}}_{\mathbf{1}}^{c}$, $\underline{\mathbf{w}}_{\mathbf{2}}^{c}$, and $\underline{\mathbf{w}}_{\mathbf{3}}^{c}$, then $\underline{\mathbf{w}}_{\mathbf{3}}^{c}$ has to be orthogonal to the plane containing $\underline{\mathbf{w}}_{\mathbf{1}}^{c}$ and $\underline{\mathbf{w}}_{\mathbf{2}}^{c}$. After computing $\underline{\mathbf{w}}_{\mathbf{1}}^{c}$ and $\underline{\mathbf{w}}_{\mathbf{2}}^{c}$ (using the iterative stages of update, orthogonalization, normalization and convergence check), the only possible direction for the third unmixing vector $\underline{\mathbf{w}}_{\mathbf{3}}^{c}$ is perpendicular to the plane containing $\underline{\mathbf{w}}_{\mathbf{1}}^{c}$ and $\underline{\mathbf{w}}_{\mathbf{2}}^{c}$. The direction for $\underline{\mathbf{w}}_{\mathbf{3}}^{c}$ can be obtained by orthogonalizing

the starting value of $\underline{\mathbf{w}}_3$ with respect to $\underline{\mathbf{w}^c}_1$ and $\underline{\mathbf{w}^c}_2$ as per (5). Since $\underline{\mathbf{w}}_1^c$, $\underline{\mathbf{w}}_2^c$ and the starting value of $\underline{\mathbf{w}}_3$ are already normalized, orthogonalization of $\underline{\mathbf{w}}_3$ will result in the required unit vector $\underline{\mathbf{w}}_3^c$. This will entirely eliminate the FICA Iteration stage for computing $\underline{\mathbf{w}}_3^c$.

Extending the same concept to n dimensions, it can be inferred that orthogonalization of the starting random value of $\underline{\mathbf{w}}_n$ with the orthonormal vectors $\underline{\mathbf{w}}_1^c \ldots \underline{\mathbf{w}}_{n-1}^c$, will directly yield the final vector $\underline{\mathbf{w}}_n^c$. Unlike the state-of-the-art methods for computing $\underline{\mathbf{w}}_n^c$ which require the entire mixed signal matrix $\mathbf{Z}$ for computing (4) and (10), Simplex FICA uses only orthogonalization which is performed using GSO. GSO requires only the $(n-1)$ previously converged vectors $\underline{\mathbf{w}}_1^c \ldots \underline{\mathbf{w}}_{n-1}^c$. If a normalized random vector is fed as an initial random vector corresponding to w_n, there will be no need to perform normalization step after orthogonalization step. Hence, by using the proposed methodology, the overall computation time required for $\underline{\mathbf{w}}_n^c$ computation reduces significantly, hereby eliminating the normalization step and the need to process L sequential inputs for the update step. Furthermore, convergence check is not needed, as $\underline{\mathbf{w}}_n^c$ is already orthonormal to all the pre-computed vectors. To summarize, computing the operations in (4)–(6) iteratively for $\underline{\mathbf{w}}_n^c$ calculation is equivalent to single GSO step, eliminating the need for entire update step, normalization step and convergence check step for $\underline{\mathbf{w}}_n^c$ computation. The advantage of this approach lies in the fact that the reduction of computation time comes with no additional hardware overhead, as the same resources which are required for executing the previous stages can be used for the last stage as well. We can conclude that Simplex FICA methodology exploited the following redundancies in the existing conventional FICA algorithm to facilitate acceleration:

- The iterative update step for nth FICA iteration becomes redundant and unnecessary.
- The normalization step becomes redundant for nth stage (enhancement over [72]).
- Convergence check for nth FICA iteration becomes unnecessary.

4.1.3 Detailed Architecture of the Accelerated Independent Component Analysis

This subsection gives the detailed architecture of the FICA methodologies discussed in the previous subsection namely nD Hybrid FICA and nD Simplex FICA. The hardware architecture implements ion for Hybrid FICA in [61] is presented in Fig. 2. Figure 2a shows the top-level view of the proposed architecture. All the samples of the input mixed signals are stored in the Memory Bank using separate data memories. Temporary memory is used to store intermediate CRM outputs, which are to be used during the next level of CORDIC. The Control Unit (CU) enables each block when necessary, and is responsible for proper synchronization and interfacing of all the blocks to maintain a cycle-accurate design. CU also keeps track of the current CORDIC level to provide the appropriate inputs and passes the outputs of the last level of CORDIC to Update Unit where the vector update step is performed. Gram-Schmidt orthogonalization, Kurtosis-based vector update, and nD Cross Product

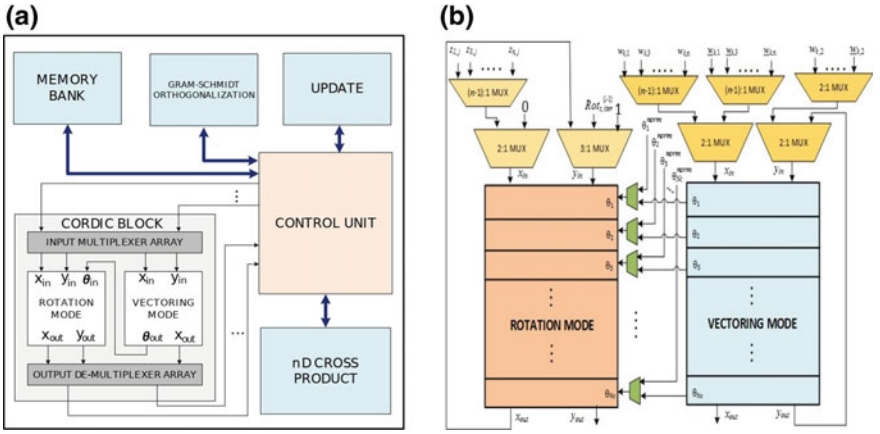

Fig. 2 **a** Top level block diagram of the architecture for nD Hybrid FICA. **b** Doubly-pipelined architecture for CORDIC rotation and vectoring mode

computation are all performed in the respective blocks shown. Outputs from the Update Unit is once again orthogonalized, and the whole iterative process is repeated until the corresponding weight vector converges or when the maximum number of iterations is reached. Inputs to CORDIC pass through a multiplexer array that sends selected signals to CRM and CORDIC Vectoring Mode (CVM), and the outputs are similarly de-multiplexed before being sent to the Control Unit. Since normalization requires only the CORDIC outputs [45], it is performed within the Control Unit itself. After computing $\underline{\mathbf{w}}^c_{\mathbf{n-1}}$, the Cross Product unit is activated to directly compute $\underline{\mathbf{w}}^c_{\mathbf{n}}$.

It is important to ensure that the hardware complexity of ICA computation is not much increased by the introduction of the Vector Cross Product operation. Hence, the generic low-complexity algorithm for nD cross product computation proposed in [73] is followed. The architecture used in [61], uses symmetry based implementation for 4D cross product as the fundamental unit [73]. To avoid the use of extra hardware intensive arithmetic units for 4D cross product, resource-sharing of the multiplies used for Gram-Schmidt Orthogonalization Unit in Fig. 2a is done. Therefore, Hybrid FICA proposed in [61] attains greater speed by making use of the same resources that are present in state-of-the art FICA implementation methodologies.

Figure 2b shows the implementation of CVM and CRM. The angle computed in CVM by adding/subtracting the micro-angles obtained at each micro-rotation stage is to be provided to CRM where it is again broken down into micro-angles. To avoid this redundancy, we make use of the doubly-pipelined architecture [74], which directly feeds the micro-angles obtained at every micro-rotation stage in CVM to the corresponding micro-rotation stage in CRM. However, during normalization, CRM is activated only during the last level of CVM [45]. Hence, we improvise the doubly-pipelined architecture by inserting a multiplexer between each micro-rotation stage of CRM and CVM as shown in Fig. 2b. The micro-angles obtained from CVM during normalization (denoted by $\theta_i^{norm}, i = 1, 2, \ldots, N_C$) are stored in a register.

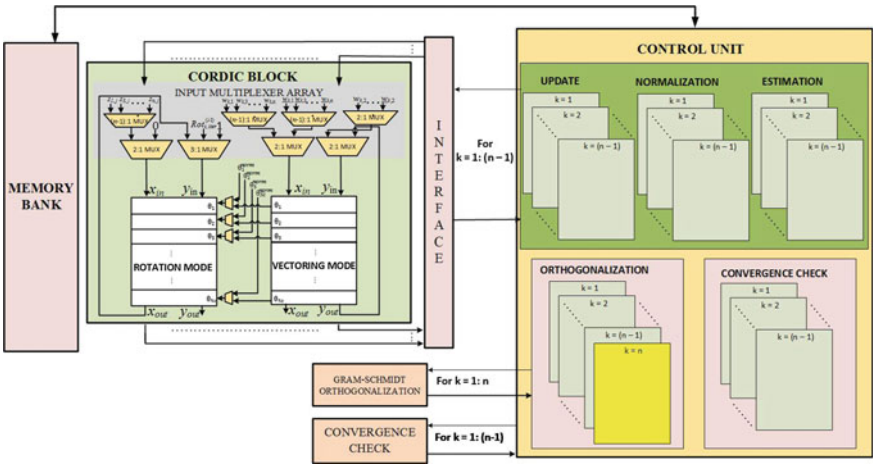

Fig. 3 Top level architectural detail diagram for nD simplex FICA

Each of these is provided as one of the inputs to the multiplexer of the corresponding micro-rotation stage whose other input is the micro-angle coming directly from CVM. The samples $z_{1,j}, z_{2,j}, \ldots, z_{n,j}$ of the preprocessed signals required during the vector update stage, and the values 0 and 1 required during normalization stage are multiplexed appropriately before being given to x and y inputs of CRM. In addition, the x-output of CRM can be directly fed to its y-input for the next level during normalization, while during vector update the x-output corresponding to each sample is stored in a temporary memory from which it is read and given as the y-input to CRM (indicated by $Rot_{x,iter}^{(l-1)}$). Similarly, the values of $\mathbf{w_k}(k = 1, 2, \ldots, n-1)$ required during normalization, and their normalized values required during an update and estimation stages are multiplexed and provided as the x and y inputs of CVM. The x-output of CVM is fed back to its y-input.

In addition to the architecture proposed in [45], an extra hardware module for $n\,D$ cross product is introduced in [61] for algorithmic and architectural improvement, as shown in Fig. 2a. Figure 2b is partially derived from [45] for CORDIC based implementation for $\mathbf{w_1^c}$ to $\mathbf{w_{n-1}^c}$ computation. Further, the CORDIC Block is shown in Fig. 2a is disabled for $\mathbf{w_n^c}$ computation.

Top level block diagram for a low complex accelerated architectural methodology for nD Simplex FICA is shown in Fig. 3. The architecture for Simplex FICA for w_1 to $w_{(n-1)}n$ computation is similar to that of Hybrid FICa as described earlier. The input mixed signal samples are stored in a Memory Bank. The intermediate CRM outputs are stored in temporary memory. Separate GSO block is used for computing the orthogonalization. Normalization, Update and estimation steps are performed using the CORDIC engine. The corresponding inputs to all the steps are generated from the Control Unit (CU) when necessary. Convergence check for all the computed weight vector after every iteration stage is performed in Convergence check block for $\underline{\mathbf{w_k}}$ where, k = 1 : (n − 1). As discussed earlier for w_n computation

only one orthogonalization step (GSO), with respect to the previously computed $w_1, w_2, \ldots w_{n-1}$ is performed. It can be noted that the proposed method is not limited to using only GSO for orthogonalization. Any orthogonalization scheme can very well be adopted. The CU ensures the proper synchronization and interfacing of all the blocks for maintaining a cycle-accurate design by enabling the various blocks at the right time. Though Bhardwaj et al. have used the CORDIC based FICA given in [45] for implementing the proposed methodology, but the proposed methodology is equally valid for any other FICA implementation.

4.2 Accelerated Approaches in String Matching

String matching is one of the most popular functions in text processing applications in which locations of strings/patterns are identified in a given database text. It is extensively used in the field of computational and information systems, with many real-world applications including web search engines, intrusion detection, information retrieval, word processing, pattern recognition, finding locations of nucleotides and amino acids in bioinformatics, etc. [14, 47, 48, 75]. Various algorithms are present in the literature that performs the operation of string matching. Depending on the number of patterns that are simultaneously searched, these algorithms can be broadly classified into a single pattern or multi-pattern matching algorithms. These include brute force searching, Knuth-Morris-Pratt algorithm, Boyer-Moore algorithm, Rabin-Karp algorithm, Aho-Corasick algorithm, Commentz-Walter algorithm, etc.

4.2.1 Hardware-Software Codesign Based Methodology for Accelerated String Matching

Hardware-software codesign is a concurrent, interconnected and coordinated design of a system that includes both hardware and software modules/components and they interact with each other to perform a complete task [76]. In the codesign based approach for system design, the desired functionality is achieved by partitioning the system into dedicated hardware and software modules. This approach facilitates the advantages like speed, power, and parallelism of hardware and flexibility, modularity and reusability of software [76]. Design constraints are met by combining the rewards offered by both hardware and software [77]. Over many decades, the research in hardware-software codesign has evolved through a number of stages and passed through multiple approaches such as focusing on partition strategies, codesign approaches in multiprocessing, multithreading, and multicore environments, codesign architectures, etc. [77].

Recently, a new paradigm is rendered by employing system-on-chip (SoC), where all components of computing and communication of a system are available on a single chip, in hardware-software codesign [78]. This approach uses SoC FPGAs

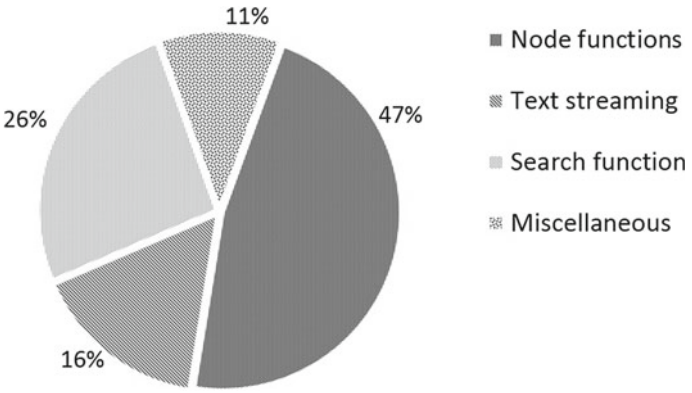

Fig. 4 Time profiling of Aho-Corasick algorithm running in software. All the values are shown as the percentage of the total time of execution of the AC algorithm

like the Zynq family from Xilinx and Stratix, Arria and Cyclone SoC families from Intel. These SoC FPGAs take away the need for standalone integrated circuits (IC) for hardware and provide a single chip solution. In addition to SoC FPGAs with on-chip ARM processors, there are a variety of softcore processors available for hardware-software codesign. These are off-the-shelf, ready to use, customizable and synthesizable processor cores that facilitate rapid prototyping and reduce the time in the design cycle. OpenRISC 1200, PicoBlaze, Leon 3 and Mico32 are open-source softcore processors while MicroBlaze, PowerPC, Nios II, and Xtensa LX are commercial softcore processors [79, 80].

Usually, in hardware-software codesign, profiling and partitioning are performed on the desired functionality of the system [76, 77]. In software profiling, the high-level description of the system functionality represented by a programming language is analyzed thoroughly for resource-intensive and time-consuming operations, functions, and tasks. This is achieved with the aid of profiling software that accurately analyze the program and provides useful insights into the various operations and functions carried in the program. In order to analyze the string matching operation using the Aho-Corasick algorithm, one of the most popular multi-pattern string matching algorithms, the time profiling operation on the algorithm implemented using C program is performed. The profiling results obtained by running the program on multiple test cases are shown in Fig. 4. It is evident that 73% of the time, a significant amount, is consumed in executing the search function and operations between the nodes of the AC finite state machine (FSM). A careful analysis of the results will lead to partition of the node functions and search function of the system into hardware, while tasks related to data control and management are assigned to software. To reconfigure the system by patterns changing with time, the functions implemented in hardware are desired to be updated quickly within the time interval by which next set of patterns is available.

Table 1 Flow of the hardware-software codeisgn methodology for string matching

Algorithm 1: Algorithmic flow of the codesign methodology for string matching
Input: Sets of patterns **S**, database for searching **dbase**
Output: locations of patterns with their ID
1: **while S** is not empty **do**
2: read patterns of set **Si** and create AC finite state machine (FSM) **-sw**
3: create a memory table for the corresponding FSM **-sw**
4: initiate hardware and transfer table to the local memory of hardware **-sw & hw**
5: perform string matching **-hw**
6: update results and communicate to the software **-hw & sw**
7: stay in standby till next set of patterns arrive **-sw & hw**
8: **end**

Abbreviations: sw—software, hw—hardware

4.2.2 Architectural Methodology for Accelerated String Matching

In the hardware-software codesign based methodology, frequently used and compute intensive functions or tasks of the underlying algorithm are offloaded to dedicated hardware while control and data management tasks are performed by software [52, 76, 77, 80]. The Substantial speedup can be achieved by employing fixed hardware accelerators for the time-consuming algorithmic and data processing tasks. The flexible software running on the processor core is well suited for executing control oriented and decision making tasks and data management. Using these guidelines, the algorithmic flow for a novel hardware-software codesign based methodology for string matching is presented in Table 1.

Given a number of sets of patterns S, the string matching operation requires to identify these patterns in the database dbase. At a given interval Ti, let Si denote a set of patterns that are changing with respect to time, while Si + 1 denotes the next set of patterns at the interval Ti + 1. The problem statement is to reconfigure the string matching system with the patterns in Si and scan the database for these patterns before the interval Ti + 1. In the methodology, the software program reads the patterns from PC or external memories and creates an AC finite state machine for these patterns. A memory table is created for the corresponding FSM using the memory based FSM implementation presented in [81]. The software program initializes the hardware accelerator and transfers the memory table of patterns to it. The string matching operation is performed by the hardware accelerator, and the search results are communicated to the software program. These steps in the flow are repetitively run for the next set of patterns of Si + 1. In the design, as soon as the patterns of Si are available, the system has to be reconfigured with them and scan the database before Si + 1 is made available. This is an essential feature of a runtime reconfigurable system.

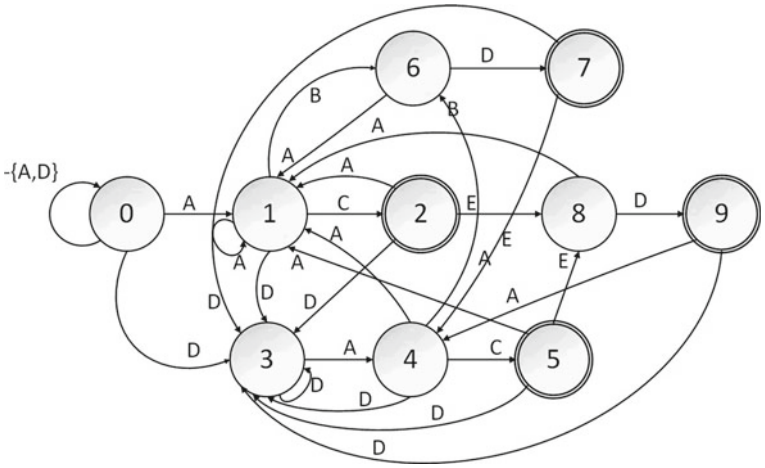

Fig. 5 Aho-Corasick FSM illustration for string matching with patterns AC, DAC, ABD and ACED

4.2.3 Memory Based FSM Implementation of Aho-Corasick Algorithm

Illustration of Aho-Corasick Algorithm

The properties of ACA including linear time complexity and the ability to simultaneously identify multiple patterns in a given text, make it advantageous than other string matching algorithms [28, 46]. Let us illustrate the ACA by considering a group of four patterns AC, DAC, ABD and ACED to be searched in a database. In the algorithm, the group of patterns is preprocessed, and an FSM is created. The searching operation is performed by passing the characters from the text or database as input to the FSM. Figure 5 shows the FSM created by ACA for the group of patterns.

In the FSM each circle is called a state or node. The initial state or root state is denoted by state 0. A character of the text is read and passed as input to the FSM and for the corresponding character, a transition of state occurs. These transitions are represented by edges or branches labelled with the corresponding character for which the transition occurs. Root state is retained when there is no matching of characters in the text while remaining states indicate partially or fully matched patterns. A double circled state indicates a valid pattern match. All the edges are made up of normal and failure transitions. Normal transitions occur when specific characters from the text are matched with the patterns, while failure transitions are useful for finding the patterns that overlap with other patterns. For the sake of simplicity, failure transitions to the root node are not represented in the diagram.

Memory Based Aho-Corasick FSM Implementation

Memory based implementation of FSM is the technique to realize the FSM using memories. Recently there are various advances in FPGA technologies including the on-chip memory growth. As a result, memory based implementation of FSMs

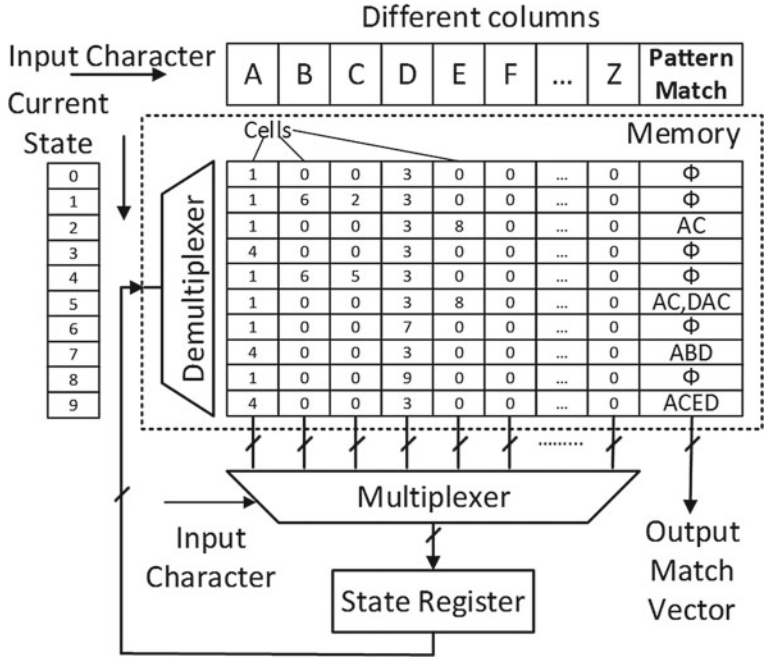

Fig. 6 Hardware details of the block RAM based Aho-Corasick FSM

on FPGAs using the on-chip memories is receiving significant research focus [81]. RAM memories including block RAM (BRAM) can be read and written during the operation runtime. This facilitates them to be employed for the implementation of different FSMs circuits. In addition to the runtime update, BRAM memories do not involve the time-consuming design steps, including synthesis, placement, and routing operations, as compared to logical elements based distributed RAM.

In a processor or computing machine, FSMs can be realized by memory tables [51, 81]. Figure 6 shows the hardware details of the block RAM based Aho-Corasick FSM for the group of patterns considered in the example. A tabular representation for realizing the FSM is also shown alongside the hardware. The string matching operation using the memory table is performed as follows. At any given time, the control is at one of the states in the FSM, and in the memory table, a row corresponding to that state is read as activated by the address generated by the state register. This row of the output of the memory is connected as inputs to the multiplexer. Out of the various inputs, which are the next states in the FSM, the multiplexer selects a particular input, i.e. state specific to the character read from the database. Let the word 'cell' denote a part of the register in memory. The inputs to the multiplexer are state-cells, while the cells corresponding to output match vectors are called output-cells. The control shifts to the next state as determined by the contents of the state register, which in turn holds the state-cell. The input character determines the transition. For

a given state, the pattern match column indicates the patterns that are matched. For a given state, no output or match is indicated by a null value in the output-cell from the pattern match column, while a non-null value indicates a match of patterns. The individual bits of the output-cell indicate their corresponding patterns matched in the database.

Memory Consumption in the Aho-Corasick FSM Implementation

The size (depth and width) of block RAM required to store the FSM table, is dependent on the size and number of patterns. For a group of S patterns each of maximum length L, the maximum number of states generated in the Aho-Corasick FSM is SL, which in turn decides the maximum depth of the block RAM. Each cell in a column excluding the cells of the pattern match column holds a state value of the FSM. The width of a state-cell is the ceiling value of log2(SL). Let the width of the pattern match column is ω bits, then for a given alphabet of α symbols, the width of each register in the block RAM is α log2(SL) + ω bits. The maximum number of bits required to represent a character from the alphabet set is decided by the value of log2(α). The value of ω decides the maximum number of overlapping patterns identified in any state. Depending on the input character symbol, an α-to-1 multiplexer selects the contents of the state-cell corresponding to that character. In other words, the input character symbol helps the transition from one state to another by activating the next state value corresponding to that character. The values of the output match vector of width ω carry the information of patterns matched in that state. For a given state, each bit in the output-cell indicates whether or not the corresponding pattern is found in the database. The values of S, L, α, and ω in the aforementioned example are 4, 4, 26 and 4 respectively. Theoretically, the value of SL is 16, but due to overlapping of certain parts of the patterns, it is 10. A block RAM of 1080 bits, width of 108 bits and depth of 10, is required to store the Aho-Corasick FSM generated by the group of patterns AC, DAC, ABD and ACED whose total size is 12 characters.

4.2.4 Hardware-Software Codesign Based Architectural Methodology for String Matching

As described earlier, the search function and the node operations of the FSM are the most time-consuming tasks in the Aho-Corasick algorithm. For an efficient design using hardware-software codesign, these tasks are well suited for acceleration using hardware. In Gudur et al. [82, 83] a novel approach for accelerated string matching that also supports fast reconfiguration by patterns changing with time is proposed. In this article, the patterns that are to be matched in the database are updated to the hardware system in real-time, and the matching operation on the database is performed in an accelerated mode using hardware-software codesign methodology. A Search Engine is designed for the Aho-Corasick FSM, and the detailed hardware architecture is shown in Fig. 7. Initially, before the start of the search operation, the block RAM in the Search Engine is configured with the data in FSM memory table by enabling memory write and memory store signals. Later, the search operation is

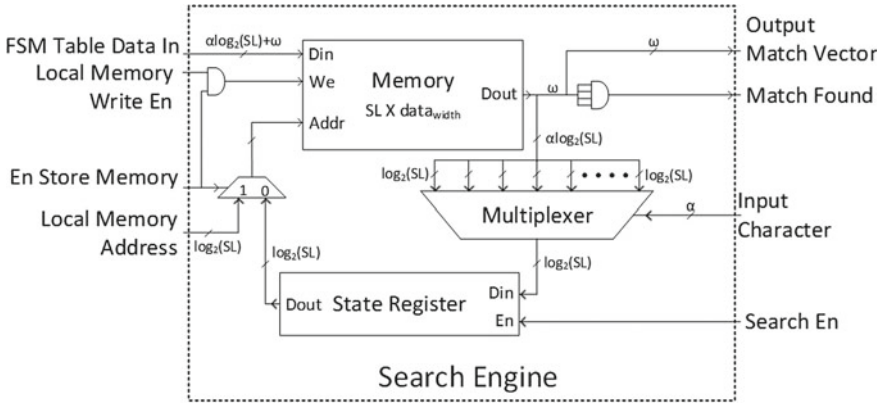

Fig. 7 Detailed hardware architecture of the search engine for AC FSM

initiated by enabling and disabling the search and memory write signals, respectively. One character at a time is read from the database, and the corresponding part of the memory output, which is a state-cell, is selected by the multiplexer. The next state address of the memory is held by a State Register connected at the output of the multiplexer, which in turn is generated by the state-cells. Bits of the Output Match Vector from the pattern match column indicates the strings that are matched in the respective states. Whenever a pattern is successfully matched, a flag is raised. In the next part, the block RAM based search engine of ACA FSM explained here is used to design the accelerated and reconfigurable string matching using hardware-software codesign.

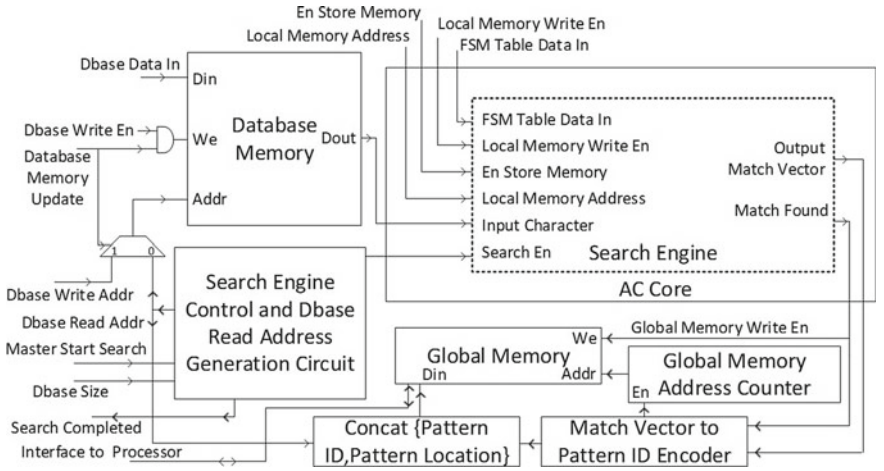

Fig. 8 Detailed hardware architecture for string matching

The detailed hardware architecture for string matching using the hardware-software codesign methodology is given in Fig. 8. The Search Engine covered in the previous section is instantiated inside an AC Core module. The module receives the data in the FSM memory table of the group of patterns and also the associated signals for controlling the local memory operations from the processor or top module where the AC core is instantiated. The Search Engine Control Logic generates the necessary signals to control the search operation in the AC core and also raises a flag for the processor whenever the search operation is completed on the given database text. A Database Memory (DM) is used to locally store the text before the search begins and it feeds the AC Core with the input characters. These characters from the database are read using the Dbase (database) Read Address Generation Circuit (DRAGC) that is used to generate the address for the DM while the searching operation is running. The bits of Output Match Vector of the AC Core indicates the patterns that are identified and they are converted to the corresponding pattern identification numbers in the Encoder. The Encoder also generates the address for the Global Memory with the help of an address counter while the concatenation circuit generates the data for this memory. The memory data input is obtained by clubbing the pattern ID and the corresponding location obtained from DRAG circuit. An interface is provided to the processor or the top module and the Global Memory to read the search results.

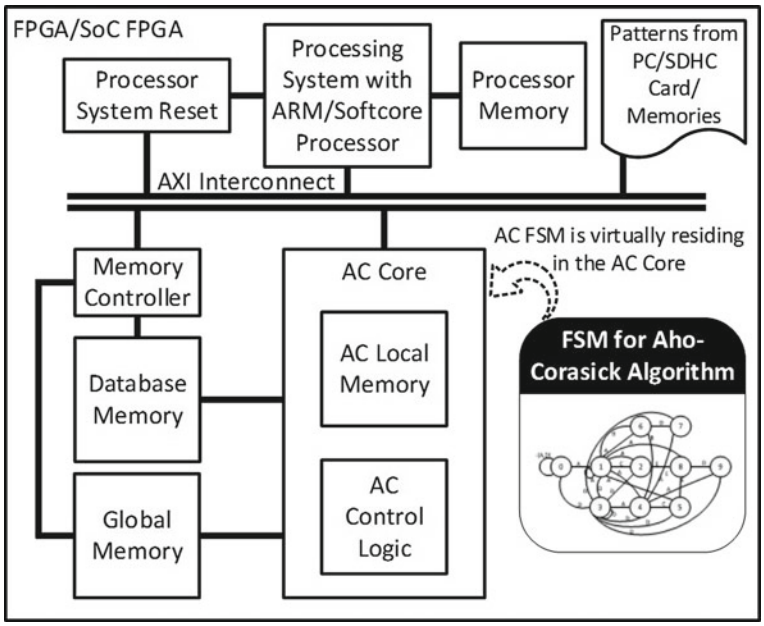

Fig. 9 System level architecture for hardware-software codesign methodology based Aho-Corasick algorithm

System level architecture for the accelerated and reconfigurable string matching using the hardware-software codesign approach is presented in Fig. 9. For ease of understanding and representation, various signals and control circuits in the above description are clubbed to form blocks representing their corresponding operations. A processing system is realized using an ARM or softcore processor. In this codesign methodology, the software part of the system is implemented using the processor. On-chip or on-board DDR memory called as Processor Memory that acts as local memory is connected to this processor for storing the compiled software instructions. Due to the limitation of on-chip memory, the DDR memory is desirable for programs that produce a large memory footprint. A synchronous reset to the entire system is provided by the Processor System Reset (PSR) block. Signals from the PSR block is used to reset all the hardware blocks in the system to their initial states. The Memory Controller facilitates a communication link between the processor and memory modules in the system. Here, Advanced Extensible Interface (AXI) memory controller is used for the AMBA AXI interconnect systems.

The AC Core block initiated by the group of patterns performs the string matching operation on the database. Memory based implementation of FSM shown in Figs. 6 and 7 are realized using the Control Logic along with the Local Memory. Depending on the contents of the state register, which holds the value of a state in the ACA FSM, a particular row is activated in the block RAM, which is used to realize Local Memory. The AC Core reads characters from the database and from this row the multiplexer selects a next state-cell value corresponding to the character. The output of the multiplexer which holds the next state is fed to the state register that acts the address for the memory. The output match vector in the activated row shows the patterns that are matched in the present state. Besides taking control actions in the AC Core, the Control Logic keeps track of the counter for the characters and value of the output match vector. The entire system is residing on an FPGA or SoC FPGA. Off-chip memories like external hard disc drives, memory cards, flash drives or any other portable memories are used to store large size databases.

The working of the system can be described as follows. The software program of the hardware-software codesign based methodology for the string matching operation is designed to read the patterns to be searched from an external Secure Digital High Capacity (SDHC) memory card or they come from a host machine. The group of patterns forms a set Si. Next, ACA FSM is generated for the corresponding patterns in the software. A memory table is created for the FSM by the software and the corresponding data is transferred to the Local Memory of the AC Core using the Control Logic. String matching operation is performed on the Database Memory by the AC Core, and the results of the search operation are updated to the processor by writing to Global Memory that is interfaced to the processor. It is evident that the AC Core is substituted for the AC algorithm, and this module acts as the hardware accelerator.

The size of the Local Memory limits the number of patterns in Si that can be searched in a single pass. For a large number of patterns, external memory is used to replace the Local Memory. In addition, as the system creates a memory table during runtime, it also supports runtime reconfiguration. This feature can also be used as an

alternate way to search a large number of patterns. For example, if the system can search ω patterns in one pass, then initially a ω number of patterns are searched in the database followed by the next ω patterns. Direct access from the AC Core to the database and global memories, removes the latency in communication and also the overload of memory operations on the software. In addition, as soon as the FSM table is stored and the search signal is enabled, the AC Core can perform string matching without the intervention of software for memory operations.

4.2.5 Application of the Codesign Methodology for String Matching in Protein Identification

As a result of the excessively rising number of proteins, hardware accelerated solutions are used for protein identification to address the bottlenecks in the computational bioinformatics pipeline [14, 27, 50, 51, 82, 83]. To demonstrate the codesign methodology, protein identification, which is a fundamental step in protein sequence analysis is used. In protein identification using tandem mass spectrometry, one of the most common procedures, the amino acid sequences of the peptide fragments obtained by mass spectrometry are matched against the large protein databases that is similar to the operation of string matching in a database text [14, 27, 50, 51, 82, 83]. The peptides that are obtained from the proteins have grown into millions in number and in addition semi, or non-specific digestion has multiplied the number of peptides by many times [27]. To scan databases for these peptide sequences and identify a protein accurately, high-speed methods employing high-density FPGAs are necessary, which can be fulfilled by the codesign methodology. In the field of proteomics, these methods can benefit the discipline of disease biomarker identification and aid disease diagnosis and prognosis [47].

The amino acid sequences of the peptide fragments are the patterns to be searched and these are used to create Aho-Corasick FSM as explained in earlier sections. The codesign methodology is useful to search proteome databases at high speed and simultaneously supports runtime reconfiguration with varying peptides patterns. The FASTA format is used to store the proteomes in database memory. A simple binary coding is used to represent different amino acids and additional symbols of the FASTA format. For protein identification the AC core is designed to keep track of the protein ID, the peptides matched and the locations of peptides in the protein sequence. These results are stored in the global memory and updated to software via the interface, where software does post-processing like the ranking of proteins according to their scores.

4.2.6 Codesign Based String Matching System Implementation on FPGA

Zynq SoC FPGA device with an ARM processor or any FPGA with a softcore processor can be useful to accomplish the accelerated, and reconfigurable hardware-

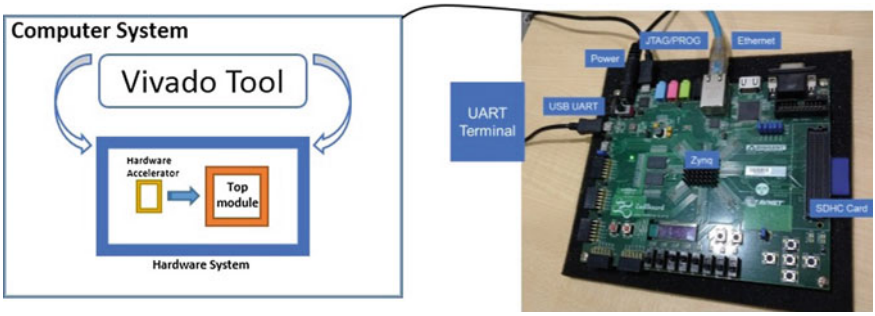

Fig. 10 A Prototype of the system implementation using Avnet Zedboard

software codesign methodology. The system designed using hardware-software codesign methodology described in earlier sections is verified using Xilinx Vivado Design Suite software tools and Avnet Zedboard development board. To examine the hardware accelerator designed in AC core, it is synthesized independently using the Vivado synthesis tool [84]. For default constraints, the maximum frequency at which the hardware accelerator can run is 316.776 MHz. Higher frequency rates can be achieved by constraining the synthesis tool more stringently at the cost of increased area and resources. The Zynq SoC FPGA has a reconfigurable hardware fabric to implement the hardware accelerator and a programmable processor to implement the software on the same chip making it an ideal choice. The system is implemented by following the embedded system design flow of the Vivado tool. Avnet Zedboard has an on board XC7Z020 SoC FPGA device, and it is used for the physical verification of the system. ARM Cortex-A9 MPCore CPU of this FPGA is employed as the processing system. The AC Core is packaged as an IP and it is interfaced with the processing system. In the system implementation on the Zedboard, patterns to be searched are read from an external SDHC memory card. An AC FSM is created for these patterns in software and converted to a memory table as explained in earlier sections. This data of the FSM memory table is stored in the local BRAM memory with the help of Control Logic. For validation of the system, on-chip memory is used for storing the database.

A prototype diagram of the system implementation on Avnet Zedboad is shown in Fig. 10. The hardware accelerator, AC core, is packaged into an IP using the Vivado tool. This custom IP is instantiated in a top module along with the ARM processing system and other essential blocks as depicted in Figs. 8 and 9. The complete hardware system is synthesized and implemented using the embedded system design flow. For interested readers, more details about embedded system design flow and custom IP packaging and an interface can be found in [84]. A bitstream file of the entire system is generated and it is used to configure the Avnet Zedboard using JTAG. A C program to implement the system using hardware-software codesign is written in SDK tool of Vivado suite following the algorithmic flow described in Table 1. The driver functions that are needed to communicate with the custom IP are written in a separate C header file. Using hardware drivers, the C program employs the hardware

accelerator for matching patterns in the databases both of which are stored on the SDHC memory card. The Zedboard configuration with the bitstream file is a one-time process as the hardware logic in the system is generic in nature and does not require to modify when patterns are changed. The results of the string matching operation can be communicated through the UART port or stored on the SDHC card. Due to the limited BRAM resources on the FPGA, the search operation on the entire database is performed in batches. When external memories are employed in place of FPGA BRAM, the entire database can be searched in a single pass. In this case, driver functions to communicate with the external memory should be written.

5 Computational Analysis

In this section, the detailed analysis of the methodologies for hardware acceleration discussed in the previous sections is presented. Various performance metrics are discussed to compare the methodologies proposed by Bhardwaj et al. and Gudur et al. [61, 71, 82, 83] with respect to the state-of-the-art methodologies.

5.1 Analysis of Accelerated Approach for Independent Component Analysis

5.1.1 Hardware Implementation and Resource Utilization

The Hybrid FICA methodology proposed by Bhardwaj et al. in [41] was implemented on Xilinx, Vertex-7 FPGA for 5D Hybrid ICA with 1024×5 samples. The design for 5D Hybrid FICA was also implemented on the ASIC platform and synthesized using Synopsys Design Compiler with UMC 90 nm standard cell libraries. The design was implemented at an operating frequency of 1 MHz, though the design was tested to work at maximum operating frequency of 176 MHz and the design was reported to consume 0.6478 mW of power at operating voltage of 1.08 V and area of 0.501 mm^2. The design was also implemented on Xilinx Vertex−7 FPGA, utilizing 14776—Slice LUTs, 13805—Registers and 331—Muxes.

FastICA has wide applications in the field of Biomedical applications, protein identification, speech processing, BCI, etc. and Hybrid FastICA is equally applicable to all the applications where conventional FastICA can be used. However, for functional validation and the practical utility of the proposed method, audio signals as shown in Fig. 11a, b, have been used for the proof of the concept. The five mixed audio signals sampled at a rate of 8 kHz are shown in Fig. 11b. To obtain a reliable comparison platform, the mixed signals were provided as inputs to the Matlab package for conventional FICA in [85] and a Matlab model of the proposed Hybrid FICA. To verify the hardware functionality of our method, a completely parameterized design aimed at generic nD Hybrid FICA with 32-bit word-length

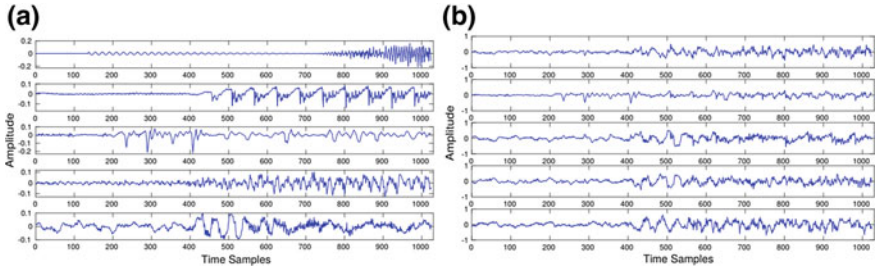

Fig. 11 **a** The original speech samples collected from 5 different sources—from top to bottom: a vehicle siren, male news-reader, female news-reader, orchestra, and a rock band. **b** The signals obtained by mixing the speech signals

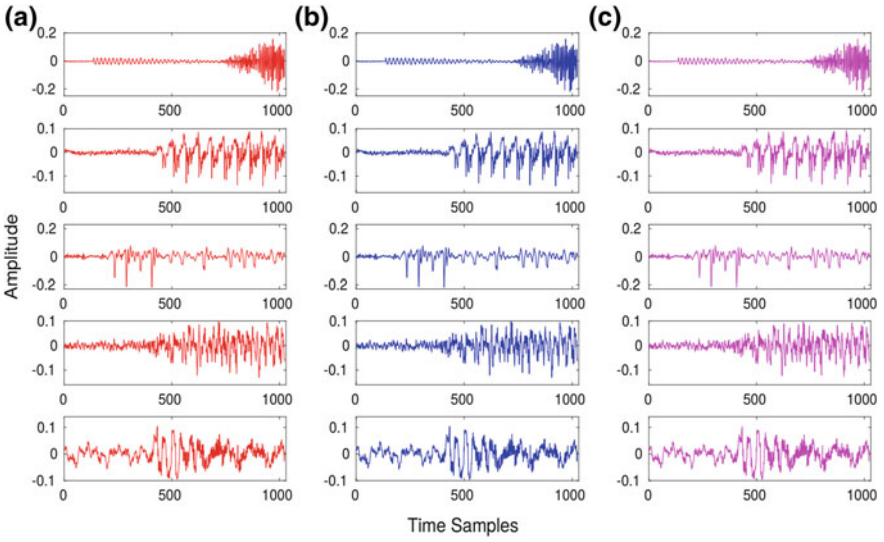

Fig. 12 **a** The original speech samples collected from 5 different sources—from top to bottom: a vehicle siren, male news-reader, female news-reader, orchestra, and a rock band. **b** The signals obtained by mixing the speech signals

was implemented using Verilog HDL and tested with the same signals used in the Matlab model (single precision floating point implementation). The mixed signals corresponding to the audio signals were input to all the three aforementioned models, and the normalized values of the estimates obtained are shown in Fig. 12a–c. It can be observed that the results obtained from both the Matlab and HDL models of Hybrid FICA match those of the conventional FICA, thereby corroborating the functional validity of the Hybrid FICA for real-time signals.

The Simplex FICA methodology proposed by Bhardwaj et al. in [71] was implemented using Verilog HDL for 6D Simplex FICA with 1024×6 samples and was synthesized on Synopsys Design Compiler using UMC 90 nm standard cell libraries.

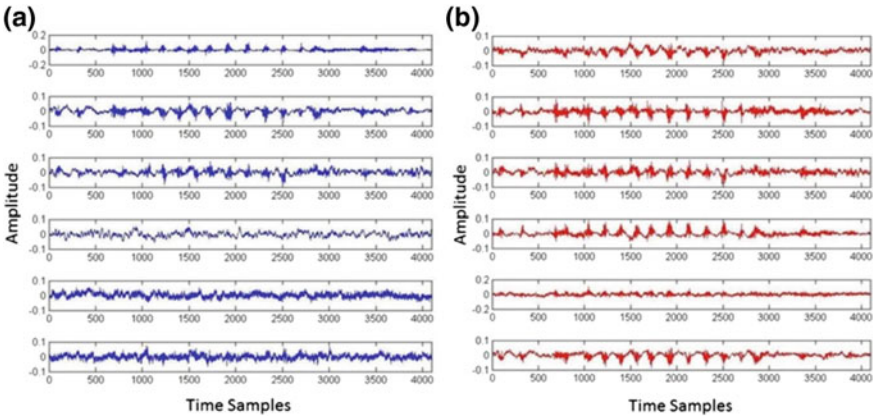

Fig. 13 **a** The EEG samples from six different sources. **b** The signals obtained by mixing the EEG signals

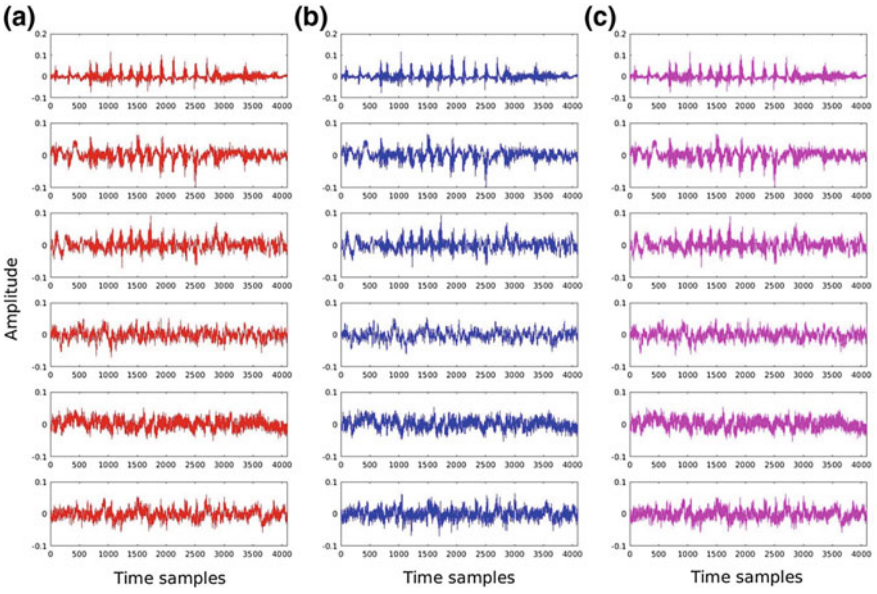

Fig. 14 **a–c** Estimated independent components obtained by performing 6D FICA for the mixed EEG signals shown in Fig. 13b using **a** Matlab model of conventional FICA, **b** Matlab model of Simplex FICA, and **c** HDL model of Simplex FICA

The design consumes 0.5703 mW of power at an operating voltage of 1.08 V and area of 0.497 mm^2 with a maximum operating frequency of 240 MHz.

For functional validation of Simplex FICA, Bhardwaj et. al. have used EEG signals although it can be validated on any biomedical signals including proteomic data

Table 2 Performance comparison with other designs

	Shyu et al. [32]	Van et al. [35]	Acharyya et al. [45]	Yang et al. [33]	Bhardwaj et al. [61]	Bhardwaj et al. [71]
Implementation approach	FPGA	ASIC	ASIC	ASIC	ASIC	ASIC
Technology	NA	90 nm	90 nm	90 nm	90 nm	90 nm
Application	Speech	EEG	Generic	ECoG	Generic	Generic
Algorithm	FastICA	FastICA	FastICA	FastICA	FastICA	FastICA
Number of channels	2	8	5	8	5	6
Maximum operating freq. (MHz)	50	100	100	11	176	240
Power dissipation (mW)	NA	16.35	0.782 @1.08V	0.0816 @0.32V	0.647	0.57036 @1.08V
Area (mm^2)	NA	1.4872	0.497	0.3969	0.501	0.497

from mass-spectrometry. The EEG signals used were taken from the Physionet [86] database which was recorded at a sampling frequency of 256 Hz. EEG data recorded from a healthy volunteer is used to validate the proposed algorithm. The EEG signals are shown in Fig. 11a, b, have been used for the proof of the concept. Figure 13a shows the six EEG signals and Fig. 13b shows the mixed EEG signals. For a reliable comparison, the method used for Hybrid FICA explained above is also used by [71]. The estimated signals obtained by using the Conventional FICA and Matlab and HDL model of Simplex FICA are plotted in Fig. 14a–c, respectively, which makes it evident that the proposed methodology is functionally correct.

Table 2 shows the comparison of accelerated methodologies for FICA namely Hybrid FICA and Simplex FICA with the state of the art designs. The area utilized for ASIC implementation of the designs using the Design Compiler can be used for comparing the area. The computation speed for Hybrid and Simplex FICA have improved significantly as will be explained further in the next subsection, whereas area of the Hybrid FICA design has increased to 0.501 mm^2 from 0.430 mm^2 in [45], as we have added the hardware corresponding to cross product. It can be noted that the area for Simplex FICA is 0.497 for 6D FICA, which is less then Hybrid FICA [61] and equal to that of [45]. We can see that the Hybrid FICA and Simplex FICA design has comparable or better area and power results with the other state-of-the-art designs as a result of addition of cross product module but the computation time for Hybrid FICA and SImplex ICA is less as compared to all the other state of the art designs as discussed in next subsection.

5.1.2 Computation Time Analysis

To obtain a generic model of the number of computation steps saved for Hybrid FICA [61], each of the steps (4)–(6) need to be considered for the nth Iteration stage

of CORDIC-based nD FICA described in (10)–(13). Denoting a number of independent components by n and number of CORDIC stages as N_{cordic}, the number of computation steps required for normalization based on CORDIC can be represented as:

$$\begin{aligned} N_{norm} &= (n-2)N_{cordic} + (n-1)N_{cordic} \\ &= (2n-3)N_{cordic} \end{aligned} \tag{16}$$

This can be derived by considering $(n-2)$ levels of CVM in feed-forward fashion [45], followed by the last level of CVM, which does not need to be counted separately since it is doubly pipelined with the first level of CRM. There are totally $(n-1)$ levels of CRM following the $(n-2)$ levels of CVM, which gives rise to the $(n-1)$ and $(n-2)$ terms in (16). The number of computation steps for CORDIC-based update step, with the frame-length L, can be expressed as:

$$N_{updt} = L(n-1) + N_{cordic} \tag{17}$$

This can be easily obtained by considering $(n-1)$ levels of doubly pipelined CVM and CRM with the L inputs to each CRM level being given sequentially. As no particular architecture for implementing Gram-Schmidt orthogonalization has been recommended, we consider N_{orth} to be a generic notation for the number of computation steps required for orthogonalizing a particular vector with a given basis vector. Therefore, the number of computation steps required for orthogonalizing $\mathbf{w_n}$ with the vectors $\underline{\mathbf{w}}_{\mathbf{1}}^{c}$ to $\underline{\mathbf{w}}_{\mathbf{n-1}}^{c}$ can be denoted as:

$$N_{orth,\mathbf{w_n}} = (n-1)N_{orth} \tag{18}$$

The number of steps required to check for convergence is denoted by N_{conv}, and may vary according to the architecture used. From (16) to (18), we can obtain the number of steps required for computing $\mathbf{w_n}$ as follows:

$$\begin{aligned} N_{\mathbf{w_n}} &= N_{norm} + N_{updt} + (n-1)N_{orth} + N_{conv} \\ &= (L + 2N_{cordic} + N_{orth})(n-1) + N_{conv} \end{aligned} \tag{19}$$

As there can be multiple iterations required to compute $\mathbf{w_n}$, the total computation steps will be:

$$N_{\mathbf{w_n},total} = i(N_{\mathbf{w_n}}) \tag{20}$$

where i is the number of iteration required. The percentage of steps saved in $\underline{\mathbf{w}}_{\mathbf{n}}^{c}$ computation can now be obtained by:

$$N_{clk\_sav\_hybrid} = \frac{N_{\mathbf{w_n},total} - N_{cp}^{nD}}{N_{\mathbf{w_n},total}} * 100 \tag{21}$$

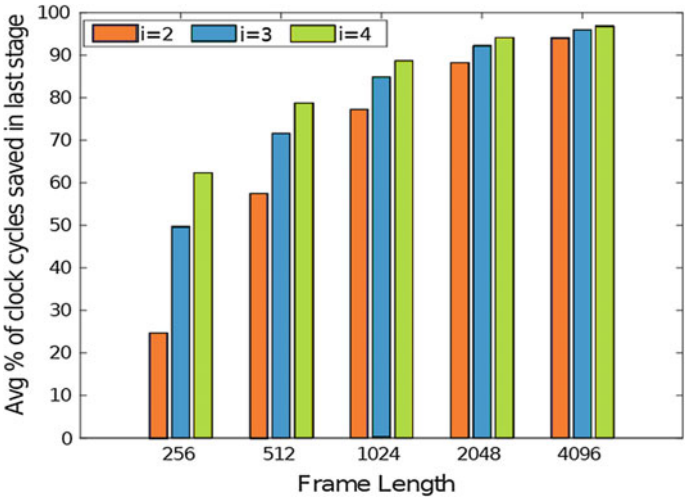

Fig. 15 Average percentage of clock cycles saved in $\mathbf{w_n}$ computation by employing Hybrid FICA in 4–7 dimensions for different values of frame-length and the number of iterations i that would have been taken by the completely CORDIC-based procedure

where N_{cp}^{nD} is the number of computation steps required for nD vector cross product computation which is implementation specific and depends on trade-offs between resources and latency.

The computation time saved in 5D Hybrid FICA performed on the speech signals was obtained by simulating its HDL model for a frame-length of 1024 samples. It was observed that 4400 clock cycles were required for one single Iteration stage required to compute $\mathbf{w_{n-1}}$, whereas the computation of $\mathbf{w_n}$ using the cross product was completed in merely 223 clock cycles. The percentage of cycles saved in the nth Iteration stage can, therefore, be given by:

$$N_{clk\_sav}^{5D} = \frac{4400i - 223}{4400i} * 100 \tag{22}$$

which is about 97% even for the least possible value of i (i.e. $i = 2$). Figure 15 shows the average percentage of clock cycles saved in the case of 4D to 7D Hybrid FICA for various frame-lengths and the number of iterations that would have been required for $\underline{\mathbf{w}}_{\mathbf{n}}^{c}$ computation without cross product. For instance, considering a frame-length of 1024 samples, let us assume that the CORDIC-based FICA would have taken 2 iterations to compute $\mathbf{w_n}$. From Fig. 15, it can be seen that the average value of the computation time savings obtained by substituting $n = 4, \ldots, 7$ in (21) is 77% of the number of cycles required for computing $\mathbf{w_n}$ without cross product. The percentage of cycles saved is further seen to increase to 85 and 88% if we assume that CORDIC-based FICA takes 3 and 4 iterations respectively to compute $\mathbf{w_n}$. Moreover, it can

be observed that the time saved by employing the proposed method significantly increases with the increase in frame-length.

For Simplex FICA presented in [71], the number of computation steps needed for w_n computation using Simplex FICA is denoted as N_{sim}^{nD} and is given by

$$N_{sim}^{nD} = N_{orth,\mathbf{w_n}} \tag{23}$$

The percentage saving of computation steps for Simplex FICA in terms of clock cycle saving for $\mathbf{w_i}$ computation, can be represented as:

$$N_{clk\_sav\_sim} = \frac{N_{\mathbf{w_n},total} - N_{sim}^{nD}}{N_{\mathbf{w_n},total}} * 100 \tag{24}$$

Using (19), (20), and (23) in (24), we get:

$$\begin{aligned} N_{clk\_sav\_sim} &= (1 - \frac{N_{orth,\mathbf{w_n}}}{N_{\mathbf{w_n},total}}) * 100 \\ &= \big(\frac{i((L+2N_C)(n-1)+N_{conv})}{N_{\mathbf{w_n},total}} \\ &+ \frac{(i-1)N_{orth,\mathbf{w_n}}}{N_{\mathbf{w_n},total}}\big) * 100 \end{aligned} \tag{25}$$

where, $N_{\mathbf{w_n},total} = i((L+2N_C)+(n-1)N_{orth}+N_{conv})$ using (19) and (20).

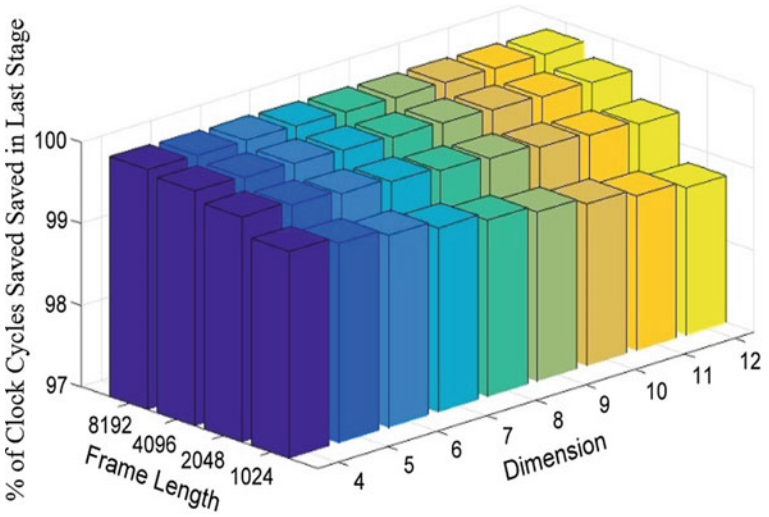

Fig. 16 Percentage clock cycles saved for $\mathbf{w_n}$ computation by using Simplex FICA with respect to the state-of-the-art design for 4D–12D with respect to different values of frame-length (L) with a fixed number of iterations ($i = 2$)

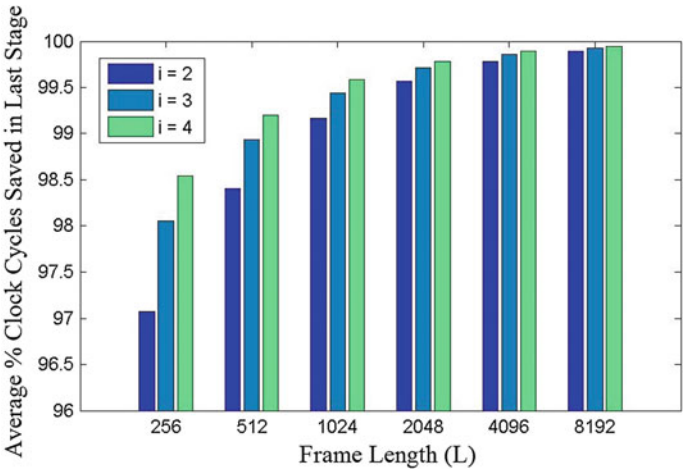

Fig. 17 Average percentage clock cycles saved for $\mathbf{w_n}$ computation by using Simplex FICA for 4D–12D with respect to different values of frame-length for varied values of the number of iterations ($i = 2, 3, 4$) taken by the state-of-the-art design

Figure 16 shows the Percentage of Clock Cycles Saved (PCCS) for $\mathbf{w_n}$ (last stage) computation by using Simplex FICA for 4–12 dimensions for different values of frame-length, with a fixed number of iterations ($i = 2$) that would be needed by the state-of-the-art $\mathbf{w_n}$ computation. For example, considering a frame-length of 1024 samples and $i = 2$ to computing $\mathbf{w_n}$, it can be observed that the PCCS obtained from Fig. 16 and for $L = 1024$, $n = 6$, $N_C = 16$ and $i = 2$ in (25) is 99.34% with respect to the number of cycles required for $\mathbf{w_n}$ computation using the conventional method. The PCCS, further increases to 99.66, 99.83 and 99.91% for the frame length of 2048, 4096 and 8192 respectively. It can be inferred from Fig. 16 that by using the proposed methodology, the time saving in terms of computation steps is very high and does not vary much on increasing the dimensions of the independent signal (98.8% for 100 dimensions, L = 8192, i = 2), hence the Simplex FICA gives good amount of PCCS for higher dimensional FICA.

Figure 17 shows the Average Percentage Clock Cycle Saving (APCCS) for w_n computation using Simplex FICA for 4D–12D with respect to different Frame Length L and the number of iterations needed for w_n computations. The APCCS for 4D–12D Simplex FICA for $L = 4096$, $i = 2$ is 99.783% and further increases to 99.855 and 99.891% for $L = 4096$, $i = 3$ and $L = 4096$, $i = 4$ respectively. It is observed from the Fig. 17 that APCCS increases with the Frame Length and also increases as the number of iterations i needed for w_n computation increases.

Table 3 Resource utilization on FPGA by codesign methodology based string matching system

Resources	Utilized	Available
LUT memory	182	17,400
LUT	3318	53,200
Block RAM	32.5	140
Flip-flop	4662	106,400
BUFG	1	32

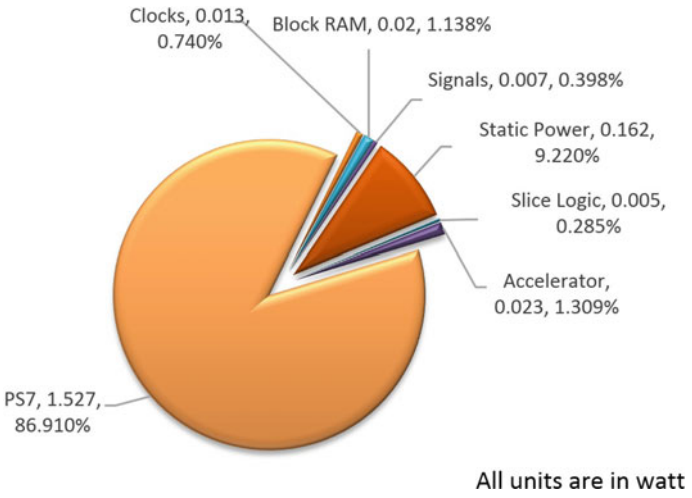

Fig. 18 Power consumption of the codesign methodology based string matching system

5.2 Analysis of Codesign Based Accelerated String Matching

5.2.1 Resource Utilization

The post-implementation results showing resources utilized by the system of Fig. 9 including the hardware accelerator are presented in Table 3. From the resources available on FPGA 3318 LUT (6.24%), 4662 FF (4.38%) and 32.50 BRAM (23.21%) are consumed by the system and total on-chip power consumption of the whole system is 1.734 W. The Vivado power analysis is used to estimate the power consumption of the system and is presented in Fig. 18. Approximately 86–88% of power is consumed by the processing system (ARM processor). The hardware accelerator in the system consumes 0.023 W which is a very small value in comparison with CPU or GPU based string matching systems.

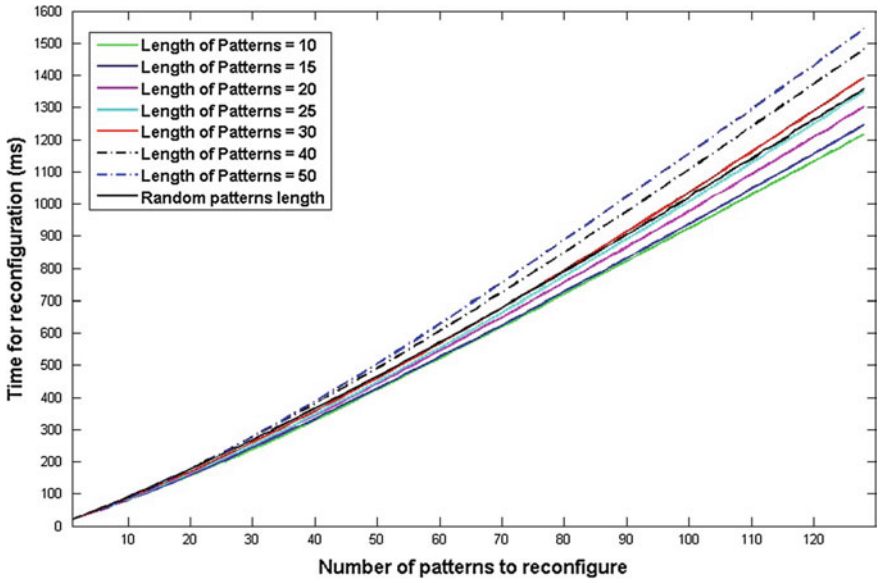

Fig. 19 Time required to reconfigure the string matching system with patterns. Dependency of reconfiguration time on the number of patterns is plotted for varying length of patterns

5.2.2 Performance on Reconfiguration Time

In applications where patterns are changed with respect to time, the system needs to be configured with the new patterns. In the system designed using the codesign methodology, an AC FSM is created and the core is reconfigured with new data of FSM memory tables. To examine the system's use for real-time reconfiguration, the effect of the number of patterns and their size on reconfiguration time of the AC Core is studied. Here different patterns of varying total sizes are considered and the reconfiguration time of the AC core obtained from a system implemented on Zedboard is plotted against the number of patterns in Fig. 19. These results are obtained for a fabric clock of 100 MHz. From the figure, it is evident that there exists a linear relation between reconfiguration time and the number of patterns; the reconfiguration time of the AC core increases linearly with the number of patterns. It is observed that the mean reconfiguration time is about a few hundreds of milliseconds value and thus the codesign methodology is worth employing in applications that demand real-time or on-field reconfiguration in string matching. This work is the first of its kind where the time required for reconfiguration of a hardware-assisted string matching system for bioinformatics applications is reported in the literature.

5.2.3 Performance Evaluation of the System in Terms of Search Time

To test the system for protein identification, UniProt proteomics data [87] is used. To demonstrate on-field reconfiguration, data of five different organisms are considered. A system that can search 32 patterns is designed using the codesign methodology. In the experiments, in each database, different sets of proteins are chosen randomly, and the databases are searched for the peptides obtained from the digestion of these proteins. PeptideMass [88], an online tool for enzymatic cleavage of proteins, is used to digest the selected proteins. The peptides obtained are stored in different patterns files with their corresponding identifiers as file names. These peptides are patterns for the string matching operation and are searched in the proteome databases stored on the SDHC memory card. The improvement of the system design using the hardware-software codesign based methodology over software-only Aho-Corasick string matching algorithm running on a workstation is tested. The workstation is running on Windows 7 operating system on Intel Xeon E5-2650 v2 CPU @ 2.60 GHz with 8 GB RAM. A similar software-only version of the ACA is also implemented using the ARM processor available on the Zynq XC7Z020 FPGA of the Avnet Zedboard. This version running on the Zedboard demonstrates a microprocessor or microcontroller tailored embedded system solution for string matching. In the system implementation using the codesign methodology, a clock of 100 MHz is used for running the hardware accelerator, and this facilitates a constant throughput of 800 Mbps for the system. The results obtained are shown in Table 4. Due to space limitation, only a few sets of results are given in the table. These results are obtained after calculating the mean values for multiple test cases in every database. On an average, there is a 4 times improvement in search time by the hardware-software codesign methodology over software-only version running on the workstation and 23 times improvement over the software running on the ARM processor on Zedboard. While calculating the gain in speed, the time required for multiple reconfigurations and also the time required for multiple searching of the same database is added to the search time. If only the time required for searching a single batch in the database is considered, then the improvement over speed is 13 and 70 times for software running on the workstation and ARM respectively.

5.2.4 String Matching in Large Proteomic Databases

To examine the practical applicability of the codesign methodology, a protein database comprised of 10 different primate animals is constructed [87]. Each database has a different number of proteins, and the total number of proteins in the concatenated database is 297,293. The total size of the constructed database is 153 MB and it has 159,654,352 amino acids. Randomly selected proteins are digested using the PeptideMass tool [88]. Figure 20 summarizes the results obtained for the large protein database. Only a few test cases are presented in the table due to space limitation. Next, to study the effect of the number of patterns and their length while searching for large databases, a set of simulated patterns is created. The number of patterns in

Table 4 Features of patterns and search time obtained using the system

Type of Dbase	#patterns[1]	#bytes[2]	Max (l)[3]	Avg (l)[4]	σ[5]	S/W (PC) ms	S/W (ARM) ms	Codesign ms
Dbase1	31.6	397.4	43.4	12.834	9.244	1511.3	9339	418.120
Dbase2	33.2	496.7	50.6	16.144	11.044	1590.1	9826	504.472
Dbase3	58.2	708.5	44.5	12.339	8.295	1912.7	10552	751.447
Dbase4	35.4	525.9	53.6	16.586	13.064	1872.7	10977	526.662
Dbase5	32.7	430.9	35.6	12.692	8.145	3341.2	18341	673.161

∗Dbase = database, S/W = Software Dbase1 = 13786.526, Dbase2 = 14954.893, Dbase3 = 14545.275, Dbase4 = 16944.043, Dbase5 = 32272.287 (all values in kB) [1]number of patterns, [2]total number of bytes in all patterns, [3]maximum length pattern, [4]average length of pattern, [5]standard deviation

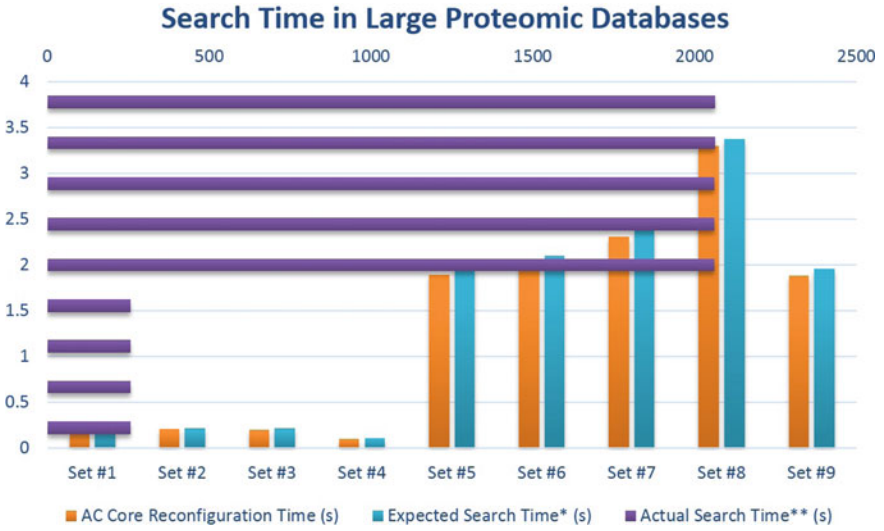

Fig. 20 Search time for string matching in large proteomic databases

each test case is 256 while their length is varied from 16, 32, 64 and 128. Finally, a test case comprising of 256 patterns of random lengths is also considered. For each case, multiple datasets are used for running the system designed using the codesign methodology. The results obtained are also presented in Fig. 20. In each case, only the mean values of the results obtained for multiple datasets are presented in the table. From the results, it is evident that the codesign methodology is applicable for searching large sized databases within a reasonable time interval.

Table 5 Comparison of codesign methodology with similar method

Comparison metric	Lei et al. [89]	Codesign
Speedup versus CPU	2X	4X
Speedup versus ARM	5X	23X
Total power (W)	1.368	1.734
Hardware accelerator power (mW)	60	23
Host PC requirement	Yes	No
Type of pattern searching	Single	Multiple

Table 6 Comparison of codesign methodology with software methods

Pattern length	Faro and Lecroq [90]		Codesign		Speed gain
	Time	Time/pattern	Time	Time/pattern	
256	1210	3.025	43.921	0.17157	17.63
128	1550	3.875	43.722	0.17079	22.69
64	1520	3.8	42.676	0.1667	22.8
32	1560	3.9	42.385	0.16557	23.55
16	1910	4.775	42.269	0.16511	28.92
8	2590	6.475	42.427	0.16573	39.07
4	2320	5.8	42.253	0.16505	35.14

5.2.5 Cross Examination with Similar Approaches

The performance of the codesign methodology with similar work reported in the literature [89, 90] is discussed as follows. Lei et al. proposed a KMP algorithm based accelerator for string matching, and Avnet Zedboard was used for the implementation [89]. As the actual time for searching is not available in the literature, the speedup is normalized for comparing speed improvement. The comparison is presented in Table 5. The codesign based methodology is 4X faster in comparison with software running on CPU while Lei et al. are 2X faster and in comparison with ARM version running on Zedboard, the codesign methodology is 23X faster while the method of Lei et al. is 5X faster. In brief, the codesign methodology is 2X–4X faster than Lei et al. Except for total power, the codesign methodology outperforms Lei et al. in all metrics since the former has higher power consumption as the processing system (PS7) consumes more power than the PS in Lei et al.

Faro et al. discussed an extensive survey of exact string matching algorithms [90]. In this article, experimental results obtained by running various algorithms implemented in C program is presented. Here, a 1.66 GHz PC with Intel Core2 processor and 2GB RAM is used for experimentation. A protein sequence of 3,295,751 length is taken from Protein Corpus for the experimental purpose (http://data-compression.info/Corpora/ProteinCorpus/). The same database is used for string matching operation using the codesign methodology. Patterns of varying lengths of 4, 8, 16, 32,

64, 128 and 256 are considered. The results are tabulated in Table 6. Faro et al. considered 400 patterns. Due to limited BRAM resources on the FPGA, 256 patterns are only considered. The search time for varying lengths of patterns and search time per pattern are examined for the database. The best time for every algorithm implemented in C program is reported by Faro et al. given in the table. On average the codesign methodology is 27 times faster than the algorithms surveyed by Faro et al. in [90]. Here, all the time units are in second. Time/Pattern indicates the mean time taken to search for one pattern in the database.

6 Conclusion

The advancements in high-throughput proteomics and bioinformatics technologies have facilitated the use of proteomic studies for disease diagnosis, disease-tailored therapeutic targets, and personalized therapy. Mass spectrometry plays a vital role in proteomics. Protein identification using mass spectrometry involves a huge amount of data processing and database searching. The computational demands posed by real-time proteomic analysis are difficult to meet. So, there is a need for accelerated solutions in the field of mass spectrometry data analysis using Independent Component analysis and string matching techniques for database searching. In this chapter, we have discussed different accelerated methodologies in the field of proteomics. Hardware accelerated, algorithmic-architectural methodologies for FICA namely Hybrid FICA and Simplex FICA and the real-time reconfigurable accelerated techniques for string matching using hardware-software codesign are discussed in detail. It is evident from the discussion that these hardware accelerated methodologies hold a promising future in the field of proteomics including domains like protein identification, biomarker discovery for disease detection, gene-sequence analysis, DNA sequencing, and Genomics.

References

1. Garret, R.H., Grisham, C.M.: Biochemistry. Cengage Learning (2013)
2. Ebbing, D., Gammon, S.D.: General Chemistry. Cengage Learning (2010)
3. Abhai, K., Verma, A., Mishra, V.N., Singh, S.: Proteomics based identification of differential plasma proteins and changes in white matter integrity as markers in early detection of mild cognitive impaired subjects at high risk of alzheimer's disease. Neurosci. Lett. **676**, 71–77 (2018)
4. Pinker, K., Chin, J., Melsaether, A.N., Morris, E.A., Moy, L.: Precision medicine and radiogenomics in breast cancer: new approaches toward diagnosis and treatment. Radiology **287**(3), 732–747 (2018)
5. Buchberger, A.R., DeLaney, K., Johnson, J., Li, L.: Mass spectrometry imaging: a review of emerging advancements and future insights. Anal. Chem. **90**(1), 240–265 (2017)
6. Bischoff, R., Luider, T.M.: Methodological advances in the discovery of protein and peptide disease markers. J. Chromatogr. B **803**(1), 27–40 (2004)

7. Boschetti, E., D'Amato, A., Candiano, G., Righetti, P.G.: Protein biomarkers for early detection of diseases: the decisive contribution of combinatorial peptide ligand libraries. J. proteomics **188**, 1–14 (2018)
8. Clarke, W., Zhang, Z., Chan, D.W.: The application of clinical proteomics to cancer and other diseases. Clin. Chem. Lab. Med. **41**(12), 1562–1570 (2003)
9. Sallam, R.M.: Proteomics in cancer biomarkers discovery: challenges and applications. Dis. markers **2015** (2015)
10. Wu, L., Qu, X.: Cancer biomarker detection: recent achievements and challenges. Chem. Soc. Rev. **44**(10), 2963–2997 (2015)
11. Petricoin, E.F., Zoon, K.C., Kohn, E.C., Barrett, J.C., Liotta, L.A.: Clinical proteomics: translating benchside promise into bedside reality. Nat. Rev. Drug Discov. **1**(9), 683 (2002)
12. Bloss, C.S., Jeste, D.V., Schork, N.J.: Genomics for disease treatment and prevention. Psychiatric Clin. **34**(1), 147–166 (2011)
13. Aebersold, R.M.M.: Mass spectrometry-based proteomics. Nature **422**, 198–207 (2003)
14. Henzel, W.J., et al.: Protein identification: the origins of peptide mass fingerprinting. J. Am. Soc. Mass Spectrom. **14**(9), 931–942 (2003)
15. Bogdán, I.A., et al.: High-performance hardware implementation of a parallel database search engine for real-time peptide mass fingerprinting. Bioinformatics **24**(13), 1498–1502 (2008)
16. Gras, R., et al.: Improving protein identification from peptide mass fingerprinting through a parameterized multi-level scoring algorithm and an optimized peak detection. Electrophoresis **20**, 3535–50 (1999)
17. Adam, B., et al.: Serum protein fingerprinting coupled with a pattern-matching algorithm distinguishes prostate cancer from benign prostate hyperplasia and healthy men. Cancer Res. **62**, 3609–3614 (2002)
18. Coombes, K., et al.: Improved peak detection and quantification of mass spectrometry data acquired from surface-enhanced laser desorption and ionization by denoising spectra with the undecimated discrete wavelet transformn. Proteomics **5**, 4107–17 (2005)
19. Mantini, D., et al.: LIMPIC: a computational method for the separation of protein signals from noise. BMC Bionform. **8**, 101 (2007)
20. Satten, G., et al.: Standardization and denoising algorithms for mass spectra to classify whole-organism bacterial specimens. Bioinformatics **20**(17), 3128–36 (2004)
21. Yasui, Y., et al.: An automated peak identification/calibration procedure for high-dimensional protein measures from mass spectrometers. J. Biomed. Biotechnol. **4**, 242–8 (2003)
22. Diamandis, E.: Mass spectrometry as a diagnostic and a cancer biomarker discovery tool: opportunities and potential limitations. Mol. Cell Proteomics **3**(4), 367–78 (2004)
23. Mantini, D., et al.: Independent component analysis for the extraction of reliable protein signal profiles from MALDI-TOF mass spectra. Bioinformatics **24**, 63–70 (2008)
24. Zerck, A., et al.: An iterative strategy for precursor ion selection for lc-ms/ms based shotgun proteomics. J. Proteome Res. **8**(7), 3239–3251 (2009)
25. Peace, R.J., et al.: Exact string matching for ms/ms protein identification using the cell broadband engine. CMBES Proc. **33**(1), (2018)
26. Benson, D., Cavanaugh, M., Clark, K., Karsch-Mizrachi, I., Lipman, D., Ostell, J., Sayers, E.: GenBank. Nucleic Acids Res. **45**(1) (2016)
27. Zhou, C., et al.: Speeding up tandem mass spectrometry-based database searching by longest common prefix. BMC Bioinform. **11**(1), 577 (2010)
28. Aho, A.V., Corasick, M.J.: Efficient string matching: an aid to bibliographic search. Commun. ACM **18**(6), 333–340 (1975)
29. Schadt, E.E., et al.: Computational solutions to large-scale data management and analysis. Nat. Rev. Genet. **11**(9), 647 (2010)
30. Aluru, S., Jammula, N.: A review of hardware acceleration for computational genomics. IEEE Des. Test **31**(1), 19–30 (2014)
31. Arram, J., et al.: Leveraging fpgas for accelerating short read alignment. IEEE/ACM Trans. Comput. Biol. Bioinform. (TCBB) **14**(3), 668–677 (2017)

32. Shyu, K.K., Lee, M.H., Wu, Y.T., Lee, P.L.: Implementation of pipelined fastICA on FPGA for real-time blind source separation. IEEE Trans. Neural Netw. **19**(6), 958–970 (2008)
33. Yang, C.H., Shih, Y.H., Chiueh, H.: An 81.6 μW fastica processor for epileptic seizure detection. IEEE Trans. Biomed. Circuits Syst. **9**(1), 60–71 (2015)
34. Mammone, N., Foresta, F.L., Morabito, F.C.: Automatic artifact rejection from multichannel scalp eeg by wavelet ica. IEEE Sens. J. **12**(3), 533–542 (2012)
35. Van, L.D., Wu, D.Y., Chen, C.S.: Energy-efficient fastica implementation for biomedical signal separation. IEEE Trans. Neural Netw. **22**(11), 1809–1822 (2011)
36. Bhardwaj, S, et al.: Online and automated reliable system design to remove blink and muscle artefact in eeg. In: 2015 37th Annual International Conference of the IEEE Engineering in Medicine and Biology Society (EMBC), pp. 6784–6787 (2015)
37. Naik, G.R., et al.: An ica-ebm-based semg classifier for recognizing lower limb movements in individuals with and without knee pathology. IEEE Trans. Neural Syst. Rehabil. Eng. **26**(3), 675–686 (2018)
38. Jiménez-González, A., James, C.J.: Extracting sources from noisy abdominal phonograms: a single-channel blind source separation method. Med. Biol. Eng. Comput. **47**(6), 655–664 (2009)
39. Jiménez-González, A., James, C.J.: Time-structure based reconstruction of physiological independent sources extracted from noisy abdominal phonograms. IEEE Trans. Biomed. Eng. **57**(9), 2322–2330 (2010)
40. Zou, X., et al.: Speech signal enhancement based on map algorithm in the ica space. IEEE Trans. Signal Proc. **56**(5), 1812–1820 (2008)
41. Lee, H.Y., et al.: Dnn-based feature enhancement using doa-constrained ica for robust speech recognition. IEEE Signal Proc. Lett. **23**(8), 1091–1095 (2016)
42. Hyvärinen, A.: Fast and robust fixed-point algorithms for independent component analysis. IEEE Trans. Neural Netw. **10**(3), 626–634 (1999)
43. Oja, E., Yuan, Z.: The fastica algorithm revisited: convergence analysis. IEEE Trans. Neural Netw. **17**(6), 1370–1381 (2006)
44. Gotze, J., Paul, S., Sauer, M.: An efficient Jacobi-like algorithm for parallel eigenvalue computation. IEEE Trans. Comput. **42**(9), 1058–1065 (1993)
45. Acharyya, A., et al.: Coordinate rotation based low complexity n-d fastica algorithm and architecture. IEEE Trans. Signal Proc. **59**(8), 3997–4011 (2011)
46. Hyyrö, H., et al.: On exact string matching of unique oligonucleotides. Comput. Biol. Med. **35**(2), 173–181 (2005)
47. Sahab, Z.J., et al.: Methodology and applications of disease biomarker identification in human serum. Biomark. Insights **2**, 117727190700200034 (2007)
48. Brudno, M., et al.: Fast and sensitive multiple alignment of large genomic sequences. BMC Bioinf. **4**(1), 66 (2003)
49. Michael, M., et al.: Siteblast-rapid and sensitive local alignment of genomic sequences employing motif anchors. Bioinformatics **21**(9), 2093–2094 (2004)
50. Alex, A.T., et al.: Hardware-accelerated protein identification for mass spectrometry. Rapid Commun. Mass Spectrom. Int. J. Devoted Rapid Dissem. Up-to-the-Minute Res. Mass Spectrom. **19**(6), 833–837 (2005)
51. Dandass, Y.S., et al.: Accelerating string set matching in fpga hardware for bioinformatics research. BMC Bioinf. **9**(1), 197 (2008)
52. Gudur, V.Y., Thallada, S., Deevi, A.R., Gande, V.K., Acharyya, A., Bhandari, V., Sharma, P., Khursheed, S., Naik, G.R.: Reconfigurable hardware-software codesign methodology for protein identification. In: 2016 38th Annual International Conference of the IEEE Engineering in Medicine and Biology Society (EMBC), pp. 456–2459 (2016)
53. Kim, H., Choi, K.I.: A pipelined non-deterministic finite automaton-based string matching scheme using merged state transitions in an fpga. PLoS ONE **11**(10), e0163535 (2016)
54. Maxfield, C.: The Design Warrior's Guide to FPGAs: Devices, Tools and Flows. Elsevier (2004)

55. Palnitkar S (2003) Verilog HDL: A Guide to Digital Design and Synthesis, vol. 1. Prentice Hall Professional
56. Dm, S., et al.: Human biomarker discovery and predictive models for disease progression for idiopathic pneumonia syndrome following allogeneic stem cell transplantation. Mol. Cell Proteomics **11**(6) (2012)
57. Brody, E., et al.: Life's simple measures: unlocking the proteome. J. Mol. Biol. **422**(5), 595–606 (2012)
58. Heikkinen, M., et al.: Independent component analysis to mass spectra of aluminium sulphate. World Acad. Sci. Eng. Technol. **26**, 173–177 (2007)
59. Chen, Y., Wolfgang, W., Hoehenwarter, W.: Comparative analysis of phytohormone-responsive phosphoproteins in arabidopsis thaliana using tio2-phosphopeptide enrichment and mass accuracy precursor alignment. Plant J. **63**, 1–17 (2012)
60. Bhardwaj, S., Raghuraman, S., Acharyya, A.: Coordinate rotation and vector cross product based hardware accelerator for nD FastICA. In: 2017 European Conference on Circuit Theory and Design (ECCTD), pp. 1–4 (2017)
61. Bhardwaj, S., et al.: Vector cross product and coordinate rotation based nd hybrid fastica. J. Low Power Electron. **14**(2), 351–364 (2018)
62. Hyvärinen, A., Oja, E.: A fast fixed-point algorithm for independent component analysis. Neural Comput. **9**(7), 1483–1492 (1997)
63. Bravo, I., Mazo, M., Lazaro, J.L., Jimenez, P., Gardel, A., Marron, M.: Novel hw architecture based on fpgas oriented to solve the eigen problem. IEEE Trans. Very Large Scale Integr. (VLSI) Syst. **16**(12), 1722–1725 (2008)
64. Volder, J.E.: The cordic trigonometric computing technique. IRE Trans. Electron. Comput. EC-**8**(3), 330–334 (1959)
65. Walther, J.S.: A unified algorithm for elementary functions. In: Spring Joint Computer Conference, pp. 18–20 (1971)
66. Adapa, B., Biswas, D., Bhardwaj, S., Raghuraman, S., Acharyya, A., Maharatna, K.: Coordinate rotation-based low complexity k-means clustering architecture. IEEE Trans. Very Large Scale Integr. (VLSI) Syst. **25**(4), 1568–1572 (2017)
67. Aggarwal, S., Meher, P.K., Khare, K.: Concept, design, and implementation of reconfigurable cordic. IEEE Trans. Very Large Scale Integr. (VLSI) Syst. **24**(4), 1588–1592
68. Bhardwaj, S., Bhagyaraja, A., Shashank, R., Jadhav, P., Biswas, D., Acharyya, A., Naik, G.R.: Low complexity single channel ica architecture design methodology for pervasive healthcare applications. In: 2016 IEEE International Workshop on Signal Processing Systems (SiPS). IEEE, pp. 39–44 (2016)
69. Shaw, R.: Vector cross products in n dimensions. Int. J. Math. Educ. Sci. Technol. **18**, 803–816 (1987)
70. Dittmer, A.: Cross product identities in arbitrary dimension. Am. Math. Mon. **101**, 887–891 (1994)
71. Bhardwaj, S., Raghuraman, S., Acharyya, A.: Simplex FastICA: an accelerated and low complex architecture design methodology for nD FastICA. IEEE Trans. Very Large Scale Integr. (VLSI) Syst. (2019)
72. Bhardwaj, S., Raghuraman, S., Acharyya, A.: Low complexity hardware accelerator for nD FastICA based on coordinate rotation. In: 2017 IEEE International Workshop on Signal Processing Systems (SiPS), pp. 1–6 (2017)
73. Acharyya, A., Maharatna, K., Al-Hashimi, B.M.: Algorithm and architecture for n-d vector cross-product computation. IEEE Trans. Signal Process. **59**(2), 812–826 (2011)
74. Sung, T., Hu, Y., Yu, H.: Doubly pipelined cordic array for digital signal processing algorithms. In: ICASSP '86. IEEE International Conference on Acoustics, Speech, and Signal Processing, vol. 11, pp. 1169–1172 (1986)
75. Rao, C.S., et al.: String matching problems with parallel approaches an evaluation for the most recent studies. Glob. J. Comput. Sci. Technol. (2013)
76. Schaumont, P.R.: The nature of hardware and software. In: A Practical Introduction to Hardware/Software Codesign, pp. 3–30. Springer (2013)

77. Teich, J.: Hardware/software codesign: the past, the present, and predicting the future. Proc. IEEE **100** (Special Centennial Issue), 1411–1430 (2012)
78. Santarini, M.: Zynq-7000 epp sets stage for new era of innovations. Xcell J. **75**, 8–13 (2011)
79. Dorta, T., Jiménez, J., Martín, J., Bidarte, U., Astarloa, A.: Reconfigurable multiprocessor systems: a review. Int. J. Reconfigurable Comput. **2010** (2010)
80. Tong, J.G., et al.: Soft-core processors for embedded systems. In: 2006 ICM'06 International Conference on Microelectronics. IEEE, pp. 170–173 (2006)
81. Senhadji-Navarro, R., et al.: Performance evaluation of RAM-based implementation of finite state machines in fpgas. In: 2012 19th IEEE International Conference on Electronics, Circuits and Systems (ICECS), pp. 225–228. IEEE (2012)
82. Gudur, V.Y., Acharyya, A.: Accelerated reconfigurable string matching using hardware-software codesign for computational bioinformatics applications. In: 2017 European Conference on Circuit Theory and Design (ECCTD), pp. 1–4 (2017)
83. Gudur, V.Y., Acharyya, A.: Hardware-software codesign based accelerated and reconfigurable methodology for string matching in computational bioinformatics applications. IEEE/ACM Trans. Comput. Biol. Bioinf. 1–1 (2019)
84. Xilinx, Inc.: Zynq-7000 all programmable SoC: embedded design tutorial. In: A Hands-On Guide Effective Embedded System Design UG1165 (v20173) (2017)
85. Gävert, H., et al.: The fastica package for Matlab (2017). https://research.ics.aalto.fi/ica/fastica/
86. Goldberger, A.L., Amaral, L.A.N., Glass, L., Hausdorff, J.M., Ivanov, P.C., Mark, R.G., Mietus, J.E., Moody, G.B., Peng, C.K., Eugene Stanley, H.: Physiobank, physiotoolkit, and physionet. Circulation **101**(23), e215–e220 (2000)
87. Bateman, A., et al.: Uniprot: a hub for protein information. Nucleic Acids Res. **43**(D1), D204–D212 (2015)
88. Gasteiger, E., et al.: Protein identification and analysis tools on the expasy server. In: The Proteomics Protocols Handbook, pp. 571–607. Springer (2005)
89. Lei, S., et al.: Scadis: a scalable accelerator for data-intensive string set matching on fpgas. In: Trustcom/BigDataSE/I SPA, 2016 IEEE, pp. 1190–1197. IEEE (2016)
90. Faro, S., Lecroq, T.: The exact online string matching problem: a review of the most recent results. ACM Comput. Surv. (CSUR) **45**(2), 13 (2013)